Tsunami Science Four Years after the 2004 Indian Ocean Tsunami

Part II: Observation and Data Analysis

Edited by
Phil R. Cummins
Laura S. L. Kong
Kenji Satake

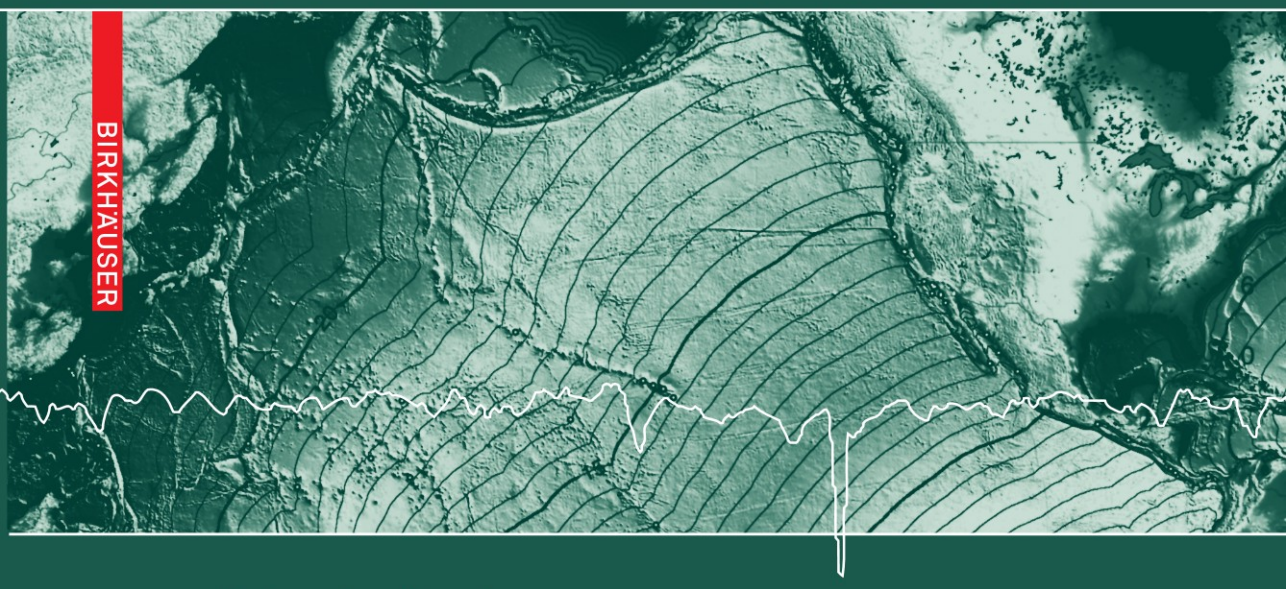

pageoph topical volumes

BIRKHÄUSER

Tsunami Science Four Years after the 2004 Indian Ocean Tsunami

Part II: Observation and Data Analysis

Edited by
Phil R. Cummins
Laura S. L. Kong
Kenji Satake

Birkhäuser
Basel · Boston · Berlin

Reprint from Pure and Applied Geophysics
(PAGEOPH), Volume 166 (2009) No. 1/2

Phil R. Cummins
Geoscience Australia
P.O. Box 378
Canberra, ACT 2601
Australia
Email: phil.cummins@ga.gov.au

Kenji Satake
Earthquake Research Institute
University of Tokyo
1-1-1 Yayoi
Bunkyo-ku
Tokyo 113-0032
Japan
Email: satake@eri.u-tokyo.ac.jp

Laura S. L. Kong
UNESCO Intergovernmental Oceanographic
Commission (IOC)
International Tsunami Information Centre
737 Bishop Street
Suite 2200
Honolulu, HI, 96813
USA
Email: l.kong@unesco.org

Library of Congress Control Number: 2009920437

Bibliographic information published by Die Deutsche Bibliothek:
Die Deutsche Bibliothek lists this publication in the Deutsche Nationalbibliografie; detailed bibliographic data is available in the Internet at <http://dnb.ddb.de>

ISBN 978-3-0346-0063-7 Birkhäuser Verlag AG, Basel · Boston · Berlin

ISBN 978-3-0346-0063-7 e-ISBN 978-3-0346-0064-4

9 8 7 6 5 4 3 2 1 www.birkhauser.ch

Contents

Pure appl. geophys. 166 (2009) 1–7
0033–4553/09/010001–7
DOI 10.1007/s00024-009-0442-0

Pure and Applied Geophysics

Introduction to ''Tsunami Science Four Years After the 2004 Indian Ocean Tsunami, Part II: Observation and Data Analysis''

PHIL R. CUMMINS,[1] LAURA S. L. KONG,[2] and KENJI SATAKE[3]

Abstract—In this introduction we briefly summarize the fourteen contributions to Part II of this special issue on *Tsunami Science Four Years After the 2004 Indian Ocean Tsunami*. These papers are representative of the new tsunami science being conducted since the occurrence of that tragic event. Most of these were presented at the session: Tsunami Generation and Hazard, of the International Union of Geodesy and Geophysics XXIV General Assembly held at Perugia, Italy, in July of 2007. That session included over one hundred presentations on a wide range of topics in tsunami research. The papers grouped into Part II, and introduced here, cover field observations of recent tsunami's, modern studies of historical events, coastal sea-level observations and case studies in tsunami data analysis.

Key words: Tsunami, tide gauge, sea level, waveform inversion, seiche, harbor resonance, numerical modeling, post-tsunami survey, tsunami warning system, runup.

1. Introduction

During the years following the 2004 Sumatra-Andaman Earthquake and subsequent Indian Ocean Tsunami (IOT), the world experienced a remarkable series of great earthquakes. The 2004 event marked the beginning of a series of earthquakes off Sumatra that included three of the ten largest earthquakes recorded since 1900 (http://earthquake.usgs.gov). During the period 2004–2007, nine earthquakes of magnitude 8 or greater occurred in the Indian and Pacific Oceans; all of which generated tsunami's, of which six were large enough to cause damage. These events coincided with a period of rapid growth in tsunami science spurred by the IOT disaster, including an expansion in earthquake and tsunami observation platforms, as well as dramatic improvements in technology and field techniques. Many observational studies of these and other events were presented in the session: Tsunami Generation and Hazard, at the International Union of Geodesy and Geophysics XXIV General Assembly in Perugia, Italy, held in July of 2007. Over

[1] Geoscience Australia, GPO Box 378, Canberra, ACT 2601, Australia. E-mail: Phil.Cummins@ga.gov.au
[2] UNESCO IOC International Tsunami Information Centre, 737 Bishop St., Ste. 2200, Honolulu, Hawaii 96813, U.S.A, E-mail: l.kong@unesco.org.
[3] Earthquake Research Institute, University of Tokyo, 1-1-1 Yayoi, Bunkyo-ku, Tokyo 113-0032, Japan E-mail: satake@eri.u-tokyo.ac.jp

one hundred presentations were made at this session, spanning topics ranging from paleo-tsunami research, to nonlinear shallow-water theory, to tsunami hazard and risk assessment. A selection of this work is published in detail in the 28 papers of the special issue of Pure and Applied Geophysics.

In this introductory paper, we briefly discuss the papers in this second part of *Tsunami Science Four Years after the 2004 Indian Ocean Tsunami*. In Section 2 we discuss field observations of recent tsunamis, while Section 3 describes some modern studies of historical events. Section 4 discusses tide gauge observations and Section 5 data analysis case studies.

2. Field Observations of Recent Tsunamis

Each damaging tsunami resulting from the series of great tsunamigenic earthquakes that occurred in 2004–2007 was followed by one or more post-tsunami surveys, and reports on three of these surveys appear in this volume. Careful observations of actual tsunami impacts, such as those presented in these reports, are invaluable for understanding tsunami runup and inundation, validating numerical tsunami models, and for interpreting geological signatures of paleo-tsunamis. The studies described below demonstrate how post-tsunami field observations can be used to infer detailed characteristics of the causative tsunami, to determine what factors influence inundation and runup, and to inform tsunami warning procedures.

LAVIGNE *et al.* (2009) provided a comprehensive summary of three months of tsunami field surveys from Banda Aceh and Lhok Nga, Indonesia in the aftermath of the 2004 Indian Ocean tsunami. Runup, wave heights, flow depths and directions, event chronologies and building damage patterns, inundation maps, high-resolution digital elevation models were collected and compiled. They reported that approximately 10 separate waves affected the region, and that the largest runups measured about 35 m with a maximum of 51 m; the highest value measured in human history from a seismically-generated tsunami. The open-source database is being made available to the community under the cooperative French-Indonesian TSUNARISQUE program to assist in better calibrating numerical models.

MACINNES *et al.* (2009) reported the results of their post-tsunami field survey of the M_w 8.3 Kuril Earthquake, which occurred on 15 November 2006, in the middle of Kuril Islands. Fortunately, they visited the islands for a paleo-tsunami survey in the summer of 2006, three months before the earthquake, hence they could compare visual observations, photographs and measurements of topographic profiles taken before and after the tsunami. While the November 2006 earthquake was followed by the January 2007 earthquake, the tsunami from the latter was smaller than that from the former, hence the authors attributed the geological traces of tsunamis to the 2006 earthquake. They found that the tsunami heights strongly depended on the local topography, and averaged about 10 m with a maximum of more than 20 m. Wherever sand was available, it was brought inland and deposited with landward thinning and fining features. Similar tsunami deposits from previous earthquakes were also found. They also described significant coastal

erosion features, such as scours, soil stripping, rock plucking or cliff retreat, at places where the runup heights were more than 10 m.

The effects of the 2006 Kuril Earthquake were also experienced in the far field. DENGLER *et al*. (2009) reported on the impact of this event in Crescent City, California, where later-arriving maximum waves and strong currents in excess of 10 knots over an 8-hour period caused an estimated US $9.2 million of damage to harbor docks despite its arrival at low tide. Crescent City is known to be historically vulnerable to tsunamis because of its coastal and undersea morphology. As a result of the 2006 tsunami, and to advise coastal officials that local conditions can cause wave amplification and strong currents, the West Coast/Alaska Tsunami Warning Center redefined its Advisory to caution that coastal threats may still persist even though significant widespread inundation was not expected for all regions. The authors also emphasized the important role of awareness as being a key for tsunami safety, especially when only modest tsunamis are expected.

3. Modern Studies of Historical Events

Several papers in this volume address the need to understand historical events in order to correctly infer what implications they may have for tsunami hazard. Historical events are most often studied by combining field observations of the type described above, with numerical or laboratory modeling, which can elucidate their source mechanisms. As demonstrated in the papers described below, an accurate understanding of the source mechanisms of historical tsunami events is important for assessing the potential for the occurrence of similar events.

SULEIMANI *et al*. (2009) used a viscous slide model coupled with shallow water equations to successfully model landslides and the ensuing local tsunami waves in Resurrection Bay, a glacial fjord in south-central Alaska, after the M_w 9.2 1964 Prince William Sound earthquake. The numerical results, in good agreement with eyewitness reports and other observational data, showed that three underwater slope failures were the major contributors to the tsunami that attacked Seward, Alaska less than five minutes after the earthquake. Their modelling approach was shown to be a useful tool for estimating landslide tsunami hazard, and their work demonstrated the need to consider these hazards in Alaska fjords where glacial sediments are accumulating at high rates on steep underwater slopes.

FRITZ *et al*. (2009) summarized two- and three-dimensional physical laboratory experiments that used a pneumatic landslide tsunami generator to model the 1958 Lituya Bay landslide tsunami, resulting in the highest wave runup (524 m) in recorded history. State-of-the-art measurement techniques were used to measure and photograph the landslide-water impact and wave generation. The two-dimensional velocity vector field showed the impact to be divided into two stages: (a) Impact and penetration with flow separation, cavity formation, and wave generation, and (b) air cavity collapse with landslide run-out and debris entrainment. The results were compared with other predictive relationships for amplitude and height since no actual tsunami heights are

available. Because this landslide-generated tsunami exhibited strong energy directivity, a three-dimensional physical model was constructed, and the surface velocities measured for future validation and benchmarking, using detailed bathymetry in a three-dimensional numerical simulation.

YELLES-CHAOUCHE *et al.* (2009) investigated the tsunamis generated from the 1856 Djidjelli earthquakes. Historical seismic intensity and tsunami wave information, combined with seismicity over the past 30 years and bathymetric and seismic reflection lines collected in 2005, were used to characterize the seismotectonics of the region and to infer the source rupture of the main earthquake and tsunami source. The numerical model results showed that much of the eastern Algerian coast and Balearic Islands were affected, with a maximum wave height of 1.5 m near the harbor of Djidjelli. This event, together with the 2003 Bourmerdes tsunami, demonstrate that the Algerian margin hosts several active tsunamigenic faults that could cause damage to the western Mediterranean and Algerian coasts.

HIRATA *et al.* (2009) reviewed multiple occurrences of tsunamigenic earthquakes along the southern Kuril subduction megathrust; one of the few areas in the world where one can test the contention that earthquake rupture occurs along characteristic segments. Tsunami data, both historic (tide gauge, field measurements, and eyewitness observations) and prehistoric (tsunami deposits), are used to provide information on rupture extent. The authors' interpretation of past studies indicates that there is substantial variability of rupture from event to event, suggesting that the idea that earthquakes repeatedly rupture characteristic segments is an oversimplification.

4. Coastal Sea-level Gauge Observations of Tsunamis

Sea-level records from coastal tide gauge stations provide some of the most detailed information available on tsunami source signatures and tsunami interaction with shallow bathymetry. They therefore have great potential to improve our understanding of potential coastal impacts of future tsunami's. They are also a critical source of information for tsunami warning systems to confirm generation of a tsunami (though data from DART (Deep-ocean Assessment and Reporting of Tsunamis) buoys are also being used for this purpose). For these reasons, understanding the quality of data from coastal tide gauges and what influences the signals recorded on them is of great importance in both progressing tsunami science and supporting tsunami mitigation. Four papers in this special issue dealt with sea-level data recorded by coastal gauges, STEPHENSON and RABINOVICH (2009), NAMEGAYA *et al.* (2009), PATTIARATCHI and WIJERATNE (2009), and ABE (2009).

STEPHENSON and RABINOVICH (2009) compiled tsunami instrumental data recorded on the Pacific Coast of Canada in 1994–2007. During these 15 years, 16 tsunamis were recorded. Eleven of these were from distant sources around the Pacific Ocean and the 2004 Indian Ocean tsunami. Three were from local earthquakes in Canada and a regional event in California, and two were of meteorological origin. Through their analysis, they

found that the background noise level was very high at Langara point, the northernmost station of British Columbia and hence an important location for a tsunami warning system. The station was therefore moved to a more protected location.

NAMEGAYA *et al*. (2009) presented results of analyses of tide gauge response characteristics and their influence on tsunami measurements. Following on from a study by SATAKE *et al*. (1988), in which tide gauge response characteristics were measured for tide gauge stations in northeast Japan, the authors made similar measurements for tide gauge stations located on the Japan Sea coast. The paper presented a thorough investigation of tide gauge response and corrections for these stations, showing that there was a wide variety of behavior between tide gauges. The results have the potential to facilitate analyses of tsunamis in the Sea of Japan, particularly the tsunami caused by the 2007 Niigataken Chuetsu-oki earthquake.

PATTIARATCHI and WIJERATNE (2009) presented summaries of sea-level records from three Sri Lanka and eleven Western Australia stations that recorded Indian Ocean tsunamis between 2004 and 2007. In comparing the station records, they showed that although the relative magnitude of the tsunami's varied due to the differences in the tsunami source, tsunami behavior at each station was similar and was affected by local and regional topography. Sea-level records from stations on the western side of Sri Lanka clearly showed reflections from the Maldives that arrived 2–3 hours after the first tsunami wave. Similarly, reflections from the Mascarene Ridge and/or Madagascar were observed about 15 hours after the first wave in records in western Australia. Tsunami waves also excited oscillations, or seiches, at a local resonance frequency that is related to the fundamental period of the offshore shelf.

ABE (2009) discussed the relation between resonant frequencies of Japanese ports and dominant periods of recent tsunamis (in 1983 and 1993) in the Japan Sea. The author measured sea level at 55 Japanese ports in comparatively calm conditions using a pressure gauge, and estimated the natural periods of harbor resonances (seiches) from the maximum spectral amplitudes. These were compared with similar analyses applied to coastal tide gauge recordings of the 1993 Hokkaido Nansei-oki and the 1983 Nihonkai Chubu-oki tsunamis. The author was able to conclude that natural oscillations were excited during the tsunamis. These new data on natural periods are an important contribution to the understanding of tsunami hazard in the bays along the Japan Sea coast.

5. Data Analysis Case Studies

The heightened tsunami activity during the period 2004–2007 contributed substantially to the pool of observational data on tsunami's, and this has spurred the development of new data analysis techniques, and increased the number of available case studies against which existing techniques could be benchmarked. The studies described below detail how this has led to improved understanding of the effects of source and bathymetry on tsunami waveforms and travel times.

BABA *et al.* (2009) investigated the degree to which finite fault inversions of seismic data for earthquake rupture patterns can be used to predict far-field tsunamis. They based their case study on the M_w 8.3 Kuril subduction zone earthquake of 15 November, 2006, which was the first teletsunami to be widely recorded by bottom pressure recorders deployed in the northern Pacific Ocean. Since these observations are not subject to the sensitivity to shallow bathymetry that introduces considerable uncertainty into coastal tide gauge measurements, any discrepancy between observed and predicted tsunami waveforms could be confidently ascribed to the source model. BABA *et al.* (2009) found that the source model obtained from seismic data, especially when seismic surface wave data are used, could be used to predict the tsunami waveforms with sufficiently high precision that they could be used in a joint inversion to better constrain earthquake source properties such as rupture velocity. The potential for use of such seismic models in a tsunami warning system to rapidly forecast teletsunami waveforms is discussed.

HÉBERT *et al.* (2009) compared several methods for characterizing the earthquake source of the M_w 8.0 2007 Peru earthquake, and then used them to model the tsunami in the far field in Nuku Hiva, Marquesas Islands, French Polynesia. A quick moment tensor inversion method (Preliminary Determination of Focal Mechanism, PDFM), available about 30 minutes after the earthquake, using seismic surface waves, gave a tsunami source that predicted far-field wave heights that were in good agreement over the first 90 minutes of tsunami wave arrivals. In contrast, the tsunami source from seismic body-wave inversion, while providing details on fault slip distribution and magnitude, produced far-field tsunami waves that were too small, thus confirming that tsunami waves are substantially more influenced by the earthquake's lower frequency components. The authors concluded that the PDFM method, complemented by inversions of the DART tsunami data, showed promise as an efficient, fast inversion method that can produce a realistic source permitting more accurate far-field wave forecasts to be calculated and used in tsunami warning applications.

WESSEL (2009) compared tsunami travel times reported in the literature with times predicted using the standard Huygens method. Over 1500 records from 127 earthquakes around the Pacific Ocean were compared. He first found large outliers in reported travel times; aside from obvious clerical errors, these outliers may be attributed to first arrivals that were missed because of their small amplitude, or to incomplete bathymetry data. Robust statistical analysis indicates that the median difference between data and predictions was less than 1 min, with an absolute deviation of 33 min. Fine bathymetry data with 2 min gridding yielded better results than a coarser 5 min grid.

Acknowledgments

Most of the papers included in this volume were presented in the tsunami session at the 2007 IUGG meeting held in Perugia, Italy. We thank all the participants who made that session such a success. We also thank the reviewers of each paper for their time and efforts, and Renata Dmowska and the editorial staff at Springer for their patience and support.

REFERENCES

ABE, K. (2009), *Excitation of resonant modes along the Japanese coast by the 1993 and 1983 tsunamis in the Japan Sea*, Pure Appl. Geophys. *166*(1–2), 117–130.

BABA, T., CUMMINS, P.R., THIO, H.K., and TSUSHIMA, H. (2009), *Validation and joint inversion of teleseismic waveforms for earthquake source models using deep ocean bottom pressure records: A case study of the 2006 Kuril megathrust earthquake*, Pure Appl. Geophys. *166*(1–2), 55–76.

DENGLER, L., USLU, B., BARBEROPOULOU, A., YIM, S.C., and KELLY, A. (2009), *The November 15, 2006 Kuril Islands-generated tsunami in Crescent City, California*, Pure Appl. Geophys. *166*(1–2), 37–53.

FRITZ, H.M., MOHAMMED, F., and YOO, J. (2009), *Lituya Bay landslide impact generated mega-tsunami: 50th anniversary*, Pure Appl. Geophys. *166*(1–2), 153–175.

HÉBERT, H., REYMOND, D., KRIEN, Y., VERGOZ, J., SCHINDELÉ, F., ROGER, J., LOEVENBRUCK, A. (2009), *The 15 August 2007 Peru earthquake and tsunami: Influence of the source characteristics on the tsunami heights*, Pure Appl. Geophys. *166*(1–2), 211–232.

HIRATA, K., SATAKE, K., TANIOKA, Y., and HASEGAWA, Y. (2009), *Variable tsunami sources and seismic gaps in the southernmost Kuril Trench: A review*, Pure Appl. Geophys. *166*(1–2), 77–96.

LAVIGNE, F., WASSMER, P., GOMEZ, C., BRUNSTEIN, D., GRANCHER, D., PARIS, R., VAUTIER, F., SETIAWAN, A., CAHYADI, R., GUNAWAN, T., FACHRIZAL, FLOHIC, F., and DE COSTER, B. (2009), *Reconstruction of tsunami inland Propagation on December 26, 2004 in Banda Aceh, Indonesia, through field investigations*, Pure Appl. Geophys. *166*(1–2), 259–281.

MACINNES, B.T., PINEGINA, T.K., BOURGEOIS, J., RAZHIGAEVA, N.G., KAISTRENKO, V.M., and KRAVCHUNOVSKAYA, E.M. (2009), *Field survey and geological effects of the 15 November 2006 Kuril tsunami in the middle Kuril Islands*, Pure Appl. Geophys. *166*(1–2), 9–36.

NAMEGAYA, Y., TANIOKA, Y., ABE, K., SATAKE, K., HIRATA, K., OKADA, M., and GUSMAN, A.R. (2009), *In situ measurements of tide gauge response and corrections of tsunami waveforms from the Niigataken Chuetsu-oki Earthquake in 2007*, Pure Appl. Geophys. *166*(1–2), 97–116.

PATTIARATCHI, C.B., and WIJERATNE, E.M.S. (2009), *Tide gauge observations of the 2004–2007 Indian Ocean tsunamis from Sri Lanka and western Australia*, Pure Appl. Geophys. *166*(1–2), 233–258.

SATAKE, K., OKADA, M., and Abe, K. (1988), *Tide gauge response to tsunamis: Measurements at 40 tide stations in Japan,* J. Marine Res. *46*, 557–571.

STEPHENSON, F. E. and RABINOVICH, A. B. (2009), *Tsunamis on the Pacific coast of Canada recorded in 1994–2007*, Pure Appl. Geophys. *166*(1–2), 177–210.

SULEIMANI, E., HANSEN, R., and HAEUSSLER, P. (2009), *Numerical study of tsunami generated by multiple submarine slope failures in Resurrection Bay, Alaska, during the Mw 9.2 1964 earthquake*, Pure Appl. Geophys. *166*(1–2), 131–152.

YELLES-CHAOUCHE, A.K., ROGER, J., DEVERCHERE, J., BRACENE, R., DOMZIG, A., HEBERT, H., and KHERROUBI, A. (2009), *The 1856 tsunami of Djidjelli (eastern Algeria): Seismotectonics, modelling and hazard implications for the Algerian coast*, Pure Appl. Geophys. *166*(1–2), 283–300.

WESSEL, P. (2009), *Analysis of observed and predicted tsunami travel times for the Pacific and Indian Oceans*, Pure Appl. Geophys. *166*(1–2), 301–324.

Pure appl. geophys. 166 (2009) 9–36
0033–4553/09/010009–28
DOI 10.1007/s00024-008-0428-3

Pure and Applied Geophysics

Field Survey and Geological Effects of the 15 November 2006 Kuril Tsunami in the Middle Kuril Islands

Breanyn T. MacInnes,[1] Tatiana K. Pinegina,[2] Joanne Bourgeois,[1]
Nadezhda G. Razhigaeva,[3] Victor M. Kaistrenko,[4] and
Ekaterina A. Kravchunovskaya[2]

Abstract—The near-field expression of the tsunami produced by the 15 November 2006 Kuril earthquake (M_w 8.1–8.4) in the middle Kuril Islands, Russia, including runup of up to 20 m, remained unknown until we conducted a post-tsunami survey in the summer of 2007. Because the earthquake occurred between summer field expeditions in 2006 and 2007, we have observations, topographic profiles, and photographs from three months before and nine months after the tsunami. We thoroughly surveyed portions of the islands of Simushir and Matua, and also did surveys on parts of Ketoi, Yankicha, Ryponkicha, and Rasshua. Tsunami runup in the near-field of the middle Kuril Islands, over a distance of about 200 km, averaged 10 m over 130 locations surveyed and was typically between 5 and 15 m. Local topography strongly affected inundation and somewhat affected runup. Higher runup generally occurred along steep, protruding headlands, whereas longer inundation distances occurred on lower, flatter coastal plains. Sediment transport was ubiquitous where sediment was available—deposit grain size was typically sand, but ranged from mud to large boulders. Wherever there were sandy beaches, a more or less continuous sand sheet was present on the coastal plain. Erosion was extensive, often more extensive than deposition in both space and volume, especially in areas with runup of more than 10 m. The tsunami eroded the beach landward, stripped vegetation, created scours and trim lines, cut through ridges, and plucked rocks out of the coastal plain.

Key words: Tsunami, Kuril Islands, coastal geomorphology, tsunami deposit, tsunami erosion.

1. Introduction

A pair of tsunamigenic great earthquakes occurred seaward of the middle Kuril Islands in November 2006 and January 2007—one of the largest earthquake doublets on record (Ammon *et al.*, 2008). The 2006 earthquake occurred along the plate boundary,

[1] Department of Earth and Space Sciences, University of Washington, Seattle, WA 98195, USA. E-mail: macinneb@u.washington.edu

[2] Institute of Volcanology and Seismology, Far Eastern Branch Russian Academy of Sciences, 683006 Petropavlovsk-Kamchatskiy, Russia.

[3] Pacific Institute of Geography, Far Eastern Branch Russian Academy of Sciences, 690041 Vladivostok, Russia.

[4] Institute of Marine Geology and Geophysics, Far Eastern Branch Russian Academy of Sciences, 693022 Yuzhno-Sakhalinsk, Russia.

whereas the 2007 earthquake was produced by normal faulting on the outer rise, similar to the interpreted source of the 1994 Shikotan earthquake (HARADA and ISHIBASHI, 2007, and earlier references).

Everywhere the 2006 and 2007 Kuril tsunamis were measured, the 2006 tsunami was larger (National Geophysical Data Center, NGDC database). Moreover, the 1994 Shikotan tsunami was an average of 1.5 times larger than the 2007 tsunami on trans-Pacific tide gages (NGDC database). The records in the database, as well as arguments we make herein, lead us to interpret our surveyed tsunami effects in the middle Kurils as the product of the 2006 tsunami.

The 15 November 2006 middle Kurils tsunami was widely reported in the media to be small, a report based principally on its early expression in northern Japan, where later tsunami waves had tide-gage water heights[1] reaching 0.6 m. Tide-gage heights in Hawaii ranged up to 0.76 m, and on the far side of the Pacific, in Crescent City, California, a 0.88-m-high wave (1.76 m peak to trough) generated $700,000-$1 million worth of damage (KELLY, 2006) in the harbor. Tide-gage records from the southern Kurils include maximum water heights of about 0.8 m (Sakhalin Tsunami Warning Center), however, there are no stations in the middle Kurils. Local runup for this tsunami remained unknown until our surveys in summer of 2007 (preliminary results reported in LEVIN *et al.,* 2008). No one lives in this remote area and logistics for visiting the islands are complex and expensive.

Two expeditions sponsored by the Institute of Marine Geology and Geophysics, Yuzhno-Sakhalinsk, Russia (IMGG) and the NSF-funded Kuril Biocomplexity Project (KBP) worked together in the middle Kurils in July and August 2007, to survey inundation, runup and geomorphic effects of the 2006 tsunami. Inundation and runup are standard descriptions of tsunami size and report the tsunami's maximum inland distance and the elevation of that position, respectively, for any given stretch of coastline (FARRERAS, 2000). Surveys of geomorphic impacts of tsunamis are less standardized and can include field descriptions or measurements of erosion, deposits, and other tsunami effects. In 2007, a total of four working groups documented tsunami effects at 130 locations in 11 bays, over a distance of about 200 km, along the rupture zone of the 15 November 2006 and 13 January 2007 earthquakes. Several members of the 2007 expeditions, including most of the authors, had surveyed parts of these islands in the summer of 2006, under the aegis of the KBP. Our prior surveying provided a remarkable opportunity to make direct measurements and comparisons, at the same time of year, of shorelines before and after the tsunamis.

2. 15 November 2006 and 13 January 2007 Earthquakes and Tsunamis

The two middle Kuril great earthquakes of 2006 and 2007 filled a seismic gap (Fig. 1). Previously, a large earthquake had not occurred in the middle Kurils Islands in at

[1] "Water height" is the term used in the NGDC catalogue for vertical deviation from zero, which is approximately equal to amplitude, which in turn is half the trough-to-peak wave height.

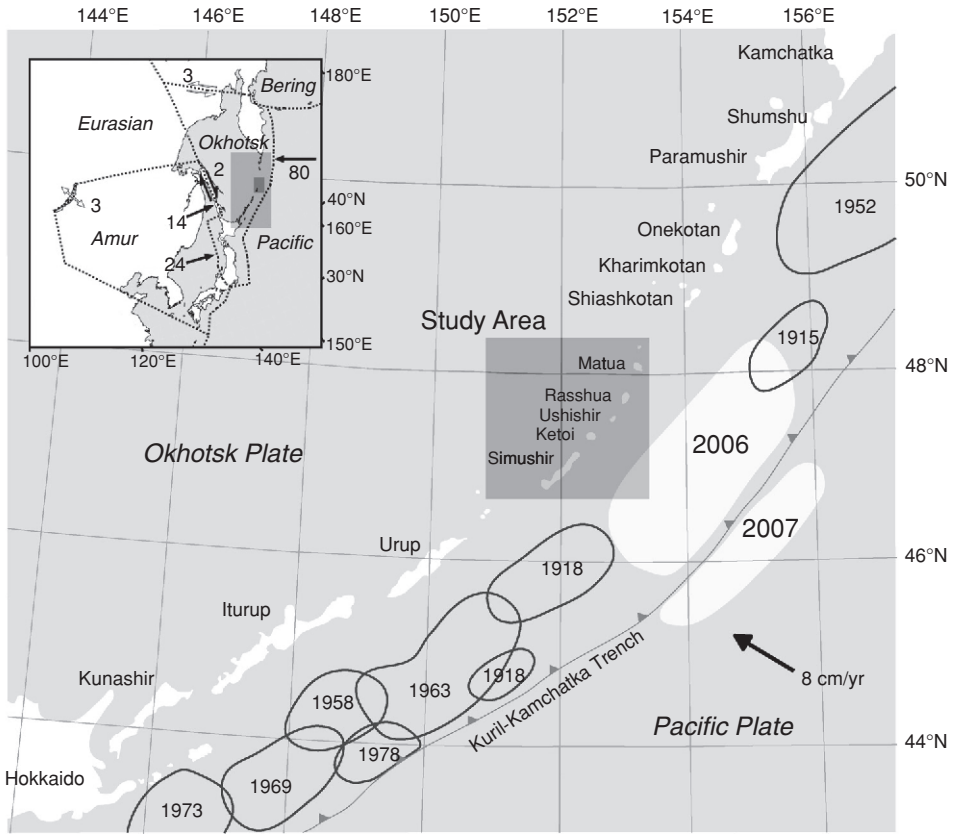

Figure 1
Tectonic setting of the Kuril Islands. Includes all historical tsunamigenic earthquakes with known source regions. Inset in the upper left: Plate tectonic map of the region including plate motions, after APEL *et al.* (2006). Measured plate motions are in mm/yr.

least 150 years—a previous event believed to have occurred along the middle Kurils (LAVEROV *et al.*, 2006), was an earthquake and tsunami experienced by Captain Snow off Simushir Island in 1780 (SNOW, 1910). The region had been interpreted as a seismic gap by Fedotov as early as 1965. However, there had been recent speculation as to whether this segment was slipping quietly (e.g., KUZIN *et al.*, 2001; SONG and SIMONS, 2003). Our paleotsunami field studies in the summers of 2006 and 2007 agree with the seismic-gap hypothesis (see below), as also confirmed by the recent earthquake doublet.

The 2006 earthquake released more total energy and lasted longer, whereas the 2007 earthquake had a higher peak energy release (AMMON *et al.*, 2008). The 15 November 2006 earthquake commenced at 11:14 UTC, according to the U.S. Geological Survey, at a depth of $\sim$30 km on the subduction zone. The epicenter for 2006 was off Simushir Island, and propagation proceeded northward (JI, 2006; VALLÉE, 2006; YAGI, 2006). The

13 January 2007 earthquake, which commenced at 04:23 UTC at a crustal depth of ~10 km, was a normal-faulting, outer-rise event on the Pacific Plate, directly east of the Kuril-Kamchatka trench (JI, 2007; VALLÉE, 2007; YAGI, 2007). According to the U.S. Geological Survey, the epicenter was approximately 100 km ESE of the 2006 event. Global CMT solutions record the 2006 event as a M_W 8.3 and the 2007 event as a M_W 8.1, although analysis of tsunami waveform inversions by FUJII and SATAKE (2008) suggest that M_W 8.1 and M_W 7.9 for 2006 and 2007, respectively, are more appropriate. AMMON *et al.* (2008) calculate M_W 8.4 for 2006 and M_W 8.1 for 2007 based on source radiation characteristics.

Both the 2006 and 2007 earthquakes produced measurable tsunamis around the Pacific Rim, although 2007 was smaller at every reported location. Observations from 113 locations for the 2006 event, and 35 locations for 2007, are archived in the National Geophysical Data Center (NGDC), Global Tsunami Database, and a few non-overlapping points in the Novosibirsk Tsunami Laboratory (NTL) Historical Tsunami Database.[2] Reported 2006 tide-gage water heights range from < 0.1 m at several locations to values of 0.4 to 0.9 m at some stations in the southern Kurils, Japan, New Zealand, Chile, the Marquesas, Hawaii, the West Coast of the U.S., and the Aleutians. Of the records of the 2007 tsunami, the maximum reported tide-gage water heights are about 0.4 m at Malokurilsk (RABINOVICH *et al.*, 2008) and Chichijima Island, ~0.3 m at Shemya in the Aleutians, and ~0.25 m at Port Orford and Crescent City, U.S.A. The closest measurements of the 2007 Kuril tsunami on a directed path of the earthquake, in Hawaii, are an average of 3.5 times less than those of the 2006 Kuril tsunami.

3. Neo-Tectonic and Geomorphic Setting

The Kuril Islands are a volcanic arc associated with subduction of the Pacific Plate under the Okhotsk Plate (Cook *et al.*, 1986) along the Kuril-Kamchatka trench. Subducting crust is ~100 million years old, and the convergence rate is 8 cm/yr (DEMETS *et al.*, 1990), excluding Okhotsk Plate motion (APEL *et al.*, 2006). The Kuril Island chain includes more than 25 islands with roundly 30 active volcanoes and many prominent volcanic edifices (GORSHKOV, 1970; MELEKESTSEV, 1980).

The islands surveyed in both 2006 and 2007, Simushir to Matua islands (Fig. 2), are morphologically different than islands to the north and south. The middle Kurils span a ~20° bend in the arc and are smaller and more widely spaced than the northern and southern islands. Primarily, the middle islands are single or multiple volcanic edifices, with the most common coastline being steep sea cliffs. Study sites fall into two broad geomorphologic categories—bouldery pocket beaches or broad embayments with gravelly to sandy shorelines (Figs. 2 and 3). The coastal plain in most field locations

[2] Note that the NGDC database reports water heights above zero, whereas the Novosibirsk database reports peak-to-trough wave heights. We are using only tide-gage records for this comparison.

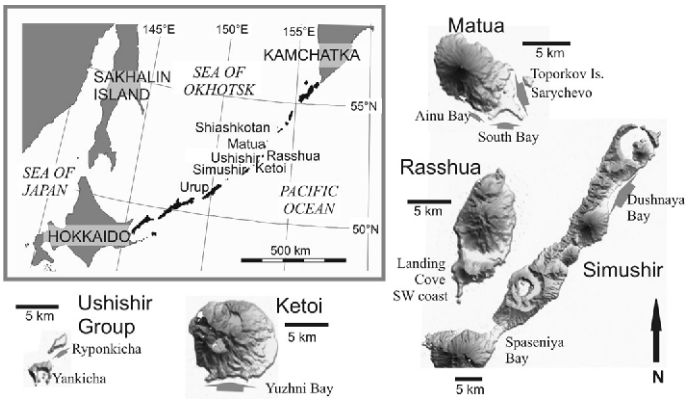

Figure 2
Overview of the basic morphology of the islands surveyed in 2007, including site names from Table 1. The scale bar for each island is 5 km.

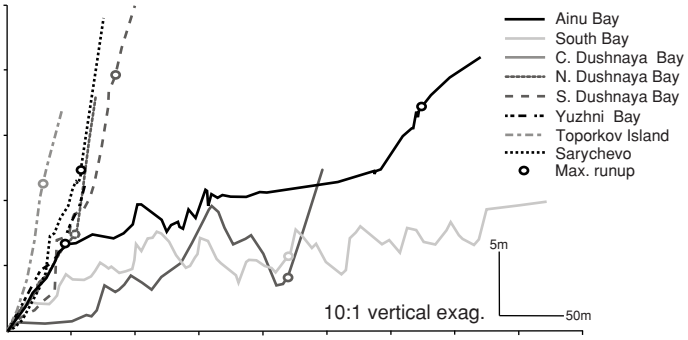

Figure 3
Example profiles that illustrate differences among short, steep coastlines (dashed lines) and broad coastal plains (solid lines). C (Central) Dushnaya Bay is an example of a profile in Table 1, where maximum runup elevation is less than the maximum elevation on the profile.

is backed by a cliff or steep slope. The largest embayments have up to 500 m of sandy coastal plain before this cliff, although more than half of the profiles measured were along rocky beaches with shoreline widths averaging around 50 m (Fig. 3).

4. Tsunami Survey Methods

Up to four teams operated simultaneously to measure topographic profiles, to record maximum runup and inundation, to collect tsunami-deposit samples and descriptions, and to make observations of erosion. Most sites visited in summer 2007 had been observed by team members previously, which helped us distinguish tsunami erosion and deposition

from other processes. Newly visited localities in 2007 include Spaseniya Bay on Simushir Island and Toporkov Island off Matua Island (Fig. 2).

Except where noted in Table 1, we made all measurements with a tripod, level and rod, with an individual measurement error of 0.3 cm vertically and 30 cm horizontally. This error does not accumulate in a given segment (until the level is moved), so that cumulative vertical error is less than 30 cm and horizontal error generally less than a few meters; each measurement was checked for error in the field. In a few cases, we used a hand level and tape, with error of 2 cm vertically per measurement and about 5% error horizontally, the latter due to irregularities on the ground. Also, where slopes were steep, we converted taped measurements trigonometrically from on-the-ground to horizontal. Whenever possible, we also checked horizontal measurements with distances calculated from GPS points (Table 1).

We measured profiles to or from local sea level and in most cases corrected for tide at the time of measurement from local tide tables. Measurements were not corrected for tide at the time of the earthquake, which began about mid-tide on the flood phase, in a low-amplitude tidal cycle (less than 0.5 m), based on tide tables and nearby tide gages; storm waves were active at the same time. Tidal range is typically 0.5–1.5 meters, thus even without corrections, error in the elevation of mean sea level is slight relative to runup.

At nearly every location surveyed, we could find evidence for an inland limit of tsunami penetration. Our primary criteria for defining runup were lines of floatable debris—typically driftwood, cut wood, plastic bottles and floats, glass floats, and styrofoam. In regions with short grasses and flowers, debris lines were obvious, and often one measurement accurately reflected runup. Where floated debris was obscured by this year's growing vegetation so that a debris line was not clear, we bushwacked, traced debris through the vegetation, and measured multiple points along 10–50 lateral meters. Both individual measurements and averages are reported in Table 1 and summarized in Table 2 and Figure 4. Single pieces of debris, such as one plastic bottle, were not considered adequate, as these bottles can blow in the wind. We observed some movement of debris material by animals, such as foxes, but it was rare. With the exception of southern Urup (briefly surveyed) and a small abandoned camp on Matua, we have no evidence that people had visited these islands since our visit in summer 2006. In a few cases, we measured heights of draped grass and seaweed on shrubs, but such flow-depth indicators were rare. Corroborative evidence of runup, not used independently, included the limit of consistently seaward-oriented stems of tall grasses and flowers, the limit of sand and gravel deposits on top of turf and dead vegetation, and the elevation of fresh erosion of turf.

5. 2006 or 2007?

We assumed our maximum runup and inundation limits were due to the 2006, not 2007, tsunami partly based on survey and catalogue data. First, the 2007 tsunami was measured to be smaller at *every* catalogued location around the Pacific. At the closest

Table 1

Table of runup and inundation of localities surveyed for the 2006 Kuril tsunami

Locality name	Latitude of profile at shore*	Longitude of profile at shore*	Runup (m)[&]	# of runup readings	Standard deviation	Max. elevation on profile seaward of inundation (m)	Inundation range[%]	Method[#]
Spaseniya Bay-36	46.84520	151.89542	**1.3**	1	-	3.9	**172**-212	HL
Spaseniya Bay-37	46.83173	151.87659	**3.9**	1	-	4.4	**141**–180	HL
Spaseniya Bay-39	46.83411	151.87962	**2.3**	1	-	3.9	**127**–146	HL
Spaseniya Bay-78	46.85281	151.90750	**4.4**	1	-	no	**115**–140	HL
Spaseniya Bay-79	46.85087	151.90409	**6.2**	1	-	no	**59**–80	HL
Spaseniya Bay-77b	46.84178	151.89000	5.7	1	-	no	**54**–109	HL
Spaseniya Bay-82	46.83668	151.88249	7.2	1	-	no	**51**–75	HL
Dushnaya Bay-24	*47.07085*	*152.18777*	8.7	1	-	no	77	HL
Dushnaya Bay-54	*47.04769*	*152.16070*	11.7	1	-	no	44	HL
Dushnaya Bay-57	*47.04684*	*152.15963*	9.3	1	-	no	115–136	HL
Dushnaya Bay-100	47.07971	152.21016	**13.3**	1	-	no	68	TL,HLT
Dushnaya Bay-101	47.07880	152.20884	***8.8***	5	0.14	no	**39**–44	TL
Dushnaya Bay-102	47.07835	152.20566	***7.7***	8	0.85	no	**50**–51	TL
Dushnaya Bay-103	47.07818	152.20214	***10.8***	10	0.48	no	**46**–49	TL
Dushnaya Bay-104	47.07809	152.19888	***13.0***	7	0.52	no	52–**52**	TL
Dushnaya Bay-105	47.07754	152.19528	***15.5***	10	0.39	no	93–**102**	TL
Dushnaya Bay-106	47.07537	152.19476	***13.0***	10	1.32	no	**66**–70	TL
Dushnaya Bay-107	47.07312	152.19315	***15.3***	12	1.90	no	**74**–85	TL
Dushnaya Bay-108	47.07124	152.19088	***11.9***	9	0.44	no	**57**–61	TL
Dushnaya Bay-109	47.07039	152.18792	***9.1***	10	0.58	no	**56**–59	TL
Dushnaya Bay-1–2006	47.06971	152.18614	***10.6***	8	0.70	no	100–**102**	TL
Dushnaya Bay-110	47.06960	152.18429	***8.8***	11	0.36	no	**107**–114	TL
Dushnaya Bay-11	47.06582	152.17981	**8.2**	1	-	8.4	**109**–115	TL
Dushnaya Bay-10	47.06772	152.18230	**9.9**	1	-	no	**121**–133	TL
Dushnaya Bay-12	47.06393	152.17726	**6.9**	1	-	no	**115**–120	TL

Table 1 Continued

Locality name	Latitude of profile at shore*	Longitude of profile at shore*	Runup (m)[&]	# of runup readings	Standard deviation	Max. elevation on profile seaward of inundation (m)	Inundation range[%]	Method[#]
Dushnaya Bay-2-2006	47.06201	152.17549	**6.7**	1	-	7.7	122–**125**	TL
Dushnaya Bay-9	47.06094	152.17313	**7.3**	1	-	12.0	151–**154**	TL
Dushnaya Bay-8	47.05979	152.17162	**8.6**	1	-	11.4	118–**120**	TL
Dushnaya Bay-7	47.05807	152.16878	**6.3**	1	-	7.1	139–**139**	TL
Dushnaya Bay-6	47.05628	152.16650	**4.4**	1	-	10.1	**98**–106	TL
Dushnaya Bay-5	47.05409	152.16471	**11.3**	1	-	no	**128**–132	TL
Dushnaya Bay-3	47.04942	152.16235	**7.9**	1	-	no	123–**135**	TL
Dushnaya Bay-2	47.04530	152.15915	**12.4**	1	-	12.7	75–**92**	TL
Dushnaya Bay-1	47.04313	152.15841	**20.0**	1	-	no	**79**–83	TL
Yuzhni Bay-1a	47.29924	152.48283	***6.5***	7	0.37	no	**39**–52	HLT
Yuzhni Bay-1b	47.29868	152.48257	***6.9***	9	0.69	no	**75**	HL
Yuzhni Bay-1c	47.29834	152.48416	***6.7***	16	0.60	no	**51**–55	HLT
Yuzhni Bay-2	47.29807	152.48616	***7.4***	9	0.24	no	**54**–58	HLT
Yuzhni Bay-3	47.29640	152.49141	***6.5***	9	0.29	no	**27**–44	HLT
Yuzhni Bay-3b	47.29979	152.48218	**10.6**	1	-	no	**47**–63	HL
Yuzhni Bay-10b	47.29966	152.47368	**6.2**	1	-	no	37	HL
Yuzhni Bay-13	*47.29774*	*152.48760*	**9.2**	1	-	no	**43**–67	HL
Yuzhni Bay-10c	47.29659	152.49009	**6.7**	1	-	no	**38**–79	HL
Yuzhni Bay-59	47.30047	152.48114	**6.8**	1	-	no	**37**–67	HL
Yuzhni Bay-61	*47.30043*	*152.48006*	**6.3**	1	-	no	52	HL
Yuzhni Bay-62	47.30022	152.47934	**6.0**	1	-	no	**18**–37	HL
Yuzhni Bay-64	47.30033	152.47762	**10.4**	1	-	no	**22**–42	HL
Yuzhni Bay-67	47.30025	152.47754	**9.7**	1	-	no	34	HL
Yuzhni Bay-69	47.29968	152.47460	**7.9**	1	-	no	**35**–54	HL
Yuzhni Bay-71	*47.29966*	*152.47368*	**6.2**	1	-	no	37	HL
Yuzhni Bay-73	47.29960	152.47238	**6.8**	1	-	no	**23**–37	HL

Table 1 Continued

Locality name	Latitude of profile at shore*	Longitude of profile at shore*	Runup (m)[&]	# of runup readings	Standard deviation	Max. elevation on profile seaward of inundation (m)	Inundation range[%]	Method[#]
Yankicha-257	47.52596	152.82620	***13.5***	2	0.21	no	57–**70**	TL
Ryponkicha-238	47.53181	152.82719	***11.7***	4	0.60	no	**50**–52	TL
Ryponkicha-245	47.53244	152.82906	***11.2***	5	0.74	no	**55**–56	TL
Ryponkicha-253	47.53632	152.83617	***11.0***	5	0.72	no	**47**–50	TL
Ryponkicha-255	47.53742	152.84057	***7.4***	3	0.59	no	25–**30**	TL
Ryponkicha-249	47.53324	152.83098	***11.2***	3	0.39	no	**42**–46	TL
Ryponkicha-251	47.53508	152.83231	**12.0**	1	-	no	45–**55**	TL
Ryponkicha-285	47.53287	152.82868	**10.1**	1	-	no	**48**–60	HL
Ryponkicha-180	47.54934	152.85081	**5.7**	1	-	no	**47**–54	HL
landing cove-507	47.70630	152.96405	**9.4**	1	-	no	**53**–56	HL
SW coast-196	47.69963	152.96543	**4.2**	1	-	no	64	HL
SW coast-198	47.69893	152.96575	**5.0**	1	-	no	66	HL
Sarychevo-120	48.08416	153.26740	***12.0***	6	0.69	no	**68**–70	TL
Sarychevo-125	48.08323	153.26612	***11.8***	4	0.04	no	**103**–118	TL
Sarychevo-129	48.08123	153.26444	***10.6***	3	0.19	no	**42**–54	TL
Sarychevo-133	48.07906	153.26357	**12.5**	1	-	no	38–**44**	TL
Sarychevo-136	48.07707	153.26329	***10.7***	4	0.08	no	**34**–36	TL
Sarychevo-69	48.07510	153.26518	**12.6**	1	-	no	59–**94**	TL
Sarychevo-73	48.07340	153.26681	**18.1**	1	-	no	93–**106**	TL
Sarychevo-79	48.07098	153.26668	***19.0***	4	0.56	no	**45**–50	TL
Sarychevo-83	48.06911	153.26872	***16.8***	4	0.57	no	**35**–38	TL
Sarychevo-86	48.06642	153.26921	***15.7***	3	0.55	no	**52**–56	TL,HLT
Sarychevo-142	48.05172	153.27181	***14.3***	3	0.22	no	51–**54**	TL
Sarychevo-145	48.05310	153.26861	***12.2***	3	0.45	no	**55**–62	TL

Table 1 Continued

Locality name	Latitude of profile at shore*	Longitude of profile at shore*	Runup (m)[&]	# of runup readings	Standard deviation	Max. elevation on profile seaward of inundation (m)	Inundation range[%]	Method[#]
Sarychevo-147	48.05498	153.26675	**17.0**	1	-	no	**48**–49	TL
Sarychevo-149	48.05728	153.26618	**15.3**	1	-	no	**56**–60	TL
Sarychevo-152	48.05941	153.26706	**21.9**	1	-	no	**41**–48	TL
Sarychevo-154	48.06177	153.26918	**16.7**	1	-	no	**26**–46	TL
Sarychevo-157	48.06401	153.26918	***12.1***	3	0.70	no	69–**79**	TL
Sarychevo-170	48.04985	153.27407	**9.9**	1	-	no	**48**–55	HL
Sarychevo-167	48.04854	153.27534	**10.4**	1	-	no	**67**–71	HL
Sarychevo-166	48.04751	153.27489	**9.6**	1	-	no	56–**56**	HL
Sarychevo-165	48.04660	153.27397	**8.6**	1	-	no	**101**–122	HL
Sarychevo-164	48.04504	153.27429	**8.6**	1	-	no	**110**–124	HL
Sarychevo-162	48.04349	153.27506	**8.1**	1	-	no	109–**116**	HL
Sarychevo-161	48.04193	153.27764	**6.1**	1	-	no	**92**–108	HL
Sarychevo-160	48.04124	153.27865	**7.3**	1	-	no	**55**–56	HL
South Bay-216	48.04199	153.24922	**5.7**	1	-	7.6	**221**–223	TL
South Bay-222	48.03976	153.23971	***7.3***	2	0.65	7.0	**170**–174	TL
South Bay-224	48.04023	153.24302	**5.7**	1	-	5.9	215–**219**	TL
South Bay-228	48.04127	153.24595	**7.1**	1	-	no	**205**–233	TL
South Bay-148	48.04234	153.25296	**4.9**	1	-	9.9	**139**–174	HL
South Bay-149	48.04244	153.25585	**6.4**	1	-	8.2	**101**–134	HL
South Bay-150	48.04267	153.25930	**5.7**	1	-	6.4	**146**–176	HL
South Bay-151	48.04202	153.26372	**7.9**	1	-	8.1	**60**–95	HL
South Bay-152	48.04034	153.26773	**7.8**	1	-	no	**126**–147	HL
South Bay-153	48.03749	153.27090	**7.8**	1	-	no	**129**–254	HL
Ainu Bay-1–2006	48.04412	153.22497	**17.1**	1	-	no	**313**–327	HLT,2006
Ainu Bay-2-2006	48.04269	153.22650	***18.1***	6	0.19	no	**411**–432	TL

Table 1 Continued

Locality name	Latitude of profile at shore*	Longitude of profile at shore*	Runup (m)[&]	# of runup readings	Standard deviation	Max. elevation on profile seaward of inundation (m)	Inundation range[%]	Method[#]
Ainu Bay-145	48.04786	153.21894	**13.6**	1	-	no	**68**–121	HL
Ainu Bay-144	48.04707	153.22058	**14.0**	1	-	no	**119**–120	HL
Ainu Bay-143	48.04599	153.22315	**17.1**	1	-	no	**200**–244	HL
Ainu Bay-139	48.04537	153.22430	**18.1**	1	-	no	**288**–315	HL
Ainu Bay-130	48.04444	153.22463	**17.1**	1	-	no	**315**–356	HL
Ainu Bay-132	48.04284	153.22588	**18.3**	1	-	no	**376**–398	HL
Ainu Bay-133	48.04266	153.22644	**20.2**	1	-	no	**417**–503	HL
Ainu Bay-126	48.04154	153.22731	**20.8**	1	-	no	**315**–436	HL
Ainu Bay-142	48.03980	153.22876	**12.9**	1	-	no	**128**–164	HL
Toporkov-237	48.07637	153.28168	***10.0***	4	0.38	no	41	HLT
Toporkov-235	48.07510	153.28164	**11.3**	1	-	no	**26**–28	HLT
Toporkov-230	48.07375	153.28205	***9.9***	2	0.31	no	**27**–42	HLT
Toporkov-231	48.07213	153.28239	***9.3***	2	1.01	no	40–**40**	HLT
Toporkov-234	48.07238	153.28224	**8.0**	1	-	no	37–**42**	HLT

* *italic*- lat/long on profile

[&] **bold**- with tide correction; *italic*- average of readings

[%] regular- field measurement; **bold**- GPS distance between shore and max runup

[#] Method- TL Transit level and rod; HLT Hand level, rod and tape; HL Hand level, rod for elevation and distance; 2006 Used profile from 2006

Table 2

Average runup and inundation for each bay surveyed, differentiated by coastal geomorphology

Island	Locality name	Coastline type	Average runup (m)	Average inundation (m)
Simushir	Spaseniya Bay	coastal plain	4.86	111
Simushir	Dushnaya Bay	coastal plain	8.08	121
Simushir	Dushnaya Bay	short, steep	12.56	65
Ketoi	Yuzhni Bay	short, steep	7.50	39
Ushishir	Yankicha, Ryponkicha	short, steep	10.43	49
Rasshua	SW coast	short, steep	6.21	61
Matua	Sarychevo	coastal plain	9.23	108
Matua	Sarychevo	short, steep	13.36	57
Matua	South Bay	coastal plain	6.64	152
Matua	Ainu Bay	coastal plain	17.02	268
Matua	Toporkov	short, steep	9.84	35

locations with records, the 2007 tsunami was five times smaller than 2006 at Yuzhno-Kurilsk ($\sim$550 km to the south of our field area), and less than half as high at Malokurilsk ($\sim$500 km to the south of our field area) (refer to RABINOVICH *et al.*, 2008 for tide gage records). Furthermore, the M_w 8.1–8.3 1994 Shikotan tsunami—comparable in earthquake mechanism to 2007 and with a larger tsunami at most trans-Pacific sites—typically produced 3–8 m (max 10 m) runup in the Habomai island group, east of Kunashir Island, close to the trench, and 1–4 m (max 6 m) in the southern Kurils themselves (YEH *et al.*, 1995; KAISTRENKO, 1997; NGDC database). Average runup at sites parallel to the 1994 source is less than 5 m, whereas the average runup we surveyed parallel to the 2006 and 2007 ruptures (see below) is about 10 m.

In addition to arguments based on measured tsunami height and runup, we argue that the effects we surveyed were primarily from 2006 because local conditions on the islands were different for the two tsunamis. A Landsat image of Dushnaya Bay from 22 November 2006 shows extensive regions without snow at lower elevations. However, weather records from December 2006 and early January 2007 in Severo-Kurilsk and Yuzhno-Kurilsk (to the north and south of the field area) indicate that there would have been snow accumulation on the islands before the 2007 tsunami. Thus a frozen, snow-covered coast in January would be less susceptible to erosion and subsequent deposition, including movement of the beach debris we used to indicate runup. Tsunamis do not necessarily erode snow (particularly if ice-covered snow) during inundation (MINOURA *et al.*, 1996).

In Dushnaya Bay on Simushir Island, there was evidence along many profiles for a smaller wave postdating the largest wave to come ashore—we cannot confidently attribute this evidence to a later wave of 2006 or to 2007. For example, we observed a thin wrack line from a smaller wave ($\sim$3–5 m elevation). Also, we observed complex tsunami deposits on several profiles, where a patchy sand deposit (average maximum elevation 5 m) lay above a layer of flattened vegetation, which, in turn, covered a

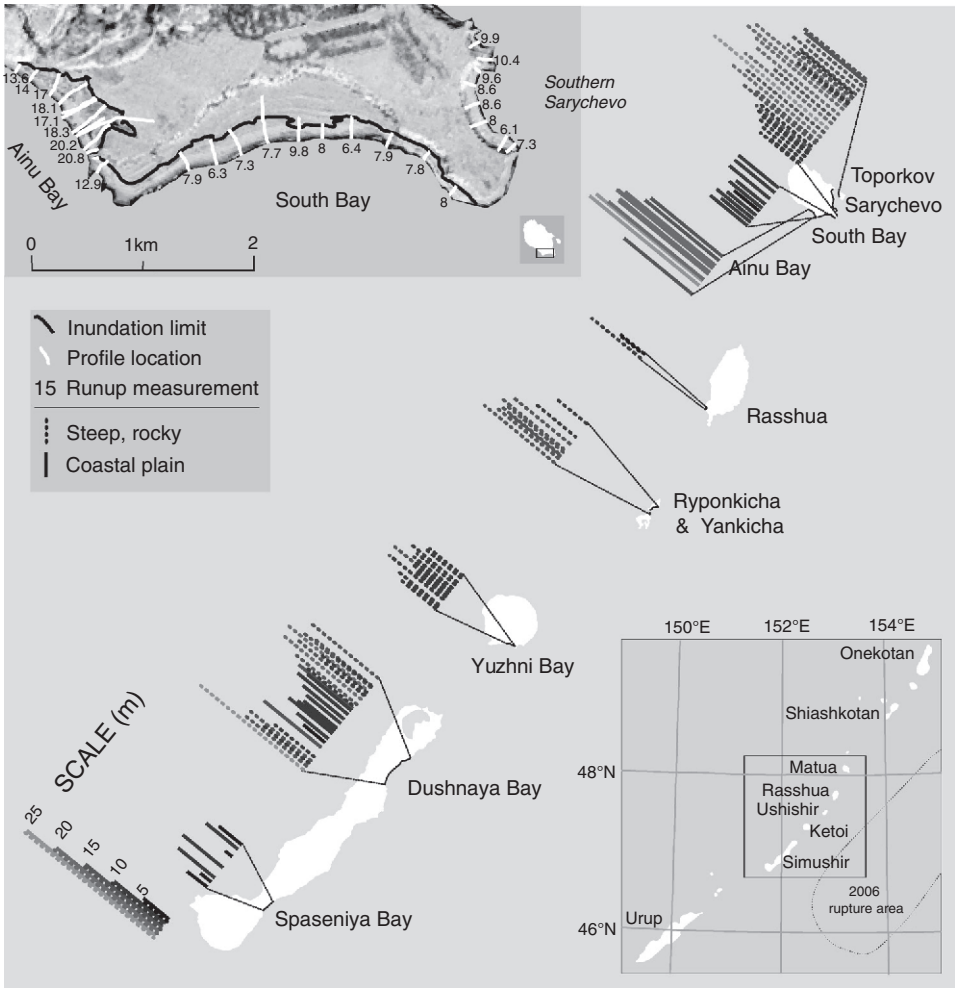

Figure 4
Summary of maximum runup of the 15 November 2006 tsunami, by location, for 130 field measurements. Values are categorized by the regional coastal geomorphology (refer to Fig. 3). Inset upper left: Detailed map of inundation and runup for southern Matua Island. Inset lower right: Location of the survey area.

continuous, coherent deposit. Such a depositional sandwich is what we expect from a second tsunami wave inundating over snow (Fig. 5), in which case these deposits would be from a smaller, 2007 tsunami.

6. Runup Observations and Inundation

Measured runup in the middle Kuril Islands (Simushir to Matua, about 200 km along strike) from the 2006 tsunami was typically 5–15 m, with a range of 2–22 m (Tables 1

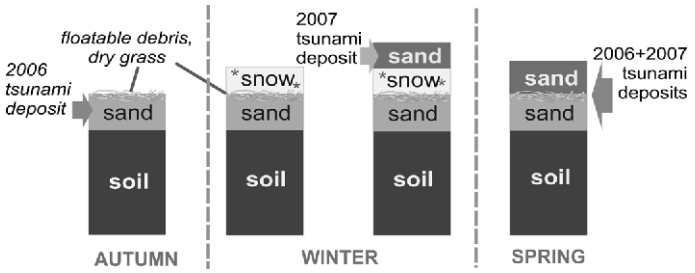

Figure 5
Schematic diagram of how the stratigraphic relationship of the 15 November 2006 and 13 January 2007 tsunami deposits appeared in the field. Snow that fell after the first tsunami would bury the 2006 deposit, floatable debris, and any vegetation still standing. The snow is not necessarily eroded in all locations by the second tsunami, and the resulting complex deposit has a thin layer of debris and vegetation in the middle.

and 2, Fig. 4), and a raw average of 10.2 m. Measured inundation varied from 20 to 500 m, with a raw average of 95 m. Average runup gives the tsunami a 3.85 on the S. Soloviev Tsunami Intensity scale (SOLOVIEV, 1972), the standard intensity scale used in the NGDC and NTL global tsunami databases:

$$I = {}^{1}/_{2} + \log_2 H_{av},$$

where H_{av} is the average height of the tsunami on the nearest coast. This scale does not take into account the distance along the shoreline of the surveyed region.

On some profiles (e.g., Central Dushnaya Bay profile in Fig. 3), seaward of maximum inundation, the tsunami over-topped beach ridges or sand dunes that were higher elevation than runup, which is by definition, elevation at maximum inundation. For these cases, Table 1 provides both runup and also maximum elevation along the profile, seaward of (maximum) inundation. Elevations along the profile do not take into account tsunami water depth, consequently the water height would have been even higher. We include the intra-profile data, in addition to runup and inundation, because they facilitate representation of the magnitude and behavior of the tsunami wave.

Variability in runup and inundation of the 2006 middle Kurils tsunami was in large part due to coastal geomorphology. Naturally, our longer inundation values are from lower, flatter coastal plains, and higher runup values generally from steep, protruding headlands (Table 2). In many of the cases we studied, the steep slope or cliff backing the coastal plain limited tsunami penetration. When a tsunami hits a reflector, such as a sea cliff, the energy not reflected back to the sea will be converted into vertical runup, increasing its height (BRIGGS *et al.*, 1996; PELINOVSKY *et al.*, 1999). Tsunami modeling will enable us to determine the degree to which coastal geomorphology, as well as bathymetry, affected tsunami runup; that work is in progress.

7. Tsunami Sediment Transport and Deposition

All affected shorelines showed evidence of erosion and deposition, and we made systematic measurements on many profiles (Table 3). Where loose sediment was available on the beach or in the nearshore, we observed deposits of sand, gravel, and cobbles on the coastal plain surface, burying turf and dead vegetation (Figs. 6B and D). Most deposits resemble sediment of the beach; more detailed analyses are forthcoming. In addition to beach sand and gravel, sediment also was derived from eroded scarps, from plucked turf and cobbles, and from artificial structures. Where the beach was composed of sediment larger than cobbles, no coherent, continuous deposit was present, although scattered boulders moved by the tsunami were common (see below). Where solid rock outcrop existed on the shore (observed on Ketoi and Matua), this rock was not noticeably affected by the tsunami.

We observed continuous tsunami sand sheets (e.g., Fig. 6D) in areas with sandy beaches, which also coincide with most low-relief profiles. As has been repeatedly seen elsewhere (c.f. SHI *et al.*, 1995; GELFENBAUM and JAFFE, 2003; BOURGEOIS, 2009), the 2006 Kurils tsunami deposits in these cases were typically thin (< 5 cm), thinning and fining landward. Over the 11 profiles where we made detailed observations, deposits were typically a few centimeters or less in thickness. Local variability in deposit thickness reflected previous topography; for example, a 0.5-cm-thick deposit locally thickened to 2–5 cm in a rodent burrow. In general, only close to the shore or in these locally low pockets did deposits exceed 5 cm in thickness.

Total volumes (average sediment thicknesses summed over distance) of sediment deposited ranged from 0.4 to 6.3 m^3/unit width (Table 3). The deposits used in these calculations were all on vegetated surfaces, with no evidence for subsequent erosion. Sediment volume is influenced by the amount of available sediment and by topographic variations controlling the velocity of the flow (GELFENBAUM and JAFFE, 2003). Profiles with less volume of sediment deposited had narrower and rockier beaches and lower runup. The largest volumes of sediment deposition came from profiles with severe beach erosion (see next section) and higher runup.

Sediment transport was not limited to sand- to cobble-sized material—across the middle Kurils, we found evidence of tsunami transport of boulders, ranging from 10's of cm to 3 m in diameter (Table 3). Moved boulders, known as *tsunami ishi* (KATO and KIMURA, 1983), were sourced from the nearshore, beach, coastal plain, and artificial structures (Fig. 6C). We easily identified tsunami *ishi* from the nearshore by recently deceased sea life on the boulders, such as attached seaweed, encrusted bryozoan communities, and kelp holdfasts. *Ishi* derived from artificial structures could generally be traced back to the dam or pier or other military structures from which they were derived. We commonly identified the source location of boulders from within the vegetated beach plain by the holes left behind (see the tsunami erosion section below for further discussion). Other than typically being clean and rounded, tsunami *ishi* that originated on the beach are associated with no identifiable characteristics so we only assume that if other

Table 3

Characteristics of onland effects of the 2006 Kuril tsunami for selected localities

Island	Locality name	Types of erosion*	Distance between erosion and max. inundation (m)	Sandy deposit noted?	Deposit volume (m^3/unit width)	Distance between deposition and max. inundation (m)	Tsunami *ishi*, minimum distance moved (m)	Evidence of smaller tsunami wave
Simushir	Dushnaya Bay-100	SB, SS	~0	yes	-	30	no	no
Simushir	Dushnaya Bay-101	SS, SC	10	yes	-	-	no	no
Simushir	Dushnaya Bay-102	SS, SC	13	yes	1.4	4	no	yes
Simushir	Dushnaya Bay-103	SS, SC	34	no	-	-	no	yes
Simushir	Dushnaya Bay-104	SB, SS, SC	10	yes	-	21	no	yes
Simushir	Dushnaya Bay-105	SB, SS, SC	14	yes	-	20	yes, 30	no
Simushir	Dushnaya Bay-106	SB, SS, SC, B	6.5	yes	-	-	yes	yes
Simushir	Dushnaya Bay-107	SB, SS, SC, P	13	no	-	-	yes	no
Simushir	Dushnaya Bay-108	SC, B, P	18	yes		10	yes	no
Simushir	Dushnaya Bay-109	SS, B, P	18	yes	0.4	13	yes, 10	no
Simushir	Dushnaya Bay-1-2006	SS, SC, B	1	yes	-	3	yes, 85	yes
Simushir	Dushnaya Bay-110	SS, SC, B	40	yes	-	-	no	yes
Simushir	Dushnaya Bay-12	SS, B	57	yes	0.9	3	no	yes
Simushir	Dushnaya Bay-2-2006	B	70	yes	1.2	2	no	yes
Simushir	Dushnaya Bay-9	SS, B	-	yes	3.0	0	no	no
Simushir	Dushnaya Bay-7	SS, B	-	yes	1.7	0	no	yes
Simushir	Dushnaya Bay-6	-	-	yes	1.2	0	no	yes
Simushir	Dushnaya Bay-2	SS, B	15	yes	0.9	3	no	no
Ketoi	Yuzhni Bay-1a	-	-	no	-	-	no	yes
Ketoi	Yuzhni Bay-1b	SB, SS	7.5	no	-	-	no	no
Ketoi	Yuzhni Bay-1c	SB, SS, SC	3.6	no	-	-	yes	no
Ketoi	Yuzhni Bay-2	SS	8	no	-	-	no	no
Ketoi	Yuzhni Bay-3	SC	0	no	-	-	no	no
Ushishir	Yankicha-257	SC	15	yes	-	9	no	no
Ushishir	Ryponkicha-238	SC, B	12	no	-	-	no	no
Ushishir	Ryponkicha-245	B	29	no	-	-	yes	no
Ushishir	Ryponkicha-253	SB	8	no	-	-	no	no
Ushishir	Ryponkicha-255	SS SC, SB	6	no	-	-	no	no
Ushishir	Ryponkicha-249	B	10	no	-	-	no	no

Table 3 Continued

Island	Locality name	Types of erosion*	Distance between erosion and max. inundation (m)	Sandy deposit noted?	Deposit volume (m^3/unit width)	Distance between deposition and max. inundation (m)	Tsunami *ishi*, minimum distance moved (m)	Evidence of smaller tsunami wave
Ushishir	Ryponkicha-251	SC	13	no	-	-	no	no
Rasshua	Landing Cove-507	SC	8	no	-	-	no	no
Matua	Sarychevo-120	SS, SC, B	11	yes	-	14	no	no
Matua	Sarychevo-125	SS, SC, B, P	9	yes	1.3	9	no	no
Matua	Sarychevo-129	T, SS, SC, B	2.5	no	-	-	yes	no
Matua	Sarychevo-133	T, SS, SC	3	yes	-	-	yes, 10	no
Matua	Sarychevo-136	T, SS	2	no	-	-	no	no
Matua	Sarychevo-69	T, SS, SC, B	5	yes	-	6	yes, 5	no
Matua	Sarychevo-73	T, SC, B	13	yes	-	34	yes, 40	no
Matua	Sarychevo-79	T, SC	5	no	-	-	yes, 20	no
Matua	Sarychevo-83	T, SS, SC	4	no	-	-	no	no
Matua	Sarychevo-86	SS, SC	4	yes	-	12	yes, 15	yes
Matua	South Bay-216	SS, B	60	yes	3.4	4	no	no
Matua	Ainu Bay-1-2006	SS, SC, B	10	yes	4.8	15	yes	yes
Matua	Ainu Bay-2-2006	SS, SC, B	6	yes	6.3	10	yes, 50	yes
Matua	Toporkov-237	T, SC	11	no	-	-	no	no
Matua	Toporkov-235	T, SC, B	2	no	-	-	no	no
Matua	Toporkov-230	T, SC	-	no	-	-	no	no
Matua	Toporkov-231	T, SC	3	no	-	-	no	no
Matua	Toporkov-234	T, SS, SC	1.5	no	-	-	no	no

*Types of erosion: T trim line; SB slope-base erosion; SS soil stripping; SC scours; B beach erosion; P rock plucking

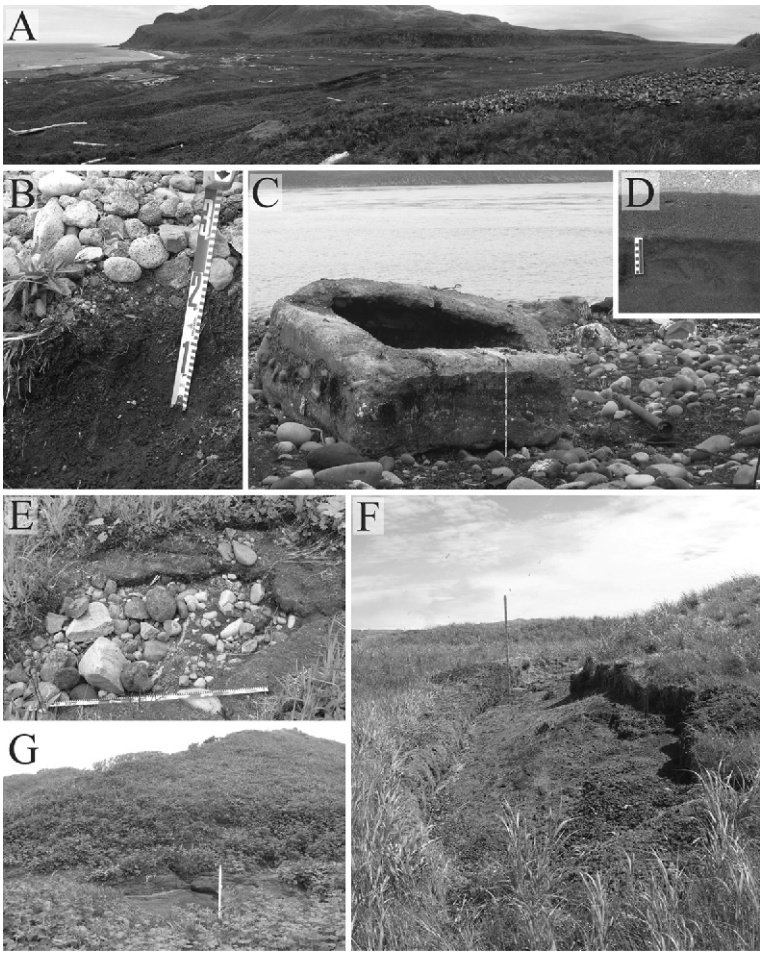

Figure 6

Deposition and erosion from the 15 November 2006 tsunami as observed in the middle Kurils. A: Ainu Bay, Matua, which experienced the maximum amount of inundation we observed (400–500 m). White flecks in the distance are large logs moved by the tsunami. B: A deposit of pebbles on top of soil and turf in Dushnaya Bay, Simushir (near profile 105). New vegetation is beginning to grow through. Measuring tape is 30 cm. C: A tsunami *ishi*, which was once an artificial structure offshore, with kelp holdfasts and bryozoan communities still attached. Measuring tape is 1 m. Sarychevo coast of Matua, profile 83. D: Continuous sand sheet from Ainu Bay, Matua, Profile 2. Here, the deposit is the thickest observed anywhere (at 20 cm thick) and is filling a drained lake bed. E: A scour pit in Dushnaya Bay, Simushir, Profile 106. Direction of flow was from right to left. Measuring tape is 1 m. F: Soil stripping in Ainu Bay, Matua, Profile 2. Turf and soil are still attached, but flipped over on the left (landward). The rod is 2 m high. G: Slope-base erosion in Dushnaya Bay, Simushir, Profile 107. The rod is 2 m high.

equivalent-sized boulders moved, the ones on the beach could have been moved. We recorded some tsunami *ishi* to have been transported at least > 85 m (Table 3), however we did not have time to conduct an exhaustive survey of all boulders transported.

8. Tsunami Erosion

Geomorphic effects of the 2006 tsunami on the landscape varied from almost unnoticeable to devastating; two of our short-term camps from the summer field season of 2006 would have been obliterated. In general, erosion is produced by local temporal or spatial increases in boundary shear stress and clearly can also be affected by bed characteristics such as grain size and cohesion. KONNO *et al.* (1961) identified three types of tsunami flow over land where erosion may occur: sheet flow, linear (or concentrated, channelized) flow, and eddy flow. Holding other factors constant (such as soil cohesion, vegetation type, etc.), sheet flow results in uniform erosion, concentrated flow in spatially variable erosion, and eddies in small-scale features. The different forms of tsunami flow are generated by topography (as in UMITSU *et al.*, 2007). Evidence is widespread for erosion from all three types of flow in the 2006 tsunami case in the middle Kuril Islands.

Far and away the two most common cases of erosion in our survey are what we call scouring and soil stripping. Documentation of scours and stripped areas are also common in tsunami literature (e.g., GELFENBAUM and JAFFE, 2003; GOFF *et al.*, 2006; KURIAN *et al.*, 2006; OKAL *et al.*, 2006), and such erosional features are typically associated with sudden changes in topography or in soil characteristics. The literature most often addresses scour associated with man-made features, such as roads, buildings, bridge pylons, etc. (e.g., GOFF *et al.*, 2006; MAHESHWARI *et al.*, 2006; MALIK *et al.*, 2006). Individual scour depressions generally form from either linear or eddy flow, but the largest scours (e.g., Fig. 7C) suggest erosional sheet flow (KONNO *et al.*, 1961). The upstream steep wall in a scour (and downstream sediment berm) form from eddies within the scour on the upstream side of the direction of flow (as in KONNO *et al.*, 1961; ALONSO *et al.*, 2002).

Visually, we identified scours in our survey by localized pits or eroded strips of coastline with a steeper wall at one end (Figs. 6E and 7C). We define a "scour" as a localized depression generated by erosion, where vegetation and topsoil are removed entirely. Scours varied in size from less than a meter in diameter, to 100's of meters long by 10's of meters wide, and had scour depths of centimeters to meters. Scours occurred in both natural and artificial landforms; those in natural settings often had sediment accumulated in the downstream end of the depression (Fig. 6E).

We identified soil stripping by removed vegetation and generally called an area stripped rather than scoured if there was not a distinct depression. In these cases, soil or sediment removal is uniform in depth and does not significantly extend below the turf zone, or in some cases, below a cinder layer near the surface (Fig. 6F). Due to its uniformity, soil stripping suggests sheet flow (c.f. KONNO *et al.*, 1961) without the development of strong eddies. Commonly in our field area, the tsunami exploited shallow networks of rodent burrows or WWII military trenches to initiate erosion and strip or "flay" the surface. In some locations, one edge of eroded turf was still attached and the upper soil layers were flipped over in the direction of flow (Fig. 6F).

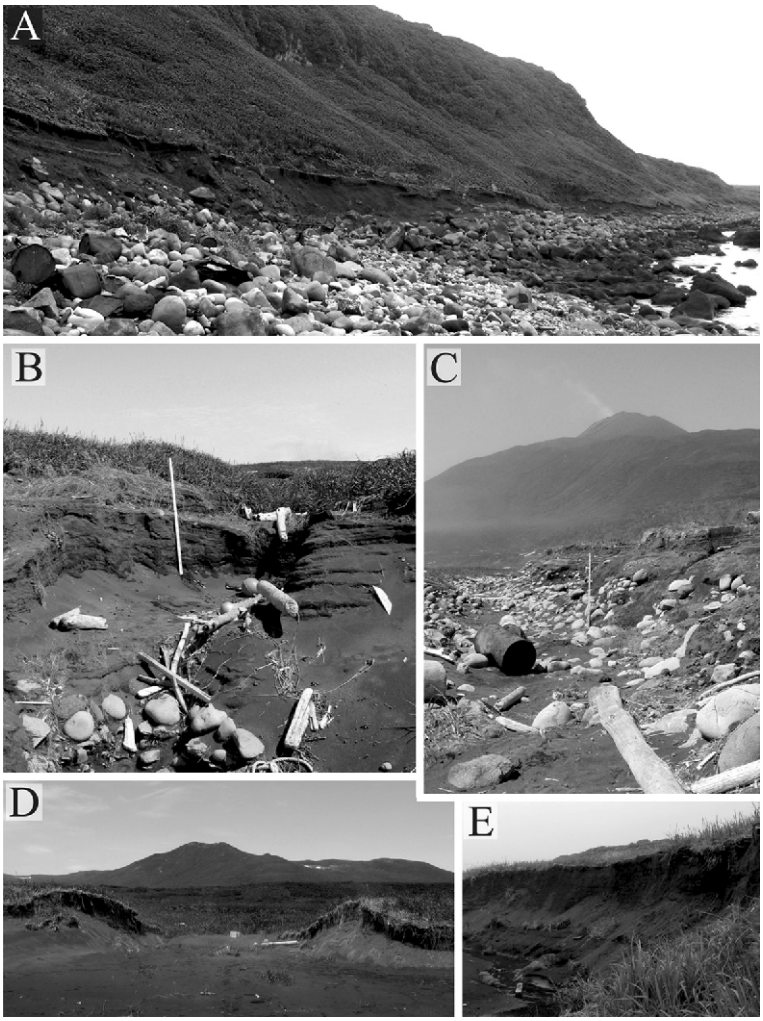

Figure 7
Examples of kinds of erosion from the 15 November 2006 tsunami as observed in the middle Kurils. A: Trim line on Matua, Sarychevo coast. B: Gullying from outflow, Ainu Bay, Matua, Profile 2. Rod is 2 m high. C: Large-scale scour that extends > 100 m laterally, in Ainu Bay, Matua, Profile 1. Rod is 2 m high. D: Breach through the first beach ridge in central Dushnaya Bay, Simushir, near Profile TKP10. Shovel in center of photo is $\sim$1.5 m high. E: *En masse* erosion of a stream channel wall in Dushnaya Bay, Simushir, near Profile TKP12. Bank height is $\sim$4 m, and the cliff was eroded back $\sim$3 m between 2006 and 2007.

The prevalent styles of erosion on middle Kurils coastlines with a narrow beach plain, where the tsunami ran up a steep slope, were trim lines and slope-base erosion. A trim line is where soil and vegetation are removed up to an approximately uniform elevation on a slope. In contrast, we define slope-base erosion as more isolated patches than trim

lines and only extending a meter or two above the change in slope. Trim lines (Fig. 7A) are visually striking and observable from a distance, and the uniformity of a trim line suggests sheet flow (c.f. KONNO *et al.*, 1961). In our survey, maximum runup and inundation were in close proximity to the location of the trim line (Table 3); the tsunami typically continued only a meter or two above and a few meters beyond the trim line. Slope-base erosion (Fig. 6G) is not as closely tied to maximum runup as trim lines are. This kind of erosion was clearly associated with sharp slope change and may have occurred during both inflow and outflow. Because slope-base erosion is selective, it suggests linear (channelized) flow, or eddy flow associated with the sharp change in slope.

Other styles of erosion we observed, plucking of rocks embedded in soil, cliff retreat of sandy back-beach edges or stream channel walls (Fig. 7E), and breaches in beach ridges (Fig. 7D), were strongly dependent on location variables. Rocks as large as 30 cm in diameter were pulled out of soil leaving distinct, coherent holes in the surface. We traced some rocks a few meters to their source hole in both the seaward and landward direction, but the tsunami also removed some boulders and cobbles entirely from land, presumably transporting them offshore. We only observed plucking in locations where the tsunami had no other source of sediment and was likely sediment starved.

Cliff retreat occurred in two forms, either *en masse*, or as scallops or gullies. *En masse*, or uniform, tsunami erosion has been previously reported along the beach edge (e.g., KURIAN *et al.*, 2006; MARAMAI and TINTI, 2007) and along a few stream channels (MARAMAI and TINTI, 2007). It is more likely to occur during inflow, when topographic effects are less important (e.g., UMITSU *et al.*, 2007). In our surveys, we identified *en masse* cliff retreat by evidence that an extended stretch of coastline eroded landward in a fairly uniform way. For example, compared to our 2006 observations, in 2007 most back-beach scarps or stream channel walls (e.g., Fig. 7E) exposed to the ocean appeared more straight and regular. We observed or measured up to > 50 m of *en masse* erosion, the largest amount occurring in Ainu Bay, Matua (MACINNES *et al.*, 2007).

Irregular scallops and gullies generally represent zones of concentrated outflow as they are produced primarily in locations where troughs intersect stream channels, or where a section of beach plain is lower then its immediate neighbors (e.g., UMITSU *et al.*, 2007). GELFENBAUM and JAFFE (2003) and UMITSU *et al.* (2007) found that incoming tsunamis flowed nearly perpendicular to the shore, but backwash returned obliquely to the shore in local topographic lows. In our survey of 2006 tsunami effects in the middle Kurils, gullies and scallops were common, especially where there was a preexisting backbeach scarp. The tsunami dug some gullies as deep as 3 m into the pre-existing beach scarp; these gullies in 2007 resembled dry waterfalls (Fig. 7B). Some of these dramatic gullies were produced or enhanced where inflow over a steep beach face was then concentrated (channelized) between two beach ridges and then outflow was focused into what we presume were pre-existing lows in the seaward-most beach ridge.

Although we are confident that most of the features we documented in our survey were due to erosion from the 15 November 2006 tsunami, the unvegetated beach is a

location of constant change, and it can be difficult to say what changes are directly related to a tsunami (or in our case, two tsunamis), especially over the course of a full year (SHEPARD *et al.*, 1950). For this reason, we paid little attention to changes on the unvegetated portion of our profiles. Besides the back-beach cliff retreat mentioned, the only other kind of beach change we could attribute to the tsunami with any amount of confidence was localized breaching through the back-beach cliff and seaward-most beach ridge. In three locations in Dushnaya Bay, we found breaches (width on the scale of meters) through the first beach ridge, at least one of which is known to have formed between 2006 and 2007 (Fig. 7D). A few older beach ridges in our field area are also breached; we tentatively suggest these breaches are preserved geomorphic change from paleotsunamis.

Where the 2006 tsunami was large, erosion extended farther inland, and commonly the inland limit of erosion exceeded that of deposition (Table 3). A direct comparison of before and after using three topographic profiles from 2006, reoccupied in 2007, shows that the tsunami removed many times more sediment than it deposited on land. Even where erosion was at a minimum, and deposits extended almost to the limit of inundation, more sediment was eroded than can be accounted for by the tsunami deposit (c.f. MACINNES *et al.*, 2007), and we presume this sediment was transported offshore.

Others have also documented beach-profile changes due to tsunami erosion. KURIAN *et al.* (2006) measured before and after (unvegetated) beach profiles in India and found some areas that experienced erosion and others that experienced deposition, but were uncertain as to what was directly from the tsunami and what was from previous or subsequent beach processes. UMITSU *et al.* (2007) also noted beaches retreated or vanished following the 2004 Indian Ocean tsunami in Indonesia and Thailand, but were not able to quantify the change. Breaches by tsunami have been previously documented in Japan from the 1960 Chile event (KONNO *et al.*, 1961) and the Maldives from the 2004 Indian Ocean event (FRITZ *et al.*, 2006).

9. Paleotsunami Deposits in the Affected Region – Preliminary Results

The presence of paleotsunami deposits in the middle Kurils indicates that ruptures at least on the scale of the 2006 event are not uncommon, and support the postulate that before 15 November 2006, the region was a seismic gap. For example, in the summer of 2006, before the 15 November 2006 tsunami, we had collected evidence of tsunami deposits as high as 20 m above sea level in Dushnaya Bay on northern Simushir (Fig. 8, profile 2006-2)—as many as three such deposits since $\sim$400 A.D. (tentative age of a marker tephra, based on correlation with dated archaeological sites).

In both 2006 and 2007 field seasons, in order to develop chronologies and determine pre-histories of eruptions, earthquakes and tsunamis, we made numerous excavations along selected profiles, using techniques as described in BOURGEOIS *et al.* (2006) (e.g., Fig. 9). In the subsurface we identified many sand layers we interpret to be tsunami

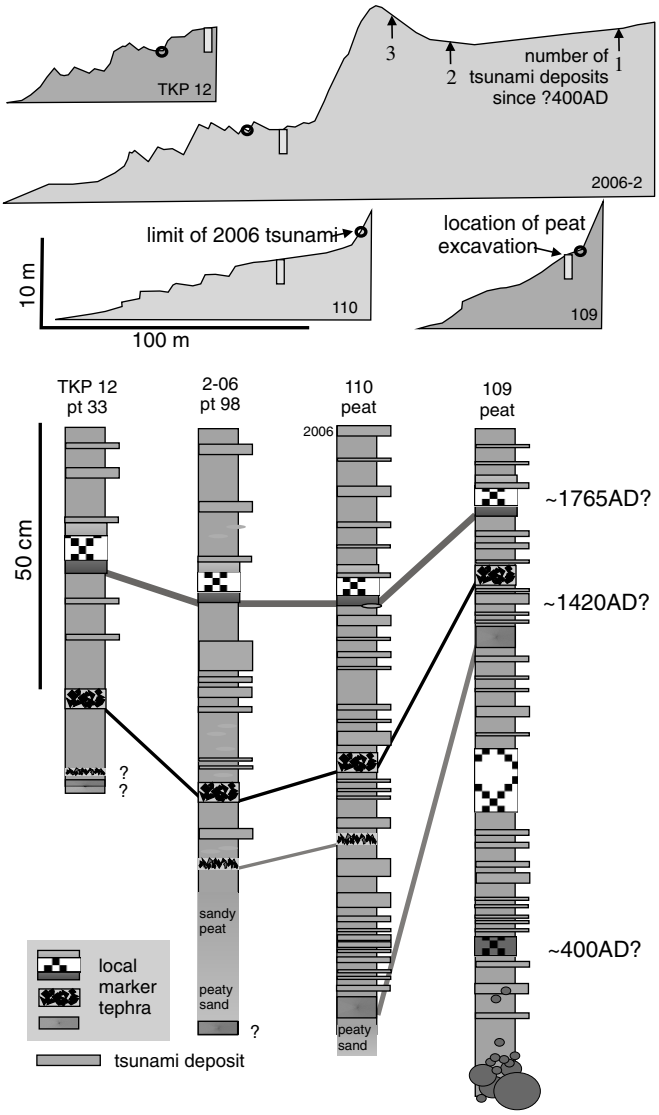

Figure 8

Paleotsunami deposits in peat sections on topographic profiles from Dushnaya Bay, Pacific Coast of northern Simushir (Fig. 2). Above: Four of 25 profiles measured in Dushnaya Bay. On each profile, the limit of the 15 November 2006 tsunami is shown by a circle, and the location of peat excavations (illustrated below) is shown by a rectangle. In addition, on profile 2006-2, the locations of three high-terrace excavations are shown with arrows, and the number of tsunami deposits present in the upper parts of those excavations indicated. Below: From a peat excavation in each profile, the logged description of tephra and tsunami deposits. The background of the sections is peat unless otherwise indicated. We show only key local marker tephra—the ones we could correlate all along the bay, in many excavations. Ages of these tephra are based on the historical record (an observed eruption c. 1765) and on radiocarbon dating of correlative archaeological sections. These dates should be taken as tentative.

deposits, based on their sheet-like geometry, (beach) sand composition, and location above storm limits. Many of our excavations have been at sites beyond the limit of the 2006 tsunami deposit (Figs. 8 and 9), indicating locally higher paleo-runup.

Herein we report only examples of the presence (not chronology or recurrence interval) of paleotsunami deposits because our age control is still being developed. This age control is and will be based on radiocarbon dating above and below marker tephra on each island. Dates reported in Figures 8 and 9 should be considered tentative.

On northern Simushir Island (Dushnaya Bay, Fig. 2), in several peat excavations at elevations at or above the limit of the 15 November 2006 tsunami, sand layers are common in the subsurface (Fig. 8). With our tentative age control, it is fair to say that tsunamis locally as large or larger than 15 November 2006 have occurred as often as once per ~100 years. Of course, some of these tsunamis might have been more local (less regional) than 2006, or triggered by submarine or coastal landslides.

On southern Matua Island (South Bay, Fig. 2; inset Fig. 4), there is also a record of a numerous prehistoric tsunamis locally larger than 15 November 2006 (Fig. 9). Compared to Dushnaya Bay on Simushir, the record is more difficult to read because cinders from the local volcano, Sarychevo, are common and thick. For example, some of the interpreted tsunami deposits on Matua are cindery beds containing beach sand.

Some previous work has been published on Holocene paleotsunami deposits south of the middle Kurils, on Kunashir and Iturup islands, north of Hokkaido (ILIEV *et al.*, 2005). On Kunashir, those authors found 17 thin sand layers intercalated with peat and lacustrine deposits. Field observations, grain-size composition, and diatom data were used to attribute the deposits to tsunamis; age control is based on radiocarbon dating and tephra

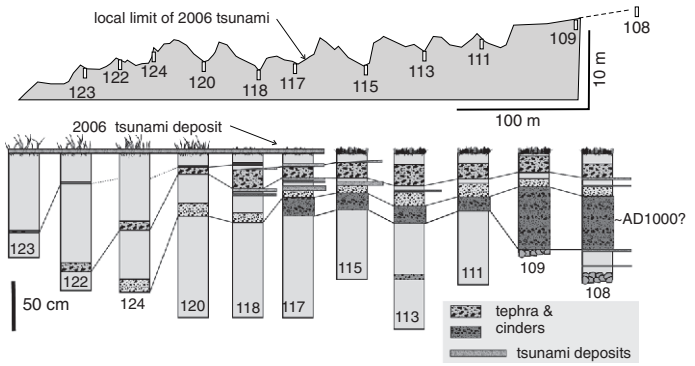

Figure 9

Profile 216, one of ten topographic profiles measured in South Bay, Matua Island (Fig. 2 and inset Fig. 4), and the logged description of excavations along that profile, simplified to include only prominent tephra. In 2006, we made ten excavations on this profile, and one nearby (108). In 2007, we mapped the 15 November 2006 tsunami deposit onto this profile, which extended just to excavation 117. Note that some paleotsunami deposits extend beyond this limit (e.g., excavations 115, 113, 108). Age control on these sections remains tentative, pending radiocarbon dates and additional work on tephra correlation.

stratigraphy. The documented sand layers are present at elevations to 7 m and inland distances up to 2.5 km. ILIEV *et al*. (2005) reported paleotsunami deposits as old as 6,000–7,000 years and attempted to correlate these deposits from Iturup to Hokkaido, with recurrence intervals for large events of about 500 yr.

10. Summary

The nearfield runup of the 15 November 2006 middle Kurils tsunami exceeds 10 times the height of water heights recorded on any Pacific Ocean tide gages (NGDC catalogue). Average runup in the middle Kurils was about 10 m, with some field sites recording > 20 m. In many locations the tsunami inundated the entire coastal plain area and reflected off cliffs backing the plain. Maximum inundation reached as far as 400 m and was mostly limited by topography.

Wherever fine-grained (primarily sand-sized) sediment was available on the beach or nearshore, we found continuous tsunami deposits. Areas deficient in sand still showed evidence of sediment transport, with tsunami *ishi* up to 3 m in diameter pulled up from offshore, transported within the coastal plain, or washed out to sea. The presence of paleotsunami deposits in the middle Kurils confirms that large ruptures in this section of the subduction zone are not uncommon, although the source characteristics of these paleoevents may vary. Many of the paleotsunami deposits are more extensive than deposits of the 15 November 2006 tsunami.

Erosion from the 2006 tsunami was greatest where runup exceeded 10 m. We predict some scours and gullies will likely be permanent alterations of the geomorphology of the coastline. At sites with high runup, erosion extended almost as far as inundation. However, erosion was minimal where runup was less than 10 m, such as in central Dushnaya Bay, Simushir; in these localities the geomorphic effect of the tsunami will be indistinguishable in the near future.

11. Future Work

We returned to the Kuril Islands in the summer of 2008, the final of three extended field seasons funded by the NSF Kurils Biocomplexity Project. The aims of the geology and tsunami team members for 2008 included visits to the Pacific coasts of Rasshua, Shiashkotan and Onekotan, where the 2006 tsunami left a record. We also visited northern Urup; our brief surveys in 2006 and 2007 showed that effects on southern Urup were minimal. With a complete set of observations, we can compare our survey results with models, e.g., by M. Nosov in LEVIN *et al*. (2008) and RABINOVICH *et al*. (2008).

From the 2007 season, we have an extensive suite of samples of the 2006 tsunami deposit along eleven profiles, and we will report in more detail on their character, following grain size analysis. For Dushnaya Bay (northern Simushir) and southern Matua,

our topographic profiles are dense enough that we will be able to generate 3-D topography. In four cases, we also have before (2006) and after (2007) profiles, and in many cases, we have quantified erosional features. Therefore, after acquiring higher resolution shallow bathymetry, we plan to model local runup and compare the geological effects to modeled tsunami behavior. We also plan for our data to present suitable benchmarks for the study of tsunami erosion and deposition (c.f. HUNTINGTON *et al.*, 2007).

As noted above, our ongoing work on paleotsunamis in the Kurils requires more radiocarbon dating, and more study of tephra chronology and correlation. Such work is a challenge because of the wide spacing of the islands, and the number of active volcanoes. However, our preliminary work is promising, and quantification of paleotsunami frequency (and possibly size) throughout the Kurils is one of our intermediate-term goals.

Acknowledgements

We are very grateful for the helpful reviews of Alexander Rabinovich, Alexei Ivashchenko and Kenji Satake. Funding for fieldwork was provided primarily by the Kuril Biocomplexity Project (NSF grant #0508109, PI Ben Fitzhugh; http://depts.washington.edu/ikip/index.shtml) and also by the Institute of Marine Geology and Geophyics, Yuzhno-Sakhalinsk, Russia (Director Boris Levin). The following people helped us collect field data in the middle Kurils: Kirill Ganzey, Sergei Chirkov, Andrei Kharlamov, Misty Nikula, Ben Fitzhugh, Boris Levin, Mikhail Nosov and Elena Sassorova.

REFERENCES

ALONSO, C.V., BENNET, S.J., and STEIN, O.R. (2002), *Predicting head cut erosion and migration in concentrated flows typical of upland areas*, Water Resources Research *38*(12), 1303, doi:10.1029/2001WR001173.

AMMON, C.J., KANAMORI, H., and LAY, T. (2008), *A great earthquake doublet and seismic stress transfer cycle in the central Kuril Islands*, Nature *451*, 561–565.

APEL, E.V., BURGMANN, R., STEBLOV, G., VASILENKO, N., KING, R., and PRYTKOV, A. (2006), *Independent active microplate tectonics of northeast Asia from GPS velocities and block modeling*, Geophys. Res. Lett. *33*, L11303, doi:10.1029/2006GL026077.

BOURGEOIS, J. (2009), *Geologic effects and records of tsunamis*. In The Sea: Volume 15, Tsunamis (eds. BERNARD, E.N. and ROBINSON, A.R.), Harvard University Press, 55–91.

BOURGEOIS, J., PINEGINA, T.K., PONOMAREVA, V., and ZARETSKAIA, N. (2006), *Holocene tsunamis in the southwestern Bering Sea, Russian Far East, and their tectonic implications*, Geol. Soc. Am. Bull. *118*(3/4), 449–463.

BRIGGS, M.J., SYNOLAKIS, C.E., KANOGLU, U., and CREEN, D.R. (1996), *Runup of solitary waves on a vertical wall*, in *Long-Wave Runup Models. In Proc. Internat. Symp.*, Friday Harbor, USA, 12–17 September 1995 (eds. H. YEH, P. LIU, C. SYNOLAKIS), World Science, pp. 375–383.

COOK, D.B., FUJITA, K., and MCMULLEN, C.A. (1986), *Present-day plate interactions in northeast Asia - North-American, Eurasian, and Okhotsk plates*, J. Geodyn. *6*, 33–51.

DEMETS, C., GORDON, R.G., ARGUS, D.F., and STEIN, S. (1990), *Current plate motions*, Geophys. J. Int. *101*, 425–478.

FARRERAS, S.F. (2000), *Post-tsunami field survey procedures: An outline*, Natural Hazards *21*, 207–214.

FEDOTOV, S.A. (1965), *Regularities of the distribution of large earthquakes of Kamchatka, the Kuril Islands and north-eastern Japan*, Akad. Nauk SSSR Inst. Fiziki Zemli Trudy *36* (203), 66–93. (in Russian).

FRITZ, H.M., SYNOLAKIS, C.E., and MCADOO, B.G. (2006), *Maldives field survey after the December 2004 Indian Ocean tsunami*, Earthquake Spectra *22*(S3), S137–S154.

FUJII, Y., and SATAKE, K. (2008), *Tsunami sources of November 2006 and January 2007 great Kuril earthquakes*, Bull. Seismol. Soc. Am. *98*(3), doi: 10.1785/0120070221.

GELFENBAUM, G. and JAFFE, B. (2003), *Erosion and sedimentation from the 17 July 1998 Papua New Guinea tsunami*, Pure. Appl. Geophys. *160*, 1969–1999.

GOFF, J., LIU, P.L.-F., HIGMAN B., MORTON R., JAFFE B.E., FERNANDO H., LYNETT, P., FRITZ, H., SYNOLAKIS C., and FERNANDO S. (2006), *Sri Lanka field survey after the December 2004 Indian Ocean tsunami*, Earthquake Spectra *22*(S3), S155–S172

GORSHKOV, G.S., *Volcanism and the Upper Mantle; Investigations in the Kurile Island Arc* (New York, : Plenum Publishing Corp. 1970), 385 pp.

HARADA, T. and ISHIBASHI, K. (2007), *Two parallel trench-normal fault planes within the Pacific slab associated with the 1994 and 2000 Kurile earthquakes as revelated by simultaneous relocation of their main shocks and aftershocks*, Earth Planets Space *59*, e25–e28.

HUNTINGTON, K., BOURGEOIS, J., GELFENBAUM, G., LYNETT, P., JAFFE, B., YEH, H., and WEISS, R. (2007), *Sandy signs of a tsunami's onshore depth and speed*, EOS, Transactions, AGU *88*(52), 577–578.

JI, C. (2006), *Rupture process of the 2006 Nov. 15 Magnitude 8.3- Kuril Island earthquake,* http://earthquake.usgs.gov/eqcenter/eqinthenews/2006/usvcam/finite_fault.php (last accessed May 2008).

JI, C. (2007), *Rupture process of the 2007 Jan. 13 Magnitude 8.1 - Kuril Island earthquake (revised),* http://earthquake.usgs.gov/eqcenter/eqinthenews/2007/us2007xmae/finite_fault.php (last accessed May 2008)

ILIEV, A.Y., KAISTRENKO, V.M., GRETSKAYA, E.V., TIKHONCHUK, E.A., RAZJIGAEVA N.G., GREBENNIKOVA, T.A., GANZEY, L.A. and KHARLAMOV, A.A., *Holocene tsunami traces on Kunashir Island, Kurile Subduction Zone*. In *Tsunamis: Case Studies and Recent Developments* (ed. SATAKE, K.), *Advances in Natural and Technological Hazards Research* (Springer, Netherlands 2005) *23*, 171–192.

KAISTRENKO, V.M., ed. (1997), *Concrete tsunami manifestation: Tsunamis of 1993 and 1994 on the Russian coast*, Geodynamics of Tectonosphere of the Pacific Eurasia Conjunction Zone, Vol. VII, Yuzhno-Sakhalinsk, 193 pp. (in Russian).

KATO, Y. and KIMURA, M. (1983), *Age and origin of so-called "Tsunami-ishi", Ishigaki Island, Okinawa Prefecture*, J. Geol. Soc. Japan *89*, 471–474.

KELLY, A. (2006), *Recent tsunami highlights need for awareness of tsunami duration*, EOS, Transactions, AGU *87*, 566–567.

KONNO, E., IWAI, J., TKAYANAGI, Y., NAKAGAWA, H., ONUKI, Y., SHIATA, T., MII, H., KITAMURA, S., KODAKA, T., and KATAOKA, J. (1961), *Geological survey on the Chile Earthquake Tsunami affected areas in the Sanriku coast, northeast Japan,* Contrib. Inst. Geol. Palaeontol. Tohoku Univ. *52*, 1–40 (in Japanese with English abstract).

KURIAN, N. P., PILLAI, A.P., RAJITH, K., MURALI KRISHNAN, B. T. and KALAIARASAN, P. (2006), *Inundation characteristics and geomorphological impacts of December 2004 tsunami on Kerala coast*, Current Science *90*(2), 240–249.

KUZIN, I.P., LOBKOVSKY, L.I., and SOLOV'EVA, O.N. (2001), *Characteristics of seismicity in the central Kurile region*, Izvestiya - Russian Academy of Sciences, Physics of the Solid Earth *37*(6), 464–473.

LAVEROV, N.P., LAPPO, S.S., LOBKOVSKY, L.I., BARANOV, B.V., KULINICH, R.G., and KARP, B.Y. (2006), *The central Kuril "gap": Structure and seismic potential*, Doklady Earth Sciences *409*, 787–790.

LEVIN, B.V., KAISTRENKO, B.M., RYBIN, A.B., NOSOV, M.A., PINEGINA, T.K., RAZHIGAEVA, N.G., SASSOROVA, E.V., GANZEI, K.S., IVELSKAYA, T.N., KRAVCHENOVSKAYA, E.A., KOLESOV, C.V., EVDOKIMOV, Y.V., BOURGEOIS, J., MACINNES, B., and FITZHUGH, B. (2008), *Manifestations of the tsunami on November 15, 2006, on the Central Kuril Islands and results of the runup heights modeling*, Transactions (Doklady) of the Russian Academy of Sciences, Earth Science Section *419* (2), 335–338.

MACINNES, B.T., BOURGEOIS J., PINEGINA, T.K., MARTIN, M. E., and KRAVCHENOVSKAYA, E.A. (2007), *Tsunami erosion: Geomorphology before and after the 15 Nov. 2006 tsunami in the Middle Kuril Islands, Russia*, EOS Trans. AGU *88*(52), Fall Meet. Suppl., Abstract OS31A–0158.

MAHESHWARI, B.K., SHARMA, M.L., and NARAYAN, J.P. (2006), *Geotechnical and structural damage in Tamil Nadu, India, from the December 2004 Indian Ocean tsunami*, Earthquake Spectra *22* (S3), S475–S493.

MALIK, J.N., MURTY, C.V.R., and RAI, D.C. (2006), *Landscape changes in the Andaman and Nicobar islands (India) after the December 2004 great Sumatra earthquake and Indian Ocean tsunami*, Earthquake Spectra *22* (S3), S43–S66.

MARAMAI, A. and TINTI, S. (1997), *The 3 June 1994 Java tsunami: A post-event survey of the coastal effects*, Natural Hazards *15*, 31–49.

MELEKESTSEV, I.V. (1980), *Volcanism and Relief Formation*, Nauka, Moscow, 212 pp. (in Russian).

MINOURA, K., GUSIAKOV, V.G., KURBATOV, A., TAKEUTI, S., SVENDSEN, J.I., BONDEVIK, S., and ODA, T. (1996), *Tsunami sedimentation associated with the 1923 Kamchatka earthquake*, Sed. Geol. *106*, 145–154.

NGDC database—National Geophysical Data Center Tsunami Database, http://www.ngdc.noaa.gov/hazard/tsu_db.shtml (last accessed May 2008).

OKAL, E.A., SLADEN, A., and OKAL, E.A.-S. (2006), *Rodrigues, Mauritius, and Reúnion islands; Field survey after the December 2004 Indian Ocean tsunami*, Earthquake Spectra *22* (S3), S241–S261.

PELINOVSKY, E., TROSHINA, E., GOLINKO, V., OSIPENKO, N., and PETRUKHIN, N. (1999), *Runup of tsunami waves on a vertical wall in a basin of complex topography*, Phys. Chem. Earth (B) *24*(5), 431–436.

RABINOVICH, A.B., LOBKOVSKY, L.I., FINE, I.V., THOMSON, R.E., IVELSKAYA, T.N., and KULIKOV, E.A. (2008), *Near-source observations and modeling of the Kuril Islands tsunamis of 15 November 2006 and 13 January 2007*, Adv. Geosci. *14*, 105–116.

SHEPARD, F.P., MACDONALD, G.A., and COX, D.C. (1950), *The tsunami of April 1, 1946,* Hawaii, Calif. Univ., Scripps Inst. Oceanography Bull. *5*, 391–528.

SHI, S., DAWSON, A. G., and SMITH, D. E. (1995), *Coastal sedimentation associated with the December 12th 1992 tsunami in Flores, Indonesia.* In Recent Tsunamis (eds. SATAKE, K., and IMAMURA, K., Pure. Appl. Geophys. *144*, 525–536.

SNOW, H.J., *In Forbidden Seas. Recollections of Sea-otter Hunting in the Kurils,* (London, E. Arnold, 1910).

SOLOVIEV, S.L. (1972), *Recurrence of earthquakes and tsunamis in the Pacific Ocean,* Volny Tsunami, Trudy Sakhnii *29*, 7–47 (in Russian).

SONG, T.A. and SIMONS, M. (2003), *Large trench-parallel gravity variations predict seismogenic behavior in subduction zones*, Science *301*, 630, doi: 10.1126/science.1085557.

TANIOKA, Y., HASEGAWA, Y., and KUWAYAMA, T. (2008), *Tsunami waveform analyses of the 2006 underthrust and 2007 outer-rise Kurile earthquakes*, Advances in Geosciences *14*, 129–134.

UMITSU, M., TANAVUD, C., and PATANAKANOG, B. (2007), *Effects of landforms on tsunami flow in the plains of Banda Aceh, Indonesia, and Nam Khem, Thailand*, Marine Geology *242*, 141–153.

VALLÉE, M. (2006) http://geoazur.unice.fr/SEISME/KURIL151106/note1.html (last accessed May 2008)

VALLÉE, M. (2007) http://geoazur.unice.fr/SEISME/KURIL130107/note1.html (last accessed May 2008)

YAGI, Y. (2006) http://www.geo.tsukuba.ac.jp/press_HP/yagi/EQ/Chishima/ (last accessed May 2008)

YAGI, Y. (2007) http://www.geo.tsukuba.ac.jp/press_HP/yagi/EQ/2007Chishima/ (last accessed May 2008).

YEH, H., TITOV, V., GUSIAKOV, V., PELINOVSKY, E., KHRAMUSHIN, V., and KAISTRENKO, V. (1995), *The 1994 Shikotan earthquake tsunamis*, Pure. Appl. Geophys. *144*(3/4), 855–874.

(Received January 1, 2008, accepted June 3, 2008)
Published Online First: February 14, 2009

Pure appl. geophys. 166 (2009) 37–53
0033–4553/09/010037–17
DOI 10.1007/s00024-008-0429-2

Pure and Applied Geophysics

The November 15, 2006 Kuril Islands-Generated Tsunami in Crescent City, California

L. DENGLER,[1] B. USLU,[2,3] A. BARBEROPOULOU,[2] S. C. YIM,[4] and A. KELLY[5]

Abstract—On November 15, 2006, Crescent City in Del Norte County, California was hit by a tsunami generated by a M_w *8.3* earthquake in the central Kuril Islands. Strong currents that persisted over an eight-hour period damaged floating docks and several boats and caused an estimated $9.2 million in losses. Initial tsunami alert bulletins issued by the West Coast Alaska Tsunami Warning Center (WCATWC) in Palmer, Alaska were cancelled about three and a half hours after the earthquake, nearly five hours before the first surges reached Crescent City. The largest amplitude wave, 1.76-meter peak to trough, was the sixth cycle and arrived over two hours after the first wave. Strong currents estimated at over 10 knots, damaged or destroyed three docks and caused cracks in most of the remaining docks. As a result of the November 15 event, WCATWC changed the definition of Advisory from a region-wide alert bulletin meaning that a potential tsunami is 6 hours or further away to a localized alert that tsunami water heights may approach warning- level thresholds in specific, vulnerable locations like Crescent City. On January 13, 2007 a similar Kuril event occurred and hourly conferences between the warning center and regional weather forecasts were held with a considerable improvement in the flow of information to local coastal jurisdictions. The event highlighted the vulnerability of harbors from a relatively modest tsunami and underscored the need to improve public education regarding the duration of the tsunami hazards, improve dialog between tsunami warning centers and local jurisdictions, and better understand the currents produced by tsunamis in harbors.

Key words: 2006 Kuril Islands earthquake, Tsunami, Crescent City, Tsunami warning system, Coastal damage, Hazard mitigation.

1. Introduction

Crescent City, located in Del Norte County on California's North Coast about 460 kilometers north of San Francisco (Fig. 1), has suffered greater impact from historic tsunamis than any other community on the West Coast of the United States (DENGLER and MAGOON, 2006). Thirty-one tsunamis have been observed at Crescent City since a tide gauge was established in 1933 (Table 1), including eleven events with maximum peak to trough wave height exceeding one meter, and four that caused damage. The most recent

[1] Humboldt State University, Arcata, CA 95521, USA. E-mail: lad1@humboldt.edu
[2] USC, Los Angeles, CA 90089, USA.
[3] NOAA PMEL, Seattle, WA 98115, USA. E-mail: Uslu@noaa.gov
[4] Oregon State University, Corvallis, OR 97331, USA. E-mail:yim@oregonstate.edu
[5] USGS, Menlo Park, CA 94025, USA. E-mail: annabelkelly@gmail.com

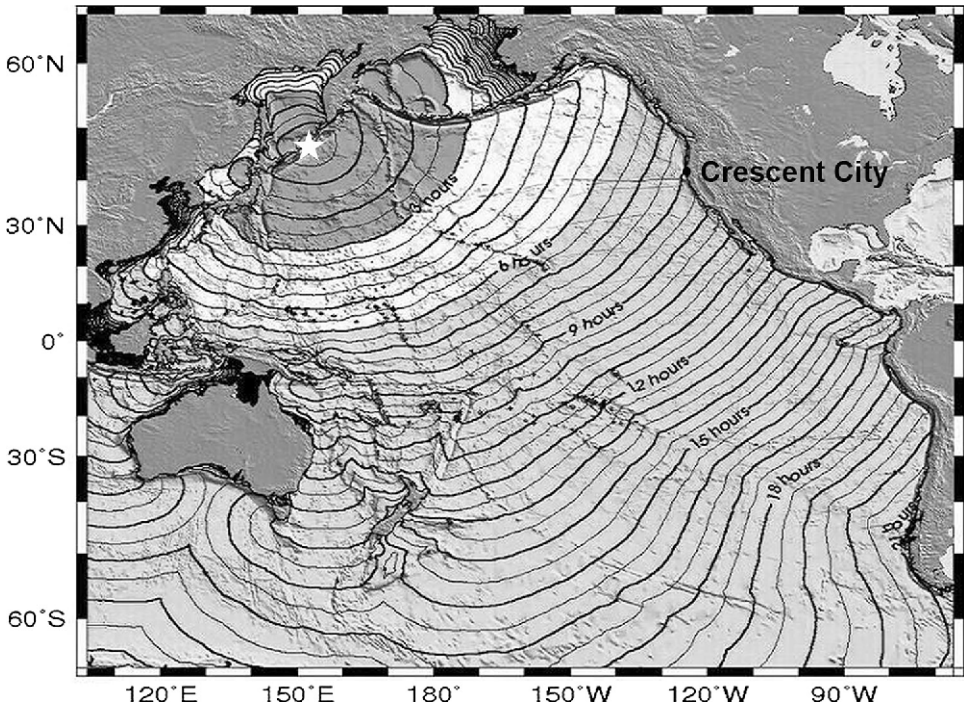

Figure 1
Location of the November 15, 2006 epicenter (star) and Crescent City, California. Travel Time map courtesy of WCATWC, NOAA.

damaging tsunami occurred on November 15, 2006 as a result of a magnitude M_w *8.3* earthquake on the central Kuril trench that caused significant damage to the floating docks in the small boat basin in Crescent Harbor. The authors visited Crescent City from November 16th to 18th, 2006, conducted interviews with officials and eyewitnesses and have continued to follow the damage assessment with County and City officials. This study examines the chronology of events on November 15, Crescent City's particular vulnerability to a modest tsunami and highlights some of the difficulties of managing a marginal tsunami event.

2. Crescent City

Crescent City, population 7,452, is the largest population center and only incorporated city in California's northernmost coastal county, Del Norte (Fig. 2). Traditionally the home of the Tolowa people, the Jedidiah Smith party in 1828 was the first group of people of European descent to explore the region. Incorporated in 1854, Crescent City was initially the center of placer gold and copper mining interests. Mining

Table 1

Tsunamis recorded at Crescent City

Date	Tsunami Source Area	Amplitude (m)	Comments
10-Nov-38	Alaska Peninsula	0.18	
06-Apr-43	N. Central Chile	0.10	
01-Apr-46	Unimak Island, Alaska	0.90	
20-Dec-46	Nankaido, Japan	0.23	
04-Mar-52	SE Hokkaido, Japan	0.18	
04-Nov-52	Kamchatka	0.93	4 boats overturned, concrete buoys moved
09-Mar-57	Central Aleutians, Alaska	0.65	
22-May-60	S. Central Chile	1.68	2 ships destroyed, $30,000 damage
13-Oct-63	Kuril Islands, Russia	0.33	
28-Mar-64	Gulf of Alaska	4.79	11 deaths, $16 million damages
04-Feb-65	W. Aleutian Islands, Alaska	0.31	
17-Oct-66	Peru	0.07	
16-May-68	Honshu, Japan	0.61	
26-Jul-71	New Ireland, PNG	0.06	
03-Oct-74	Peru	0.08	
07-May-86	Aleutian Islands, Alaska	0.06	
25-Apr-92	Cape Mendocino, California	0.55	Seiche in harbor
01-Sep-94	Mendocino fault, N. Calif	0.07	
04-Oct-94	Kuril Islands, Russia	0.50	
30-Jul-95	N. Chile	0.11	
03-Dec-95	S. Kuril Islands	0.14	
17-Feb-96	Papua, Indonesia	0.18	
10-Jun-96	Central Aleutians, Alaska	0.14	
22-Jun-01	S. Peru	0.20	
25-Sep-03	Hokkaido, Japan	0.18	
26-Dec-04	Indonesia	0.31	
15-Jun-05	Gorda basin, N. Calif	0.10	
03-May-06	Tonga Islands	0.27	
15-Nov-06	Kuril Islands, Russia	0.88	$9.2 million damages to docks
13-Jan-07	Kuril Islands, Russia	0.23	
15-Aug-07	S. Peru	0.16	

From the National Geophysical Data Center Global Tsunami Database. Amplitudes are zero to peak values.

activities declined in the later 1800s to be replaced by logging and a small fishing industry. The small boat basin, built in the early 1970s as part of the post 1964 tsunami reconstruction in Crescent City, currently holds about 100 small commercial fishing boats and numerous recreational craft. On November 15, 2006 at least 75 commercial crab boats were preparing for the beginning of crab season on December 1.

Crescent City is well known for its vulnerability to tsunamis. The community has been affected by earthquake-generated tsunamis located throughout the Pacific basin, including ten from the northwestern Pacific (Japan, Kuril Islands, Kamchatka), seven each from South America and Alaska and several from the southwestern Pacific. The worst historic event was the tsunami caused by the March 28, 1964 9.2 (M_w) Alaskan

Figure 2
Aerial view of Crescent City and the locations of the small boat basin (box) and tide gauge (arrow). Docks on the west (left) side of the small boat basin are lettered E, F, G, H from north to south.

earthquake that inundated 29 city blocks, killed 11 and caused an estimated 15 million in losses (DENGLER and MAGOON, 2006; LANDER *et al.*, 1993).

Only three small near-source tsunamis have been recorded at Crescent City (Table 1). Several paleoseismic studies have looked for evidence of past tsunamis in the Crescent City area (ABRAMSON, 1998; GARRISON-LANEY, 1998; PG&E, 2003) and deposits interpreted as tsunami sands have been found in a number of locations. Numerical modeling as part of the California Division of Mines and Geology Earthquake Planning Scenario for an earthquake on the southern Cascadia subduction zone showed flooding about twice as far inland as the 1964 event (BERNARD *et al.*, 1994; TOPPOZADA *et al.*, 1995). More recent modeling results (USLU *et al.*, 2007) show that rupture on the southern portion of the Cascadia subduction zone with additional slip on the Little Salmon fault poses the greatest risk for the Crescent City area.

Crescent City is unusual on the US West Coast for the large amplitude and unusual long duration of tsunami signals compared to nearby coastal sites. Two of the reasons are straightforward: exposure and bathymetry. Crescent City is unique along the northern California coast, with the majority of the town at low elevation highly exposed to the ocean. The combination of geology and tectonics has thrust Point St. George out into the ocean and created a natural south-facing crescent-shaped bay that funnels tsunamis from all directions into the harbor area. Offshore, the Mendocino fracture zone extends nearly 4000 km offshore of the northern California coast, creating an elevation step in the Pacific sea floor that acts as a wave-guide focusing higher amplitude tsunami waves at northern California and southern Oregon (KOWALIK *et al.*, 2008).

Tsunamis at Crescent City are characterized by long duration and peak amplitudes delayed to the fourth or later cycle (DENGLER and MAGOON, 2006; NOAA, 2005). Investigators considering this anomaly have postulated several possible reasons. WILSON

and TORUM (1968) proposed that the 30 to 35 minute period oscillations noted in the 1964 tsunami "would accord with the third harmonic of the incident tsunami wave" which they reported as a 1.77-hour period. They suggest the shape and bathymetry offshore between Pt. St. George and Patrick's Point could be the cause. KEULEGAN *et al*. (1969) in analyzing the high-speed water level recordings taken during the May 1960 tsunami at Citizen's Dock and Dutton's Dock at Crescent City, note that "predominate periods of 80.0, 33.0, 22.0, and 18.0 minutes are clearly defined in all cases and can be accepted with confidence. These predominate periods are in good agreement with periods computed by consideration of the oscillations of the Crescent City area from the offshore area to the beach". ROBERTS and KAUPER (1964) suggested that the submarine morphology and direction of propagation of the (1964) tsunami were the cause of the focusing of the wave energy at Crescent City. Trapped edge waves or a combination of effects may be partly responsible for the relatively high waves at Crescent City (DENGLER and MAGOON, 2006). More recently, KOWALIK *et al*. (2008) and HORILLO *et al*. (2008) look at both the far-field travel path effects and the near-shore resonance and conclude that both combine to account for the amplification at Crescent City.

3. The November 15, 2006 Warning Chronology

The Kuril Islands trench marks the boundary between the Pacific and North American plates and is one of the most rapidly converging plate boundaries in the world. The Tonga and Loyalty-Vanuatu trenches are the only boundaries where subduction occurs more rapidly (STEIN and OKAL, 2007). At least 44 earthquakes of probable magnitude 7 or larger have been generated on the Kuril trench since 1700; 23 of which have generated tsunamis (NGDC, 2008). Since 1958, seven earthquakes of magnitude 7.9 or larger have occurred on the Kuril trench, five generating tsunamis that were recorded at the tide gauge in Crescent City harbor. Prior to 2006, no Kuril tsunami had caused damage at Crescent City.

On November 15, 2006 at 11:14 UTC (3:14 AM PST on the US West Coast) a M_w *8.3* earthquake occurred in the Kuril Islands trench. The West Coast Alaska Tsunami Warning Center (WCATWC) issued an initial alert bulletin 15 minutes after the earthquake (Fig. 3). WCATWC has several forecasting tools to estimate water heights throughout its area of responsibility. An initial projection of water heights at Crescent City based on historic Kuril events and the size and location of the epicenter gave a maximum amplitude estimate at Crescent City of about 0.5 meter zero to peak (TWC model in Fig. 3). NOAA's Pacific Marine Environmental Laboratory (PMEL) has developed a modeling tool, SIFT (Short-term Inundation Forecasting for Tsunamis) that was being used on an experimental basis by WCATWC on November 15. SIFT uses precomputed scenarios for earthquake-generated tsunamis throughout the Pacific basin that can be adjusted as actual water-level data from the Deep-ocean Assessment and Recording of Tsunamis (DART^{TM}) network becomes available. PMEL provided SIFT

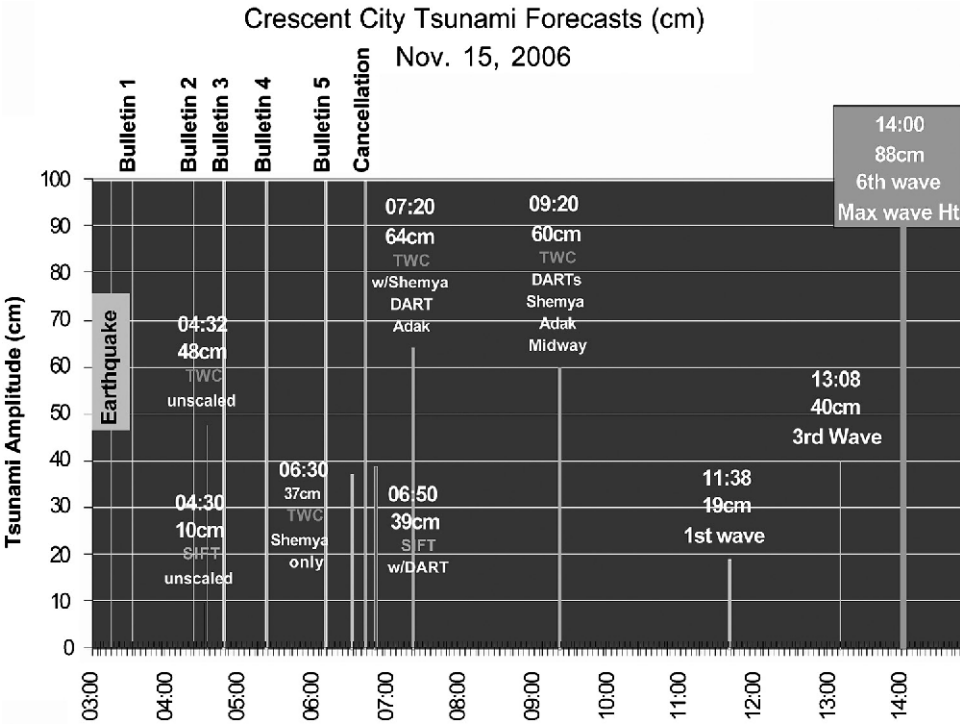

Figure 3
Time line (PST) of tsunami bulletins issued by WCATWC, forecasted water-level data at Crescent City and actual wave amplitudes (zero to peak in cm). SIFT stands for the Short-term Inundation Forecasting for Tsunamis model. TWC stands for the Tsunami Warning Center Projections. Data and graphic provided by WCATWC.

forecast estimates to the WCATWC during the November 15 event. The initial unscaled (no water level data constraints) SIFT forecast estimated a peak tsunami amplitude at Crescent City of only 10 cm. Both the initial TWC and SIFT projections were available at 4:30 AM PST, about an hour and fifteen minutes after the earthquake. A SIFT hindcast using DART data made after the event projected a peak amplitude of 55 cm at Crescent City (Whitmore, personal communication).

Subsequent bulletins were issued at approximately half-hour intervals expanding warning and watch areas (Fig. 3; Table 2). The peak Shemya tide gauge water-level recordings arrived shortly before 6:30 AM PST. The TWC projections were recomputed and the peak water-level amplitude for Crescent City was forecast to be 37 cm. Relatively low water heights measured by tide gauges in Japan and elsewhere in the western Pacific indicated that a large tsunami was not expected along the Alaskan or the US Pacific Coast. WCATWC canceled the Warning and Watch for Alaska and the North American West Coast at 6:41 AM PST, about three and a half hours after the earthquake.

Table 2

Chronology

TIME PST	Bulletins & Communication
3:14	Earthquake occurs.
3:31	1st WCATWC Bulletin - Information Bulletin M 7.7 - No Watch, Warning.
3:44	NEIC Preliminary Earthquake Magnitude 7.8.
4:10	2nd WCATWC Bulletin - M 8.1, Warning Attu to Dutch Harbor, AK, Watch Dutch Harbor to Vancouver Island, BC; tsunami unconfirmed; 1st arrival at CC 11:38 AM PST.
4:17	California State Warning Center (CSWC) contacted CA Operational Areas (Counties) via California Warning System (CAWAS).
4:42	NEIC preliminary moment tensor magnitude - 7.7.
4:35	Crescent City received paged notification of Advisory.
4:46	3rd WCATWC Bulletin - M 8.1, Warning Attu to Sand Point, AK, Watch Sand Point to Cape Flaherty, WA, tsunami unconfirmed.
5:21	4th WCATWC Bulletin - M 8.1, Warning Attu to Sand Point, AK, Watch Sand Point to Cape Flaherty, WA, tsunami confirmed 30 cm Hanasaki, Japan.
6:09	5th WCATWC Bulletin - M 8.1, Warning Attu to Sand Point, AK, Watch Sand Point to Cape Flaherty, WA, tsunami confirmed 30 cm Hanasaki, Japan, 20 cm Shemya, AK
6:40	Global Moment Tensor Project - Revised magnitude 8.3
6:41	6th WCATWC Bulletin - M 8.1, Warning and Watch Cancelled, NO TSUNAMI DANGER EXISTS FOR ALASKA/ BRITISH COLUMBIA/ WASHINGTON/ OREGON OR CALIFORNIA.
6:51	Crescent City notified by CSWC of cancellation.
9:23	CSWC received call from WC/ATWC on status of tsunami. “No warning, watch or advisory in effect. Crescent City may experience wave surges but damage not expected.” Message faxed to Humboldt County. First surges expected at 11:38 AM.
9:30	Humboldt County OES forwards message to Crescent City, contacts NWS Weather Forecast Office Eureka.
9:30 - 11:00	NWS Weather Forecast Office Eureka Warning Coordination Meteorologist contacts emergency personnel in Humboldt and Del Norte Counties. Beaches and harbor areas are cleared.
11:40 - 12:00	First surge observed by Crescent City Harbor Master as a gentle change in water level with 1 foot peak-to-trough range.
13:00	Harbor Master observes very strong currents in the Small Boat Basin, boats oscillating. Harbor Master and assistant go into the Boat Basin to secure boats.
14:00 - 14:30	Docks G, F and E docks begin breaking up. Two boats set adrift.
15:30	Special Weather Statement issued by NWS Weather Forecast Office Eureka, potentially dangerous current alert in Humboldt and Del Norte County Harbors until 8:00 PM.

At the peak of the warning alert (Bulletin 5), the coastline from the western Aleutians Islands to Sand Point on the Alaska Peninsula was placed in a Tsunami Warning, and Sand Point to northern Washington was placed in a Tsunami Watch. During the elevated alert period, Crescent City was never placed above an Advisory.

WCATWC continued to monitor the tsunami as it was recorded at Midway (48 cm zero to peak) and in Hawaii (76 cm at Maui) (Fig. 4). The TWC projections were recomputed at 7:20 AM PST with the Shemya data and the closest DART station and suggested amplification on the northern California and southern Oregon coast’s and water levels of over 60 cm at Crescent City, considered near the threshold of damage. A fourth

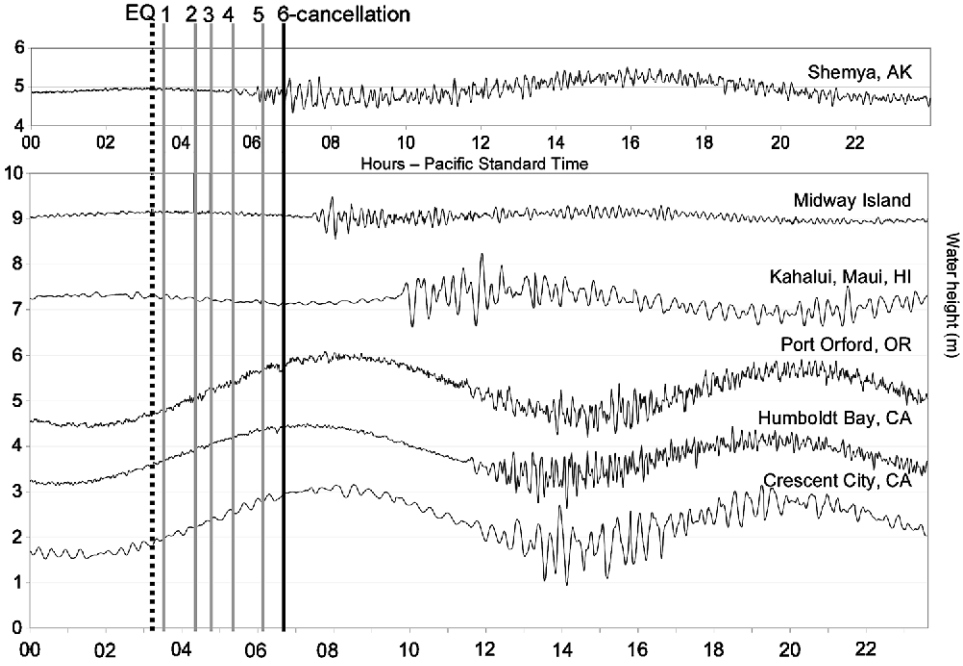

Figure 4
National Ocean Services (NOS) tide gauge recordings for six Pacific stations. Time (PST) of the earthquake and the six WCATWC bulletin times are noted. Figure courtesy of WCATWC.

TWC projection using two DARTs, and Shemya, Adak and Midway tide gauge data showed similar results. WCATWC was concerned that these water heights might cause problems at some localities in northern California and southern Oregon and contacted the State Warning Points in Oregon and California to tell them that the water range (peak to trough) might approach one meter but the tsunami was not expected to be damaging. The dispatcher at the California State Warning Point forwarded the information to Humboldt County, just south of Del Norte County, but was unaware that Crescent City was in a different county. In California, most of the State Office of Emergency Services (OES) officials were participating in a earthquake drill and, because the State was not placed in any official alert status under existing protocols, were not notified of the WCATWC concern and did not participate in the decision-making process. Humboldt County officials did forward the message to Del Norte County OES and also contacted the Eureka Forecast Office of the National Weather Service (NWS).

4. November 15, 2006 Response and Impacts at Crescent City

Humboldt and Del Norte County emergency managers in discussion with the NWS Eureka Forecast office became convinced that the tsunami threat was real and deployed

sheriff and Coast Guard personnel to clear the beach and harbor areas in both counties. The Crescent City small boat basin and the outer basin were cleared of most people by 11:30 AM PST. The Harbor Master and several other people at the harbor in Crescent City observed a modest rise and lowering of the water level between 11:40 and noon and the Crescent City tide gauge recorded an initial 38 cm peak to trough water level change (Fig. 4). People in the harbor area were surprised to observe extremely strong currents starting around 1 PM PST. The Harbor Master noticed boats rocking in the harbor and went with an assistant to secure boats on F and G Docks. He did not associate the strong currents with the tsunami event and was unaware that a tsunami event lasted longer than the first surge (Young, personal communication; KELLY *et al*., 2006). The Harbor Master described the tsunami as a river in flood within the harbor and estimated the currents at 10 to 12 knots. The currents were strong enough to completely submerge a tethered 0.7 m diameter float near the mouth of the basin (Fig. 5). The strongest currents were observed between 2 and 2:30 PM, associated with the sixth tsunami oscillation, a peak-to-trough water level change of 1.76 m (Fig. 3).

Dock G, closest to the entrance of the boat basin broke up first. Three boats were moored to Dock G and two, moored directly to the dock, were set adrift. A third was moored directly to the piling and remained secured. Floating sections of Dock G collided with Dock F as it began to fail and G F sections piled into Dock E, causing extensive damage (Figs. 6a, c, d). As the slips broke off and converged, two boats were popped onto the docks (Fig. 6b). Fortunately there were few boats moored at the most extensively damaged docks. Harbor Master Richard Young attributed the dock breakup to the currents pinning the pile ring against the pilings. The small boat basin was built in the early 1970s and the floating docks were connected to the metal pilings by a metal pile ring. The docks were unable to adjust to the changing water level allowing about a half meter of water to flow over the surface (Young, personal communication) (Fig. 7). The

Figure 5
Entrance to small boat basin during peak surge. Note the water boil in the foreground. Arrow points to a 0.7 m diameter tethered float that is nearly completely submerged by the flow. Photo by A. Winogradov.

Figure 6
Damage in the Crescent City small boat basin. A) Broken sections of Dock F. B) Sail boat popped up on dock by slips converging. C) Displaced slips of Dock F. D) Bolt connecting slip to dock pulled from concrete.

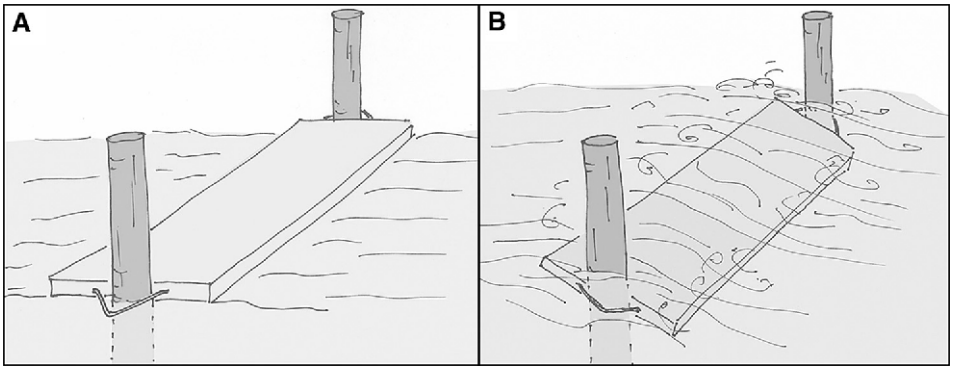

Figure 7
Schematic of the small boat basin floating docks. A) Floating docks in the small boat basin are attached to metal pilings by metal pile rings. Under normal conditions the pile rings do not constrict movement and the buoyant docks can adjust to changing water levels. B) During the tsunami, strong currents pushed the pile rings against the pilings creating friction that resisted the buoyancy forces of the dock. Over a foot of water was observed flowing over the tops of the docks.

currents pulled the pile ringbolts out of the concrete dock and broke the braces supporting the slips (see Fig. 6d). Young and an assistant were on the docks as they began breaking up, and were fortunately able to get out of the dock area before the worst damage occurred.

It was low tide when the strongest surges occurred and the tsunami never caused the water level to exceed the normal tidal variation. The initial damage estimates (Winogradov, personal communication) were on the order of $700,000 and State OES officials decided that it was not necessary to request an official State Emergency declaration. An underwater assessment of the docks conducted four months later showed extensional cracks in most of the floating docks in the basin. In addition, the county will be required to put extensions on the pilings and caps on the top so that it will be impossible for the floating docks to be lifted off of the piling. The most recent estimate to replace the floating docks and modify the pilings is $9.2 million (Winogradov, personal communication). As of December 2008, no repair work had begun.

The November 15 tsunami was observed throughout the Pacific basin. In Hawaii, surges of water overran the parking lot at the small boat harbor at Nawiliwili Bay on Kauai, and reached the highway near Laniakea on Oahu. A woman swimming at Waikiki suffered cuts when she was sucked through an opening in the seawall as the water receded. On the central California coast at Santa Cruz, the tsunami tossed boats in the harbor and momentarily trapped two boaters in a small sailboat against a dock. Post-tsunami field surveys in 2007 measured peak runup elevations reaching 20 m in the unpopulated Kuril Islands near the epicenter (BOURGEOIS *et al.*, 2007). Only at Crescent City, was the damage significant.

5. Discussion

The December 26, 2004 Indian Ocean tsunami brought an awareness of tsunamis to the global community and focused much scientific and mitigation attention on extreme tsunami events. The November 15, 2006 tsunami illustrates the opposite end of the tsunami spectrum and highlights the vulnerability of harbors from a relatively modest tsunami. There are four issues this event brings to the fore.

1) *Awareness*: First and most important, the November 15 tsunami underscored a persistent problem for tsunami hazard mitigation — a lack of awareness of both government officials and the public of what a tsunami looks like and how long the danger period may persist. Crescent City has a history of tsunamis and much greater awareness than most coastal communities. Tsunamis are featured prominently on banners throughout the town; there are many interpretive signs, photos and high water marks from the 1964 tsunami. However, no one we interviewed was aware that a tsunami could manifest as strong currents, could gain in strength after the first surge and might last several hours (KELLY, 2006). There was also little awareness of previous tsunamis in the area, other than 1964.

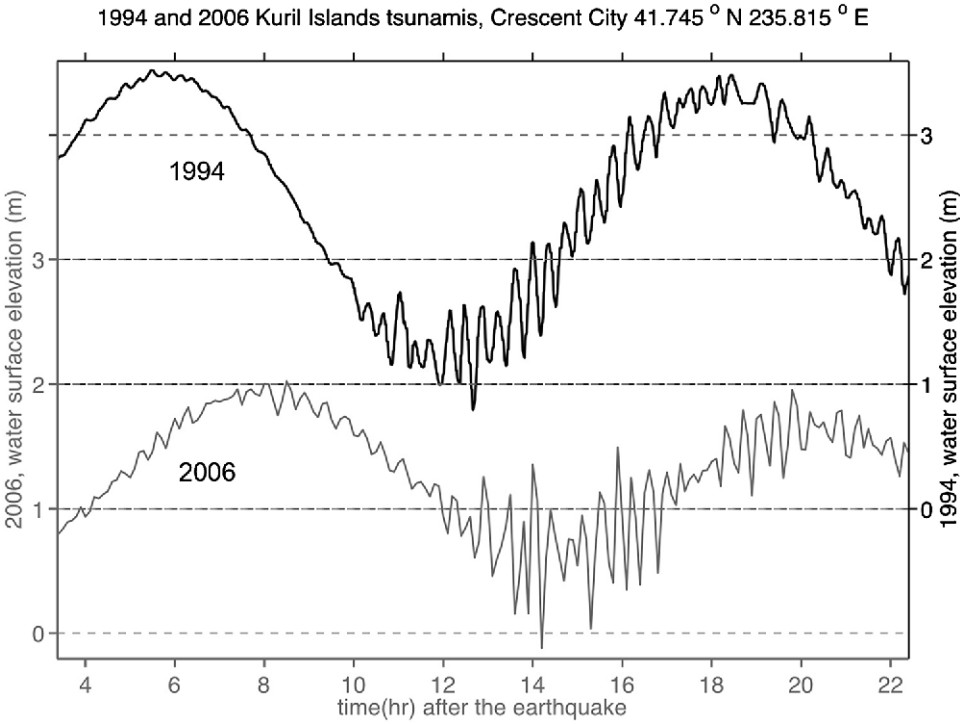

Figure 8
Crescent City marigrams of Kuril Islands tsunamis relative to travel time from the source. Upper plot, October 4, 1994; lower plot, November 15, 2006. In both cases the largest amplitude cycles are delayed from the initial onset by several hours.

On October 4, 1994 a similar-sized earthquake occurred in the Kuril Islands, about 500 km southwest of the 2006 earthquake. It had the same magnitude and triggered tsunami alert bulletins that culminated in a tsunami warning for the entire Pacific basin. At Crescent City, boats were evacuated from the harbor and stayed offshore for five hours. The 1994 marigram from Crescent Harbor (Fig. 8) was remarkably similar in character to 2006. The largest amplitude signal was the seventh cycle, and arrived a little more than two hours after the first wave. The 1994 tsunami lasted at least through an entire tidal cycle.

No one in the Harbor District or in the local government was aware that recordings of the 1994 tsunami existed and when we showed them the record, they wished they had been aware of them early in the event. Past events always carry a caveat, however. The 1994 event, generated by the same size earthquake in nearly the same location produced peak amplitudes only half that of the 2006 event and no damage. Four other Kuril Islands-generated tsunamis had been recorded at Crescent City prior to 2006 and none caused damage. Subtle changes in fault orientation can make significant differences in

directionality of the tsunami, and, in locations like Crescent City, make the difference between a damaging and non-damaging event (DENGLER *et al*., 2008). The 2006 event underscores the need for conservatism in emergency response; relying too heavily on past events in this case might have lowered the threat assessment. The boundary between no damage and significant damage is very narrow at Crescent City, and response should err on the side of caution.

Tsunami education programs must incorporate what is known about the characteristics of tsunamis in a particular region, the range in potential events and repeat over and over that the first surge in locations like Crescent City is never the largest.

2) *The Warning System*: The 2006 tsunami brought out a weakness in the existing tsunami warning product suite. All of the damage at Crescent City occurred more than 6 hours after alerts had been cancelled by WCATWC. At the time of the event, there were only two categories of bulletins: Alert (Warning, Watch, Advisory) status that put a large region into the same status, and Information, which meant there was no threat level. The difference in the three Alert status levels referred to the threat horizon: Warning meant a potentially damaging tsunami would arrive within 3 hours, Watch between 3 and 6 hours and Advisory status meant the first arrival was at least 6 hours away. WCATWC was faced with the choice of putting the entire region of northern California and southern Oregon into a Warning, or issuing no alert at all. The forecast tools correctly predicted that there was no Pacific-wide tsunami threat and it would have been inappropriate to evacuate all of the coastal areas in the region. WCATWC and local officials developed an *ad hoc* response to the situation, initiating an informal dialog that largely worked. Beach areas and harbors were cleared and no one was injured in the event. However, by the time this dialog occurred, it was too late to safely take boats in the harbor to deep water and some avoidable damage did occur.

WCATWC and state and local emergency officials were able to use the lessons of the 2006 tsunami to develop a new warning product suite that redefined Advisory to include threats to localized areas like Crescent City without throwing an entire region into an elevated status.

> *"A tsunami advisory is issued due to the threat of a potential tsunami which may produce strong currents or waves dangerous to those in or near the water. Coastal regions historically prone to damage due to strong currents induced by tsunamis are at the greatest risk. The threat may continue for several hours after the arrival of the initial wave, but significant widespread inundation is not expected for areas under an advisory. Appropriate actions to be taken by local officials may include closing beaches, evacuating harbors and marinas, and the repositioning of ships to deep waters when there is time to safely do so. Advisories are normally updated to continue the advisory, expand/contract affected areas, upgrade to a warning, or cancel the advisory."* (WCATWC message definition)

This new product, implemented in early 2008, was used on an interim basis on January 13, 2007 when a M_w 8.1 earthquake occurred close to the 2006 epicenter. The initial

magnitude estimate was 8.4 and there was concern of similar or greater impacts, especially because of the weakened state of the surviving docks. Hourly conferences between WCATWC, regional NWS forecast offices and regional/state emergency officials were held with a considerable improvement in the flow of information to local coastal jurisdictions. SIFT forecasts were made more widely available and updated as DART water height measurements became available. The magnitude was downgraded to 8.1, recorded water heights were below that of 2006, and SIFT projected water heights were on the order of half the 2006 levels, and it was deemed that no tsunami threat existed. In Crescent City, officials contacted all of the boat owners in the harbor, informed them of the event and gave them the option of taking their boats out of the harbor. No one chose to evacuate and the general consensus was that communications worked well (Winogradov, personal communication).

3) *Tsunami currents*: Strong currents caused all of the damage at Crescent City. The Harbor Master estimated the current velocity between 10 and 12 knots based on the visual appearance. No video footage was taken of the event and there are no direct ways to measure the flow rate. Numerical modeling (DENGLER *et al.*, 2007) gave an average current velocity at the Crescent City tide gauge location of about 0.6 m/sec, an order of magnitude smaller than the Harbor Master estimates. The floating docks in the harbor failed because the strong currents pinned the pile rings against the pilings so that they were unable to adjust to the rapidly changing water levels. Newer dock/piling connecting systems that employ rollers may solve this problem, nevertheless it is essential to understand the current regime to develop design solutions.

What happened on November 15, 2006 was not unique to Crescent City's harbor. All harbors are vulnerable to the strong currents produced by tsunamis. Without an understanding of the velocity regime, design solutions are only guesses. There are no measuring systems deployed at present to measure the strong currents produced by tsunamis. Crescent City's harbor is an ideal location to develop such an instrumentation system. Modest tsunamis are recorded at Crescent City with an average recurrence of about two years. Understanding the tsunami current regime is an essential first step to designing structures to resist tsunamis in harbors and also an important parameter in calibrating numerical models.

4) *Crescent City's tsunami vulnerability:* The 2006 tsunami reignited the debate about the cause of tsunami amplification at Crescent City. Research efforts in the 1960s (WIEGEL, 1965; WILSON and TORUM, 1967, 1968; ROBERTS and KAUPER, 1964; KEULEGAN, 1969) looked at focusing, edge waves and resonance. More recent studies (USLU *et al.*, 2007; USLU, 2008; KOWALIK *et al.* 2008; and HORRILLO *et al.*, 2008) examine distant and near-shore bathymetry and scattering impacts.

There is no way to resolve this debate without better data on how the northern California and southern Oregon coasts respond to tsunamis. There is presently only one NOS (National Ocean Service) tide gauge besides Crescent City between Cape Mendocino, California and Gold Beach, Oregon. The North Spit gauge in Humboldt Bay near Eureka, California is located in very shallow water inside the mouth of

Humboldt Bay and does not give an open coast response. WIEGEL (1965) speculated that the amplification at Crescent City was not confined to Crescent Harbor and likely occurred over a large area — from Patricks Point about 65 km south of Crescent City to Point St. George, 10 km to the northwest. WCATWC forecast tools suggest an area of amplification over an even larger area, from Cape Mendocino to Port Orford, Oregon. To solve the debate, more tidal instrumentation is needed along the northern California and Oregon coasts. At the minimum, existing instruments at Trinidad, California 75 km south of Crescent City and Brookings, Oregon 35 km north, should be upgraded to a one minute sampling so they can be used for tsunami research. Ideally, additional instruments should be installed at selected locations along the northern California and Oregon coast's to solve the edge wave, resonance, focusing debate.

6. Conclusion

The 2006 tsunami highlighted the vulnerability of harbors from a relatively modest tsunami, problems with the tsunami warning system for a marginal event, awareness issues and the particular susceptibility of the Crescent City harbor area. A marginal tsunami event such as that generated by the 2006 Kuril Islands earthquake was capable of causing nearly $10 million in damages. The strongest surges arrived at low tide and the same event may have caused even more damage at a higher tide level. The event led to a redefinition of WCATWC products to allow for alerting selected vulnerable coastal locations. It also illustrated a persistent problem for tsunami hazard mitigation — a lack of awareness of both government officials and the public of the duration of tsunami hazard and the need to emphasize the long-time period over which a tsunami may pose risks in all education materials.

Tsunamis generated by the Kuril Islands and Japan trenches are not the worst-case tsunami scenarios for Crescent City. Crescent City is at greater risk from great events on the Alaska-Aleutian trench and near-source tsunamis generated by the Cascadia subduction zone (USLU *et al*., 2007; USLU, 2008). However, northwestern Pacific events in historic times have been the most frequent source region to generated tsunamis recorded at Crescent City and, as the 2006 tsunami illustrates, have the potential to have considerable financial impact and pose risks to the users of Crescent Harbor. What happened in Crescent City on November 15, 2006 could occur in any coastal community and it underscores the need to better understand the lower end of the tsunami spectrum and the boundary between damaging and non-damaging events.

Acknowledgements

We thank Paul Whitmore and Bruce Turner, WCATWC, for their willingness to discuss the warning protocol and sequence of events with us. Costas Synolakis provided

funding for Barberopoulou and Uslu to travel to Crescent City. The USGS supported A. Kelly's travel. We also thank Richard Young, Harbor Master, Allen Winogradov, Del Norte County OES, Dan Larkin, Humboldt County, OES and Jim Goltz, California OES for their recollections of the events. Thanks to the numerous Crescent City residents who shared their experiences and observations with us.

References

Abramson, H. (1998), *Evidence for tsunamis and earthquakes during the last 3500 years from Lagoon creek, a coastal freshwater marsh, Northern California*, unpublished Masters Thesis, Humboldt State University, Arcata, CA 95521, 76 pp.

Bernard, E., Mader, C., Curtis, G., and Satake, K. (1994), *Tsunami Inundation Model Study of Eureka and Crescent City, California*, NOAA Technical Memorandum ERL PMEL-103, National Oceanic and Atmospheric Administration, Seattle, Washington, 80 pp.

Bourgeois, J., Pinegina, T., Razhegaeva, N., Kaistrenko, V., Levin, B., MacInnes, B., and Kravchunovskaya, E. (2007), *Tsunami runup in the Middle Kuril Islands from the great earthquake of 15 Nov., 2006*, EOS Transact. Am. Geophys. Union *88* (52), Fall Meet Suppl., Abstract S51C-02.

Dengler, L. A. and Magoon, O.T. (2006), *Reassessing Crescent City, California's tsunami risk*. In Proc. 100th Anniversary Earthq. Conf., [CD-ROM], 18–22 April 2006, San Francisco, paper R1577.

Dengler, L., Uslu, B., and Barberopoulou, A. (2007). *Tsunami Hazard in Crescent City, California from Kuril Islands earthquakes*, EOS Transact. Am. Geophys. Union *88* (52), Fall Meet Suppl., Abstract S53A-1012.

Dengler, L., Uslu, B., Barberopoulou, A., Borrero, J., and Synolakis, C. (2008), *The vulnerability of Crescent City, California to tsunamis generated by earthquakes in the Kuril Islands region of the northwestern Pacific*, Seismol. Res. Lett. *79*(5), 608–619.

Garrison-Laney, C. (1998), *Diatom Evidence for Tsunami Inundation from Lagoon Creek, a Coastal Freshwater Pond, Del Norte County, California*, unpublished Masters Thesis, Humboldt State University, Arcata, CA 95521, 97 pp.

Horrillo, J., Knight, W., and Kowalik, Z. (2008), *Kuril Islands tsunami of November 2006: 2. Impact at Crescent City by local enhancement*, J. Geophys. Res. *113*, C01021, doi:10.1029/2007JC004404.

Kelly, A., Dengler, L., Uslu, B., Barberopoulou, A., Yim, S., and Bergen, K. (2006), *Recent tsunami highlights need for awareness of tsunami duration*, EOS Transact. Am. Geophys. Union *87* (50), 566–567.

Keulegan, G. H., Harrison, J., and Matthews, M.J. (1969), *Theoretics in the design or the proposed Crescent City Harbor tsunami model*, US Army Corps of Engineers.

Kowalik, Z., Horrillo, J., Knight, W., and Logan, T. (2008), *Kuril Islands tsunami of November 2006: 1. Impact at Crescent City by distant scattering*, J. Geophys. Res. *113*, C01020, doi:10.1029/2007JC004402.

Lander, J. F., Lockridge, P.A., and K, M.J. (1993), *Tsunamis affecting the West Coast of the United States 1806–1992*, NGDC Key to Geophysical Record Documentation No. 29, NOAA, NESDIS, NGDC, 242 pp.

National Geophysical Data Center (NGDC) (2008), *NOAA/WDC Historical Tsunami Data Base, Boulder, Colorado*, http://www.ngdc.noaa.gov/hazard/tsu_db.shtml

NOAA Center for Tsunami Research (2005), *Crescent City, CA 1960 and Hilo, HI 1964 Tsunamis*, http://nctr.pmel.noaa.gov/tsu_cc60hh64.html

Pacific Gas and Electric Company (PG&E) (2003), *Humboldt Bay ISFSI Safety Analysis Report, December 2003*, Report to the Nuclear Regulatory Commission, Washington D.C.

Roberts, J. A. and Kauper, E. A. (1964), *The effects of wind and precipitation on the modification of the South Beach, Crescent City, including An appendix on the focusing of tsunami energy at Crescent City*. Atmospheric Research Group.

Stein, S., and Okal, E.A. (2007), *Ultralong period seismic study of the December 2004 Indian Ocean earthquake and implications for regional tectonics and the subduction process*, Bull. Seismol. Soc. Am. *97*, No1A, doi:10.1785/0120050617

TOPPOZADA, T., BORCHARDT, G., HAYDON, W., and PETERSEN, W. (1995), *Planning scenario in Humboldt and Del Norte Counties, California for a great earthquake on the Cascadia subduction zone*, California Division of Conservation, Division of Mines and Geology Special Publication 115, 159 pp.

USLU, B. (2008), *Deterministic and Probabilistic Tsunami Studies in California from Near and Farfield Sources*, unpublished Ph.D. Thesis, University of Southern California, Los Angeles, CA.

USLU, B., BORRERO, J.C., DENGLER, L., and SYNOLAKIS, C.E. (2007), *Tsunami inundation at Crescent city generated by earthquakes along the Cascadia subduction zone*, Geophys. Res. Lett. *34*, L20601.

WHITMORE, P. (2007), personal communication, West Coast Alaska Tsunami Warning Center, Palmer, AK 99645.

WIEGEL, R.L. (1965), *Protection of Crescent City, California from tsunami waves*, Report for the Redevelopment Agency of the City of Crescent City, 5 March 1965, Berkeley, California, 114 pp.

WILSON, B.W., and TORUM, A. (1967), *Final Report: Engineering Damage from the Tsunami of the Alaskan Earthquake of March 27, 1964*, Coastal Engineering Research Center, Corps of Engineers, U.S. Army, Contract No. DA-49-055-CIVENG-66-6, Science Engineering Associates, San Marino, CA.

WILSON, B.W., and TORUM, A. (1968), *The tsunami of the Alaskan earthquake, 1964: Engineering evaluation,* Tech. Memo No. 25, Coastal Engineering Research Center, U.S.. Army Corps of Engineers, Washington, D.C., 401 pp.

WINOGRADOV, A. (2007), personal communication, Del Norte County Office of Emergency Services, Crescent City, CA 95531.

YOUNG, R. (2007), personal communication, Crescent City Harbor District, Crescent City, CA 95531.

(Received December 31, 2007, accepted June 17, 2008)
Published Online First: February 6, 2009

Pure appl. geophys. 166 (2009) 55–76
0033–4553/09/010055–22
DOI 10.1007/s00024-008-0438-1

Pure and Applied Geophysics

Validation and Joint Inversion of Teleseismic Waveforms for Earthquake Source Models Using Deep Ocean Bottom Pressure Records: A Case Study of the 2006 Kuril Megathrust Earthquake

TOSHITAKA BABA,[1,2] PHIL R. CUMMINS,[2] HONG KIE THIO,[3] and HIROAKI TSUSHIMA[4]

Abstract—The importance of accurate tsunami simulation has increased since the 2004 Sumatra-Andaman earthquake and the Indian Ocean tsunami that followed it, because it is an important tool for inundation mapping and, potentially, tsunami warning. An important source of uncertainty in tsunami simulations is the source model, which is often estimated from some combination of seismic, geodetic or geological data. A magnitude 8.3 earthquake that occurred in the Kuril subduction zone on 15 November, 2006 resulted in the first teletsunami to be widely recorded by bottom pressure recorders deployed in the northern Pacific Ocean. Because these recordings were unaffected by shallow complicated bathymetry near the coast, this provides a unique opportunity to investigate whether seismic rupture models can be inferred from teleseismic waves with sufficient accuracy to be used to forecast teletsunami. In this study, we estimated the rupture model of the 2006 Kuril earthquake by inverting the teleseimic waves and used that to model the tsunami source. The tsunami propagation was then calculated by solving the linear long-wave equations. We found that the simulated 2006 Kuril tsunami compared very well to the ocean bottom recordings when simultaneously using P and long-period surface waves in the earthquake source process inversion.

Key words: Earthquake, tsunami, Kuril subduction zone, waveform inversion.

1. Introduction

The vast majority of large teletsunami are generated by undersea earthquakes. Because these earthquakes generate seismic waves which travel much faster than the tsunami, it is possible to develop a warning system based on the use of the seismic waves to detect a potentially tsunamigenic earthquake well before the arrival of the tsunami at shores distant from the earthquake epicenter. In practice, the magnitude and location of an earthquake are used to infer whether there is the potential for generation of a large tsunami, in which case a warning is initiated and sea-level data are monitored to confirm

[1] Research Program for Plate Dynamics, Institute for Research on Earth Evolution, Japan Agency for Marine-Earth Science and Technology, 3173-25 Showa-machi, Kanazawa-ku, Yokohama 236-0001, Japan.

[2] Geoscience Australia, GPO Box 378, Canberra ACT 2601, Australia. E-mail: phil.cummins@ga.gov.au

[3] URS Group Inc., 556 El Dorado Street, Pasadena, California 91101, USA.

[4] Research Center for Prediction of Earthquakes and Volcanic Eruptions, Tohoku University, 6-6 Aza-Aoba, Aramaki, Aoba-ku, Sendai 980-8578, Japan.

whether or not a large tsunami has actually been generated. To our knowledge, more detailed seismic information about the properties of the earthquake that generated the tsunami, such as its slip distribution, is not currently used operationally in any tsunami warning system.

While teletsunami amplitudes are not expected to be strongly influenced by details of the slip distribution on the earthquake fault (GEIST and DMOWSKA, 1999), recent events have shown that there are important exceptions to this general rule. Events such as the $M_w = 9.3$ (STEIN and OKAL, 2007) Sumatra-Andaman earthquake of 2004, with a fault length of over 1200 km (see AMMON *et al.*, 2005 and CHLIEH *et al.*, 2007, among others), are so large that coastlines even 1,000 km distant from the earthquake are still within a fault length's distance from the rupture area and may therefore experience tsunami heights that are sensitive to the spatial distribution of fault slip. Even for smaller events, slip may be concentrated at depth on the megathrust, as in the $M_w = 8.7$ Nias earthquake of 28 March, 2005 (e.g., BRIGGS *et al.*, 2006), or it may be concentrated at shallow depth near the trench, as in the $M_w = 7.8$ Java earthquake of 17 July, 2006 (AMMON *et al.*, 2006). In such cases, the resulting tsunami may be much smaller or larger, respectively, than would be expected based on estimates of the earthquake magnitude alone. At least in cases such as these, detailed fault slip models would seem to be useful in modelling tsunami waveforms.

With recent advances in the number of seismographic stations telemetering data in real time, detailed seismic models of the earthquake source can potentially be obtained soon after an earthquake has occurred. This may allow rapid tsunami modelling to be performed that can contribute to tsunami warning information disseminated to potentially affected coastlines. There are many questions that need to be answered before such modelling can be utilized in the operation of a tsunami warning center. One fundamental question which this paper seeks to answer is: Can seismic data provide sufficiently accurate models of the slip distributions of large tsunamigenic earthquakes to be reliably used in teletsunami modelling? While both seismic (KIKUCHI and KANAMORI, 1991) and tsunami (SATAKE, 1987) data are routinely used separately to estimate slip distributions for large earthquakes, they are rarely used together (see, however, SATAKE, 1993; TANIOKA *et al.*, 1995; JOHNSON *et al.*, 1996; KONCA *et al.*, 2007; SATAKE and TANIOKA, 1995; DELOUIS *et al.*, 2002; KOKETSU *et al.*, 2004; ICHINOSE *et al.*, 2005 and CHLIEH *et al.*, 2007, for examples of joint inversion using various combinations of seismic, tsunami and geodetic data). One reason for this is that tsunami data have hitherto been taken from coastal tide gauges, which can be very sensitive to the shallow bathymetry in their immediate vicinity. This makes it very difficult to judge whether any discrepancy between observed tsunami waveforms and those predicted based on a fault slip model is due to an inaccuracy in the model, or to inaccurate (or poorly modelled) bathymetry. This situation has changed in recent years with the deployment of a network of ocean bottom pressure recorders (BPRs) in the Pacific Ocean, which record tsunami waveforms in the deep-ocean where they are less sensitive to small variations in bathymetry.

In this paper we consider the use of seismic data for determining the slip distribution of a magnitude 8.3 Kuril earthquake that occurred on 15 November, 2006. This

earthquake was the first large tsunamigenic earthquake to occur in the northern Pacific Basin since the establishment of networks of BPRs. Seismic body- and surface-wave data are used to estimate slip models for the earthquake, and these slip models are used to generate seafloor displacement that is used as an initial condition for tsunami propagation. The computed tsunami waveforms are then compared with data recorded by the BPRs to determine whether the seismic slip models are sufficiently accurate to be used in modelling teletsunami waveforms.

2. Seismic and Tsunami Observations of the 15 November, 2006 Kuril Islands Earthquake

As estimated by the USGS's National Earthquake Information Center (NEIC), the 15 November, 2006 Kuril Islands earthquake occurred at 11:14:16 UTC, with hypocentral parameters as indicated in Table 1. Although the earthquake caused no fatalities, it generated a teletsunami which injured one person in Hawaii and caused damage in Crescent City, California. Also listed in Table 1 are the Centroid Moment Tensor (CMT) estimates made by the NEIC and the Global CMT Project. Since both moment tensor solutions indicate a shallow thrust event, we assumed that this earthquake ruptured along the boundary between the subducting Pacific Plate and the North American Plate. Therefore, rather than adopting the strike and dip of either of the moment tensor solutions from Table 1, we used the strike of the Kuril Trench, 220°, and a dip, 10°, defined as the average dip of the plate boundary determined in a marine seismic survey of the Kuril Trench (NAKANISHI *et al*., 2004). We assumed that rupture occurred over a 400 $\times$ 140 km^2 area of this fault plane, with its upper edge along the trench axis. In the modelling of seismic waves and tsunami described below, we have divided this rupture surface into 20 $\times$ 20 km^2 square subfaults, with 20 subfaults along strike and 7 down the dip of the rupture area.

2.1 Seismic Data

Due to their relatively short wavelengths, seismic body waves have more potential to resolve spatial details of earthquake fault slip patterns than do surface wave or tsunami

Table 1

Source parameters for the 15 November, 2006 Kuril earthquake

Source	Lat.(°N)	Lon.(°E)	Depth (km)	Strike (°)	Dip (°)	Rake (°)	M_w
NEIC Hypocenter	46.61	153.23	30	-	-	-	-
NEIC MT	46.68	153.22	7	270	16	121	7.9
Global CMT	46.75	154.32	13	214	15	92	8.3
This study	46.68	153.22	20	220	10[1]	90 $\pm$ 45	8.4

Fault geometry parameters obtained from azimuth of trench axis and the seismic velocity model of NAKANISHI *et al*. (2004)

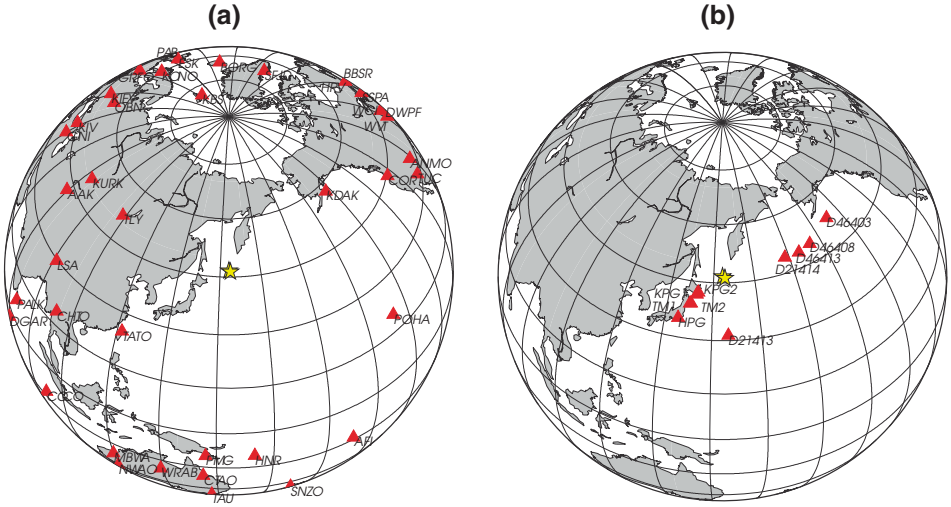

Figure 1
Geographic distribution of stations (triangles) that recorded observations of the 2006 Kuril earthquake used in this study: (a) Seismic stations, (b) ocean-bottom pressure (tsunami) gauges. Stars show location of the epicenters of the 2006 and 2007 Kuril earthquakes.

data. However, inversions for fault slip using only body-wave data may be less stable than those which use longer-wavelength data such as surface-wave or tsunami data. In this study we consider the use of surface-wave and body-wave data, both independently and jointly, to investigate the issue of stability vs. resolution. We downloaded the available GSN (Global Seismological Network) data from the Data Management Center of the Incorporated Research Institutions for Seismology. The seismic stations whose data were used to estimate the earthquake slip distribution are shown in Figure 1a. We have avoided stations closer than 30° and greater than 90° from the epicentre, to avoid waveforms which are sensitive to upper mantle structure or contain diffracted energy, respectively. All records had the instrument response removed via a 'water-level' deconvolution.

The 25 vertical P waveforms used in the inversion were bandpasss-filtered to remove energy outside the 4 mHz to 4 Hz passband. The time window used for the P-wave analysis was taken to include 190 sec after the arrival of the P wave. Following the method of KIKUCHI and KANAMORI (1991), point-source P-wave Green's functions are calculated for the center of each subfault using the Haskell propagator matrix method of BOUCHON (1976), which accounts for crustal structure and depth phases near the source. The observed P-wave arrivals are aligned with those on the synthetics to remove any travel-time anomalies due to laterally heterogeneous velocity structure along the source-receiver paths. Thus, the slip pattern obtained through P-wave analysis is constrained relative to the earthquake epicentre.

For surface waves, 24 Rayleigh and 22 Love waves were bandpass-filtered from 3.0 to 6.0 mHz, with a varying analysis window that depended on distance via Rayleigh and Love wave phase velocities appropriate for the 3.0–6.0 mHz passband. Point-source surface wave synthetics were calculated for each subfault using the method of KANAMORI and STEWART (1976) including phase velocity corrections for 3-D structure (EKSTRÖM *et al*., 1997). No arbitrary shifts are applied to the surface wave data, so that they do constrain the absolute position of slip pattern.

The near-source seismic velocity structure used for both body- and surface-wave calculations was based on a marine seismic survey result performed in the southern Kuril subduction zone (NAKANISHI *et al*., 2004).

2.2 BPR Tsunami Data

The locations of the BPRs used in this study are shown in Figure 1b. We downloaded data from Deep Assessment and Reporting of Tsunamis (DART, see e.g. TITOV *et al*., 2005) buoys in the northeastern Pacific, as well as from seafloor cable BPRs (HIRATA *et al*., 2002; IWASE *et al*., 2003) off Japan, from the web sites http://nctr.pmel.noaa.gov/Dart/ and http://www.jamstec.go.jp/scdc/top_e.html, respectively. We also used BPR data from other cable systems off Japan (TM1 and TM2, see Fig. 1b) operated by Tohoku University (KANAZAWA and HASEGAWA, 1997). These instruments record pressure fluctuations caused by phenomena such as ocean tides, seismic waves and vertical displacement at the seafloor as well as tsunami. In order to remove the non-tsunami signals from the data, we used a data processing procedure similar to that of HIRATA *et al*. (2003). In the tsunami frequency band, BPR pressure data are converted to sea-surface disturbances via $\Delta P = \rho g \Delta h$, where ΔP is water pressure fluctuation, ρ is the density of seawater (1.0 gm/cm^3), g is the gravitational acceleration at the earth's surface (9.8 m/s^2), and Δh is sea-level fluctuation. Short-period components such as pressure vibrations related to Rayleigh waves were removed by applying a block mean filter with a width of 100 sec to the original records (Fig. 2b). The theoretical tide at each BPR location was calculated using the Naotide software (MATSUMOTO *et al*., 2000) and was subtracted from the block-mean filtered data. Because some residual tidal signal remains after removing the theoretical tide, we also applied a high-pass filter with a corner frequency of 120 min, after which the dominant signal on all recordings was the tsunami. The first-arriving tsunami wave with a height of about 2.5 cm can be seen at KPG1 in Figure 2c.

For modelling the BPR data, we used finite-difference tsunami modelling software developed by SATAKE (1995), which solves the linear longwave equation including the Coriolis force. The tsunami computation area was defined from 120 E to 220 E and 15 N to 65 N to contain the ocean-bottom pressure gauges shown in Figure 1b. The bathymetric grid data with an interval of 2' was created by re-sampling the GEBCO bathymetry dataset (http://www.ngdc.noaa.gov/mgg/gebco/grid/1mingrid.html) in order to save computation time. Total grid points are 3000 $\times$ 1500 points. The time step used in the computation was 3 sec in order to satisfy the stability condition of the finite-

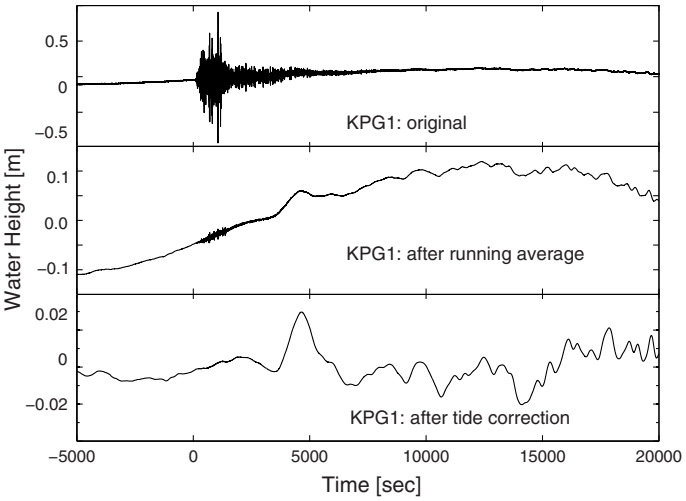

Figure 2
(a) Original water pressure fluctuation recorded at KPG1. The short-period disturbance due to seismic waves is seen. (b) After removal of the short-period components by a block mean filter. (c) Tsunami waveforms are retrieved after removal of the long-period ocean tide components.

difference scheme. The tsunami initial condition is assumed to be equal to the vertical ocean bottom deformation due to the faulting, which was computed using the equations of OKADA (1985).

3. *Inversion of Seismic Data for the 2006 Kuril Earthquake and Comparison with Deep-ocean BPR Data*

We employed an inversion to determine the temporal and spatial distribution of slip on the fault plane. Both surface and body waves were inverted for fault slip using the multiple-time window algorithm of THIO *et al.* (2004), which is a modified form of the slip inversion method developed by HARTZELL and HEATON (1983). This method involves the construction of the normal equations:

$$\begin{pmatrix} C_d^{-1}A \\ \lambda_1 S \\ \lambda_2 M \end{pmatrix} x = \begin{pmatrix} C_d^{-1}b \\ 0 \\ 0 \end{pmatrix}. \tag{1}$$

The elements of matrix **A** consist of Green's functions of seismic waves for body and/or surface waves, calculated as discussed above by using unit slip point sources at the center of each subfault, **S** is a matrix of smoothing constraints and **M** is a minimization criterion. λ_1 and λ_2 are hyperparameters which weight the smoothing and minimization criteria, respectively, and were chosen by trial and error as the maximum weights that did not significantly degrade the fit to the observed waveforms. Finally, C_d is a data

covariance matrix. Following HARTZELL and LANGER (1993) we use a diagonal matrix whose values are such that each trace in the vector *b* will have a peak value of 1. Thus, when body- and surface-wave data, and later tsunami data, are inverted simultaneously, they are all included with normalized amplitude, and no attempt was made to use any other relative weighting for the different datasets.

A least-squares inversion with positivity constraint is applied to the normal equations (1) using the Householder reduction method of LAWSON and HANSON (1974). As discussed by HARTZELL and LANGER (1993), among others, the positivity constraint is needed to prevent instability in the inversion, which may manifest itself in adjacent subfaults taking on equal and opposite slips. The rake angle of the slip was allowed to vary, however, within the range 90 $\pm$ 45 degrees.

The subfault underlying the epicenter determined by the USGS (Table 1) was used as the starting point for rupture in the inversion. The maximum speed of rupture propagation was assumed to be 1.8 km/sec, and each subfault was permitted to slip over 30 sec after the passing of rupture front. The slip on each subfault was parameterized with triangles of 5.0 sec half-width, so that each subfault could slip over 5 time steps of 5.0 sec duration, allowing for some variation in rupture velocity. The time step and triangle half-width were chosen to match the frequency content of the observed P-waves, and the assumption of 1.8 km/sec maximum rupture velocity was tested using the match of observed and predicted tsunami data described below.

3.1 Inversion of Seismic P-Waves

We first carried out a slip inversion using only direct P-wave data. The obtained cumulative slip distribution is shown in Figure 3a. An area of high slip appears in an "L-shape" pattern extending about 140 km to the northeast and mainly down-dip from the hypocenter. The maximum slip is 5.0 m. The total seismic moment obtained is 5.20×10^{21} Nm (M_w 8.4), which is larger than that estimated by the Global CMT project (3.4×10^{21} Nm). The variance reduction (VR) of the P waves determined by $(1-\Sigma(d_{obs}-d_{cal})^2/\Sigma d_{obs}^2)$ is 67%, where d_{obs} and d_{cal} indicate normalized observed and calculated waveforms, respectively. We also independently calculated the synthetic surface waves derived from the obtained source model and obtained the VR value of 56% for the surface waves (Table 2).

The predicted tsunami waveforms are shown in Figure 3b. The arrivals of the computed tsunami are about 2 or 3 min earlier, and the amplitudes are slightly smaller than these of the observed waveforms for the Japanese pressure gauges (KPG1, KPG2, TM1, TM2, HPG). We can see a second small peak (shown by arrows in Fig. 3b) on the observed tsunami records at KPG1, KPG2, TM1 and TM2, which is not reproduced in the simulation. The waveform fits for the DART stations (D21424, D46413, D46408 and D46403) are worse; the period of the computed tsunami is inconsistent with the observed waveforms. The first peaks of the computed tsunami are earlier than observed ones by several minutes. The VR of the tsunami waveforms was calculated to be 60%.

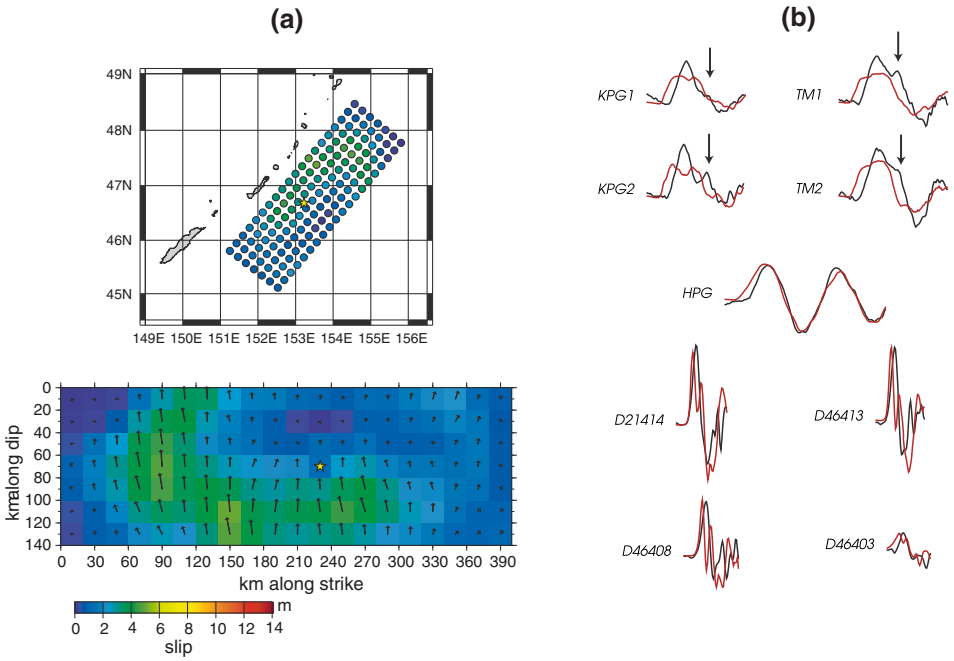

Figure 3

(a) Cumulative slip distribution of the 2006 Kuril earthquake estimated from the inversion of P waves only. The colour shows the slip amount and arrows represent the motion of hanging wall relative to footwall. The star denotes the hypocenter. (b) Comparison of the deep-ocean tsunami waveforms. Black and red lines show the observed and predicted tsunami waveforms, respectively, with the latter calculated from the slip model shown in (a). The small second peaks on the tsunami record (shown by arrows) are not produced by the simulation.

Table 2

Parameters describing slip models obtained using different combinations of P-wave, surface wave, BPR tsunami waveform data, and corresponding variance reductions

Data types used	Max. Slip (m)	Moment ($\times 10^{21}$ Nm)	P wave VR (%)	Surface VR (%)	BPR Tsunami VR (%)	Total VR (%)
P wave only	5.0	5.20	67	56	60	61
P wave and surface wave	12.8	5.33	58	84	73	73
P wave, surface wave, and BPR tsunami	11.8	5.01	58	84	81	74

3.2 Inversion of Seismic P-Waves and Surface Waves

The slip distribution obtained by using both P wave and long-period surface waves is quite different from the P-wave only model (Fig. 4a). The patch of highest slip is located near the trench just east of the epicenter. The maximum slip has increased to 12.8 m. A separate area of smaller slip is imaged farther down-dip. The total seismic moment is

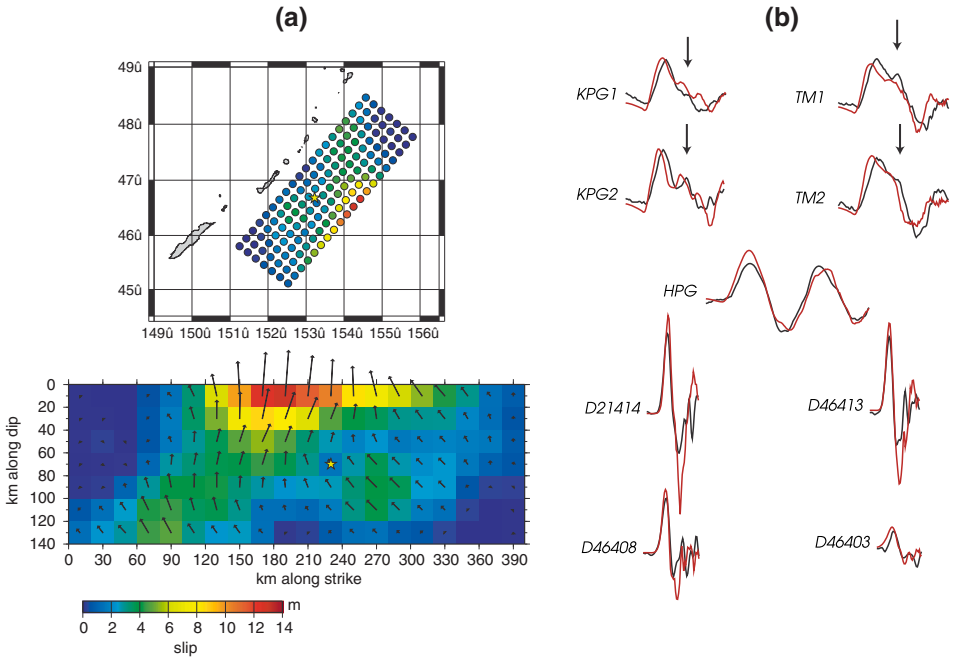

Figure 4

(a) Cumulative slip distribution of the 2006 Kuril earthquake estimated from the combined inversion of P waves and long-period surface waves. The colour shows the slip amount and arrows represent the motion of hanging wall relative to footwall. The star denotes the hypocenter. (b) Comparison of the deep-ocean tsunami waveforms. Black and red lines show the observed and predicted tsunami waveforms, respectively, with the latter calculated from the slip model shown in (a). The small second peaks on the tsunami record (shown by arrows) are produced by the simulation.

about 5.33×10^{21} Nm. The VR values of 58% and 84% are obtained for the P wave and the surface waves, respectively, for this model. This indicates that the waveform fitting of the surface waves is much improved without a substantial deterioration of the P-wave fit (Table 2).

In Figure 4b, we compare the observed tsunami waveforms with the predicted ones from the source model. For KPG1, KPG2, TM1, and TM2, the tsunami waveforms match the observations better than the simulation derived from the inversion based on P waves only. The maximum amplitudes are well retrieved and the waveforms are very similar to the observed waveforms. The small peaks in the first tsunami wave (shown by arrows in Fig. 4b) are also seen in the simulated tsunami waves. However, for these BPRs the calculated tsunami waveforms appear to arrive about 2 min earlier than the observed waveforms. This may indicate that the accuracy of the bathymetric data is insufficient to predict the tsunami travel times. To reach the Japanese stations, the first tsunami waves propagate along the Kuril trench, where rapid changes in seafloor topography may not be accurately represented in the bathymetry data. The accuracy of the bathymetric data will

be discussed below. The timing of the maximum peaks and period of the tsunami waveform are better predicted in the simulation for the D21414, D46413, D46408 and D46403. However, the first draw-downs following the maximum peaks on the computed tsunami waves are much larger than the observations. The VR of the tsunami waveforms is 73%, which is better than the result using only the P waveforms.

3.3 Inversion of Seismic P-Waves, Surface Waves, and BPR Tsunami Waveforms

All the data, the P wave, the long-period surface wave and the BPR tsunami waveforms, were finally inverted to estimate our preferred source model for the 2006 Kuril earthquake (Fig. 5a). The pattern of the cumulative slip distribution does not change from the result of the P and surface wave inversion, while the slip amount is slightly decreased. The maximum slip was estimated to be 11.8 m in the shallowest subfault near the trench. The total moment is 5.01×10^{21} Nm, which is equivalent to M_w 8.4. The VR of the P and surface waves are still good, at 58% and 84%, respectively. The

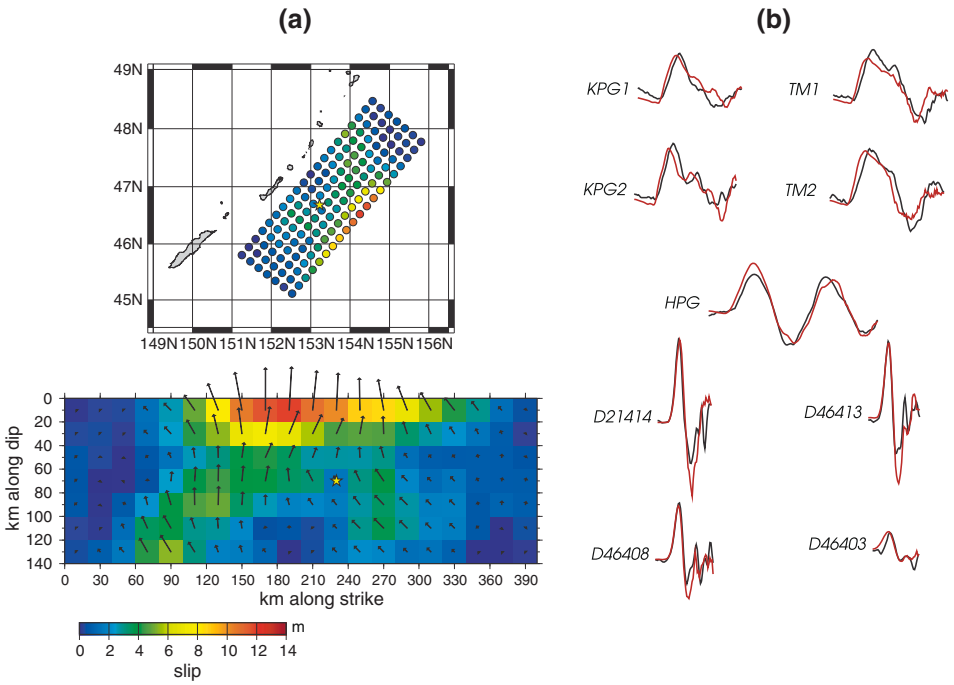

Figure 5

(a) Cumulative slip distribution of the 2006 Kuril earthquake estimated from the simultaneous inversion of P waves, long-period surface waves and tsunami. The colour shows the slip amount and arrows represent the motion of hanging wall relative to footwall. The star denotes the hypocenter. (b) Comparison of the deep-ocean tsunami waveforms. Black and red lines show the observed and calculated tsunami waveforms respectively, with the latter calculated from the slip model shown in (a).

offshore tsunami waves are also reproduced well, especially at DART stations, where the computed amplitude, timing and period of tsunami waveforms adequately fit the observations (Fig. 5b). The VR of the tsunami waveforms is better (81%) than obtained above, which is obviously due to the fact that the tsunami waveforms were inverted together with the seismic waves. A comparison of observed and calculated the P and surface waves are shown in Figure 6.

4. Discussion

Models for the slip distribution of the 2006 Kuril earthquake obtained in recent studies (FUJII and SATAKE, 2008; JI, 2007; AMMON *et al.*, 2008; YAGI, 2006; and YAMANAKA, 2006) are summarized in Table 3. Except for YAGI (2006), all of the models indicate that most of the fault slip occurred over an area that extends from about 100 km east to 200 km northeast of the hypocenter (see, e.g., Fig. 4). The seismic models of JI (2007), YAMANAKA (2006), and this study all exhibit pronounced peaks in slip about 100 km due east of the hypocenter, while the tsunami model of Fujii and Satake and the seismic model of AMMON *et al.* (2008) each show a less peaked slip distribution, with maximum slip located about 200 km northeast of the hypocenter. The models exhibit considerable variation in maximum slip and seismic moment.

The main differences between the slip pattern obtained here and in the other recent studies are the pronounced peak in slip 100 km east of the hypocenter and the high seismic moment, of over 5×10^{21} Nm. We found that increased smothing in our inversion resulted in models similar to those of FUJII and SATAKE (2008) and AMMON *et al.* (2008), having a considerably reduced maximum slip. This increase in smoothness, however, came at the expense of a poorer fit to the Love waves used in our inversion. We note that Love waves were likewise used in the inversion of JI (2007), which also had a sharp peak in slip 100 km east of the hypocenter, but were not used in AMMON *et al.* (2008), whose model was not sharply peaked. Also, 1-D velocity models with decreasing rigidity at shallow depth were used to convert from moment to slip in this study and that of JI (2007), which would amplify slip at shallow depth where these studies exhibit sharp peaks in slip, compared to the constant rigidity used in the model of AMMON *et al.* (2008).

While the seismic models of JI (2007) and AMMON *et al.* (2008) have moments higher (18% and 39%, respectively) than the GlobalCMT value of 3.3×10^{21} Nm (http://www.globalcmt.org), the moment obtained here is even more so—by over 50%. The high moment of our model relative to these other seismic models is due to the fact that we assumed a relatively shallow fault dip, based on the seismic survey of NAKANISHI *et al.* (2004). The well-known trade-off of dip with seismic moment (KANAMORI and GIVEN, 1981) accounts for an increase in our estimated seismic moment of 46% over the GlobalCMT fault model with 15° dip. This trade-off also explains why the larger dip used in YAMANAKA (2006) has resulted in a seismic moment 35% less than the GlobalCMT result. On the other hand, the tsunami model of FUJII and SATAKE (2008) appears to have a

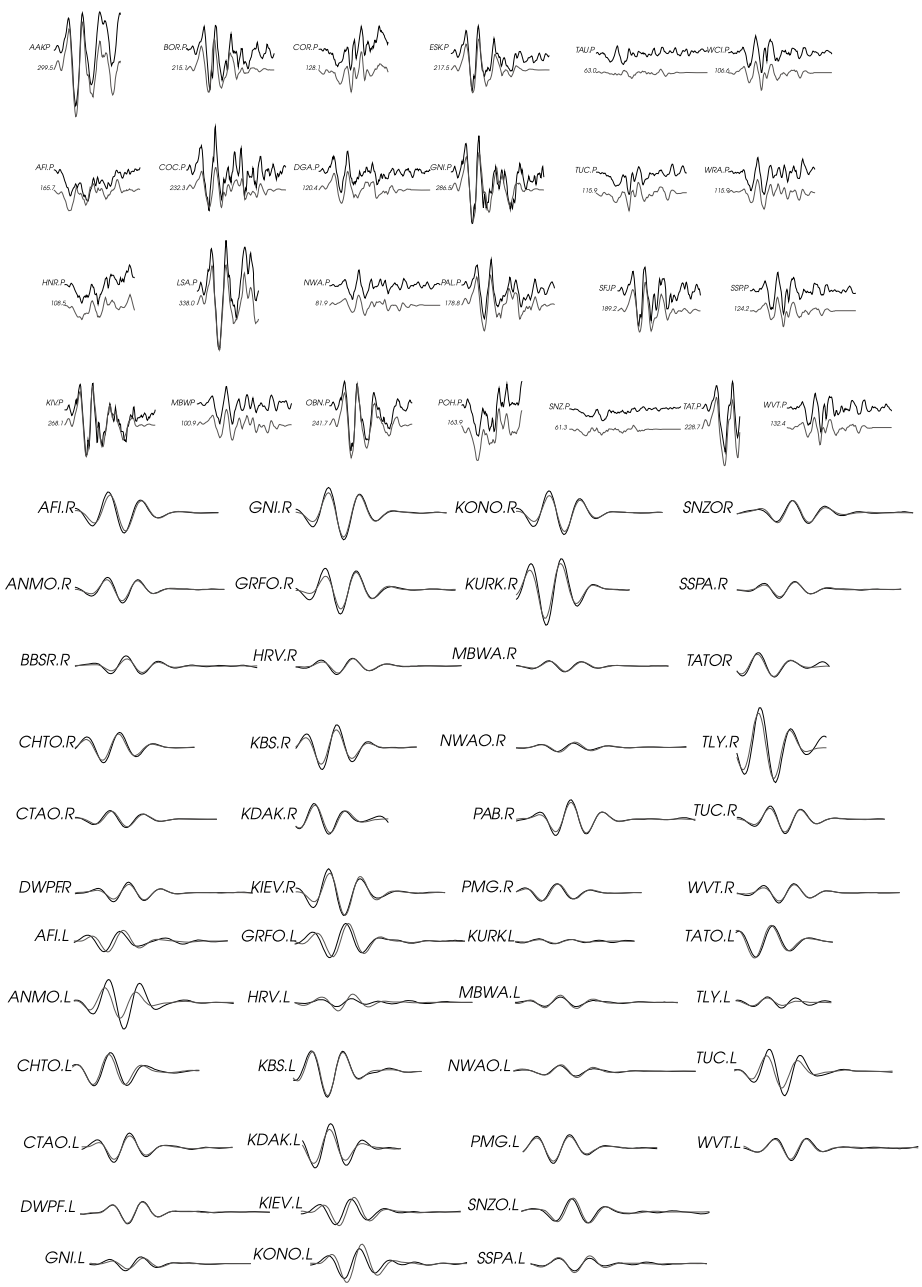

Figure 6
Comparison between observed (black) and calculated (red) waveforms for all seismic waves used in the simultaneous inversion for the 2006 Kuril earthquake. Station names and components (P: P wave, R: Rayleigh wave, L: Love wave) are shown.

Table 3

A comparison of models of fault slip for the 2006 Kuril earthquake estimated by recent studies

Study	Strike (°)	Dip (°)	Depth (km)	Max. Slip (m)	Moment ($\times 10^{21}$ Nm)
FUJII and SATAKE (2008)	214	15	5–31	6.8	2.0
	214	8–15	5–24	7.4	2.5
JI (2007)	220	15	8–40	9	3.9
AMMON *et al*. (2008)	215	15	17–52	7	4.6
YAGI (2006)	214	15	2–36	7.7	1.6
YAMANAKA (2006)	220	25	5–30	12.6	2.1
This study: P and surface wave P,	220	10	17–42	12.8	5.3
surface wave, and BPR	220	10	17–42	11.8	5.1

seismic moment considerably less than the GlobalCMT value—40% less for the constant dip case, even though it has the same dip as the GlobalCMT solution. We speculate that this may be due to the large subfaults (50 km × 50 km) used in this model, which have resulted in appreciable slip at shallow depth—about 5 m at 5 km depth. Since our fault model allows slip to be concentrated at greater depth, it can accommodate the higher slip required for agreement with the seismic data without resulting in an overprediction of the tsunami amplitude (since slip at greater depth is less efficient at generating a tsunami through seafloor deformation). Finally, we note that an up-dip limit of rupture at 10–15 km depth is consistent with the seismogenic zone inferred by NAKANISHI *et al*. (2004) for the southern Kuril subduction zone, based on the rupture area of the 1973 Nemuro-oki earthquake and thermal constraints on the frictional properties of the Kuril megathrust.

Below we consider other aspects of our slip model for the 2006 Kuril earthquake, including constraints on rupture velocity, the accuracy of bathymetry data for modelling the tsunami data, as well as the possibility that excitation and dispersion of tsunami energy may not be adequately accounted for in our tsunami modelling.

4.1 Constraints on Rupture Velocity

The pattern of slip is potentially sensitive to the maximum rupture velocity assumed in the inversion. For a given source duration, fault slip is spread over a wider area when the rupture velocity is high, and it is conversely concentrated when the rupture velocity is low. In order to find the optimal maximum rupture speed of the 2006 Kuril earthquake, we draw curves of VR of the P and surface waveforms calculated from slip models obtained by varying the maximum rupture speed in a range from 1.5–2.5 km/sec (Fig. 7). It is difficult to find the maximum point of the P and surface wave VR curves, indicating that the seismic data do not constrain the maximum rupture speed well.

We simulated tsunami waveforms derived from the source process obtained by changing the maximum rupture velocity and calculated the VR for the tsunami

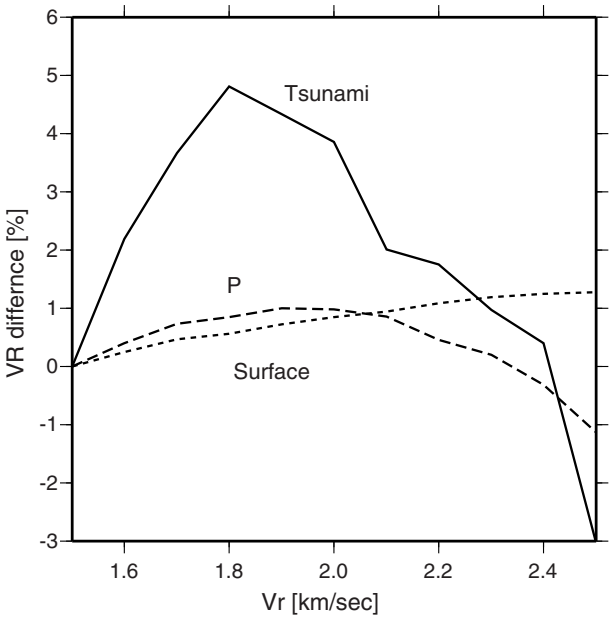

Figure 7
Relationship between variance reductions and the maximum rupture velocity (Vr) for the 2006 Kuril earthquake.

waveforms (Fig. 7). The maximum tsunami VR is successfully found at the maximum rupture speed of 1.8 km/sec. By itself tsunami data cannot resolve rupture velocity, because rupture speeds are much faster than the velocity of tsunami propagation—the tsunami velocity is only about 0.2 km/sec over water depths of 4000 m. However, tsunami data can help resolve rupture velocity when used in conjunction with seismic data, because its sensitivity to the slip pattern can resolve the trade-off in rupture area vs. rupture velocity inherent in the use of teleseismic data. A maximum rupture velocity of 1.8 km/sec was therefore applied for all inversions for the 2006 Kuril earthquake.

4.2 Accuracy of Bathymetric Data

Tsunami in the deep-ocean propagates at a velocity proportional to the square root of ocean depth. Although the GEBCO bathymetric dataset used for the tsunami calculations presented above is gridded at 1', the resolution of the original bathymetric soundings used to construct the grid can be much sparser. Especially near rapid changes in seafloor topography such as ocean trenches, gridded bathymetry data sets such as GEBCO may include significant errors in bathymetry. Even though deep-ocean tsunami calculations are less sensitive to errors in bathymetry, such errors gradually accumulate in tsunami calculations over long distances, and may result in a difference in tsunami waveforms in

Table 4

Comparison of water depths at the BPRs used in this study

	OBPG (m)	GEBCO (m)	Difference (m) (OBPG-GEBCO)
KPG1	2279	2218	+61
KPG2	2233	2210	+23
THK1	1563	1563	0
THK2	954	1007	–53
HPG1	1176	756	+420
D21414	5311	5511	−200
D46413	5572	5632	−60
D46408	5372	5242	+130
D46402	4711	4732	−21
D46403	4510	4484	+26
D51407	4710	4710	0

far-field. We here discuss the accuracy of the bathymetric data used in our tsunami calculation.

The ocean bottom pressure is an independent measurement for the water depth, which can be inferred from the hydrostatic condition expressed by $P = \rho gh$, where P is ocean bottom pressure, ρ is density of water, g is gravitational acceleration and h is water depth. We here compare the water depths observed at BPRs and included in the GEBCO bathymetric dataset used in the tsunami calculation in Table 4. The water depths measured by BPRs are consistent with the GEBCO data set at several sites. Especially at THK1 and D51407, the differences are less than 1 m. However, significant differences of more than 100 m in the water depth are seen at three sites. The maximum difference reaches 420 m at station HPG1 located near a small island (Hatsushima), where the seafloor topography is complicated. A comparison of high-resolution swath bathymetry data around the Japan Trench surveyed by the Japan Agency for Marine-Earth Science and Technology with the GEBCO dataset shows a systematic discrepancy up to 600 m along the Japan Trench axis (Fig. 8). The GEBCO bathymetric dataset was used for the far-field tsunami calculation in the finite-difference scheme because it covers the whole Earth with uniform gridding space. However, such a global dataset may not accurately represent rapid changes of topography that occur in areas such as ocean trenches.

The Kuril trench axis is also a region where bathymetry changes rapidly and which the tsunami must pass over in order to arrive at the Japanese BPRs. We do here a trial calculation of the tsunami travel times to estimate whether an error in the bathymetric data could explain the observed difference in tsunami travel time. Tsunami propagation speed is expressed by square root of gh, which is 264 m/sec over the trench axis, assuming an average water depth of 7000 m. We next suppose that the water depth is deeper by 600 m, based on the comparison with the high-accuracy sea beam data, that is 7600 m, and the tsunami speed becomes 275 m/sec. The distance from the epicenter of the 2006 Kuril earthquake to KPG1 is about 900 km. This difference in the water depths

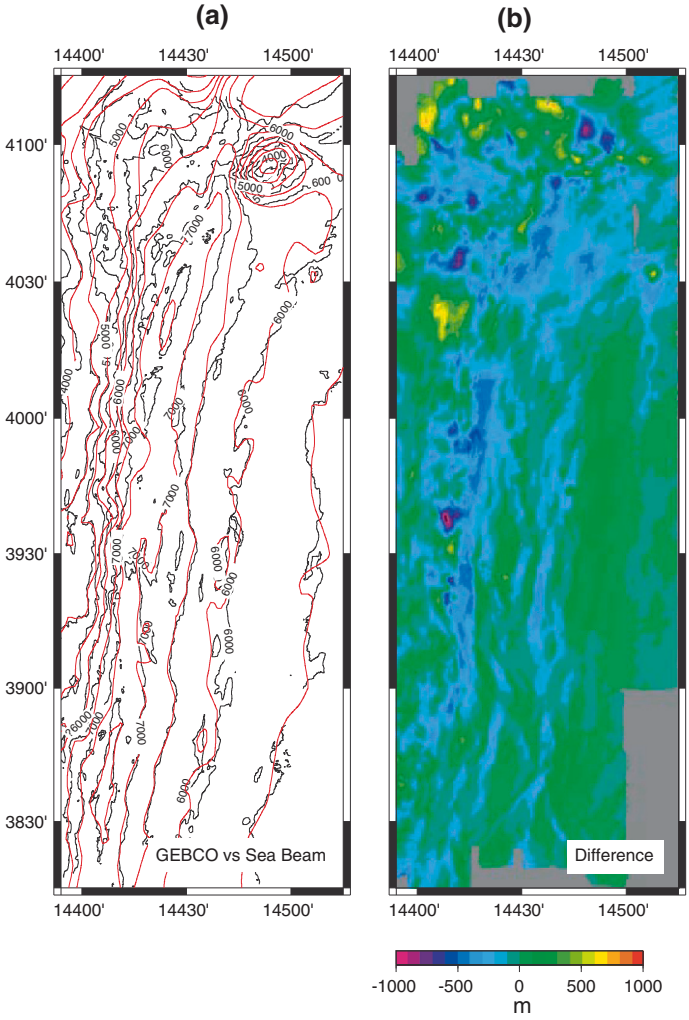

Figure 8

(a) Comparison of the GEBCO bathymetric dataset (red contours) and the high-resolution swath bathymetry data (black contours) around the Japan Trench. (b) The difference between GEBCO and the swath dataset.

produces a difference in the tsunami travel times of about 2 and half minutes at KPG1. As shown in Figure 5b, the calculated tsunami waveforms appear shifted in time by 2–3 minutes earlier than the waveforms observed on the Japanese BPRs, which would be consistent with a bathymetry error of 600 m along the Kuril Trench. Thus, the discrepancy in observed and calculated tsunami arrival times for BPRs along the Japanese coast may be due to water depths along the Kuril trench axis that are shallower by several hundreds meters on average than the bathymetric dataset we used in the tsunami calculation.

4.3 Initial Sea-surface Elevation and Tsunami Waveform Dispersion

As discussed in TANIOKA *et al*. (2008) and RABINOVICH *et al*. (2008), the procedure used here to calculate the initial sea-surface elevation, which assumes it is identical to the vertical coseismic displacement of the sea floor, is not valid for small-scale sources in deep water. This issue can be addressed by either applying the technique of KAJIURA (1963) to smooth the spatial pattern of seafloor displacement, or by numerically simulating the three-dimensional hydrodynamical response of the ocean to a sudden shift in the seafloor. RABINOVICH *et al*. (2008) adopted the latter approach when computing tsunami from both the 2006 Kuril earthquake considered here and a later Kuril event which occurred on 13 January 2007. As shown in RABINOVICH *et al*. (2008, Fig. 6), while the three-dimensional simulation of tsunami excitation makes a dramatic difference in the pattern of initial sea-surface displacement for the 2007 earthquake, it makes less difference for the 2006 event considered here. Although in the latter case a sharp maximum in seafloor displacement is reduced from 2.7 to 1.9 m, the broader pattern of seafloor displacement is relatively unchanged. As pointed out by TANIOKA *et al*. (2008), the dramatic difference in the tsunami excitation between the two events is due to the considerably narrower pattern of seafloor deformation produced by the 2007 earthquake. Unlike the 2006 event, which occurred on the shallowly dipping megathrust of the Kuril subduction zone, the 2007 event occurred on a steeply-dipping fault in the oceanic plate near the outer rise. This difference in fault dip results in a projection of the fault slip area onto the seafloor which is much narrower for the 2007 event than for the 2006 event (approximately 30 km and over 60 km, respectively—see Figs. 6a and 6b of RABINOVICH *et al*., 2008). Although the result of RABINOVICH *et al*. (2008) suggests the seafloor deformation pattern of the 2006 Kuril earthquake is close to the limit at which the assumption that this pattern is identical to the initial sea-surface elevation breaks down, our success in modelling the resulting tsunami using the seismic model suggests it is still a reasonable approximation for this event.

The same reasoning suggests that dispersion of tsunami energy is less a concern for the tsunami generated by the 2006 Kuril earthquake than for that generated by the 2007 event. Figure 9 illustrates spectragrams for the two tsunami's, both recorded at BPR D21414. Figure 9a shows that most of the tsunami energy recorded for the 2006 event is confined to the 0–2 mHz frequency band, arriving between 7500 and 8250 seconds after the earthquake. The energy arriving within this bandwidth exhibits little dispersion, consistent with the dispersion curve indicated in the figure: the latter is steep in the 0–2 mHz band, predicting only small dispersion. The spectragram for the 2007 event (Fig. 9b), on the other hand, shows that much of the tsunami energy recorded for this event extends through the frequency band 0–3 mHz, and dispersion in the energy above 2 mHz is evident (again, consistent with the dispersion curve). The wider area of the seafloor elevated by the 2006 event due to its occurrence on the shallowly-dipping megathrust has excited lower frequency tsunami energy that is little affected by dispersion, while the narrow area of sea floor elevated by the 2007 outer rise event on a steeply-dipping fault has excited higher frequency tsunami energy that is affected by dispersion.

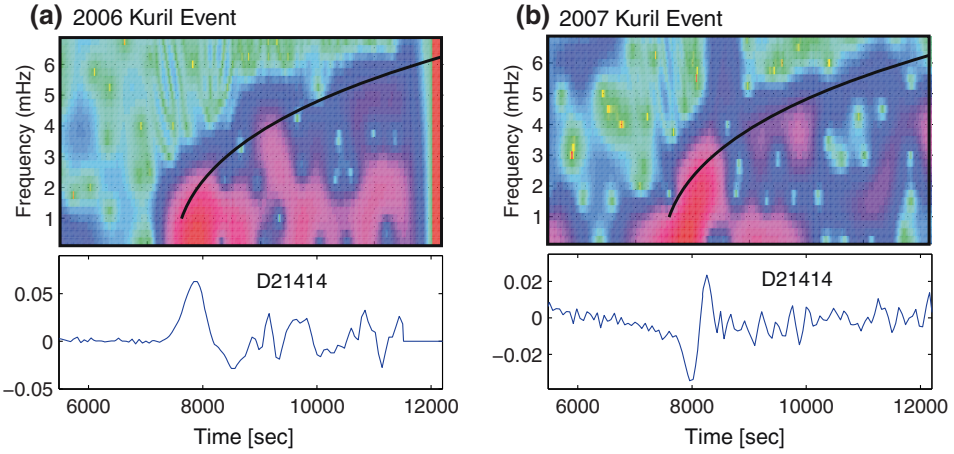

Figure 9
Spectrograms calculated using waveform data from BPR D21414 for: (a) The 15 November, 2006 Kuril earthquake, and (b) the 13 January 2007 Kuril Earthquake. Approximate dispersion curves calculated for 6000 m water depth are indicated.

4.4 Implications for Teletsunami Forecasting

According to the result shown in Figs. 3 and 4 of the 2006 Kuril earthquake, the slip model derived using only P waves is clearly different from the slip model of P and long-period surface waves. There may be several reasons for this inaccuracy in the P-wave slip model. Teleseismic body waves can be very sensitive to fault orientation as well as near-source structure, including the slope of the seafloor (WIENS, 1987; OKAMOTO and MIYATAKE, 1989). They can also be affected by large-scale, laterally heterogeneous velocity structure along the path between source and receiver; although this can be removed by aligning observations and synthetics along the P-wave arrival, it is at the expense of any information on absolute position, and the result is therefore dependent on the accuracy of the presumed hypocenter. This study suggests that slip inversions using P-wave data alone can be unstable, in the sense that different models appear to be able to satisfy the data almost equally well. The P wave only and the P wave + surface wave slip models obtained above differed substantially in their slip distributions, however while the latter model leads to a substantial 28% improvement in surface wave VR over the P wave only model, the corresponding reduction of the P-wave VR is only 9% after including the surface wave data. The inclusions of long-period surface wave data also resulted in a model which gave a much better fit to the BPR tsunami waveforms, resulting in a tsunami VR of 73%, and was able to match subtle features of the tsunami waveforms.

The variance reduction of the teletsunami waveforms can be improved to 81% with the inclusion of BPR data. However, for the configuration of seismic and BPR platforms available at the time of the earthquakes considered here, this increased accuracy is achieved only at the expense of a significant delay in the acquisition of the data required

to achieve it. To obtain a source model achieving a 73% VR in teletsunami data, it took 63 minutes from the initiation of earthquake rupture for the surface and body waves to arrive at the recording stations. In contrast, the first tsunami waveforms did not begin to arrive at the nearest BPR (KPG2 in Fig. 1) until 54 minutes after rupture initiation, the full tsunami waveform used in the inversion was not recorded by this nearest BPR until 134 minutes, and it took 294 minutes for all of the tsunami waveforms useful for inversion of the source to be recorded. While the time it takes for tsunami waveforms to be recorded depends on the location of the earthquake and the BPRs, the larger delay for the tsunami data is fundamentally due to the slower propagation of tsunami vs. seismic waves. Since the processing time needed for the slip inversion is only a few minutes, the larger delay needed to reduce the VR by including BPR data may be important in the context of tsunami warning. On the other hand, because tsunami generation can be enhanced by non-seismic mechanisms such as submarine landslides, BPR data would seem to provide an indispensible check on seismic models of the tsunami source.

5. Conclusion

Accurate and rapid forecasts of teletsunami waveforms could potentially be used as part of a tsunami warning system to forecast impacts on coastlines likely to be affected by a tsunami. The potential for such forecasts has been demonstrated for source models inferred from deep-ocean BPRs (TITOV *et al.*, 2005), and the US National Oceanic and Atmospheric Administration is in the process of greatly expanding the network of deep-ocean BPRs that could be used for this purpose. Less attention has been paid to the use of tsunami source models derived from seismic data, in part because the only data that could be used to validate such models were from coastal tide gauges, and these data can be very sensitive to details of coastal bathymetry that are often poorly known. Since the expansion of the network of deep-ocean BPRs, whose data can be expected to be less sensitive to bathymetry than to details of the tsunami source, it is now possible to validate seismic models of the tsunami source.

The goal of this study was to use the first occurrence of a large tsunamigenic earthquake to be recorded by an extensive network of deep-ocean BPRs in the Pacific Ocean, to test whether seismic data could be used to forecast the teletsunami recorded at the BPRs. Seismic data from the 15 November, 2006 Kuril earthquake were inverted to obtain two candidate models for the spatial distribution of slip on the Kuril megathrust: One model was obtained by inverting only P waves, and the other used both P- and long-period surface waves. Both models forecast teletsunami waveforms that were a reasonable match to the observations, with variance reductions (VRs) of 60% and 73%, respectively.

The source model obtained using both P and surface waves, however, produced teletsunami waveforms with a better match to the observations. While P-wave data appear to be sensitive to details of the earthquake rupture process, source inversion using P-wave data alone appears to be less stable than the combined use of P- and

surface-wave data. We speculate that this instability in the P-wave only inversions may be due to, or at least exacerbated by, sensitivity of the P-wave data to factors that may be either poorly constrained or not well represented in the forward modelling, such as fault orientation and near-source velocity structure. (Although we did not present them in this paper, inversions using S waves indicated that similar considerations apply to them). We conclude that the use of the long-period surface waves with P waves was very effective in stabilizing the teleseismic inversion and resulted in improving the accuracy of the deep-ocean teletsunami forecasting for the 2006 Kuril earthquake.

Our results have been obtained only for 1 event, which is a megathrust event on the Kuril Trench. Other studies (CHLIEH *et al*., 2007; AMMON *et al*., 2006, among many others) likewise suggest that seismic waveform data can be used to obtain reliable slip models for large megathrust events. The situation is not as clear for other, intraplate events which can also be tsunamigenic, including outer rise events such as the 2007 Kuril earthquake as well as the 1933 Sanriku and 1977 Sumba earthquakes. For these and other intraplate earthquakes it is not always clear what the fault orientation is, and this can have a pronounced influence on tsunami generation. Also slip on a steeply dipping fault may result in a narrow pattern of seafloor deformation, for which some assumptions often used in modelling tsunami generation and propagation, in particular the excitation and dispersion discussed in section 4.3, may not be valid. We are investigating these issues using data from the 2007 Kuril earthquake, which was also recorded by numerous of BPRs in the Pacific Ocean. These results will be published in a subsequent, companion paper.

Acknowledgements

We thank the editor, K. Satake, and the reviewers I. Fine, T. Lay, and A. Rabinovich for their careful and constructive reviews, and also the U.S. National Oceanic and Atmospheric Administration, the Japan Agency for Marine-Earth Science and Technology and Tohoku University for providing BPR data, and the Data Management Center of the Incorporated Research Institutions for Seismology for access to the seismic data used in this study.

REFERENCES

AMMON, C.J., JI, C., THIO, H.-K., ROBINSON, D., NI, S., HJORLEIFSDOTTIR, V., KANAMORI, H., LAY, T., DAS, S., HELMBERGER, D., ICHINOSE, G., POLET, J., and WALD, D. (2005), *Rupture process of the 2004 Sumatra-Andaman earthquake*, Science *308*, 1133–1139, doi: 10.1126/science.1112260.

AMMON, C.J., KANAMORI, H., LAY, T., and VELASCO, A.A. (2006), *The 17 July 2006 Java tsunami earthquake*, Geophys. Res. Lett. *33*, L24308, doi:10.1029/2006GL028005.

AMMON, D.J., KANAMORI, H., and LAY, T. (2008), *A great earthquake doublet and seismic stress transfer cycle in the central Kuril Islands*, Nature, *45*, 561–565.

BOUCHON, M. (1976), *Teleseismic body wave radiation from a seismic source in a layered medium*, Geophys. J. R. Astr. Soc. *47*, 515–530.

BRIGGS, R.W., SIEH, K., MELTZNER, A.J., NATAWIDJAJA, D., GALETZKA, J., SUWARGADI, B., HSU, Y.-J., SIMONS, M., HANANTO, N., SUPRIHANTO, I., PRAYUDI, D., AVAUAC, J.-P., PRAWIRODIRDJO, L., and BOCK, Y. (2006), Deformation and slip along the Sunda megathrust in the great 2005 Nias-Simeulue earthquake, Science *311*, 1897–1901.

CHLIEH, M., AVOUAC, J.-P., HJORLEIFSDOTTIR, V., SONG, T.-R. A., JI, C., SIEH, K., SLADEN, A., HEBERT, H., PRAWIRODURDJO, L., BOCK, Y., and GALETZKA, J. (2007), *Coseismic slip and afterslip of the Great M_w 9.15 Sumatra-Andaman Earthquake of 2004*, Bull. Seismol. Soc. Am. *97*, S152–S173, doi:10.1785/0120050631.

DELOUIS, B., GIARDINI, D., LUNDGREN, P., and SALICHON, J. (2002), *Joint inversion of InSAR, GPS, teleseismic, and strong-motion data for the spatial and temporal distribution of earthquake slip: Application to the 1999 Izmit main shock*, Bull. Seis. Soc. Am. *92*, 278–299.

EKSTRÖM, G., TROMP, J., and LARSON, E.W.F. (1997), *Measurements and global models of surface wave propagation*, J. Geophys. Res. *102*(B4), 8137–8157.

FUJII, Y. and SATAKE, K. (2008), *Tsunami sources of the November 2006 and January 2007 great Kuril earthquakes,* Bull. Seismol. Soc. Am, *98*, 1559–1571.

GEIST, E. L. and DMOWSKA, R. (1999), *Local tsunamis and distributed slip at the source*, Pure Appl. Geophys. *154*, 485–512.

HARTZELL, S. H. and HEATON, T. H. (1983), *Inversion of strong ground motion and teleseismic waveform data for the fault rupture history of the 1979 Imperial Valley, California, earthquake*, Bull. Seismol. Soc. Am. *73*, 1553–1583.

HARTZELL, S., and LANGER, C. (1993), *Importance of model parameterization in finite fault inversions; application to the 1974 M_w 8.0 Peru earthquake*, J. Geophys., Res., *98,* 22,123–22,134.

HIRATA, K., AOYAGI, M., MIKADA, H., KAWAGUCHI, K., KAIHO, Y., IWASE, R., MORITA, S., FUJISAWA, I., SUGIOKA, H., MITSUZAWA, K., SUYEHIRO, K., KINOSHITA, H., and FUJIWARA, N. (2002), *Real-time geophysical measurements on the deep seafloor using submarine cable in the southern Kurile subduction zone*, IEEE J. Oceanic Eng., *27*, 170–181.

HIRATA, K., TAKAHASHI, H., GEIST, E., SATAKE, K., TANIOKA, Y., SUGIOKA, H., and MIKADA, H. (2003), *Source depth dependence of small-tsunamis recorded with ocean-bottom pressure gauges: The January 28, 2000 Mw 6.8 earthquake off Nemuro Peninsula, Japan*, Earth Planet. Sci. Lett. *208*, 305–318.

ICHINOSE, G. A., SOMERVILLE, P., THIO, H. K., MATSUSHIMA, S., and SATO, T. (2005), *Rupture process of the 1948 Fukui earthquake (M 7.1) from the joint inversion of seismic waveform and geodetic data*, J. Geophys. Res. *110*, doi:10.1029/2004JB003437.

IWASE, R., ASAKAWA, K., MIKADA, H., GOTO, T., MITSUZAWA, K., KAWAGUCHI, K., HIRATA, K. and KAIHO, Y. (2003), *Off Hatsushima Island observatory in Sagami Bay: Multidisciplinary long-term observation at cold seepage site with underwater mateable connectors for future use*, Proc. 3rd International Workshop on *Scientific Use of Submarine Cables and Related Technologies*, pp 31–34.

JI, C. (2007), *Rupture process of the 2006 Nov. 15 Magnitude 8.3 Kuril Island earthquake*, http://earthquake.usgs.gov/eqcenter/eqinthenews/2006/usvcam/fite_fault.php,

JOHNSON, J. M., SATAKE, K., HOLDAHL, S. R. and SAUBER, J. (1996), *The 1964 Prince William Sound earthquake: Joint inversion of tsunami and geodetic data*, J. Geophys. Res. *101*(B1), 523–532.

KAJIURA, K. (1963), *The leading wave of a tsunami*, Bull. Earthq. Res. Inst. *41*, 535–571.

KANAMORI, H. and GIVEN, J. W. (1981), *Use of long-period surface waves for rapid determination of earthquake-source parameters*, Phys. Earth Planet. Inter. *27*, 8–31.

KANAMORI, H. and STEWART, G.S. (1976), *Mode of the strain release along the Gibbs fracture zone, Mid-Atlantic ridge*, Phys. Earth Planet. Int. *11*, 312–335.

KANAZAWA, T. and HASEGAWA, A. (1997), *Ocean-bottom observatory for earthquakes and tsunami off Sanriku, north-east Japan using submarine cable*, Paper presented at International Workshop on Scientific Use of Submarine Cable, Inst. of Electr. and Electr. Eng., Okinawa, Japan.

Kikuchi, M. and KANAMORI, H. (1991), *Inversion of complex body waves-III*, Bull. Seismol. Soc. Am. *81*, 2335–2350.

KOKETSU, K., HIKIMA, K., MIYAZAKI, S., and IDE, S. (2004). *Joint inversion of strong motion and geodetic data for the source process of the 2003 Tokachi-oki, Hokkaido, earthquake*, Earth Planets and Space *56*, 329–334.

KONCA, A. O., HJORLEIFSDOTTIR, V., SONG, T.-R. A., AVOUAC, J.-P., HELMBERGER, D. V., JI, C., SIEH, K., BRIGGS, R., and MELTZNER, A. (2007), *Rupture kinematics of the 2005 M_w 8.6 Nias-Simeulue earthquake from the joint inversion of seismic and geodetic data*, Bull. Seismol. Soc. Am. *97*, S307–S322.

LAWSON, C. L. and HANSON, R. J. *Solving Least-squares problems*, 340 pp., (Prentice-Hall, Series in Automatic Computation, 1974).

MATSUMOTO, K., TAKANEZAWA, T., and OOE, M. (2000), *Ocean tide models developed by assimilating TOPEX/POSEIDON altimeter data into hydrodynamical model: A global model and a regional model around Japan*, J. Oceanogr. *56*, 567–581.

NAKANISHI, A., SMITH, A. J., MIURA, S., TSURU, T., KODAIRA, S., OBANA, K., TAKAHASHI, N., CUMMINS, P.R., and KANEDA, Y. (2004), *Structural factors controlling the coseismic rupture zone of the 1973 Nemuro-Oki earthquake, the southern Kuril Trench seismogenic zone*, J. Geophys. Res. *109*, doi:10.1029/2003JB002574.

OKADA, Y. (1985), *Surface deformation due to shear and tensile faults in a half space*, Bull. Seismol. Soc. Am. *75*, 1135–1154.

OKAMOTO, T. and MIYATAKE, T. (1989), *Effects of near source seafloor topography on long-period teleseismic P waveforms*, Geophys. Res. Lett. *11*, 1309–1312.

RABINOVICH, A. B., LOBKOVSKY, L. I., FINE, I. V., THOMSON, R. E., IVELSKAYA, T. N., and KULIKOV, E. A. (2008), *Near-source observations and modeling of the Kuril Islands tsunamis of 15 November 2006 and 13 January 2007*, Adv. Geosci. *14*, 105–116.

SATAKE, K. (1987), *Inversion of tsunami waveforms for the estimation of a fault heterogeneity: Method and numerical experiments*, J. Phys. Earth *35*, 241–254.

SATAKE, K. (1993), Depth distribution of coseismic slip along the Nankai Trough, Japan, from joint inversion of geodetic and tsunami data, J. Geophys. Res. *98*, 4553–4565.

SATAKE, K. (1995), *Linear and nonlinear computations for the 1992 Nicaragua earthquake tsunami*, Pure Appl. Geophys., *144*, 455–470.

SATAKE, K. and TANIOKA, Y. (1995), *Tsunami generation of the 1993 Hokkaido Nansei-Oki earthquake*, Pure Appl. Geophys. *144*, 803–821.

STEIN, S. and OKAL, E. A. (2007), *Ultralong period seismic study of the December 2004 Indian Ocean Earthquake and implications for regional tectonics and subduction process*, Bull. Seismol. Soc. Am. *97*, S279–S295.

TANIOKA, Y., SATAKE, K., and RUFF, L. (1995), *Total analysis of the 1993 Hokkaido Nansei-Oki earthquake using seismic wave, tsunami, and geodetic data*, Geophys. Res. Lett. *22*(1), 9–12.

TANIOKA, Y., HASEGAWA, Y., and KUWAYAMA, T. (2008), *Tsunami waveform analysis of the 2006 underthrust and 2007 outer-rise Kurile earthquakes*, Adv. Geosci. *14*, 129–143.

THIO, H. K., GRAVES, R. W., SOMERVILLE, P. G., SATO, T., and ISHII, T. (2004), *A multiple time window rupture model or the 1999 Chi-Chi earthquake from a combined inversion of teleseismic, surface wave, strong motion, and GPS data*, J. Geophys. Res. *109*, B08309, doi:10.1029/2002JB002381.

TITOV, V.V., GONZÁLEZ, F.I., BERNARD, E.N., EBLE, M.C., MOFJELD, H.O., NEWMAN, J.C., and VENTURATO, A.J. (2005), *Real-time tsunami forecasting: Challenges and solutions*. Nat. Hazards *35*(1), Special Issue, U.S. National Tsunami Hazard Mitigation Program, 41–58.

WIENS, D.A. (1987), *Effects of near source bathymetry on teleseismic P waveforms*, Geophys. Res. Lett. *14*, 761–764.

YAGI, Y. (2006), *Fault rupture imaging of the Nov. 15, 2006 earthquake that occurred off Chishima*, http://www.geo.tsukuba.ac.jp/press_HP/yagi/EQ/Chishima/ (in Japanese).

YAMANAKA, Y. (2006), *Earthquake note No. 183*, http://www.eri.u-tokyo.ac.jp/sanchu/Seismo_Note/2006/EIC183.html (in Japanese).

(Received April 14, 2008, revised September 1, 2008)

Pure appl. geophys. 166 (2009) 77–96
0033–4553/09/010077–20
DOI 10.1007/s00024-008-0432-7

Pure and Applied Geophysics

Variable Tsunami Sources and Seismic Gaps in the Southernmost Kuril Trench: A Review

KENJI HIRATA,[1] KENJI SATAKE,[2,4] YUICHIRO TANIOKA,[3] and YOHEI HASEGAWA[1,5]

Abstract—In the southernmost Kuril Trench, the tsunami source regions vary their along-trench extent even among earthquakes occurring within the same segment. Recent studies suggest that the tsunami source of the 1952 Tokachi-oki earthquake (M 8.1) differs from but partially overlaps with that of the 2003 Tokach-oki earthquake (M 8.0). Furthermore, the along-trench extent among the earthquakes seems to differ between deep and shallow portions of the subduction interface. A seismic gap has been recognized along the deep subduction interface between the sources of the 1952 and 1973 earthquakes. We propose that the gap is now larger, including both shallow to deep portions of the interface between the 1973 and 2003 earthquakes. Variability in spatial extent of large subduction earthquakes in both along-trench direction and trench-normal direction makes it difficult to forecast future earthquakes in the southernmost Kuril Trench.

Key words: Kuril Trench, Tokachi-oki, Nemuro-oki, tsunami.

1. Introduction

In March 2003, the Earthquake Research Committee of the Japanese government announced a long-term forecast for great (M $\sim$ 8) earthquakes along the Kuril Trench (EARTHQUAKE RESEARCH COMMITTEE, 2004). The committee estimated that the probability that a great earthquake with a magnitude of nearly 8.1 will occur in the next 30 years (starting March 2003) was 60% for offshore Tokachi, Hokkaido (Fig. 1). In the forecast, the committee assumed that a great earthquake recurs in a demarcated offshore segment following a Brownian-passage-time probability distribution with a characteristic recurrence interval. The characteristic recurrence interval was estimated from intervals between great earthquakes in the 19th and 20th centuries. The offshore segment for the

[1] Seismology and Volcanology Research Department, Meteorological Research Institute, 1-1 Nagamine, Tsukuba 305-0052, Japan. E-mail: khirata@mri-jma.go.jp

[2] Active Fault Research Center, National Institute of Advanced Industrial Science and Technology, Site C7 1-1-1 Higashi, Tsukuba 305-8567, Japan.

[3] Institute of Seismology and Volcanology, Hokkaido University, N10W8 Kita-ku, Sapporo 060-0810, Japan.

[4] Earthquake Research Institute, University of Tokyo, 1-1-1 Yayoi, Bunkyo-ku, Tokyo 113-0032, Japan.

[5] Seismological and Volcanological Department, Japan Meteorological Agency, 1-3-4, Ote-machi, Chiyoda-ku, Tokyo 100-8122, Japan.

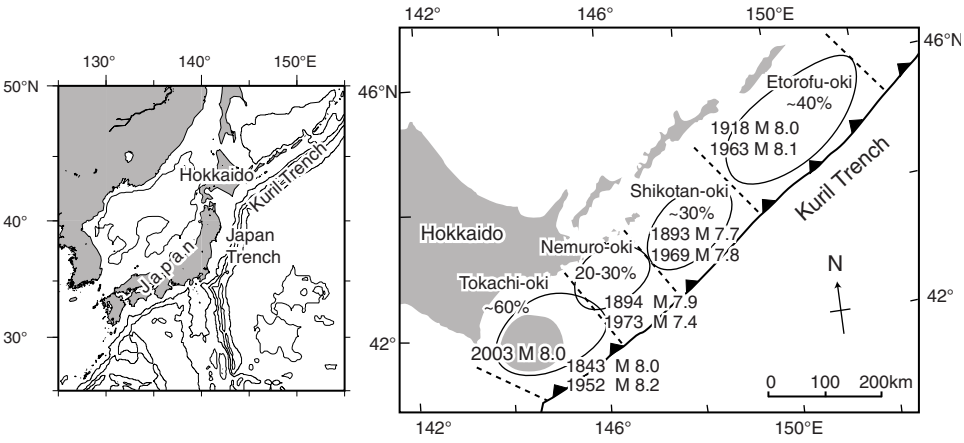

Figure 1

Location of Kuril Trench (left) and the source regions of great earthquakes along the southern Kuril trench (right). Recurrence of earthquakes in the 19th and 20th centuries in each segment (bordered by dashed lines), as well as the probabilities (in the next 30 years) forecasted before the 2003 Tokachi-oki earthquake are shown (EARTHQUAKE RESEARCH COMMITTEE, 2004). Magnitudes of these events are on the Japanese scale, based on instrumental or historical data (UTSU, 1999) (after SATAKE *et al.*, 2005).

forthcoming Tokachi-oki earthquake was estimated from evidence such as the aftershock distribution of the 1952 Tokachi-oki earthquake (M 8.1) and its rupture area (Fig. 1).

On the 26th of September 2003, about six months after the announcement of the long-term forecast, a great earthquake with a magnitude of M 8.0 occurred off Tokachi. Although its magnitude was nearly as predicted (M 8.1), the source area was slightly smaller than predicted; the source area did not extend to the eastern part of the forecasted one (SHIMAZAKI, 2005). Studies based on seismic waveforms, aftershock distribution, GPS crustal deformation, and tsunamis from the 2003 Tokachi-oki earthquake have all suggested that the source area was confined near the Tokachi coast, though these studies showed minor discrepancies.

Soon after the source process of the 2003 event was unveiled, its relationship with the 1952 Tokachi-oki earthquake was extensively investigated. Waveform inversion of regional strong motion records (YAMANAKA and KIKUCHI, 2003) and re-examination of the aftershock distribution (HAMADA and SUZUKI, 2004) of the 1952 event suggested that the 2003 event was a recurrence of the 1952 event. In contrast, studies of the 1952 and 2003 tsunamis suggest that both source areas partially overlap, but do not coincide. The reason why different results were obtained probably owes to insufficient amounts and quality of observed data such as seismic waves and tsunamis in 1952.

In this paper, we review studies on tsunamis from the 1952 and 2003 Tokachi-oki earthquakes and then explain why the 2003 source differs from the 1952 source. In addition, we review studies on tsunamis from the 1973 Nemuro-oki earthquake (M 7.4), a large earthquake that occurred in the offshore segment adjoining the 1952 source area to

the northeast. Finally, we discuss the spatial extent of tsunami sources along the southernmost Kuril Trench from the 17th through 21st centuries.

2. *The 1952 Tokachi-oki Earthquake Tsunami*

A great earthquake occurred off Tokachi, Hokkaido at 10:23 a.m. (Japan Local Time (JLT)), on March 4, 1952. The hypocentral parameters re-examined by the Japan Meteorological Agency (JMA) (1982) are: 41°48'02''N, 144°08'03''E, h = 0 km, and M_J (magnitude scale of JMA) 8.2. In 1952, on the other hand, the Central Meteorological Observatory, the former organization of JMA, assigned a hypocenter of 42°09'N, 143°52'E, h = 45 km, and M = 8.0 from the macroscopic seismic intensity distribution (CENTRAL METEOROLOGICAL OBSERVATORY, 1953). The Central Meteorological Observatory named this event the 1952 (27th year in the Showa era of Japan) Tokachi-oki earthquake.

The earthquake generated tsunamis that caused damage along the Pacific coast in northern Japan (Hokkaido and Tohoku regions). The most striking damage appeared at Kiritappu, eastern Hokkaido, because icebergs with thicknesses of nearly 60 cm and floating boats, in the ocean, were carried to land by the tsunami (CENTRAL METEOROLOGICAL OBSERVATORY, 1953).

Field surveys were carried out soon after the earthquake (CENTRAL METEOROLOGICAL OBSERVATORY,1953; KUSUNOKI and ASADA, 1954; TAMIYA and NAKAMURA, 1953; HYDROGRAPHIC OFFICE, THE FIRST DISTRICT MARITIME SAFETY BUREAU, 1954). Figure 2 shows tsunami runup heights (open circles) from the 1952 Tokachi-oki earthquake along the Hokkaido coast measured by field surveys. The tsunami runup heights were 1.5–3.5 m along the Tokachi coast (between Cape Erimo and Kushiro). In contrast, runup heights were 2–6.5 m between Konbumori and Kiritappu. The maximum tsunami height of 6.5 m was reported at Senpoushi (CENTRAL METEOROLOGICAL OBSERVATORY, 1953). However, other values of 2.0–4.4 m for tsunami heights at Senpoushi were also reported by other survey reports (KUSUNOKI and ASADA, 1954; TAMIYA and NAKAMURA, 1953; HYDROGRAPHIC OFFICE, THE FIRST DISTRICT MARITIME SAFETY BUREAU, 1954).

HASEGAWA *et al*. (2004) interviewed a man in his seventies who had witnessed the inundation of Senpoushi by the 1952 tsunami. The eyewitness was still able to exactly show the geographic point of the maximum tsunami runup at Senpoushi in 1952. By correcting for a local landform change between 1952 and 2003, HASEGAWA *et al*. (2004) confirmed that the maximum runup height at Senpoushi in 1952 was approximately 6 m (Fig. 3) and that there was no ice sheet which might affect tsunami runup behavior in Akkeshi Bay in 1952. HASEGAWA *et al*. (2004) regarded the other runup heights of 2.0–4.4 m reported at Senpoushi as inaccurate values, which might be caused by misidentifying the maximum wave, or indication of locally complicated runup behavior within the village of Senpoushi.

By using tsunami travel times measured on tide gauge records and given by eyewitness accounts, HATORI (1973) located the 1952 tsunami source off Tokachi

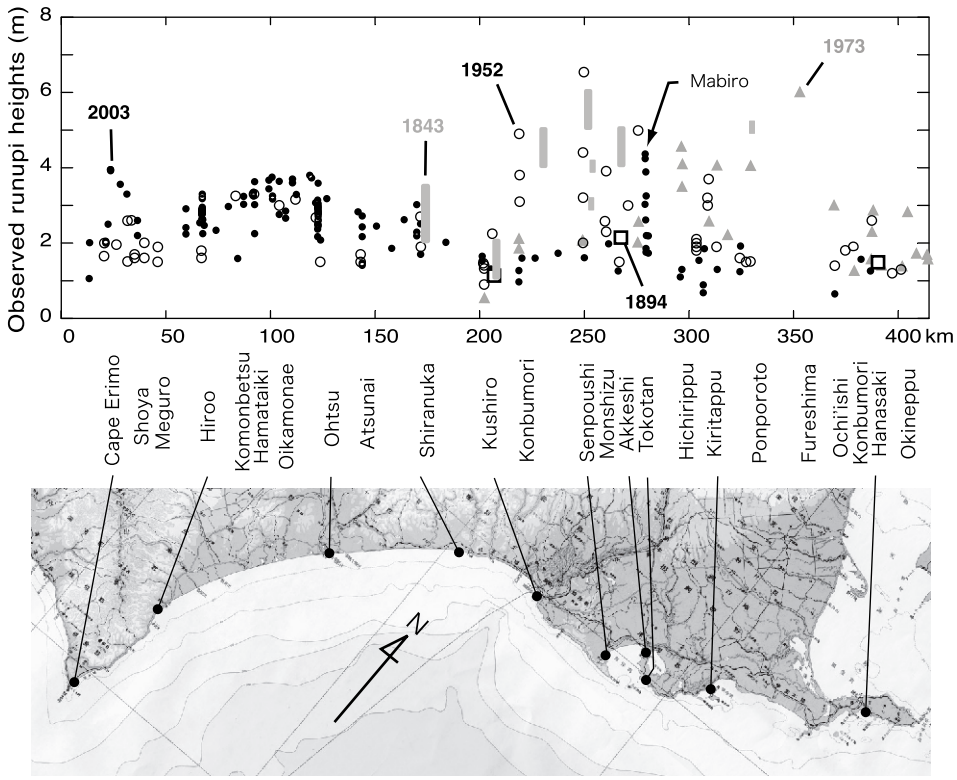

Figure 2
Runup heights from tsunamis along the Pacific coast of eastern Hokkaido off Tokachi and Nemuro from the 1843 earthquake (ranges estimated from historical documents by HATORI, 1984 and TSUJI, 1994), the 1894 Nemuro-oki earthquake (HATORI, 1974a), the 1952 Tokachi-oki earthquake (CENTRAL METEOROLOGICAL AGENCY, 1953; KUSUNOKI and ASADA, 1954), the 1973 Nemuro-oki earthquake (JAPAN METEOROLOGICAL AGENCY, 1974), and the 2003 Tokachi-oki earthquake (TANIOKA *et al*., 2004a). Modified from the original figure of SATAKE *et al.* (2005).

(Fig. 4a). HIRATA *et al*. (2003), who inverted tide gauge records of the 1952 event, proposed that the 1952 tsunami source possibly extended to Akkeshi, farther east of the tsunami source of HATORI (1973) (Fig. 4b). Recently, SATAKE *et al*. (2006) re-examined the 1952 tsunami source by using tsunami waveform inversions of tide gauge records, correcting for tide gauge clocks. They also suggested that observed tide gauge records in 1952 are well explained when the tsunami source (uplift area) extends to near the trench off Akkeshi, though their slip distribution is slightly different from that of HIRATA *et al*. (2003) (Figs. 4c, d).

Because there was only one tide gauge station (Kushiro) to the northeast of the 1952 tsunami source, the northeast portion of the 1952 tsunami source is poorly resolved. Recently, HIRATA *et al*. (2007) examined the reliability of tsunami travel times from 32 eyewitness accounts northeast of Kushiro in 1952, which had been described in technical

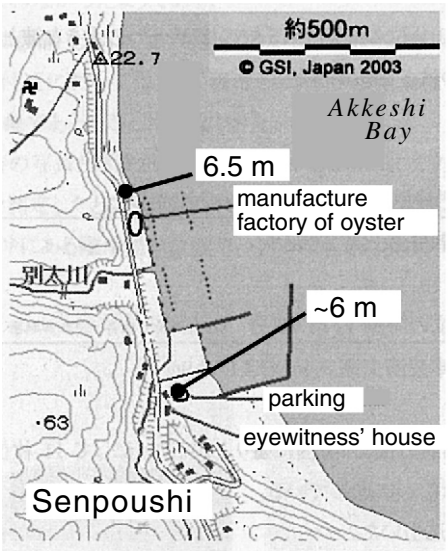

Figure 3
Runup heights at Senpoushi from the 1952 Tokachi-oki earthquake tsunami. About 50 years after the earthquake, HASEGAWA *et al*. (2004) confirmed that tsunami runup in 1952 reached nearly 6 m near an eyewitness' house, based on detailed accounts by the eyewitness who is still alive. The runup height of 6.5 m north of the oyster factory is a value measured by staff of the Central Meteorological Observatory in 1952 (modified from HASEGAWA *et al*., 2004).

reports published in 1953 and 1954. They found that most of the reported tsunami travel times marked the time of the maximum water level rather than the onset time of the first arrival, and concluded that the northeast edge of the 1952 tsunami source extended to at least Akkeshi Bay, and probably farther east. Because the travel times that eyewitnesses reported have no information about systematic time delay/progress, however, the conclusion by HIRATA *et al*. (2007) holds only if the clocks of the eyewitnesses are all correct. To obtain a more reliable solution, one must examine other tide gauge records which might be stored in foreign countries such as Russia, after checking the accuracy of the tide gauge clocks.

3. 1973 Nemuro-oki Earthquake Tsunami

At 0:55 pm (JLT) of 17th June 1973, a large earthquake occurred off eastern Hokkaido. JMA determined the hypocentral parameters: 42°58'N, 145°57'E, $h = 40$ km, and M_J 7.4. The tsunami generated by the earthquake caused damage in the coastal region from the Nemuro Peninsula to Kushiro. The tsunami and earthquake injured 22 people, damaged 65 boats, and destroyed 25 port facilities (JAPAN METEOROLOGICAL AGENCY, 1974). JMA named the earthquake the 17th June 1973

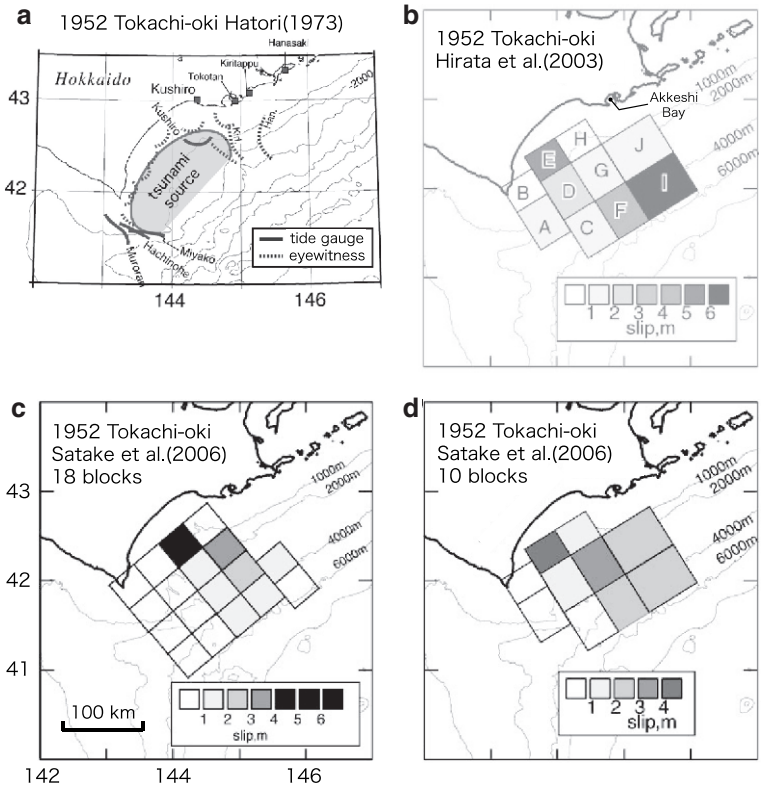

Figure 4

Source models for the 1952 Tokachi-oki earthquake. (a) Tsunami source area estimated by HATORI (1973) using tsunami travel times measured on tide gauge records and interviews from eyewitnesses. (b) Slip-distribution model estimated by HIRATA *et al*. (2003) using tsunami waveform inversion. (c) and (d) are 18-block and 10-block models, respectively, of slip distributions estimated by SATAKE *et al*. (2006) using tsunami waveform inversion.

Nemuro-Hanto-oki (off Nemuro Peninsula) earthquake. We refer to it as the 1973 Nemuro-oki earthquake hereafter.

Tsunami runup heights are distributed as shown by gray triangles in Figure 2 (JAPAN METEOROLOGICAL AGENCY, 1974). From Kushiro to Senpoushi, observed runup heights were lowest, decreasing from 2 m to 0.5 m. From Hichirippu to Ponporoto, runup heights were 2–5 m. Farther to the east (from Ochi'ishi to Okineppu), runup heights were 1–3 m. Although in Fureshima, west of Ochi'ishi, runup height was reported as 6 m, the JAPAN METEOROLOGICAL AGENCY (1974) regarded this height as an abnormal value owing to the collision between two inundating flows which sandwiched a dairy farmer's house and ran up farther onshore. However, we found descriptions in the same report that the runup height was 3 m at paved stones of the dairy farmer's house and nearly 5 m at coastal sand dunes, 0.5 km east of the house (JAPAN METEOROLOGICAL AGENCY, 1974). Therefore,

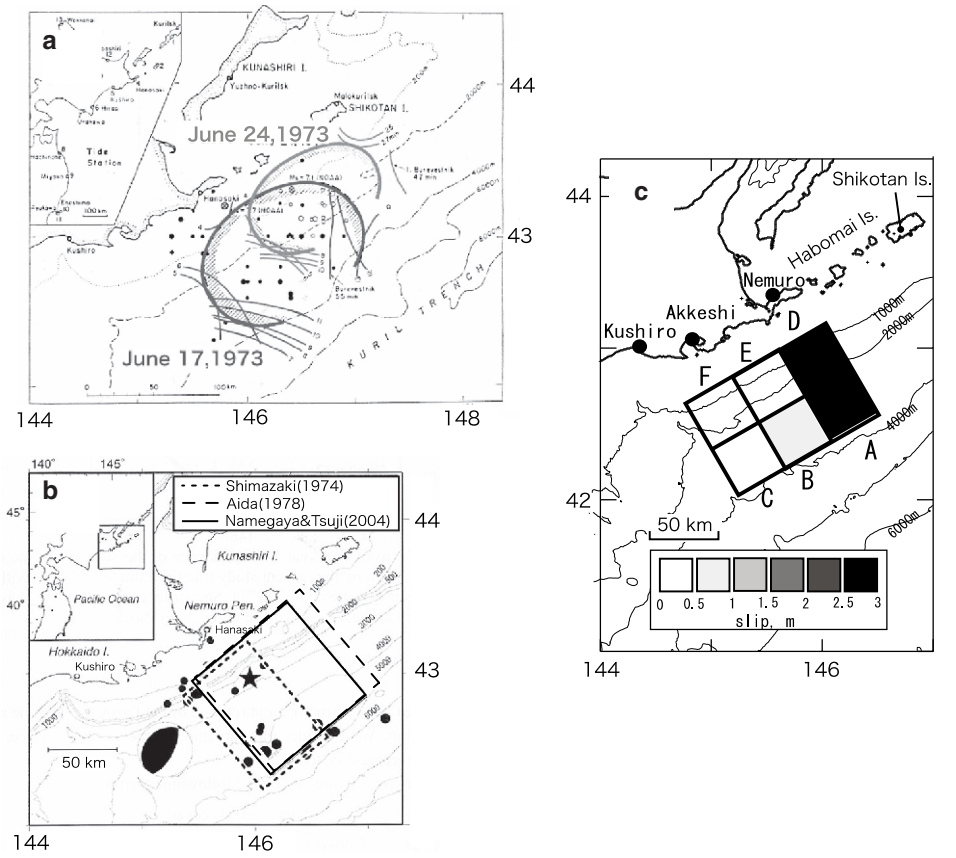

Figure 5

Source models of the 1973 Nemuro-oki earthquake. (a) Tsunami source area estimated by HATORI (1974a) using tsunami travel times (modified from HATORI, 1974a). Tsunami source corresponding to the largest aftershock of 24th June 1973 is also depicted. (b) Rectangular fault models estimated by SHIMAZAKI (1974) (dotted line), AIDA (1978) (broken line), and NAMEGAYA and TSUJI (2004) (solid line) (modified from NAMEGAYA and TSUJI, 2004). (c) Slip-distribution model estimated by TANIOKA et al. (2007) using tsunami waveform inversion.

tsunami runup heights in Fureshima are considered to be 3–5 m, which is almost comparable to the large heights observed between Hichirippu and Ponporoto.

In contrast with the 1952 Tokachi-oki tsunami, tide gauge records with good station coverage were obtained along the coast of northeast Honshu, Hokkaido, and Kuril Islands. HATORI (1974a, 1975) located the 1973 tsunami source area offshore between the Nemuro Peninsula and Shikotan Island by using tsunami travel times, recorded on tide gauge records in Japan and reported in a Russian technical report (Fig. 5a). AIDA (1978) tried to obtain an appropriate rectangular fault model by numerical simulations of tide gauge records in 1973 (Fig. 5b), although he failed to explain the observed records as he noted. SHIMAZAKI (1974) put forward a rectangular fault model by analyzing seismic

waves, crustal deformation data, and tsunamis (Fig. 5b). NAMEGAYA and TSUJI (2004) proposed another rectangular fault model through tsunami forward modeling of Japanese tide gauge records (Fig. 5b). Recently, TANIOKA *et al*. (2007) estimated the slip distribution of the 1973 Nemuro-oki earthquake by using tsunami waveform inversion of Japanese tide gauge records (Fig. 5c). The spatial extent and amounts of slip as well as slip-distribution pattern in the model of TANIOKA *et al*. (2007) are nearly identical to those estimated by a seismic waveform inversion (YAMANAKA, 2006), indicating that deep and shallow portions of the plate interface during the 1973 Nemuro-oki earthquake had ruptured along different lengths; the rupture zone is narrow at depth although relatively wide up-dip (Fig. 5c). These models indicate that the 1973 Nemuro-oki earthquake source is limited to an offshore region between Kiritappu and Habomai Islands. In particular, the western side of the source model is well constrained by Japanese tide gauge records.

4. 2003 Tokachi-oki Earthquake Tsunami

At 4:50 a.m. (LT) of 26 September, 2003, another great earthquake occurred off Tokachi. JMA determined the hypocentral parameters as follows: 41°46.5'N, 144°04.9'E, h = 45 km, and $M_J = 8.0$ (JAPAN METEOROLOGICAL AGENCY, 2005). The location of the 2003 epicenter coincides with the 1952 epicenter within errors. JMA named the event the 2003 Tokachi-oki earthquake. The earthquake generated a tsunami which damaged coastal regions of Hokkaido and northern Honshu. According to the SAPPORO DISTRICT METEOROLOGICAL OBSERVATORY (2004), a regional observatory of the JMA, the earthquake caused no deaths but two persons, who were fishing at the Tokachi coast, were missing. Many fishing boats in Ohtsu Port, Hokkaido, were displaced on land by the tsunami. In Kushiro, a large amount of wood was swept away from a lumberyard. In Tohoku (northern Honshu), farms of oysters and scallops in Rikuzen-Takada and Miyako were heavily damaged.

Tsunami field surveys were conducted by universities, institutes and the JMA immediately after the event (HASEGAWA *et al*., 2004; TANIOKA *et al*., 2004a). Tsunami runup heights of the 2003 Tokachi-oki earthquake tsunami are plotted by closed circles in Figure 2. Runup heights were 2–4 m from Hyakunin-hama, on the eastern side of Cape Erimo, to Ohtsu port. They gradually decreased farther east of Ohtsu port. Runup heights finally reduced to only 1–2 m to the east of Kushiro except Mabiro. Maximum runup heights of nearly 4 m were observed at Mabiro (Fig. 6). However, such high values were confined only within a 500-m-long section of about 2-km-long beach in Mabiro (Fig. 7). On either side of this 500-m-long section, runup heights suddenly decreased to less than 2 m (Fig. 2). HASEGAWA *et al*. (2004) could not reproduce such spike-like large runup even when a fine bathymetric grid size of 25 m was used in the coastal region as part of a nonlinear tsunami computation that included runup (Fig. 7). These facts indicate that such a spike-like runup distribution at Mabiro is caused by a very local bathymetric

Figure 6
Tsunamis arrived at Mabiro in 2003. (a) A relatively low water level after the 2003 tsunami arrived in Mabiro. Breakwater appeared about 2 m above sea level. (b) The highest water level when tsunami runup reached 4 m on the beach, minutes past 6:30 AM(LT). The breakwater disappeared fully below sea level. In (a) and (b), the sea surface seemed to be relatively calm. Clock time when the photo (a) was taken is unknown although it was taken in the early morning of September 26. (c) Runup measurement in Mabiro.

feature such as a local focusing of tsunami energy around the Daikoku Island, a small island off Mabiro (Fig. 7) (HASEGAWA *et al*., 2004; TANIOKA *et al*., 2004a).

The 2003 tsunami source was located off Tokachi by HATORI (2004) and HIRATA *et al*. (2004) (Figs. 8a, b). From a tsunami waveform inversion, TANIOKA *et al*. (2004b) suggested that the effective slip was limited to only off Tokachi, with maximum slip occurring off Hiroo (Tokachi port) (Fig. 8c). OHGAKI and IMAMURA (2004) obtained a similar result to TANIOKA *et al*. (2004b) by tsunami forward modeling. All of these source models are well constrained by using tide gauge records with a relatively good station coverage. These studies suggest that the 2003 tsunami source was confined near the Tokachi coast, but did not extend to off Akkeshi.

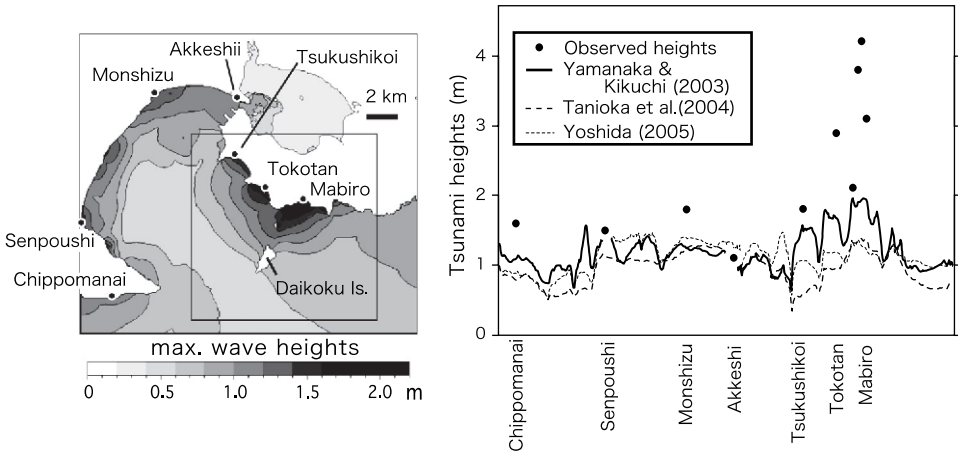

Figure 7

(Right) Runup heights measured around Akkeshi Bay and theoretical runup heights calculated using the source models estimated from seismic wave inversions (YAMANAKA and KIKUCHI, 2003; YOSHIDA, 2005) and tsunami inversion (TANIOKA *et al.*, 2004b). All of the theoretical tsunami height distributions cannot reproduce the observed, spike-like runup near Mabiro. (Left) Model domain used in tsunami calculation. The minimum grid size of 25 m is used within a coastal region shown by a small rectangle but a grid size of 75 m is used outside it. Larger grids with sizes of 225 m and 675 m are used farther outside of the left-hand side of the map, although it is not displayed (modified from HASEGAWA *et al.*, 2004).

5. *The Tsunami Sources of the 1952 and 2003 Tokachi-oki Earthquakes and their Relationships with the Tsunami Source of the 1973 Nemuro-oki Earthquake*

A discrepancy in tsunami runup height distribution between the 1952 and 2003 tsunamis suggests that these tsunami sources are not the same: The runup heights were over 4 m in a region from Konbumori to Kiritappu (a section of 220–310 km in the abscissa of Fig. 2) in 1952, whereas runup heights were less than 2 m (except Mabiro) in the same region in 2003. The largest runup heights over 3 m were observed in Hyakunin-hama (20–30 km in the abscissa) and in a region from Hiroo to Ohtsu (70–120 km in the abscissa) in 2003.

According to HIRATA *et al.* (2004), the observed discrepancy in tsunami runup height distributions between 1952 and 2003 can be qualitatively explained by a difference in the spatial extent of the tsunami sources (Fig. 9). A tsunami source extending to off Akkeshi can yield a similar pattern to observed runup distribution in 1952, whereas a tsunami source confined near the Tokachi coast can explain the observed runup distribution in 2003. The spatial distribution of tsunami runup heights observed in 1973 is quite different from that in 1952 and 2003 (Fig. 2).

HATORI (1975) suggested that there is a nearly 80-km-long gap between the 1952 tsunami source (HATORI, 1973) and the 1973 tsunami source (HATORI, 1974a, 1975) (Fig. 10a). Comparison between slip distributions for the 1952 earthquake (right panel of Fig. 10b; the 18 block model of SATAKE *et al.*, 2006) and 1973 earthquake (TANIOKA *et al.*,

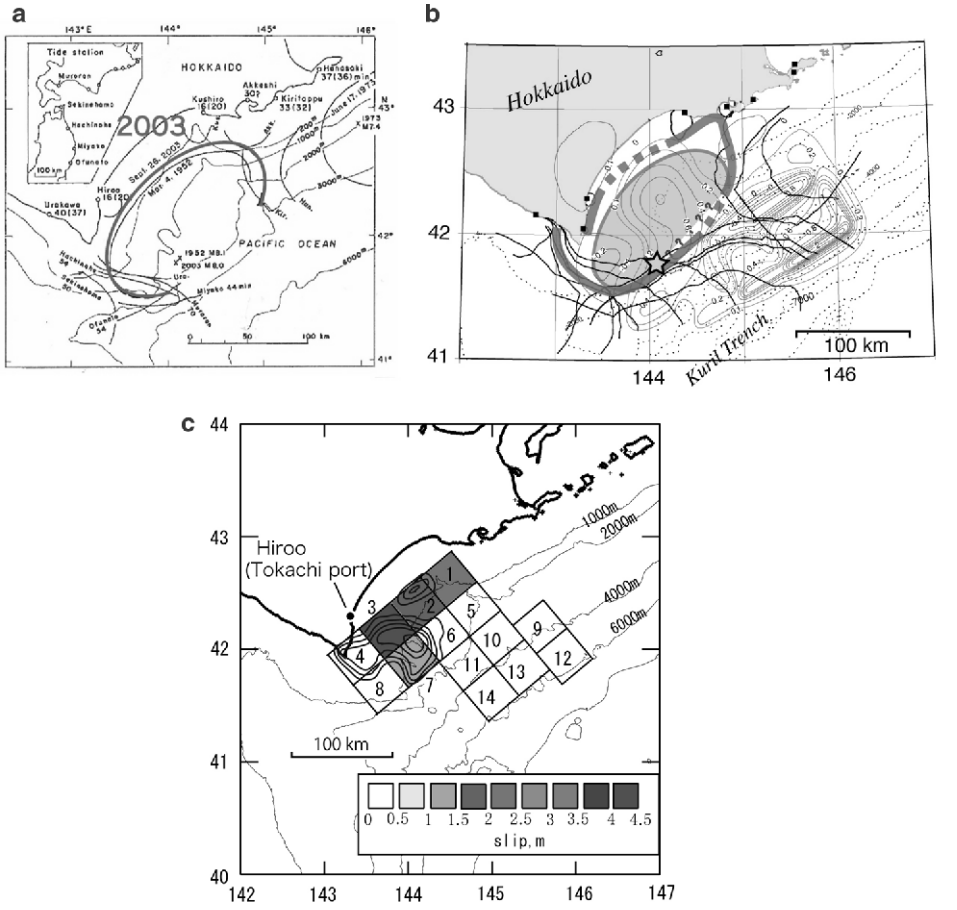

Figure 8

Source models of the 2003 Tokachi-oki earthquake. (a) Tsunami source area (thick curve) determined by HATORI (2004) (b) Tsunami source area (thick gray curve) determined by HIRATA *et al*. (2004). Both source areas are estimated using tsunami travel times. Back-projected, imaginary tsunami wave fronts are plotted by thin curves in both of (a) and (b). (c) Slip-distribution model estimated by TANIOKA *et al*. (2004b) using tsunami inversion. Contours represent slip distribution calculated for a seismic source model and estimated by YAMANAKA and KIKUCHI (2003).

2007) also shows a similar gap with an along-trench length of about 80 km but confined only to the deeper part of the subduction interface off Akkeshi. This can be confirmed visually from corresponding seafloor displacements (left panel of Fig. 10b). The seismic gap seems to have existed since 1894. It is interesting that two M 7 earthquakes, Aug. 12, 1961 (M 7.2) and Nov. 15, 1961 (M 6.9), occurred in and near the gap off Akkeshi (Fig. 10b). However, if we accept the 10 block model of SATAKE *et al*. (2006) as the 1952 earthquake source, such a gap becomes considerably smaller, if it exists, than in the former case (Fig. 10c). The slip distribution for the 1952 Tokachi-oki earthquake

estimated by HIRATA *et al*. (2003) is roughly the same as the 10 block model of SATAKE *et al*. (2006). Therefore, if we accept the source model of HIRATA *et al*. (2003), such a gap between the 1952 and 1973 earthquakes is also quite small or possibly nonexistent. Examination of eyewitness accounts for the 1952 tsunami by HIRATA *et al*. (2007) seems to suggest that any gap, if it exists, is no more than the 80-km-long. The size, or even the existence, of this seismic gap is thus somewhat ambiguous. In any case, we cannot identify any seismic gap in the shallow portion of the subduction interface between the 1952 and 1973 earthquakes.

On the contrary, we can identify a distinct gap along the subduction interface (right panel of Fig. 10d) or in seafloor displacement (left panel of Fig. 10d) between the 1973 earthquake (TANIOKA *et al*., 2007) and 2003 earthquake (TANIOKA *et al*., 2004b). This seismic gap clearly extends from near the trench to the deeper portion along the subduction interface. This seismic gap has existed since 1952 and overlaps with the

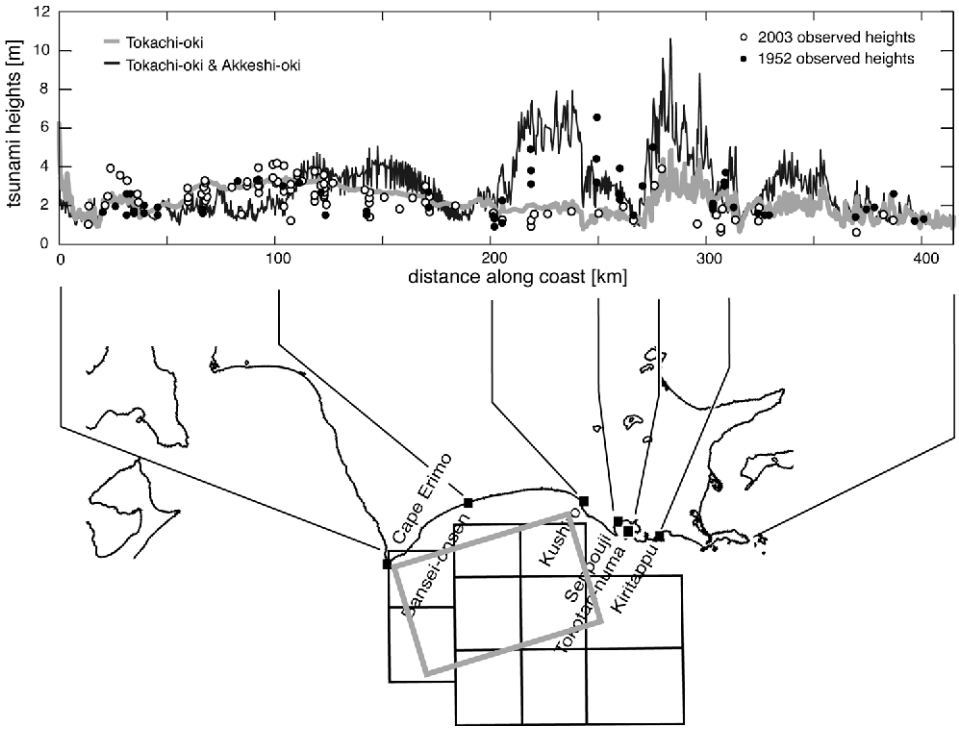

Figure 9

Runup heights of the 1952 and 2003 Tokachi-oki earthquake tsunamis. (Top) Solid and open circles indicate runup heights measured in 1952 and 2003, respectively. The thick gray line represents runup heights computed from a tsunami source model located only off Tokachi. The thin solid line is computed from another tsunami source model extended from Tokachi to Akkeshi. (Bottom) The solid rectangle represents a tsunami source model (fault model) located only off Tokachi. Thick gray rectangles are another tsunami source model (fault model) extending from Tokachi to Akkeshi (modified from HIRATA *et al*., 2004).

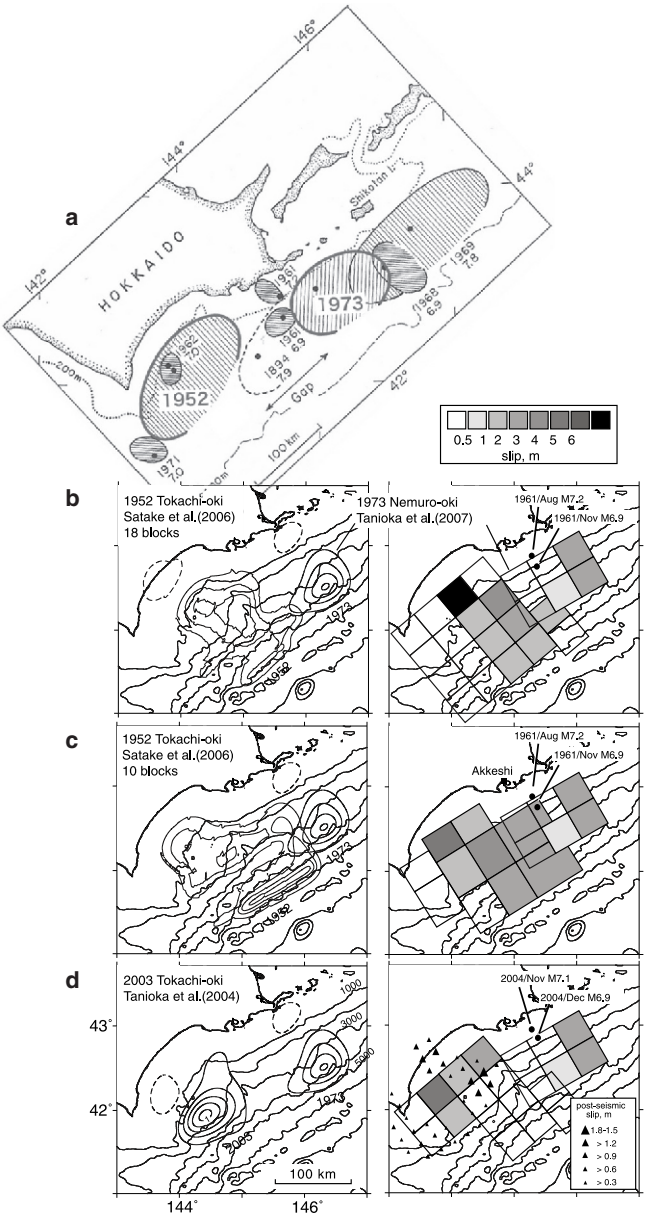

Figure 10

(a) Tsunami source areas of the 1952 Tokachi-oki and 1973 Nemuro-oki earthquakes (HATORI, 1974a). (b) Calculated seafloor displacement (left) and slip distribution (right) of the 1952 Tokachi-oki earthquake (18-block model of SATAKE *et al*., 2006) and 1973 Nemuro-oki earthquake (TANIOKA *et al*., 2007). (c) The same as (b) except displaying the 10-block model of SATAKE *et al*. (2006), instead of their 18-block model, for the 1952 Tokachi-oki earthquake. (d) Calculated seafloor displacement (left) and slip distribution (right) of the 2003 Tokachi-oki earthquake (TANIOKA *et al*., 2004b) and 1973 Nemuro-oki earthquake (TANIOKA *et al*., 2007). The distribution of slow post-seismic slip during the year after the 2003 earthquake (BABA *et al*., 2006) is shown by triangles. In (b), (c), and (d), the contour interval for seafloor displacement is 0.2 m.

seismic gap along the deep interface that has existed since 1894. Two M 7 earthquakes, Nov. 29, 2004 (M 7.1) and Dec. 6, 2004 (M 6.9), occurred in the deeper part of the gap in late 2004. Thus, there is a similarity between the 1952 and 2003 Tokachi-oki earthquakes in that both earthquakes were followed by M 7 subduction thrust earthquakes occurring in and near the possible seismic gap off Akkeshi.

Slow post-seismic slip after the 2003 event was observed by GPS networks (MIYAZAKI *et al*., 2004) and ocean-bottom pressure gauges (BABA *et al*., 2006). The southeastern part of the slow post-seismic slip seems to erode the western part of the seismic gap between the 2003 and 1973 earthquake sources (Fig. 10d). Such a post-seismic slip might be occurring around the coseismic slip region of other large subduction earthquakes such as the 1952 Tokachi-oki earthquake or the 1973 Nemuro-oki earthquake. However, this cannot be confirmed because neither GPS networks nor ocean-bottom pressure gauges were deployed before the 1990s.

6. Tsunami Sources in the Southernmost Kuril Trench prior to the 20th Century

Large tsunami events in the southernmost Kuril Trench off Tokachi and Nemuro have been recorded in 1843 and 1894. Prior to the 20th century, tsunami runup heights were estimated from information such as damage that was reported in historical documents. Runup heights of the 1894 tsunami were estimated by HATORI (1974a, b) and heights of the 1843 tsunami were estimated independently by HATORI (1984) and TSUJI (1994). Estimated tsunami runup heights in 1843 and 1894 are shown in Figure 2. Runup height data in 1894 (open squares) are very sparse but are significantly different from those in 1952. Runup height data in 1843 are limited (gray vertical bars) but seem similar to the distribution around Akkeshi in 1952 (SATAKE and YAMAKI, 2005).

Only the tide gauge record at Ayukawa for the 1894 earthquake is preserved. Recently, TANIOKA *et al*. (2007) numerically modeled the Ayukawa tide gauge record to examine the 1894 earthquake source. They examined only the waveform shape, because of the poor accuracy of clocks in the tide gauge record, and concluded that the along-trench length of the 1894 earthquake was nearly 200 km (Fig. 11). The length is considerably longer than the length of about 80 km for the 1973 source (Fig. 5c).

Tsunami waveforms should be different if the corresponding tsunami sources are different. According to SATAKE and YAMAKI (2005), the location of the Ayukawa tide gauge station has not changed since 1894. Shallow bathymetry and breakwater geometry around the station also has not significantly changed. However, the tide gauge records observed at Ayukawa from the 1894, 1952, 1973 and 2003 tsunamis differ significantly (Fig. 12). The discrepancy suggests differences among the tsunami sources (SATAKE and YAMAKI, 2005).

During the last decade, studies on tsunami deposits in eastern Hokkaido have shown that earthquakes larger than those in the 19–20th centuries occurred in the southernmost Kuril Trench. In Kiritappu, prehistoric sand sheets of marine origin extend as much as

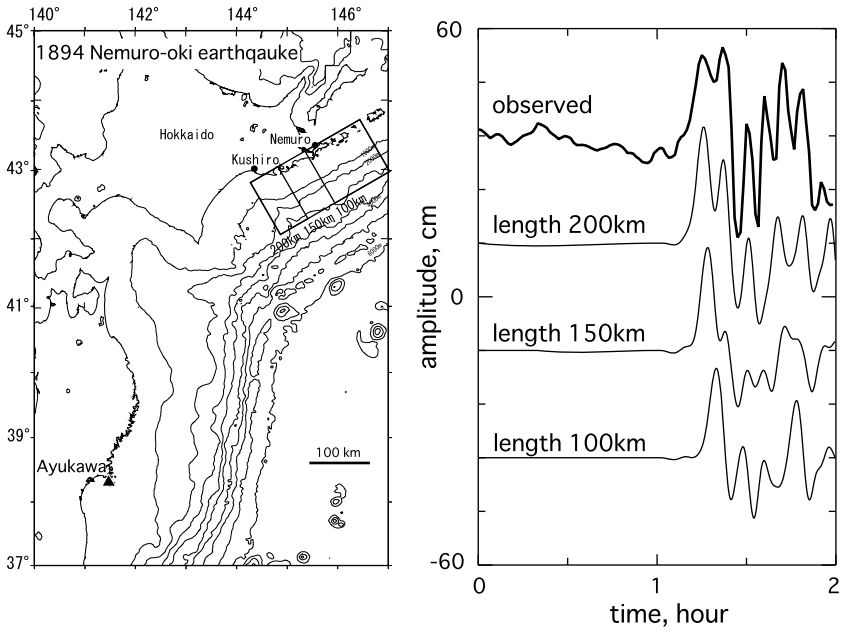

Figure 11
Modeling of the Ayukawa tide gauge record in the 1894 earthquake (modified from TANIOKA *et al*., 2007). (Left) Model domain used in the tsunami calculation. Three rectangular fault models with different along-trench lengths are assumed. (Right) Comparison between observed and calculated tide gauge records. All waveforms are aligned along the time of the first peak of the tsunami.

3 km inland across a beach-ridge plain (NANAYAMA *et al*., 2003), whereas the 1952 tsunami penetrated about 1 km from the coast (CENTRAL METEOROLOGICAL AGENCY, 1953). At Kiritappu and elsewhere, a stratigraphic series of extensive sand sheets, intercalated with dated volcanic ash layers, showed that the unusually large tsunamis occurred every 500 years on average over the past 2,000–7,000 years, with the youngest of the extensive sand sheets dated in the 17th century (NANAYAMA *et al*., 2003). SATAKE *et al*. (2005) modeled the 17th century's prehistoric tsunami by a large rectangular fault 100-km-wide (trench-normal) by 300-km-long (along-trench) located off Tokachi through Nemuro. The computed inundation area nearly matched the observed distribution of the 17th century's tsunami deposits.

7. New Interpretation on Spatial Extent of Large Subduction Earthquakes in the Southernmost Kuril Trench

From the runup height distributions and macroscopic seismic intensity, SATAKE *et al*. (2005) modified from the original demarcation of HATORI (1984), and introduced three offshore segments in the southernmost Kuril Trench: Tokachi-oki, Akkeshi-oki,

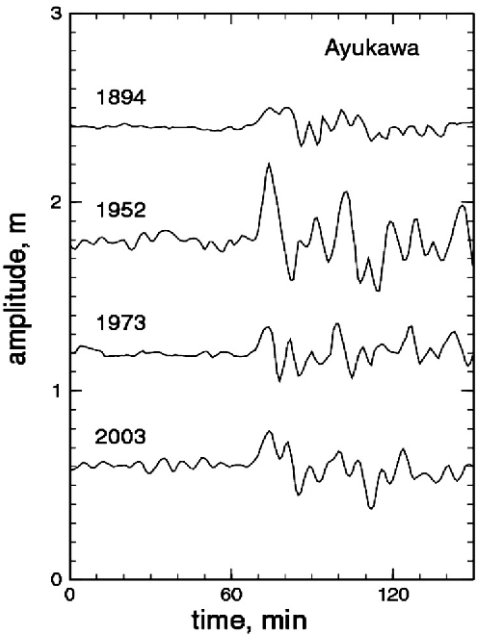

Figure 12
Comparison of the tide gauge records observed at Ayukawa since the end of the 19th century. All the records are aligned at the onset time of the first upward wave (after SATAKE and YAMAKI, 2005).

and Nemuro-oki segments. In the descriptions given previously, we have showed that the source regions vary among earthquakes of the 17th through 21st centuries. The 2003 Tokachi-oki earthquake ruptured only the Tokachi-oki segment, whereas the 1952 Tokachi-oki earthquake extended over both the Tokachi-oki and Akkeshi-oki segments. The 1843 event ruptured at least the Akkeshi-oki segment (SATAKE *et al*., 2005) and it seems to have extended farther to the west by considering macroscopic seismic intensity distribution (HATORI, 1984). It is possible that the 1843 event extended farther to the east but data for the 1843 event is too limited to discuss the possibility further. The 1973 Nemuro-oki earthquake ruptured only the Nemuro-oki segment, whereas the 1894 event probably ruptured not only the Nemuro-oki segement but also the Akkeshi-oki segment, although the southwestern edge of the ruptured interface is somewhat unclear.

From the spatial extent of the slip distributions in 1952, 1973, and 2003 (Fig. 10), we modify the segmentation of SATAKE *et al*. (2005) so that the spatial extent of large subduction earthquakes along the southernmost Kuril Trench is discriminated between shallow (light gray bars in Fig. 13) and deep (dark gray bars) portions of the subduction interface (Fig. 13). A seismic gap possibly remained only in the deep subduction interface between the 1952 and 1973 earthquakes. Strain increase in and around the gap promoted the occurrence of two M 7 earthquakes there (Fig. 10b, c). In contrast, both the 1952 and 1973 earthquakes ruptured the shallow interface nearly 10090 (Fig. 10b, c). On

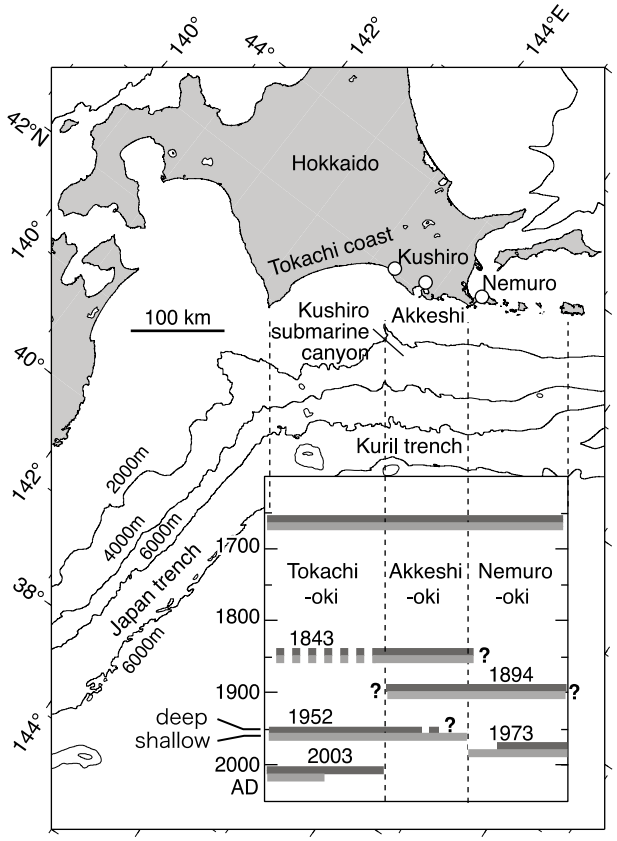

Figure 13
New interpretation of the space-time extent of great earthquakes along the southernmost Kuril Trench from the 17th through 21st centuries (modified from SATAKE *et al*., 2005). Deep and shallow parts of the megathrust have ruptured along different lengths, indicated by darker and lighter shading, respectively.

the other hand, the 2003 Tokachi-oki earthquake ruptured the deep interface more than it did the shallow interface (Fig. 10d). Neither deep nor shallow ruptures extended into the segment offshore Akkeshi in 2003 (Fig. 10d). The Akkeshi segment therefore remained as a distinct seismic gap in 2003, with respect to the 1973 earthquake. The strain increase in the unruptured Akkeshi segment prompted two M 7 earthquakes there in late 2004, which released a fraction of the accumulated strain. In the western part of the seismic gap recognized after 2003, a significant slow post-seismic slip occurred (Fig. 10d). However, it does not seem to have extended through the Akkeshi segment (MIYAZAKI *et al*., 2004; BABA *et al*., 2006).

Source regions varied their along-trench extent even among the earthquakes occurring within the same segment in the southernmost Kuril Trench. Furthermore, the along-trench extent of the source regions seems to differ between deep and shallow portions of the subduction interface.

8. Conclusion

In this paper we have thoroughly reviewed studies of tsunamis occurring in the southernmost Kuril Trench, including the most recent works published in 2007. Recent studies using waveform inversions of tide gauge records from the 1952 and 2003 Tokachi-oki earthquakes suggest that the 2003 tsunami source is significantly different from the 1952 tsunami source (HIRATA *et al.*, 2003; TANIOKA *et al.*, 2004b; SATAKE *et al.*, 2006). Other evidence from tsunami first arrivals (HIRATA *et al.*, 2004; HIRATA *et al.*, 2007) and tsunami runup height distributions (TANIOKA *et al.*, 2004a; SATAKE *et al.*, 2005) between 1952 and 2003 strongly support this idea. We conclude, at least from the viewpoint of tsunami evidence, that the 1952 and 2003 events do not share an identical rupture extent.

We propose a new interpretation of the spatial extent of large subduction earthquakes in the southernmost Kuril Trench. Possibly a small seismic gap has developed since 1894, limited only in the deep subduction interface, between the 1952 and 1973 earthquakes. The width of the gap is as long as a few to several tens of kilometers parallel to the trench, if it exists. On the other hand, there remains a larger seismic gap between the 1973 and 2003 earthquakes since 1952. The size of this gap reaches $\sim$150 km and $\sim$100 km in the shallow and deep portions, respectively, of the megathrust seismogenic zone. The later large seismic gap includes the small seismic gap that might have existed since 1894.

Variability in the spatial extent of large subduction earthquakes in both the along-trench direction and trench-normal directions makes it difficult to forecast future earthquakes in the southernmost Kuril subduction zone. In addition to spatial heterogeneity of coseismic rupture, slow post-seismic slip that was found following the 2003 Tokachi-oki earthquake provides additional complexity in understanding future earthquake rupture along the subduction interface.

Acknowledgements

This work is partially supported by the funding program (PI: Professor Naoshi Hirata): Special Coordination Fund for Promoting Science and Technology, Ministry of Education, Culture, Sports, Science and Technology (MEXT). Comments by two reviewers, Eric L. Geist and Yuichi Namegaya, and the editor, Phil Cummins enhanced the manuscript.

REFERENCES

AIDA, I. (1978), *Reliability of a tsunami source model derived from fault. Parameters*, J. Phys. Earth *26*, 57–73.

BABA, T., K. HIRATA, T. HORI, and H. SAKAGUCHI (2006), *Offshore geodetic data conducive to the estimation of the afterslip distribution following the 2003 Tokachi-oki earthquake*, Earth Planet. Sci. Lett. *241*, 281–292.

CENTRAL METEOROLOGICAL OBSERVATORY (1953), *Report of the Tokachi-Oki earthquake of March 4, 1952*, Q. J. Seismol. *17*, 135 (in Japanese).

EARTHQUAKE RESEARCH COMMITTEE (2004), *Long-term evaluation of seismicity along the Kuril Trench*, Publications of Earthquake Research Committee *II*, 1–74 (in Japanese).

HAMADA, N. and Y. SUZUKI (2004), *Re-examination of aftershocks of the 1952 Tokachi-oki earthquake and a comparison with those of the 2003 Tokachi-oki earthquake*, Earth, Planets, Space *56*, 341–345.

HASEGAWA, Y., Y. YOSHIDA, Y. HAYASHI, M. KOBAYASHI, A. KAMIKAWA, K. KABATA, and T. MATSUYAMA (2004), *Study on tsunami generation process based on detailed analysis of tsunami run-up heights. In Report of Emergent Research on the 2003 Tokachi-oki Earthquake* (ed. N. Hirata), the Special Coordination Funds for Promoting Science and Technology, MEXT, 229–249. (in Japanese).

HATORI, T. (1973), *Reexamination of the wave source of the 1952 Tokachi-oki tsunami*, Zisin *2*, 26, 206–208 (in Japanese with English abstract and figure captions).

HATORI, T. (1974a), *Source area of the tsunami off the Nemuro Peninsula in 1973 and its comparison with the tsunami in 1894*, Bull. Earthq. Res. Inst. *13*, 67–76 (in Japanese with English abstract and figure captions).

HATORI, T. (1974b), *Size and source area of tsunamis in and around eastern Hokkaido*. In *Report of Research on the Nemuro-Hanto-Oki Earthquake of June 17, 1973* (ed. Y. Sakai), the Special Coordination Funds for Natural Disaster Research in 1973, Monbusho, 248–256 (in Japanese with English abstract and figure captions).

HATORI, T. (1975), *Tsunami activity in eastern Hokkaido after the Nemuro Peninsula earthquake in 1973*, Zisin *28*, 461–471 (in Japanese with English abstract and figure captions).

HATORI, T. (1984), *Source area of the east Hokkaido tsunami generated in April, 1843,* Bull. Earthq. Res. Inst. *59*, 423–431 (in Japanese with English abstract and figure captions).

HATORI, T. (2004), *Size and source area of the 2003 Tokachi-oki earthquake*, Research Reports of Tsunami Engineering, Disaster Control Research Center, Tohoku University, 21, 93–98 (in Japanese with English abstract and figure captions).

HIRATA, K., E.L. GEIST, K. SATAKE, Y. TANIOKA, and S. YAMAKI (2003), *Slip distribution of the 1952 Tokachi-oki earthquake (M 8.1) along the Kuril trench deduced from tsunami waveform inversion*, J. Geophys. Res. *108* (B4), 2196 doi: 10.1029/2002JB001976.

HIRATA, K., Y. TANIOKA, K. SATAKE, S. YAMAKI, and E.L. GEIST (2004), *The tsunami source area of the 2003 Tokachi-oki earthquake estimated from tsunami travel times and its relationship to the 1952 Tokachi-oki earthquake*, Earth, Planets, and Space, *56*, 367–372.

HIRATA, K., K. SATAKE, S. YAMAKI, Y. TANIOKA, Y. YAMANAKA, and T. NISHIMURA (2007), *Examination of the northeast edge of the 1952 Tokachi-oki earthquake tsunami source based on eyewitness accounts stated in previously published reports*, Zisin *2*, 60, 21–42 (in Japanese with English abstract and figure captions).

HYDROGRAPHIC OFFICE, THE FIRST DISTRICT MARITIME SAFETY BUREAU (1954), *Observations on the phenomena caused by the Tokachi-oki earthquake*. In *The Survey Report of the Tokachi-oki Earthquake of 4th March, 1952* (ed. The Survey Committee of the Tokachi-oki earthquake), 209–219 (in Japanese).

JAPAN METEOROLOGICAL AGENCY (1982), *Revised table of major earthquakes in and around Japan (1926–1960)*, Seismol. Bull. Japan Meteorol. Agency, Supplement vol. 6, pp. 109 (in Japanese).

JAPAN METEOROLOGICAL AGENCY (1974), *Research report on the Nemuro-Hanto-Oki earthquake of June 17, 1973*, Technical Report of the Japan Meteorological Agency, 87, pp. 102 (in Japanese).

JAPAN METEOROLOGICAL AGENCY (2005), *Research report on the 2003 Tokachi-oki earthquake*, Technical Report of the Japan Meteorological Agency, *126*, pp. 231 (in Japanese).

KUSUNOKI, H. and H. ASADA1 (1954), *Report on the survey of the "Tsunami" in Hokkaido caused by the Tokachi earthquake*. In *The Survey Report of the Tokachi-oki Earthquake of 4th March, 1952* (ed. The Survey Committee of the Tokachi-oki Earthquake), 273–285 (in Japanese).

MIYAZAKI, S., P. SEGALL, J. FUKUDA, and T. KATO (2004), *Space-time distribution of afterslip following th 2003 Tokachi-oki earthquake: Iplications for variations in fault zone frictional properties*, Geophys. Res. Lett. *31*, L0623, doi:10.1029/2003GL019410.

NAMEGAYA, Y. and Y. TSUJI (2005), *Delayed peaks of tsunami waveforms at Miyako from earthquakes east off Hokkaido*. In *Tsunamis: Case Studies and Recent Developments* (ed. K. Satake), Advances in Natural and Technological Hazards Research (Springer), *23*, 115–134.

NANAYAMA, F., K. SATAKE, R. FURUKAWA, K. SHIMOKAWA, B.F. ATWATER, K. SHIGENO, and S. YAMAKI (2003), *Unusually large earthquakes inferred from tsunami deposits along the Kuril trench*, Nature *424*, 660–663.

OHGAKI, K. and F. IMAMURA (2004), *Numerical Analysis of the 2003 Tokachi-earthquake tsunami to understand its characteristic using field data*, Ann. J. Coastal Engin. JSCE *51*, 271–275 (in Japanese).

SAPPORO DISTRICT METEOROLOGICAL OBSERVATORY (2004), Report on investigation for the 2003 Tokachi-oki earthquake *The earthquake and tsunami from a viewpoint of damages*, Sapporo District Meteorological Observatory, March 2004, 127 pp. (in Japanese).

SATAKE, K., K. HIRATA, S. YAMAKI, and Y. TANIOKA (2006), *Re-estimation of tsunami source of the1952 Tokachi-oki earthquake*, Earth, Planets, Space *58*, 535–542.

SATAKE, K., F. NANAYAMA, S. YAMAKI, Y. TANIOKA, and K. HIRATA (2005), *Variability among tsunami sources in the 17th–21st centuries along the southern Kuril Trench*, Tsunami *Case Studies and Recent Developments* (ed. K. Satake), Advances in Natural and Technological Hazards Research (Springer), *23*, 157–170.

SATAKE, K. and S. YAMAKI (2005), *Tsunami source regions of the Tokachi-oki and Nemuro-oki earthquakes between 19th and 21st centuries*, The Earth Monthly, Special Vol. *49*, 168–172 (in Japanese).

SHIMAZAKI, K. (1974), *Nemuro-oki earthquake of June 17, 1973: A lithospheric rebound at the upper half of the interface*, Phys. Earth Planet. Inter. *9*, 314–327.

SHIMAZAKI, K. (2005), *Long-term earthquake forecast along the Kuril trench and the forecasted Tokachi-oki earthquake of 2003*, The Earth Monthly, Special Vol. *49*, 21–26 (in Japanese).

TAMIYA, M. and N. NAKAMURA (1953), *On tsunamis accompanied with the Tokachi-oki earthquake*, The Hydrographic Bull. Supplement *10*, 10–22 (in Japanese).

TANIOKA, Y. *et al*. (2004a), *Tsunami runup heights of the 2003 Tokachi-oki earthquake*, Earth, Planets, Space *56*, 359–365.

TANIOKA, Y., K. HIRATA, R. HINO, and T. KANAZAWA (2004b), *Slip distribution of the 2003 Tokachi-oki earthquake estimated from tsunami waveform inversion*, Earth, Planets, Space *56*, 373–376.

TANIOKA, Y., K. SATAKE, and K. HIRATA (2007), *Recurrence of recent large earthquakes along the Southernmost Kurile-Kamchatka Subduction Zone*, Geophy. Monograph Series *172*, American Geophysical Union, 145–152.

TSUJI, Y. (1994), *Illustrated another story (19), The Kushiro-oki earthquake in Tenpou era*, Newsletter, Seismol. Soc. Japan, *5*(6), 20 (in Japanese).

UTSU, T. (1999), *Seismicity Studies: A Comprehensive Review*, University of Tokyo Press, 876 pp (in Japanese).

YAMANAKA, Y. and K. KIKUCHI (2003), *Source process of the recurrent Tokachi-oki earthquake on September 26, 2003, inferred from teleseismic body waves* Earth, Planets, Space *55*, e21–24.

YAMANAKA, Y. (2006), *Asperity map in Hokkaido and southern Kurile arc*, The Earth Monthly *28*, 427–431 (in Japanese).

YOSHIDA, Y. (2005), *Source process determined by strong motion seismograms*. In *Report on the Tokachi-oki earthquake in 2003*, Technical Report of the Japan Meteorological Agency, 126, 9–14 (in Japanese).

(Received January 15, 2008, accepted June 23, 2008)
Published Online First: February 6, 2009

Pure appl. geophys. 166 (2009) 97–116
0033–4553/09/010097–20
DOI 10.1007/s00024-008-0441-6

Pure and Applied Geophysics

In situ Measurements of Tide Gauge Response and Corrections of Tsunami Waveforms from the Niigataken Chuetsu-oki Earthquake in 2007

YUICHI NAMEGAYA,[1] YUICHIRO TANIOKA,[2] KUNIAKI ABE,[3] KENJI SATAKE,[1,5] KENJI HIRATA,[4] MASAMI OKADA,[4] and ADITYA R. GUSMAN[2]

Abstract—Linear and nonlinear responses of ten well-type tide gauge stations on the Japan Sea coast of central Japan were estimated by *in situ* measurements. We poured water into the well or drained water from the well by using a pump to make an artificial water level difference between the outer sea and the well, then measured the recovery of water level in the well. At three tide gauge stations, Awashima, Iwafune, and Himekawa, the sea-level change of the outer sea is transmitted to the tide well instantaneously. However, at seven tide gauge stations, Nezugaseki, Ryotsu, Ogi, Teradomari, Banjin, Kujiranami, and Naoetsu, the sea-level change of the outer sea is not always transmitted to the tide well instantaneously. At these stations, the recorded tsunami waveforms are not assured to follow the actual tsunami waveforms. Tsunami waveforms from the Niigataken Chuetsu-oki Earthquake in 2007 recorded at these stations were corrected by using the measured tide gauge responses. The corrected amplitudes of the first and second waves were larger than the uncorrected ones, and the corrected peaks are a few minutes earlier than the uncorrected ones at Banjin, Kujiranami, and Ogi. At Banjin, the correction was significant; the corrected amplitudes of the first and second upward motion are +103 cm and +114 cm, respectively, while the uncorrected amplitudes were +96 cm and +88 cm. At other tide gauge stations, the differences between the uncorrected and corrected tsunami waveforms were insignificant.

Key words: *In situ* measurement, Tide gauge response, Corrected tsunami waveform, The Niigataken Chuetsu-oki Earthquake in 2007.

1. Introduction

A large earthquake occurred off the coast of Niigata Prefecture, Japan, at 10:13 a.m. (JST) July 16th, 2007. The Japan Meteorological Agency (JMA) estimated its magnitude to be 6.8 and named it the Niigataken Chuetsu-oki Earthquake in 2007. About 1,300

[1] Geological Survey of Japan, National Institute of Advanced Industrial Science and Technology (AIST), Central 7, Higashi 1-1-1, Tsukuba 305-8567, Japan. E-mail: yuichi.namegaya@aist.go.jp

[2] Faculty of Science, Hokkaido University, Kita 10 Nishi 8, Kita-ku, Sapporo 060-0810, Japan.

[3] The Nippon Dental University College at Niigata, Hamaura-cho 1-8, Chuo-ku, Niigata 951-8580, Japan.

[4] Meteorological Research Institute, Japan Meteorological Agency, Nagamine 1-1, Tsukuba 305-0052, Japan.

[5] Earthquake Research Institute, the University of Tokyo, Yayoi 1-1-1, Bunkyo-ku, Tokyo 113-0032, Japan.

houses were completely destroyed around the source area and 15 people were killed. The earthquake was accompanied by a tsunami with maximum amplitude of about 1 m recorded at the tide gauge station at Banjin, Kashiwazaki City, near the source region.

Three types of tide gauge systems are generally used in Japan: a well type, which records vertical motion of a float in a tide well connected with one or more intake pipes to the outer sea; a pressure type, which records hydrostatic pressure; and an acoustic type, which records distance between the sea surface and the sensor by acoustic waves. The tide gauge system of Banjin is of the well type. For this type, because of the narrow and/or long intake pipe, waves such as the astronomical tide with periods longer than several hours are faithfully recorded, but short-period waves with periods of less than several seconds such as wind wave or swell are mostly cut off. The response to a tsunami, having energy in the intermediate-period band of a few to a few ten minute periods is not well known. The intake pipes of tide gauge stations on the Japan Sea coast are usually narrow because of the severe sea conditions in winter. Therefore, in order to estimate the actual, or true, tsunami waveforms from the tide gauge records, it is necessary to correct them using the measured tide gauge response.

There have been several studies on tide gauge response. SHIPLEY (1963) studied a tide gauge system where the tide well is connected to the outer sea by an intake pipe. CROSS (1967) studied a tide gauge system in which the tide well is directly connected to the outer sea at an orifice without an intake pipe. They proposed a nonlinear response such that the temporal change of the water level in the well is proportional to the square root of the level difference between the outer sea and the well by using Bernoulli's theorem.

NOYE (1974a) examined a well system with long intake pipe, and proposed a linear response such that the temporal change of the water level in the well is proportional to the level difference between the outer sea and the well, assuming the flow in the intake pipe is a steady Poiseuille flow. If the length of the intake pipe is not too long and/or the diameter is not too small, the linear and nonlinear responses should be combined for tide gauge corrections (NOYE, 1974b).

LOOMIS (1983) calculated a nonlinear response to pseudo-tsunami by using running white noise, and showed that the larger the amplitude or the broader the spectrum of the tsunami, the greater the difference between the original and corrected waveforms.

OKADA (1985) carried out *in situ* measurements of the tide gauge response at Maizuru, Japan, and concluded that the observation was in better agreement with a nonlinear response than with a linear response. He also corrected the tsunami waveform of the 1983 Nihonkai-chubu (Japan Sea) earthquake (M_w 7.9) tsunami at Fukaura, Japan, using the nonlinear response.

SATAKE *et al.* (1988) conducted *in situ* measurements of the response at 40 tide gauge stations on the coasts of northern Japan, and corrected tsunami waveforms of the 1983 earthquake using nonlinear responses. For this tsunami, the amplitudes recorded at some tide gauge stations were considerably smaller than the visually observed inundation heights (KINOSHITA *et al.*, 1984). The maximum tsunami heights corrected by SATAKE *et al.* (1988) agreed well with the visually observed ones. SATAKE *et al.* (1988) also

estimated the theoretical hydraulic coefficients of the tide gauge response, but they concluded that the theoretical coefficients poorly coincided with those obtained by *in situ* measurements.

These previous studies mainly considered the effects of nonlinear response. However, since the lengths and diameters of the intake pipes of tide wells in Japan vary, we cannot exclude the possibility that some of the tide gauge response may include a linear component as proposed by NOYE (1974b). Moreover, about 20 years have passed since the previous studies, and circumstance of the intake pipes might be different. For example, the tide gauge stations at Naoetsu and Ogi moved after the measurements by SATAKE *et al*. (1988).

In the present study, we carry out *in situ* measurements at ten tide gauge stations. They are located at Nezugaseki (38°33'48"N, 139°32'45"E), Ogi (37°48'53"N, 138°16'52"E), and Kujiranami (37°21'24"N, 138°30'30"E), operated by the Geographical Survey Institute (GSI), at Awashima (38°28'04"N, 139°15'18"E) operated by Japan Coast Guard (JCG), at Iwafune (38°11'29"N, 139°25'51"E), Ryotsu (38°05'00"N, 138°26'10"E), Teradomari (37°38'36"N, 138°45'58"E), Banjin (37°21'55"N, 138°31'51"E), Naoetsu (37°11'06"N, 138°15'12"E), and Himekawa (37°02'22"N, 137°50'11"E), operated by Niigata Prefecture (Fig. 1). We estimate the tide gauge

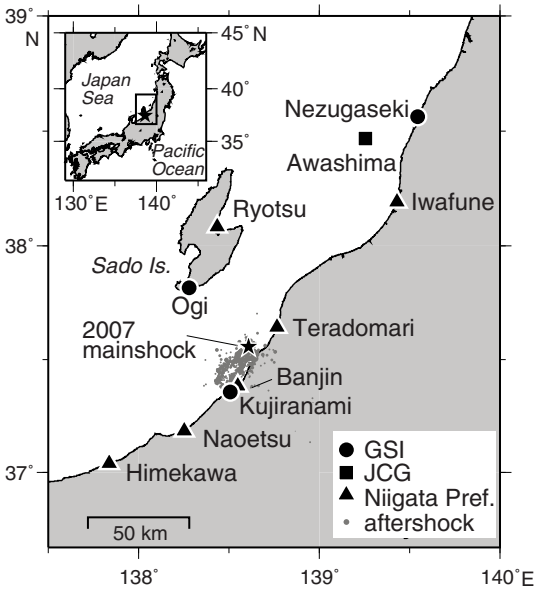

Figure 1

Location of the tide gauge stations whose responses were estimated by *in situ* measurements in the present study. The circles, square, and triangles indicate the tide gauge stations operated by Geographical Survey of Japan (GSI), Japan Coast Guard (JCG), and Niigata Prefecture, respectively. The aftershocks (gray dots) located by JMA within 1 day after the main shock (star) are also shown.

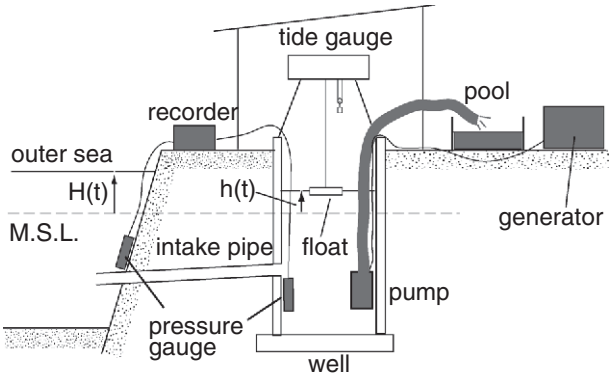

Figure 2
Schematic diagram for a typical tide gauge well structure in Japan. The pressure gauges, recorder, pump, pool, and generator (colored gray) are set up temporarily for *in situ* measurements. $H(t)$ and $h(t)$ denote the water levels of the outer sea and the well, respectively, above the mean sea level (M.S.L.).

responses with linear and nonlinear effects combined. Using the measured responses, we also correct the tsunami waveforms of the Niigataken Chuetsu-oki Earthquake in 2007.

2. Theory and Method for Tide Gauge Response and Tsunami Waveform Correction

2.1. Linear and Nonlinear Responses of Tide Well

In a typical tide well in Japan (Fig. 2), the well is connected to the outer sea with a long and narrow intake pipe. It usually records the long-period waves like astronomical tides and the vertical deformation due to long-term crustal motion, and short-period waves like wind wave or swell are cut off due to the existence of the narrow intake pipe. However, a tsunami having intermediate periods of a few to a few tens of minutes may not be faithfully recorded, because the change in the outer sea level caused by a tsunami is sometimes so large and rapid that the tide gauge system cannot follow it instantaneously.

When the water level in the well becomes different from the outer sea level, the nonlinear response based on Bernoulli's theorem is expressed as

$$\frac{dh(t)}{dt} = W\mathrm{sgn}\{H(t) - h(t)\}\sqrt{2g|H(t) - h(t)|}, \tag{1}$$

where t, $H(t)$, $h(t)$, and g denote time, the outer sea and the well levels, and gravitational acceleration, respectively (Fig. 2). The operation $\mathrm{sgn}(x)$ indicates the sign function. It takes the value $+1$ when there is inflow, and it takes the value -1 when there is outflow. The value, W, is a non-dimensional coefficient of the nonlinear response (nonlinear coefficient) to be estimated by *in situ* measurements (e.g. SATAKE *et al.*, 1988).

When the intake pipe is long and/or narrow, the flow in the intake pipe becomes like a steady Poiseuille flow (e.g., NOYE, 1974b). In this case, the response becomes linear, and is described as

$$\frac{dh(t)}{dt} = \frac{1}{G}\{H(t) - h(t)\}, \tag{2}$$

where G is the coefficient of the linear response with unit of time (linear coefficient), also to be estimated by *in situ* measurements.

When the length of the intake pipe is not too long and/or the diameter is not too small, the response of the well level is regarded as a combination of linear and nonlinear responses. Then, the response can be described as

$$\frac{dh(t)}{dt} = gW^2 \mathrm{sgn}\{H(t) - h(t)\}\left\{-G + \sqrt{G^2 + \frac{2|H(t) - h(t)|}{gW^2}}\right\}, \tag{3}$$

(e.g., NOYE, 1974b). Note that equation (3) becomes a nonlinear equation (1), when the linear response is negligible, that is, $G = 0$. Because of the long and/or narrow intake pipes, we consider equation (3).

2.2. *In situ Measurement of Tide Well Response*

The nonlinear coefficient W can be calculated by theoretical hydraulic considerations. However, SATAKE *et al*. (1988) pointed out that the theoretical coefficients can be as much as ten times larger than those obtained by *in situ* measurements. The large discrepancy is attributed to the inaccurate estimation of the friction in the intake pipe, because theoretical considerations do not account for the effect of marine organisms and sediment on it. Therefore, the actual coefficients should be estimated by *in situ* measurements.

In the *in situ* measurement, we first prepare two pressure gauges, a pump, pool, and generator (the gray symbols shown in Fig. 2). One pressure gauge is set up in the well and the other is set up near the mouth of the intake pipe in the outer sea. The pump is set up in the well, and the generator, which supplies electric power for the pump, and pool are set up on the ground near the well.

Next, water in the well is drained up to the pool by the pump until the water level in the well becomes significantly lower than that of the outer sea. Then we stop the pump, and measure the naturally recovering water level by using the pressure gauge, until the water level in the well becomes the same as that of the outer sea. This measurement is for the response of inflow from the outer sea to the well (inflow experiment).

We also carry out *in situ* measurements for outflow. In this case, we set up the pump in the pool filled with sea water. We then pour the water from the pool to the well, increasing the water level in the well with respect to the outer sea (outflow experiment). The pool is needed for the outflow experiments, but at Ryotsu and Himekawa, we directly poured water from the outer sea, because the tide well is located so close to the outer sea.

These inflow and outflow measurements are similar to SATAKE *et al.* (1988), however, they observed the well-water levels manually with a sampling interval of about 3 sec, because portable pressure gauges were not available. Moreover, they did not observe the outer sea level, and regarded it as the same as that in the well after the recovery. For our case, we measured the water levels both of the outer sea and the well by pressure gauges whose sampling interval is 1 sec for the tide well and 2 sec for the outer sea. We also manually observed the water level in the well with a sampling interval of about 3 sec, and recorded it by video camera.

2.3. Estimation of Linear and Nonlinear Coefficients G and W

In order to obtain the linear and nonlinear coefficients G and W in equation (3), we adopt a grid search method. First, we assume a W-G plane with a search area of $0.00001 \leqq W \leqq 0.01$ and $0 \leqq G \leqq 100$ sec, represented by 1,000 × 1,000 grid points with intervals of $\Delta W = 0.00001$ and $\Delta G = 0.1$ sec (Fig. 3a). Next, the recovering well levels after stopping the pump are calculated from equation (3) by the Runge-Kutta method, using

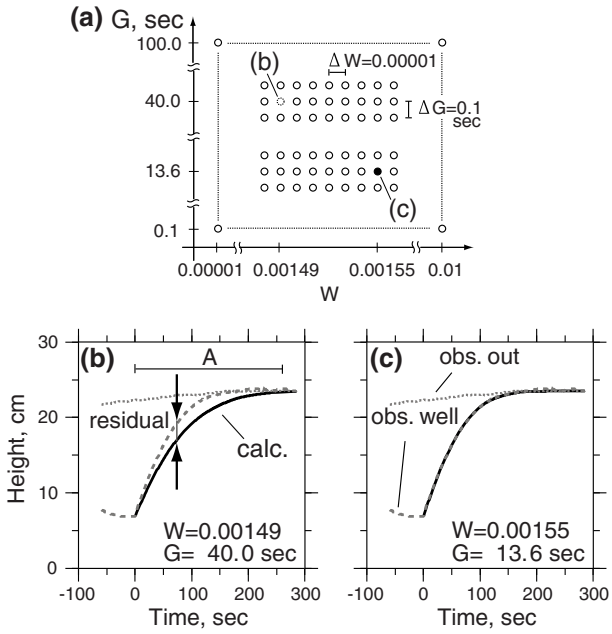

Figure 3

Schematic illustration of the grid-search method (see text). (a) Schematic W-G plane used for the grid search method. (b) Observed recovering well level (gray dashed line) for inflow and calculated one (solid line) by the Runge-Kutta method using the trial values for the coefficients $W = 0.00149$ and $G = 40.0$ sec at Banjin. The outer sea level is also shown (gray dotted line). The belt A indicates the time range in which the TASR is calculated. (c) Same as (b), but using the estimated linear and nonlinear coefficients which give the minimum TASR.

the coefficients at each grid point (W, G) as trial values (Fig. 3b). The temporally averaged-squared residual (TASR) between the observed and calculated levels is also calculated for each grid point, from the time the pump was stopped until the well water level reaches the same level of the outer sea. Then, the values of G and W which take the minimum TASR are regarded as the linear and nonlinear coefficients (Fig. 3c). We estimate the coefficients for inflow and outflow separately.

Because the water levels of the outer sea and the well are measured separately using two portable pressure sensors, the average level of the well after the recovery is set to be the same as that of the outer sea.

2.4. Corrections of Tide Gauge Records

The corrections of tide gauge records using the combined linear and nonlinear responses can be expressed as follows (NOYE, 1974b),

$$H(t) = h(t) + G\frac{dh(t)}{dt} + \frac{1}{2gW^2}\left(\frac{dh(t)}{dt}\right)^2 \mathrm{sgn}\left(\frac{dh(t)}{dt}\right). \tag{4}$$

Note that positive dh/dt means inflow and negative means outflow. Therefore, the coefficients obtained by the inflow and outflow experiments should be used for the positive and negative dh/dt, respectively.

3. Results of in situ Measurements

3.1. Linear and Nonlinear Coefficients

We carry out the inflow and outflow experiments at ten well-type tide gauge stations, and estimate the linear and nonlinear coefficients G and W by the grid search method. The results are shown in Figure 4, and Tables 1 and 2. At Nezugaseki, Ryotsu, Ogi, Teradomari, Banjin, Kujiranami, and Naoetsu, significant differences of the water levels between the outer sea and well could be produced using the pump, and the coefficients are obtained by the grid search method. A smallest value for the nonlinear coefficient W is estimated to be 0.00061 for the inflow and 0.00055 for the outflow at Kujiranami, while the largest value is estimated to be 0.00684 for the inflow at Teradomari and 0.00321 for the outflow at Naoetsu. Equations (3) and (4) indicate that the small nonlinear coefficient yields long recovery time and large water-level difference. The recovery times at Kujiranami, where the nonlinear coefficients take small values, are in fact long, while those at Naoetsu and Teradomari, where the nonlinear coefficients take large values, are short. At Nezugaseki, because of the severe sea condition at the time of measurement, strong short-period wave energy was transmitted to the tide well. Therefore, the TASR at Nezugaseki is large and the estimation of the linear and nonlinear coefficients might include some errors. Moreover, comparison of the recovering well levels between inflow

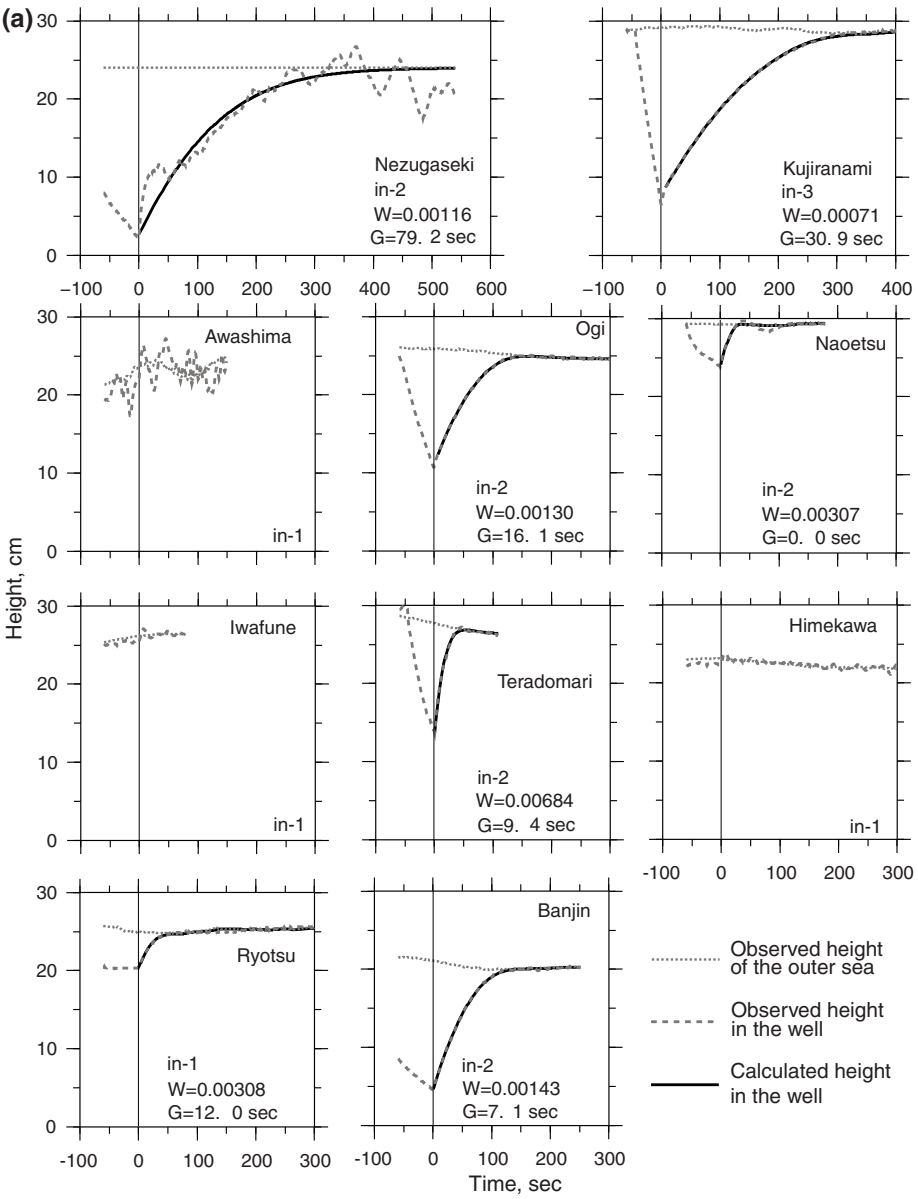

Figure 4

Results of the *in situ* measurements for ten tide gauge stations. (a) The observed recovering well levels (gray dashed lines) for inflow, outer sea levels (gray dotted lines), and the calculated recovering well levels (solid lines) using the estimated linear and nonlinear coefficients G and W (see Table 1). The code name indicates the experiment; e.g., in-2 is the second inflow experiment. Because the significant differences of the water levels between the outer sea and the well could not be made at Awashima, Iwafune, and Himekawa, the linear and nonlinear coefficients are not estimated. At Nezugaseki, because the pressure gauge in the outer sea was out of order, the outer sea level is assumed to be as indicated. (b) Same as (a), but for the outflow experiments.

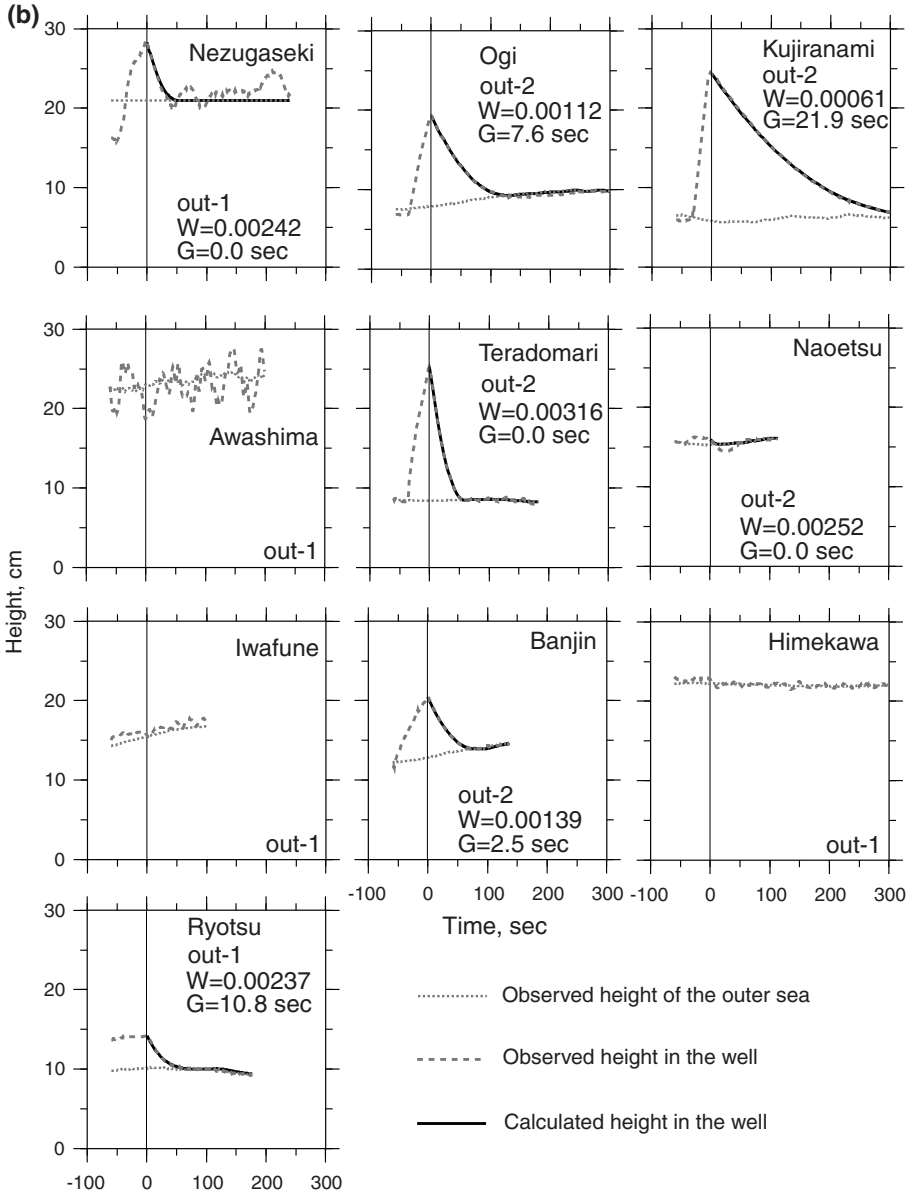

Figure 4
contd.

Table 1

The linear and nonlinear coefficients estimated from the in situ inflow experiments

Station	No.	W	G (sec)	TASR (m^2)	A	Ww	$TASR_w$	Obs. Date
Nezugaseki	1	0.00070	100.0	8.14E-04		0.00743	1.33E-03	22 Nov., 07
	2	0.00116	79.2	2.89E-04	*	0.00705	3.00E-03	
Awashima								23 Nov., 07
Iwafune								13 Sep., 07
Ryotsu	1	0.00308	12.0	5.95E-07	*	0.00183	2.29E-06	19 Sep., 07
	3	0.00303	11.7	7.85E-07		0.00180	2.49E-06	
Ogi	1	0.00126	10.8	5.68E-07		0.00113	1.81E-06	19 Sep., 07
	2	0.00130	16.1	2.79E-07	*	0.00109	2.65E-06	
Teradomari	2	0.00684	9.4	8.33E-06	*	0.00404	2.16E-05	13 Sep., 07
	3	0.00506	6.4	1.13E-05		0.00389	1.74E-05	
Banjin	1	0.00155	13.6	7.25E-07		0.00130	4.41E-06	11 Sep., 07
	2	0.00143	7.1	5.00E-07	*	0.00132	1.23E-06	
	3	0.00142	4.7	7.68E-07		0.00135	1.23E-06	
Kujiranami	1	0.00079	34.2	2.62E-06		0.00065	8.92E-06	11 Sep., 07
	2	0.00061	35.1	2.34E-06		0.00051	5.30E-06	
	3	0.00071	30.9	8.34E-07	*	0.00061	5.10E-06	
Naoetsu	1	0.00299	0.0	5.41E-07		0.00299	5.41E-07	12 Sep., 07
	2	0.00307	0.0	5.40E-07	*	0.00307	5.40E-07	
	3	0.00324	0.0	6.15E-07		0.00324	6.15E-07	
	4	0.00296	0.0	8.00E-07		0.00296	8.00E-07	
Himekawa								20 Sep., 07

The values of G and W with symbol * in column A are the best linear and nonlinear coefficients used for the corrections of tsunami waveforms. TASR is the temporally averaged-squared residual (in m^2). The subscript "w" denotes the values of the nonlinear response, which is estimated by the grid search method, assuming that the linear coefficient $G = 0$.

and outflow at Nezugaseki shows that the artificial water-level difference for inflow is much larger than and the recovery for inflow is slower than those for outflow. This discrepancy is attributed to an insufficient setting for the outflow experiment at Nezugaseki where the recovery time is considerably long. The amount of water pumped from the pool was not sufficient to raise the well water level enough to conduct the outflow experiment. Therefore, the coefficients for outflow at Nezugaseki may be unreliable.

At Naoetsu and Teradomari, the linear coefficient G is estimated as zero. This means that the tide gauge response for inflow and/or outflow is completely nonlinear at these sites.

At Awashima, Iwafune, and Himekawa, no significant difference of the water level between the outer sea and well could be produced using the pump both for the inflow and outflow experiments. Such an insignificant difference suggests that the outer sea-level change transmits to the well almost instantaneously, and the tsunami waveforms recorded in the well can be regarded as the actual or true tsunami waveforms of the outer sea. Therefore, in the present study, no corrections are made for the recorded tsunami waveforms at the above three tide gauge stations. The observed oscillation in inflow experiment at Awashima can be explained by the characteristic oscillation of the tide gauge system consisting of intake pipe and tide well.

Table 2

The linear and nonlinear coefficients estimated from the in situ outflow experiments

Station	No.	W	G (sec)	TASR (m^2)	A	Ww	$TASR_w$	Obs. Date
Nezugaseki	1	0.00242	0.0	9.59E-07		0.00242	9.59E-07	22 Nov., 07
Awashima								23 Nov., 07
Iwafune								13 Sep., 07
Ryotsu	1	0.00237	10.8	8.21E-07	*	0.00160	1.75E-06	19 Sep., 07
	2	0.00209	6.4	1.06E-06		0.00168	1.37E-06	
Ogi	1	0.00132	22.7	6.83E-07		0.00100	3.80E-06	19 Sep., 07
	2	0.00112	7.6	4.19E-07	*	0.00103	7.76E-07	
Teradomari	1	0.00309	0.0	5.81E-06		0.00309	5.81E-06	13 Sep., 07
	2	0.00316	0.0	5.68E-07	*	0.00316	5.68E-07	
Banjin	1	0.00143	3.2	8.13E-07		0.00135	8.95E-07	11 Sep., 07
	2	0.00139	2.5	3.26E-07	*	0.00134	3.67E-07	
Kujiranami	1	0.00055	1.8	1.33E-06		0.00055	1.61E-06	11 Sep., 07
	2	0.00061	21.9	8.61E-07	*	0.00055	2.70E-06	
Naoetsu	1	0.00273	0.0	5.46E-07		0.00273	5.46E-07	12 Sep., 07
	2	0.00252	0.0	2.86E-07	*	0.00252	2.86E-07	
	3	0.00298	0.0	1.58E-06		0.00298	1.58E-06	
	4	0.00244	0.0	1.09E-06		0.00244	1.09E-06	
	5	0.00321	0.0	2.53E-06		0.00321	2.53E-06	
Himekawa								20 Sep., 07

The legend is the same as Table 1.

During the inflow experiments at Iwafune and Himekawa, we could not produce significant water level differences, and the flow in the intake pipe was steady. We measured the steady flow rate of 2.6 liter/sec at Iwafune, and 3.5 liter/sec at Himekawa by using a scaling bucket.

At Iwafune, the intake pipe was cleaned in February 2007, which is 7 months before the experiment or 5 months before the tsunami. Hence the tide response is good at this station. At Nezugaseki, it was also cleaned in October 2007, which is 1 month before the experiment but 4 months after the tsunami. Therefore, the obtained linear and nonlinear coefficients at Nezugaseki may not be the same as those at the time of the tsunami from the Niigataken Chuetsu-oki Earthquake in 2007.

During the inflow experiments at Kujiranami and Ogi, the backward (rebound) flow from the pump into the well was observed just after we stopped the pump. Hence, the observed well level recovered more quickly than the well level governed by equation (3) does (Fig. 5a). In these cases, as the initial condition for the Runge-Kutta method, we use the observed well level at the time when the backward flow is just completed rather than when we stopped the pump (Fig. 5b).

At Teradomari and Naoetsu, inertial oscillations were observed after the well level recovered to the outer sea level (Fig. 5c). This phenomenon cannot be explained by equation (3), and therefore, the mean level of the oscillation is considered as the outer sea level just after the recovery (region A in Fig. 5c).

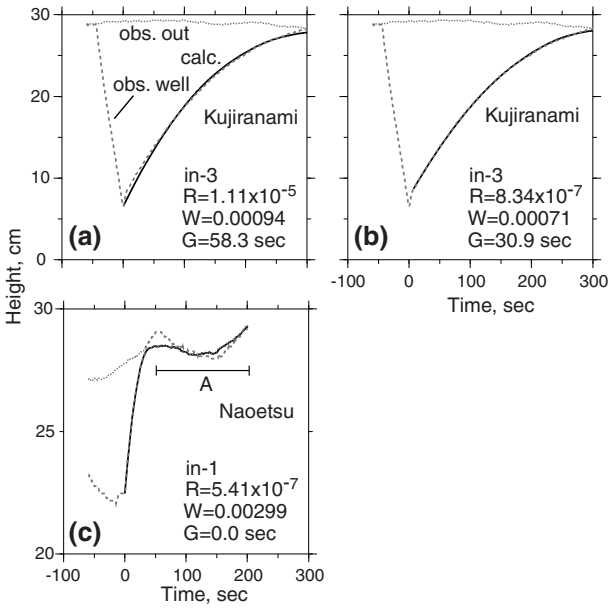

Figure 5

(a) Recovering well level (the black solid line) for the third inflow experiment (in-3) at Kujiranami calculated by the Runge-Kutta method with the initial height at t = 0 (just after we stopped the pump). The gray dotted and dashed lines are the observed outer sea and the well levels, respectively. R, W, and G denote TASR and nonlinear and linear coefficients, respectively. Because of the influence of the backward flow, the calculated recovering well level does not completely coincide with the observed one even if the linear and nonlinear coefficients estimated by the grid-search method are used. (b) Recovering well level for the same case as (a) calculated with the initial height at t = 7 sec (when the backward flow from the pump ended). In this case, the calculated recovering well level coincides with the observed one. (c) Recovering sea level for the first inflow experiment (in-1) at Naoetsu calculated by referencing the outer sea level to the mean well level in range A.

3.2. Best Linear and Nonlinear Coefficients

Several inflow and outflow experiments were carried out at each tide gauge station, and the linear and nonlinear coefficients are estimated by a grid search method for each experiment. In the present study, among the estimated linear and nonlinear coefficients for each experiment, those with the minimum TASR are regarded as the best pairs for inflow or outflow at the tide gauge station. For example, at Banjin, we made three inflow experiments and two outflow experiments, and the linear and nonlinear coefficients of the second inflow and outflow experiments yield the minimum TASR (Tables 1 and 2). Hence the pairs $W = 0.00143$ and $G = 7.1$ sec for inflow and $W = 0.00139$ and $G = 2.5$ sec for outflow are regarded as the best linear and nonlinear coefficients at Banjin.

To confirm the reproducibility of experiments, we check the distributions of TASR for the inflow and outflow experiments at each tide gauge station (Fig. 6). The figure shows that the distribution of TASR is similar for repeated inflow or outflow experiments at each tide gauge station, and indicates that repeated experiments yield similar results.

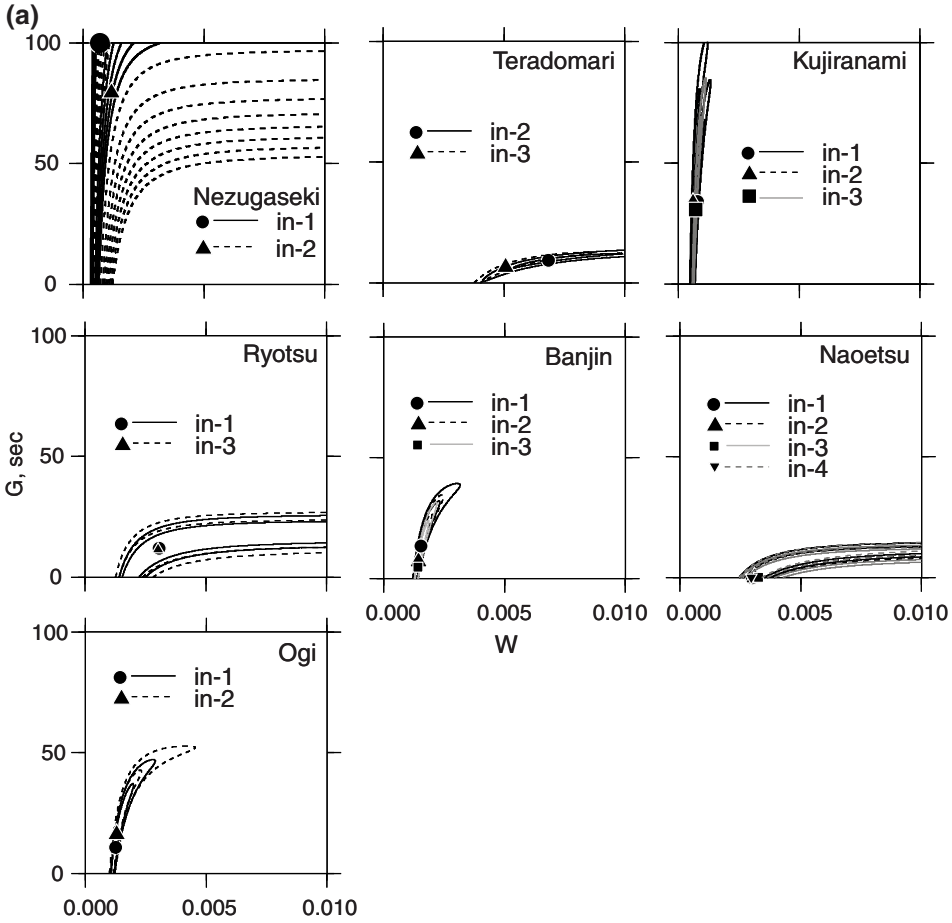

Figure 6

(a) Contour plot of the temporally averaged squared residual (TASR) of observed and calculated recovering well levels for inflow. The range of the contour lines is from 2×10^{-4} to 2×10^{-3} m^2 with intervals of 2×10^{-4} m^2 for Nezugaseki, while the range is from 1×10^{-5} to 2×10^{-5} m^2 with intervals of 1×10^{-5} m^2 for the other stations. The different lines (solid and dashed) and symbols indicate the different experiments. At Awashima, Iwafune, and Himekawa, the contour lines of TASR are not estimated because the responses of these tide gauges insignificantly influence recorded tsunami waveforms. (b) Same as (a), but for outflow. At Nezugaseki, only one outflow experiment was carried out, and therefore, the comparison is not made.

3.3. Nonlinear Response

The tide gauge response is modeled by a combination of linear and nonlinear response at Nezugaseki, Ryotsu, Ogi, Teradomari, Banjin, and Kujiranami, because the estimated best coefficients of G are not zero (Table 1). The nonlinear coefficients W are also estimated by the grid search method, assuming that the linear coefficients G are zero, correspond to a pure nonlinear response as adopted by the previous study (e.g., SATAKE

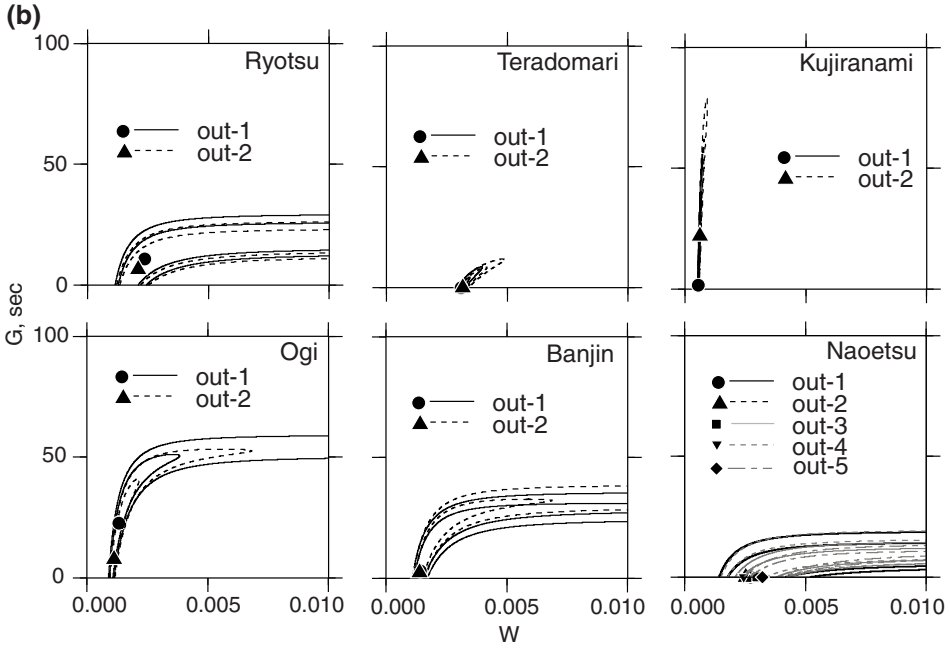

Figure 6
contd.

et al., 1988). We denote this nonlinear coefficient *Ww,* and the corresponding TASRw are also shown in Tables 1 and 2. In fact, TASRw is larger than or equal to the TASR. The effect of *W* and *Ww* on the waveform correction will be discussed in Section 4.3.

4. Correction of Tsunami Waveforms of the Niigataken Chuetsu-oki Earthquake in 2007

4.1. Correction of the Tsunami Waveforms using the Best Linear and Nonlinear Coefficients

In the previous section, we found that the correction for tide gauge response is necessary at Nezugaseki, Ryotsu, Ogi, Teradomari, Banjin, Kujiranami, and Naoetsu, but not at Awashima, Iwafune, and Himekawa. In this section, the tsunami waveforms of the Niigataken Chuetsu-oki Earthquake in 2007 at the former seven tide gauge stations are corrected using equation (4) and the best linear and nonlinear coefficients.

The original tide gauge records are digitally recorded at a sampling interval of 30 sec at Nezugaseki, Ogi and Kujiranami, and 6 sec at Teradomari. We resampled them at 60 sec interval for the correction. At Ryotsu, Banjin, and Naoetsu, the tsunami waveforms were recorded in analogue form. Hence we manually digitized the tsunami waveforms

recorded on the paper sheets. We also resampled the digitized records at 60 sec intervals. Generally, manual digitization inevitably includes reading errors which mainly consist of high frequency components. In order to minimize these errors, a moving average filter, consisting of a Hanning window with 4 min full width, was applied to the digitized records. Because it makes the peaks of the records blunt, the peak values are replaced by the original ones, so that the original peak values are retained. The astronomical tide is removed by fitting polynomial functions.

The above tsunami waveforms at a sampling interval of 60 sec are corrected by using equation (4) with the best linear and nonlinear coefficients (Fig. 7). Note that in equation (4), we use the best coefficients of inflow for the upward motion, and those of outflow for the downward motion. At Banjin, where the largest amplitudes were originally recorded,

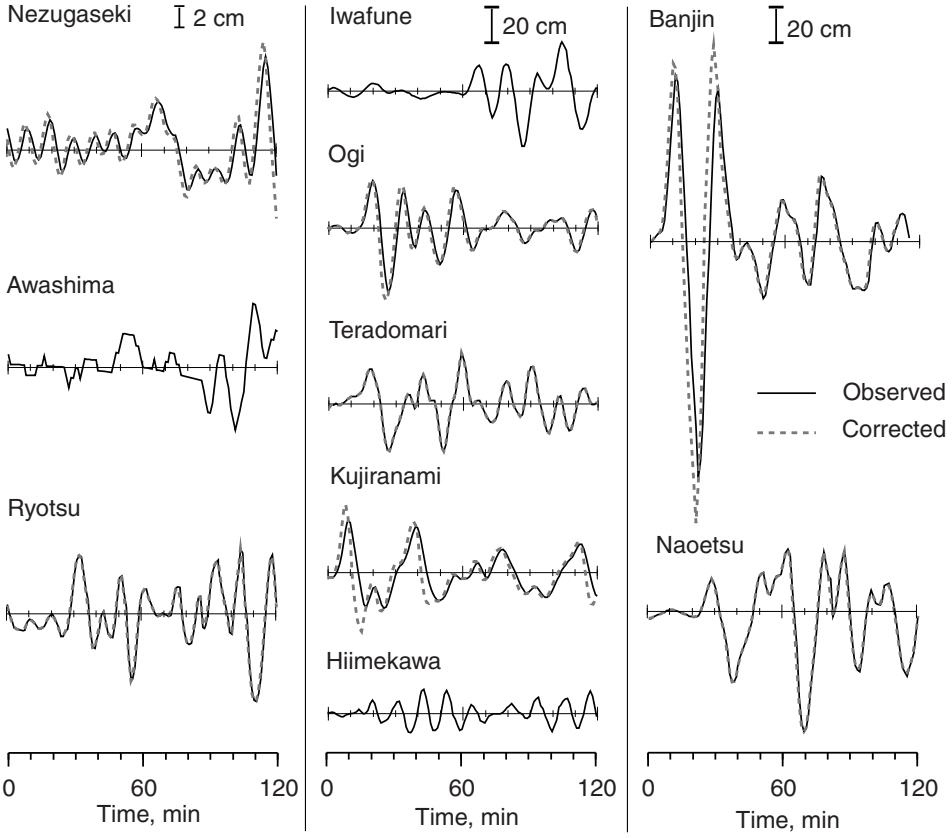

Figure 7

Corrected (gray dashed lines) and observed (black solid lines) tsunami waveforms of the Niigataken Chuetsu-oki Earthquake in 2007. Note the different amplitude scales for the left column. The tsunami waveforms at Nezugaseki, Ryotsu, Ogi, Teradomari, Kujiranami, Banjin, and Naoetsu are corrected. At the other tide gauge stations, only the original tsunami waveforms are shown because these tide gauge responses had no significant influence on the recorded tsunami waveform.

the first upward, downward, and second upward amplitudes after the correction become +103 cm, −163 cm, and +114 cm, respectively, while those of the original record are +96 cm, −137 cm, and +88 cm. It is noteworthy that the corrected waveform shows that the second upward amplitude becomes larger than the first one. The appearance of the above peaks shifts to at most a few minutes earlier than the peaks of the uncorrected records. Moreover, around Banjin tide gauge station, it was reported that the tsunami climbed up a quay, and the ground was slightly inundated. The inundation height was visually observed as 110 cm above the sea level at the time of tsunami arrival (Fig. 8). This height is in good agreement with the corrected maximum amplitude of +114 cm, indicating that the correction is reliable.

At Kujiranami, the corrected first upward and downward amplitudes become +41 cm and −31 cm, while those of the original records are +33 cm and −17 cm, respectively. The appearance of the above peaks also shifts to a few minutes earlier than the uncorrected

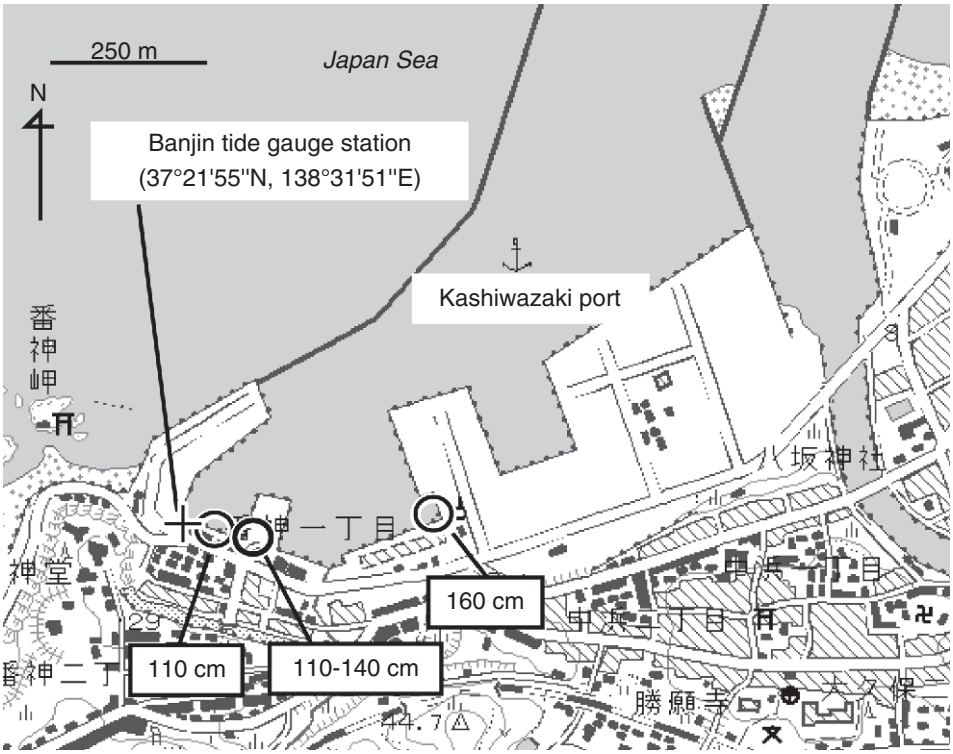

Figure 8
Map around the Banjin tide gauge station. The numerals indicate the tsunami inundation height of the Niigataken Chuetsu-oki Earthquake in 2007 above the sea level at the time of tsunami arrival. Around here, subsidence of a few cm was reported by GSI (NISHIMURA *et al.*, 2008), but the amount can be neglected in comparison with the tsunami inundation height. A topographical map with 1:25,000 scale provided by GSI is used.

peaks. At Ogi, the original waveform is similarly corrected. However, at Ryotsu, Teradomari, and Naoetsu, the corrected waveforms are similar to the original ones, despite values of G and W for these stations that would suggest a significant influence of both nonlinear and linear response components. This unexpected result is attributed to the relatively small amplitudes and long periods of the tsunami. At Nezugaseki, as mentioned in Section 3.1, the intake pipe was cleaned after the tsunami but before our *in situ* measurement. Therefore, the linear and nonlinear coefficients obtained by the *in situ* measurement may not represent the tide gauge response at the time of the tsunami, but we correct it tentatively using the coefficient only for the inflow (see Section 3.1).

4.2. Effects of Variance of Linear and Nonlinear Coefficients on the Correction

For the correction of tsunami waveforms, we used the best linear and nonlinear coefficients estimated from the repeated experiments as mentioned in Section 3.2. How do the corrected waveforms change if we use other pairs of coefficients? In order to examine the effect, we correct the tsunami waveforms by using all the pairs of the coefficients estimated by each experiment. For example, at Kujiranami, we carried out three inflow experiments and two outflow experiments. Hence three pairs for inflow and two pairs for outflow were estimated. Therefore, six corrected tsunami waveforms can be obtained, because the pairs for inflow and outflow are needed to correct the upward and downward waveforms, respectively. Comparison of these waveforms shows that there is a discernable difference in the corrected waveforms only at Kujiranami. The largest difference is obtained by the combinations of the linear and nonlinear coefficients of the third inflow and the second outflow experiments, and the second inflow and the second outflow experiments (Fig. 9), nonetheless the difference is insignificant. This indicates that variance in measurement of the coefficients does not influence the correction of tsunami waveforms significantly.

4.3. Effect of Linear Response

The results in Section 3.1 show that the linear response is needed for the correction of the tsunami waveforms at Nezugaseki, Ryotsu, Ogi, Teradomari, Banjin, and Kujiranami. What is the contribution of the linear response to the tsunami waveform correction? In order to examine the effect, we correct the tsunami waveforms by using the coefficients *Ww* in Tables 1 and 2, which are the nonlinear coefficients estimated by the grid search method by assuming the linear coefficient G is zero. At Nezugaseki the correction using *Ww* does not change the waveform, while the appearance of the corrected peaks with the combined linear and nonlinear coefficients becomes a few minutes earlier (Fig. 10a). This indicates that the effect of the linear response is larger than the nonlinear response, although it is still insignificant for correcting the tsunami waveforms. At Kujiranami, the negative amplitude corrected by using the nonlinear coefficient *Ww* is slightly larger than that by combined linear and nonlinear coefficients G and W (arrow in Fig. 10b).

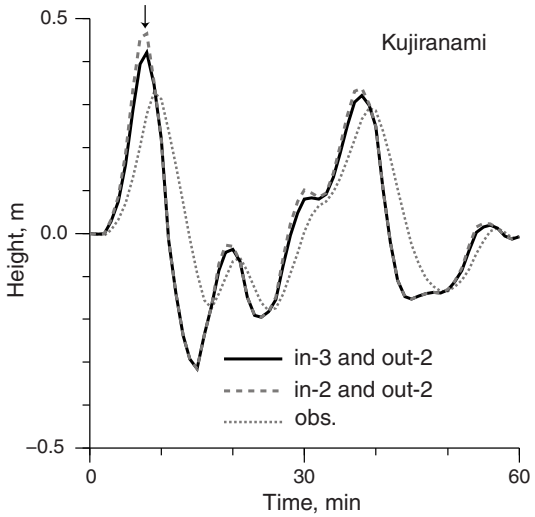

Figure 9
Comparison of the observed tsunami waveform with the corrected ones at Kujiranami. The correction using both linear and nonlinear coefficients for the third inflow and the second outflow experiments is shown by a solid line, while for the second inflow and outflow experiments shown by a gray dashed line. The original record is shown by a dotted line. The amplitudes of the first peak (arrow) are slightly different.

However, the difference is small compared with the difference between corrected and original tsunami waveforms. At the other tide gauge stations, no differences were recognized. That is to say, for the tsunami of the Niigataken Chuetsu-oki Earthquake in

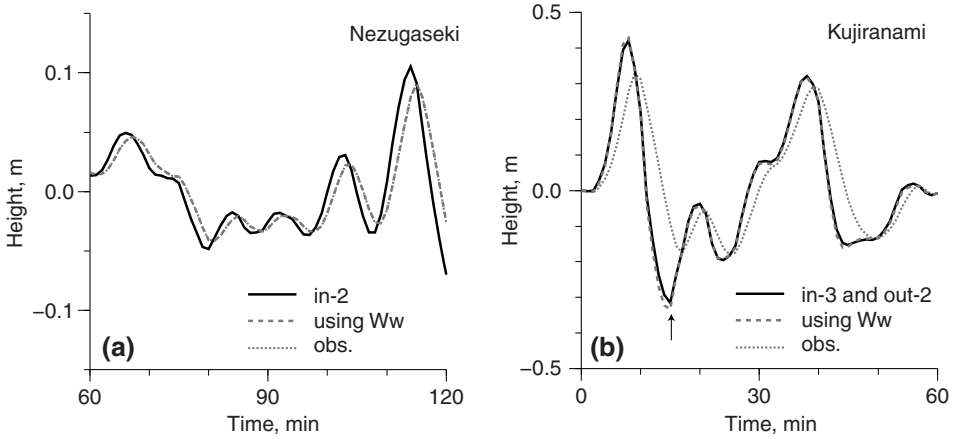

Figure 10
(a) Comparison of the corrected tsunami waveforms using the nonlinear-only coefficients *Ww* (gray dashed line) with those using the combined coefficients *G* and *W* (black solid line) at Nezugaseki. The original waveform (dotted line) is also shown. (b) Same as (a) but at Kujiranami. The difference was only at the negative peak (arrow).

2007, the effect of the linear response can be neglected. However, this does not necessarily mean that the linear response can always be neglected for other cases.

5. Conclusion

We carried out *in situ* measurements for the linear and nonlinear tide gauge responses at ten tide gauge stations, Nezugaseki, Awashima, Iwafune, Ryotsu, Ogi, Teradomari, Banjin, Kujiranami, Naoetsu, and Himekawa, on the Japan Sea coast of central Japan, and corrected the tsunami waveforms of the Niigataken Chuetsu-oki Earthquake in 2007. The results are summarized as follows.

(1) At Nezugaseki, Ryotsu, Ogi, Teradomari, Banjin, and Kujiranami, both linear and nonlinear components of the tide gauge response must be considered for the intermediate periods of a few to a few tens of minutes characteristic of tsunami energy. At Naoetsu, only the nonlinear component of the tide gauge response influences the tsunami waveform. At Awashima, Iwafune, and Himekawa, the response of the tide system negligibly effects the tsunami waveform, so that the correction was unnecessary.
(2) We corrected the tsunami waveforms from the Niigataken Chuetsu-oki Earthquake in 2007 with the measured tide gauge responses at Nezugaseki, Ryotsu, Ogi, Teradomari, Banjin, Kujiranami, and Naoetsu. The corrected amplitudes become higher and the peaks appear a few minutes earlier than the original ones at Banjin, Kujiranami, and Ogi. At Banjin, the original first upward amplitude of +96 cm, the first downward one of −137 cm, and the second upward one of +88 cm become +103 cm, −163 cm, and +114 cm, respectively. The amplitude of +114 cm coincides with the tsunami inundation height by visual observation. At the other stations, the differences of original and corrected tsunami waveforms are insignificant.
(3) The corrected tsunami waveform by the nonlinear coefficients is slightly different from that by the combined linear and nonlinear ones at Kujiranami. However, the difference is considerably smaller than the amplitudes of the first and second tsunami waves on the original tide gauge records and/or on the corrected tsunami waveforms. At the other tide gauge stations, the difference is insignificant. Therefore, the effect of the linear response for the tsunami of the Niigataken Chuetsu-oki Earthquake in 2007 can be neglected.

The tide gauge stations whose response was estimated in this study are a well type and located on the coast of the Japan Sea where the sea condition is severe in winter, and the intake pipes therefore need to be narrow. Our study indicates that tide gauge response to tsunami must be considered for such stations, particularly when the recorded tsunami period is short and the amplitude is large. While tide gauges usually respond well to record tsunami for other cases, other types (pressure gauges and acoustic gauges) are less costly and free from the effects of intake pipes.

Acknowledgements

Geographical Survey Institute, Japan Coast Guard, and Niigata Prefecture kindly provided us their tide gauge records and gave us permissions for our *in situ* measurements. Editor Phil R. Cummins and two anonymous referees provided valuable comments which improved the paper. This study was partially supported by Special Coordination Funds for Promoting Science and Technology, from Ministry of Education Sports, Culture, Science and Technology. Most of the figures were generated by using General Mapping Tools (WESSEL and SMITH, 1998).

REFERENCES

CROSS, R. H. (1967), *Frequency response of tide gages*, Technical Rep. Univ. California, *HEL 16-4*, 16 p.

KINOSHITA, T., KUMAGAI, S., TSUJI, Y., OGAWA, N., NUMANO, N., ABE, O., and KONISHI, T. (1984), *Survey research report on the disaster of the Nihonkai-Chubu earthquake*, Principal Disaster Rep. *23*, National Research Center for Disaster prevention, Tsukuba, 165 p (in Japanese).

LOOMIS, H. G. (1983), *The nonlinear response of a tide gage to a tsunami*, Proc. 1983 Tsunami Symp., pp. 177–185.

NISHIMURA, T., TOBITA, M., YARAI, H., OZAWA, S., MURAKAMI, M., YUTSUDO, T., ISHIMOTO, M., UMESAWA, T., TOYOFUKU, T., KAWAMOTO, S., AMAGAI, T., FUJIWARA, M., SUZUKI, A., ENYA, S., SASAKI, T., YOKOKAWA, M., OOMORI, S., TANOUE, S., IKEDA, H., NEMOTO, M., SUITO, H., HAYASHI, F., UNE, H., KOARAI, M., and TSUZAWA, M. (2008), *Crustal deformation and a preliminary fault model of the 2007 Chuetsu-oki earthquake observed by GPS, InSar, and leveling*, Earth Planet. Space *60*, 1093–1098.

NOYE, B. J. (1974a), *Tide-well systems II: The frequency response of a linear tide-well system*, J. Mar. Res. *32*, 155–181.

NOYE, B. J. (1974b), *Tide-well systems III: Improved interpretation of tide-well records*, J. Mar. Res. *32*, 183–194.

OKADA, M. (1985), *Response of some tide-wells in Japan to tsunamis*, Proc. Int. Tsunami. Symp., pp. 208–213.

SATAKE, K., OKADA, M., and ABE, K. (1988), *Tide gauge response to tsunamis: Measurements at 40 tide gauge stations in Japan*, J. Mar. Res. *46*, 557–571.

SHIPLEY, A., M. (1963), *On measuring long waves with a tide gauge*, Deut. Hydr. Zeitschr. *16*, 136–140.

WESSEL, P. and SMITH, W. H. F. (1998), *New, improved version of the Generic Mapping Tools released*, EOS Trans. AGU *79*, 579.

(Received January 27, 2008, accepted July 21, 2008)
Published Online First: February 14, 2009

Pure appl. geophys. 166 (2009) 117–130
0033–4553/09/010117–14
DOI 10.1007/s00024-008-0436-3

Pure and Applied Geophysics

Excitation of Resonant Modes along the Japanese Coast by the 1993 and 1983 Tsunamis in the Japan Sea

KUNIAKI ABE

Abstract—We observed seiches at 55 ports in Japan facing the Japan Sea and obtained dominant periods from their maximum spectral amplitudes. These periods were mostly determined ranging from 10 to 40 minutes. They were compared with dominant periods of the 1993 Hokkaido Nansei-oki tsunami and the 1983 Nihonkai Chubu-oki tsunami at the same ports. As a result, relations of dominant periods between seiches and tsunamis are classified into three types. The first one is fundamental mode excitation, the second is higher mode excitation and the third is no excitation. Plotting the maximum spectral amplitude normalized at an epicentral distance of 50 km versus the ratio of the tsunami dominant period to the seiche dominant period, we obtained resonance curves having maxima at one. This fact shows a contribution of resonance to the amplification. Thus it is recognized that the dominant period of seiching is an important factor in interpreting amplification and resonance of tsunami.

Key words: Seiche, Tsunami, Japan Sea, resonant mode.

1. Introduction

Many tide gauge observations of tsunamis have established that the maximum tsunami amplitude rarely occurs during the first peak-trough cycle. It is difficult to understand this behavior because tsunamis are generated by fault motion with no oscillation. Accordingly, it is necessary to consider some superposition of waves to explain an amplitude increase at a later time. KATO *et al.* (1961) arrived at the idea of resonance to explain the different behavior between the 1960 Chilean tsunami and the 1933 Sanriku tsunami. ABE (2005) carried out observations of seiching at bays along the Sanriku coast, Japan, to obtain the dominant period of each observation, and constructed resonance curves by plotting the amplitude ratio between the mouth and head of each bay as a function of tsunami period normalized by seiche period. He showed that tsunami inundation heights observed at the head of bays along the Sanriku coast facing the Pacific Ocean are explained from resonance curves using the dominant periods. In contrast to the Sanriku coast, the coast of Japan bordering the Japan Sea, has a simple coastline. During the last 25 years there have

Nippon Dental University, College at Niigata, Hamauracho 1-8, Chuouku, Niigata City 951-8580, Japan. E-mail: abeku@ngt.ndu.ac.jp

been two large tsunamis in the Japan Sea: The 1993 Hokkaido Nansei-oki and the 1983 Nihonkai Chubu-oki tsunamis. Many tide gauge records of these tsunami are useful for analyzing tsunami amplification. In this paper I analyze the spectra of these observations to better understand the relation between tsunami amplification and seiching.

2. *Seiche Observations*

Observations of seiching at ports, including heads of bays, were conducted intermittently along the Japanese coast of the Japan Sea during the period from November 22, 2002 to December 25, 2006. Due to the simple coastline, bays are limited in number and many observation places are ports including ones facing the open sea. The fifty-five observation points distribute from Hokkaido to Kyushu in Japan as shown in Figure 1. Variations of sea level were recorded by a pressure gauge hung along the wall

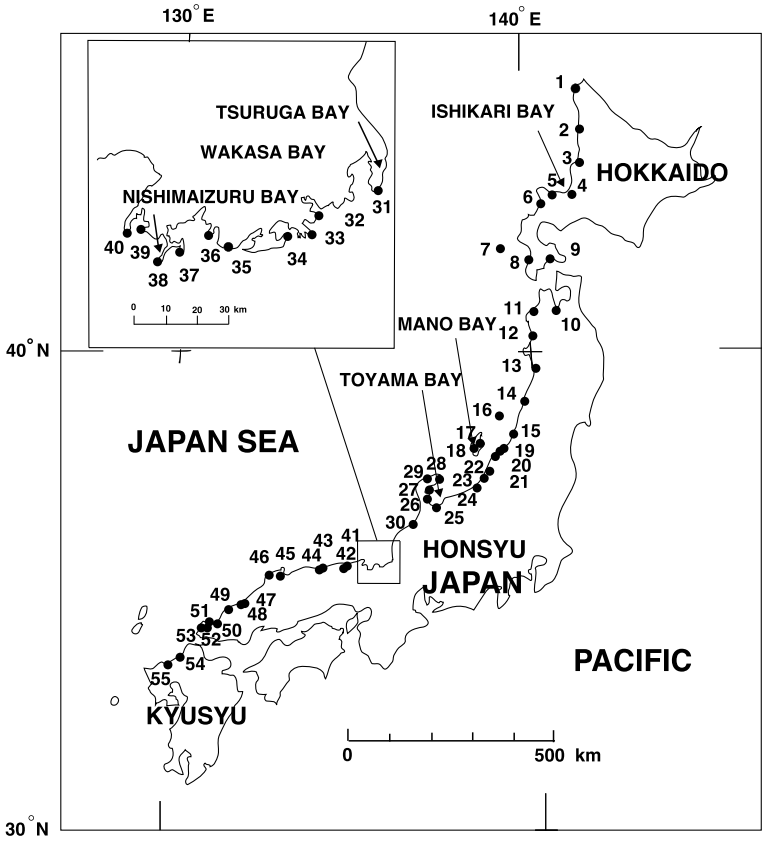

Figure 1
Observation points of seiche (solid circle).

of a quay in a port (ABE, 2005). Data were acquired for total durations of six hours with a sampling interval of one minute in comparatively calm sea conditions. The amplitude data were stored in a recorder and transferred to a computer via memory card. The time histories were transformed to smooth spectra in the frequency range of 0.06–2.4 mHz (6.9–177 min. in period).

3. Observed Spectra and the Dominant Periods in the Seiche

The dominant period T_0 is defined as the period of the maximum amplitude in the seiche spectrum for each observation point. The numbers corresponding to observation points are indicated in Figure 1. Examples of obtained spectra are shown in Figure 2. These are characterized by a single peak and referred to here as 'single-peak' spectra. A single-peak spectrum is defined as containing no second peak in amplitude higher than one-third of the maximum level, so that the dominant period is clearly defined. Eleven observation points are included in this category as shown in Figure 2, and occupy 20% of all the observation points. Most of these observation points are in large bays such as Ishikari, Toyama and Wakasa. This is not the case, however, for Sakata (No.14), Naoetsu (No.23), Kanazawa (No.30) and Sawada (No.18). The former three points are in comparatively large ports and the last one is on a beach at the head of Mano Bay. The dominant period for the single-peak spectra is always longer than 33 minutes. The rest of the observations are characterized as 'multiple-peak' spectra. The multiple-peak spectra were observed at open coasts, small islands or asymmetrical bays. Six examples of multiple-peak spectra are shown in Figure 3, in which Haboro, Fukuoka are on the open coast, Awashima is on a small island and Ryotsu, Toyama, Sakaikou are in asymmetrical bays. Dominant periods are also defined for the multiple-peak spectra. Hereafter, the dominant period of the seiche spectrum is called the seiche period.

A histogram of the observed seiche periods is shown in Figure 4. The seiche period varies from a minimum value of 7.1 minutes at Aomori port (No. 10) to a maximum value of 167 minutes at Tsuruga port (No. 31). The most frequently occurring range for the seiche period was 10–20 minutes, which accounted for 25% of all the data. The number of observation points with seiche period ranging from 10 to 40 minutes reaches 31 and corresponds to more than half, 56%. It forms an approximately continuous distribution as shown in Figure 4.

4. Dominant Periods of the 1993 and 1983 Tsunamis

The 1993 Hokkaido Nansei-oki tsunami and the 1983 Nihonkai Chubu-oki tsunami are treated for comparison. The former was caused by the Hokkaido Nansei-oki earthquake, registering a magnitude of 7.8, and the latter was caused by the Nihonkai

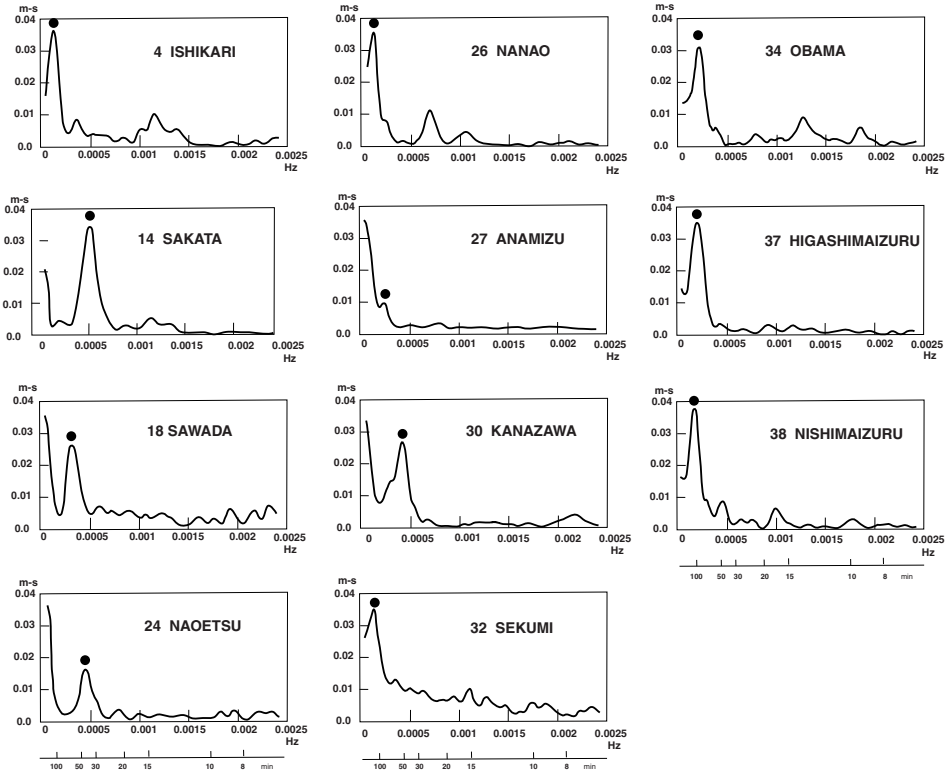

Figure 2
Amplitude spectra of single-peak seiche. The dominant periods are indicated by solid circles.

Chubu-oki earthquake, having magnitude of 7.7. Both of these tsunamis impacted the coast as waves higher than 10 meters spread throughout the Japan Sea. The marigrams were collected from thirty tide stations and the amplitude spectra were obtained for six hours from the origin times. These tsunami waveforms were corrected for the response of the tide gauges using recovery times measured by SATAKE *et al.* (1988). For tide stations without such data, an average recovery time of 269 s was applied as used by ABE (2003). The dominant period T_t is defined as the period of the maximum amplitude of the tsunami spectra, using the same method as used for the seiche observations. The tide stations used are shown in Figure 5.

5. *Comparison of Spectra between Tsunami and Seiche*

The spectra of tsunamis observed at each tide station are compared with the spectrum of the seiche that was observed nearest the tide station in the same bay or

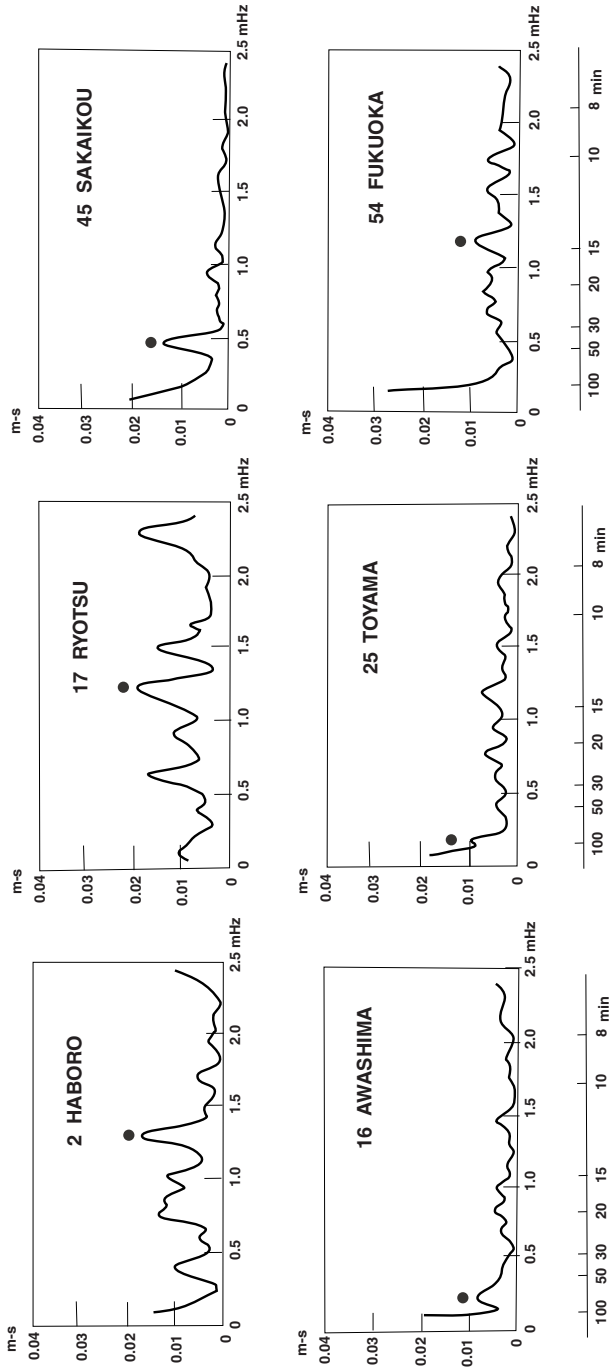

Figure 3
Example of multi-peak seiche spectra. The dominant periods are indicated by solid circles.

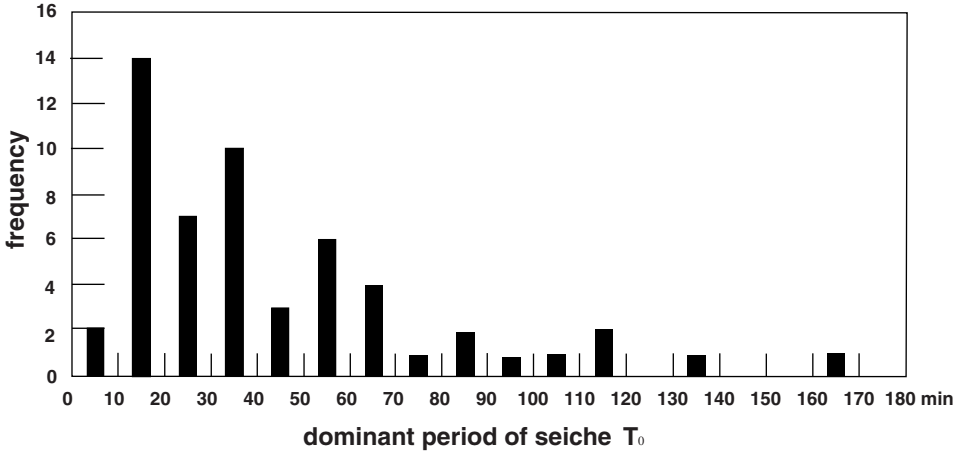

Figure 4
Histogram of dominant periods observed in seiche.

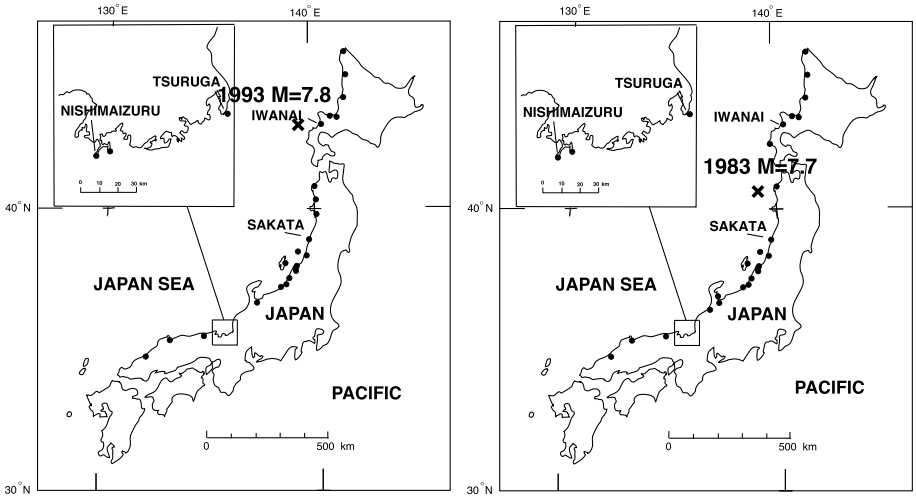

Figure 5
Tide stations at which dominant periods of tsunami were observed. Left: 1993 tsunami. Right: 1983 tsunami.

port. Four examples are shown in Figure 6. The first case is for Iwanai tide station and the seiche at Iwanai port (No. 6). The tsunami amplitude is as large as ten times that of the seiche and the period component consists of two or three peaks in contrast to the isolated peak of the seiche. A dominant period of 23 minutes of the 1993 tsunami is almost equal to the seiche period of 21 minutes, a difference of only 2 minutes. Since the seiche period is approximately the fundamental mode of the bay (ABE, 2005),

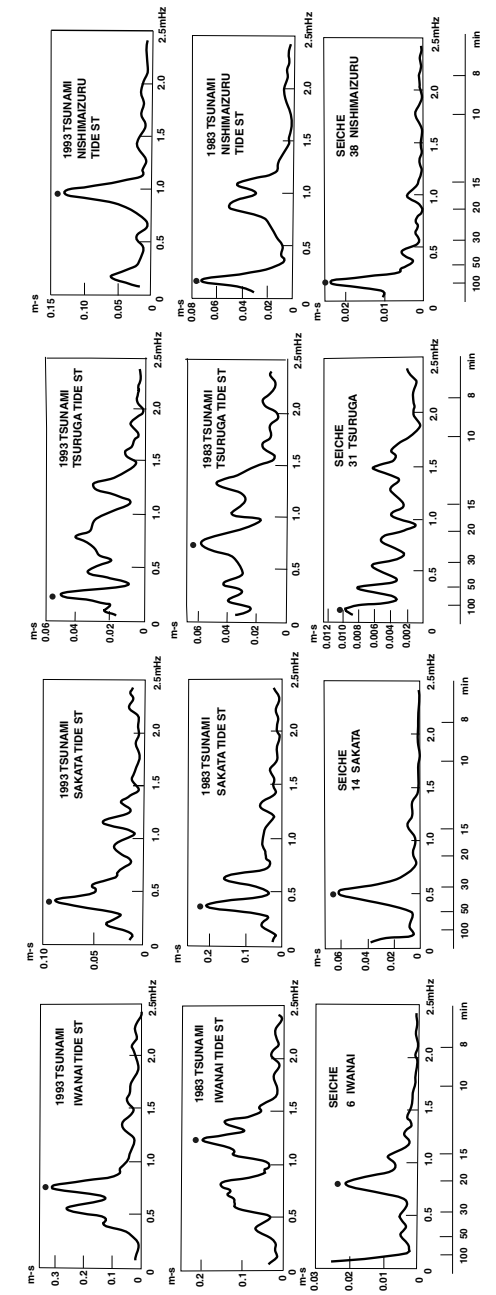

Figure 6
Amplitude spectra of tsunamis and seiche. From top to bottom: 1993 tsunami, 1983 tsunami and seiche. (a) Iwanai, (b) Sakata, (c) Tsuruga, (d) Nishimaizuru. Dominant periods of tsunamis and seiche are indicated by solid circles.

this indicates that the 1993 tsunami excited the fundamental mode with a node at the head of the bay. The spectrum for the 1983 tsunami also has a peak at the natural period, even though the maximum amplitude was observed at 14 minutes period. This again suggests that the fundamental mode was excited by the tsunami incident to Iwanai.

The second example is that of the Sakata tide station and Sakata port (No. 14). The dominant periods of the 1993 tsunami and the 1983 tsunami are 40 and 44 minutes, respectively. On the other hand the seiche period of Sakata port is 33 minutes. These spectra are dominated by energy at periods of 20 minutes or more. It is interesting that the dominant period of 40 minutes in the 1993 tsunami recorded at Sakata is almost equal to twice the dominant period observed at the Iwanai tide station for the same tsunami, and the dominant period of 44 minutes in the 1983 tsunami is almost equal to three times the dominant period at Iwanai tide station for the same tsunami. The fact that the ratio is integer suggests that the observed periods have the same origin.

The third case is that of Tsuruga tide station and Tsuruga bay (No. 31). The spectra of the tsunamis at Tsuruga have many peaks with an irregular interval. On the other hand the seiche observed there consists of many peaks with an almost regular interval. It is classified as a multiple peak spectrum as described above. This bay is asymmetrical in shape, with a dominant period of 167 minutes having the longest period of the peaks in the seiche spectrum. The multiple peaks are related to the higher modes. The dominant periods of the 1993 tsunami and the 1983 tsunami are 64 and 22 minutes, respectively, which correspond to higher modes identified in the seiche spectrum.

The fourth case is that of the Nishimaizuru tide station and Nishimaizuru bay (No. 38). It is noted that the tsunami spectra are represented by two peaks at 17 and 93 minutes period. The 17-minute peak dominated in the 1993 tsunami but the 93-minute peak dominated in the 1983 tsunami. The seiche period of 93 minutes is represented as a single peak as shown in Figure 2. It coincides with the dominant period of the 1983 tsunami. On the other hand 17 minutes dominated in the 1993 tsunami. The two modes correspond to the fundamental and a higher mode, as suggested by the latter as about one fifth the period of the fundamental mode.

6. Correlation between Seiche Period and Tsunami Dominant Periods

At the same port and bay the dominant periods of tsunamis are compared with the seiche period. The correlations are shown in Figure 7. In the figure, straight lines of 1:1, 1:3, 1:5 and 1:7 as the ratio of tsunami dominant period to seiche period are indicated. Since the seiche period probably is that of the fundamental mode at a bay or port, dominant periods of tsunami for 1:1 are the fundamental modes. When we approximate a bay or port as a rectangular bay of length L and sea depth h, we obtain a resonance period T_n from Merian's formula as follows:

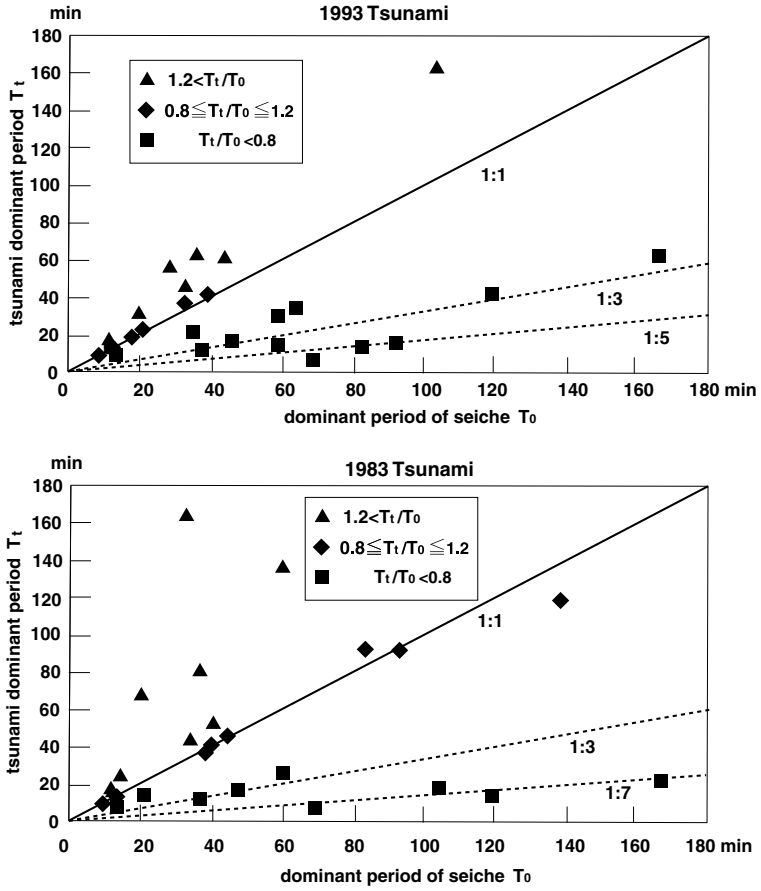

Figure 7
Correlation relation of tsunami dominant period to dominant period of seiche. Groups I, II and III are shown with diamond, rectangle and triangle, respectively. Top: 1993 tsunami. Bottom: 1983 tsunami.

$$T_n = \frac{4L}{(2n+1)\sqrt{gh}},$$

in which g is the gravitational acceleration at the Earth's surface and n is an integer. Assuming the seiche period as the fundamental mode we will obtain the periods of higher modes as

$$T_n = \frac{T_0}{2n+1}.$$

Thus the higher mode is represented as the ratio of odd numbers such as 1:3,1:5,1:7, etc.

It is observed that most of the tsunami dominant periods are explained as being the fundamental mode (seiche period) and a higher mode in the area T_t / $T_o \leqq 1.2$. In this

area the tsunami was trapped in the bay or port and proper oscillations were excited. On the other hand in the area $T_t / T_o > 1.2$ this trapping did not occur and the tsunami period has no particular relation to the seiche period. The long-period components were observed at tide stations distant from the epicenter.

For example the longest-period peak in the 1983 tsunami spectra is observed at Wakkanai (No. 1 in Fig. 1) being located at the northern tip of Hokkaido. The location relative to the epicenter shows an oblique incidence, which is not favorable for exciting secondary seiche undulations (e.g., NAKAMURA and WATANABE, 1961). Thus, we can classify all the data into three groups, as indicated in Figure 7. One is a group of fundamental mode excitation around the line of 1:1. Another one is a group of higher mode excitation around lines of 1:3, 1:5 and 1:7. The rest comprise a group corresponding to no excitation of proper oscillations. Assuming an error of 20% for the 1:1 line we obtain 7 and 9 tide stations for the 1993 tsunami and the 1983 tsunami, respectively. They correspond to 27% and 33%, respectively, of the observations. This is the first group (Group I). The second group is defined as tide stations having dominant periods smaller than the lower limits to the 1:1 line. Twelve and nine tide stations belong to this group for the 1993 and 1983 tsunamis, respectively (Group II). The third group is defined as tide stations for the periods larger than the upper limit of the first group. It consists of 7 and 9 tide stations for the 1993 tsunami and the 1983 tsunami, respectively (Group III). The classifications are shown in Figure 7 using three different symbols.

In the distribution we can notice a critical transition from the fundamental mode to higher modes in the 1993 tsunami and identify the critical point at 40–44 minutes of tsunami dominant period. The existence of this transition implies that the 1993 tsunami has most of its energy confined to a period range shorter than this critical value. The one observation that does not fit this interpretation is the Toyama tide station, which has a dominant tsunami period of 167 minutes. In contrast, it is concluded that the 1983 tsunami consists of a broader spectrum of energy that extends to periods longer than 119 minutes.

The different character of modal excitation for the two tsunamis is illustrated in the histogram of Figure 8. The ratio of higher mode to fundamental mode excitation is 1.7 and 1.0 for the 1993 tsunami and the 1983 tsunami, respectively. Excitation of higher modes is larger in the 1993 tsunami. It suggests that the former is more dominated by short-period energy in comparison with the latter.

7. Resonance

The dominant period ratio T_t / T_0 is defined as the dominant period of tsunami T_t relative to the seiche period T_0. The normalized amplitude of the tsunami dominant period is also defined as the amplitude at the epicentral distance of 50 km, reduced by a formula which has amplitude inversely proportional to the square root of the epicentral distance, i.e., it is assumed that tsunami amplitude decreases due to geometrical spreading. The normalized amplitude is plotted against the dominant period ratio for both tsunamis as shown in

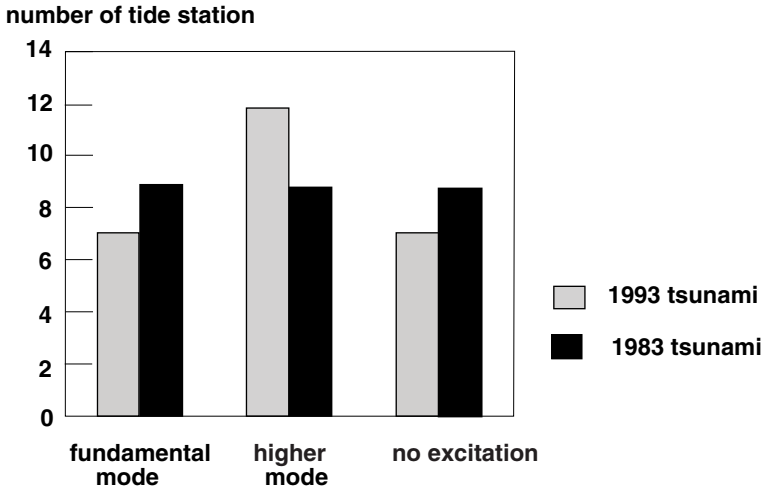

Figure 8
Histograms of mode excitation in the 1993 and the 1983 tsunamis.

Figure 9. It is found that data concentrate around 1 in the abscissa and the maxima occur near one in both cases. This result was expected from the concentration around lines 1:1 as shown in Figure 7. The concentration around 1 and the amplitude increase at 1 supports the idea that the amplification of the tsunami is caused by a resonance due to local bathymetry. An exceptional observation is the large amplitude of the 1993 tsunami observed at Nishimaizuru. This may be due to some unknown mechanism such as focusing. The fact that the maximum in the resonance curve appears at 1 implies that the fundamental mode is more important than higher modes in the amplification.

8. Discussions

HONDA *et al.* (1908) also estimated dominant periods of seiche records near some of the observation points used in the present study. According to them they are as follows: 22.6 min (Niigata); 11.6–12.4, 14.5–17.2, 22.0–25.5, 30–35.8, and 43 min (Kashiwazaki); 37.6 min (Naoetsu); 12.5–16.4, 21.9, 28.0–33.0, and 81.5 min (Wazima); 56.7 and 62.7–67.7 min (Tsuruga); and 11.9–12.9 min (Tonoura). In our study, the corresponding dominant periods were observed to be as follows: 44 min (No. 21 Niigata westport), 46 min (No. 23 Kashiwazaki), 38 min (No. 24 Naoetsu), 30 min (No. 29 Wazima), 167 min (No. 31 Tsuruga) and 13 min (No. 47 Tonoura). At Naoetsu, Wazima and Tonoura our result agrees with that of HONDA *et al.* (1908). At Niigata our period of 44 min is almost twice their result of 22.6 min, and at Tsuruga our result of 167 min is about three times their result of 56.7 min. The fact that the dominant period ratios were integers suggests that HONDA *et al.* (1908) observed higher mode excitation.

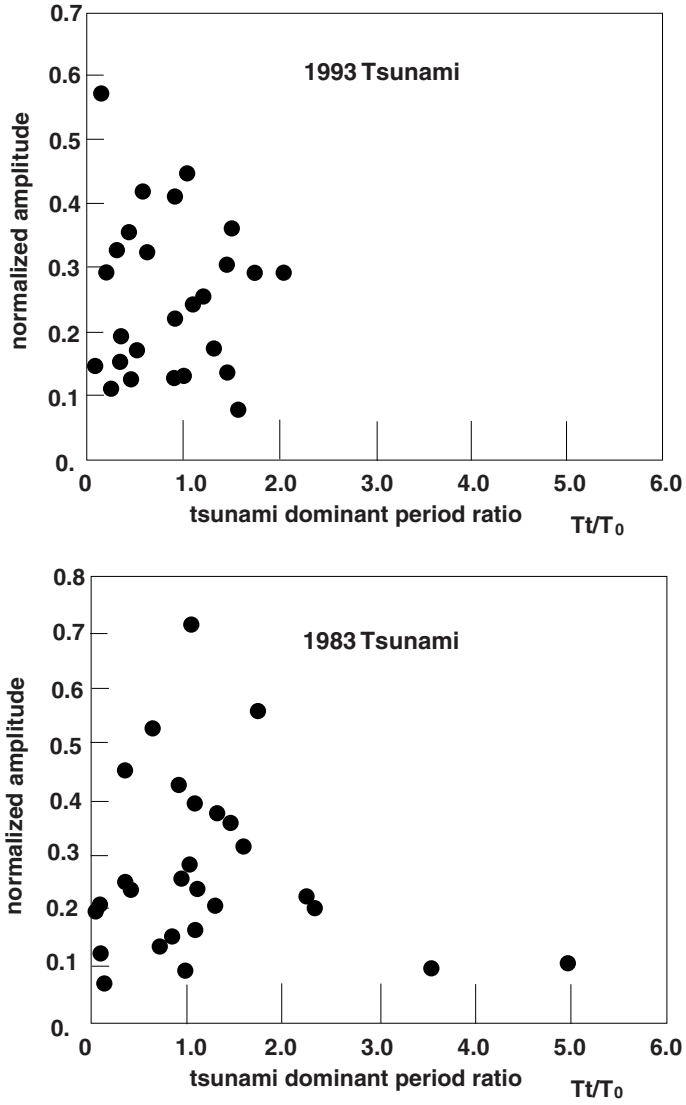

Figure 9
Normalized maximum spectral amplitude versus the dominant period of tsunami relative to seiche period in the 1993 tsunami (top) and the 1983 tsunami (bottom).

NAKANO and UNOKI (1962) studied seiche observed at tide stations around Japan. They identified undulations that accompanied storm surge, tsunami and meteorological disturbances, etc., from tide gauge records for intervals of one month to 26 years. In their results they listed frequently observed periods as follows: 26–27, 38, and 45–55 min (Wakkanai); 18–22 and 42–60 min (Miyazu); 40, 45, 50, 55, 60, 70 and 80 min (Sakaikou);

and 11–12 min (Tonoura). Our result is as follows: 33, 52, 36 and 13 min for Wakkanai (No. 1), Sakaikou (No. 45), Miyazu (No. 40) and Tonoura (No. 47), respectively. There is a maximum difference of 5 minutes between them, which seems insignificant when we consider that measured seiche periods are subject to some variation (see below).

RABINOVICH (1997) proposed a method to separate source spectra of tsunami from observed tide gage spectra using the background spectra observed before the tsunami arrival. He approximated the tsunami spectrum observed at a tide station as a multiple of source spectrum and background spectrum. Our result shows that the dominant period of the seiche is reproduced in tsunamis at many tide stations. According to his approximation this may be explained by the generated tsunami having energy at periods similar to the seiche periods.

ABE (2007) estimated tsunami source lengths for the 1993 tsunami and the 1983 tsunami by analyzing the first wave. Assuming a sea depth of 2500 and 2000 m he obtained the lengths of 169 and 126 km for the 1993 and 1983 tsunami, respectively. We can calculate the period from the wavelength and the long-wave velocity. Assuming the length to be one wavelength and the same sea depths used by ABE (2007), we obtain periods of 18 and 15 min for the 1993 and 1983 tsunamis, respectively. These values are in the range of the most frequently appearing dominant periods, as described in Section 3. This is in agreement with the amplification resulting from resonance.

AIDA *et al.* (1975) observed seiche at Onagawa Bay in northeast Japan and investigated its change with time. They found that the seiche energy is mainly in the fundamental mode, whose period varies seasonally from 37 to 42. Their result implies that we should adopt at least 5 minutes as the potential error in our measurements of dominant period. This amounts to 14% in the relative error. We conservatively assumed 20% relative error in our classification of mode excitation. It should be noted, however, that this reflects seasonal variation and its geographic variability in addition to measurement error.

9. Conclusion

Seiches were observed at fifty-five observation points consisting of ports and bays facing the Japan Sea along the Japanese coast, and the dominant periods (resonant periods) were determined from the maximum spectral amplitudes. Most of the seiche periods are found to range from 10 to 40 minutes. They are compared with dominant periods of the 1993 and 1983 tsunamis observed at the same ports on tide gauges. The result shows that resonant oscillations of ports or bays, including the higher seiche modes, were excited by the tsunami. Where no excitation of resonant oscillation occurred, this is explained as being due to oblique incidence. The fact that the amplification as a function of the ratio of tsunami and seiche dominant periods attains its maximum at a ratio of one indicates resonance between tsunami and bay or port. The dominant seiche period is therefore an important factor to consider in interpreting tsunami amplification.

Acknowledgements

The author is grateful for a preparation of tide gauge records for the 1993 and the 1983 tsunamis to Japan Meteorological Agency, Ports and Harbor Bureau, Hydrographic, Oceanographic Department of Japan Coast Guard and Prefecture Offices. A Research Promotion Grant from The Nippon Dental University supports this study.

References

Abe, K. (2003), *Source model of a small tsunami accompanied with a volcanic earthquake at Kouzu-shima on July 1, 2000*, Zisin *2*, *56*, 181–187 (in Japanese).

Abe, K. *Tsunami resonance curve on dominant periods observed at bays*. In *Tsunamis: Case Studies and Recent Developments* (ed. K. Satake) (Springer Publishing 2005) pp. 97–113.

Abe, K. (2007), *Phase representing source lengths of tsunami in tide gauge records*, Pure Appl. Geophys. *164*, 453–463.

Aida, I., Koyama M., Date D. and S. Sakashita. (1975), *Long-period waves in the vicinity of Onagawa Bay (III)—Time change of the seiche characteristics in the bay*. J. Oceanog. Soc. Japan *31*, 61–70.

Honda, K., Terada, T., Yoshida, Y., and Isitani, D. (1908), *The secondary undulations of oceanic tides*, J. Coll. Sci., Imper. Univ. Tokyo, *24*, 1–110.

Kato, Y., Suzuki, Z., Nakamura, K., Takagi, A., Emura, K., Ito, M., and Ishida, H. (1961), *The Chile tsunami of 1960 observed along the Sanriku coast of Japan*, Sci. Rep. Tohoku Univ., Ser. 5, Geophys. *13*, 107–125.

Nakamura, K. and Watanabe, H. (1961), *Tsunami forerunner observed in case of the Chile tsunami of 1960*, Report on the Chilean Tsunami, Field Investigation Committee for the Chilean Tsunami, pp. 82–99.

Nakano, M. and Unoki S., (1962), *On the seiches (The secondary undulations of tides) along the coasts of Japan*, Records of Oceanographic Works in Japan, No. 6, 169–214.

Rabinovich, A. B. (1997), *Spectral analysis of tsunami waves: Separation of source and topography effects*, J. Geophys. Res. *102*(C6), 12663–12676.

Satake, K., Okada, M., and Abe, K., (1988), *Tide gauge response to tsunamis: Measurements at 40 tide stations in Japan*, J. Mar. Res. *46*, 557–571.

(Received December 17, 2007, accepted September 15, 2008)
Published Online First: February 16, 2009

Pure appl. geophys. 166 (2009) 131–152
0033–4553/09/010131–22
DOI 10.1007/s00024-004-0430-3

Pure and Applied Geophysics

Numerical Study of Tsunami Generated by Multiple Submarine Slope Failures in Resurrection Bay, Alaska, during the M_W 9.2 1964 Earthquake

ELENA SULEIMANI,[1] ROGER HANSEN,[1] and PETER J. HAEUSSLER[2]

Abstract—We use a viscous slide model of JIANG and LEBLOND (1994) coupled with nonlinear shallow water equations to study tsunami waves in Resurrection Bay, in south-central Alaska. The town of Seward, located at the head of Resurrection Bay, was hit hard by both tectonic and local landslide-generated tsunami waves during the M_W 9.2 1964 earthquake with an epicenter located about 150 km northeast of Seward. Recent studies have estimated the total volume of underwater slide material that moved in Resurrection Bay during the earthquake to be about 211 million m^3.

Resurrection Bay is a glacial fjord with large tidal ranges and sediments accumulating on steep underwater slopes at a high rate. Also, it is located in a seismically active region above the Aleutian megathrust. All these factors make the town vulnerable to locally generated waves produced by underwater slope failures. Therefore it is crucial to assess the tsunami hazard related to local landslide-generated tsunamis in Resurrection Bay in order to conduct comprehensive tsunami inundation mapping at Seward. We use numerical modeling to recreate the landslides and tsunami waves of the 1964 earthquake to test the hypothesis that the local tsunami in Resurrection Bay has been produced by a number of different slope failures. We find that numerical results are in good agreement with the observational data, and the model could be employed to evaluate landslide tsunami hazard in Alaska fjords for the purposes of tsunami hazard mitigation.

Key words: Landslide-generated tsunamis, numerical modeling, 1964 Alaska earthquake, Resurrection Bay, Seward.

1. Introduction

On March 28, 1964, the Prince William Sound area of Alaska was struck by the largest earthquake ever recorded in North America. This magnitude M_W9.2 megathrust earthquake generated the most destructive tsunami experienced in historical times by Alaskans and, further south, by people on the West Coast of the United States and Canada. Of the 131 fatalities associated with this earthquake, 122 were caused by tsunami waves (LANDER, 1996). Although tragic, the number of deaths was fortunately far smaller than in the case of the 2004 Indian Ocean tsunami due to low population density on the Alaska coast. As a result of the earthquake, more than twenty local tsunamis were

[1] Geophysical Institute, University of Alaska Fairbanks, 903 Koyukuk Dr., Fairbanks AK 99775-7320. E-mail: elena@gi.alaska.edu

[2] USGS, Alaska Science Center, 4210 University Dr., Anchorage, AK 99508-4626.

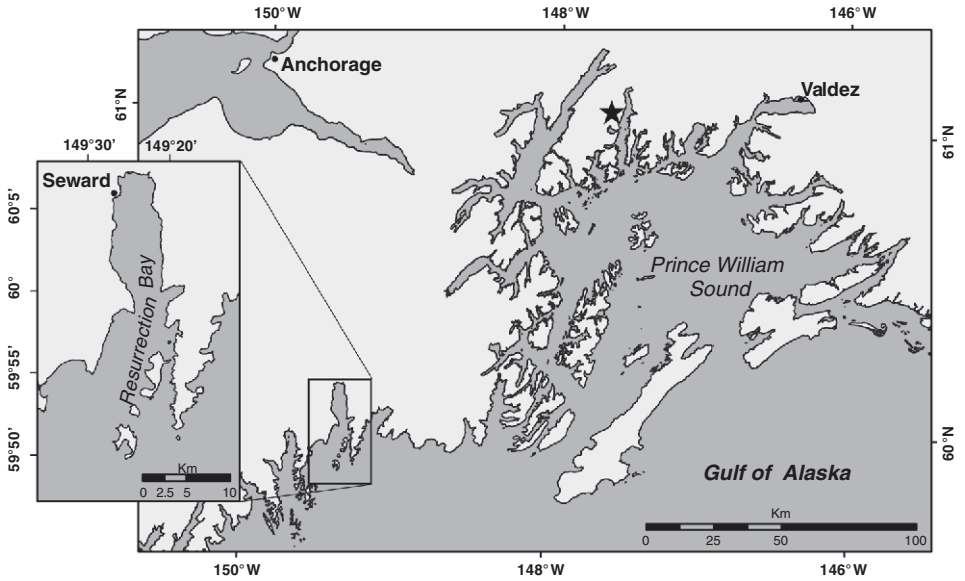

Figure 1
Location map of Resurrection Bay and Seward in the Gulf of Alaska. The star indicates the epicenter of the M_W 9.2 1964 earthquake.

generated by submarine and subaerial landslides in coastal Alaska, in addition to the major tectonic tsunami that was generated by displacement of the ocean bottom between the trench and the coastline. Local tsunamis caused most of the damage and accounted for 76% of the tsunami fatalities. Also, they arrived almost immediately after the shaking began, leaving no time for warning or evacuation. The community of Seward in Resurrection Bay (Fig. 1) suffered from the combined effects of local landslide-generated waves and the major tectonic tsunami that propagated from the main earthquake rupture zone in the Gulf of Alaska. The earthquake triggered a series of slope failures offshore of Seward, which resulted in landsliding of part of the coastline into the water, along with the loss of the port facilities. The town sustained great damage, and 12 people perished due to the tsunamis. Seward has grown considerably since the 1964 earthquake. As an ice-free harbor, it is an important supply center for Interior Alaska. The town is one of the major tourist destinations in Alaska. Seward hosts more than 90 cruise-ship dockings per year, and it is also a port for the state ferry system. Because local tsunamis were responsible for most of the damage and deaths in Seward during the 1964 earthquake, the future potential of similar events needs to be evaluated for comprehensive inundation mapping. Underwater slides could be triggered almost instantaneously during a future large earthquake, with tsunami waves arriving without warning, as they did in 1964. For tsunami hazard mitigation it is important to estimate the inundation areas, depths of inundation and velocity currents in Resurrection Bay.

Tsunamis caused by submarine slope failures are a serious hazard in glacial fjords of coastal Alaska and other high-latitude fjord coastlines. LEE *et al*. (2002) studied different environments of the US Exclusive Economic Zone and found that Alaskan fjords are likely the most susceptible environment to slope failures. In a fjord setting, rivers and streams drain the glacier that initially eroded the valley, forming a fjord-head delta and depositing sediment that easily looses strength during an earthquake. HAMPTON *et al*. (1996) note that in a fjord environment, where the deltaic sediment is deposited rapidly, the sediment builds up pore-water pressures and could liquefy under extreme low tide conditions or ground-shaking due to low static shear strength. BORNHOLD *et al*. (2001) identify the most common triggering mechanisms that can cause underwater slope failures as earthquakes, extreme low tides, and construction activities in ports and harbors. Because of these diverse mechanisms, prediction of landslide-generated tsunamis is a challenging task. Estimation of landslide tsunami risk for a coastal community requires assessment of locations of potential underwater failures using high-resolution bathymetry, known or reasonably estimated physical parameters of the underwater materials, and an adequate numerical model. The most probable locations of unstable sediment bodies in Resurrection Bay will be at the head of the bay where the Resurrection River had constructed a delta, and steep submarine slopes located elsewhere in the bay (HAEUSSLER *et al*., 2007).

This paper is the first numerical modeling study of tsunami waves in Resurrection Bay that utilizes the recent findings of the large-scale submarine slope failures in the bay during the 1964 earthquake (HAEUSSLER *et al*., 2007). It was shown that submarine failures initiated along the fjord walls at shallow depths and sediment was transported 6 to 13 km into the deepest part of the basin. The total volume of slide material that moved in Resurrection Bay during the earthquake was estimated to be about 211 million m^3 (HAEUSSLER *et al*., 2007). The purpose of this study is to recreate the sequence of tsunami waves observed in Resurrection Bay during the 1964 earthquake, and to test the hypothesis that the local tsunami was produced by a number of different slope failures. We perform numerical modeling of submarine slides and associated water waves and compare numerical results with the observations. In this preliminary analysis, our goal is not to model the inundation of dry land, but to create a foundation for future studies that will address runup of landslide-generated waves in Resurrection Bay. We will show that our modeling approach is a useful tool for estimating the landslide tsunami hazard at Seward and other tsunami-prone communities in southern Alaska.

2. Tsunami Hazard in Resurrection Bay

Resurrection Bay is a deep glacial fjord, typical of many in south-central and southeastern Alaska. KULIKOV *et al*. (1998) analyzed tsunami catalog data for the North Pacific Coast and showed that this region has a long history of tsunami waves generated by submarine and subaerial landslides, avalanches and rockfalls. The authors also found

Figure 2 ▶

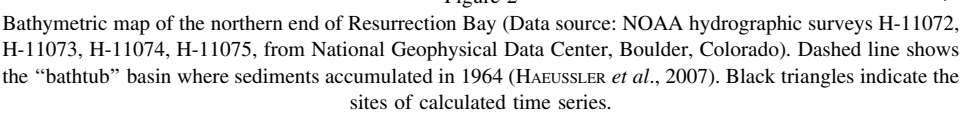

Bathymetric map of the northern end of Resurrection Bay (Data source: NOAA hydrographic surveys H-11072, H-11073, H-11074, H-11075, from National Geophysical Data Center, Boulder, Colorado). Dashed line shows the "bathtub" basin where sediments accumulated in 1964 (HAEUSSLER *et al*., 2007). Black triangles indicate the sites of calculated time series.

that, in the majority of cases, tectonic tsunamis that arrive in bays and fjords from the open ocean have relatively small amplitudes, but a great number of local landslide-generated tsunamis have considerably larger wave amplitudes. For example, as a result of the 1964 earthquake, about 20 local submarine and subaerial landslide tsunamis were generated in Alaska (LANDER, 1996). Following the earthquake, Seward was the only place hit by both landslide-generated tsunamis and a major tectonic tsunami (HAEUSSLER *et al*., 2007), while several other communities experienced only locally generated waves (PLAFKER *et al*., 1969). KULIKOV *et al*. (1998) also noted that, due to the sparse population of the area, the actual number of historical landslide tsunami events is unknown, and probably much greater than the number of events observed or recorded. BORNHOLD *et al*. (2001) addressed the problem of estimation of risk from landslide-generated tsunami waves for the coast of Alaska and British Columbia. They outlined the specific features of the long-term prediction of landslide-generated tsunamis at selected sites, and developed an approach for estimating tsunami risk. The long-term approach consists of two steps: analysis of historical events and verification of model results with runup observations at the site; and numerical simulation of hypothetical tsunami scenarios. Although for many communities historical observations do not exist, Seward is an exception. The effects of the 1964 earthquake and tsunami waves in Resurrection Bay, including wave amplitudes and extent of inundation, are well documented (WILSON and TØRUM, 1968; LEMKE, 1967) and are ideal for numerical modeling studies.

2.1. Study Area and Tsunami Waves of March 28, 1964

The town of Seward is located at the northwest corner of Resurrection Bay, and is built mostly on the alluvial fan of Lowell Creek. Lowell Point, Tonsina Point, and the Fourth of July Creek (Fig. 2) are locations of other alluvial fans that extend into the bay as fan deltas (LEMKE, 1967). The entire head of Resurrection Bay is a fjord-head delta that was built by the Resurrection River. HAEUSSLER *et al*. (2007) used the word "bathtub" to describe a flat depression in the middle of the bay extending north to south (Fig. 2). The deepest part of the bathtub is about 300 meters. The average pre-earthquake offshore slopes in the vicinity of Seward ranged from 10° to 20°, decreasing to 5° at the depth of about 200 m (LEMKE, 1967). Today, the same area has an average slope of about 25° (LEE *et al*., 2006). A natural barrier formed by Caines Head and a glacial sill divide the bay into two deep basins, separated by a narrow "neck" with maximum depth above the sill of 195 m. This sill inhibits sediment transport by tidal currents to the southern part of the bay (HAEUSSLER *et al*., 2007). Our study focuses on the northern basin of Resurrection Bay, north of the sill area (Fig. 2).

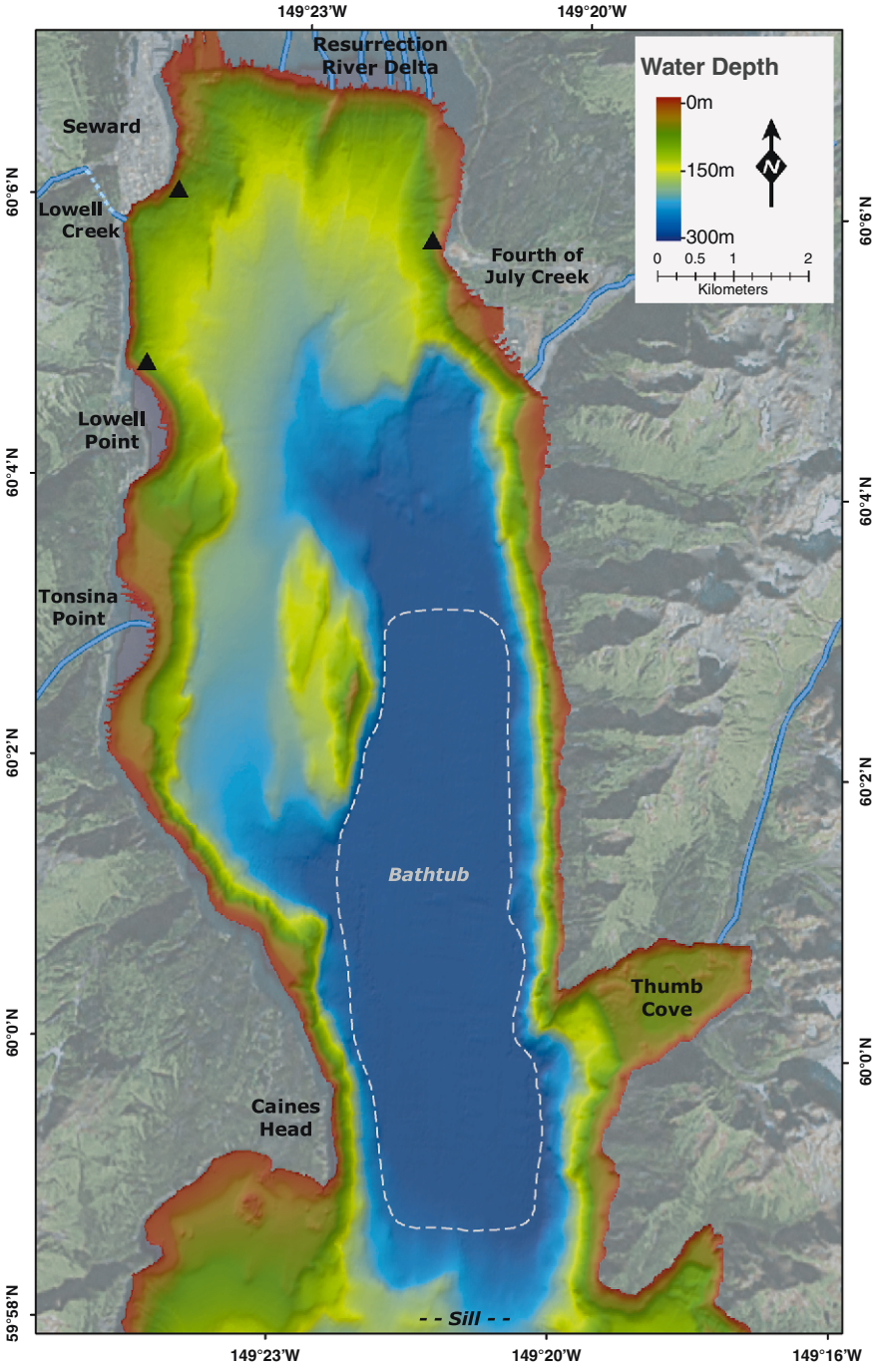
149°23'W
149°20'W
Resurrection River Delta
Seward
Lowell Creek
Fourth of July Creek
Lowell Point
Tonsina Point
Bathtub
Thumb Cove
Caines Head
- - Sill - -
Water Depth
0m
150m
300m
0 0.5 1 2
Kilometers
N
60°6'N
60°4'N
60°2'N
60°0'N
59°58'N
149°16'W

There were several types of waves observed in Resurrection Bay on March 28, 1964: landslide-generated waves, a tectonic tsunami wave train, and probably seiches (WILSON and TØRUM, 1968), all resulting in a complicated wave pattern. The Seward tide gauge was located on a dock that collapsed into the bay as a result of massive submarine slope failures. The instrument was heavily damaged, and the record was lost. Although the sequence of waves was reconstructed from observations provided by eyewitnesses, there are uncertainties in the time estimates of wave arrivals (WILSON and TØRUM, 1968). Table 1 is a portion of the eyewitness report compiled by WILSON and TØRUM (1968) that covers the period when the ground was shaking. An initial drawdown of water was observed at the Seward waterfront about 30 seconds after the ground started to shake. At the same time, fuel tanks ruptured, leaked, and subsequently exploded; the tanks slid into the bay, and the receding water was covered with burning oil. The highest wave at Seward was about 6–8 m high observed about 1.5-2 minutes after the shaking began (Table 1). The tectonic tsunami wave, covered with burning oil, came into the bay about 25 minutes after the earthquake, spanning the entire width of the bay (WILSON and TØRUM, 1968). This wave was as high as the initial landslide-generated waves. Because the source of local waves in the bay ceased at the end of ground-shaking (WILSON and TØRUM, 1968), about 20 minutes before the arrival of the tectonic tsunami, we can assume that these events are independent, and model them separately. In this paper we focus only on waves generated by local submarine slope failures in Resurrection Bay.

2.2. *Justification for the Study*

Geologic investigations were conducted in the Resurrection Bay area right after the earthquake by several researchers (LEMKE, 1967; WILSON and TØRUM, 1968; PLAFKER *et al.*, 1969; SHANNON and HILTS, 1973). From these studies, it was concluded that strong ground motion during the earthquake caused several submarine slope failures along the Seward waterfront and other areas within upper Resurrection Bay. HAMPTON et al. (1996) described the triggering mechanism as dynamic forces imposed by large seismic accelerations that added to the downslope component of the gravitational force on the

Table 1

Observations at Seward waterfront during the earthquake (from WILSON and TØRUM, 1968)

Estimated time points and heights (zero time is at the start of the quake)

Whiteness	Source	Time	Feet
Ted Pedersen		30 seconds	Drawdown at Standard Oil Dock
Hal Gilfillen	Genie Chance	45 ”	
Robert Clark		45 ”	
Many Eyewitnesses	Genie Chance	1.5–2 minutes	+20–25 feet at ARR docks
	BERG *et al.* (1964)		Rose over box cars on RR tracks
	LANTZ and KIRKPATRICK (1964)		Reached corner of Third Avenue and Washington

steep slopes of the Lowell Creek and Resurrection River deltas. HAMPTON *et al*. (2002) notes that the stability of the sediment was also decreased by the low tidal level at the time of the earthquake, and by the rapid drawdown of water due to the initial slope failure, which prevented the pore water from draining from the sediment quickly enough to maintain hydrostatic conditions. The underwater slope failures generated large waves that were observed during ground shaking (WILSON and TØRUM, 1968). The major factors that contributed to the total volume and aerial extent of the slide material were the long duration of ground motion (3 to 4 min), the configuration of underwater slopes, and the type of sediment forming these slopes, unconsolidated and fine-grained materials (LEMKE, 1967). HAMPTON *et al*. (1996) added that high artesian pressure within aquifers of the delta combined with the extra load caused by waterfront artificial fill and the shoreline development also contributed to the slope failures. The authors summarized all the environmental loads in Resurrection Bay and concluded that although it was a unique combination of conditions, most of them had been documented separately during slope failures in other fjords.

Studies by LEE *et al*. (2006) and HAEUSSLER *et al*. (2007) provided analysis of pre- and post-earthquake bathymetric data and high resolution subbottom profiles of Resurrection Bay and showed convincing evidence of massive submarine landsliding. They utilized a 2001 NOAA high-resolution multibeam bathymetry survey of Resurrection Bay to study the morphology and depth changes of the fjord bottom. A shaded relief map derived from this bathymetric data shows a variety of sea-floor features related to submarine slides. LEE *et al*. (2006) identified remains of the Seward waterfront that failed in 1964 as a result of strong ground-shaking. These remains are visible as blocky debris extending offshore Seward for about 750 m (Fig. 3). The authors also identified dispersed debris flows that correspond to failures of the Resurrection River delta, and they concluded that the 1964 earthquake could potentially have triggered different failure types simultaneously. HAEUSSLER *et al*. (2007) concluded that several failures initiated along the fjord walls at relatively shallow depths, and the mass flows produced by these failures transported most of the material as far as 6 to 13 km into the bathtub, covering the entire basin with a flow deposit.

Engineering studies conducted after the 1964 earthquake (LEMKE, 1967) showed that additional onshore and submarine landslides can be expected along the Seward waterfront in the event of another large earthquake, and that sediment from the Resurrection River and smaller creeks will continue to accumulate on underwater slopes of Resurrection Bay. The recent results of sediment chemistry monitoring in Port Valdez, located in a glacial fjord setting similar to that of Resurrection Bay (Fig. 1), demonstrated high sediment accumulation rates of about 1.5 cm/year at the head of the fjord (SAVOIE *et al*., 2006). Sediment could be released not only by the ground-shaking due to an earthquake, but also by other triggering events, such as extreme low tide conditions and construction activities. Because short-term prediction of landslide tsunamis is not applicable for tsunami risk assessment (BORNHOLD *et al*., 2001), we will need to use the long-term approach described at the beginning of section 2 for estimating the local

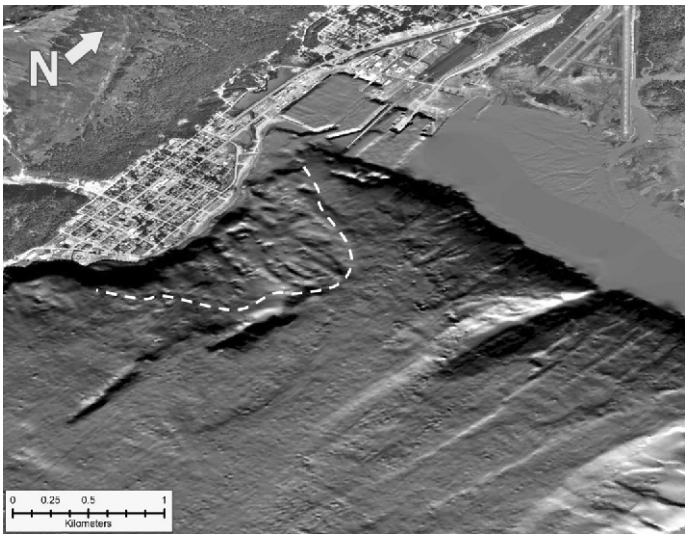

Figure 3
Oblique bathymetric image, overlain with aerial photograph, of the northwest corner of Resurrection Bay, offshore of the Seward waterfront. Dashed line delineates the blocky debris that are remains of the 1964 waterfront failure. The scale was made for the downtown Seward.

tsunami hazard at Seward. The essential part of this approach is numerical modeling of historical landslide tsunami events, as well as simulating future hypothetical underwater slope failures.

3. Model Description

A number of studies of tsunami waves generated by landslides employed depth-integrated numerical models. HARBITZ (1992) simulated tsunamis generated by Storegga slides using linear shallow water equations. JIANG and LEBLOND (1992, 1994), FINE *et al.* (1998), THOMSON *et al.* (2001), IMAMURA *et al.* (2001), TITOV and GONZALEZ (2001) used nonlinear shallow water approximation to model the slide-water system as a two-layer flow. LYNETT and LIU (2002) discussed the limitations of the depth-integrated models with regards to landslide-generated waves, and developed fully nonlinear weakly dispersive model for submarine slides that is capable of simulating waves from relatively deep water to shallow water. The model was later extended to employ the multilayer approach (LYNETT and LIU, 2004a, 2004b) that allowed for accurate simulation of landslides in shallow and intermediate water (LYNETT and LIU, 2005). GRILLI and WATTS (2005) derived and validated a two-dimensional fully nonlinear dispersive model that does not have any restrictions on tsunami amplitude, wavelength, or landslide depth, and describes the motion of the landslide by that of its center of mass.

To simulate tsunami waves produced by multiple underwater slope failures in Resurrection Bay on March 27, 1964, we use a three-dimensional numerical model of a viscous underwater slide with full interactions between the deforming slide and the water waves that it generates. This model was initially proposed by JIANG and LEBLOND (1994). FINE *et al*. (1998) improved the model by including realistic bathymetry, and also by correcting errors in the governing equations. The model assumptions as well as its applicability to simulate underwater mudflows are discussed by Jiang and LeBlond in their formulation of the viscous slide model (JIANG and LEBLOND, 1992, 1994). The model uses long-wave approximation for water waves and the deforming slide, which means that the wavelength is considerably greater than the local water depth, and the slide thickness is considerably smaller than the characteristic length of the slide along the slope (JIANG and LEBLOND, 1994). ASSIER-RZADKIEWICZ *et al*. (1997) argued that the long-wave approximation could be inaccurate for steep slopes, that is for slopes greater than 10°. RABINOVICH *et al*. (2003) studied the validity of the long-wave approximation for slopes greater than 10° and found that for the slope of 16° the possible error was 8%, and for the maximum slope in their study of 23° the possible error was 15%. Based on this analysis, for the average pre-earthquake offshore slopes that ranged from 10° to 20° in the vicinity of Seward, the possible error introduced by a slide moving down these higher gradient slopes could be around 10%.

The advantage of the vertically integrated model that includes two horizontal dimension effects is its ability to simulate real landslide tsunami events using high-resolution numerical grids based on multibeam bathymetry data. Although model runs require use of high-performance computing, the computational times are still reasonable. This model was successfully applied to simulate tsunami waves in Skagway Harbor, Alaska, generated by collapse of the PARN dock on November 3, 1994 (FINE *et al*., 1998; THOMSON *et al*., 2001). The results of numerical simulations were in good agreement with the tide gauge record in Skagway Harbor, one of the numerous fjords in southeastern Alaska. RABINOVICH *et al*. (2003) simulated potential underwater landslides in British Columbia fjords, settings that are similar to Resurrection Bay, and demonstrated that this model can be used for tsunami hazard assessment.

3.1. Model Equations

The geometry of the slide is shown in Figure 4. The physical system consists of two layers: The upper one is water with density ρ_1, and the lower layer is slide material with density ρ_2 and dynamic viscosity μ. The slide is assumed to be an incompressible viscous fluid. We assume a sharp interface between the layers, with no mixing allowed between water and sediments. The disturbance of the water surface produced by slide motion is described by free surface elevation $\xi(x, y, t)$ and horizontal components of water velocity $u(x, y, t)$ and $v(x, y, t)$. The horizontal velocity of the slide $\mathbf{U}$ has components $U(x, y, t)$ and $V(x, y, t)$. The thickness of the slide is $D(x, y, t)$, the undisturbed water depth is $H(x, y)$, and $H_t(x, y, t) = H + \xi - D$ is the total water depth above the slide. The equations for the

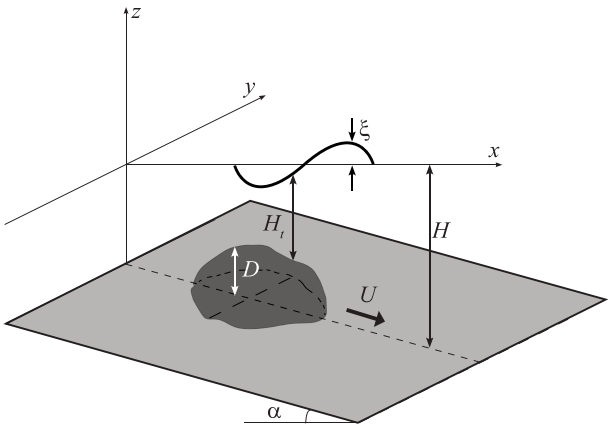

Figure 4
Geometry of a submarine landslide.

slide were initially derived under the assumption that the underwater slide rapidly reaches its equilibrium velocity (JIANG and LEBLOND, 1994), which means that changes of horizontal components of the slide velocity in the vertical direction can be approximated by a parabolic function. It is also assumed that the slide mass does not cross the boundary of the computational domain.

The slide equations that we use in this study are the equations from JIANG and LEBLOND (1994) that were corrected by FINE *et al*. (1998):

$$\frac{\partial U}{\partial t} - \frac{1U}{5D}\frac{\partial D}{\partial t} + \frac{4}{5}\left(U\frac{\partial U}{\partial x} + V\frac{\partial U}{\partial y}\right) = -\frac{3}{2}g\left(\frac{\partial D}{\partial x} - \frac{\partial H}{\partial x}\right) - \frac{3}{2}g\frac{\rho_1}{\rho_2}\frac{\partial H_t}{\partial x} - \frac{3\mu U}{\rho_2 D^2}, \quad (1)$$

$$\frac{\partial V}{\partial t} - \frac{1V}{5D}\frac{\partial D}{\partial t} + \frac{4}{5}\left(U\frac{\partial V}{\partial x} + V\frac{\partial V}{\partial y}\right) = -\frac{3}{2}g\left(\frac{\partial D}{\partial y} - \frac{\partial H}{\partial y}\right) - \frac{3}{2}g\frac{\rho_1}{\rho_2}\frac{\partial H_t}{\partial y} - \frac{3\mu V}{\rho_2 D^2}, \quad (2)$$

$$\frac{\partial D}{\partial t} = -\frac{2}{3}\left(\frac{\partial (DU)}{\partial x} + \frac{\partial (DV)}{\partial y}\right). \quad (3)$$

The equations that describe the upper layer are the nonlinear shallow water equations:

$$\frac{\partial u}{\partial t} + u\frac{\partial u}{\partial x} + v\frac{\partial u}{\partial y} = -g\frac{\partial \xi}{\partial x}, \quad (4)$$

$$\frac{\partial v}{\partial t} + u\frac{\partial v}{\partial x} + v\frac{\partial v}{\partial y} = -g\frac{\partial \xi}{\partial y}, \quad (5)$$

$$\frac{\partial H_t}{\partial t} = -\frac{\partial (H_t u)}{\partial x} - \frac{\partial (H_t v)}{\partial y}. \quad (6)$$

The variable that couples the two systems of equations is the total water depth above the slide, $H_t(x, y, t)$. In this study we do not calculate the inundation of dry land due to

landslide-generated waves, which implies that the normal velocity component is set to zero at the shoreline. At the open boundary, we apply the radiation boundary condition for surface waves.

3.2. Data

The two data sets used in this study are the bathymetry of Resurrection Bay, and the initial distribution and thickness of the slide material. In order to simulate underwater slope failures of 1964 in Resurrection Bay, we use a bathymetry grid of 15-m resolution that covers the northern part of the bay (Fig. 2). The source of the data is the 2001 NOAA high-resolution multibeam survey of Resurrection Bay, and the 2006 survey of the Seward harbor and surrounding areas (LABAY and HAEUSSLER, 2008, in press).

HAEUSSLER *et al*. (2007) have conducted a comprehensive study of submarine slope failures in Resurrection Bay during the 1964 earthquake. The location and extent of submarine mass failures were estimated based on analysis of pre- and post-earthquake bathymetry. The authors created a bathymetric difference grid that shows depth changes in the bay resulting from the 1964 slope failures. The estimated total volume of slide material is 211 million m^3 (HAEUSSLER *et al*., 2007). A map of the slide thickness, derived from the bathymetric difference grid, is shown in Figure 5. This distribution of the slide material serves as an initial condition for the slide surface in system of equations (1)–(3). HAEUSSLER *et al*. (2007) identified ten different landslide areas and calculated their volumes (Fig. 5). We use their results shown in Figure 5 to better understand the contribution of different slide complexes to the observed tsunami amplitudes in Resurrection Bay.

4. Numerical Simulation of the 1964 Landslides and Tsunami

We use an explicit in time finite-difference method to numerically solve equations (1)–(6) on a staggered leap-frog grid. Thomson *et al*. (2001) describe the construction of the numerical scheme and provide the final discretized equations. The computational domain is shown in Figure 2. This area is covered by a grid of 711 $\times$ 1310 grid points with horizontal space steps $\Delta x = 13.75$ m and $\Delta y = 15$ m, and time step $\Delta t = 0.01$ sec. SHANNON and HILTS (1973) conducted a subsurface geotechnical investigation of materials that failed in Resurrection Bay during the 1964 earthquake. They found that the density of the slide material ranged from 2.0 $g \cdot cm^{-3}$ to 2.11 $g \cdot cm^{-3}$. We do not have any measurements of the slide viscosity, but sensitivity studies by RABINOVICH *et al*. (2003) demonstrated that the influence of kinematic viscosity on tsunami wave heights is small. We assume slide density of $\rho = 2.0$ $g \cdot cm^{-3}$ and slide viscosity of $\mu = 0.05$ $m^2 \cdot s^{-1}$. The upper and lower surfaces of the slide mass are defined by the initial slide thickness distribution (Fig. 5), and they are given on the same 711 $\times$ 1310 grid used for bathymetric data. The slide thicknesses are added to the bathymetry values in order to

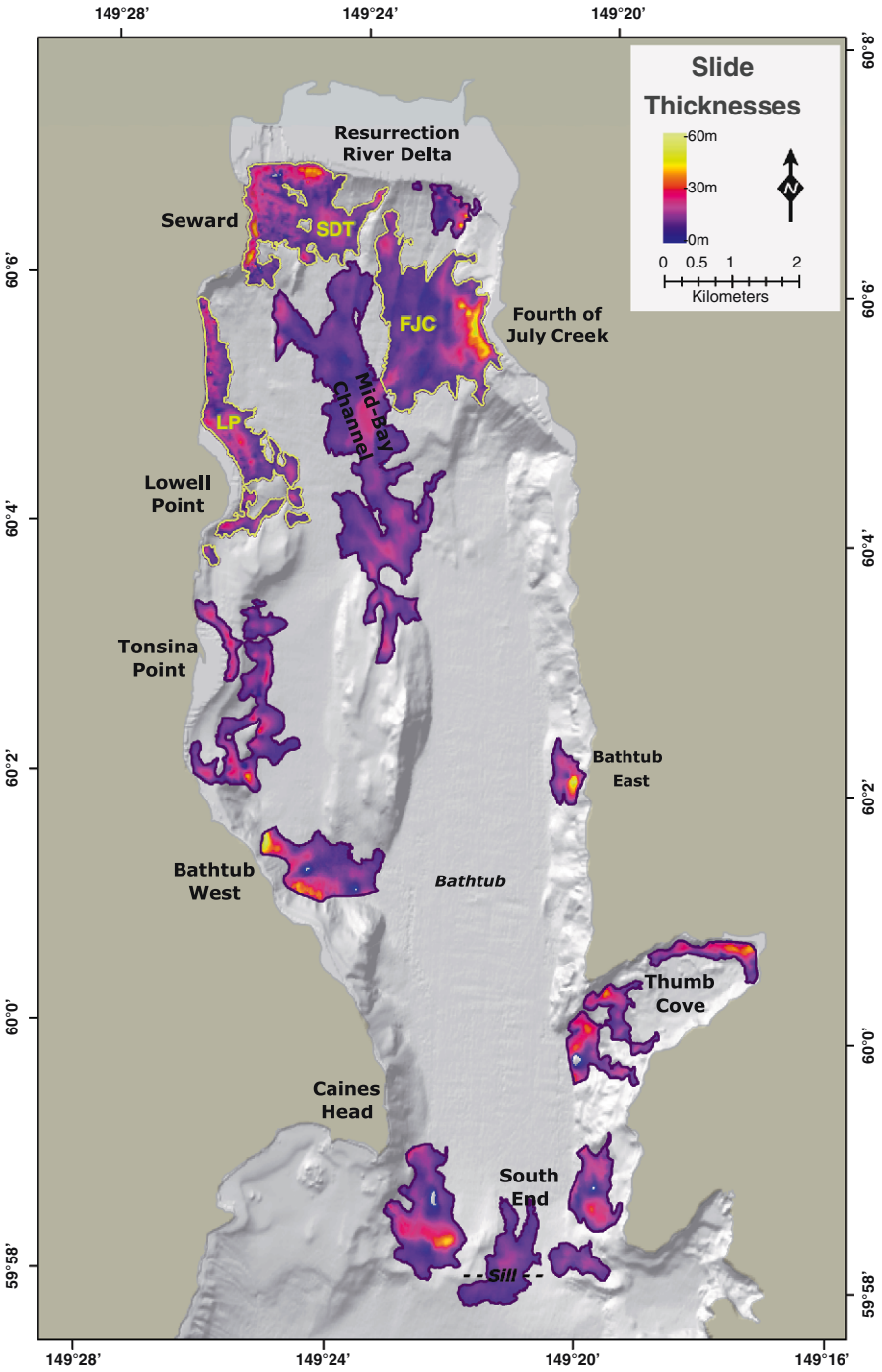
149°28'
149°24'
149°20'
149°16'
60°8'
60°6'
60°4'
60°2'
60°0'
59°58'
Slide
Thicknesses
60m
30m
0m
0 0.5 1 2
Kilometers
N
Resurrection
River Delta
Seward
SDT
FJC
Fourth of
July Creek
Mid-Bay
Channel
LP
Lowell
Point
Tonsina
Point
Bathtub
East
Bathtub
West
Bathtub
Thumb
Cove
Caines
Head
South
End
Sill

◀ Figure 5
Reconstructed thicknesses and initial extent of slide bodies that were mobilized during the 1964 earthquake (modified from HAEUSSLER *et al.* (2007)).

define the pre-earthquake depths in Resurrection Bay. It is assumed that the slide mass is initially at rest, and gravity is the only driving force. Although it is possible that individual slides were triggered at different times after the initial ground shaking, there is no independent evidence to support this hypothesis. Therefore we assume in the model that all slides start moving at the same time.

4.1. Movement of the Sediments and Propagation of Surface Waves

The initial thickness and extent of the slide mass is shown in Figure 5. The strong ground shaking associated with the earthquake acted as a trigger that released unstable sediments in the bay. The slide masses moved downslope, spreading out and filling the bathtub from all directions (Fig. 6). Because the bottom of the bathtub is nearly flat, slide speed decreased dramatically when the sediments reached the deepest part of the fjord (Figs. 6C, D). Only a relatively small amount of sediments from the South End slide complex (Fig. 5) moved out of the basin to the southern slope of the glacial sill that extends across the bay and keeps sediment in the basin (Fig. 6D). Results of numerical simulations show that it took about 30 minutes for the sediment flow to completely cover the bathtub.

The wave modeling results show that each slope failure produced a cylindrical wave with a crest propagating toward the opposite shore, and the trough moving toward the generation area (Fig. 7). This wave pattern is in agreement with previous numerical studies of waves generated by viscous underwater slides (THOMSON *et al.*, 2001; RABINOVICH *et al.*, 2003). In frame B ($t = 40$ sec), the wave crests from the Lowell Point (LP), Seward downtown (SDT), and Fourth of July Creek (FJC) slides are clearly visible (white dashed lines). At $t = 1$ min the crests pass the middle of the bay and continue moving toward the opposite shores, while the wave from the LP slide is approaching the southern end of Seward (Fig. 7C). At $t = 1$ min 40 sec the wave from the FJC slide hits Seward at the southeastern point of the fan delta (Frame D, white dashed line). Frames D and E show complicated patterns of multiple reflections and wave interactions in the bay. About 5 minutes after the beginning of ground shaking the wave action subsides (Fig. 7F). Our modeling results agree with the observation that sliding appeared to terminate at the end of the shaking (that lasted about 4.5 minutes), and therefore the source of the waves ceased as well. This is consistent with the assumption that most of sediments was released during the period of ground shaking.

The waves generated in the southern part of the bay by the South End and Thumb Cove slide complexes (Fig. 5) propagated mostly to the west, in the direction of Caines Head, and to the south, toward the open boundary (Figs. 7B, C). Two waves, produced by the eastern and western slides of the South End slide complex, are visible on frames C and D (yellow arrows), diffracting around Caines Head.

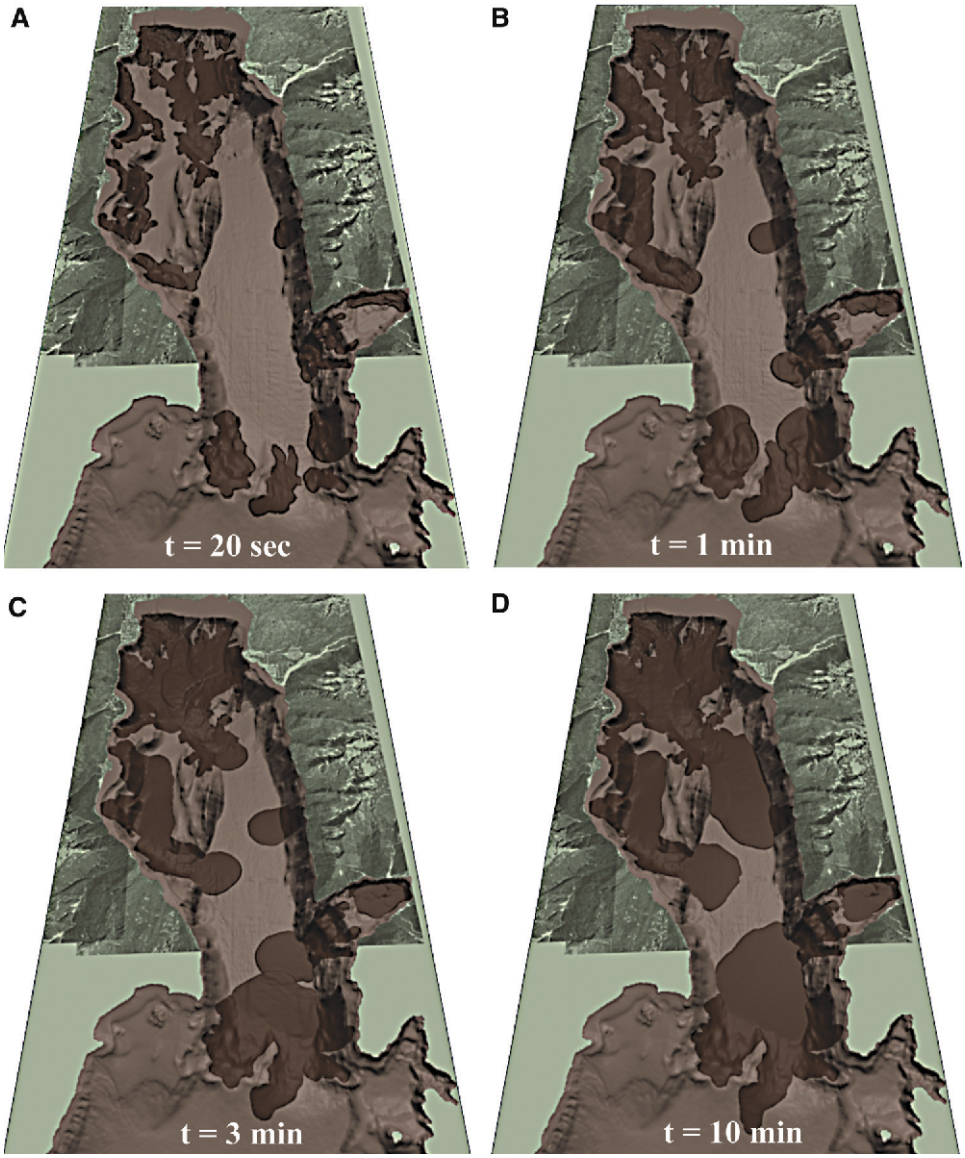

Figure 6
Snapshots from the numerical simulation of slide mass.

4.2. Simulated Wave Records

We conducted a numerical experiment to investigate how individual slide failures contributed to the observed tsunami amplitudes. The equations that describe water waves in this problem are nonlinear shallow water equations. The time series of water waves

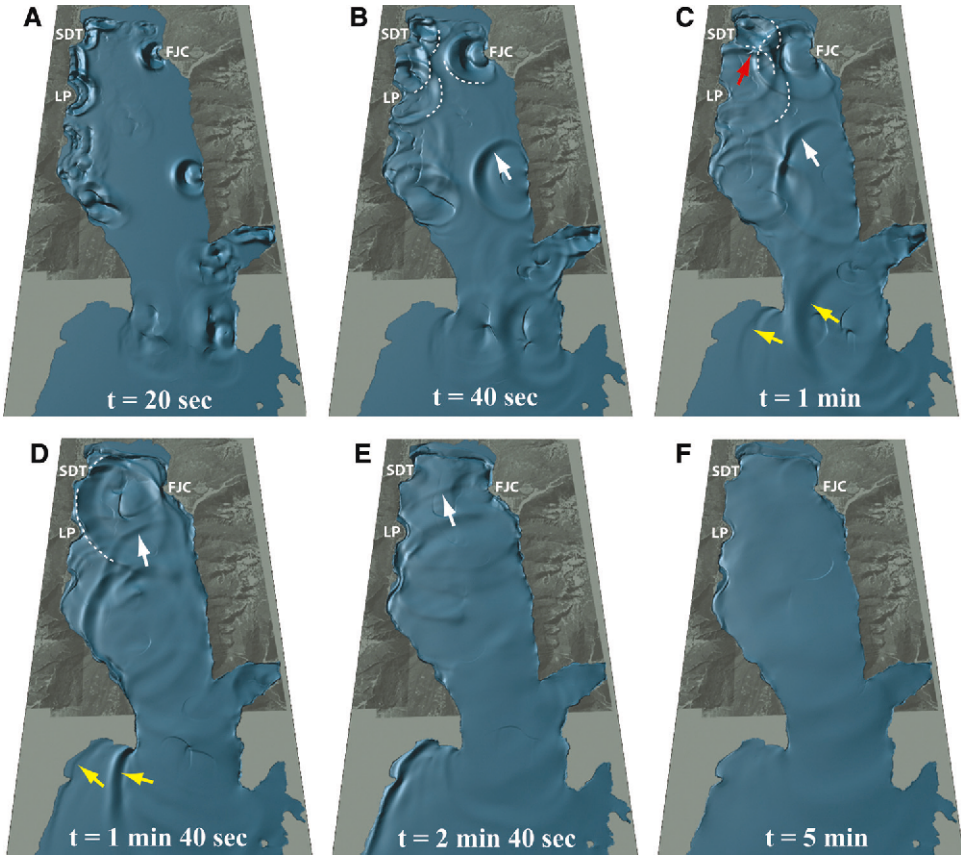

Figure 7
Snapshots from numerical simulation of surface waves in Resurrection Bay generated by the moving slide mass. Slide locations: SDT - Seward downtown, LP - Lowell Point, FJC - Fourth of July Creek. Dashed lines and arrows indicate positions of different wave fronts (see text for reference).

generated by multiple slope failures cannot generally be represented as a linear superposition of a time series of waves generated by individual slides. This is especially true if interacting waves propagate at a small angle with respect to each other and for a long enough time for nonlinear effects to grow. But in cases where the relative angles are not small, and especially when waves propagate in the opposite directions (crossing waves) with very small interaction time, the nonlinear effects can be neglected. For example, in the scope of shallow water equations, the mathematical problem of two crossing waves is equivalent to a problem of a wave reflecting from a vertical wall (PELINOVSKY, 1996), in which case the nonlinear effects have been shown to be minimal. In our analysis we superpose the waves that propagate either in the opposite directions or at angles greater than 45° with short interaction time, and therefore the linear approximation is valid.

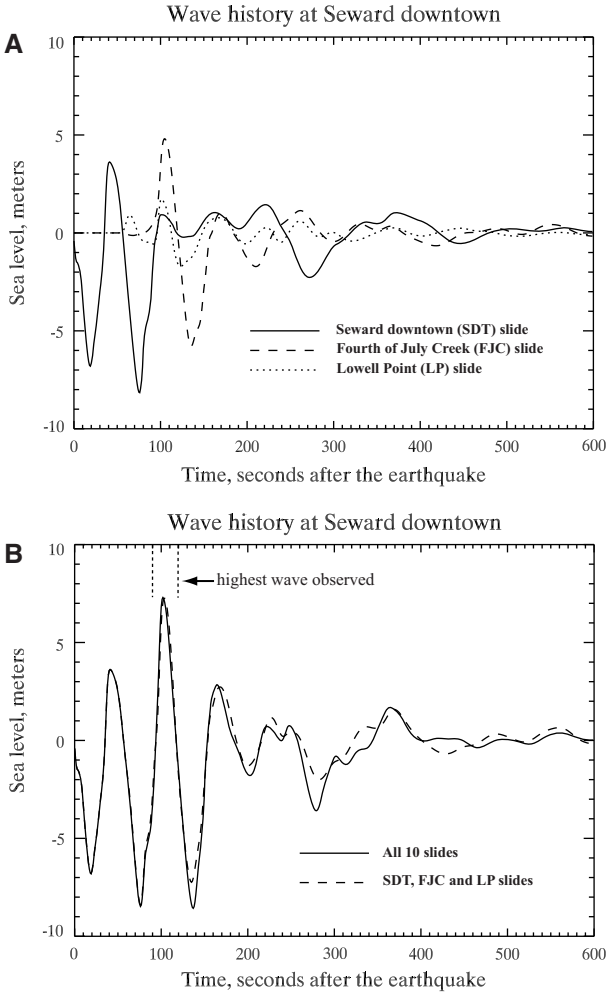

Figure 8
Simulated water level at Seward downtown.

The numerical experiment consisted of three steps. First, we selected the slides that are the closest to Seward, and also have substantial volumes and relatively shallow initiation depth. In Figure 5 these slide complexes are: SDT (Seward downtown, 27.5 million m^3), LP (Lowell Point, 18.1 million m^3) and FJC (Fourth of July Creek, 35 million m^3). We modeled each of these slides separately, and calculated time histories for generated waves at all three locations shown in Figure 2. Then, we modeled the three slides together, and calculated the time histories at the same locations. Finally, we calculated time histories for waves resulting from all 10 slides.

The results of the water level simulation at Seward are shown in Figure 8. The Seward slide first generated a trough, which was observed as a massive drawdown of

water about 30 seconds after the initial ground shaking in the waterfront area, followed by the wave crest (Fig. 8a). The highest simulated wave at Seward was the one generated by the FJC slide that arrived in 1 min 40 seconds after the earthquake. It was the superposition of this wave and two smaller crests from the Seward slide and the Lowell Point slide that resulted in the maximum observed wave height at Seward (Table 1). Figure 8b shows the time series of waves resulted from the slides SDT, LP, and FJC combined, compared to the time series of waves generated by all slides. It is evident that the waves generated by slides in the lower part of the bay had relatively little impact on the wave amplitudes in the upper bay during ground shaking (first 250 seconds).

As was the case in Seward, the initial trough at Fourth of July Creek (Fig. 9a) was generated by the local slide, but the following crest was not as high as the crest generated by the Seward slope failure. The waves from the opposite shore, induced by the SDT slide and the LP slide, arrived at Fourth of July Creek almost at the same time, in about 105 sec, and their superposition generated the highest crest at this location. This was probably the wave that, according to observations, ran inland 400 meters (WILSON and TØRUM, 1968). Figure 9b shows that the amplitude of the second trough is much smaller if the wave field is calculated from all 10 slides, compared to its amplitude produced by the slides in the upper bay only. This trough was diminished by the superimposed wave crest produced by the Bathtub East failure (Fig. 5), which arrived to Fourth of July Creek in about 140 sec. This crest is indicated by the white arrow on frames B–E of Figure 7.

The Lowell Point time series are shown in Figure 10. There is a short first positive wave at this location, due to a combination of the slide geometry and the location of the time series point (Figs. 2 and 5). The slide complex consists of two major areas, and the crest from the northern part of the slide that propagates toward the opposite shore reaches the time series point faster than the trough from the southern section of the slide complex does. The wave from Fourth of July Creek arrives at Lowell Point in 1 min 40 sec, and the wave from Seward arrives 20 sec later (Fig. 10a). Superposition of these waves (Figure 10b) generates a 6.5 m high crest at Lowell Point.

5. Discussion and Conclusions

We performed numerical simulations of tsunami waves generated by submarine slides in Resurrection Bay, Alaska, during the M_W 9.2 1964 earthquake. Our numerical results confirm the hypothesis that tsunami waves observed in Seward during and immediately after the earthquake resulted from multiple submarine slope failures (LEE *et al.*, 2006; HAEUSSLER *et al.*, 2007). Results of numerical simulation of water waves at Seward for the first 5 minutes after the initial ground shaking are in good agreement with the eyewitness observations (Fig. 8b, Table 1). Our numerical experiments were designed to investigate the relative contributions of different submarine slide complexes. The results show that the Seward downtown (SDT) slide, the Lowell Point (LP) slide, and the Fourth of July

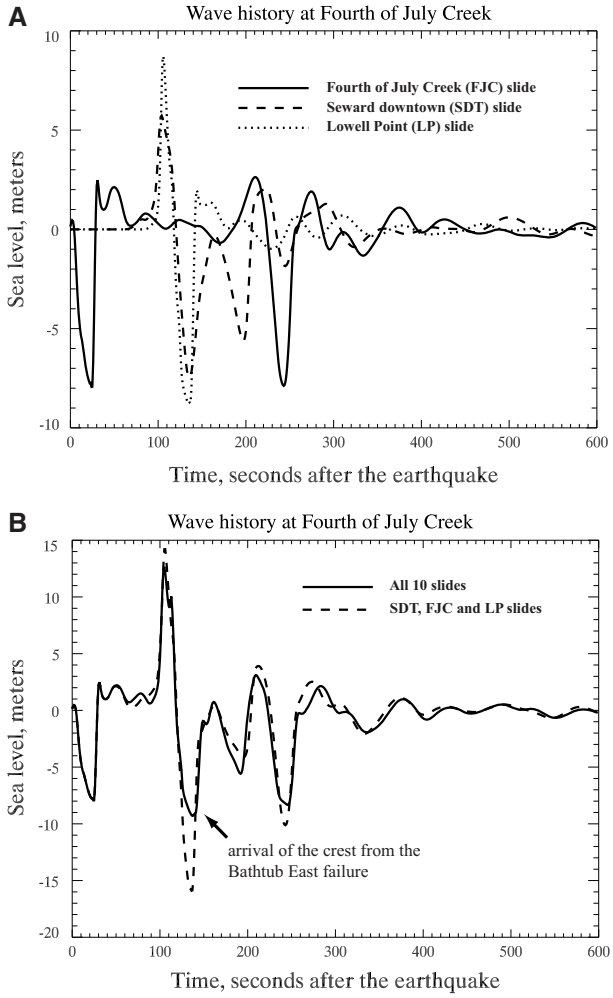

Figure 9
Simulated water level at Fourth of July Creek.

Creek (FJC) slide were the major contributors of tsunami wave energy in the upper bay during the first 3 minutes after slide initiation.

Eyewitness descriptions of events at Seward on March 27, 1964 (WILSON and TØRUM, 1968) report that a 6–8 m high, north-moving wave arrived at the Seward waterfront 1.5-2 minutes after the earthquake. The simulated time history at downtown Seward (Fig. 8b) agrees very well with observation of this wave (Table 1). Also, several observers noted the north-moving wave crossing the wave coming from the east. We interpret these observations as the interaction of the waves generated by the LP and FJC slides (Fig. 7, frame C, red arrow). The numerical results show that the highest waves at Seward were

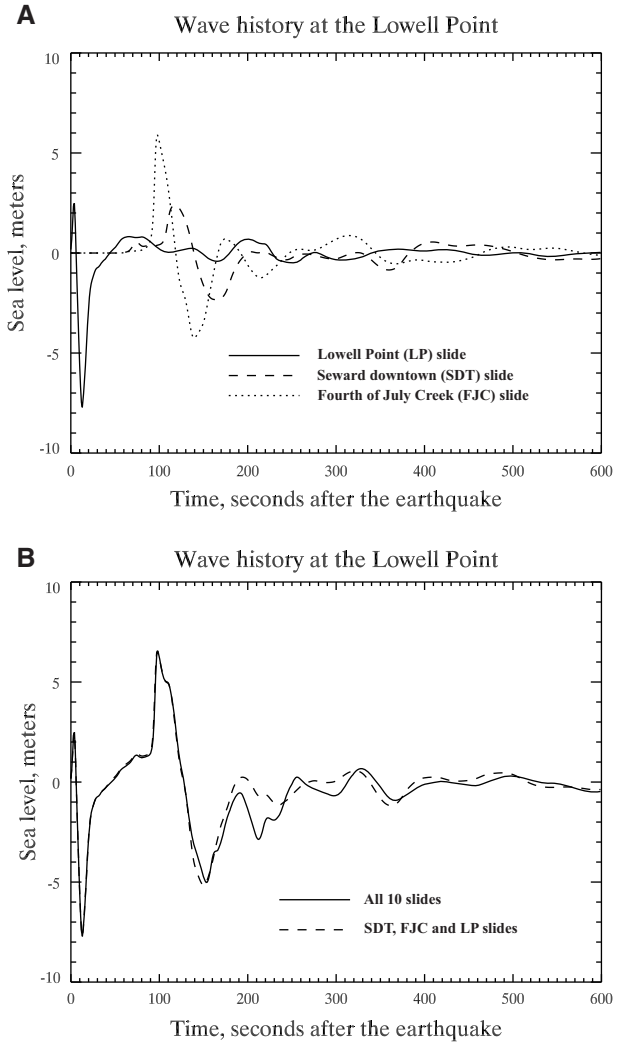

Figure 10
Simulated water level at the Lowell Point.

the result of positive interference of the three major waves in the upper part of Resurrection Bay, generated by the SDT, LP and FJC slides (Fig. 8b).

WILSON and TØRUM (1968) describe "boils" of water observed about 1.5 km west of the Fourth of July Creek and speculate they could be the result of an underwater slide. Numerical experiments conducted by FINE *et al*. (2003) show that the total wave energy generated by a slide strongly depends on the initial position of the slide. For submarine slides, wave amplitude quickly decreases when initial depth of the slide increases. It is unlikely that the sliding mass could have generated a big wave in the middle of the bay, at

a depth of about 200 m. It is possible, though, that the Mid-Bay Channel slide experienced a delayed trigger, caused by the motion of the FJC slide when the latter reached the middle of the bay and scoured the bottom (HAEUSSLER *et al.*, 2007). This would have caused a significant increase in the total volume of the moving mass. This hypothesis could be verified by additional numerical experiments.

Observers at Lowell Point reported a wave coming from Seward, and at the same time, a wave radiating toward Fourth of July Creek (WILSON and TØRUM, 1968). We interpret these observations as waves generated by SDT and LP slides. The highest reported wave at Lowell Point was about 6 m high (WILSON and TØRUM, 1968), which agrees with the modeling results (Fig. 10b).

Future work will include simulation of runup of tsunami waves generated by slope failures in Resurrection Bay and comparison of results with inundation patterns observed in 1964. For the purposes of tsunami hazard mitigation, we plan to study tsunami waves generated by hypothetical underwater slides and estimate the landslide tsunami hazard. Engineering studies conducted after the 1964 earthquake in Seward and Valdez (LEMKE, 1967; COULTER and MIGLIACCIO, 1966; SHANNON and HILTS, 1973) concluded that underwater slope failures have not improved slope stability, meaning that the same slopes could fail again during the next large earthquake. Moreover, some of the streams draining into Resurrection Bay, such as Lowell Creek and Fourth of July Creek, have been rerouted by humans. These creeks are now depositing sediments in new locations, which may lead to new unstable sediment accumulations and future submarine slides.

Acknowledgments

This study was supported by NOAA grants 27-014d and 06-028a through Cooperative Institute for Arctic Research, and by the USGS. We thank Michelle Coombs, Chris Waythomas and anonymous reviewers for helpful suggestions that improved this manuscript. The authors also thank Keith Labay for the construction of the high-resolution DEM of Resurrection Bay, and Dave West for data processing in ArcGIS and his help in preparing the figures. Numerical calculations for this work are supported by a grant of High Performance Computing (HPC) resources from the Arctic Region Supercomputing Center (ARSC) at the University of Alaska Fairbanks as part of the US Department of Defense HPC Modernization Program. We thank ARSC specialists Miho Aoki and Sergei Maurits for visualizations of computational results.

REFERENCES

ASSIER-RZADKIEWICZ, S., MARIOTTI, C., and HEINRICH, P. (1997), *Numerical simulation of submarine landslides and their hydraulic effects*, J. Waterw. Port. Coast. Ocean. Eng. *123*(4), 149–157.

BERG, E., COX, D., FURUMOTO, A., KAJIURA, K., KAWASUMI, H., and SHIMA, E. (1964), *Field survey of the tsunami of 28 March 1964 in Alaska*, Report, Hawaii Institute of Geophysics (unpublished).

BORNHOLD, B., THOMSON, R., RABINOVICH, A., KULIKOV, E., and FINE, I. (2001), *Risk of landslide-generated tsunamis for the coast of British Columbia and Alaska*. In *An Earth Odyssey*, Proc. Canadian Geotechn. Conf., pp. 1450–1454.

COULTER, H. and MIGLIACCIO, R. (1966), *Effects of the Earthquake of March 27, 1964, at Valdez, Alaska*, U.S. Geolog. Survey Prof. Paper 542-C, 36 pp.

FINE, I., RABINOVICH, A., KULIKOV, E., THOMSON, R., and BORNHOLD, B. (1998), *Numerical modelling of landslide-generated tsunamis with application to the Skagway Harbor tsunami of November 3, 1994*. In Proc. Int. Conf. on Tsunamis, Paris, pp. 211–223.

FINE, I., RABINOVICH, A., THOMSON, R., and KULIKOV, E., *Numerical modeling of tsunami generation by submarine and subaerial landslides*. In: *Submarine Landslides and Tsunamis*, (Yalciner, A., Pelinovsky, E., Okal, E., Synolakis, C., eds.), (Kluwer 2003), pp. 69–88.

GRILLI, S. and WATTS, P. (2005), *Tsunami generation by submarine mass failure. I : Modeling, experimental validation, and sensitivity analysis*, J. Waterw. Port. Coast. Ocean. Eng. *131*(6), 283–297, DOI 10.1061/(ASCE)0733-950X(2005)131:6(283).

HAEUSSLER, P., LEE, H., RYAN, H., LABAY, K., KAYEN, R., HAMPTON, M., and SULEIMANI, E. (2007), *Submarine slope failures near Seward, Alaska, during the M9.2 1964 earthquake*. In: *Submarine Mass Movements and their Consequences*, (Lykousis, V., Sakellariou, D., Locat, J., eds.), pp. 269–278.

HAMPTON, M., LEE, H., and LOCAT, J. (1996), *Submarine landslides*, Rev. Geophys. *34*, 33–59.

HAMPTON, M., LEMKE, R., and COULTER, H. (2002), *Submarine landslides that had a significant impact on man and his activities: Seward and Valdez, Alaska*. In: *Submarine Landslides: Selected Studies in the US Exclusive Economic Zone*, (Schwab, W., Lee, H., Twichell, D., eds.), U.S. Geolog. Survey Bull., pp. 123–134.

HARBITZ, C. (1992), *Model simulations of tsunamis generated by the Storegga Slides*, Marine Geol. *105*, 1–21.

IMAMURA, F., HASHI, K., and IMTEAZ, M., *Modeling for tsunamis generated by landsliding and debris flow*. In: *Tsunami Research at the End of a Critical Decade*, (Hebenstreit, G.T., ed.), (Kluwer 2001), pp. 209–228.

JIANG, L. and LEBLOND, P. (1992), *The coupling of a submarine slide and the surface waves which it generates*, J. Geophys. Res. *97*(C8), 12,731–12,744.

JIANG, L. and LEBLOND, P. (1994), *Three-dimensional modeling of tsunami generation due to a submarine mudslide*, J. Phys. Oceanogr. *24*(3), 559–572.

KULIKOV, E., RABINOVICH, A., FINE, I., BORNHOLD, B., and THOMSON, R. (1998), *Tsunami generation by landslides at the Pacific coast of North America and the role of tides*, Oceanology *38*(3), 361–367.

LABAY, K. and HAEUSSLER, P. (2008, in press), *Combined high-resolution LIDAR topography and multibeam bathymetry for upper Resurrection Bay, Seward, Alaska*, U.S. Geolog. Survey Digital Data Series.

LANDER, J. (1996), *Tsunamis affecting Alaska. 1737–1996*, No. 31 in NGDC Key to Geophysical Research, National Geophysical Data Center, Boulder, Colorado.

LANTZ, B. and KIRKPATRICK, M., *Seward Quake, Good Friday, 1964* (Kirkpatrick Printing Co., Seward, Alaska 1964).

LEE, H., SCHWAB, W., and BOOTH, J. (2002), *Submarine landslides: An introduction*. In: *Submarine Landslides: Selected Studies in the U.S. Exclusive Economic Zone*, (Schwab, W., Lee, H., Twichell, D., eds.), U.S. Geolog. Survey Bull., pp. 1–13.

LEE, H., RYAN, H., KAYEN, R., HAEUSSLER, P., DARTNELL, P., and HAMPTON, M. (2006), *Varieties of submarine failure morphologies of seismically-induced landslides in Alaska fjords*, Norwegian J. Geology *86*, 221–230.

LEMKE, R. (1967), *Effects of the Earthquake of March 27, 1964, at Seward, Alaska*, U.S. Geolog. Survey Prof. Paper 542-E, 48 pp.

LYNETT, P. and LIU, P.F. (2002), *A numerical study of submarine landslide generated waves and runup*, Proc. Roy. Soc. London *A 458*, 2885–2910.

LYNETT, P. and LIU, P.F. (2004a), *A two-layer approach to water wave modeling*, Proc. Roy. Soc. London *A 460*, 2637–2669.

LYNETT, P. and LIU, P.F. (2004b), *Linear analysis of the multi-layer model*, Coastal Eng. *51*, 439–454.

LYNETT, P. and LIU, P.F. (2005), *A numerical study of the runup generated by three-dimensional landslides*. J. Geophys. Res. *110*(C03006), DOI 10.1029/2004JC002443.

PELINOVSKY, E. (1996), *Tsunami Waves Hydrodynamics*, Institute of Appl. Phys., RAS, Nizhny Novgorod, Russia.

PLAFKER, G., KACHADOORIAN, R., ECKEL, E., and MAYO, L. (1969), *Effects of the Earthquake of March 27, 1964 on various communities*, U.S. Geolog. Survey Prof. Paper *542-G*, 50 pp.

RABINOVICH, A.B., THOMSON, R.E., BORNHOLD, B.D., FINE, I.V., and KULIKOV, E.A. (2003), *Numerical modelling of tsunamis generated by hypothetical landslides in the Strait of Georgia, British Columbia*, Pure Appl. Geophys. *160*(7), 1273–1313.

SAVOIE, M., SAVOIE, J., TREFRY, J., SEMMLER, C., WOODALL, D., TROCINE, R., BROOKS, J., and MCDONALD, T. (2006), *Port Valdez sediment coring program: Final 2004 monitoring report*, Kinnetic Laboratories, Inc., Contract No. 961.04.1 for Prince William Sound Regional Citizens' Advisory Council.

SHANNON, W. and HILTS, D., *Submarine landslide at Seward*. In *The Great Alaska Earthquake of 1964*. Engin. (National Academy of Sciences Washington, D.C. 1973), pp. 144–156.

THOMSON, R.E., RABINOVICH, A.B., KULIKOV, E.A., FINE, I.V., and BORNHOLD, B.D., *On numerical simulation of the landslide-generated tsunami of November 3, 1994 in Skagway Harbor, Alaska*. In: *Tsunami Research at the End of a Critical Decade* (Hebenstreit, G.T., ed.), (Kluwer 2001), pp. 243–282.

TITOV, V. and GONZALEZ, F., *Numerical study of the source of the July 17, 1998 PNG tsunami*. In: *Tsunami Research at the End of a Critical Decade*, (Hebenstreit, G.T., ed.), (Kluwer 2001), pp. 197–207.

WILSON, B. and TØRUM, A. (1968), *The tsunami of the Alaskan Earthquake, 1964: Engineering evaluation*, U.S. Army Corps of Engineers, Technical Memo. *25*, 401 pp.

(Received February 16, 2008, accepted June 18, 2008)
Published Online First: February 6, 2009

Pure appl. geophys. 166 (2009) 153–175
0033–4553/09/010153–23
DOI 10.1007/s00024-008-0435-4

Pure and Applied Geophysics

Lituya Bay Landslide Impact Generated Mega-Tsunami 50th Anniversary

HERMANN M. FRITZ, FAHAD MOHAMMED, and JESEON YOO

Abstract—On July 10, 1958, an earthquake M_w 8.3 along the Fairweather fault triggered a major subaerial landslide into Gilbert Inlet at the head of Lituya Bay on the southern coast of Alaska. The landslide impacted the water at high speed generating a giant tsunami and the highest wave runup in recorded history. The mega-tsunami runup to an elevation of 524 m caused total forest destruction and erosion down to bedrock on a spur ridge in direct prolongation of the slide axis. A cross section of Gilbert Inlet was rebuilt at 1:675 scale in a two-dimensional physical laboratory model based on the generalized Froude similarity. A pneumatic landslide tsunami generator was used to generate a high-speed granular slide with controlled impact characteristics. State-of-the-art laser measurement techniques such as particle image velocimetry (PIV) and laser distance sensors (LDS) were applied to the decisive initial phase with landslide impact and wave generation as well as the runup on the headland. PIV provided instantaneous velocity vector fields in a large area of interest and gave insight into kinematics of wave generation and runup. The entire process of a high-speed granular landslide impact may be subdivided into two main stages: (a) Landslide impact and penetration with flow separation, cavity formation and wave generation, and (b) air cavity collapse with landslide run-out and debris detrainment causing massive phase mixing. Formation of a large air cavity — similar to an asteroid impact — in the back of the landslide is highlighted. A three-dimenional pneumatic landslide tsunami generator was designed, constructed and successfully deployed in the tsunami wave basin at OSU. The Lituya Bay landslide was reproduced in a three-dimensional physical model at 1:400 scale. The landslide surface velocities distribution was measured with PIV. The measured tsunami amplitude and runup heights serve as benchmark for analytical and numerical models.

Key words: Tsunami, landslide, landslide generated tsunami, natural hazard, nonlinear gravity water waves, wave runup, near-field wave characteristics, slide energy conversion, three-phase flow, Alaska.

1. Introduction

Lituya Bay is a T-shaped tidal inlet that cuts through the coastal lowlands and the foothills flanking the Fairweather Range of the St. Elias Mountains on the southern coast of Alaska shown in Figure 1a. The stem corresponding to the main part of the T-shaped bay is 12 km long and extends northeastward from the bay entrance. The width of the stem ranges from 1.2 to 3.3 km except at the entrance, which is only 300 m wide. The bay fills and slightly overflows a depression carved by a valley glacier of which Lituya, North Crillon and Cascade glaciers are remnants. Submarine contours show a pronounced

School of Civil and Environmental Engineering, Georgia Institute of Technology, 210 Technology Circle, Savannah, GA 31407, U.S.A. E-mail: fritz@gatech.edu

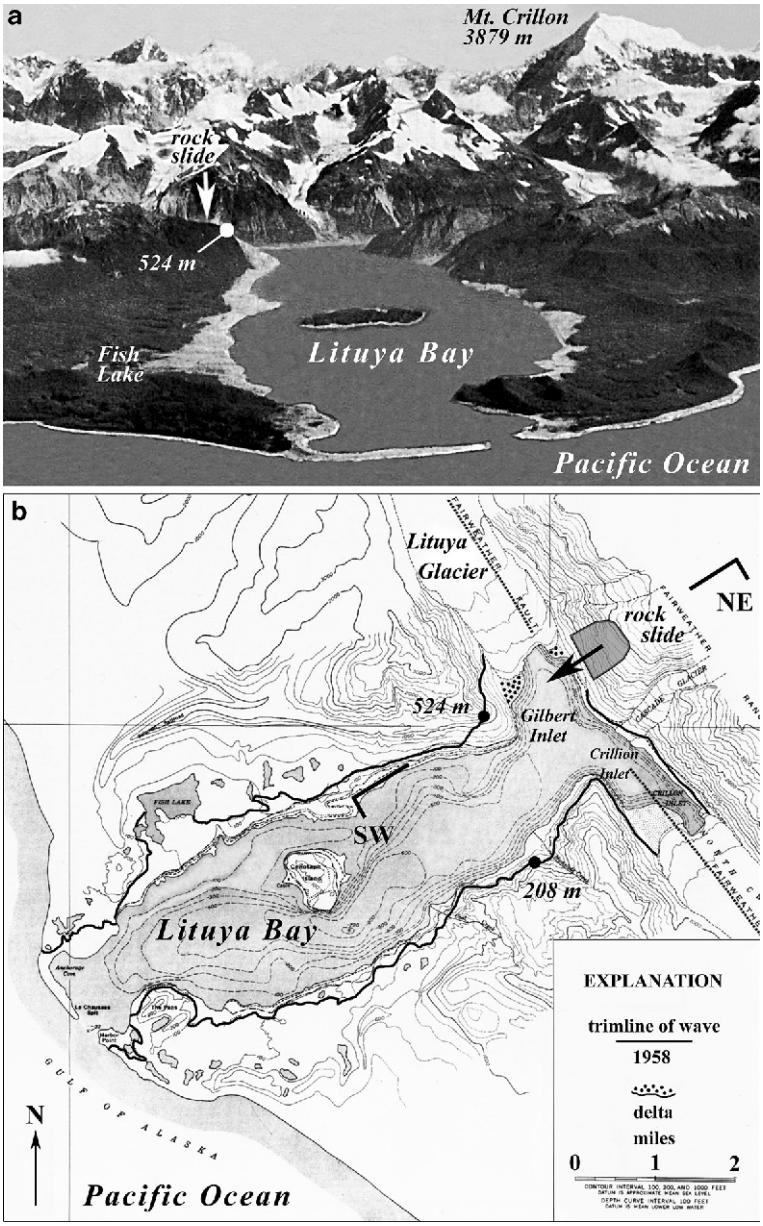

Figure 1

Lituya Bay, Alaska: (a) Overview in August 1958 (MILLER, 1960). Forest destroyed to a maximum elevation of 524 m and a maximum distance of 1100 m from high-tide shoreline at Fish Lake due to a giant tsunami generated on 10 July 1958 by a landslide at the head of the bay. (b) Map showing topographic and bathymetric contours, trace of Fairweather fault, 1958 landslide and trimline of tsunami runup (MILLER, 1960).

U-shaped trench with steep walls and a broad flat floor sloping gently downward from the head of the bay to a maximum depth of 220 m. Minimum depth at the entrance of the bay is 10 m. At the head of the bay the walls are fjord-like glacially over-steeped. The walls have been buttressed by glaciers until recently. Radiocarbon dates on high moraines suggest retreat of glaciers only in the last millennium (SLINGERLAND and VOIGHT, 1979). The two arms at the head of the bay are part of a great trench that extends tens of kilometers to the northwest and southeast as a topographic expression of the Fairweather transform fault shown in Figure 1b.

Giant waves have occurred in Lituya Bay probably five times during the last two centuries emphasizing the unique geologic and tectonic setting of the bay. Frequent occurrence of giant waves in Lituya Bay, as compared to other similar bays, is attributed to the combined effect of recently glaciated steep slopes, highly fractured rocks and deep water in an active fault zone, heavy rainfall, frequent freezing and thawing (MILLER, 1960). Three extreme wave runup heights in 1853 or 1854, 1936 and 1958 carved sharp trimlines of chopped trees to elevations beyond 100 m on to the slopes of Lituya Bay. Photographic evidence and eyewitness accounts suggest two additional giant waves occurred possibly in 1874 and 1899 (MILLER, 1960). In 1853 or 1854 a giant wave caused forest destruction on Lituya Bay shores to a maximum elevation of 120 m. A landslide from the steep wall on the south shore of Lituya Bay near Mudslide Creek is the likely source directly opposite to the maximum destruction on the north shore. The trimline of the 1936 waves reached a maximum height of 150 m above sea level on the northeast wall of Crillon Inlet and indicates a wave generation near the head of Crillon Inlet. MILLER (1960) suggests a landslide or rock avalanche from the southwest wall of Crillon Inlet, opposite the high point on the trimline. In 1958 the largest wave runup of 524 m in recorded history was observed on a spur ridge on the southwest wall of Gilbert Inlet. Only the 1958 event is further considered here as the exact sources of the earlier events remain to be confirmed by bathymetric and geologic surveys of the seafloor.

2. 1958 Landslide Impact and Tsunami Runup

Beginning at 06:16 UTC on July 10, 1958, the southwest sides and bottoms of Gilbert and Crillon Inlets moved northwestward and relative to the northeast shore at the head of the bay, on the opposite side of the Fairweather fault. Total movements of 6.4 m horizontally and 1 m vertically were estimated for the earthquake M_w 8.3 (TOCHER and MILLER, 1959). Intense shaking in Lituya Bay continued for 1 to 4 minutes according to two eyewitnesses that anchored in the bay. Between 1 and 2½ minutes after the earthquake was first felt a large mass of rock slid from the northeast wall of Gilbert Inlet (Fig. 2). The landslide was triggered impulsively by fault movement and intense earthquake vibrations. It is highly probable that the entire mass plunged into Gilbert Inlet as a unit at the time of the earthquake. PARARAS-CARAYANNIS (1999) classified the mass movement as subaerial rockfall to distinguish from gradual processes of ordinary

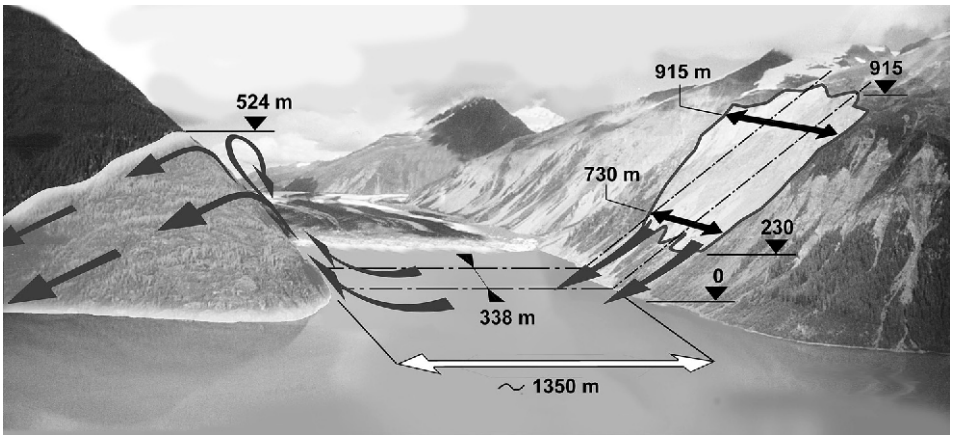

Figure 2
Gilbert Inlet illustration showing landslide dimensions, impact site and tsunami runup to 524 m on spur ridge directly opposite to landslide impact. Direction of view is north and the front of Lituya Glacier is set to 1958 post-slide position. Illustration background is synthesized from two aerial photos recorded in 1997 (Photos: courtesy of Charles L. Mader).

landslides whereas MILLER (1960) judged it to be near the borderline between landslide and rockfall as defined by SHARPE (1938) and VARNES (1958). The landslide occurred in an area of previously active sliding to an elevation of 915 m on a slope averaging 40°. The rocks are mainly amphibole and biotite schists with an estimated density of 2.7 t/m^3. The dimensions of the slide on the slope are accurate, but the thickness of the slide mass normal to the slope could be estimated only roughly (MILLER, 1960). The main mass of the slide presumably involved a prism of rock roughly triangular in cross section, with width dimensions from 730 m to 915 m (MILLER, 1960; SLINGERLAND and VOIGHT, 1979), a slope parallel length of 970 m (SLINGERLAND and VOIGHT, 1979), a maximum thickness of about 92 m normal to the slope, and a center of gravity at about 610 m elevation (MILLER, 1960). Dimensions are illustrated in Figure 2. Miller estimated the slide volume from these as 30.6×10^6 m^3.

Prior to the landslide low deltas of gravel had built out into Gilbert Inlet at the southeast and northwest margins of the Lituya Glacier front. Part of the slide must have hit the Lituya Glacier and glacial gravel deltas due to the pre-slide location of slide mass, deltas and glacier front (MILLER, 1960). The Lituya Glacier front was characterized by a vertical wall normal to the Gilbert Inlet axis after the event (Figs. 3a, b). During the event as much as 400 m of ice had been sheared off on parts of the glacier front and the gravel deltas were pushed or washed away. The landslide impact created a giant tsunami and a resulting maximum tsunami runup of 524 m in straight prolongation of the slide axis on a spur ridge on the southwest shore of Gilbert Inlet (Figs. 3a, b, c).

The maximum tsunami runup of the 1958 event was incomparable at the time to any other event outside of Lituya Bay. The 524 meter runup is seven times larger than

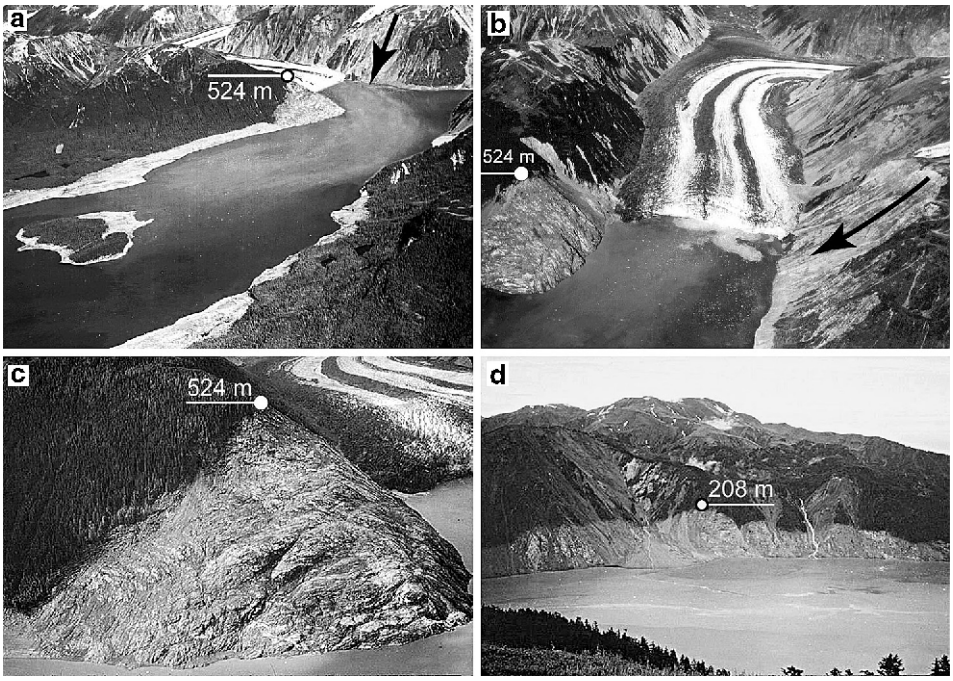

Figure 3
Trimlines carved by tsunami in 1958: (a) NE-view of Lituya Bay from Cenotaph Island to Gilbert Inlet with landslide scar at the head of the bay and trimlines of destructed forest with 524 m runup on spur ridge. (b) NW-view of Gilbert Inlet with landslide scar, post-event Lituya Glacier front, forest destruction and soil erosion down to bedrock. (c) N-view of spur ridge. (d) S-view of trimline in the Mudslide Creek area on the south shore of Lituya Bay with wiped out trees to an elevation of 208 m. (Photos: courtesy of USGS).

the highest tsunami runup of 75 m observed 1936 in Norwegian Lake Loen (JØRSTAD, 1968) and roughly doubles wave runup heights in the Vajont reservoir, Italy (MÜLLER, 1964) and Spirit Lake, U.S.A. (VOIGHT *et al.*, 1983). A simplified 3-D physical model of Lituya Bay at a 1:1,000 scale was constructed at the University of California, Berkeley (R.L. WIEGEL in MILLER, 1960, pp. 65-66). Wiegel concluded from physical model observations, that a sheet of water washed up the slope opposite to the landslide to an elevation of at least three times the water depth for a slide impacting Gilbert Inlet as a unit and very rapidly. At the same time a large wave, several hundred feet high, moved in the southerly direction, causing a peak rise to occur in the vicinity of Mudslide Creek. Unfortunately no measured data are available from these three dimensional experiments. The highest mark of chopped trees at an elevation of 208 m on the south shore trimline is shown in Figure 3d. WIEGEL (1964) estimated the hydrodynamic forces exerted on the trees by the wave as roughly ten times greater than the force necessary to snap or uproot trees.

3. Physical Model of Gilbert Inlet

Based on the generalized Froude similarity a cross section of Gilbert Inlet was rebuilt at a 1:675 scale in a two-dimensional physical laboratory model (L × W × H: 11 m, 0.5 m and 1 m) by FRITZ *et al.*, 2001. The Froude similarity has been confirmed by a laboratory scale series (HELLER *et al.*, 2008). The modeled Gilbert Inlet cross section is shown in Figure 4a and its NE-SW orientation in Figure 1b. The prismatic Gilbert Inlet slice rebuilt in the model is shown in Figure 2. The width of 338 m represented in the 2-D model corresponds to 40% of the mean slide width of 823 m (SLINGERLAND and VOIGHT, 1979). The volume per unit width $V_s' = 37.2 \times 10^3$ m^3/m$'$ was estimated by equal distribution of the total slide volume $V_s = 30.6 \times 10^6$ m^3 over an averaged slide width of 823 m. This is a conservative assumption neglecting the volume concentration in the slide center due to roughly triangular slide cross sections along the slope. The indicated geometry corresponds to the physical model assumptions with a hill slope angle α and a headland angle β of both 45°. The simplified Gilbert Inlet bathymetry roughly corresponds to bedrock of the glacially carved U-shaped trench. Pre-slide gravel deltas

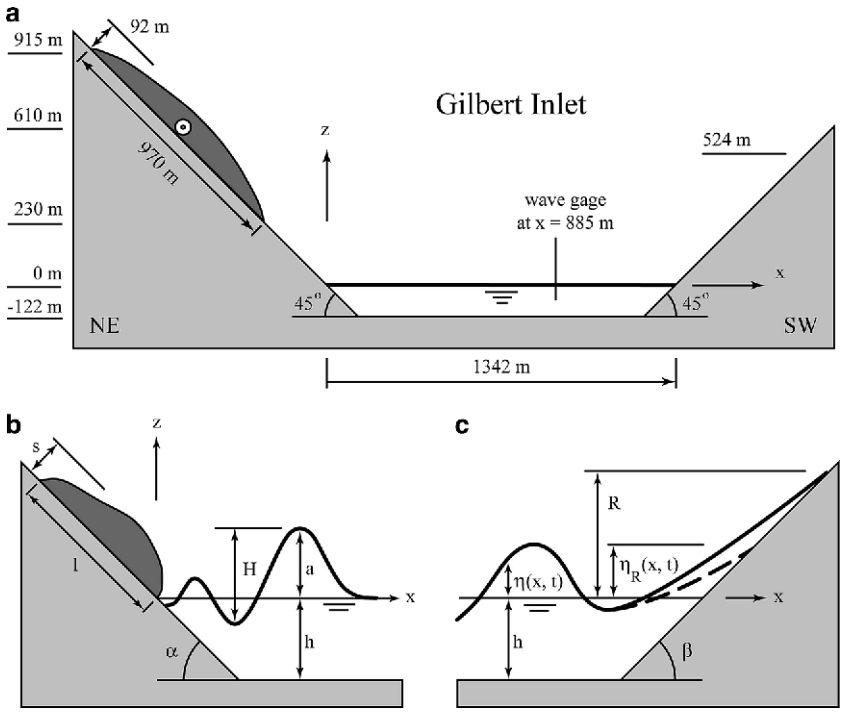

Figure 4
(a) Cross section of Gilbert Inlet along slide axis in NE to SW orientation shown in Figure 1b. Geometry corresponds to physical model assumptions and simplifications. (b) Notation for landslide impact and wave propagation; (c) notation for wave runup.

along parts of the glacier front shown in Figure 1b were neglected. The assumed stillwater depth $h = 122$ m matches the maximum water depth in Gilbert Inlet. The notation for landslide impact, wave propagation and wave runup are defined (Figs. 4b, c).

Radial or lateral wave spreading is neglected in the two-dimensional model. In northern direction the impact area is confined to the Lituya Glacier front. In this specific topographic situation wave height reduction due to 3-D effects is further limited by the small ratio of 1.6 between propagation distance and slide width. Therefore it is expected that the present 2-D model can give a good estimate of wave and runup heights in Gilbert Inlet.

The dynamic slide impact characteristics were controlled with a specifically designed pneumatic landslide generator shown in Figure 5 (FRITZ and MOSER, 2003). The pneumatic landslide generator models the transition from block slide motion to granular flow. The first stage with acceleration up to the granulate release velocity corresponds to block sliding whereas the second stage from granulate release to impact into the water body is purely gravity driven granular flow.

Three different measurement techniques were built into the physical model: Laser distance sensors (LDS), particle image velocimetry (PIV) and capacitance wave gauges

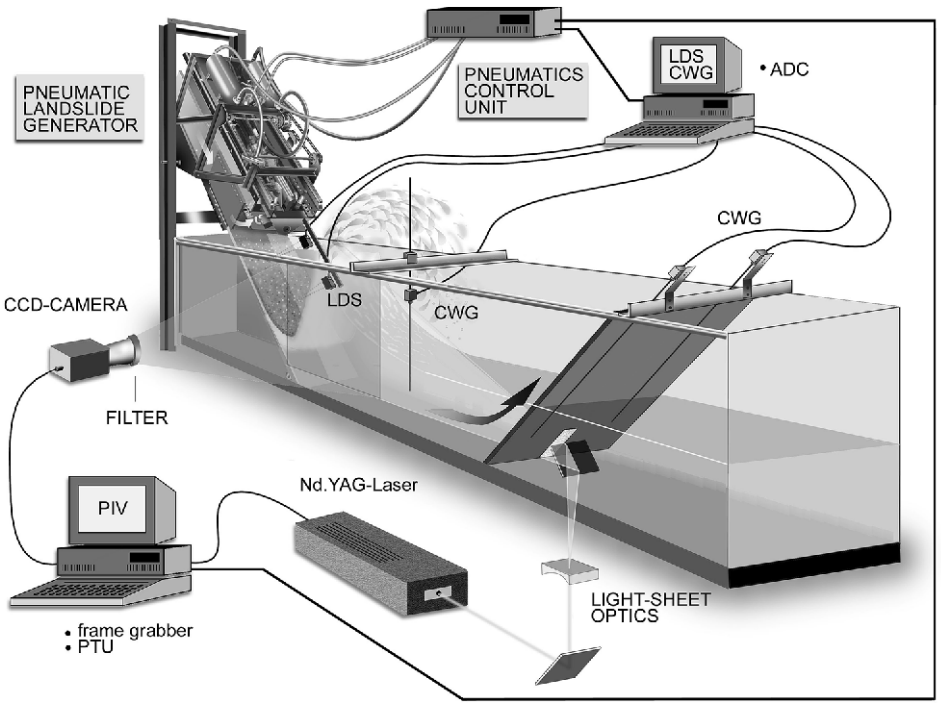

Figure 5
Experimental setup with pneumatic installation and measurement systems: Laser distance sensors (LDS), capacitance wave gages (CWG) and particle image velocimetry (PIV).

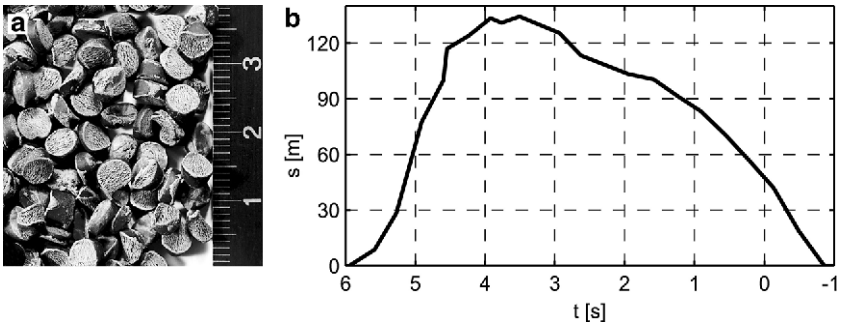

Figure 6
(a) Granulate: PP-$BaSO_4$, $d_g = 4$ mm, $\rho_g = 2.64$ g/cm^3; (b) granular slide profile scanned with a laser distance sensor orthogonal to ramp at location $x = -67$ m and $z = 67$ m.

(CWG). The laser-based digital PIV-system was introduced in FRITZ (2002a). The planar PIV provided instantaneous velocity vector fields in the slide impact area and gave insight into the kinematics of wave generation (FRITZ *et al.*, 2003a). Water displacement volumes and rates were extracted from the PIV recordings (FRITZ *et al.*, 2003b). Instantaneous image areas as large as 529(H) × 516(V) m in prototype scale were acquired. By means of cross-correlation analysis instantaneous 2D-2C velocity vector fields were computed using an adaptive multi-pass algorithm (SCARANO and RIETHMULLER, 1999) and second-order correlation (HART, 2000). Spatial resolution is determined by the window size of 8.4 × 8.4 m used in cross-correlation analysis. Time resolution of the PIV-system for 2D-2C velocity vector field estimation was 0.6 Hz in prototype time scale.

The landslides were modeled with an artificial granular material (PP-$BaSO_4$) shown in Figure 6a. The granulate properties were: grain density $\rho_g = 2.64$ t/m^3, grain diameter $d_g = 4$ mm, bulk slide density $\rho_s = 1.62$ t/m^3, bulk slide porosity $n_{\text{por}} = 39\%$, effective internal friction angle $\phi' = 43°$, and dynamic bed friction angle $\delta = 24°$ (FRITZ, 2002b). The slip between the bed and the granular mass was dominant, resulting in slug-type flow (SAVAGE, 1979). Its grain density perfectly matches the estimated schist density of $\rho_s = 2.7$ t/m^3 and resulted in a slide mass per unit width of $m' = 98.5 \times 10^3$ t/m′. The assumed porosity corresponds to data from Alpine debris flows (TOGNACCA, 1999). Slide profiles before impact are scanned with two laser distance sensors. A landslide profile recorded orthogonal to the ramp and 67 m above the stillwater level is shown in Figure 6b. The maximum slide thickness of 134 m equals 1.4 times the pre-motion slide thickness of 92 m (MILLER, 1960). This increase of 40% in slide thickness is necessary in the model to compensate for the void fraction present in granular flow in order to match the slide mass-flux per unit width. The prototype landslide porosity likely also increased due to fragmentation of the schist slide mass prior to impact. The generated slide length before impact was conservatively estimated to 748 m with the mean slide velocity of 110 m/s and the slide profile duration of 6.8 s. The mean landslide impact velocity v_s of

110 m/s is estimated assuming free fall equations for a slide centroid at 610 m elevation (LAW and BREBNER, 1968; NODA, 1970). The kinetic impact energy of the landslide is at the upper limit neglecting frictional losses. This gives an impact slide Froude number of 3.18 based on the definition $F = v_s/(gh)^{1/2}$. The slide Froude number relates the mean impact velocity v_s of the centroid to the shallow water wave propagation velocity (NODA, 1970). Scale effects regarding viscosity and surface tension may be assumed smaller than 5% (STIVE, 1985; MÜLLER, 1995).

Wave features during propagation and runup are determined with capacitance wave gages (CWG). One CWG records the wave profile at $x = 885$ m and two CWGs record wave runup profiles on the headland ramp. Laser distance sensors and capacitance wave gauges are sampled at 20 Hz in prototype time scale (FRITZ *et al.*, 2001).

4. 2-Dimensional Experimental Results

A series of experiments was conducted with the assumptions for Lituya Bay topography, bathymetry, landslide impact velocity, mass and shape described in the physical model section. The waves generated by the granulate inflow (Fig. 6b) and recorded with a capacitance wave gauge at location $x = 885$ m are shown in Figure 7a. The wave propagating away from the impact area in positive x-direction creates a single initial peak at $t = 16$ s with a maximum positive amplitude $a = 152$ m. In the two-dimensional model of Gilbert Inlet the single outward travelling wave is reflected back and forth from both headland and landslide ramps. The main trailing peaks recorded on the wave gauge have altering propagation directions from positive to negative x-direction, respectively. The second peak ($a = 85$ m, $t = 48$ s) on the wave record corresponds to the wave reflection from the headland propagating in the negative x-direction. An experiment without the headland ramp showed that the first wave trough ($\eta = 37$ m, $t = 30$ s) is truncated by the reflection from the headland and not fully developed. In the experiment without headland ramp a flat trough with a negative amplitude $a = -10$ m was recorded behind the single outward travelling wave crest. Therefore the total wave height is estimated to $H = 162$ m. The measured wave height to stillwater depth ratio $H/h = 1.33$ is well beyond any breaking criterion (DEAN and DALRYMPLE, 1991). The experimental run without headland ramp showed that breaking and transformation to a nonlinear bore initiated roughly at $x = 1500$ m — after the beginning of the headland ramp at location $x = 1342$ m. The third main peak ($a = 111$ m, $t = 93$ s) and the fifth peak ($a = 57$ m, $t = 180$ s) correspond to the wave reflected back from the landslide slope. The fourth peak ($a = 73$ m, $t = 129$ s) and the sixth peak ($a = 57$ m, $t = 214$ s) are wave reflections from the headland ramp. This partial back and forth wave reflection in Gilbert Inlet could account for the "jumping and shaking" reported by one eyewitness (MILLER, 1960).

The corresponding wave runup recorded by a capacitance wave gage on the headland ramp is shown in Figure 7b. The runup gauge record acquired parallel to the 45° inclined

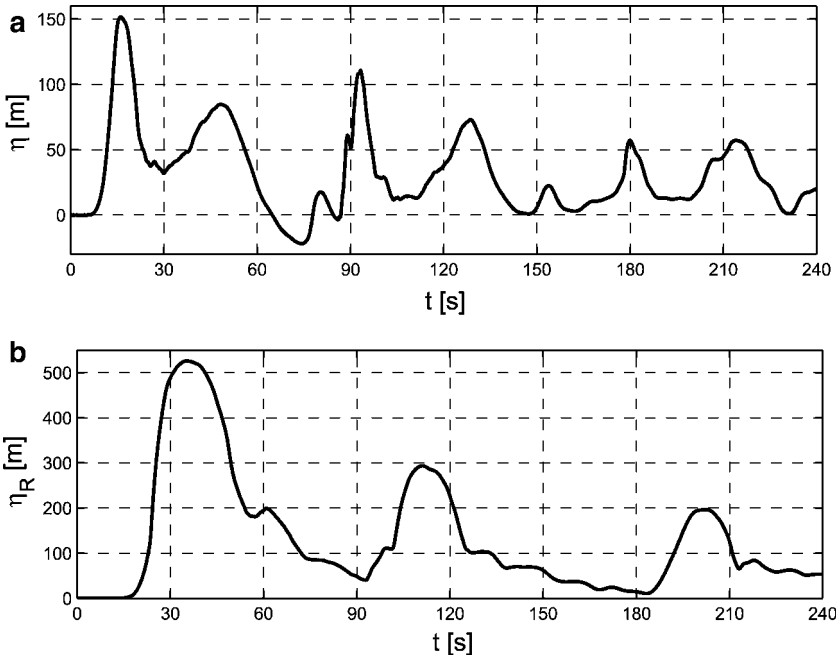

Figure 7
(a) Tsunami record at location $x = 885$ m; (b) tsunami runup record on headland ramp at locations $x = 1342$ m + η_R measured with capacitance wave gauges.

headland ramp is transformed into an elevation record. On the headland ramp a maximum runup height of $R = 526$ m is measured at $t = 35$ s. The measured runup of 526 m perfectly matches the highest elevation of 524 m on the trimline of forest destruction in Gilbert Inlet. The two trailing peaks on the runup record correspond to the first and second reflection of the single initial wave runup. The peak-to-peak period increases from 76 s to 91 s. This decay in propagation velocity with diminishing wave amplitude is due to the characteristic amplitude dispersion of nonlinear waves.

A sequence of twelve instantaneous velocity vector plots computed with PIV is shown in Figure 8. The sequence starts at t = 0.76 s after landslide impact and continues with a time step of 1.73 s covering roughly a time span of 20 s. Instantaneous velocity vector plots provide insight into kinematics during landslide impact and tsunami generation. The entire process may be subdivided into two main stages: (a) Slide impact and penetration (Fig. 8a), flow separation (Fig. 8b), cavity formation (Figs. 8c, d, e, f) while slide penetration velocity exceeds wave propagation velocity, and (b) cavity collapse (Figs. 8g, h), slide run-out along channel bottom, slide detrainment and deposition (Figs. 8i, j, k, l) as the wave overtakes the landslide and propagates out of the impact area. At the beginning of the cavity collapse (Fig. 8g) the splash amplitude exceeds 200 m in elevation at $x = 600$ m and $t = 11.14$ s before decaying

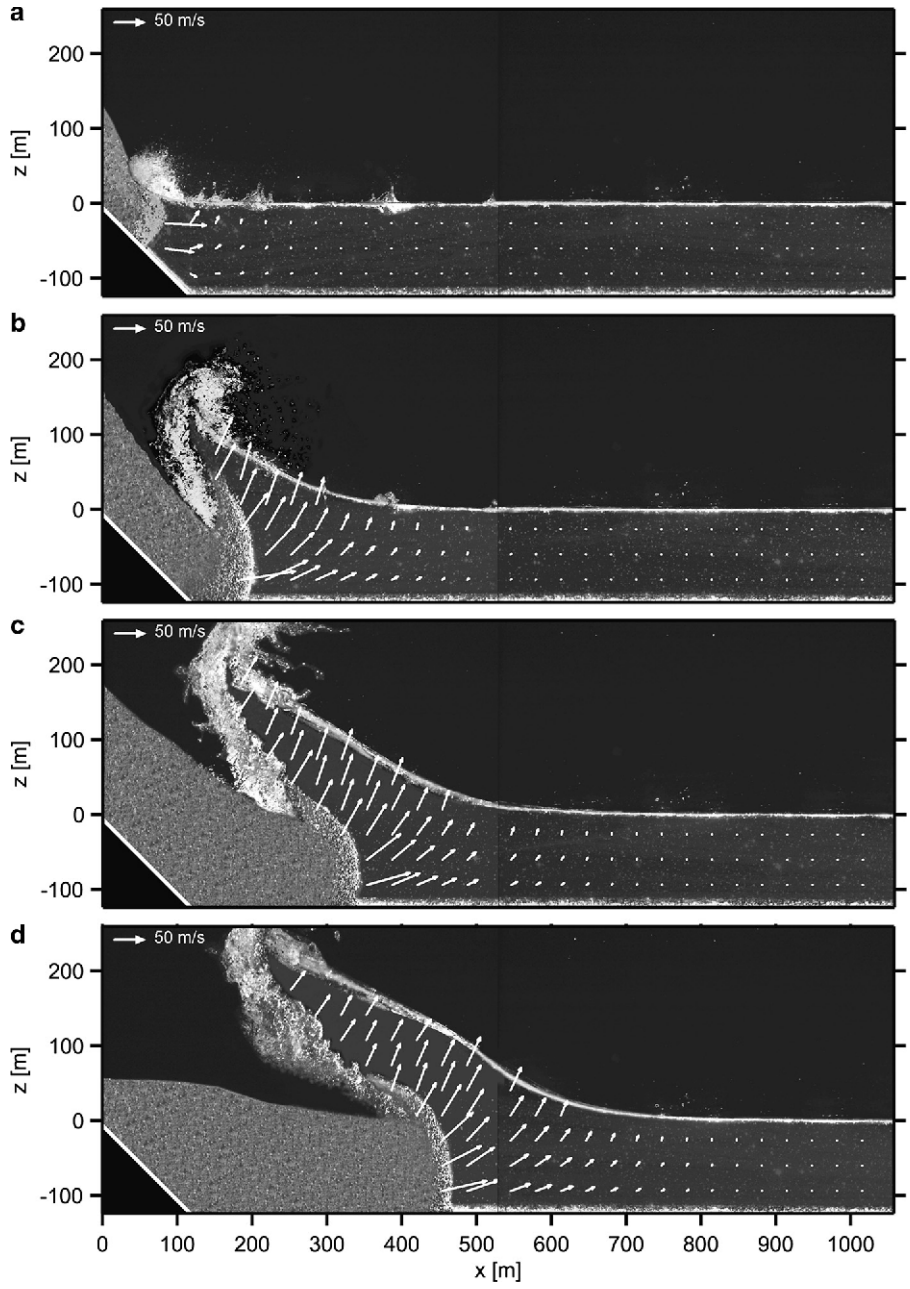

Figure 8
PIV velocity vector plot sequence of two synchronized granular slide impact experiments with juxtaposed areas of view and upscaled parameters: F = 3.18, v_s = 110 m/s, m' = 98.5 × 10^3 t/m′, h = 122 m, $\alpha = \beta = 45°$, time increment 1.73 s with first image at t = 0.76 s after impact.

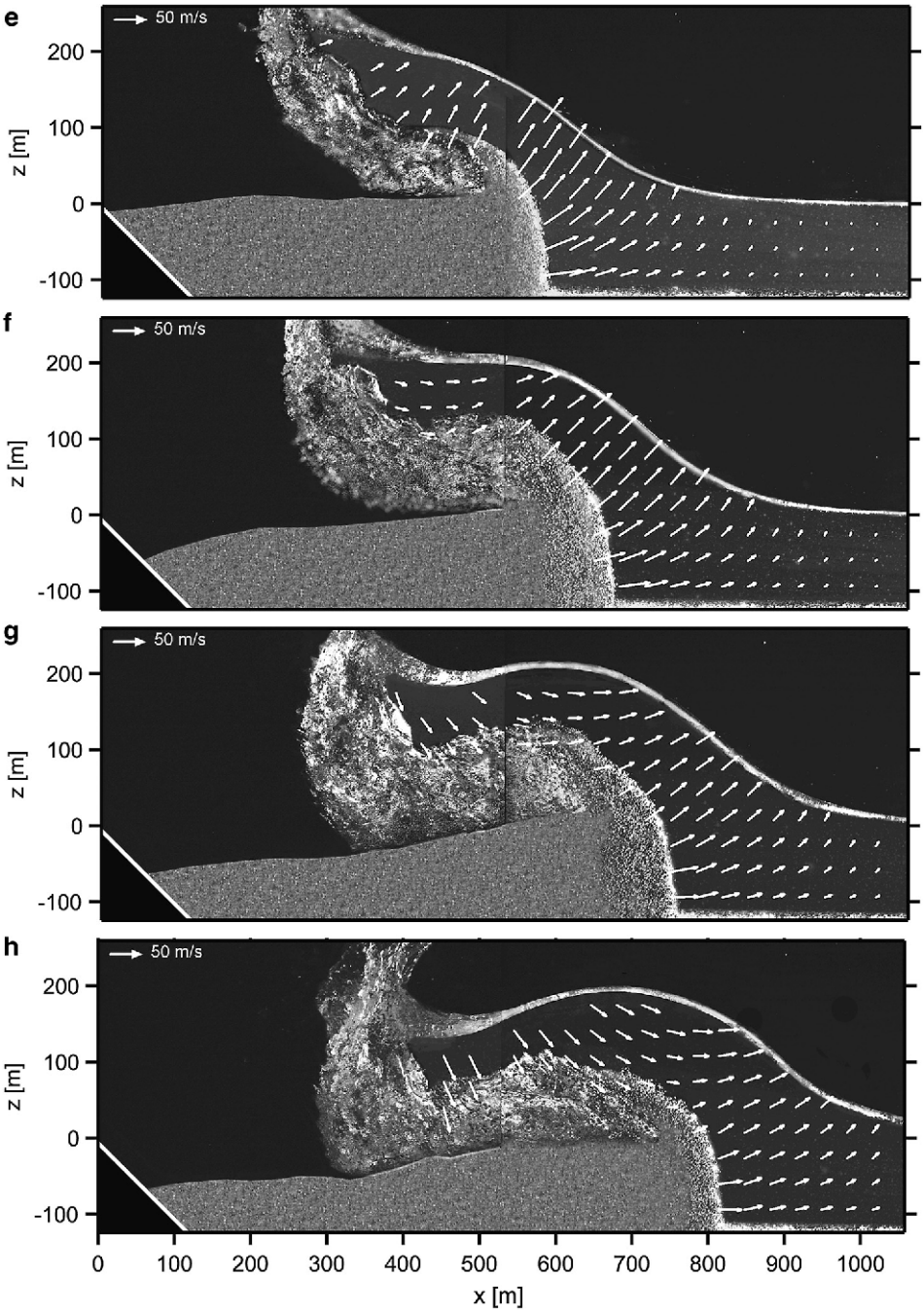

Figure 8
contd.

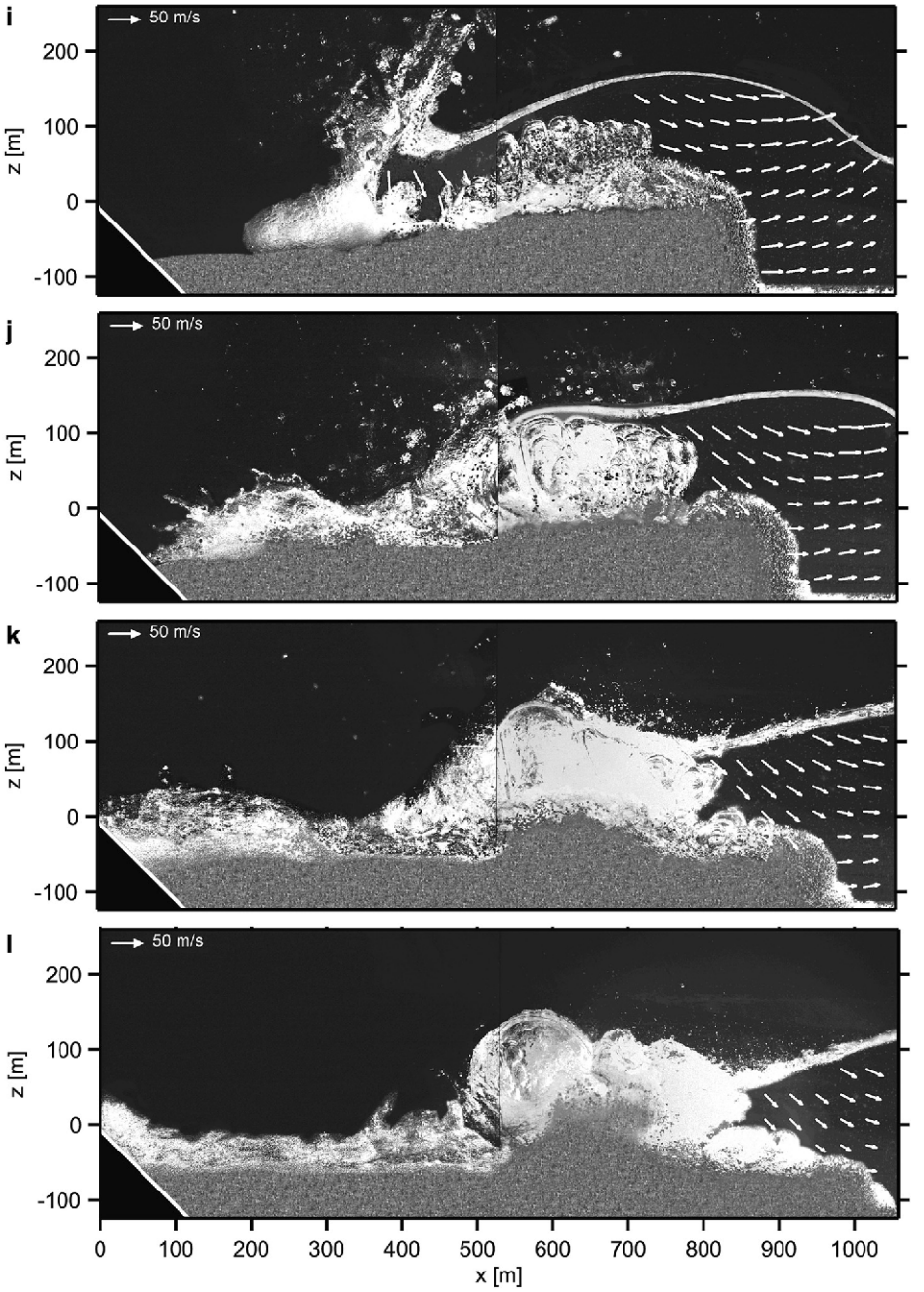

Figure 8
contd.

synchronously with the cavity collapse to a tsunami wave with $a = 152$ m at $t = 16$ s and $x = 885$ m (Fig. 7a). A high velocity gradient at the slide-water interface during impact and penetration causes sediment transport on the slide front leading to a sheet flow effect (Fig. 8b). The three phases — granular material, water and air — are clearly separated along distinct borderlines before flow reattachment occurs (Fig. 8h). Flow reattachment traps a large volume of air in the back of the landslide (Fig. 8i), which leads to large cavity formation (Fig. 8j), bubble break-up and massive phase mixing (Figs. 8k, l). Slide detrainment further increases phase mixing. The granular slide is deformed due to impact and deflection at the channel bottom reaching a maximum thickness and minimum length (Fig. 8d). The slide front forms an almost vertical wall with culminating height at the beginning of the cavity collapse (Figs. 8f, g). Thereafter the slide front thickness decays with slide run-out (Figs. 8j, k, l).

A sequence of eight PIV velocity vector plots acquired during tsunami runup on the headland is shown in Figure 9. The view area begins above the stillwater level. The sequence starts at $t = 23.28$ s after landslide impact and continues with a time step of

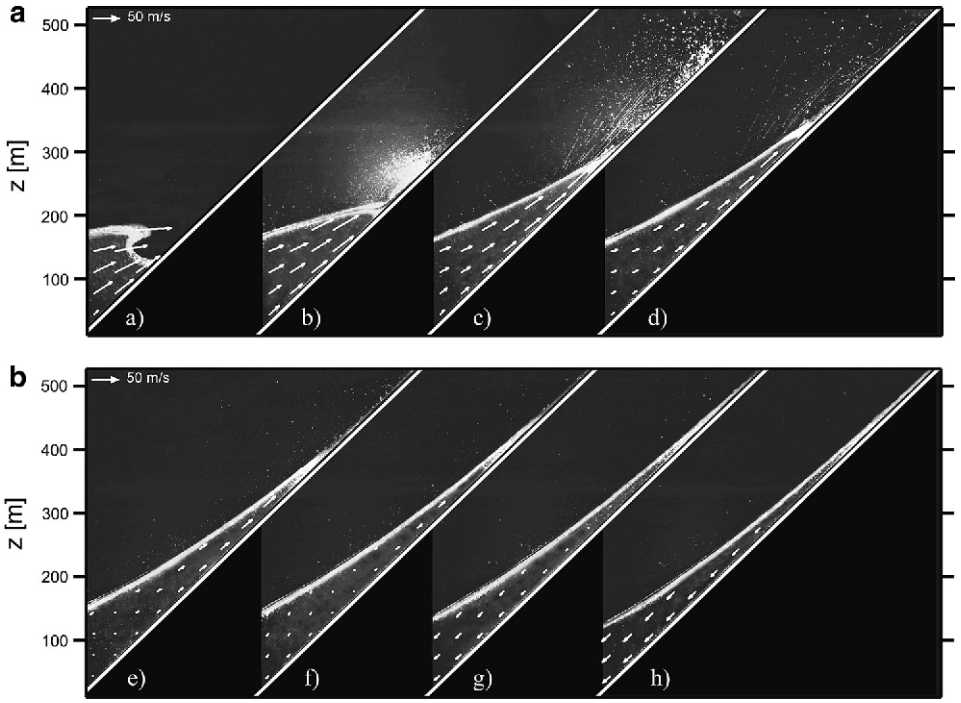

Figure 9
PIV velocity vector plot sequence of tsunami runup on headland slope created by a landslide impact with upscaled parameters: F = 3.18, $v_s = 110$ m/s, $m' = 98.5 \times 10^3$ t/m′, $h = 122$ m, $\alpha = \beta = 45°$, time increment 1.73 s, first image at $t = 23.28$ s after impact, lower left image corner at location $x = 1353$ m and $z = 11$ m.

1.73 s covering roughly a time span of 12 s. At $t = 23.28$ s the wave is shown prior to plunging onto the headland ramp. The wave amplitude has increased beyond 180 m. Wave-breaking during runup is initiated but does not fully develop due to the steep slope. The runup process is more surging than breaking and therefore with little air-entrainment (SYNOLAKIS, 1987; JENSEN *et al*., 2003). In the following images the wave surges up the headland slope with high velocity. At t = 30.2 s (Fig. 9e) an instantaneous stagnation point appears in the lower left corner of the velocity vector field. The stagnation point propagates up the headland ramp phase shifted to the runup wave front. In the area below the stagnation point water rushes down the headland ramp, whereas above the stagnation point water still surges upward. Therefore the sheet of water located on the headland ramp thinned significantly at the lower end by t = 35 s when the time of maximum runup height is reached (Fig. 9h). Sufficient water rushed up the headland slope to cause the flooding observed in Lituya Bay as estimated by MADER (1999) with numerical simulations of Lituya Bay outside the immediate impact area.

5. Comparison with two-dimensional Predictive Models

Various predictive relationships for the landslide-generated tsunami amplitude are compared with the Lituya Bay benchmark experiment as no field data are available on the tsunami height itself. Characteristic for highly non-linear waves is the large difference between the wave crest and the wave trough amplitudes. Predicting solely the total wave height H is insufficient and misleading (FRITZ *et al*., 2006). The comparison between the measured and predicted wave amplitudes and heights using the various equations is shown in Table 1.

The equation by FRITZ *et al*. (2004) for the maximum leading crest amplitude matched the measured crest amplitude $a = 155$ m. The relationship presented by KAMPHUIS and BOWERING (1970) from tray impact experiments matched the measured wave height $H = 162$ m. NODA (1970) used linear wave theory to predict the form of the wave motion produced by a body falling vertically into a tank. The theoretical solution underestimates the maximum wave amplitude with $a = 122$ m by 20%. The linear solution does not distinguish between the wave crest and trough amplitudes. Hence the trailing wave trough is massively overestimated. NODA (1970) obtained a theoretical solution for the case of a horizontally penetrating wall, which overestimates the measured wave crest amplitude by a factor of three. Similar overestimations may be produced by depth averaging shallow water equations in the wave generation area (MADER, 1999). SLINGERLAND and VOIGHT (1982) derived an empirical regression from two case studies, which overestimate the measured wave height by a factor of two. The empirical formula of HUBER and HAGER (1997) for 2-D-impulse wave characteristics predicts a wave height of $H = 94$ m, which underestimates the wave height by a factor of 1.8. Rough estimations of slide thickness from photos (HUBER, 1980) indicate that Huber's slides at comparable impact Froude

Table 1

Lituya Bay 1958 benchmark comparison of wave amplitude and runup predictions

Reference	Equations and remarks	a_C [m]	a_T [m]	H [m]	R [m]
Fritz *et al.* (2001) (scale model case study)	measured	152	10	162	530
Fritz (2002); Fritz *et al.* (2004) (granular slide model)	$\frac{a_C}{h} = 0.25\left(\frac{v_s}{\sqrt{gh}}\right)^{1.4}\left(\frac{s}{h}\right)^{0.8}$	155			
Huber and Hager (1997) (granular slide model)	$H = 0.88\sin\alpha\left(\frac{\rho_s}{\rho_w}\right)^{1/4}\left(\frac{V_s}{b}\right)^{1/2}\left(\frac{h}{x}\right)^{1/4}$			94	
Kamphuis and Bowering (1970) (block/weighted tray model)	$\frac{H}{h} = \left(\frac{v_s}{\sqrt{gh}}\right)^{0.7}\left(0.31 + 0.2\log\left(\frac{l_s s}{h^2}\right)\right) + 0.35e^{-0.08(x/h)}$			159	
Noda (1970) (theoretical solution)	$\frac{\eta(x,t)}{s} = f\left(\frac{v_s}{\sqrt{gh}}, \frac{x}{h}\right)$	122			
Noda (1970) (piston model)	$\frac{a_C}{h} = 1.32\left(\frac{v_s}{\sqrt{gh}}\right)$	515			
Slingerland and Voight (1982) (granular bag model)	$\log\left(\frac{a_C}{h}\right) = -1.25 + 0.71\log\left(\frac{1}{2}\frac{\rho_s}{\rho_w}\frac{V_s}{h^3}\frac{v_s^2}{gh}\right)$	329			
Mader and Gittings (2002)	full Navier-Stokes numerical simulation	170			580
Hall and Watts (1953) (R only based on measured H by Fritz *et al.*, 2001)	$\frac{R}{h} = 3.1\left(\frac{H}{h}\right)^{1.15}$				526
Synolakis (1987) (R only based on measured H by Fritz *et al.* 2001)	$\frac{R}{h} = 2.831\sqrt{\cot\beta}\left(\frac{H}{h}\right)^{5/4}$				493

numbers were thinner $s < h$. The present study and the sliding block experiments conducted by Noda (1970) and Kamphuis and Bowering (1970) showed a strong dependency of the generated wave heights on the slide impact thickness and the slide Froude number $F = v_s/(gh)^{0.5}$. The relationship given by Fritz *et al.* (2004) is recommended to predict the maximum leading crest amplitude a, because the relationship presented by Kamphuis and Bowering (1970) allows only the prediction of the total wave height H. The Lituya bay cross section was modeled numerically by Mader and Gittings (2002), Quecedeo *et al.* (2004) and Weiss and Wuennemann (2007) with full Navier-Stokes hydrodynamic codes in two dimensions. Both the Hall and Watts (1953) and Synolakis (1987) solutions for solitary wave runup on an impermeable slope match the experimentally measured wave runup and the observed elevation of forest destruction in Lituya Bay with predictions of $R = 526$ m and $R = 493$ m based on the experimentally measured incident wave parameters $H = 162$ m and $h = 122$ m (Fritz *et al.*, 2001). This confirms the conclusion drawn by Slingerland and Voight (1979) using back-calculation of wave height from runup that a wave height of about 160 m was necessary to produce the wave runup in Gilbert Inlet.

6. Three-dimensional Landslide Tsunami Experiments

The coupling between landslide motion and three-dimensioinal tsunami wave propagation and runup is of critical importance given the local, strongly-directional source mechanism. A unique pneumatic landslide generator was designed by the authors at Georgia Tech and installed at the NEES Tsunami Wave Basin (TWB) at OSU as shown in Figure 10. The apparatus simulated the impact of landslides that occur both above and below the water's surface. The landslide tsunami generator was constructed as an open aluminum box that is mounted on a steel slide and filled with up to 1,350 kg of gravel. The box accelerates down the slide by means of four pneumatic pistons. The granular mass is accelerated inside the box and released by opening the front tarp while the sled is slowed down pneumatically. The box measures 2.1 m by 1.2 m by 0.3 m with subdivisions to adjust initial slide length and thickness, and is placed on a slide that can vary in length. The box itself is able to travel approximately 2 m before the gravel is released down the 2H:1V slope at initial velocities up to 5 m/sec. Using cameras placed above and within the water, the researchers measured the shape, length, and thickness of the gravel masses while they were in motion.

The measured front velocity of the granular landslide and the corresponding acceleration are shown in Figure 11. The landslide velocity prior to release from the box is measured using the string pot data from the slide box. The landslide velocity after release from the box is measured from the image sequences recorded by a 2-megapixel PIV camera. The impact velocity of the landslide is compared to the velocity evolution of a dry granular landslide run. The PIV camera is setup at a distance of 6.8 m perpendicular to the hill slope providing an approximate 15 m^2 (4.5 m by 3.38 m) view area. A characteristic image sequence is shown in Figure 11b. This image sequence highlights the lateral spreading of the granular landslide after exiting the slide box prior to impact on

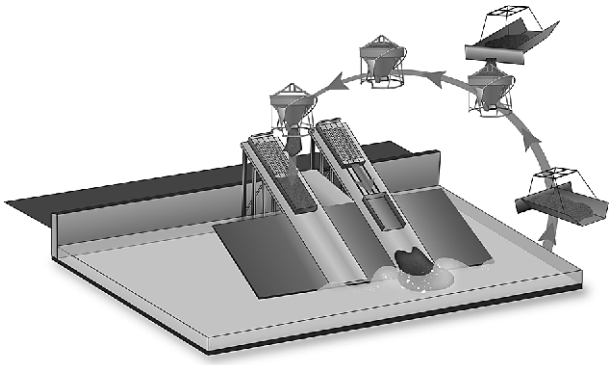

Figure 10
Granular landslide tsunami generator deployed in the three-dimensional NEES Tsunami Wave Basin at OSU in 2006/2007.

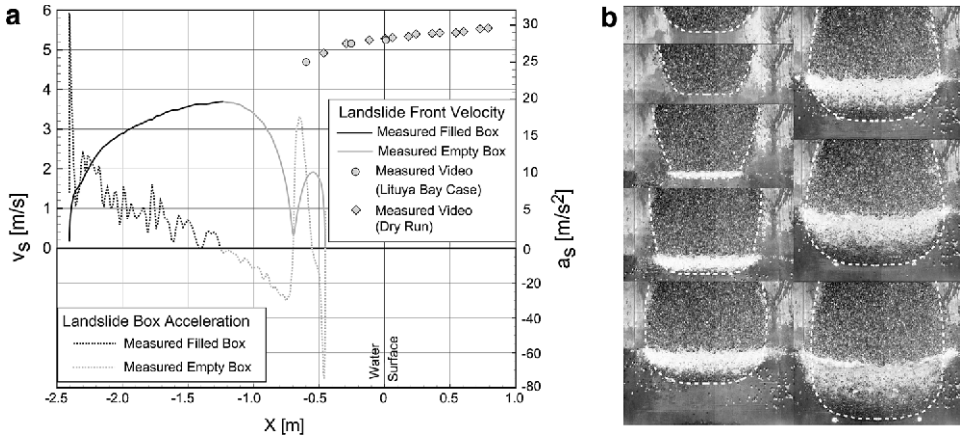

Figure 11
Granular Landslide kinematics at F = 3.2: (a) granular landslide front kinematics with transition from pneumatic acceleration inside the landslide generator to subaerial gravity slide; (b) lateral spreading and deformation of the granular landslide on the hill slope in a video image sequence.

the water body. The landslide shape is geometrically similar to the Lituya Bay landslide shown in Figure 2 at a 1:400 scale. The granular landslide front velocity prior to impact on the water surface was calculated from recorded subaerial landslide shown in Figure 11a. At the impact, a landslide velocity of 5.26 m/s was measured, which corresponds to an impact slide Froude number of 3.07 based on a still water depth 0.3 m and the definition $F = v_s/(gh)^{1/2}$. This corresponds to a full three- dimensional physical model of the Lituya Bay landslide at a 1:400 scale. Hence the pneumatic landslide generator can reproduce landslide velocities scaled to real world physical events.

The recorded high-resolution image sequences were processed with PIV to analyze the landslide characteristics at the impact location and the wave generation process by measuring the surface velocity field. The speckle patterns generated by the landslide granulate surface were used for iterative multi-pass cross-correlation analysis with decreasing window sizes down to 32 by 32 pixels. A PIV velocity vector plot of the landslide surface shortly after impact corresponding to a 1:400 scale landslide model of the three-dimensional Lituya Bay landslide is shown in Figure 12a. The landslide front penetrated below the water surface enabling the PIV based analysis of the water surface in the impact zone, which was seeded with 5 mm diameter naturally buoyant tracer particles prior to each experiment. The granular landslide deposits were scanned with an acoustic multi-transducer array (Fig. 12b). Unfortunately the Lituya Bay landslide deposit has not been surveyed to date, which would be necessary to compare physical model results with the landslide deposits in the field. The proposed landslide deposit mapping was conducted, for example, in Lake Lucerne, Switzerland (SCHNELLMANN *et al.*, 2002).

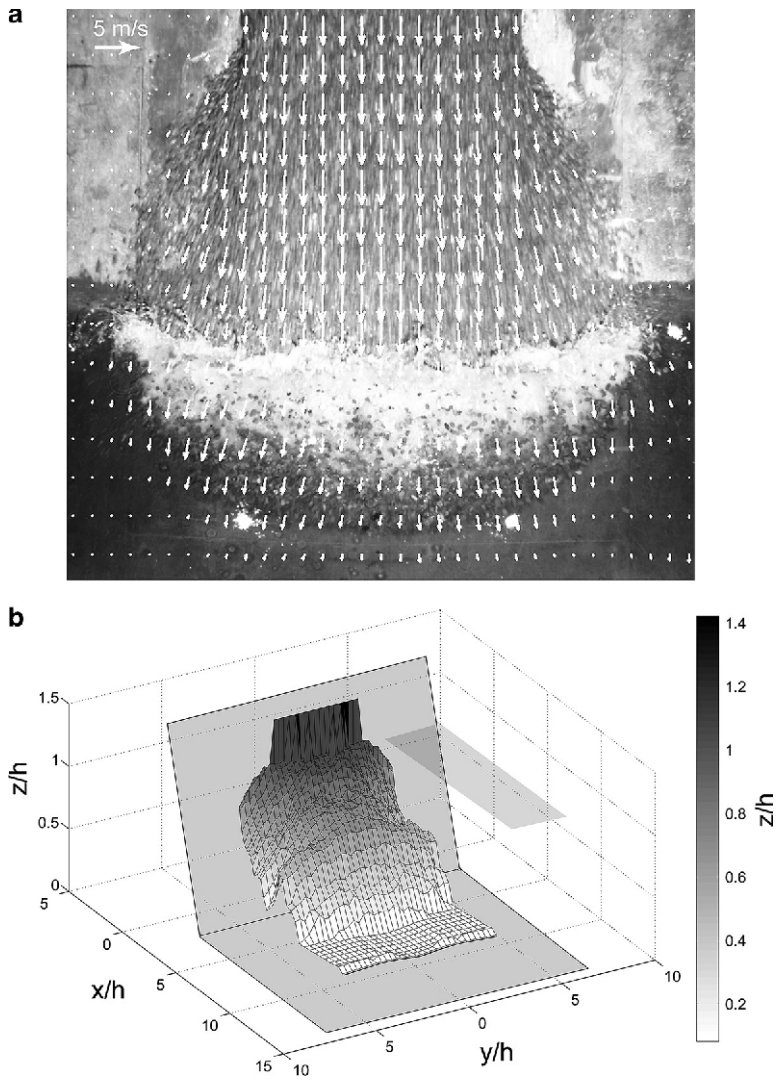

Figure 12
Landslide tsunami generation in 3-D: (a) PIV velocity vector plot of the landslide surface shortly after impact with the landslide front penetrating below the water surface and tsunami wave generation (note: the displayed number of vectors is reduced for visibility); (b) granular landslide deposit scanned with an acoustic multi-transducer array.

Wave gauges were placed to measure the size and shape of the tsunami waves that were generated, including the lateral onshore runup. The locations of wave and runup gauges in the tsunami wave basin measuring 48.8 m by 26.5 m by 2.1 m (L $\times$ W $\times$ H) at OSU are shown in Figure 13a. The scaled gauge locations are based on a 0.3 m water depth, which corresponds to a 1:400 scale model given the 122 m water depth at the

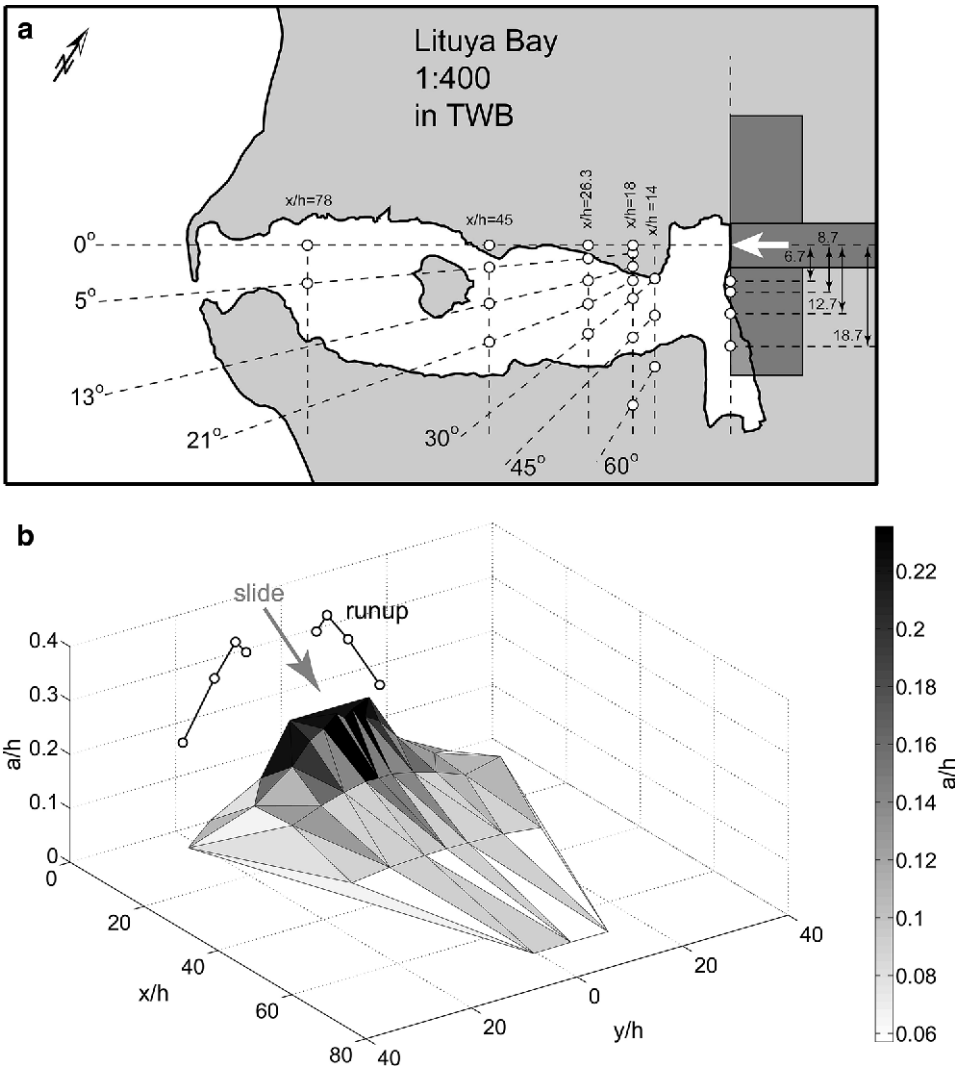

Figure 13
Landslide tsunami propagation in 3-D: (a) Locations of wave and runup gauges in tsunami wave basin at OSU based on a 1:400 scale Lituya Bay water depth with superimposed Lituya Bay coastline for reference; (b) tsunami amplitude attenuation with strong directional component and the high wave runup as edge waves along the hill slope.

impact site in Lituya Bay. The scaled Lituya Bay coastline is superimposed to highlight the complicated setting. The detailed fully three-dimensional bathymetry and topography of Lituya Bay would have to be reconstructed in the physical model to enable a direct comparison between the measurements and the observations in the field. The tsunami amplitude attenuation and the wave runup along the hill slope are shown in Figure 13b.

The recorded wave profiles were extremely directional, unsteady, nonlinear, and located mostly in the intermediate water depth wave regime. Among the principal differences between a tectonic-generated tsunami and a landslide-generated tsunami is that the latter has a strong directional component that can be devastating to the immediate area. Because it has a shorter wavelength, however, it dissipates quickly over a short distance. Landslide tsunamis exhibit a more dispersive and strongly directional propagation than tectonic tsunamis. Currently more than 60 successful runs have been completed and the main tsunamigenic parameters identified that will serve as key benchmarks for numerical models. However a fully three-dimensional benchmark of the Lituya Bay with the detailed bathymetry remains to be conducted to validate numerical simulations of the entire Lituya Bay with three-dimensional tsunami generation, propagation and runup.

7. Conclusions

The two-dimensional physical model at 1:675 scale of the Lituya Bay 1958 event includes landslide impact, tsunami generation, propagation and runup on headland. A unique pneumatic landslide generator was used to generate a high-speed granular slide with controlled impact velocity and shape. State-of-the-art laser measurement techniques such as particle image velocimetry (PIV) and laser distance sensors (LDS) were applied to cope with an extremely unsteady three phase flow due to high speed granular slide impact, high velocity gradients, flow separation, cavity formation, wave generation and runup. A granular slide with density and volume given by MILLER (1960) impacting at a mean velocity of 110 m/s generates a large air cavity and an extremely nonlinear wave beyond breaking criterion, which remains nonbreaking due to the short propagation distance to the headland runup. The formation of a large air cavity is highlighted (FRITZ *et al*., 2001). The predictive tsunami amplitude equation by FRITZ *et al*. (2004) matches the experimentally measured tsunami amplitude in Gilbert Inlet. The experimentally measured wave runup matches the trimline of forest destruction on the spur ridge in Gilbert Inlet. Back-calculations of wave height from observed trimline of forest destruction using HALL and WATTS (1953) and SYNOLAKIS (1987) runup formulas equal the measured wave height in Gilbert Inlet. Further research on slide impact characteristics, wave generation and energy conversion using three-dimensional models is necessary. MADER and GITTINGS (2002), QUECEDO *et al*. (2004) as well as WEISS and WUENNEMANN (2007) reproduced the physical model results of the Lituya Bay landslide tsunami with full Navier-Stokes models in two dimensions. A three-dimenional pneumatic landslide tsunami generator was designed, constructed and successfully deployed in the tsunami wave basin at OSU. The Lituya Bay landslide was reproduced in a three-dimensional physical model at 1:400 scale. The landslide surface velocities distribution was measured with PIV. The landslide deposits in Lituya Bay should be mapped to validate the experiments and establish a baseline bathymetry prior to a possible future landslide tsunami in Lituya Bay. A detailed three-dimensional benchmark experiment of the Lituya

Bay remains to be conducted with the exact bathymetry to validate numerical simulations of the entire Bay with three-dimensional tsunami generation, propagation and runup.

Acknowledgments

This research work is supported by the National Science Foundation under Grant No. CMS-0421090. Any opinions, findings, and conclusions or recommendations expressed herein are those of the author(s) and do not necessarily reflect the views of the National Science Foundation. The two-dimensional experiments conducted at VAW (ETH Zürich) were supported by the Swiss National Science Foundation, grant number 2100-050586.97.

References

Dean, R.G. and Dalrymple, R.A., *Water wave mechanics for engineers and scientists. Advanced Series on Ocean Engineering* 2 (World Scientific, Singapore 1991).

Fritz, H.M., Hager, W.H. and Minor, H.-E. (2001), *Lituya Bay case: rockslide impact and wave runup*, Science of Tsunami Hazards *19*(1), 3–22.

Fritz, H.M., *PIV applied to landslide generated impulse waves*, In (Adrian, R.J. *et al*., eds) *Laser Techniques for Fluid Mechanics*, pp. 305–320 (Springer, New York, Berlin, Heidelberg 2002a).

Fritz, H.M., *Initial phase of landslide generated impulse waves*, In (Minor, H.-E., ed.) *VAW Mitteilung 178* (Versuchsanstalt für Wasserbau, Hydrologie und Glaziologie, ETH Zürich 2002b).

Fritz, H.M. and Moser, P. (2003), *Pneumatic landslide generator.* Int. J. Fluid Power *4*(1), 49–57.

Fritz, H.M., Hager, W.H. and Minor, H.-E. (2003a), *Landslide generated impulse waves, Part 1: Instantaneous flow fields*, Exp. Fluids *35*, 505–519.

Fritz, H.M., Hager, W.H., and Minor, H.-E. (2003b), *Landslide generated impulse waves, Part 2: Hydrodynamic impact craters*, Exp. Fluids *35*, 520–532.

Fritz, H.M., Hager, W.H., and Minor, H.-E. (2004), *Near field characteristics of landslide generated impulse waves*, J. Waterway, Port, Coastal, and Ocean Engrg., ASCE *130*, 287–302.

Fritz, H.M., Physical modeling of landslide generated tsunami. In (A. Mercado-Irizarry and P.L.-F. Liu, eds) *Caribbean Tsunami Hazard* (World Scientific, Singapore 2006), pp. 308–324.

Hall, J.V., Jr. and Watts, G.M. (1953), *Laboratory investigation of the vertical rise of solitary waves on impermeable slopes*, Tech. Memo *33*, U.S. Army Corps of Engineers, Beach Erosion Board.

Hart, D., *PIV error correction.* In *Laser Techniques Applied to Fluid Mechanics*, selected papers from the 9th Internat. Symp., Lisbon 1998, Portugal. (Eds. Adrian, R.J. *et al*.) (Springer, New York 2000).

Heller, V., Hager, W.H., and Minor, H.-E. (2008), *Scale effects in subaerial landslide generated impulse waves*, Exp. Fluids *44*(5), 691–703, doi:10.1007/s00348-007-0427-7.

Huber, A., *Schwallwellen in Seen als Folge von Bergstürzen* (in German), *VAW-Mitteilung 47*, (Ed. Vischer, D.) (Versuchsanstalt für Wasserbau, Hydrologie und Glaziologie, ETH Zürich 1980).

Huber, A. and Hager, W.H. (1997), *Forecasting impulse waves in reservoirs. Dix-neuvième Congrès des Grands Barrages* C31:993–1005. Florence, Italy. Commission International des Grands Barrages, Paris.

Jensen, A., Pedersen, G.K., and Wood, D.J. (2003), *An experimental study of wave runup at a steep beach*, J. Fluid Mech. *486*, 161-188, doi:10.1017/S0022112003004543.

Jørstad, F. (1968), *Waves generated by landslides in Norwegian fjords and lakes.* Norwegian Geotechnical Institute Publication *79*:13–32, Norwegian Geotechnical Institute, Oslo.

Kamphuis, J.W. and Bowering, R.J. (1970), *Impulse waves generated by landslides.* In *Proc. 12th Coastal Engin. Conf.* ASCE *1*, 575–588.

LAW, L. and BREBNER, A. (1968), *On water waves generated by landslides*, *3rd Australas. Conf. on Hydraulics and Fluid Mechanics*, Sydney, Paper *2561*, 155–159.

MADER, C.L. (1999), *Modelling the 1958 Lituya Bay mega-tsunami*. Science of Tsunami Hazards *17*(2), 57–67.

MADER, C.L. and GITTINGS, M.L. (2002), *Modeling the 1958 Lituya Bay mega-tsunami, II*. Science of Tsunami Hazards *20*(5), 241–250.

MILLER, D.J. (1960), *Giant waves in Lituya Bay, Alaska*, Geological Survey Professional Paper *354*-C, U.S. Government Printing Office, Washington D.C.

MÜLLER, D., *Auflaufen und Überschwappen von Impulswellen an Talsperren* (in German). *VAW-Mitteilung* 137 (Ed. Vischer, D.) (Versuchsanstalt für Wasserbau, Hydrologie und Glaziologie, ETH Zürich 1995).

MÜLLER, L. (1964), *The rock slide in the Vajont Valley*. Rock Mech. Eng. Geol. *2*(3–4), 148–212.

Noda, E. (1970), *Water waves generated by landslides*, J. Waterw. Harbors Coastal Eng. Div. ASCE *96*(WW4), 835–855.

PARARAS-CARAYANNIS, G. (1999), *Analysis of mechanism of tsunami generation in Lituya Bay*, Science of Tsunami Hazards *17*(3), 193–206.

QUECEDO, M., PASTOR, M., and HERREROS, M.I. (2004), *Numerical modelling of impulse wave generated by fast landslides*, Int. J. Numer. Meth. Engin. *59*, 1633–1656. doi: 10.1002/nme.934.

SAVAGE, S.B. (1979), *Gravity flow of cohesionless granular materials in chutes and channels*, J. Fluid Mech. *92*, 53–96.

SCARANO, F. and RIETHMULLER, M. (1999), *Iterative multigrid approach in PIV image processing with discrete window offset*, Experiments in Fluids *26*, 513–523.

SCHNELLMANN, M., ANSELMETTI, F.S., GIARDINI, D., MCKENZIE, J.A., and WARD, S.N. (2002), *Prehistoric earthquake history revealed by lacustrine slump deposits*, Geology *30*(12), 1131–1134.

SHARPE, C.F.S., *Landslides and Related Phenomena* (Columbia Univ. Press, New York 1938).

SLINGERLAND, R.L. and VOIGHT, B., *Occurrences, properties and predictive models of landslide-generated impulse waves*, Rockslides and Avalanches *2*, 317–397 (Ed. Voight, B) *Developments in Geotechnical Engin.* 14B (Elsevier, Amsterdam 1979).

STIVE, M.J.F. (1985), *A scale comparison of waves breaking on a beach*, Coastal Engin. *9*, 151–158.

Synolakis, C.E. (1987), *The runup of solitary waves*, J. Fluid Mech. *185*, 523–545.

TOCHER, D. and MILLER, D.J. (1959), *Field observations on effects of Alaskan earthquake of 10 July, 1958*, Science *129*, 394–395.

TOGNACCA, C., *Beitrag zur Untersuchung der Entstehungsmechanismen von Murgängen (in German)*, *VAW-Mitteilung* 164 (Ed. Minor, H.-E.) (Versuchsanstalt für Wasserbau, Hydrologie und Glaziologie, ETH Zürich 1999).

VARNES, D.J. (1958), *Landslide types and processes*, Highw. Res. Board Spec. Rep. *29*, Natl. Acad. Sci.-Natl. Res. Counc. Publ. *544*, 22–47.

VOIGHT, B., JANDA, R.J., GLICKEN, H., and DOUGLASS, P.M. (1983), *Nature and mechanics of the Mount St. Helens rockslide-avalanche of 18 May 1980*, Géotechnique *33*, 243–273.

WEISS, R. and WUENNEMANN, K. (2007), *Understanding tsunami by landslides as the next challenge for hazard, risk and mitigation: Insight from multi-material hydrocode modeling*, EOS Trans. AGU *88*(52), Fall Meet. Suppl., Abstract S51C-06.

WIEGEL, R.L., *Oceanographical Engineering* (Prentice-Hall, Englewood Cliffs, N.J. 1964).

(Received December 31, 2007, revised September 2, 2008)
Published Online First: February 6, 2009

Pure appl. geophys. 166 (2009) 177–210
0033–4553/09/010177–34
DOI 10.1007/s00024-008-0440-7

Pure and Applied Geophysics

Tsunamis on the Pacific Coast of Canada Recorded in 1994–2007

FREDERICK E. STEPHENSON[1] and ALEXANDER B. RABINOVICH[1,2]

Abstract—In the last 15 years there have been 16 tsunami events recorded at tide stations on the Pacific Coast of Canada. Eleven of these events were from distant sources covering almost all regions of the Pacific, as well as the December 26, 2004 Sumatra tsunami in the Indian Ocean. Three tsunamis were generated by local or regional earthquakes and two were meteorological tsunamis. The earliest four events, which occurred in the period 1994–1996, were recorded on analogue recorders; these tsunami records were recently re-examined, digitized and thoroughly analysed. The other 12 tsunami events were recorded using digital high-quality instruments, with 1-min sampling interval, installed on the coast of British Columbia (B.C.) in 1998. All 16 tsunami events were recorded at Tofino on the outer B.C. coast, and some of the tsunamis were recorded at eight or more stations. The tide station at Tofino has been in operation for 100 years and these recent observations add to the dataset of tsunami events compiled previously by S.O. WIGEN (1983) for the period 1906–1980. For each of the tsunami records statistical analysis was carried out to determine essential tsunami characteristics for all events (arrival times, maximum amplitudes, frequencies and wave-train structure). The analysis of the records indicated that significant background noise at Langara, a key northern B.C. Tsunami Warning station located near the northern end of the Queen Charlotte Islands, creates serious problems in detecting tsunami waves. That station has now been moved to a new location with better tsunami response. The number of tsunami events observed in the past 15 years also justified re-establishing a tide gauge at Port Alberni, where large tsunami wave amplitudes were measured in March 1964. The two meteorological events are the first ever recorded on the B.C. coast. Also, there have been landslide generated tsunami events which, although not recorded on any coastal tide gauges, demonstrate, along with the recent investigation of a historical catastrophic event, the significant risk that landslide generated tsunami pose to coastal and inland regions of B.C.

Key words: Tsunami records, British Columbia, tide gauge, meteorological tsunami, landslide generated tsunami, tsunami catalogue.

1. Introduction

The Pacific Coast of Canada, in the province of British Columbia (B.C.) extends from approximately 48°N to 55°N, a distance of about 775 kilometres. However, this coast is a complex network of inlets, straits, passes, sounds, and narrows, which has a coastline length, including islands, of approximately 27,300 kilometres (THOMSON, 1981).

[1] Department of Fisheries and Oceans, Canadian Hydrographic Service, Institute of Ocean Sciences, 9860 West Saanich Road, Sidney, B.C. V8L 4B2, Canada.
E-mail: Fred.Stephenson@dfo-mpo.gc.ca; Alexander.Rabinovich@dfo-mpo.gc.ca

[2] Russian Academy of Sciences, P.P. Shirshov Institute of Oceanology, 36 Nakhimovsky Prosp., Moscow, 117997, Russia E-mail: A.B.Rabinovich@gmail.com

Significant parts of this coastline are susceptible to the effects of tsunamis generated within the Pacific basin (RAPATZ and MURTY, 1987; MURTY, 1992; CLAGUE *et al*., 2003). Geological and geophysical evidence gathered along the western coastline of Vancouver Island, as well as on the Washington and Oregon coasts, show that major Cascadia earthquakes accompanied by destructive tsunamis have an average recurrence interval of about 500 years (CLAGUE and BOBROWSKY, 1999; CLAGUE *et al*., 2003). Trans-Pacific tsunamis caused by major earthquakes elsewhere in the Pacific "Rim of Fire" can also significantly affect the B.C. coast (MURTY, 1992; CLAGUE, 2001). The March 1964 Alaska earthquake with magnitude $M_w = 9.2$ produced a catastrophic tsunami which swept southward from the source area in Prince William Sound along the B.C. coast causing about $10 million in damage (WIGEN and WHITE, 1964; CLAGUE, 2001; CLAGUE *et al*., 2003). According to RAPATZ and MURTY (1987) and HEBENSTREIT and MURTY (1989) for the coast of British Columbia there is also a high potential risk of destructive tsunamis caused by local major earthquakes. The coasts and underwater slopes of B.C. contain significant amounts of unstable material, so submarine and subaerial landslides, slumps and rock falls and associated tsunamis are often the secondary effects of earthquakes (EVANS, 2001; RABINOVICH *et al*., 2003).

Until the mid-1980s all tide gauges on the B.C. coast were analogue. Records of reasonably high quality were collected (WIGEN, 1983), but with the exception of a very rudimentary automated warning system at Tofino and Langara, sea-level records were not available for real-time analysis in response to potential tsunami events. Basic information could be obtained from gauge attendants by radio or telephone, but the record could only be analysed and digitised days or weeks after the event. The accuracy of these instruments was a few centimetres and WIGEN (1983) was able to identify some tsunami as small as 6 cm. Given that the typical range of tide at these stations is about 5 metres it was impossible to identify any events with tsunami wave heights smaller than that. In the 1980s the Canadian Hydrographic Service (CHS) began to operate both digital and analogue gauges at key stations on the B.C. coast. This provided access to the data in real-time by either telephone modem or Meteor Burst communication. For the most part though, on-site data storage and throughput considerations limited the data sampling interval to 15 minutes.

The destructive tsunamis of the last decade (e.g., Shikotan tsunami of October 4, 1994) initiated a major upgrade of the existing Tsunami Warning and Permanent Water Level Network (PWLN) stations on the B.C. coast (see Fig. 1). The new digital instruments were designed to continuously measure sea-level variations with considerably higher precision than earlier analogue gauges, and to store corresponding sea-level samples every minute; a significant improvement from the previous digital instruments. During the period 1999–2001 near-continuous series of high-quality 1-minute sea-level data were collected at all stations and two weak tsunamis (the trans-Pacific Peru tsunami of June 23, 2001 and the local Queen Charlotte tsunami of October 12, 2001) were recorded (RABINOVICH and STEPHENSON, 2004). These two observed tsunami events, and the high quality of the data from the new instruments, initiated a review of tide gauge records for the period 1981–1998. The review identified four events in the 1990s in

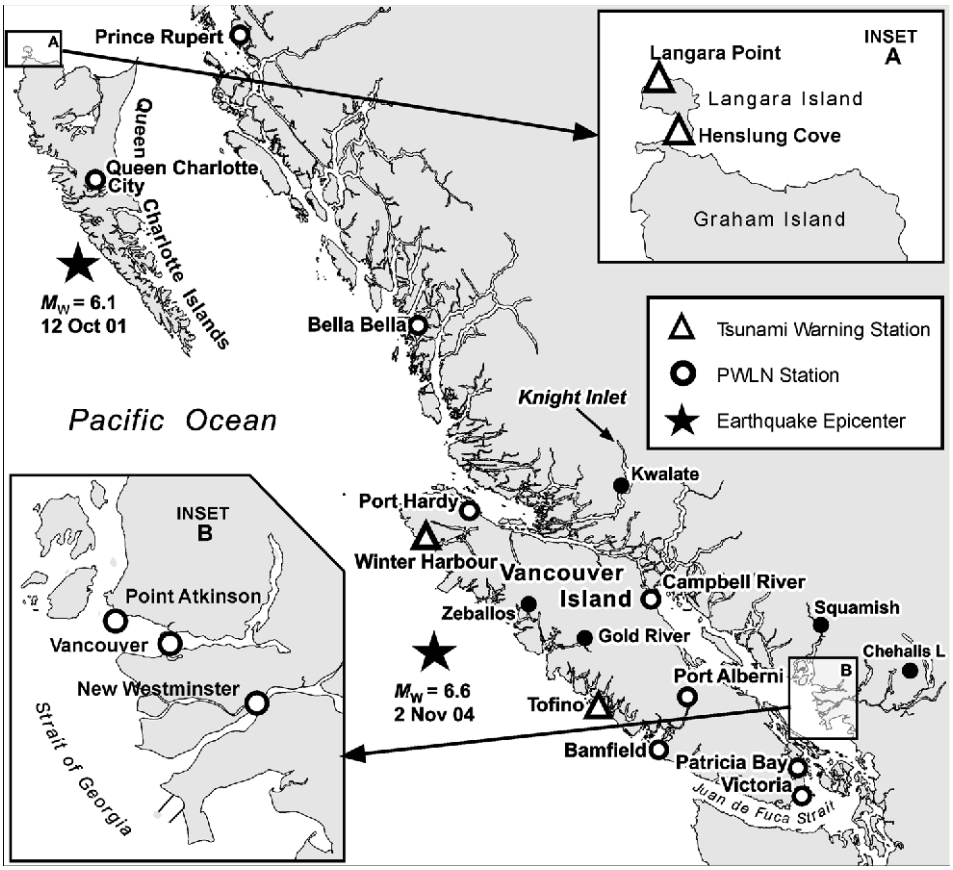

Figure 1
A map showing the location of Permanent Water Level Network (PWLN) and Tsunami Warning stations on the coast of British Columbia. Also shown are epicenters of the earthquakes of October 12, 2001 and November 2, 2004 (stars) and locations of some geographical sites mentioned in the text (solid circles).

addition to two events previously described by González *et al*. (1991) and González and Kulikov (1993). As had been indicated by González *et al*. (1991) the Alaska earthquake events of November 30, 1987 and March 6, 1988 produced tsunami "observed in Alaska, B.C. and the Hawaiian Islands." These weak tsunami events were observed at Langara Island near the northern coast of the Queen Charlotte Islands (Fig.1) and had heights of 14 cm and 11 cm, respectively. A review of analogue records from four stations on the west coast of Vancouver Island (Tofino, Gold River, Zebellos and Winter Harbour) failed to identify a tsunami at any of these locations for either of the Alaska events. The tsunami wave recorded at Langara Island either did not reach the southern B.C. coast, or it was too small to be detected on any of these analogue records.

Of the sixteen tsunami events observed since 1994, eleven were far-field events from various areas of the Pacific, three were local (B.C. coast) or regional (less than 3 hrs

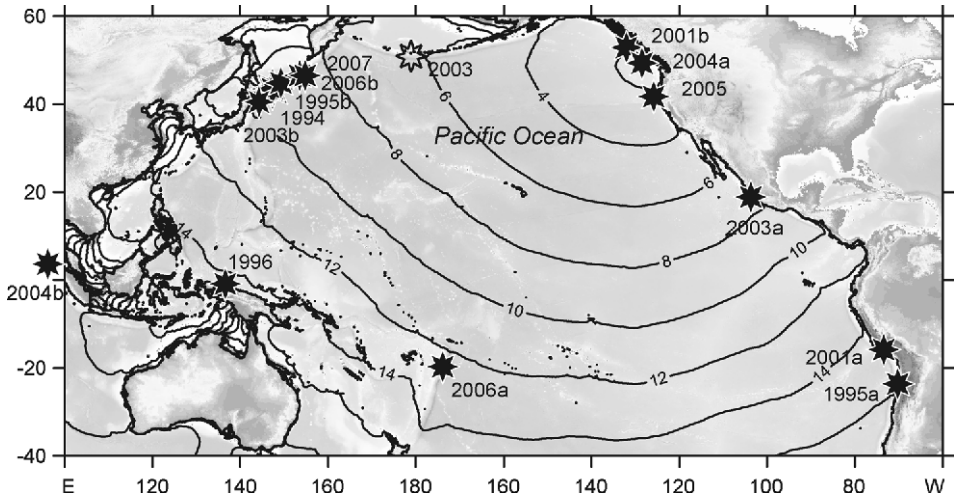

Figure 2
A map showing earthquake epicenters that have produced tsunami observed on the B.C. coast (1994–2007). Also shown is the epicenter of the 2003 Rat Islands earthquake (clear star), which did not produce tsunami waves measurable on the coast of B.C. Solid thin lines are 2-hourly inverse isochrones of the tsunami travel time from any point in the Pacific Ocean to Tofino.

tsunami travel time from the source region) events, and two were meteorological tsunamis (Fig. 2). All of these sixteen tsunami events were recorded at Tofino on the outer B.C. coast and some of the tsunamis were recorded at eight or more stations. The tide station at Tofino has been in operation for 100 years and these recent observations add to the dataset of tsunami events compiled previously by S.O. WIGEN (1983) for the period 1906–1980. WIGEN detected 43 tsunami events for this 75-year period. All these events were far-field, with no local or regional events, and no meteorological tsunamis identified.

The fact that the 16 tsunami events observed since 1994 were all recorded at Tofino demonstrates that Wigen's selection of this station for his study was an excellent choice. In addition, Tofino was the location of the maximum observed wave height for 5 of the 15 events. Tofino as a Tsunami Warning station plays a key role for the B.C. coast. Our experience indicates that if a tsunami signal has been detected in the Tofino record, it could be also detected in some other records; however, if there is no tsunami signal in Tofino, there is very little chance that such signal will be found at other sites. We might say that Tofino is an "alarm bell" that always rings in the case of a tsunami. Some of the other "bells" (other stations) sometimes ring louder, but they do not ring as reliably.

This paper will first look at the seismically generated events, and these will be organized in four groups: (1) Far-field events for the period 1994–1998 (analogue instruments), (2) far-field events for the period 1999–2007, (3) local and regional events, and (4) a major event where no tsunami was detected. Two meteorological tsunami events will then be described, followed by a discussion of two recent landslide tsunami

events. The paper will conclude with a discussion of the knowledge gained from these events and how this knowledge is being applied to enhance Canadian tsunami warning and mitigation capabilities.

2. Seismically Generated Tsunamis

2.1. 1994–1998

As mentioned previously, the analogue records from stations on the coast of Vancouver Island were checked for evidence of tsunami events during the period 1981–1998. Altogether we checked about 20 major events (trans-Pacific tsunamis or strong local tsunamis), with particular attention to events observed on the nearby coast of Alaska and on the West Coast of the U.S.A. (cf., LANDER, 1996, 2003). We were able to identify a definite tsunami signal for four events. Table 1 lists these four far-field tsunami events that occurred during the period 1994–1996; the locations of the epicentres of the corresponding earthquakes are shown in Figure 2. The October 4, 1994 Kuril Islands tsunami was well known, as it resulted in a Tsunami Warning being issued for the west coast of North America (see RABINOVICH *et al*., 2006b for discussion of this warning). The other three events had not been identified previously in B.C. records.

1994 Shikotan tsunami. The Shikotan (Kuril Islands) earthquake on October 4, 1994 had a magnitude of $M_w = 8.3$. On Shikotan Island, one of the South Kuril Islands closest to

Table 1

Summary of the 16 recorded tsunami events that occurred between 1994 and 2007. The locations of earthquake epicenters for events 2001b and 2004a are shown in figure 1; all others are shown in Figure 2

Year, Event*	Date	Earthquake parameters				Obs.	Station, Max. height (cm)
		Location	Lat.	Long.	M_w		
1994	04 Oct	Kuril Is., Russia	43.8 N	147.3 E	8.3	5	Port Alberni (26.2)
1995a	30 Jul	Antofagasta, Chile	23.3 S	70.3 W	8.0	6	Port Alberni (24.9)
1995b	03 Dec	Kuril Is., Russia	44.7 N	149.3 E	7.9	5	Port Alberni (37.5)
1996	17 Feb	Irian Jaya, Indonesia	0.9 S	137.0 E	8.2	6	Port Alberni (36.7)
2001a	23 Jun	Peru	16.3 S	73.6 W	8.4	8	Tofino (15.1)
2001b	12 Oct	Queen Charlottes, Canada	52.6 N	132.2 W	6.1	4	Winter Harbour (22.7)
2003a	22 Jan	Colima, Mexico	18.8 N	104.1 W	7.5	3	Tofino (10.5)
2003b	25 Sep	SE Hokkaido I., Japan	41.8 N	143.9 E	8.3	5	Winter Harbour (10.0)
2004a	02 Nov	Vancouver I., Canada	49.0 N	129.2 W	6.6	2	Tofino (10.8)
2004b	26 Dec	Sumatra, Indonesia	3.3 N	96.0 W	9.3	6	Winter Harbour (21.0)
2005a	15 Jun	N. California, USA	41.3 N	126.0 W	7.2	2	Tofino (4.3)
2005b	09 Dec	Vancouver I., Canada	Meteotsunami			11	Tofino (15.5)
2006a	03 May	Tonga Islands	20.2 S	174.1 W	7.9	6	Winter Harbour (10.8)
2006b	15 Nov	Kuril Is., Russia	46.6 N	153.3 W	8.3	10	Langara (38.5)
2007a	13 Jan	Kuril Is., Russia	46.2 N	154.5 W	8.1	8	Langara (17.1)
2007b	13 Jul	Vancouver I., Canada	Meteotsunami			3	Victoria (10.2)

the epicentre, ground-shaking was extremely intense, and maximum runup of 10 m was observed (YEH *et al.*, 1995). A runup of approximately 1.8 m was reported soon after the earthquake at Nemuro (Japan) and a Pacific-wide Tsunami Warning was issued. At that time, only the Tsunami Warning stations at Winter Harbour and Bamfield were equipped with digital instruments and these were the only records utilized. These digital records indicated maximum wave heights of 19.8 cm at Winter Harbour and 9.3 cm at Bamfield. The recent review of the analogue records revealed that the wave was also recorded at Tofino, Port Alberni and Victoria, and that a maximum wave height of 26.2 cm was measured at Port Alberni. The digitized tsunami records (with predicted tides removed and high-pass filtered with a 3-hour Kaiser-Bessel window) for these three stations, and for the stations at Winter Harbour and Bamfield, are shown in Figure 3. The first-wave reached the B.C. coast 8 h 25 m after the earthquake and there was good agreement between the expected and observed wave arrival times at all five stations. At each of the stations the first-wave arrival was positive (a crest) and the maximum wave arrived four or more hours after the first wave.

1995 Chile (Antofagasta) tsunami. On July 30, 1995 an earthquake near Antofagasta in Northern Chile ($M_w = 8.0$) generated a tsunami which was recorded at six tide gauges on the B.C. coast—the same five stations as the previous event in October 1994, as well as

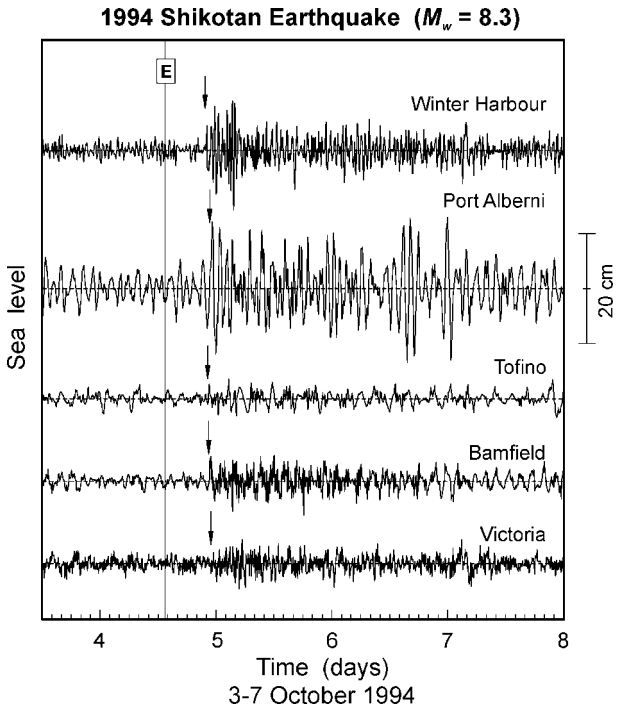

Figure 3
Tsunami records of the Shikotan tsunami of October 4, 1994. Solid vertical line labeled "E" denotes the time of the main earthquake shock; arrows indicate the first tsunami arrival.

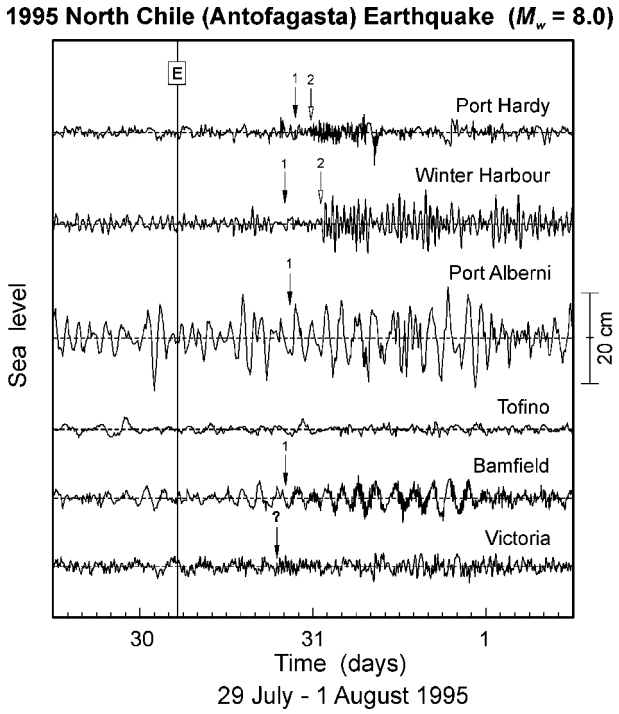

Figure 4
As for Figure 3 but for the Antofagasta tsunami of July 30, 1995. Arrows and numbers indicate arrivals of the first and second tsunami wave train. Solid vertical line labelled ''E'' denotes the time of the main earthquake shock.

Port Hardy. A maximum wave height of 24.9 cm was observed at Port Alberni. The digitized high-pass filtered tsunami records for these six stations are shown in Figure 4. At Winter Harbour the arrival of the first train of waves is not clear, but the arrival of the second train is evident approximately 4 hours later. At Bamfield the record clearly shows both a low-frequency modulating oscillation and high-frequency waves. The high frequency waves, with a period of about 12 minutes, are a common characteristic of tsunami at Bamfield. The tsunami was observed at Port Hardy, Tofino and Victoria, but at each of these stations the tsunami was small and in some instances irregular.

1995 Kuril Islands (Iturup) tsunami. On December 3, 1995 an $M_w = 7.9$ earthquake occurred near Iturup Island (the southern Kuril Islands). A tsunami was observed at the same five stations as the October 1994 Kuril Islands event, and once again the largest wave height (37.5 cm) was at Port Alberni. The digitized tsunami records for Port Alberni, Winter Harbour, Bamfield, Tofino and Victoria are shown in Figure 5. At Bamfield, the first train of high-frequency (12 min) relatively small waves is followed approximately 4.5 h later by a second train of more energetic waves with a period of about 80 min. The arrival of this second train of waves corresponds well with the maximum wave heights at Port Alberni.

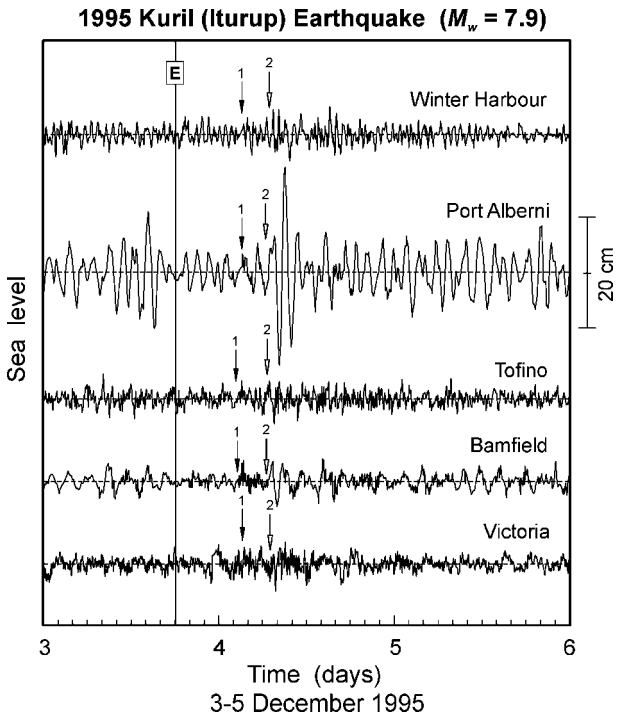

Figure 5
As for Figure 4 but for the Kuril Islands (Iturup) tsunami of December 3, 1995.

1996 Irian Jaya tsunami. The last of the four events identified from the review of the analogue records was the $M_w = 8.2$ earthquake which occurred near Irian Jaya (Indonesia) on February 17, 1996. This tsunami was observed at the same six stations as the July 1995 Chile event. The digitized records for this tsunami are shown in Figure 6. It is noteworthy that tsunami generated near Indonesia rarely reach the coast of B.C.. WIGEN (1983) was able to identify only three tsunami events originating from this region of the Pacific, and in each of these cases the maximum wave height observed at Tofino was less than 10 cm (actually, two of these events are dubious). For the 1996 event the maximum wave height observed at Tofino was only about 5 cm,[1] but larger waves were observed at the other five stations and at each of these stations the first wave arrival was positive (a crest). Once again the maximum wave height (36.7 cm) was recorded at Port Alberni.

These four tsunami events were all far-field events and were from three distinct regions of the Pacific—Russia, Chile and Indonesia. All four of these events were recorded at the same five stations—Victoria, Bamfield, Tofino, Port Alberni and Winter Harbour. The

[1] This estimate for Tofino is unreliable: The main tide gauge was not working during the event, for this reason we used the record from a reserve digital tide gauge with 5-min sampling but with unknown response characteristic.

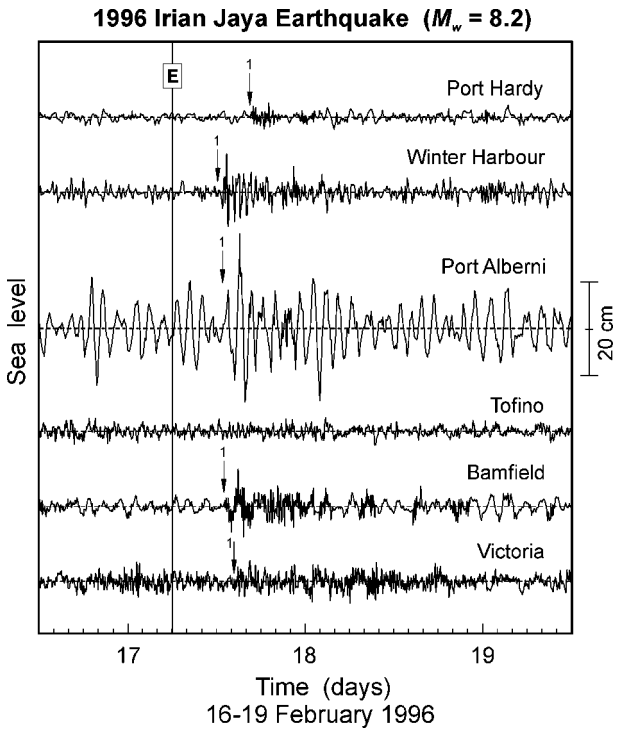

Figure 6
As for Figure 3 but for the Indonesia (Irian Jaya) tsunami of February 17, 1996.

Indonesia and Chile events were also weakly observed at the sixth station—Port Hardy. For each of these events the maximum wave heights were recorded at Port Alberni and at Winter Harbour. Surprisingly, the signals at Tofino were quite modest in each instance. The maximum wave height at Tofino was smaller than at Bamfield for three of the four events and comparable to Bamfield for the fourth event. In contrast, the maximum wave height at Tofino was greater than at Bamfield for every one of the 12 events since 2001.

Tofino is a unique station in that it is one of only two B.C. stations designed expressly for Tsunami Warning. Each of the three stilling wells has a horizontal intake pipe connecting it to the sea. While this provides a linear response to the incoming signal, it requires the horizontal intake to be well maintained. This has been the case in recent years and these horizontal intake pipes are now checked and cleaned annually. WIGEN (1983) noted that, as a result of sediment build-up in the intake pipes at Tofino, "from 1975 to 1978 response may have been diminished" and "from 1979 through 1980 the gauge may at times have been unable to respond to a smaller tsunami, or register accurately a larger one." It now seems that this problem continued for a much longer period of time. A more detailed review of the residuals (observed heights minus predicted heights) may identify additional periods when the station's response was reduced. It seems very likely that 1994–1996 will be one of those periods.

2.2. 1999–2007: Distant Events

Seven tsunami events with distant or far-field sources have been observed on the B.C. coast since the upgraded digital instruments were installed in 1998. Two of these events, Peru (2001) and Sumatra (2004) have been partly discussed in previous papers (RABINOVICH and STEPHENSON, 2004; RABINOVICH *et al*., 2006a); the other five far-field events have not been described previously. These are the Colima, Mexico tsunami (2003), the Hokkaido (Tokachi-oki) tsunami (2003), the Tonga tsunami (2006), and two recent tsunami events with source regions in the Central Kuril Islands (2006 and 2007).

2001 Peru tsunami. The Peru earthquake ($M_w = 8.4$) on June 23, 2001 generated a widespread tsunami, which was observed at distant locations around the Pacific, including Australia and Japan (cf., OKAL *et al*., 2002). Most of the energy went southwestward, i.e., in the direction of New Zealand and Australia. However, a certain portion of the energy also went poleward (to the north and south) along the coasts of the Americas. The tsunami event was clearly evident at three stations on the west coast of Vancouver Island (Tofino, Winter Harbour and Bamfield) as well as at five other locations on the B.C. coast or in adjoining waterways (RABINOVICH and STEPHENSON, 2004).

To better display the data a high-passed Kaiser-Bessel filter with a 3-hour window was used (cf., EMERY and THOMSON, 2003). Several well-defined packets of long waves were apparent in each of these records, and the maximum tsunami wave heights were mainly associated with the second or third packet at a time 1.5–2.0 days after the earthquake event (Fig. 7), i.e., 1.0–1.5 days after the expected tsunami arrival times. Also, a significant increase of wave energy (compared with normal background noise) during the tsunami event was observed to persist for more than four days. Such a prolonged "ringing" could only be explained by persistent incoming wave energy. These features suggest that the tsunami waves measured on the coast of B.C. were mainly edge waves, which propagated along the continental coast from the source region to the observational sites.

The 2001 Peru tsunami waves detected on the B.C. coast demonstrated clearly that the data quality from the upgraded PWLN instruments had improved considerably and become appropriate to detect even weak tsunami events. Though the 2001 wave heights were relatively small (from 3.7 cm in Queen Charlotte City to 15.1 cm in Tofino) the tsunami signal was quite clear and easily distinguishable from the background noise.

2003 Colima tsunami. The Colima earthquake ($M_w = 7.5$) on January 22, 2003 created strong damage in Colima State (Mexico), killed 18 people and produced a small tsunami that was recorded by several tide gauges on the Pacific coast of Mexico with a maximum trough-to-crest height of 122 cm at Manzanillo (ORTIZ *et al*., 2003). The tsunami was observed at three stations on the outer B.C. coast (Fig. 8). The largest observed wave height was 10.5 cm at Tofino. The initial waves reached the B.C. stations about 7 hours after the earthquake event. Approximately 14 hours later a second train of waves arrived

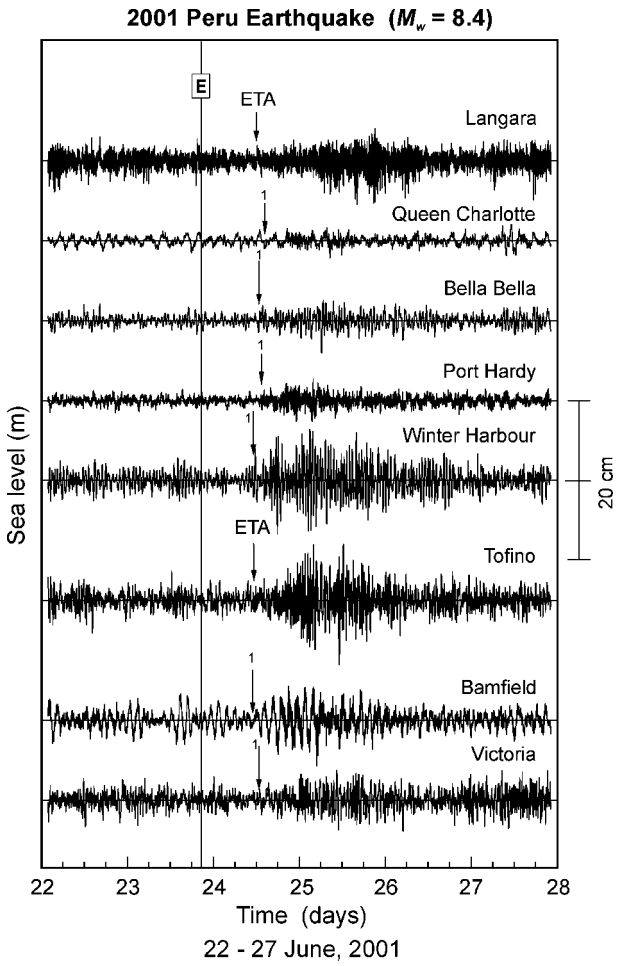

Figure 7
As for Figure 3 but for the Peru tsunami of June 23, 2001.

and this was followed by a third wave train another 8 hours later. This mirrors the sequence of events following the Peru tsunami in 2001 and suggests that once again the tsunami waves measured on the coast of B.C. were mainly edge waves, which propagated along the continental coast from the source region.

2003 Hokkaido (Tokachi-oki) earthquake. A great earthquake on September 25, 2003 ($M_w = 8.3$) injured more than 700 people and produced severe damage in southeastern Hokkaido. The associated tsunami was observed along the entire Pacific coast of Japan. The maximum wave height (254 cm) was recorded at Tokachiko (southeastern coast of Hokkaido Island), maximum runups on this coast were more than 4 m (TANIOKA *et al.*, 2004). Tsunami waves were also observed on the coast of Alaska, at many sites in the Hawaiian Islands and at eight stations on the coasts of Oregon and California with a

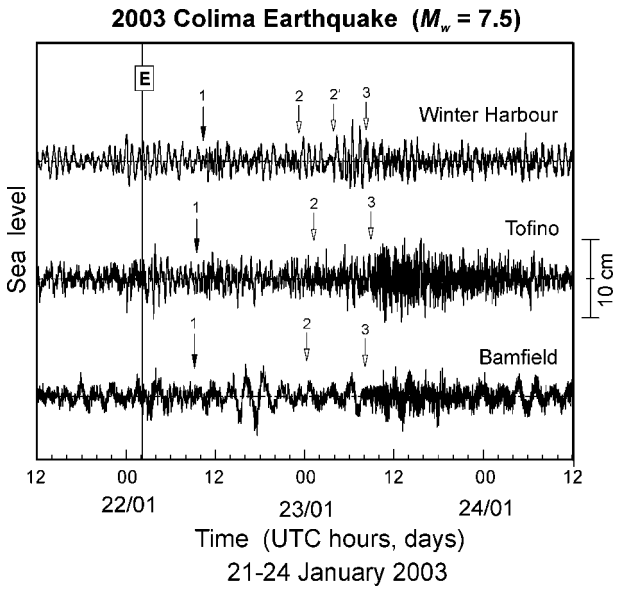

Figure 8
As for Figure 4 but for the Mexico (Colima) tsunami of January 22, 2003.

maximum wave height (trough-to-peak) of 35 cm at Crescent City, CA and 4–9 cm at the other seven sites. These West Coast gauges had a 6-minute sample interval, and would therefore slightly underestimate the actual maximum height. Tsunami waves were expected to be recorded at some stations on the coast of B.C. However, the immediate post-event examination of tide gauge data did not reveal evident tsunami signals. Working on the present paper, we re-examined the data and came to the conclusion that the 2003 Hokkaido tsunami waves had, in fact, been detected on this coast.

Figure 9 shows the records of six stations on or near the outer (Pacific) coast of B.C. (Fig. 1); time of the main shock and estimated arrival time (ETA) for Tofino are indicated (ETA for Langara is approximately 1.5 h earlier, for Victoria 1 h later, while for the other three stations it is approximately the same as for Tofino). The same disturbance ($\sim$1.5 wavelengths beginning from a crest), arriving at the time of ETA is clearly seen at Tofino, Bamfield, Port Hardy and Victoria (indicated by arrows in Fig. 9). The height of this initial disturbance ranges from 3.5 cm to $\sim$7 cm. The same disturbance is apparently seen at Winter Harbour (indicated by an arrow with a question mark) but it is masked by earlier induced seiches. In general, the post-ETA oscillations observed at two neighbouring stations, Tofino and Winter Harbour, in particular the timing of the largest waves, are highly correlated, supporting the assumption of their mutual tsunami origin. The largest observed wave heights are 8 cm at Tofino, 10 cm at Winter Harbour, and $\sim$5.5 cm at Bamfield and Victoria. The Langara record (top record in Fig. 9) is very noisy, preventing identification of tsunami waves at this site.

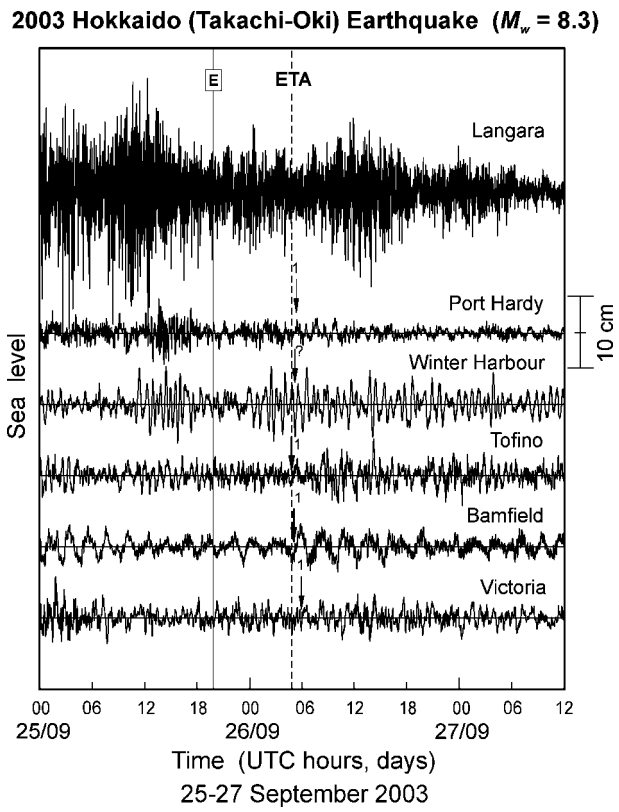

Figure 9
As for Figure 3 but for the Hokkaido (Tokachi-oki) earthquake of September 25, 2003. Dashed vertical line labeled "ETA" denotes the expected tsunami arrival time for the Tofino Warning Station. Tsunami waves have not been identified in the record of Langara, which was too noisy.

2004 Great Sumatra tsunami. The Sumatra megathrust earthquake on December 26, 2004 ($M_w = 9.3$) generated a catastrophic tsunami that caused widespread damage in coastal areas throughout the Indian Ocean. It was soon apparent that this tsunami had the potential to be a global-scale tsunami. We expected the Sumatra tsunami would propagate into the North Pacific and given the excellent tsunami observations collected on the B.C. coast in 2001–2004, supposed that it would be recorded by many PWLN stations.

Several criteria were used to identify the 2004 Sumatra tsunami waves in the B.C. records. The most important criteria were: (1) Close agreement between the expected tsunami arrival times and the observed times of arriving tsunami waves; (2) agreement between nearby stations (it is much easier to detect tsunami wave arrival for a group of stations than for a single tide gauge); (3) the presence of dominant periods in the arriving waves; and (4) relatively sharp amplification and abrupt temporal structure change in the observed longwave observations. The high quality of the instruments, the 1-minute sampling interval, as well as the cumulative effects of the detection criteria enabled us to

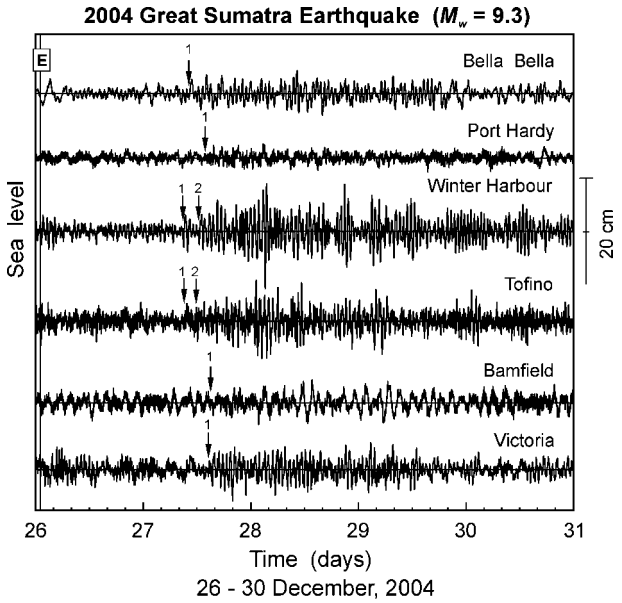

Figure 10
As for Figure 4 but for the Great Sumatra tsunami in the Indian Ocean of December 26, 2004.

recognize a tsunami signal at six of the stations on the B.C. coast (RABINOVICH *et al.*, 2006a). The maximum wave heights ranged from 21.0 cm at Winter Harbour to 4.5 cm at Port Hardy (Fig. 10). Tsunami energy for these stations was principally in the 45–60 minute range. In addition, the observed wave heights, tsunami arrival times, and the general character of the wave trains for stations in the North Pacific were all found to be in good agreement with the results of numerical computations (TITOV *et al.*, 2005b).

Further analysis demonstrated that the 2004 Sumatra tsunami waves were actually recorded along the entire Pacific Coast of North America, from Mexico to the Aleutian Islands, with maximum measured wave heights at Manzanillo (Mexico)—89.3 cm, Crescent City (CA)—60.5 cm, and Port San Luis (CA)—53.0 (RABINOVICH *et al.*, 2006a). The main properties of the waves observed on the coasts of Alaska, Oregon, California (CA) and B.C. were approximately the same, despite significant differences in wave heights and oscillation frequencies associated with the resonant features of the station sites.

All B.C. records had a wave-train structure with maximum recorded waves mainly in the second or third trains (i.e., 18–24 hours after the first wave arrival). Wave trains at neighbouring stations (e.g., Tofino and Winter Harbour) are highly correlated, indicating that they are related through properties inherent to the open-ocean tsunami wavefield. A pronounced feature of the tsunami records for the B.C. and West Coast U.S. sites is the very long (> 3.5 days) ringing (Fig. 10). Similar long-period ringing of tsunami waves for the entire coast of North America was observed by MILLER *et al.* (1962) following the

1960 Chile earthquake. Such long-duration ringing is only possible if persistent external energy "pumping" is provided through continued arrival of the open-ocean tsunami energy. This additional energy may be associated with waves reflected from the continental margins or other large-scale topographic features, which may, in turn, account for the wave-train structure of the tsunami waves.

2006 Tonga tsunami. The Tonga Islands earthquake on May 3, 2006 ($M_w = 7.9$) was felt throughout the surrounding islands. It produced a widespread Pacific tsunami with substantial wave heights in the near field, although no damage or fatalities were reported. Measured heights (peak-to-trough) of approximately 0.5 m were recorded at a number of islands in the SW Pacific and at Kalului, Hawaii. The wave was also observed in Japan and New Zealand, where the maximum wave heights were 0.15 m. On the West Coast of North America the wave was observed at a number of locations from Santa Barbara, CA to King Cove, AL. The maximum observed wave height on the coast of North America was 0.54 m at Crescent City. On the B.C. coast the tsunami was observed at six locations. The maximum recorded wave height was 10.8 cm at Winter Harbour on the west coast of Vancouver Island. The travel time to the B.C. coast was 12–14 hours and the arrival of the tsunami is clearly shown in de-tided plots with a high-passed Kaiser-Bessel filter with 3-hour window used (Fig. 11).

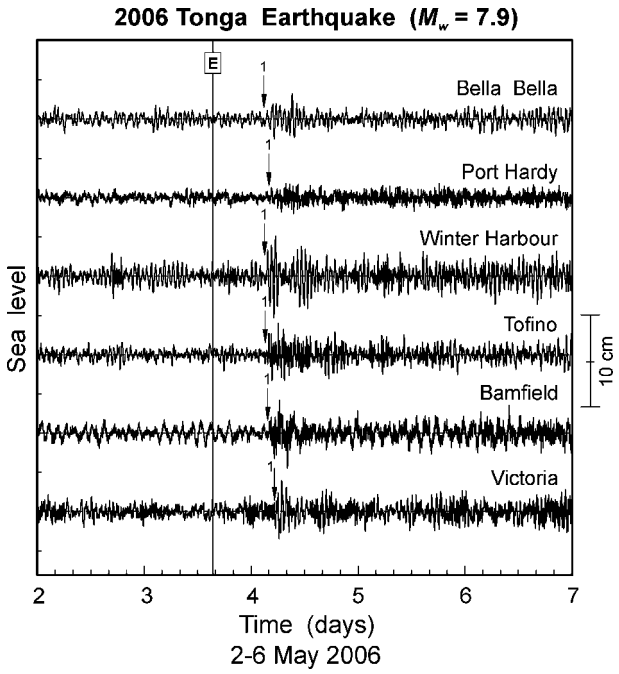

Figure 11
As for Figure 3 but for the Tonga tsunami of May 3, 2006.

2006 and 2007 Kuril Islands tsunamis. Two of the most recent events, the central Kuril Islands earthquakes on November 15, 2006 and January 13, 2007, produced tsunamis clearly observed at stations on the B.C. coast. The maximum wave height in each instance was recorded at Langara Island −38.5 cm and 17.1 cm, respectively. The November 15, 2006 event ($M_w = 8.3$) generated a trans-oceanic tsunami, the strongest tele-tsunami in the Pacific since the 1964 Alaska tsunami (RABINOVICH *et al*., 2008a). Tsunami wave heights were recorded at more than 100 tide gauge stations throughout the Pacific, including ten stations on the B.C. coast (Fig. 12). Two of these ten stations were the recently installed Tsunami Warning station at Henslung Cove, where the maximum wave height was 28.2 cm, and the recently reactivated station at Port Alberni, where the

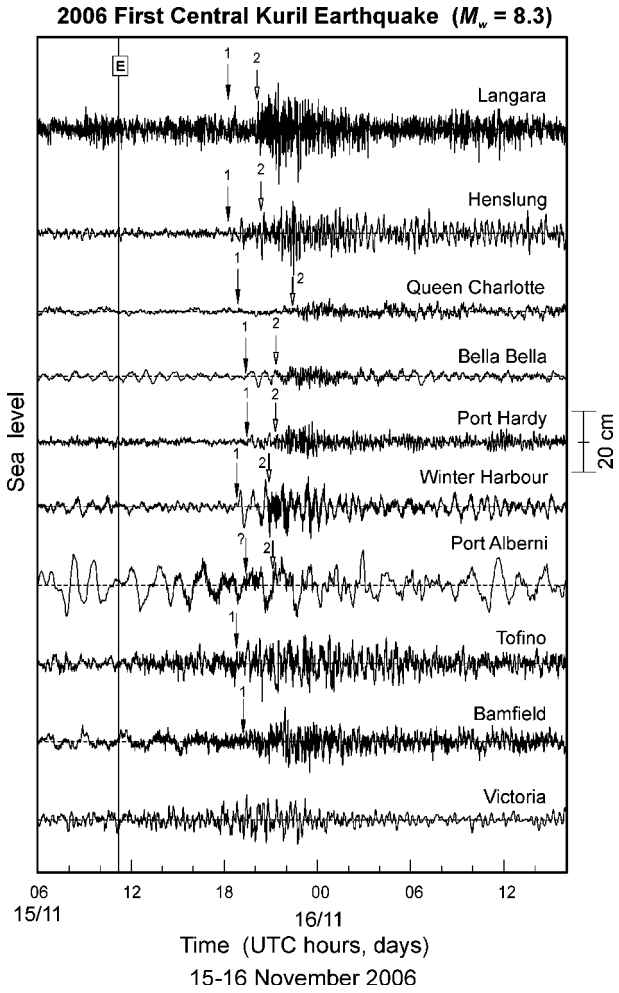

Figure 12
As for Figure 4 but for the Central Kuril Islands tsunami of November 15, 2006.

maximum wave height was 24.5 cm. At eight stations where the first wave arrival was clearly determined, it was positive (a crest). At many of the stations the first train of waves was followed by a second train of high frequency waves approximately two hours later.

The second central Kuril Islands earthquake ($M_w = 8.1$) occurred on January 13, 2007. It produced a tsunami that was observed at 8 locations on the B.C. coast (Fig. 13). The maximum observed wave height was 17.1 cm at Langara Island. At each of the seven stations shown in Fig. 13 plus Langara the first wave arrival was positive (a crest) and at all stations except Victoria the first train of waves was followed by a second train of high frequency waves approximately two hours later. The tsunami was not observed at Port

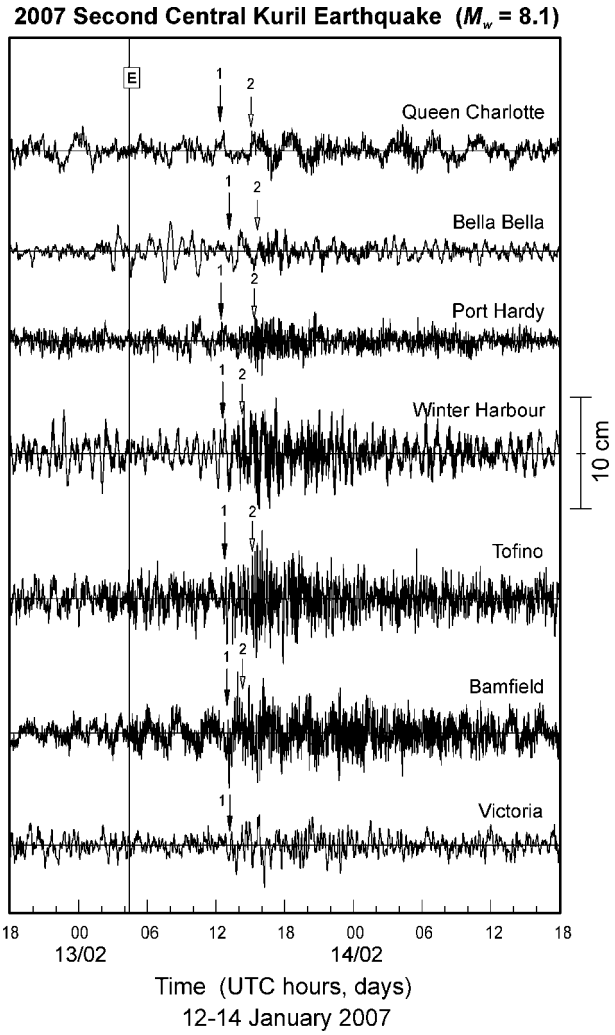

Figure 13
As for Figure 4 but for the Central Kuril Islands tsunami of January 13, 2007.

Alberni, probably because of a strong mismatch between the typical periods of this tsunami in the open ocean (from a few minutes to approximately 20 min, cf. RABINOVICH *et al*., 2008a) and the eigen periods of Alberni Inlet (about 112 min, cf. FINE *et al*., 2008).

2.3. 1997–2007: Local and Regional Events

WIGEN (1983) studied tsunamis recorded at Tofino during the period 1906–1980 and identified 43 events. These were all far-field tsunamis, with no local or regional events. Our examination of analogue records for the period 1981–1998 also had not revealed any local tsunami events. However, during the last 10 years, i.e., since the installation of high-quality digital instruments, there have been two local events and one regional event identified in the records.

2001 Queen Charlotte Islands tsunami. An earthquake of magnitude $M_w = 6.1$ occurred on October 12, 2001 on the continental slope of the Queen Charlotte Islands at 52.63° N, 132.20° W (Fig. 1). Shaking was felt all over the Queen Charlotte Islands and on the adjacent mainland. The earthquake epicentre was located just to the east of the major strike-slip Pacific-North American plate boundary known as the Queen Charlotte Transform Fault. A well constrained moment tensor solution based on regional broad-band data from B.C. and Alaska shows that the earthquake had almost pure thrust faulting. Rupture initiated at a depth of about 22 km, typical for many earthquakes in this region, and the center of energy release as determined by the regional moment tensor solution was at a depth of 14 km.

Despite its relatively low magnitude, this underwater earthquake generated a tsunami which was clearly recorded by four tide gauges on the coast of Vancouver Island—Bamfield, Tofino, Winter Harbour, and Port Hardy (RABINOVICH and STEPHENSON, 2004; RABINOVICH *et al*., 2008b). Maximum wave heights for the four gauge sites were quite consistent, ranging from a minimum of 11.3 cm at Bamfield to a maximum of 22.7 cm at Winter Harbour (Fig. 14). Unfortunately, the Langara tsunami station was not in operation during this event, while at other PWLN stations, including nearby stations Queen Charlotte, Bella Bella, and Prince Rupert (Fig. 1) the tsunami was not detected, apparently because of coastal sheltering and spatial energy decay. The duration of "ringing" at Bamfield, Tofino, Winter Harbour and Port Hardy was relatively short, lasting for only 6–8 hours.

Despite an obvious increase of long-wave energy during the event (Fig. 14), the exact arrival time (and the respective travel time) of the first wave were not clearly delineated in the records. In this case, the tsunami-driven seiches simply augmented the atmospherically generated seiches (eigen oscillations) that were occurring in the corresponding bays, inlets or harbours at the time. This earthquake has some of the characteristics typical of a "tsunami earthquake" (cf., KANAMORI, 1972; ABE, 1979) because the effective source is larger than would be expected from the magnitude of the generating earthquake. It is likely that the rupture extended into the soft sediments of

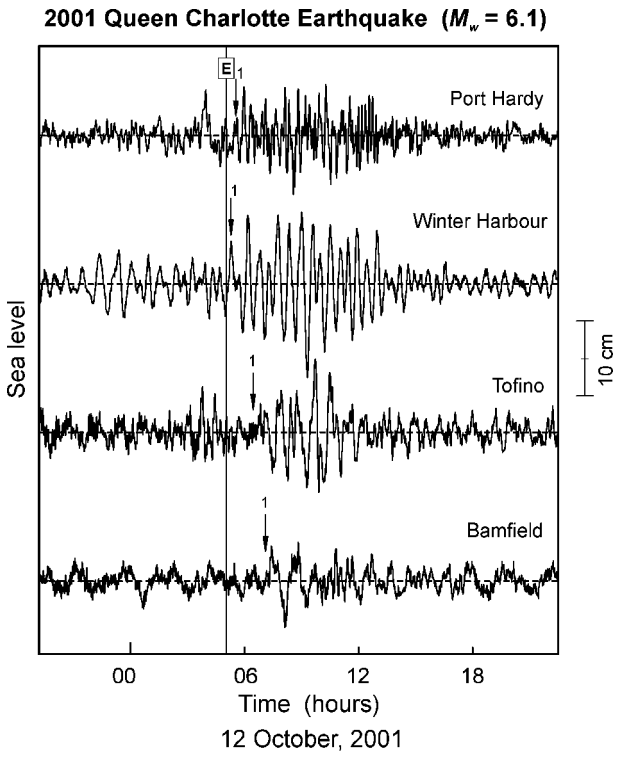

Figure 14
As for Figure 4 but for the Queen Charlotte tsunami of October 12, 2001.

the Queen Charlotte terrace, thus exceeding the effective displacement for a typical earthquake of this size.

2004 Vancouver Island tsunami. An intense swarm of earthquakes occurred about 200 km west of Vancouver Island during the first week of November 2004. Over 700 earthquakes were detected. While swarm activity is not uncommon in the tectonically active, thin oceanic lithosphere west of Vancouver Island, this swarm was unusual because it did not occur along any of the previously recognized offshore fault zones (RABINOVICH *et al.*, 2008b). The largest event ($M_w = 6.6$) was on November 2 at 10:02 UTC at an effective depth of 9 km. The earthquake epicentre (49.01°N, 129.18°W) was located within the region of the Explorer Plate about 190 km from Port Hardy and 230 km from Tofino. The earthquake was felt at Alert Bay, Bamfield and Port Alice on Vancouver Island, but there were no reports of damage. Locations and focal mechanisms from regional moment tensor solutions of the larger earthquakes reveal a previously unknown left-lateral strike-slip fault about 80-km long within the Explorer Plate. It trends about 15 degrees counter-clockwise to the very active Nootka Fault Zone. Rupture length of the largest earthquake ($M_w = 6.6$) in the sequence swarm was about 40 km, estimated

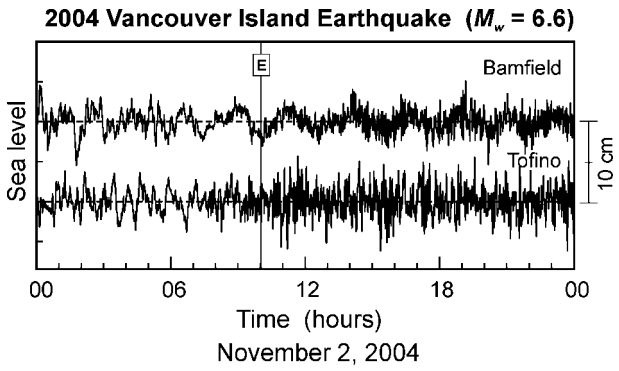

Figure 15
As for Figure 4 but for the Vancouver Island tsunami of November 2, 2004.

from the empirical Green's Function technique using surface waves. While most of the motion was strike-slip, there was a small thrust component with the east side down.

Examination of the digital records for nearby tide gauge stations—Winter Harbour, Port Hardy, Tofino, Bamfield, and Victoria (Fig. 1) reveals that the November 2004 earthquake generated a weak tsunami, which was only measurable at Tofino and Bamfield on the outer southwest coast of Vancouver Island (Fig. 15). The maximum recorded trough-to-crest wave heights of 10.8 cm at Tofino and 7.5 cm at Bamfield, are approximately 35% smaller than for the October 2001 Queen Charlotte Islands tsunami. This suggests that the November 2004 earthquake was a markedly less efficient source mechanism.

The observed tsunami travel times of 52 min and 75 min for Tofino and Bamfield respectively, were in reasonable agreement with the expected tsunami travel times of 58 min and 70 min. The first tsunami semiwave recorded on the coast was negative (wave trough) agreeing with the east side down motion of the fault. This caused a negative wave to travel outward to the southeast and a positive wave to move outward to the northwest.

2005 California tsunami. An $M_w = 7.2$ earthquake occurred on June 15, 2005 seaward of northern California off the west coast of North America. Based on the earthquake location and source parameters the possibility existed for a locally destructive tsunami and a Regional Tsunami Warning was issued. Tsunami waves were recorded at four stations in California and Oregon with the maximum trough-to-crest wave height of 27.7 cm observed at Crescent City, CA. Tsunami waves of 0.5 and 1.5 cm were also recorded by open-ocean DART buoys 46404 and 46405, respectively, closely matching wave heights derived from numerical models (Rabinovich *et al.*, 2006b). The tsunami signal was clearly detected at Tofino and Bamfield on the coast of Vancouver Island (B.C.) with arrival times in good agreement with estimated arrival times (Fig. 16).

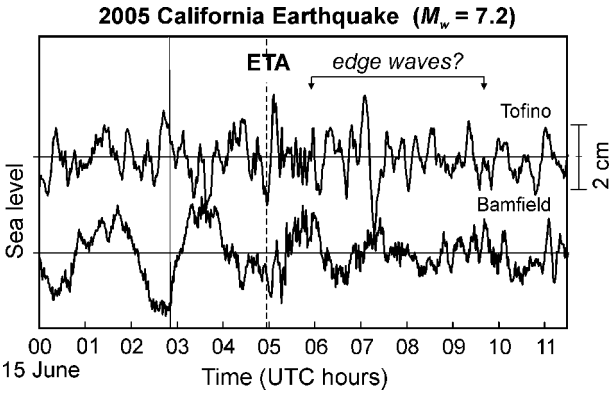

Figure 16
As for Figure 4 but for the California tsunami of June 15, 2005.

At both Tofino and Bamfeld the first observed wave was negative and had respective trough-to-crest heights of 3.3 cm and 1.8 cm.

The first tsunami waves to arrive at Tofino were irregular, but were followed an hour later by a train of regular waves with typical periods of about 22 min. The regular waves persisted for about four hours and had maximum trough-to-crest wave heights of 4.3 cm. It has been speculated (RABINOVICH *et al.*, 2006b) that the more regular train of waves was associated with edge waves. Tsunami signals were also identified at Winter Harbour and Port Hardy, but they were less than 1 cm.

2.4. Events where no Tsunami was Identified

Table 1 lists 16 tsunami events observed during the study period. There was, however, one significant event that has not been identified in the tide gauge records on the coast of B.C. This was the tsunami associated with the November 17, 2003 ($M_w = 7.8$) Rat Islands earthquake (Aleutian Islands). The earthquake produced a tsunami which was observed at a number of locations along the west coast of North America.

2003 Rat Islands earthquake. The earthquake occurred near Amchitka Island in the Rat Islands (Aleutian Islands, Alaska). The earthquake was the largest to occur in North America since the Denali earthquake ($M_w = 7.9$) of November 3, 2002, and the largest in the region of the Aleutian Islands since the $M_w = 7.9$ earthquake in June 1996. A small tsunami was recorded locally (52 cm at Shemya, 20 cm at Adak) and across the Pacific in Hawaii (65 cm at Kahului and 44 cm at Hilo) and Chile (30 cm at Caldera and 8–10 cm at several other stations). The November 17, 2003 tsunami was observed at several stations in Oregon and California, with maximum wave heights varying between 10 cm and 22 cm. The tsunami was also recorded by deep-ocean DART station D171 ($\sim$7 cm) and this record was successfully used to numerically simulate and predict tsunami waves

Table 2

Maximum wave height (cm) observed at stations on the coast of British Columbia

Year, Event*	Stations							
	Victoria	Bamfield	Tofino	Port Alberni	Winter Harbour	Port Hardy	Bella Bella	Langara/ Henslung
1994	8.7	9.3	6.1	26.2	19.8	x	x	x
1995a	8.2	12.2	3.0	24.9	13.2	7.2	x	x
1995b	6.4	9.7	10.0	37.5	11.1	–	x	x
1996	9.1	13.9	5.0	36.7	15.1	5.2	x	x
2001a	7.4	9.7	15.1	x	12.9	5.4	6.7	9.5
2001b	–	11.3	18.2	x	22.7	14.5	–	x
2003a	–	8.0	10.5	x	8.5	–	–	x
2003b	5.5	5.5	8.0	x	10.0	4.5	–	x
2004a	–	7.5	10.8	x	–	–	–	x
2004b	11.7	4.5	15.4	x	21.0	4.5	9.0	x
2005a	0	2.6	4.3	x	< 1	< 1	–	x
2005b	13.9	14.5	15.5	x	10.7	8.0	7.5	x
2006a	9.0	5.6	6.9	x	10.8	3.7	5.7	x
2006b	17.5	21.4	25.4	24.5	23.9	13.5	8.6	38.5 / 28.2
2007a	7.4	7.3	10.3	x	9.0	5.3	4.5	17.1 / x
2007b	10.2		3.4					

as shown in Table 1 and Fig. 2

"x" indicates the station was not operational, or the record was not checked

"–" indicates the record showed no evidence of a tsunami

on the coasts of the Hawaiian Islands (TITOV *et al.*, 2005a). The records from six B.C. stations were analysed, but no signal was identified in any of them (Fig. 17).

In general, our ability to detect tsunami waves in a tide gauge record depends strongly on the signal-to-noise ratio (the ratio between tsunami and background oscillations). Infragravity waves generated by nonlinear interaction of wind waves and tsunami-like, atmospherically-induced seiches create serious problems in identifying weak tsunamis (RABINOVICH and STEPHENSON, 2004; see also RABINOVICH *et al.*, 2006a). In fact, one of the main purposes of any preliminary analysis of tide gauge data is to reduce the background noise level and thereby improve the tsunami-to-noise ratio. Once a tide gauge record has been de-tided several criteria are used to identify tsunami waves (see discussion on the 2004 Sumatra tsunami in Section 2.2). However, based on these criteria for the November 17, 2003 event (Fig. 17) we cannot unambiguously detect tsunami waves, either because these waves are too weak or because background oscillations are too strong.

Note that the Rat Islands tsunami should have been recorded at least at Langara, the station located relatively close to the source area. However, the signal at Langara is very noisy and was of no use for this particular event, or for the 2003 Hokkaido tsunami. The observational problems at Langara are discussed in more detail in the next section.

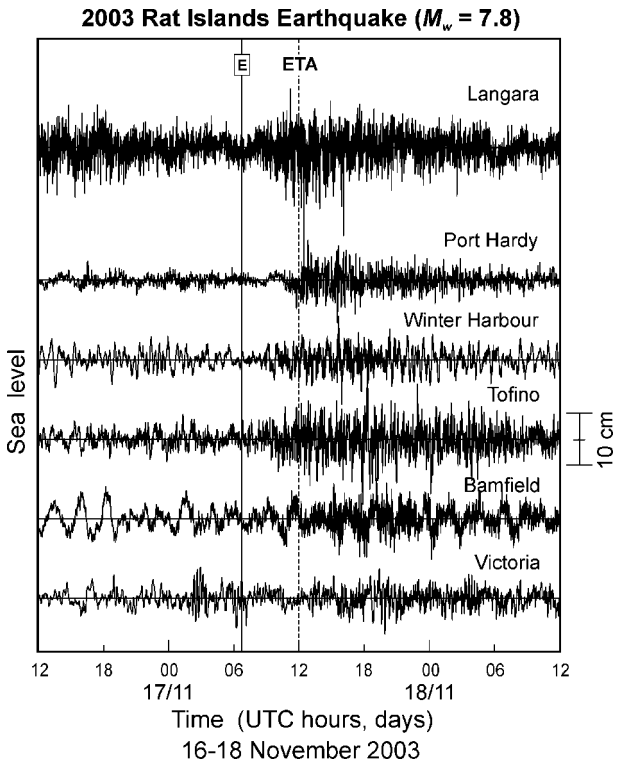

Figure 17
As for Figure 3 but for the Rat Islands earthquake of November 17, 2003.

In addition to this event, there were ten other events where the tidal records were checked for evidence of a tsunami and where no tsunami could be identified in the records. These earthquake events are listed in Table 3.

Table 3

Earthquake events (1994–2007) where no tsunami could be identified in the records of B.C. tide stations

Year	Date	Time (UTC)	M_w	Source area	Where recorded	Type of recording
1996	February 21	12:51	7.5	Northern Peru	Peru, Chile, Mexico, Hawaii	Analogue
1996	June 10	04:04	7.9	Adak, Aleutian Is.	Alaska, Hawaii, US west coast	Analogue
1997	April 21	12:02	7.7	Santa Cruz Is. (Solomon Is.)	Pacific Is., Japan	Analogue
1997	December 5	11:27	7.8	Kamchatka	Russia, Aleutian Is., Hawaii	Analogue
1998	July 17	08:49	7.0	Papua New Guinea	PNG, Japan	Digital
2000	November 16	04:54	8.0	New Ireland, PNG	Solomon Is.	Digital
2001	January 10	16:03	7.1	Kodiak I., Alaska		Digital
2001	February 17	05:02	6.3	Queen Charlotte Is., BC		Digital
2002	March 5	21:16	7.5	Mindanao, Philippines	Philippines	Digital
2002	September 8	18:44	7.6	Papua New Guinea	PNG, Japan	Digital
2003	November 17	06:43	7.8	Rat Islands., Alaska	Chile, Hawaii, US west coast	Digital

2.5. Observational Problems

Previous studies have confirmed that the Langara Point station has a very noisy signal, making detection of small tsunami events very difficult. To improve our tsunami detection capability at that important site (located close to Alaska and the Aleutian Islands, the regions with the highest seismic risk) and to estimate the influence of local topographic factors, a second gauge was installed at Henslung Cove on the south side of Langara Island.

We believe that this intensive high-frequency background noise at Langara (Figs. 9 and 17) is due to the particular location of the respective station on the outer (oceanic) coast of Langara Island where it is exposed to storm waves and swell. The nonlinear interaction of wind waves or swell generates a specific type of long waves known as *infragravity (IG) waves* (cf., BATTJES, 1988). These waves have typical periods of 30 s to 300–600 s and length scales from 100 m to 10 km. The occurrence of relatively high-frequency long waves is highly correlated with the modulation of groups of storm or swell waves. In general, the significant high-frequency background noise is likely related to the IG-waves (a common feature of several US tide gauges, in particular, Shemya (Aleutian Islands), Charleston (Oregon), Arena Cove, Point Reyes, Port San Luis, and Santa Monica (California) (RABINOVICH *et al.*, 2006a)). The tsunami signal at these stations is often buried in high levels of noise associated with IG-waves, creating major difficulties in identifying weak tsunami waves and detecting their exact arrival time at some stations.

In contrast to the Langara Point tide gauge, an instrument installed in Henslung Cove, on the south side of Langara Island (8 km from the old location, see the inset in Fig. 1), was sheltered from storm waves and swell and associated IG-waves. In addition, although both stations use pneumatic bubbler tide gauges equipped with differential pressure transducers, the gauge at Henslung Cove has a gas buffer volume which improves measurement accuracy. Figure 18a shows the de-tided signals from both of these stations for a two-month period in 2004. Three segments of those residual (longwave) plots are shown in greater detail in Figure 18b. These records clearly show that low-frequency oscillations at the two stations almost coincide, but the Langara signal is much noisier due to high-frequency oscillations and suffers from periodic "spikes."

The Langara Point gauge has no gas buffer volume (reservoir bell). A comparison of the records late on Julian Day 110 shows quite clearly that the Langara Point record most closely matches the Henslung Cove record at the times of the spikes. This is when the orifice point is the actual point of the measurement. Between the spikes wave action is causing gas to escape from the bubbler line faster than it can be replenished and the reference point has moved some distance up the bubbler line.

The Tsunami Warning station for the northern B.C. coast has been moved from Langara Point to a new location at Henslung Cove and in this new location appears to respond well to tsunami events. More time is required to fully assess the response of this station to a number of tsunami scenarios.

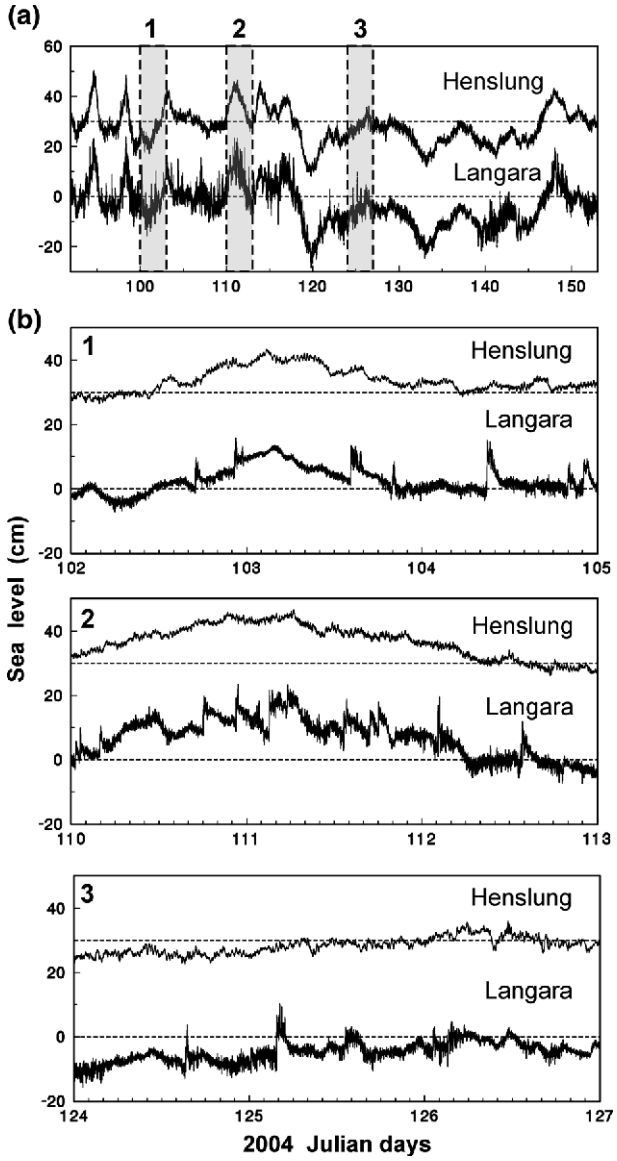

Figure 18
(a) Residual sea-level oscillations (predicted tide removed) for Henslung Cove and Langara Point records for a two month period in 2004 (top panel) and (b) three-zoomed segments (panels 2–4). Each of the high resolution plots covers a period of 3 days.

In section 2.1 it was noted that the maximum wave heights observed at Tofino (1994–1996) were unusually small with irregular oscillations and no clearly defined arrival times. This was almost certainly due to siltation in the horizontal intake pipes. In order for the wells to respond correctly to the incoming signal the horizontal intakes need to be

well maintained. This has been the case since new digital instruments were installed in 1998, and these horizontal intake pipes are now checked and cleaned annually. A more detailed review of the residuals (observed heights minus predicted heights) may identify additional periods when the station's response was reduced. It seems very likely that 1994–1996 will be one of those periods and there may be other periods after 1981 when siltation was a problem; e.g., the two Alaska tsunami events studied by González *et al.* (1991) may not have been observed at Tofino for this reason.

The largest tsunami ever recorded on the B.C. coast was at Port Alberni on March 28, 1964 (Wigen and White, 1964; Fine *et al.*, 2008) and that station was in continuous operation from 1970 to 1997, however, lulled by a long period of little tsunami activity and faced with budget restrictions the station was then shut down. It was only as a result of the review of analogue records (1981–1997) that the importance of Port Alberni for tsunami research was again appreciated. The station was reactivated in 2006 and, along with the station at Bamfield, provides important observations for ongoing study and tsunami modelling of Barkley Sound and Alberni Inlet.

The twelve tsunami events recorded on the B.C. coast since 1998, and the analysis of the data collected has clearly shown that a sampling interval of 1 min is appropriate for this region. Changing the data recording to 6-min sample intervals would reduce the data storage and data transmission costs, however, the Nyquist period in that case would become 12 min. The major topographic admittance peaks at most of the stations were determined to be located at periods less than 12 min (cf., Rabinovich and Stephenson, 2004; Fine *et al.*, 2008). Also some of the recent tsunami events (2001 Queen Charlotte; 2004 Vancouver Island; 2005 California; 2006 and 2007 Kuril Islands) had major source energy at relatively high frequencies (cf., Rabinovich and Stephenson, 2004; Rabinovich *et al.*, 2006b, 2008b). Thus, reducing the sample interval to 6 minutes would deprive us of some important information about long waves in the tsunami frequency band and may create serious aliasing problems (cf., Emery and Thomson, 2003). At the same time, there is no apparent reason to reduce the sample interval to 30 or 15 sec; this can be important for investigation of IG-waves, but is not crucial for tsunami waves.

3. Landslide-Generated Tsunami

As mentioned earlier, the coasts and underwater slopes of B.C. contain significant amounts of unstable material, so submarine and subaerial landslides, slumps and rock falls, and associated tsunamis are often the results of earthquakes. Extended periods of heavy rain can also produce conditions that trigger landslides, particularly in coastal areas with very steep slopes. Some landslide generated tsunami events on the B.C. coast have been documented in the scientific literature, e.g., Kitimat (Murty, 1979) and Knight Inlet (Bornhold *et al.*, 2007). These conditions are not limited to tidal waters, as many lakes and rivers in B.C. have similar conditions (steep slopes, unstable material, periods of heavy rain) (cf., Evans, 2001).

Historical Kwalate landslide-generated tsunami. The Kwalate landside-generated tsunami event is historical and occurred in Knight Inlet roughly 400 years ago. An 840-m high rock avalanche descended into the water of Knight Inlet and produced a tsunami which destroyed the aboriginal community of Kwalate on the opposite side of the inlet (BORNHOLD *et al.*, 2007). This tsunami is thought to have killed 100 or more inhabitants. The initial interest and "awareness" of this tsunami was due to a traditional First Nations oral narrative of the event, and scientific investigation of the village site and the slide site began in 2005. Tsunami height estimates for possible scenarios were subsequently determined and range from 1 m to 6 m. Many parts of the B.C. coast are remote and sparsely populated (e.g., Knight Inlet). These coastal areas are generally susceptible to tsunamis generated by landslides and rock avalanches. As the pace of development increases in these coastal areas the potential for rare but possibly devastating tsunami events need to be considered as part of the planning and development process.

2006 Squamish submarine landslide. Two additional tsunami events have been identified and investigated in the past five years. The first event occurred in 2006 at Squamish, about 40 km north of Point Atkinson (see Fig. 1). Squamish is located at the head of Howe Sound on a low-lying area adjacent to the Squamish River. The site is typical of many inlets on the B.C. coast – a deep water fiord-like inlet with a river at its head where silt carried by the river forms a small shallow delta. At Squamish this shallow delta area is adjacent to a "deep water, break-bulk" terminal and dredging is required to maintain sufficient water depth on the approaches to the terminal berths. Hydrographic surveys are carried out, as required, to monitor changes to the delta. The seaward edge of this growing delta is steep and unstable and therefore susceptible to submarine landslides.

In October 2006 it was noted that one of the navigation buoys marking the approach to the terminal had moved a considerable distance seaward. The buoy was recovered and repositioned. Two multibeam surveys of this area, the first in March 2006 and the second in November 2006, provided a detailed map of the underwater landslide event. The slump occurred on the steep slope of the delta front, an area with initial water depths of 0–50 m. After the landslide, the water depths in this area increased by 10–20 m. The debris field is clearly visible, flowing downslope from the slide site in a southwest direction for a distance of about 1 km and ending at the bottom of the inlet in a water depth of approximately 120 m. This debris field has a height of 5–10 m along its length.

The record of the tide station at Point Atkinson was studied for any evidence of a tsunami, but no definitive tsunami event was identified there or observed at Squamish. The height of the possible tsunami in the area of the slide is unknown, but given that the wharf deck and assembly area of the bulk terminal are less that 2 m above the highest normal tide, and only 1 m above the historical extreme high water as measured at Point Atkinson, a moderate tsunami event, if it occurred during a time of high water, could cause considerable damage. The areas adjacent to the Squamish River and the bulk terminal were surveyed twice more in 2007 to monitor the movement and growth of this

area. These surveys indicate that the delta front immediately in front of the river mouth is slowly growing and will at a future date again become unstable.

2007 Chehalis Lake landslide-generated tsunami. Chehalis Lake is a small lake approximately 8-km long and 1-km wide located in the coastal mountains about 80-km east of Vancouver (see Fig. 1). On or about December 4, 2007 a landslide into Chehalis Lake, during a period of heavy rain, produced a tsunami with a maximum wave height in excess of 10 m in the vicinity of the landslide area and of 4–10 m throughout the lake. The volume of the slide has been estimated to be 2 million m^3.

One campground opposite the slide site was completely destroyed and two other campgrounds on the lake were severely damaged by the tsunami. Fortunately, there was no one using any of the campgrounds at the time. Had this landslide been triggered by an earthquake, during the summer months when the campgrounds were full, there could have been considerable loss of life. In addition, the shore of the lake was scoured of all vegetation and a large pile of floating log debris, covering approximately 13 hectares, was deposited at the outlet to the lake about 7 km from the site of the landslide. This large pile of debris poses a risk to the environment of the river (fish habitat) and to the properties and infrastructure located downstream.

4. Meteorological Tsunami Events

The earlier study of tsunamis at Tofino (WIGEN, 1983) identified no meteorological tsunami events, and no such events had been identified in B.C. prior to December 2005. The trigger for the 2005 meteorological tsunami event was alarm software incorporated into each of the three B.C. Tsunami Warning stations (Tofino, Winter Harbour and Langara, see Fig. 1). On this occasion it was the Tsunami Warning station at Tofino that detected an abnormal variation in sea level and issued an alarm message. Without this feature this event would likely have been overlooked, as stations on the B.C. coast routinely have seiches superimposed on the tidal signal. This feature did not exist for the many years when water levels were recorded using analogue recorders. It could be that meteorological tsunamis are a fairly common event on the B.C. coast.

Meteorological tsunami of December 9, 2005. Unusual sea-level measurements took place on December 9, 2005 along the entire coast of B.C. from Prince Rupert to Victoria, a distance of approximately 1000 km. These unusual sea-level variations were also observed at eight stations in Washington State. No seismic events had occurred that could generate a noticeable tsunami, and therefore the waves are ascribed to be of meteorological or atmospheric origin, and most probably a manifestation of high-frequency irregularities in atmospheric pressure as the weather was calm that day.

Examination of the sea-level records showed that stations on both the open ocean and in the sheltered straits recorded noticeable tsunami-like oscillations. Tofino, Bamfield, and Winter Harbour in B.C., and Neah Bay and Toke Point in Washington are all located along the ocean coast and are relatively open to waves arriving from the open ocean. On the other hand, Patricia Bay, Vancouver and Point Atkinson in B.C., and Port Angeles, Port Townsend, Friday Harbor, Cherry Point, Seattle and Tacoma in Washington are located in areas more protected from tsunami coming from the open ocean. The wave oscillations continued for approximately 9–12 hours and had mainly irregular (polychromatic) characteristics with dominant periods of 10 to 60 min. A very clear time shift between oscillations observed at various sites suggests that the disturbance propagated from north to south (Fig. 19).

The generation mechanism of such waves is thought to be related to Proudman resonance resulting from a rapidly propagating low-pressure system (RABINOVICH, 2008). MONSERRAT *et al.* (2006) proposed that the international community considers adopting a general term independent of geographic location to describe such oscillations. The term "meteorological tsunami" seems to be the best. It is important to distinguish very clearly the difference between "meteorological tsunamis" and storm surges, since the latter have periods from several hours to several days, while the former have the same periods as ordinary tsunami waves (from a few minutes to a few hours). Tsunami catalogues often contain a number of events described as "probably of meteorological origin."

Meteorological tsunami of July 13, 2007. A second meteorological tsunami event occurred on the morning of July 13, 2007. It was first noticed in the record of the Patricia Bay station during the daily quality control check of that station's data. Later in the day a call was received from a resident of Thetis Island, located about 37 kilometres north of Patricia Bay, asking if a tsunami had occurred that morning at about 5:15 PDT (12:15 UTC). Anomalous oscillations are clearly seen in the observed water level records for Patricia Bay and Victoria, and are also identifiable in the record for Tofino (Fig. 20). There was no earthquake at that time that could have directly or indirectly produced a tsunami.

During the final preparation of this paper another meteorological tsunami occurred in the region on February 25, 2008. This event is similar to the event of December 9, 2005; significant tsunami-like oscillations of non-seismic nature were observed at several stations of British Columbia and Washington. Atmospheric pressure records found for the period of this event indicate that these oscillations were induced by a sharp pressure jump of $\sim$1 hPa.

In general, it appears that meteorological tsunamis are quite common in this region. Their examination is crucial because of two important reasons: (1) The necessity to distinguish meteorological tsunamis from ordinary tsunamis, to reduce the number of false alarms and to improve the Tsunami Warning System; (2) to avoid possible risk associated directly with meteorological tsunamis: for example a recent destructive meteorological tsunami on June 25, 2006 produced 30 million euros of damage on Menorca Island, Western Mediterranean (MONSERRAT *et al.*, 2006; RABINOVICH, 2008).

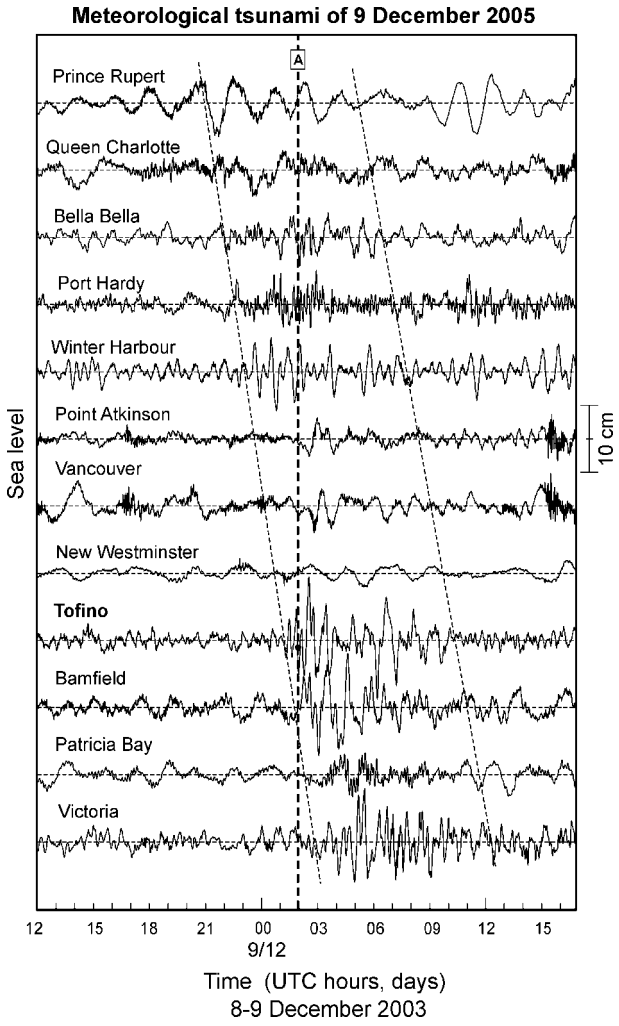

Figure 19

The meteorological tsunami of December 9, 2005 recorded at the B.C. PWLN and Tsunami Warning stations. The non-tidal signal triggered the automatic tsunami alarm of the Tofino tide gauge. The dashed line with the label "A" marks the time of that automatic alarm. The station plots are ordered by latitude (from north to south.).

5. Discussions and Conclusions

Sixteen tsunamis have been measured at locations on the British Columbia coast over the past 15 years. None of these tsunamis were destructive or placed coastal communities at risk, however, these events have provided valuable information on the character of tsunamis at a number of coastal locations and also the performance of our instrumentation

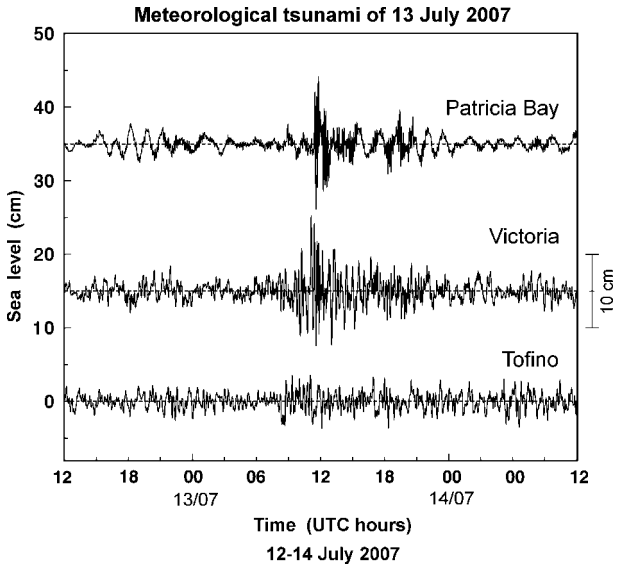

Figure 20
The meteorological tsunami of July 13, 2007 observed at 3 tide gauges on the B.C. coast.

at some of the stations. This information has resulted in modifications to our coastal network and to the measuring systems at some of those locations.

These data have verified that the Tsunami Warning stations at Tofino and Winter Harbour on the west coast of Vancouver Island and the PWLN station at Bamfield are reliable indicators of tsunamis from both regional and far-field events. Most tsunami events are also recorded at Victoria and Port Hardy, however, at each of these stations the signal is smaller and/or not as timely due to the location of the station. The station at Port Alberni, which had been shut down for almost 10 years, has now been reactivated and will be an excellent station for detecting and measuring future tsunamis.

The Tsunami Warning station at Langara Point has been moved to a new location at Henslung Cove and in this new location appears to respond well to tsunami events. More time is required to fully assess the response of this station to a number of tsunami scenarios.

The Tofino station operates well if properly maintained. Insufficient maintenance has affected the quality of the station record in the past and this may be the case during the period 1994–1996 when four tsunami events were recorded. More investigation will be required to determine if this is in fact the case and to determine if any other tsunami events are likely to have been under measured.

The detection and measurement of tsunamis on the B.C. coast is challenging because the range of tide is large and at many locations in harbours or inlets seiching is a common phenomenon. The modern instrumentation, with higher sample rates and better

resolution, and the data analysis tools have significantly improved our ability to detect and analyse tsunami events. The automated detection algorithm on the Tsunami Warning station gauge at Tofino alerted us to the meteorological tsunami event on December 9, 2005 and should be effective for other meteorological or landslide-generated tsunami. Consideration should be given to incorporating this algorithm into the software of all stations in the B.C. network. Incorporating microbarometers into some of the Tsunami Warning and PWLN stations would also increase our ability to detect and analyse meteorological tsunami events.

The NEPTUNE cable-linked seafloor observatory is presently being installed off the B.C. coast. While not specifically designed as a tsunami warning system, the NEPTUNE tsunami array will contribute substantially to our understanding of tsunamis and their propagation off western North America.

In addition to the residual plots (tidal signal removed) included in this paper, frequency-time plots and plots showing the spectra of background and tsunami oscillations at the tide gauge locations have also been extremely valuable tools for understanding these tsunami events. Space precludes including some of this material in the paper, however, examples are available in other publications (e.g., RABINOVICH *et al.*, 2006a, 2006b, 2008b).

The new tide gauge hardware has been in operation since early 1999. During this period the data return has been in excess of 99.6% from the network. The present network is reliable, and the data it provides are accurate and timely. It is important to note that most of the tsunamis recorded on the B.C. coast have trough-to-crest heights less than 20 cm, and over the last 37 years none have had heights greater than 40 cm. When a potentially tsunamigenic earthquake occurs, the West Coast and Alaska Tsunami Warning Center (WC/ATWC) provides information on the location and magnitude of the event, as well as expected tsunami arrival times at various locations around the Pacific Coast. Soon after the predicted tsunami arrival time at a coastal location emergency response personnel expect to begin receiving information on the observed tsunami. Response staff must be able to quickly and accurately estimate the wave heights of arriving waves, determine if the measured signals are tsunami or merely atmospherically generated seiches, and assess the danger of the arriving waves for the coastal communities. That information must then be passed to the WC/ATWC and to local emergency response personnel.

Acknowledgements

We are grateful to Don Jodrell, Canadian Hydrographic Service for helping with Figure 1. We would like to thank Prof. Kenji Satake, Editor, and our reviewers, Drs. Liujuan Tang and Timothy Walsh for their valuable comments and suggestions. Partial support for Alexander Rabinovich was provided by the Russian Foundation on Basic Research (RFBR) grant, Project 08–05-13582-ofi-c.

REFERENCES

ABE, K. (1979), *Size of great earthquakes of 1837–1974 inferred from tsunami data*, J. Geophys. Res. *84*, 1561–1568.

BATTJES, J.A. (1988), *Surf-zone dynamics*, Annual Rev. Fluid Mech. *20*, 257–293.

BORNHOLD, B.D., HARPER, J.R., MCLAREN, D., and THOMSON, R.E. (2007), *Destruction of the First Nations village of Kwalate by a rock avalanche-generated tsunami*, Atmosphere-Ocean *45*(2), 123–128.

CLAGUE, J.J. and BOBROWSKY, P.T. (1999), *The geological signature of great earthquakes off Canada's west coast*, Geoscience *26*(1), 1–15.

CLAGUE, J.J. (2001), *Tsunamis.* In *A Synthesis of Geological Hazards in Canada* (ed. Brooks, G.R.) Geol. Surv. Canada, Bulletin *548*, 27–42.

CLAGUE, J.J., MUNRO, A., and MURTY, T. (2003), *Tsunami hazard and risk in Canada*, Natural Hazards *28*(2–3), 433–461.

EMERY, W.J. and THOMSON, R.E. *Data Analysis Methods in Physical Oceanography*, 2nd and Revised Edition (Elsevier, Amsterdam, 2003) 638 pp.

EVANS, S.G. (2001), *Landslides*. In *A Synthesis of Geological Hazards in Canada* (ed. Brooks, G.R.) Geol. Surv. Canada, Bulletin *548*, 43–79.

FINE, I.V., CHERNIAWSKY, J.Y., RABINOVICH, A.B., and STEPHENSON, F.E. (2008), *Numerical modeling and observations of tsunami waves in Alberni Inlet and Barkley Sound, British Columbia*, Pure Appl. Geophys. *165*(11–12), 2019–2044.

GONZÁLEZ, F.I., MADER, C.L., EBLE, M.C. and BERNARD, E.N. (1991), *The 1987–88 Alaska Bight tsunamis: Deep ocean data and model comparisons*, Natural Hazards *4*, 119–139.

GONZÁLEZ, F.I. and KULIKOV, E.A. (1993), *Tsunami dispersion observed in the deep ocean*, In *Tsunamis in the World* (ed. Tinti, S.) (Kluwer Acad. Publ., Dordrecht 1993), pp. 7–16.

HEBENSTREIT, G.T. and MURTY, T.S. (1989), *Tsunami amplitudes from local earthquakes in the Pacific Northwest region of North America. Part 1: The outer coast*, Marine Geodesy *12*, 189–209.

KANAMORI, H. (1972), *Mechanism of tsunami earthquakes*, Phys. Earth Planet. Int. *6*, 346–359.

LANDER, J. (1996), *Tsunamis affecting Alaska: 1737–1996*, USDC/NOAA, Boulder, CO, 195 pp.

LANDER, J. (2003), *Two decades of global tsunamis: 1982–2002*, Science of Tsunami Hazards *21*(1), 3–88.

MILLER, G.R., MUNK, W.H., and SNODGRASS, F.E. (1962), *Long-period waves over California's borderland. Part II, Tsunamis*, J. Mar. Res. *20*(1), 31–41.

MONSERRAT, S., VILIBIĆ, I., and RABINOVICH, A.B. (2006), *Meteotsunamis: Atmospherically induced destructive ocean waves in the tsunami frequency band*, Natural Hazards Earth Syst. Sci. *6*, 1035–1051.

MURTY, T.S. (1979), *Submarine slide-generated water waves in Kitimat, British Columbia,* J. Geophys. Res. *84*(C12), 7777–7779.

MURTY, T.S. (1992), *Tsunami threat to the British Columbia coast*, Geotechnique and Natural Hazards, BiTech. Publ., Vancouver, BC, 81–89.

OKAL, E.A., DENGLER, L., ARRAYA, S., *et al*. (2002), *Field survey of the Camaná, Peru tsunami of June 23, 2001,* Seism. Res. Lett. *73*(6), 907–920.

ORTIZ, M., GONZÁLEZ, J.I., RAMÍREZ-MONDRAGÓN, N.A., and FARRERAS, S.F. (2003), *Quick field survey of the 22 January 2003 (M 7.8) Colima-Mexico earthquake-tsunami*, Tsunami Newsletter *35*(1), 3–5.

RABINOVICH, A.B. (2008), *Seiches and harbour oscillations.* In *Handbook of Coastal and Ocean Engineering* (ed. Kim, Y.C.) (World Scientific, Singapore) (in press).

RABINOVICH, A.B. and STEPHENSON, F.E. (2004), *Longwave measurements for the coast of British Columbia and improvements to the tsunami warning capability*, Natural Hazards *32*(3), 313–343.

RABINOVICH, A.B., THOMSON, R.E., BORNHOLD, B.D., FINE, I.V., and KULIKOV, E.A. (2003), *Numerical modeling of tsunamis generated by hypothetical landslides in the Strait of Georgia, British Columbia*, Pure Appl. Geophys. *160*, 1273–1313.

RABINOVICH, A.B., THOMSON, R.E., and STEPHENSON, F.E. (2006a), *The Sumatra Tsunami of 26 December 2004 as observed in the North Pacific and North Atlantic Oceans*, Surveys in Geophysics *27*, 647–677.

RABINOVICH, A.B., STEPHENSON, F.E., and THOMSON, R.E. (2006b), *The California Tsunami of 15 June 2005 along the coast of North America*, Atmosphere-Ocean *44*(4), 415–427.

RABINOVICH, A.B., LOBKOVSKY, L.I., FINE, I.V., THOMSON, R.E., IVELSKAYA, T.N., and KULIKOV, E.A. (2008a), *Near-source observations and modeling of the Kuril Islands tsunamis of 15 November 2006 and 13 January 2007*, Advances in Geosciences *14*, 105–116. www.adv-geosci.net/14/105/2008/

RABINOVICH, A.B., THOMSON, R.E., TITOV, V.V., STEPHENSON, F.E., and ROGERS, G.C. (2008b), *Locally generated tsunamis recorded on the coast of British Columbia*, Atmosphere-Ocean *46*(3), 343–360.

RAPATZ, W.J., and MURTY, T.S. (1987), *Tsunami warning system for the Pacific Coast of Canada*, Marine Geodesy *11*, 213–220.

TANIOKA, Y., HIRATA, K., HINO, R., and KANAZAWA, T. (2004), *Slip distribution of the 2003 Tokachi-oki earthquake estimated from tsunami waveform inversion*, Earth Planets Space *56*, 373–376.

THOMSON, R.E. (1981), *Oceanography of the British Columbia Coast*, Can. Spec. Publ. Fish. Aquat. Sci. *56*, Ottawa, 291 pp.

TITOV, V.V., GONZÁLEZ, F.I., BERNARD, E.N., EBLE, M.C., MOFJELD, H.O., NEWMAN J.C., and VENTURATO, A.J. (2005a), *Real-time tsunami forecasting: Challenges and solutions*, Natural Hazards *35*, 41–58.

TITOV, V.V., RABINOVICH, A.B., MOFJELD, H., THOMSON, R.E., and GONZÁLEZ, F.I. (2005b), *The global reach of the 26 December 2004 Sumatra tsunami*, Science *309*, 2045–2048.

WIGEN, S.O. (1983), *Historical studies of tsunamis at Tofino, Canada.* In *Tsunamis—Their Science and Engineering* (eds. Iida K. and Kawasaki, T.) (Terra Sci. Publ. Comp., Tokyo, Japan, 1983), pp. 105–119.

WIGEN, S.O. and WHITE, W.R.H. (1964), *Tsunami of March 27–29, 1964, West coast of Canada*, Report, Department of Mines and Technological Surveys.

YEH, H., TITOV, V., GUSIAKOV, V., PELINOVSKY, E., KHRAMUSHIN, V., and KAISTRENKO, V. (1995), *The 1994 Shikotan earthquake tsunamis*, Pure Appl. Geophys. *144*, 855–874.

(Received April 14, 2008, accepted July 6, 2008)

Pure appl. geophys. 166 (2009) 211–232
0033–4553/09/010211–22
DOI 10.1007/s00024-008-0439-0

Pure and Applied Geophysics

The 15 August 2007 Peru Earthquake and Tsunami: Influence of the Source Characteristics on the Tsunami Heights

HÉLÈNE HÉBERT,[1] DOMINIQUE REYMOND,[2] YANN KRIEN,[1] JULIEN VERGOZ,[1] FRANÇOIS SCHINDELÉ,[1] JEAN ROGER,[1] and ANNE LOEVENBRUCK[1]

Abstract—The tsunami caused by the 2007 Peru earthquake (M_w 8.0) provoked less damage than by the seismic shaking itself (numerous casualties due to the earthquake in the vicinity of Pisco). However, it propagated across the Pacific Ocean and small waves were observed on one tide gauge in Taiohae Bay (Nuku Hiva, Marquesas, French Polynesia). We invert seismological data to recover the rupture pattern in two steps. The first step uses surface waves to find a solution for the moment tensor, and the second step uses body waves to compute the slip distribution in the source area. We find the slip distribution to consist of two main slip patches in the source area. The inversion of surface waves yields a scalar moment of 8.9 10^{20} Nm, and body-wave inversion gives 1.4 10^{21} Nm. The inversion of tsunami data recorded on a single deep ocean sensor also can be used to compute a fault slip pattern (yielding a scalar moment of 1.1 10^{21} Nm). We then use these different sources to model the tsunami propagation across the Pacific Ocean, especially towards Nuku Hiva. While the source model taken from the body-wave inversion yields computed tsunami waves systematically too low with respect to observations (on the central Pacific Ocean DART buoy as on the Polynesian tide gauge), the source model established from the surface-wave inversion is more efficient to fit the observations, confirming that the tsunami is sensitive to the low frequency component of the source. Finally we also discuss the modeling of the late tsunami arrivals in Taiohae Bay using several friction coefficients for the sea bottom.

Key words: Seismological source, Moment tensor inversion, Body-wave inversion, DART inversion, Tsunami numerical modeling, Pacific Ocean, French Polynesia.

1. Introduction and Objectives

On August 15, 2007, at 23:40 UTC, a M_w 8.0 earthquake occurred off the Peruvian coast on a shallow portion of the subduction zone where the Nazca plate subducts beneath the South American plate at a rapid convergence rate of about 6.5 to 7.0 cm/yr (KENDRICK *et al.*, 2003). In addition to numerous casualties and severe damage in the region of Pisco, the sea-floor displacement associated to the quake triggered a destructive tsunami, as normal given the earthquake magnitude and such a shallow hypocentral depth. The run-up reported along the coastline measured up to almost 10 m locally, and on average 3 to 5 m along at least 100 km of the Peruvian coast (SLADEN *et al.*, 2007c; FRITZ *et al.*, 2008; http://www.eeri.org/lfe/pdf/peru_coast_tsunami.pdf).

[1] CEA, DAM, DIF, F-91297 Arpajon, France.
[2] Laboratoire de Géophysique, CEA, BP 640, 98713 Papeete, Tahiti, French Polynesia.

This event occurred in an area frequently struck by major thrusting events, immediately north to the 12 November, 1996 M_w 7.7 earthquake. Further southward, the 1868 historical seismic gap has been partly ruptured by the M_w 8.4 23 June 2001 earthquake, however the identified gap may correspond to a magnitude 9 event as in 1868 (DORBATH *et al.*, 1990). This seismic gap, together with the nearby gap corresponding to the North Chile 1877 earthquake (DELOUIS *et al.*, 1997; CHLIEH *et al.*, 2004), constitute large areas expected to produce major earthquakes (COMTE and PARDO, 1991). Such being the case, the 2001 Peru earthquake seems to have ruptured a significant part of the 1868 gap, while the 1877 remains unbroken (Fig. 1).

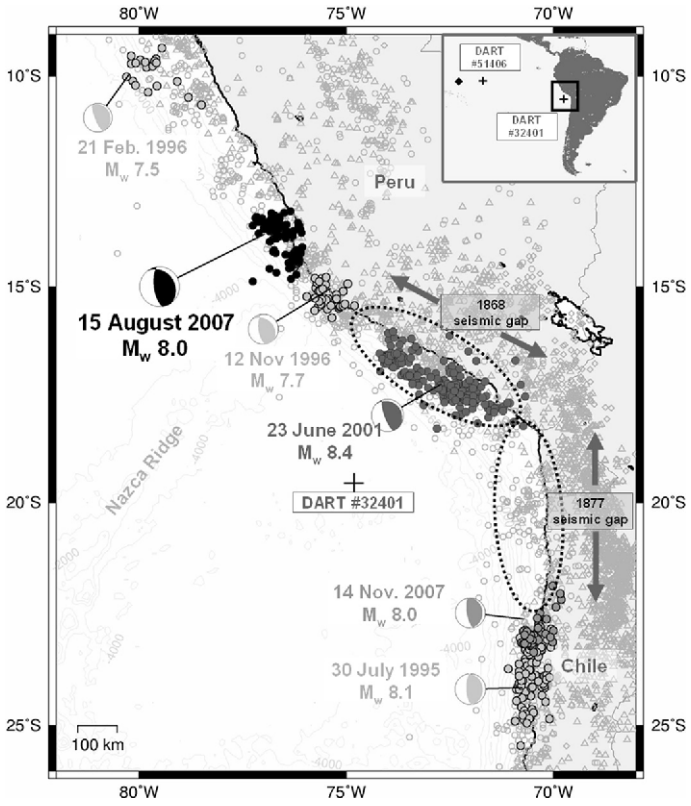

Figure 1

Context of the Peru-Chile border subduction zone, with recent major seismic ruptures highlighted. Background subduction seismicity in grey is taken from USGS NEIC catalogue, with a symbol depending on the focal depth (circle, $z < 50$ km, triangle, $50 < z < 150$ km, and diamond, $150 < z < 500$ km). For each major event displayed, one-year aftershocks are plotted, defining the extent of the rupture (taken from USGS database). Ellipses recall the historical seismic gaps, the 1877 still devoid of recent ruptures, except with the recent 14 November, 2007 event which may have started to fill the gap. Note the lack of shallow seismicity along the 1877 gap, contrasting with the high level of deep seismicity. DART sensors studied are also plotted with crosses. Inset shows the mean direction from the source area to the Marquesas (French Polynesia).

While it is well known which seismological parameters are relevant to issue a warning (location, seismic moment, and focal depth), the difficulty in determining the accurate level of impact and possible flooding for specific bays and harbors is real, particularly because the actual azimuth and rupture direction are difficult to define in the first minutes after the quake, and yet they define the area where the maximum impact is expected. Recent events in 2006 have also stressed the need for cautious appraisal of tsunami impact in remote sites, as was the case for Crescent City during the November 15, 2006 tsunami initiated in the Kuril Islands. The Marquesas Islands (French Polynesia) are among these remote far-field sites where the impact can be strong, but highly dependent upon the fault azimuth and rupture direction (HÉBERT *et al*., 2001a, b; OKAL and HÉBERT, 2007).

The dependence on relation with the seismic moment is the first-order aspect to take into account (TALANDIER and OKAL, 1989), however corrections including azimuthal influence and propagation distance are now considered (REYMOND *et al*., 2007) to help define more accurately the expected level of tsunami impact. In addition, the slip heterogeneities during the rupture may also influence the impact in the far field, as was already observed in the Indian Ocean (HÉBERT *et al*., 2007).

The 15 August 2007 event presents the opportunity to discuss the influence of the seismic rupture characteristics on the tsunami heights, especially in the far field. Seismic inversions have been performed to rapidly compute the moment and to obtain the slip distribution. Another insight to the earthquake source is also given by a simple inversion of the tsunami waves recorded on a single DART signal located off Chile. Then we compare tsunami heights computed in the far field (French Polynesia) using the various source models considered, and we emphasize the influence of the source characteristics on these water heights. Our results finally allow us to discuss the relevant parameters of the source that facilitate improvement of the tsunami hazard assessment, and that could be considered in the frame of real-time modeling.

2. *Seismological Overview of the 15 August 2007 Earthquake*

Given the magnitude and depth quickly determined on August 15, 2007, a tsunami information bulletin was first issued by the Pacific Tsunami Warning Center at 23:54 UTC, while the estimated magnitude was then only M_w 7.5. Subsequently an expanding regional warning (M_w 7.9) was issued at 00:19 UTC, based on the variable-period mantle magnitude M_m (OKAL and TALANDIER, 1989; REYMOND *et al*., 1991; SCHINDELÉ *et al*., 1995) (further information available on http://www.prh.noaa.gov/ptwc/messages/pacific/2007/).

Meanwhile in Tahiti (French Polynesia) the TREMORS system, similarly based on M_m, provided at 00:35 UTC a rapid estimation of the seismic moment corresponding to M_w 8.1. The Polynesian Tsunami Warning System (CPPT: Centre Polynésien de Prévention des Tsunamis) then issued a yellow warning bulletin for the Marquesas Islands at 00:57 UTC. While the PTWC finally cancelled the warning at 02:10 UTC, the

warning in Polynesia was revised to the orange level at 03:50 UTC for the Marquesas, since these islands are well known to amplify tsunami waves coming from Chilean and Peruvian subduction earthquakes. Finally the alert was cancelled at 11:30 UTC, two hours after the arrival of the waves. During the watch level, only coastal sites and light boats have been evacuated. No damage was observed.

2.1 PDFM Inversion

A method of quick inversion of seismic moment tensor using very small data sets (named PDFM: Preliminary Determination of Focal Mechanism) started in 1997 with the goal of deriving early focal mechanism solutions for strong earthquakes in the context of tsunami warning. Good knowledge of the seismic source is obviously of crucial importance in tsunami warning because the tsunami excitation is strongly dependent on focal depth, earthquake size (seismic moment), and fault geometry. The method is based on the early suggestion by ROMANOWICZ and SUAREZ (1983), that focal solutions can be obtained by inverting only spectral amplitudes of mantle waves (and discarding the phase information). It has been verified (REYMOND and OKAL, 2000) that this approach is particularly robust with respect to uncertainties in epicentral location and exact origin time; these parameters being relatively imprecise under real-time operational conditions. The cost of working with modulus of spectra is an indeterminacy of 180 degrees in strike and slip angles that can be lifted by considering a few critical first motion polarities. The PDFM method also had been applied to study large historical earthquakes such as the great Banda Sea earthquake of February 1, 1938 (OKAL and REYMOND, 2003), for which no definitive focal mechanism has been published. Precise timing corrections are not available for these historical earthquakes; such technical limitations constitute an obstacle for standard CMT inversions which use the phase velocity, but is not problematic for the PDFM method which needs only spectral amplitude without the phase information.

For the 15 August, 2007 earthquake PDFM inversion, 48 stations from IRIS were used (Fig. 2). The inversion itself was made between 114 s and 293 s, using a total of 576 spectral amplitudes, originating from 48 Rayleigh waves and 24 Love waves (the signals were checked visually, and those showing bad signal-to-noise ratios on the horizontal components were removed manually). Details of the inversion process are explained in previous works (REYMOND and OKAL, 2000). The spectral amplitudes of Rayleigh and Love waves are related through a nonlinear system to the components of the moment tensor and of the excitation coefficients of the surface waves, computed with the PREM model (DZIEWONSKI and ANDERSON, 1981). The signals are corrected from the propagation, using a regionalized earth model of $10° \times 10°$ degrees, in 7 tectonic regions (similar to correction of distance in the computation of mantle magnitude M_m, see OKAL and TALANDIER, 1989).

The nonlinear system is solved iteratively, using the generalized inversion method of TARANTOLA (1987); the quality of the inversion is controlled with the condition number defined by the ratio of the largest to the smallest eigenvalue of the model matrix of partial

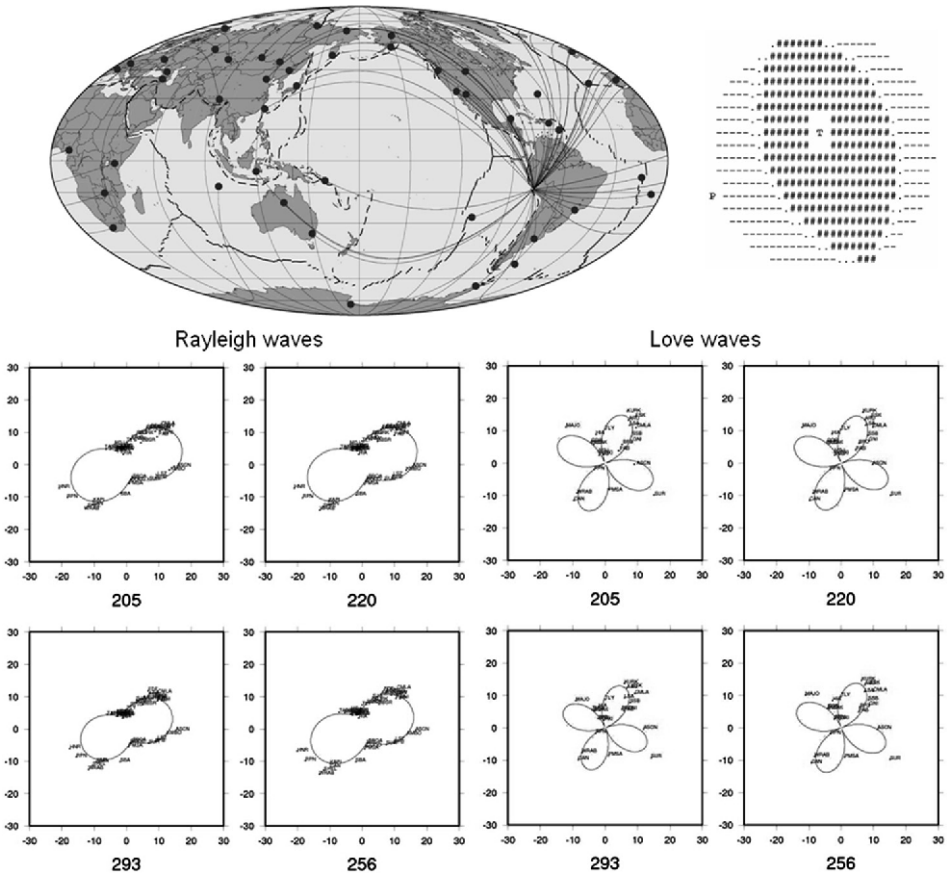

Figure 2

Preliminary Determination of Focal Mechanism (PDFM) inversion based on 48 stations (location on top). The solution yields a best double couple moment of 8.9 10^{20} Nm, with principal axes (T) Val = -8.76 10^{20} Nm, Plg = 83°, Azm = 30°, (N) Val = -0.2210^{20} Nm, Plg = 4°, Azm = 157°, and (P) Val = 8.98 10^{20} Nm, Plg = 006, Azm = 248, corresponding to nodal planes NP1 (strike = 343° dip = 39° slip = 97°) and NP2 (strike = 154° dip = 51° slip = 84°). The quality of the solution obtained is verified by comparing the radiation patterns at the source, at several periods, to the observed spectral amplitudes calculated in the stations used. Since the representation is made in the frequency domain, the units are in cm; the graphics are the same for both Rayleigh and Love waves.

derivatives (relative to the moment tensor elements). Since the result of the inversion is the moment tensor itself, the principal axes of constraint are solved as the eigenvectors of the moment tensor, and the best double couple gives the scalar moment M_0; the nodal planes are then computed from the (T) and (P) axis.

It is also worth mentioning that the PDFM method (like other published CMTs) calculates only the focal geometry and scalar moment, but not the slip distribution along the fault; consequently an average uniform slip over the entire fault area is assumed. This remark is important for the next, because the earth surface deformation computed

with this homogeneous slip model (with OKADA's formula, 1985) is injected as the static displacement in tsunami simulation.

Results for the Peruvian earthquake of 15 August, 2007 are summarized on Figure 2. Without surprise, the mechanism is a quasi-pure thrust faulting (rake 97°), with the principal nodal plane that corresponds approximately to the plane defined by the subduction zone.

The Centroid Moment Tensor determined at Harvard (http://www.globalcmt.org/) exhibits a strike (324°) more consistent with the mean trench direction than the azimuth found in PDFM inversion (343°). This could be explained by the fact that the inversion is made at a very long period, and thus integrates the multiple sources that can occur: the resulting fault plane solution would be an average of the smaller ones. The CMT dip angle (24°) is also less steep than that of the PDFM (39°), the latter, again could be more representative for the deeper part of the subduction.

Despite an ill-conditioned resolution (the condition number is equal to 342), it has also been possible to determine the focal depth from the residual errors computed at several focal depths, and retaining the depth corresponding to the smallest value of residuals, thus 40 km.

2.2 Body-wave Inversion

Body waves recorded on teleseismic broadband stations allow recovery of the fault characteristics (focal mechanism, depth and duration of the rupture, slip distribution and rupture velocity). The method employed here (VALLÉE and BOUCHON, 2004) considers the rupture as a succession of slip patches breaking at different velocities. As it is very simple to implement, this method is routinely used after large events, and provides interesting characteristics especially for tsunami warning.

We use 16 IRIS stations with epicentral distances from 35° to 90° and well sampled various azimuths for this body-wave inversion. Signals are bandpass-filtered between 120 s and 40 s, and the misfits are calculated on 170 s windows for P waves, 210 s windows for SH waves. The rise time is assumed to be the same for each subfault, and fixed to 12 s.

In this 2-patch inversion, 12 parameters are inverted: the small and large axes of the 2 elliptic patches (2×2 parameters), the slip and rupture velocity for each patch (2×2 parameters) and the position of the center of each patch relative to the hypocenter (2×2 parameters).

The fault geometry used here is fixed using the mean parameters of the CMT solution, thus with a 27° dip angle, and a 324° azimuth of the fault. The hypocentral depth was fixed to 37 km. Then each patch axes and slip value is retrieved on 5×5 km^2 sub-fault planes. In addition a mean rupture velocity is also determined using the rise times found for each patch. For early warning purposes, the method can also be implemented without waiting for the CMT solution. In that case it relies on a preliminary low frequency estimation that is subsequently refined with a higher frequency approach, on two patches

if necessary; the entire process can be achieved within less than 30 minutes after the main shock.

We find here two main slip patches (Fig. 3) with values locally reaching more than 9 m, and yielding a seismic moment of 1.4 10^{21} Nm, consistent with M_w 8.0 (a 35 Nm^2 rigidity is used). The southernmost patch is actually close to the city of Pisco where the strongest damage occurred. We also note that both patches are defined in areas where the rate of aftershocks is rather low. The relationship between aftershock activity and coseismic slip on asperities has been debated recently in the Indian Ocean (HSU *et al*., 2006; KONCA *et al*., 2007). Although the seismological inversion here is only carried out to the first order, the highest slip areas similarly seem to be consistent with lower aftershock occurrence. Results of other body-wave inversions available (e.g., http://www.tectonics.caltech.edu/slip_history/2007_peru/pisco.html; Chen Ji (UCSB) and Yueha Zeng (NEIC): http://earthquake.usgs.gov/eqcenter/eqinthenews/2007/us2007gbcv/finite_fault.php) also highlight these two areas of high slip, although with a smoother pattern giving smaller slip values on larger patches.

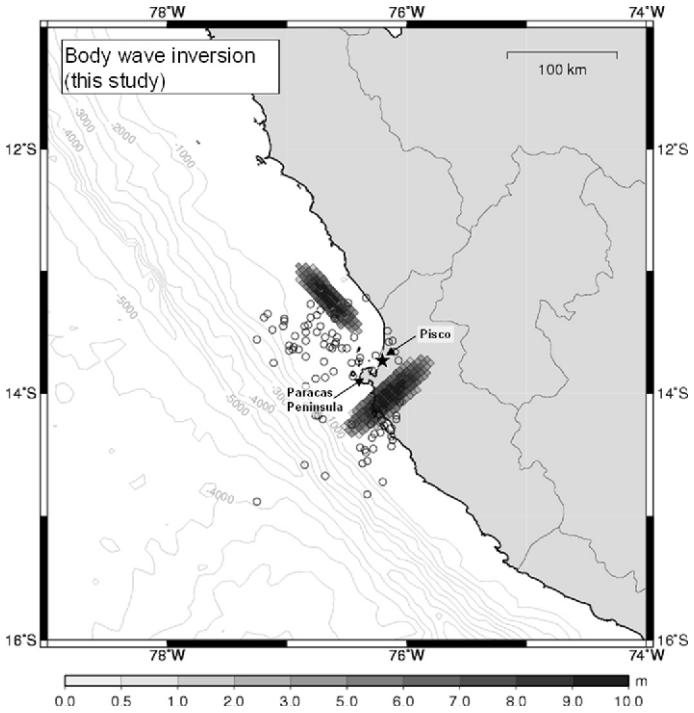

Figure 3

Slip distribution on the fault plane obtained by inversion of teleseismic body waves. The fault geometry is derived from the CMT solution (http://www.globalcmt.org/) and the inversion yields the slip values and the rupture velocity. Open circles are the aftershocks determined by USGS during the first three months following the main shock. The southernmost patch, located south of Pisco, is consistent with the highest damage observed in the area.

Finally, we also observe that the mean direction defined by both patches is close to the azimuth defined in the PDFM inversion, thus oblique with respect to the trench axis, confirming the integration made by the latter approach that probably yields an integrated view of the main rupture patches.

3. Propagation of the 15 August 2007 Tsunami in Pacific Ocean

The seismological inversion of the earthquake retrieves the seismic moment and defines the main slip pattern on the fault. In this section, we show that the tsunami signal observed in the deep ocean can also be used to examine the fault pattern. Then we use the different earthquake sources presented to study the far-field impact of the tsunami in the Marquesas (French Polynesia).

3.1 Method of Tsunami Modeling

We assume here that the tsunami is triggered by the coseismic deformation of the seabottom, considered as instantaneous (1 to 2 minutes for this kind of magnitude) with respect to tsunami periods (from 15 to 30 minutes). This coseismic deformation is computed from a model of elastic dislocation (OKADA, 1985), as a function of the fault geometry and ground elastic parameters. The fault parameters and the seismic moment M_0 are provided by the moment tensor analysis of seismic waves, and are related by $M_0 = \mu ULW$, where μ is the rigidity, U is the average slip amount and L (W) the length (width) of the fault plane.

Since tsunami wavelengths (hundreds of kilometers) are much larger than the ocean depth (a few kilometers), tsunamis are considered "long" or shallow water gravity waves. Under this assumption, the hydrodynamic equations describing the conservation of mass (1) and momentum (2) can be depth-averaged:

$$\frac{\partial(\eta + h)}{\partial t} + \nabla.[\mathbf{v}(\eta + h)] = 0, \tag{1}$$

$$\frac{\partial(\mathbf{v})}{\partial t} + (\mathbf{v}.\nabla)\mathbf{v} = -\mathbf{g}\nabla\eta + \sum \mathbf{f}, \tag{2}$$

where h is the sea depth and η the water elevation above the mean sea level, $\mathbf{v}$ is the depth-averaged horizontal velocity vector, $\mathbf{g}$ is the gravity acceleration and $\mathbf{f}$ additional forces such as bottom friction and Coriolis forces. Coriolis forces are usually negligible and bottom friction will be further discussed in the results.

In the shallow water theory, for small amplitudes and nondispersive propagation, the wave velocity c is simply given by $c = (gh)^{1/2}$, the long-wave celerity. When approaching the coasts, the water depth h decreases and the wave velocity slows. As periods remain approximately constant, wavelengths decrease and the conservation of energy in a smaller volume of water produces nonlinear waves with amplitudes of the

order of the water depth. This amplification effect (shoaling effect) is responsible for the large waves observed onshore, which can flood and devastate significant areas close to the shores.

Equations (1) and (2) are solved in spherical coordinates by means of a finite-difference method, centered in time, and using an upwind scheme in space (HEINRICH *et al*., 1998; HÉBERT *et al*., 2001a). To deal with shoaling and resonance effects close to the shores, tsunamis are simulated over a set of nested bathymetric grids characterized by an increased resolution close to the shores. The numerical stability is ensured under the Courant-Friedrich-Lewy condition defining the time step Δt such as $\Delta t << \Delta x/c$, where c is the wave velocity and Δx the grid cell dimension.

In this study we use five levels of imbricated grids to compute proper amplification in the Marquesas bays. The grids used have been briefly described in previous works, and have been validated for various scenarios allowing definition of hazard maps for the Marquesas (SLADEN *et al*., 2007a and 2007b). In addition to the 4' grid describing the ocean, derived from ETOPO2 dataset (SMITH and SANDWELL, 1997), they consist of a 1' grid describing the archipelago, a 300-m grid describing the surroundings of Nuku Hiva Island, a 60-m grid describing the approach to the Taiohae Bay and finally a 15-m grid describing the Taiohae bay. This latter high resolution grid includes topographic data allowing to compute runup, through a method extrapolating values on wet cells towards dry cells (KOWALIK and MURTY, 1993). Even though these grids are available for several bays in the Marquesas, we present here results for the Taiohae Bay, where the tide gauge recorded well the 2007 tsunami waves.

3.2 Constraints Given by the DART Sensors

The tsunami triggered by the 15 August 2007 Peruvian earthquake was well recorded by the Chilean DART 32401 (Deep-ocean Assessment and Reporting of Tsunamis) deployed off Chile (see location on Fig. 1), and operated within the frame of the Pacific Tsunami Warning System by the Chilean Hydrographic and Oceanographic Service of the Chilean Navy (SHOA). On the 15 August 2007, this DART sensor was the only one to record the tsunami in the ocean in this area close to the epicenter. The signal exhibits a 6-cm positive first wave confirming the propagation of significant tsunami waves in the ocean (Fig. 4a), and observed about 50 minutes after the quake. These data, compared to modeling results based on precomputed scenarios, enable the identification of the regions of highest tsunami exposure, a few hours after the main shock. For instance, 4 to 5 hours after the quake, the Short-term Inundation Forecasting for Tsunami (SIFT) delivered a map of maximum expected wave heights showing that French Polynesia was within one of the maximum lobes (now revised on http://nctr.pmel.noaa.gov/peru20070815.html; WEI *et al*., 2008).

A second DART system (DART 51406), located in the central Pacific Ocean (see location on Fig. 1) also recorded the tsunami waves, with peak-to-trough amplitudes not exceeding 4 cm (Fig. 4b). This record was however originally substantially noisier than

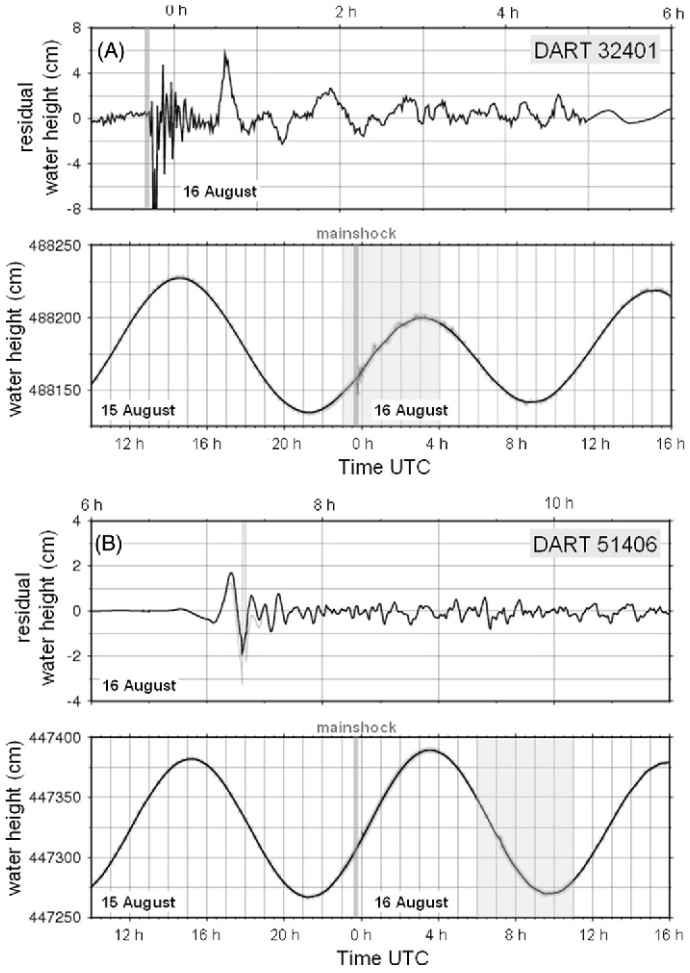

Figure 4

Tsunami records on two DART systems (Deep ocean Assessment and Reporting of Tsunamis) in the Pacific Ocean (see their location on Fig. 1). For each DART, the raw signal is displayed in the lower panel. The signal is filtered using a Gaussian filter removing periods larger than 120 min, and the residual is shown in each upper panel. The grey area in the bottom indicates the focus displayed on the upper panel. The time of the earthquake is recalled with the grey line. For DART 51406, some erroneous points occurring on the first trough were removed. High-frequency signals originally present in the dataset at the time of tsunami arrival were located at the present negative leading wave (around 7 h) (see text).

that recorded at DART 32401, and the recently revised signal available on the NOAA NDBC (National Data Buoy Center) surprisingly exhibited a negative leading wave while the original signal only contained a high-frequency signal probably related to the triggering of high-frequency acquisition when the tsunami waves arrive. Modeling results described later will also indicate that this negative leading wave may not be the actual

tsunami signal; all the more as the coseismic deformation due to a subduction earthquake is not expected to produce a negative leading wave oceanwards.

Our objective here was not originally to invert tsunami data to recover the fault pattern, since the records available do not favor a good azimuthal distribution, and detailed modelings in Peruvian bays where tide gauges could be available, and improve the coverage, require considerable effort beyond our purpose. However, preliminary tests on the single DART 32401 record showed that the inversion yielded an interesting fault pattern, not completely consistent with seismological inversions, however worthy of examination.

We defined 12 subfaults in the epicentral area, covering the aftershock area, characterized by 50 $\times$ 50 km^2 dimensions, and with a mean geometry close to those used in seismological inversions (using the focal geometry published by the Harvard CMT: strike 324°, dip 27° and rake 64°) (Fig. 5a). The Green's functions corresponding to each subfault were computed using the linear version of the equations, using here the 2' bathymetric grid taken from ETOPO2. Then the inversion to recover the slip distribution was simply performed using the Non-Negative Least-Square method which we already used in the Indian Ocean (SLADEN and HÉBERT, 2008).

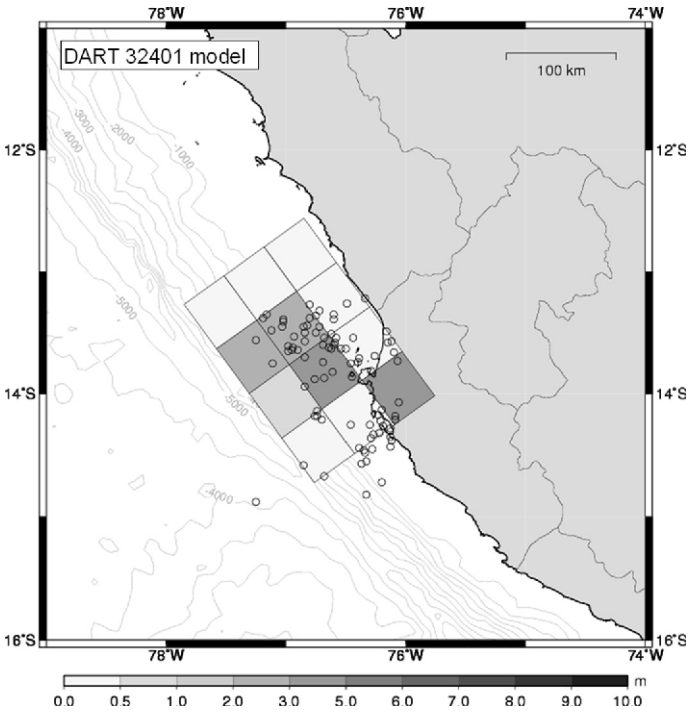

Figure 5
Slip values obtained when inverting the DART 32401 data on 50 $\times$ 50 km^2 subfaults. The slip pattern is significantly different from the one obtained in Figure 3, and concentrates considerable slip in shallower parts of the fault, although also in the area south of Pisco

Synthetical tests performed with the checkerboard approach underlined the need to use only the first waveforms of the DART signal (about 120 min). However, regardless of the approach and the time window used, the inversion was not robust for the deeper part of the fault involved, whereas the inversion led to a shallow pattern close to the one input for the shallowest sub-faults.

Using only the DART 32401 on a time window of 120 minutes, the obtained slip distribution (Fig. 5) does not appear to be extremely consistent with the body-wave seismological inversion. The common point is a high slip southwards of Pisco and the Paracas Peninsula, retrieved in most of the published seismological inversions. However, the average correlation between the low-slip area and the aftershock sequence almost disappears, and significant slip appears in the shallowest part of the source area. This may result from the poor robustness evidenced in synthetical tests as regards the deepest part of the fault. Thus contrary to the seismological inversion, one of the highest slip areas is in the shallowest portion of the fault, and, more generally, the sub-faults characterized by the highest slip values are complementary to those found using seismological data. The obtained model yields a seismic moment of $1.1\ 10^{21}$ Nm.

The tsunami waves due to the different earthquake and tsunami sources have been modeled and compared to the available data. The model derived from the DART inversion obviously does match very well the DART 32401 signal, for the 120 minutes considered in the inversion, and also for the subsequent long wavelength trends (Fig. 6) (the RMS obtained from the inversion process was smaller than 1 cm). By comparison, neither the PDFM nor the body-wave inversion is able to fit the first recorded peak of the tsunami, which exhibits a shorter period and a higher amplitude compared to the modeling results. Both seismological inversions indeed provide a zero-to-peak amplitude never exceeding 2 cm, compared to the 5 cm observed amplitude. These sources are thus unable to produce the high and narrow observed peak that probably arises from a shallow source.

3.3 Comparison with DART 51406

The data recorded by the DART 51406, of poorer quality, are not very satisfactorily fit by any of the models tested (Fig. 7). Whereas all models yielded arrival times rather correct for DART 32401, only the time arrival due to the body-wave inversion is close to the signal inception. However, as mentioned before, the signal of the DART 51406 is rather suspect in the minutes preceding the apparent arrival, and a 15-min shift in tsunami modeling, in deep water, is rather surprising. Thus we cast doubts on the quality of this record.

However, it is worth noting that for this DART record, the tsunami model using the body-wave inversion model (Fig. 7, middle) has already lost more energy than the tsunami model using the PDFM inversion as a source (Fig. 7, top): the amplitudes rather similar for both models on DART 32401 are now lower by at least 50% for the DART 51406. This confirms that this model may be characterized by shorter tsunami periods (shorter slip patches) that are less efficiently propagated across the ocean in a non-

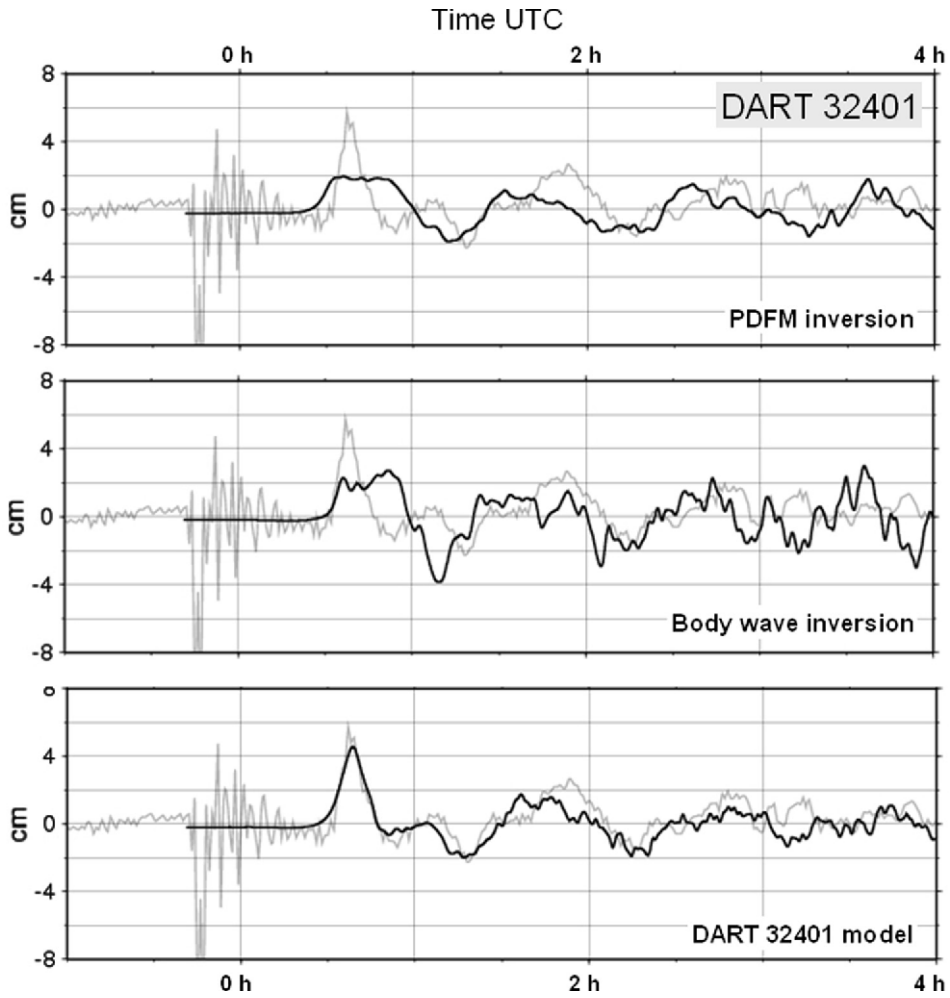

Figure 6
Comparison of tsunami modeling results with the tsunami observation on DART 32401, for various source models.

dispersive model. On the other hand, an average uniform slip along the entire fault (as assumed with PDFM) generates longer tsunami periods losing less energy in the far field. The model taken from the inversion of a single DART produces an amplitude apparently close to the one observed (Fig. 7, bottom).

3.4 Tsunami Pattern in the Pacific Ocean

The maximum water heights computed after 13 hours of propagation have been plotted (Fig. 8). They underline the less energetic tsunami when the model uses the

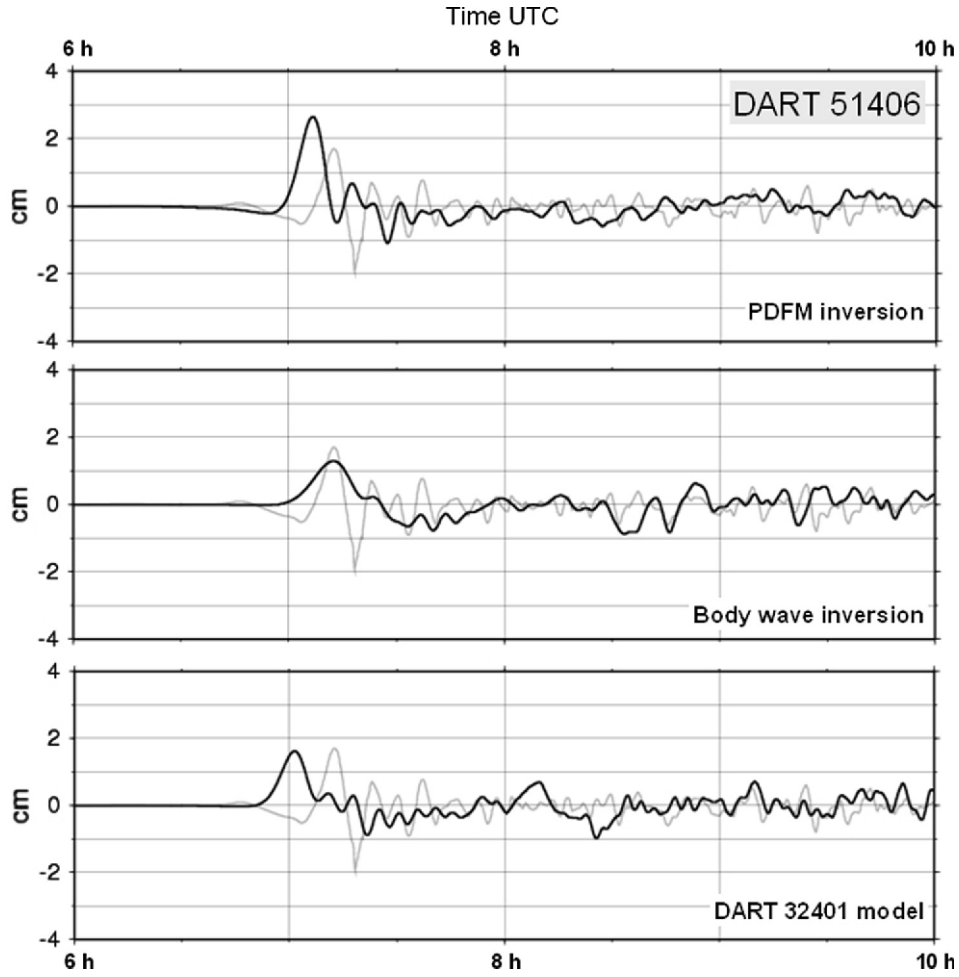

Figure 7
Same as Figure 6, for the central Pacific DART 51406. Note that all tsunami models exhibit a positive first arrival not consistent with the negative arrival obtained when the raw data are filtered and de-tided, casting doubt on this part of the observed signal.

results of the body-wave inversion as a source (Fig. 8, middle) which is associated with the smallest seismic moment retrieved. The most energetic model is derived from the PDFM inversion and also from the DART inversion, with both patterns being rather close. The PDFM model is weaker towards the region south to the source, probably due to the azimuth's inconsistency with tectonics, whereas the body wave and the DART models use an azimuth derived from CMT, more consistent with the subduction direction.

As usual, the bathymetric features characterizing the oceanic seafloor strongly guide the distribution of tsunami maximum values (HÉBERT *et al.*, 2001a, b and 2007), from the Nazca Ridge close to the source, to the alignments of the southeast Pacific. The fracture

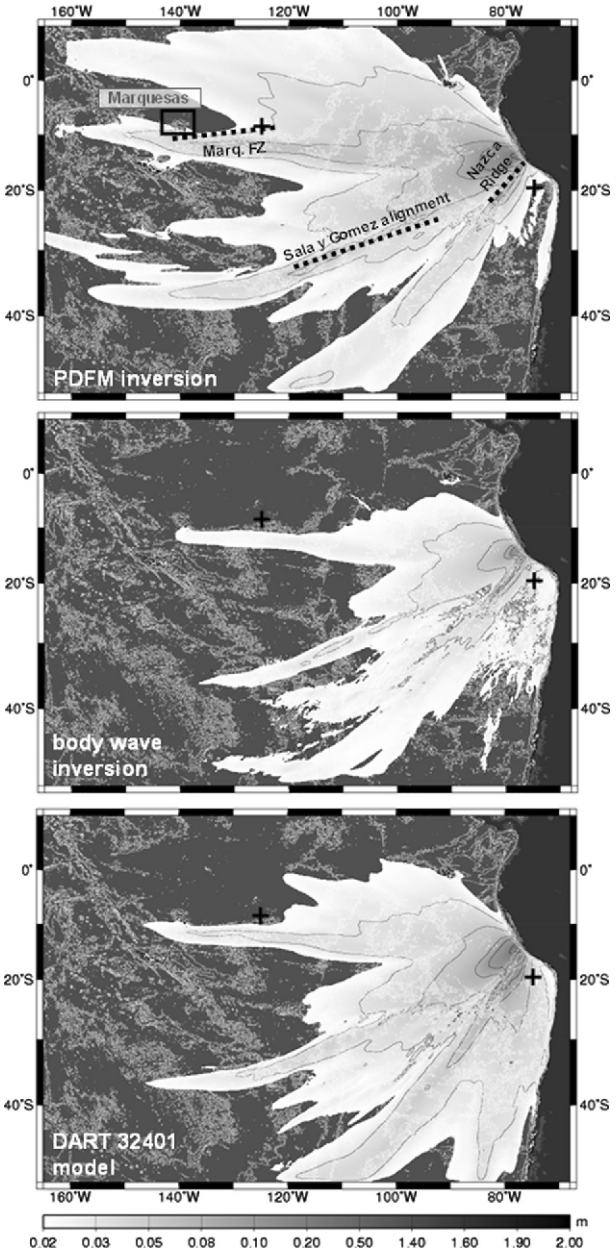

Figure 8

Maximum water heights in the Pacific Ocean, computed after thirteen hours of propagation, and for the three principal source models. The poorly constrained DART inversion is only slightly different from the pattern obtained using the PDFM inversion, except for the area south of the source area. The tsunami model based on the body-wave inversion is significantly lower.

zones also probably trap part of the tsunami energy, such as the Marquesas Fracture Zone that may catch one of the principal lobes just before its arrival in the archipelago (Fig. 8). The central lobe, present for all the sources, is probably influenced by a series of shallow, localized seamounts forming the Sala y Gomez alignment, that relay and favor the propagation of highest amplitudes.

Finally, the source taken from body-wave inversion (Fig. 8, middle) only radiates, moderately across the ocean, consistent with the results presented. As for all the models, the Nazca Ridge and Sala y Gomez alignment trap part of the energy at the beginning of the propagation and subsequentially towards the central Pacific Ocean.

4. Observations and Modeling Results in the Marquesas

4.1 Context

In French Polynesia, one of the most important natural hazards is the tsunami hazard, mainly arising from the central location of the Polynesian Islands in the Pacific Ocean, where transoceanic tsunamis occur several times a century (SCHINDELÉ *et al.*, 2006). Among the archipelagos, the Marquesas are the most sensitive to these long waves originating around the Pacific, because these high volcanic islands, contrary to the low atolls, are not protected by any coral reef and offer wide bays directly open towards the ocean. In addition, submarine slopes are very mild in the 0–200-m bathymetric range and favor the tsunami amplification when the wave celerity decreases close to the coast. In the 1990's several tsunamis originating from Japan, Peru, Chile and Mexico, caused varied damage in the Marquesas, from almost unnoticed (in 1994, from Kurile, and 1995, from Mexico), to a significant flooding (in 1995, from Chile and 1996, from Peru), especially in the Tahauku Bay (Hiva Oa) (GUIBOURG *et al.*, 1997; HEINRICH *et al.*, 1998; HÉBERT *et al.*, 2001a). As mentioned before, the key source parameter controlling the impact in the far field is the fault azimuth, posing a significant hazard level for tsunamis triggered in the Tonga, the Aleutian and the Peru-Chile events (HÉBERT *et al.*, 2001b; SLADEN *et al.*, 2007a, b). More generally, most of the major historical tsunamis triggered in these regions have been observed in the Marquesas (OKAL *et al.*, 2004; OKAL and HÉBERT, 2007; SCHINDELÉ *et al.*, 2006).

4.2 Observations

Within the Polynesian tsunami warning system operated in the frame of the basin-wide Pacific Tsunami Warning System, four tide gauges are deployed in harbors and designed for real-time transmission: one in Tahiti (Papeete harbor), one in Mangareva (Rikitea), and two in the Marquesas (Taiohae Bay in Nuku Hiva and Tahauku Bay in Hiva Oa). In August 2007, unfortunately only one gauge was recording, in Taiohae, with a sampling rate of 2 minutes.

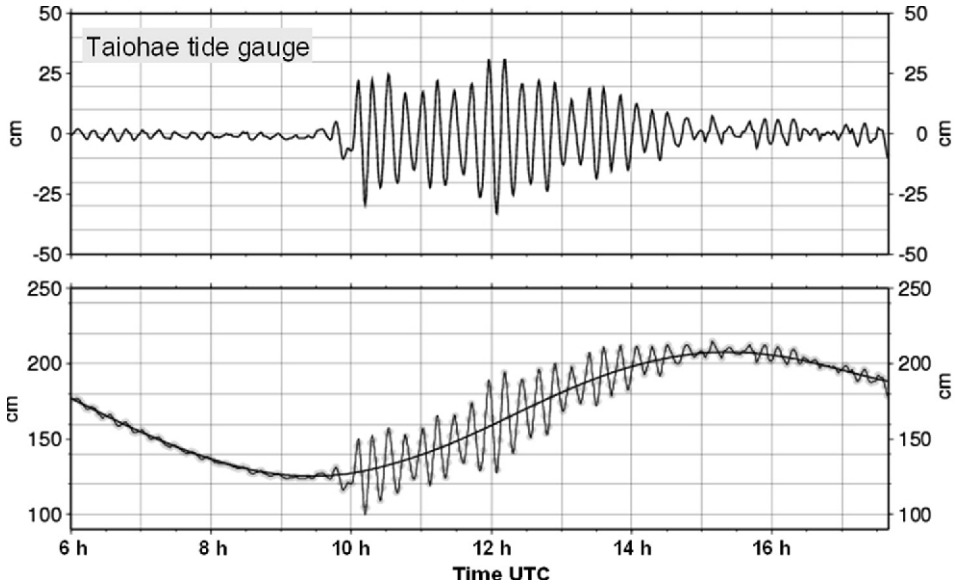

Figure 9
Tide gauge signal observed in Taiohae Bay (Nuku Hiva Island, Marquesas Archipelago) on 16 August. The raw signal (bottom) is de-tided using a Gaussian filter removing periods larger than 120 min (same as data in Fig. 4), yielding the residual (top). Note the duration of the signal amounting to about five hours.

The tsunami arrival is observed at low tide, at about midnight local time (10 h UTC on 16 August) (Fig. 9). When de-tided, the signal exhibits a series of waves with rather constant periods (about 15 min). This noteworthy monochromatic behavior has already been observed for this wide bay where the period of resonance always seems to be close to 15 minutes (HÉBERT *et al.*, 2001a). On the 15 August 2007, the peak-to-trough amplitudes reach 50 cm during the first 2 hours, and even 60 cm about 2 hours after the arrival. The tsunami arrivals last at least 4 hours, and clearly decrease after 5 hours. A relative increase of the amplitudes also occurs at about 12 h UTC, 2 hours after the first arrivals. This may reflect a delayed arrival due to scattered tsunami waves, and a detailed study of the animated, computed oceanic free surfaces indeed indicates that the Tuamotu Plateau located about 500 km southwest the Marquesas may be a good candidate for this secondary source.

4.3 Modeling Results in Taiohae (Nuku Hiva)

The model using the seismological PDFM inversion provides amplitudes rather close to the observed amplitudes, but for the 4 to 6 first waves (Fig. 10, top). Thereafter the amplitudes computed increase and exceed the observed signal by at least 40 to 50%. The tsunami waves computed using the source derived from body-wave inversion (Fig. 10, middle) are constantly too low for the first waves, and are close to the observation about

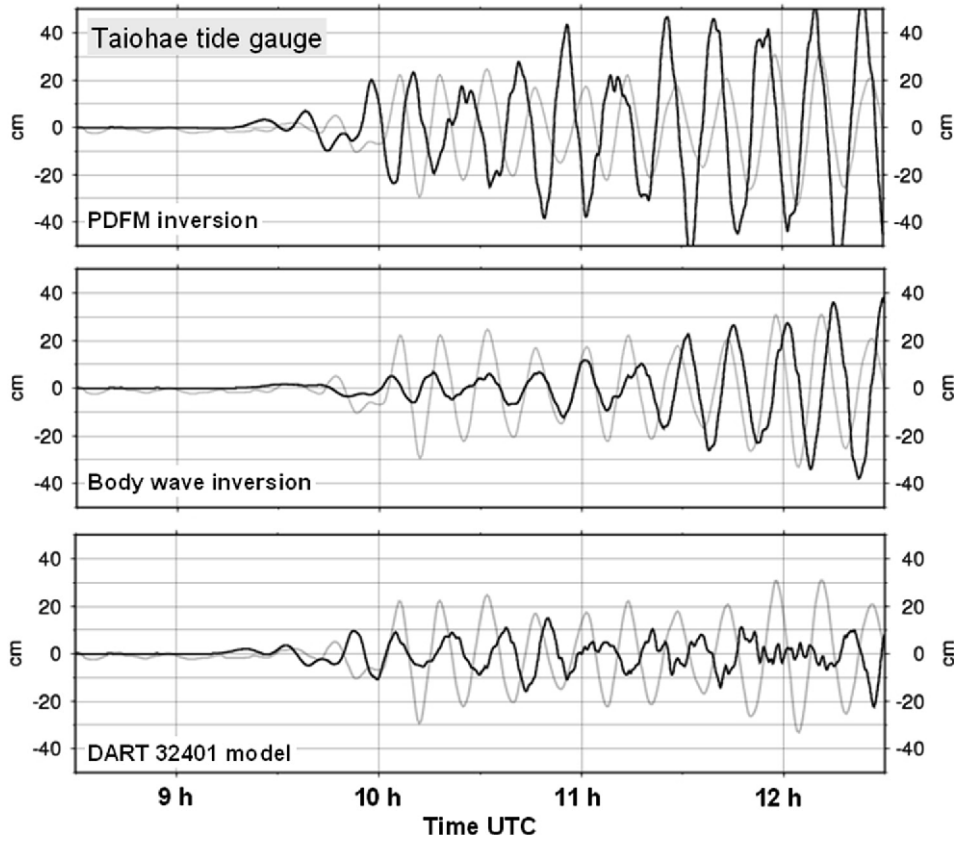

Figure 10
Comparison of the Taiohae signal with three different tsunami models. As in the Pacific Ocean, the model based on the body-wave inversion is too weak to explain the observations. Most of the models arrive too early compared to the observations, as was the case on the DART 51406 (see Fig. 51406).

90 minutes after the first arrival. The model derived from the single DART inversion is quite similar to the latter (Fig. 10, bottom), but keeps inadequately small amplitudes throughout the first 2 hours.

These results underline that the PDFM model accounts rather well for the observations, when the tsunami record is considered during the first 90 minutes. Due to numerical dispersion or instabilities, the model then excessively increases and cannot trustfully match the observations.

On the other hand the PDFM-and DART-based models, which explain most of the first amplitudes of the tsunami, arrive too early with respect to the observed signal (by at least 5 to 10 minutes), as was already the case on the DART 51406. This delay was not observed on the DART 32401 and may be related to particular local conditions unexplained to date.

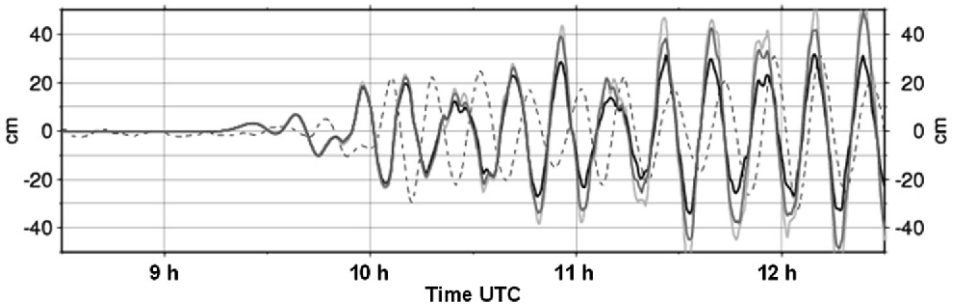

Figure 11
Effect of the friction term on the tsunami modeling in Taiohae Bay. The observation is displayed with the dashed line. The modeling results (solid lines) are plotted for a model without friction (light grey), with a Chezy coefficient of 20 (dark grey) and of 10 (black).

Finally we also took the opportunity to study the effect of bottom friction in the Taiohae harbor on the modeling results. Several formulations of the bottom friction exist in the literature; one of the most frequent involves the Chezy friction coefficient that depends on the Reynolds number and the seabottom roughness (LIU *et al.*, 1994). We tested here several values of the Chezy coefficient that are uniformly ascribed to the Taiohae Bay. For a Chezy coefficient of 30, the waveforms computed are not very different from the waveform computed without any friction, nonetheless the differences become significant as soon as the Chezy coefficient decreases to 20 (differences of 5 to 10%) and even to 10 (differences reaching 40%) (Fig. 11). The friction is more perceptible after the first tsunami waves (from 11 h UTC), when precisely the previous modeling results tend to overestimate the observations. Thus allowing for the seabottom friction may sound reasonable to improve the fit of late observations. Unfortunately, the Chezy coefficient required to improve this match is very low (10), and is usually considered only for areas covered with buildings or dense forests (MADER and CURTIS, 1991). Thus it is rather unlikely that such a coefficient is physically realistic in the Taiohae Bay, however it highlights the need for dissipation terms in our modeling of the late tsunami arrivals.

5. Discussion and Conclusion

This study allows us to discuss the main features of the 15 August 2007 earthquake that triggered a significant tsunami. The inversion of the seismic moment tensor provides a moment magnitude of 8.0 consistent with other results, and evidences a mean azimuth not strictly consistent with the regional trench direction. However, this azimuth is in proximity to the mean direction defined by the two main slip patches identified in the body-wave teleseismic inversion. This inversion yields an important patch just in the region south of Pisco, in good agreement with the major damage observed here, and a second patch confined to the deepest part of the trench, to the northwest of the first patch.

Although it should not be considered as too robust, the inversion of the single DART data having recorded the tsunami close to the source area has been carried out. The slip pattern obtained is disparate from the one obtained by the body-wave inversion, confirming the fact that the tsunami waves are obviously more influenced by the lower frequency component of the earthquake source, and not that sensitive to details less than 50 km in extent.

It may also be illusory to recover the slip pattern on the actual fault thanks to tsunami data only, especially with a single DART record. Indeed inversion of tsunami data should more likely be used to recover the initial seafloor deformation, since imaging the rupture on the fault plane implies additional uncertainties depending on the subduction zone characteristics, including many uncertainties on the sediment cover. The direct inversion of the seafloor deformation would avoid the construction of sub-fault fixed geometries that can be unsuitable for some earthquakes (either the geometry or the mechanical properties input in the elastic model). Regardless the tsunami modeling of the DART-derived source, though underestimating the observation, provides a valuable complement to the inversion of seismic moment tensor to improve the tsunami warning in the far field. To date the distribution of DART buoys is not homogeneous off the major subduction zones, although in the future, inversions including seismological, GPS and tsunami data, should greatly contribute to advancing the accuracy of tsunami warnings.

This study also allowed us to discuss the coastal impact of the tsunami in French Polynesia, where unfortunately only one tide gauge was able to record the waves. The observed wave train persists about five hours, with a relative maximum occurring two hours after the first arrival. These data are best fit using the model derived from the PDFM inversion, while the source model derived from the body-wave inversion and the DART inversion are rather excessively low. After the two first hours of signal, the best models overestimate the observations. Adding seafloor friction allows to improve the fit, however the coefficient that must be input is poorly realistic in terms of the nature of seafloor. These results remind us that tsunami modeling is usually correct for the first wave trains, and that our method requires additional dissipation for the subsequent wave trains.

In conclusion this study is also promising regarding the tools that can be developed for real-time tsunami warning. An efficient inversion of surface waves together with tsunami data should facilitate definition of a realistic source for the tsunami waves underway. The current computing capacity allows for the estimation of the sea-level heights in remote places in the first hours following the event, readily in advance with respect to the actual arrival, and the improvement of parallel computing should significantly decrease this computing duration to consider real-time computing as feasible in the shortterm. This, of course, should be complementary to the precomputed database, an element necessary for the inversion of tsunami data. Despite its complex rupture pattern, partially beneath the coast, the 2007 Peru earthquake gives some reliable indications towards this purpose, showing that the amplitudes of the remote first wave trains are well forecasted.

Acknowledgements

The original manuscript benefited from constructive reviews by S. Weinstein and S. Barrientos. This work was partly supported by French Agence Nationale de la Recherche under contract ANR-05-CATT-016-01. We thank Anthony Sladen for fruitful discussions regarding his early models and tsunami observations in Peru. Support from CEA is also acknowledged. Figures were drawn using the GMT software (WESSEL and SMITH, 1998).

REFERENCES

CHLIEH, M., DE CHABALIER, J.-B., RUEGG, J.-C., ARMIJO, R., DMOWSKA, R., CAMPOS, J., and FEIGL, K.L. (2004), *Crustal deformation and fault slip during the seismic cycle in the North Chile subduction zone, from GPS and InSAR observations*, Geophys. J. Int. *158*, 695–711.

COMTE, D. and PARDO, M. (1991), *Reappraisal of great historical earthquakes in the Northern Chile and Southern Peru seismic gaps*, Nat. Hazards *4*, 23–44.

DELOUIS, B., MONFRET, T., DORBATH, L., PARDO, M., RIVERA, L., COMTE, D., HAESSLER, H., CAMINADE, J.P., PONCE, L., KAUSEL, E., and CISTERNAS, A. (1997), *The $M_w = 8.0$ Antofagasta (Northern Chile) earthquake of 30 July 1995: A precursor to the end of the large 1877 gap*, Bull. Seismol. Soc. Am. *87* (2), 427–445.

DORBATH, L., CISTERNAS, A., and DORBATH, C. (1990), *Assessment of the size of large and great historical earthquakes in Peru*, Bull. Seismol. Soc. Am. *80*, 551–576.

DZIEWONSKI, A.M. and ANDERSON, D.L. (1981), *Preliminary reference Earth model*, Phys. Earth Planet. Inter. *25*, 197 – 256.

FRITZ, H. M., KALLIGERIS, N., BORRERO, J.C., BRONCANO, P., and ORTEGA, E. (2008), *The 15 August 2007 Peru tsunami runup observations and modeling*, Geophys. Res. Lett. *35*, L10604, doi:10.1029/2008GL033494.

GUIBOURG, S., HEINRICH P., and ROCHE, R. (1997), *Numerical modeling of the 1995 Chilean tsunami. Impact on French Polynesia*, Geophys. Res. Lett. *24*, 775–778.

HÉBERT, H., HEINRICH, P., SCHINDELÉ, F., and PIATANESI, A. (2001a), *Far-field simulation of tsunami propagation in the Pacific Ocean: Impact on the Marquesas Islands (French Polynesia)*, J. Geophys. Res. *106*, C5, 9161–9177.

HÉBERT, H., SCHINDELÉ, F., and HEINRICH, P. (2001b), *Tsunami risk assessment in the Marquesas Islands (French Polynesia) through numerical modeling of generic far-field event,* Nat. Hazards Earth Syst. Sci. *1*, 233–242.

HÉBERT, H., SLADEN, A., and SCHINDELÉ, F. (2007), *Numerical modeling of the Great 2004 Indian Ocean Tsunami focus on the Mascarene Islands*, Bull. Seismol. Soc. Am. *97*, 1A, S208–S222.

HEINRICH, P., SCHINDELÉ, F., GUIBOURG, S., and IHMLÉ, P. (1998), *Modeling of the February 1996 Peruvian tsunami*, Geophys. Res. Lett. *25*, 2687–2690.

HSU, Y., SIMONS, M., AVOUAC, J., GALETZKA, J., SIEH, K., CHLIEH, M., NATAWIDJAJA, D., PRAWIRODIRDJO, L., and BOCK, Y. (2006), *Frictional afterslip following the 2005 Nias-Simeulue earthquake*, Science *312*, 1921–1926.

KENDRICK, E., BEVIS, M., SMALLEY, R.J., BROOKS, B., VARGAS, R.B., LAURÍA, E., and FORTES, L.P.S. (2003), *The Nazca-South America Euler vector and its rate of change*, J. South Amer. Earth Sci. *16*, 125–131.

KONCA, A., HJORLEIFSDOTTIR, V., SONG, T. R.-A., AVOUAC, J.-P., HELMBERGER, D., JI, C., SIEH, K., BRIGGS, R., and MELTZNER, A. (2007), *Rupture kinematics of the 2005, M_w 8.6, Nias-Simeulue earthquake from the joint inversion of seismic and geodetic data*, Bull. Seismol. Soc. Am. *97*, S307–322.

KOWALIK, Z. and MURTY, T.S. (1993), *Numerical simulation of two-dimensional tsunami runup*, Marine Geodesy *16*, 87–100.

LIU, P.L.-F., CHO, Y.-S., YOON, S.B., and SEO, S.N. (1994), *Numerical simulations of the 1960 Chilean tsunami propagation and inundation at Hilo, Hawaii*. In, Y. Tsuchiya, N. Shuto, (eds.), *Tsunami: Progress in Prediction, Disaster Prevention and Warning. Advances in Natural and Technological Hazards Research*, vol. 4. (Kluwer Academic Press, 1994), pp. 99–115.

MADER, C.L. and CURTIS, G. (1991), *Modeling Hilo, Hawaii tsunami inundation*, Sci. Tsunami Hazards *9*, 85–94.

OKADA, Y. (1985), *Surface deformation due to shear and tensile faults in a half-space*, Bull. Seismol. Soc. Am. *75*, 1135–1154.

OKAL, E.A., and TALANDIER, J. (1989) *Mm: A variable-period mantle magnitude*, J. Geophys. Res. *94*, 4169–4193.

OKAL, E.A. and REYMOND, D. (2003), *The mechanism of the great Banda Sea earthquake of 01 February 1938: Applying the method of Preliminary Determination of Focal Mechanism to a historical event*, Earth Planet. Sci. Lett. *216*, 1–15.

OKAL, E.A. BORRERO, J.C., and SYNOLAKIS, C.E. (2004), *The earthquake and tsunami of 17 November 1865: Evidence for far-field tsunami hazard from Tonga*, Geophys. J. Int. *157*, 164–174.

OKAL, E.A. and HÉBERT, H. (2007), *Far-field modeling of the 1946 Aleutian tsunami*, Geophys. J. Int. *169*, 1229–1238.

REYMOND, D., HYVERNAUD, O., and TALANDIER, J. (1991), *Automatic detection, location and quantification of earthquakes: Application to Tsunami Warning,* Pure Appl. Geophys. *135*, 361–382.

REYMOND, D. and OKAL, E.A. (2000), *Preliminary determination of focal mechanisms from the inversion of spectral amplitudes of mantle waves*, Phys. Earth Planet. Inter. *121*, 249–271.

REYMOND., D., OKAL, E.A., HÉBERT, H., and LOEVENBRUCK, A. (2007), *Far-field tsunami amplitude estimations from numerical simulations and empirical laws*, Eos Trans. AGU *88* (52), Fall Meet. Suppl., Abstract S53A–1037.

ROMANOVICZ, B.A. and SUÁREZ, G. (1983), *On an improved method to obtain the moment tensor and depth of earthquakes from the amplitudes spectrum of Rayleigh waves*, Bull. Seismd. Soc. Am. *73*, 1513–1526.

SCHINDELÉ, F., HÉBERT, H., SLADEN, A., and REYMOND, D. (2006), *L'aléa tsunami en Polynésie française: synthèse des observations et des mesures*, C. R. Geoscience *338*, 1133–1140.

SCHINDELÉ, F., REYMOND, D., GAUCHER, E., and OKAL, E.A. (1995), *Analysis and automatic processing in near-field of the eight 1992–1994 tsunamigenic earthquakes: Improvements in real-time tsunami warning*, Pure Appl. Geophys. *144*, 381–408.

SLADEN, A. and HÉBERT, H. (2008), *On the use of satellite altimetry to infer the earthquake rupture characteristics: application to the 2004 Sumatra event*, Geophys. J. Int. *172*, 707–714.

SLADEN, A., HÉBERT, H., SCHINDELÉ, F., and REYMOND, D. (2007a), *Evaluation of far-field tsunami hazard in French Polynesia based on historical data and numerical simulations*, Nat. Hazards Earth Syst. Sci. *7*, 195–206.

SLADEN, A., HÉBERT, H., SCHINDELÉ, F., and REYMOND, D. (2007b), *L'aléa tsunami en Polynésie française: Apports de la simulation numérique*, C. R. Geoscience *339*, 303–316.

SLADEN, A., KONCA, O., FIELDING, E., PERFETTINI, H., AUDIN, L., TAVERA, H., AVOUAC, J.-P., SIMONS, M., and HELMBERGER, D. (2007c), *Source characteristics of the 2007 Pisco earthquake (M_w = 8.0), Central Peru*, EOS Trans. AGU *88* (52), Fall Meet. Suppl., Abstract S13A–1055.

SMITH, W.H.F. and SANDWELL, D.T. (1997), *Global seafloor topography from satellite altimetry and ship depth soundings*, Science *277*, 1956–1962.

TALANDIER, J. and OKAL E.A. (1989), *An algorithm for automated tsunami warning in French Polynesia, based on mantle magnitudes*, Bull. Seismol. Soc. Am. *79*, 1177–1193.

TARANTOLA, A. (1987), Inverse Problem Theory: Methods for Data Fitting and Model Parameter Estimation (Elsevier 1987), 613 pp.

VALLÉE, M., and BOUCHON, M. (2004), *Imaging coseismic rupture in far field by slip patches*, Geophys. J. Int. *156*, 615–630.

WEI, Y., BERNARD, E.N., TANG, L., WEISS, R., TITOV, V.V., MOORE, C., SPILLANE, M., HOPKINS, M., and KANOGLU, U. (2008), *Real-time experimental forecast of the Peruvian tsunami of August 2007 for U.S. coastlines*, Geophys. Res. Lett. *35*, L04609, doi:10.1029/2007GL032250.

WESSEL, P., and SMITH W.H.F. (1998), *New, improved version of Generic Mapping Tools released*, EOS Trans. AGU, *79* (47), 579. pp

(Received January 12, 2008, revised September 30, 2008, accepted October 14, 2008)
Published Online First: February 14, 2009

Pure appl. geophys. 166 (2009) 233–258
0033–4553/09/010233–26
DOI 10.1007/s00024-008-0434-5

Pure and Applied Geophysics

Tide Gauge Observations of 2004–2007 Indian Ocean Tsunamis from Sri Lanka and Western Australia

CHARITHA B. PATTIARATCHI[1] and E. M. SARATH WIJERATNE[2]

Abstract—Tide gauge data collected from Sri Lanka (three stations) and Western Australia (eleven stations) during the Indian Ocean tsunamis, which occurred in December 2004, March 2005, July 2006, and September 2007, and incorporated five tsunamis, were examined to determine tsunami behaviour during these events. During the December 2004 tsunami, maximum wave heights of 3.87 m and 1.75 m were recorded at Colombo (Sri Lanka) and Bunbury (Western Australia), respectively. The results indicated that although the relative magnitudes of the tsunamis varied, the tsunami behaviour at each station was similar. This was due to the effect of the local and regional topography. At all tide gauges, the spectral energy corresponding to periods between 20 and 85 minutes increased during the tsunami. The sea-level data obtained from the west and south coasts of Sri Lanka (Colombo and Kirinda) indicated the importance of wave reflections from the Maldives Island chain, which produced the maximum wave two to three hours after the arrival of the first wave. In contrast, Trincomalee on the east coast did not show evidence of a reflected wave. Similarly, along the west coast of Australia, the highest waves occurred 15 hours after the arrival of the first wave. Here, based on travel times, we postulated that the waves were reflected from the Mascarene Ridge and/or the Island of Madagascar. Reflected waves were not present in the 2006 tsunami, where the primary waves propagated away from topographic features. One of the main influences of the tsunami was to set up oscillations at the local resonance frequency. Because Sri Lanka and Western Australia have relatively straight coastlines, these oscillations were related to the fundamental period of the shelf oscillation. For Colombo, this corresponded to 75-minute period, whereas in Geraldton and Busselton (Australia), the four-hour period was most prominent; at Jurien Bay and Fremantle, the resonance period was 2.7 hours.

Key words: Tide gauge, Sri Lanka, Western Australia, tsunami, wave reflection, seiches.

1. Introduction

The Indian Ocean experienced its most devastating natural disaster through the action of a tsunami resulting from an earthquake off the coast of Sumatra on 26 December 2004, which caused widespread damage to property and human lives, with over 250,000 deaths in the region and millions left homeless (WALTER, 2005). This event revealed the destructive effects of tsunamis, with a maximum runup exceeding 30 m in Banda Aceh

[1] School of Environmental Systems Engineering, The University of Western Australia, 35 Stirling Highway, Crawley, WA 6009, Australia. E-mail: chari.pattiaratchi@uwa.edu.au

[2] Oceanography Division, National Aquatic Resources Research and Development Agency (NARA), Crow Island, Colombo 15, Sri Lanka. E-mail: emsw@nara.ac.lk

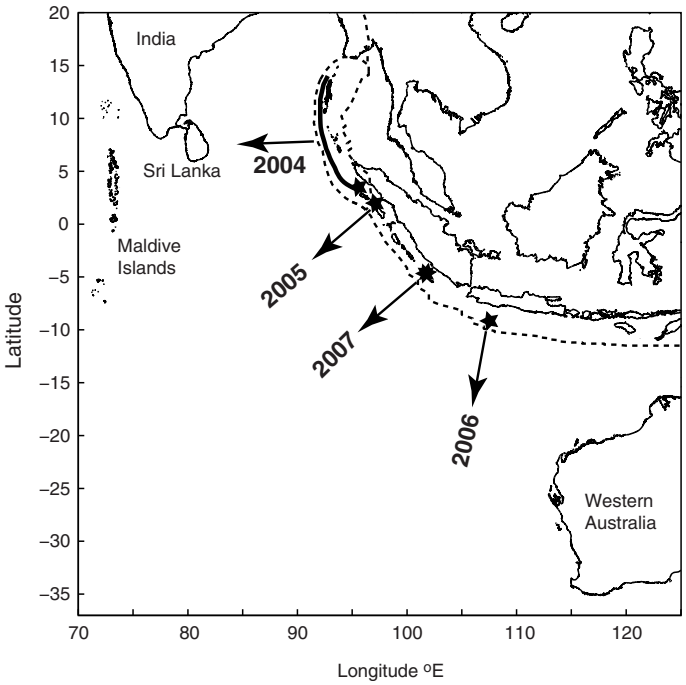

Figure 1
Map of the eastern Indian Ocean showing the location of the earthquake epicentres (indicated by stars) and direction of the primary wave propagation for the 2004, 2005, 2006, and 2007 tsunamis. Note that there were two earthquakes in September 2007 within 12 hours. The dashed line indicates the plate boundary; the thick black line indicates the area of rupture for the 2004 tsunami.

and 10 m at several sites in Sri Lanka (INOUE *et al.*, 2007); in Western Australia, the impact was much less, with a maximum total water level of 2.6 m recorded at Geraldton. The December 2004 tsunami was followed by considerably smaller basin-wide tsunamis in 2005, 2006, and 2007 (Fig. 1; Table 1). Although these tsunamis caused loss of lives and damage to property in the immediate vicinity of the tsunami generation region in Indonesia, regions located far from the earthquake epicentre (e.g., Sri Lanka, Western

Table 1

Details of Indian Ocean tsunamis 2004–2007 (see Figure 1 for locations)

Year	Date	Time of earthquake (UTC)	Earthquake magnitude	Epicentre location
2004	26 December	00:58	9.1	3.32° N 95.854° E
2005	28 March	16:09	8.6	2.07° N 97.01° E
2006	17 July	08:19	7.7	9.22° S 107.32° E
2007	12 September	11:10	8.5	4.52° N 101.37° E
		23:49	7.9	2.51° N 100.91° E

Australia) did not experience the tsunami's damaging impacts; however, local sea-level recording stations documented the characteristics of each tsunami.

Tsunamis in the Indian Ocean are rare, with ~ 24 tsunamis reported over a 2000-year period prior to 2004 (DOMINEY-HOWES *et al*., 2007). The 2004 tsunami is considered to be the third tsunami recorded globally, i.e., observed in oceans other than the ocean where the tsunami was generated (RABINOVICH and THOMSON, 2007). The globally recorded tsunamis were: (1) The Krakatoa volcanic explosion in 1883 (CHOI *et al*., 2003); (2) the Chilean tsunami in 1960 (RABINOVICH and THOMSON, 2007); and, (3) the December 2004 event, which was recorded in most of the global sea-level measurement stations across all the major oceans (TITOV *et al*., 2005; MERRIFIELD *et al*., 2005; WOODWORTH *et al*., 2005; DRAGANI *et al*., 2006; NAGARAJAN *et al*., 2006; RABINOVICH and THOMSON, 2007). RABINOVICH and THOMSON (2007) presented detailed analyses of the sea-level records from the Indian Ocean region for the 2004 event. In this paper, we present previously unreported data from the 2004 event from tide gauges from Sri Lanka and Western Australia (the Colombo tide record was reconstructed using an offshore tide gauge) together with data from Indian Ocean tsunami events, which occurred in 2005, 2006, and 2007.

The destructive effects of tsunamis in coastal regions are usually limited to several hours. However, a much neglected tsunami effect is the set-up of coastal oscillations (seiches), which can last for three to five days after the impact of the tsunami and affect port operations and coastal sea levels. These oscillations were predominant in all of the sea-level time series presented in this paper, and the nature of these oscillations was also examined.

This paper is organised as follows: Section 2 presents background information on tsunami impacts and tidal characteristics of the study regions (Sri Lanka and Western Australia); methods are presented in Section 3, followed by analysis of the sea-level records for the tsunami events from 2004 to 2007 in Section 4; Section 5 presents an analysis of the continental shelf seiches induced by the tsunami.

2. Study Regions

2.1. Sri Lanka

Sri Lanka is located off the southern tip of India (Fig. 1). The island has a length of 445 km, a width of 225 km, a total area of 65,610 km^2, and a coastline of 1760 km, which mainly consists of sandy materials with intermittent stretches of granite rock or sandstone. It has a population of over 20 million, of which 4.85 million people live within 1 km of the coast, which makes up only 4% of the land mass.

Sri Lanka has a narrow continental shelf (range: 2.5–25 km), with a mean distance between the coast and the 200-m-depth contour of 20 km; at some locations, especially along the southern coast, this distance is reduced to < 3 km (Fig. 2a). The shelf is

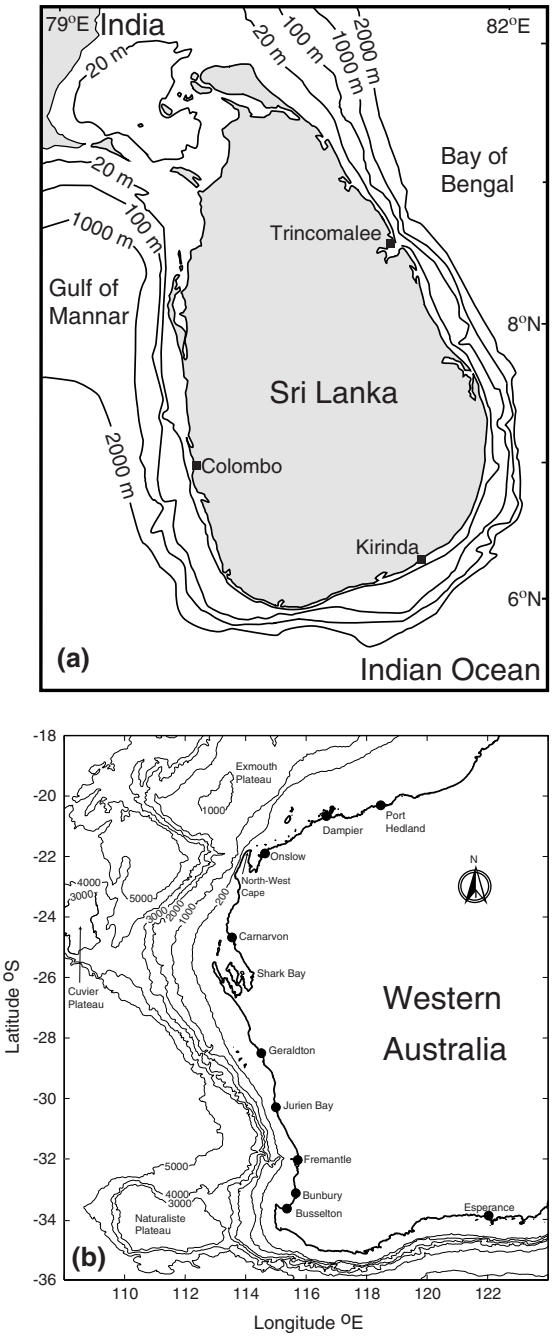

Figure 2
Locations of the tide gauges in (a) Sri Lanka and (b) Western Australia. Bathymetry contours are in metres.

narrowest around the southern part of Sri Lanka and broadens to merge with the Indian continental shelf towards the north and northeast. The continental shelf is also shallower (30–90 m) than the mean global shelf depth (75–125 m). The continental slope is steep, with a rapid increase in water depth to $\sim$4000 m. The narrow continental shelf and the steep continental slope mean Sri Lanka is extremely vulnerable to the action of tsunamis, as the shoaling effect occurs over a shorter distance and there is a negligible amount of energy dissipated over the continental shelf region. Sri Lanka is most vulnerable to tsunamis generated from the Sunda Arc region, located approximately 1500 km to the east (Fig. 1). There are also no major submarine topographic features between the tsunami source region and Sri Lanka to dissipate or refract the tsunami waves. As a result, Sri Lanka was the second-most affected country for the 2004 tsunami event.

Sri Lanka has a semi-diurnal, micro-tidal regime with a maximum tidal range of $\sim$0.5 m along the entire coast. The tides around Sri Lanka are controlled by the oceanic tides of the Arabian Sea (west coast) and the Bay of Bengal (east coast), which results in a phase difference in the tides between the east and west coasts. For example, the tides in Trincomalee are exactly out-of-phase with the tides in Colombo, with low water in Colombo corresponding to high water at Trincomalee.

Although Sri Lanka lies in the direct path of a tsunami from the Sunda Arc, the only documented impact of a tsunami, prior to 2004, was due to the 1883 Krakatoa eruption (Choi *et al*., 2003). The resulting tsunami was reported in newspaper articles in Sri Lanka, with impacts reported from Galle, Negombo, and Arugam Bay where there was one casualty. The reported maximum wave height was 1 m, and the tsunami impacted Sri Lanka five to seven hours after the eruption (Choi *et al*., 2003). It is likely Sri Lanka was affected by the tsunamis in the Bay of Bengal in 1881 (Ortiz and Billham, 2003), 1941 (Murty and Rafiq, 1991), and 1994 (Synolakis *et al*., 1995), but the effects of a small tsunami would not have caused any damage and thus would have been undetected. The 1994 East Java earthquake, which occurred on 3 June 1994, was recorded in tide gauges in Oman (B. Kilonsky, pers. comm., 2005). As Sri Lanka lies between the source region and Oman, the tsunami would have propagated past Sri Lanka; however, no tide records from Sri Lanka exist to confirm this.

2.2. *Western Australia*

Western Australia's coast is over 20,000 km and comprises one-third of the Australian continent. The northern section of Western Australia (east of Onslow, Fig. 2a) has a wide continental shelf. Although this region is closest to the Sunda Arc region (Fig. 1), the wide continental shelf has a large influence on tsunami impacts at the shoreline (Pattiaratchi and Woo, 2000). The presence of the Exmouth Plateau influences tsunami propagation through refraction, with a concentration of energy along the coastline (Legget, 2006). The continental shelf is narrowest (< 20 km) at North-West Cape (Fig. 2b); its width increases to the south of North-West Cape to Shark Bay (where it is up to 80 km), decreases to Jurien Bay (Fig. 2b), and then increases to the south.

Along the west coast, the narrowest shelf is at Jurien Bay; thus the tsunami's arrival was first recorded at this location.

The location of Cuvier Plateau to the west of Shark Bay strongly influenced deep water tsunami propagation through refraction (LEGGET, 2006). Here, the presence of the plateau causes the refraction of tsunami wave energy onshore, concentrating energy in the region between Geraldton and the offshore regions of Shark Bay (Fig. 2b).

There is a large variation in the tidal chacteristics along the coast, with the northern section (east of Onslow, Fig. 2b) experiencing semi-diurnal tides, with a maximum spring tidal range exceeding 10 m to the east of Port Hedland (Fig. 2b). The section between Onslow and Carnarvon (Fig. 2b) experiences mixed tidal conditions, with a maximum tidal range of 2–3 m. The coastline between Geraldton and Esperance (Fig. 2b) expriences diurnal tides, with a maximum range of < 1 m. The low tidal range in this region means that even a small tsunami or seiche (> 0.25 m) results in a significant proportion of the local tidal range.

Western Australia is susceptible to the action of tsunamis generated by earthquakes in the Sunda Arc region (Fig. 1). Although there have been many earthquakes in the region (DOMINEY-HOWES, 2007), tsunamis have been observed (either through visual records or tide gauges) only for the events in 1883 (Krakatoa), 1977 (Sumbawa), 1994 (East Java), and the 2004–2007 tsunami events described in this paper. A summary of these events is presented below (see also PATTIARATCHI and WOO, 2000, and DOMINEY-HOWES *et al.*, 2007).

- The 1883 tsunami was associated with the eruption of Krakatoa volcano on 27 August 1883. A maximum runup height of 1.5 m was observed at Cossack (near Dampier, Fig. 1). Tsunami waves corresponding to this volcanic explosion were also observed at Geraldton, Carnarvon, and Fremantle.
- The 1977 tsunami was due to the 7.9-magnitude Sumbawa earthquake, which occurred on 19 August, 1977. GREGSON *et al.* (1979) described the tsunami associated with this earthquake. A 4-m-high wave was observed at Barrow Island by fishermen while the lighthouse keeper at Cape Leveque reported a 6-m-high wave. This is the highest tsunami-generated wave reported in Australia. At Point Samson, six to eight 4.6-m-high waves were observed, and in Dampier, four waves of 2–2.5 m in height were observed.
- The 1994 tsunami resulted from the 7.2-magnitude East Java earthquake, which occurred on 3 June, 1994. The time series from the water level recorders obtained from coastal stations along the northwest region indicated small changes in the water level. This was due to the fact that the tide gauges were set to record at 15-minute intervals and therefore may not have accurately measured the maximum wave heights. Examination of the damage resulting from the tsunami revealed the tsunami would have reached heights up to 4 m along the NorthWest Cape, with reduced values of 2–3 m between Exmouth and Dampier (PATTIARATCHI and WOO, 2000).

3. Methods

Data were obtained from tide gauges in Sri Lanka and Western Australia (Fig. 2). In Sri Lanka, data were obtained from tide gauges operated and maintained by the National Aquatic Resources Research and Development Agency (NARA). The sea-level recording station at Colombo, within the Mutwal fishery boat harbour, was established as a global sea-level observing system (GLOSS) station in August 2004. The tide gauges consisted of two floats with a digital recording system, and were set to record measurements at two-minute intervals. During the 2004 tsunami, after recording the first wave, the floats were stuck at the bottom of the stilling well at 0430 UTC (1030 local time), 40 mins after the arrival of the intitial wave (Fig. 3) when the water level dropped below the lowest level of the well. The floats were reset by the second author (EMSW) and then recorded data from 1000 UTC (1400 local time). Thus data were missing for 3.5 hours, coinciding with the arrival of the highest waves. This is in contrast to the 5 hours 40 minutes reported by RABINOVICH and THOMSON (2007) who used the data archived by the University of Hawaii Sea Level Centre using data from a single encorder. Using data recorded by both encorders, we have decreased the amount of missing data. An offshore bottom mounted tide gauge (InterOcean S4DW wave and current recorder maintained by Lanka Hydraulic Institute, Ltd), located in 16-m-water depth, a distance 5 km from the coastline, recorded water levels at 10-minute intervals throughout the tsunami event.

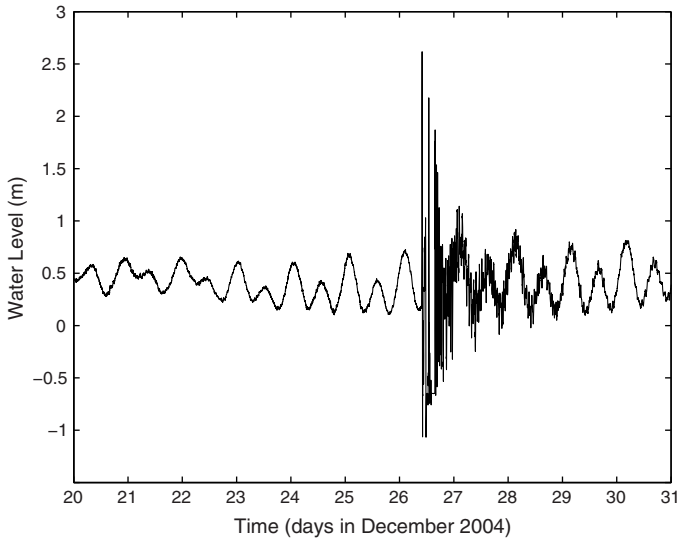

Figure 3
Time series of the water level record from Colombo, Sri Lanka, from 20 to 31 December, 2004 showing the scale of the tsunami with respect to the tidal range and also the presence of high frequency oscillations subsequent to the tsunami.

The S4DW water level data were used to determine the missing data from the Colombo tide gauge as follows: The Colombo data, for one day before and after the tsunami, were re-sampled at 10-minute intervals and compared with the S4DW water level record. The missing data were then interpolated with reference to the S4DW data, and the Colombo time series was re-sampled at 2-minute intervals (Fig. 4). Subsequent to reconstruction, the spectral characteristics of both series were found to be very similar (not shown). There was an excellent correspondence between the two-time series after the reconstruction of the Colombo data (Fig. 4a). It should be noted that the floats accurately recorded a single wave after the floats were partly dislodged at around 1200 (Fig. 4b), but were dislodged completely after the largest wave at 1330. After the 2004 tsunami, the sampling interval on the Colombo tide gauge was changed to one minute. The sea-level recording station at Trincomalee (Fig. 2), which was established in 2005 (subsequent to the March 2005 tsunami), also had a sampling interval of one minute.

A Coastal Leasing micro-tide pressure gauge located inside the Kirinda fishery harbour measured the March 2005 tsunami (Fig. 2). The instrument recorded the sea level at five-minute intervals, with an accuracy of ± 1 cm.

In Western Australia, data were obtained from tide gauges that the Department for Planning and Infrastructure (http://www.dpi.wa.gov.au/) operates and maintains. All sea-level stations recorded the sea level at five-minute intervals. The residual time series were obtained by subtracting the predicted tide from the observed tide at each recording station.

The tidal time series were subjected to Fourier analysis to identify the dominant frequencies in the records. This was undertaken in two ways: (1) the records for five consecutive days immediately before and after the tsunami were used to construct the auto-spectrum and identify the changes in the spectral energy before and after the tsunami; and (2) the auto-spectra were used to construct time–frequency plots and determine the longer-term changes in the spectral energy distribution. Here, time series of 2048 points were used to estimate power spectra using the 'Welch' method (LITTLE and SHURE, 1988) using Fast Fourier Transform (FFT) method. Subsequent spectra were calculated using a 50% overlap (i.e., 1024 points).

4. Tide Gauge Records of Tsunamis

4.1. December 2004 Tsunami

Sri Lanka. The Colombo tide gauge data indicated the tsunami arrived at 0352 UTC (0952 local time) as a leading elevation wave reaching a maximum height of 2.65 m over 10 minutes (Table 2); that is, the highest water level for the initial wave was reached at 0402 UTC (1002 local time).

During the tsunami, the float in the stilling well was stuck at bottom of the tide gauge; the missing data were reconstructed using an offshore tide gauge (see Section 3).

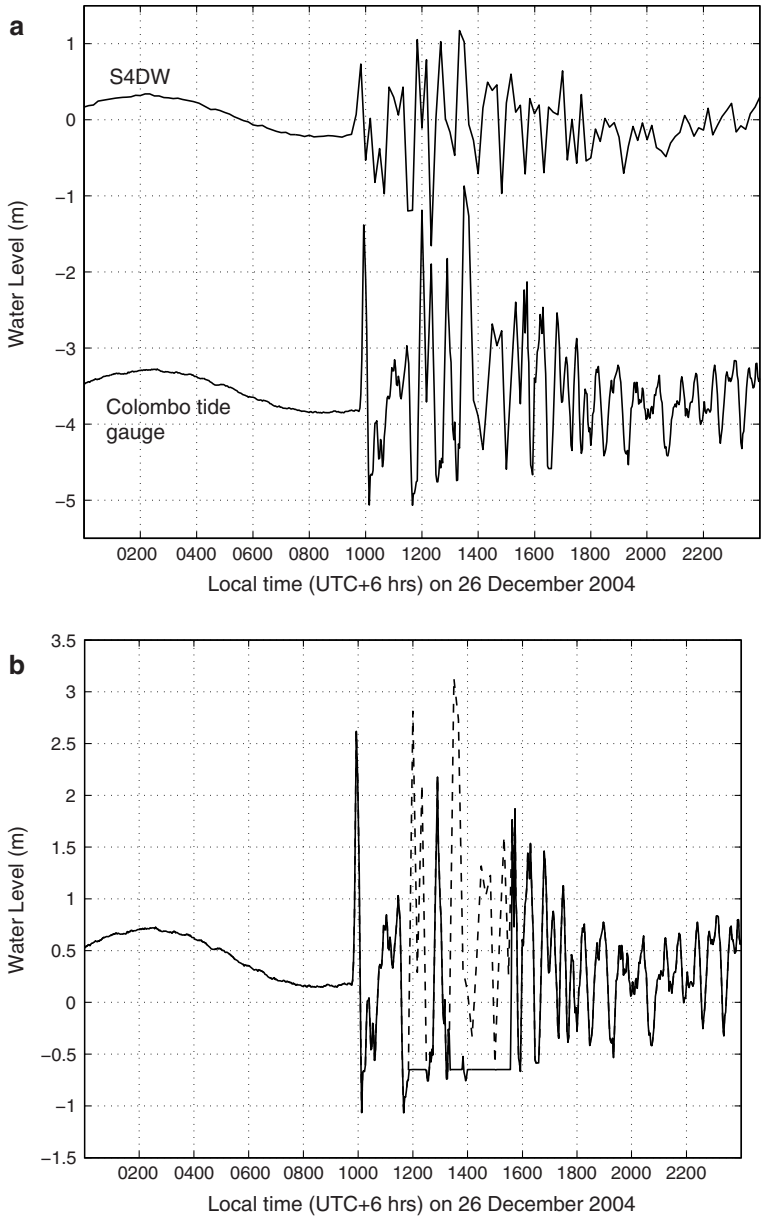

Figure 4
(a) Time series of the offshore S4DW tide gauge and Colombo tide gauge sea levels on 26 December, 2004. Note the Colombo data were offset by −4 m. (b) Time series of the reconstructed Colombo tide gauge sea level on 26 December, 2004. The dashed lines show the reconstructed data.

Table 2

Characteristics of the 26 December 2004 tsunami as recorded by tide gauges

Station	Initial wave		Maximum wave	
	Arrival time/date (UTC)	Wave height[+]	Elapsed time (number)	Wave height
Colombo	03:52 26/12/04	2.3 m	2 h 08 m (3)	3.87 m
			3 h 38 m (6)	3.87 m
Carnarvon	07:40 26/12/04	0.38 m	15 h 20 m (25)	1.14 m
Geraldton	07:20 26/12/04	0.13 m	15 h 15 m (19)	1.65 m
Jurien Bay	07:05 26/12/04	0.47 m	6 h 30 m (10)	0.90 m
Fremantle	07:40 26/12/04	0.33 m	7 h 20 m (9)	0.60 m
Bunbury	08:05 26/12/04	0.60 m	13 h 35 m (18)	1.75 m
Busselton	07:55 26/12/04	0.54 m	13 h 15 m (19)	1.15 m
Esperance	09:00 26/12/04	0.11 m	12 h 00 m (17)	0.44 m

[+] Maximum wave height is listed as the trough to crest height.

The resulting time series (Fig. 4) showed that in Colombo, the highest water level of 3.13 m occurred during the sixth wave, 3.5 hours after the first wave at 0730 UTC (1330 local time). As a result of the previously missing data, many authors (e.g., LIU *et al.*, 2005) reported eyewitness accounts that the third wave along the west coast, which arrived at ~0600 UTC (1200 local time), was the highest. INOUE *et al.* (2007) reported that the arrival of the second wave was between 0400 and 0900 UTC (1000 and 1500 local time). The reconstructed sea-level record confirmed some of these findings with respect to Colombo (Table 2):

(1) The initial wave, which arrived at 0352 UTC, was a leading elevation wave with a maximum height of 2.65 m.
(2) The second highest water level of 2.81 m was reached at 0600 UTC (1200 local time).
(3) The highest water level of 3.13 m was reached at 0730 UTC (1330 local time).
(4) The maximum wave height (trough to crest) was 3.87 m, with the two waves at 0600 UTC and 0730 UTC having the same height.

The timings of the above waves could be confirmed by the personal experiences of the first author (CBP) who was present in Sri Lanka and experienced the first and subsequent waves along the coast while driving on a road (Galle Road) that runs parallel to the coast to the south of Colombo.

The above results suggested the waves along the west coast of Sri Lanka had many sources, with the highest waves reflected from the Maldives Island chain. The elapsed time for the tsunami's deep water propagation from Sri Lanka to the Maldives Island chain and return was ~two hours. Thus the second largest wave in the record, which occurred at 1200 (Fig. 4), could be attributed to the reflection from the Maldives Island chain. KOWALIK *et al.* (2007) showed through numerical modelling that the reflected waves from Sri Lanka and the Maldives Island chain were often larger than the primary

wave. The results from the Colombo tide gauge, where the highest waves were those resulting from the wave reflected from the Maldives Island chain, confirmed this finding.

Western Australia. The tide gauge data along the west coast indicated that the tsunami waves were first recorded at Jurien Bay at 0705 UTC, with a travel time of six hours and three minutes (Table 2). The continental shelf offshore Jurien is the narrowest along this part of the coast. The waves were then incident at Geraldton (0720), Carnarvon (0740), Fremantle (0740), Busselton (0755), Bunbury (0805), and Esperance (0900). Esperance is located along the southern coast (Fig. 2b) and is farthest away from the source region, which explained the late arrival time. The initial waves all indicated an increase in the water level, corresponding to leading elevation waves, and the heights along the west coast ranged from 0.33 m at Fremantle to 0.60 m at Bunbury (Fig. 5 and Table 2). Esperance recorded an initial wave height of 0.11 m.

Examination of the residual time series, maximum wave heights, and the elapsed time between the initial and maximum waves indicated several features:

(1) The maximum wave heights (Table 2), recorded at Carnarvon, Geraldton, Bunbury, and Busselton all exceeded the maximum spring tidal range at these locations.
(2) At Geraldton, although initial oscillations due to the tsunami waves were observed at 0720 UTC, there was a lag of five hours before the highest water level (2.6 m relative to datum) was reached at 1210 GMT, which coincided with the tidal high water (Fig. 6). However, the highest waves (trough to crest) were recorded ~ 10 hours later

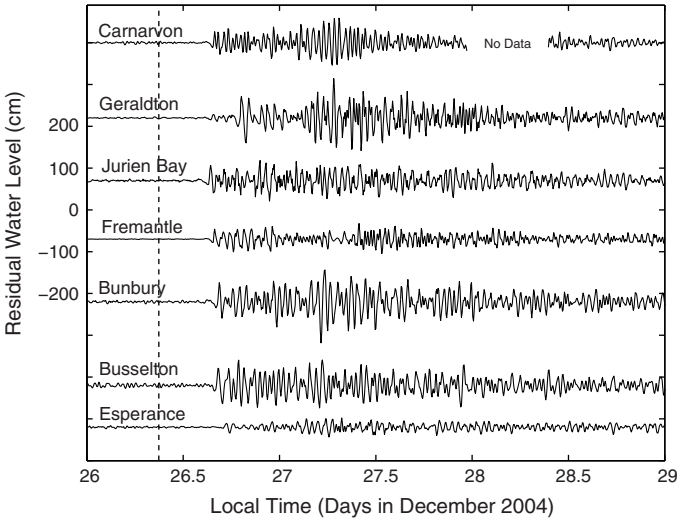

Figure 5
Time series of residual sea level from coastal stations located along the west coast of Australia. The dashed line shows the time of the earthquake. (Note: local time is +8 hrs UTC).

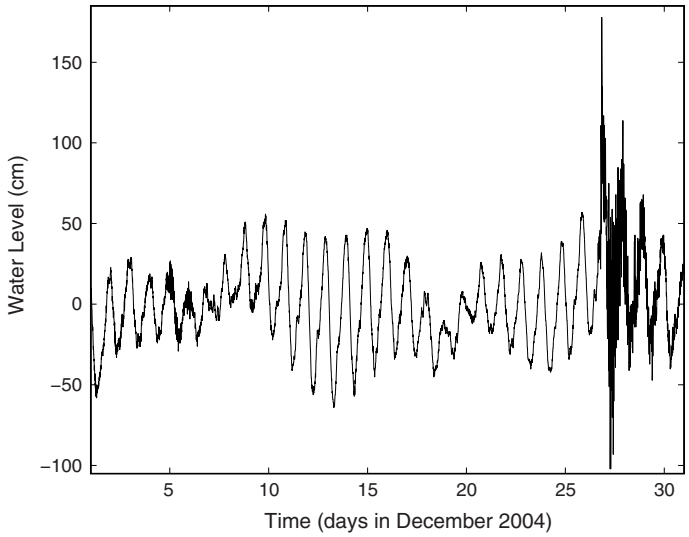

Figure 6
Time series of the water level record from Geraldton, Western Australia, for December, 2004 showing the scale of the tsunami with respect to the tidal range and also the presence of high frequency oscillations subsequent to the tsunami (also note the high frequency oscillations from 4 to 8 December).

and were associated with a wave group (see 3 below). The highest waves coincided with the low water and thus the lowest water level (−0.60 m) was recorded at this time (Fig. 6). The water levels recorded at Geraldton during this event were the highest and lowest levels recorded at this station, which has been in continuous operation for more than 40 years.

(3) The residual time series indicated the arrival of a group of waves with higher wave heights at all stations except at Fremantle and Jurien Bay (Fig. 5) some 13–15 hours after the arrival of the initial wave (Table 2). The maximum wave height (crest to trough) at each of these stations (Carnarvon, Geraldton, Bunbury, Busselton, and Esperance) was also recorded during the passage of this wave group. KOWALIK *et al.* (2007) examined the energy flux of the tsunami waves between Australia and Antarctica across longitude 140° onto the Pacific Ocean and predicted that the highest energy flux was ∼21 hours after the source earthquake. The wave group at Bunbury, Busselton, and Esperance was recorded ∼19 hours after the source earthquake. As the cross section (longitude 140°) at which the energy flux calculations were made was located to the east of these stations (Fig. 1), it is likely this wave group was responsible for the high energy flux predicted by KOWALIK *et al.* (2007). KOWALIK *et al.* (2007) attributed the source of this higher energy to reflected waves from the Maldives and Seychelles (Mascarene Ridge). However, the time lag of 13–15 hours suggested that the Island of Madagascar could also have been responsible for the reflection.

(4) The highest (trough to crest) wave was recorded at Bunbury (1.75 m; Table 2), which coincided with the arrival of the wave group. However, as the wave group arrived at Bunbury near to low water, the maximum water level was lower than that recorded at Geraldton (see 2 above).

4.2. March 2005 Tsunami

Sri Lanka. Tide gauges at Colombo and Kirinda (Fig. 2a) recorded initial tsunami wave heights of 0.3 m and 0.7 m, respectively, with the travel times to Colombo and Kirinda being two hours and 56 minutes and three hours and 24 minutes, respectively (Fig. 7; Table 3). At Kirinda, the first wave arrived almost at low tide; the wave heights then increased, reaching a maximum height of 2.7 m two hours and 24 minutes after the arrival of the first wave (Fig. 8). The approximate 2.5-hour time interval corresponded to the elapsed time from the tsunami wave reflected from the Maldives Island chain; hence, similar to the December 2004 tsunami, the highest waves were due to reflection from the Maldives Island chain. It should be noted that the wave height recorded at Kirinda was larger than wave heights recorded elsewhere in the region—Cocos Island (10–22 cm), the Maldives (10 cm)—and were similar to those recorded near the earthquake zone—3 m on the southern edge of Simeulue Island and 2 m recorded on the west coast of Nias Island (RASTOGI and JAISWAL, 2006).

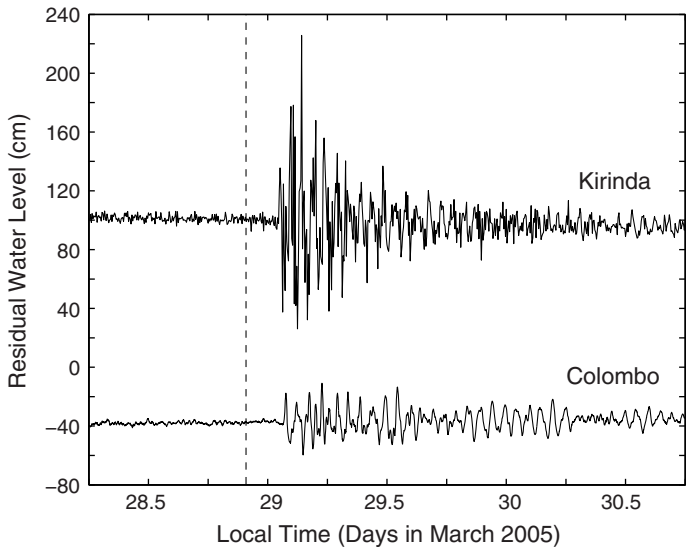

Figure 7
Time series of residual sea level from Kirinda and Colombo, Sri Lanka, 29 March, 2005.

Table 3

Characteristics of the 28 March 2005 tsunami as recorded by tide gauges

Station	Initial wave		Maximum wave	
	Arrival time/date (UTC)	Wave height	Elapsed time (number)	Wave height
Colombo	19:32 28/03/05	0.23	4 h 17 m (5)	0.43 m
Kirinda	19:05 28/03/05	0.56	2 h 24 m (7)	2.7 m
Carnarvon	22:20 28/03/05	0.07 m	14 h 45 m (25)	0.30 m
Geraldton	22:10 28/03/05	0.05 m	3 h 55 m (5)	0.40 m
Jurien Bay	21:45 28/03/05	0.08 m	12 h 35 m (11)	0.38 m
Fremantle	21:45 28/03/05	0.20 m	14 h 05 m (16)	0.32 m
Bunbury	22:15 28/03/05	0.17 m	12 h 45 m (10)	0.49 m
Busselton	22:20 28/03/05	0.19 m	15 h 25 m (16)	0.49 m
Esperance	01:45 29/03/05	0.05 m	3 h 00 m (4)	0.11 m

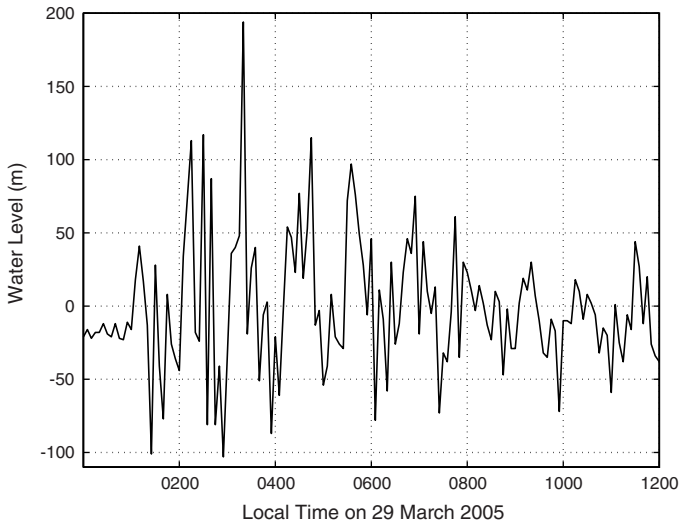

Figure 8
Time series of the water level record from Kirinda, Sri Lanka, on 29 March, 2005.

Western Australia. All the tide gauges along the WA coast recorded the tsunami waves (Fig. 9), but the waves had considerably smaller amplitudes than those in Sri Lanka, with heights ranging between 11% and 50% of the heights recorded for the December 2004 tsunami (Table 3). The maximum wave heights ranged between 0.11 m (Esperance) and 0.49 m (Bunbury and Busselton). However, the tsunami arrival patterns were similar to the 2004 event: The waves first arrived at Jurien Bay and Fremantle, followed by Geraldton, Bunbury, Busselton, Carnarvon, and Esperance.

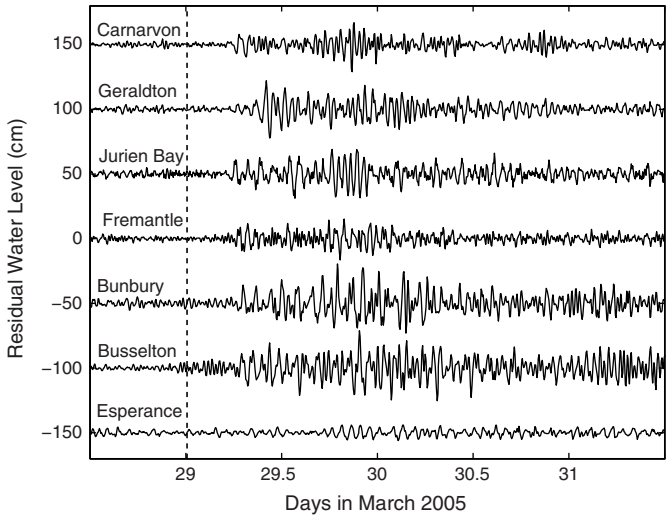

Figure 9
Time series of the residual water level records from Western Australia for 28 March to 1 April, 2005. The dashed line shows the time of the earthquake. (Note: local time is +8 hrs UTC).

The features identified during the 2004 events (see Section 4.1) were also observed. These included: (a) The lag of several hours (∼four hours) before the arrival of the highest wave at Geraldton; and (b) the presence of a second group of waves 13–15 hours after the arrival of the initial wave at all stations (Fig. 9 and Table 3). The maximum wave heights (crest to trough) at all stations, except Geraldton and Esperance, were also recorded during the passage of this wave group. It should be noted that the second wave group, which was not clearly identified at Jurien Bay and Fremantle for the 2004 event, was present during the 2005 event (Fig. 9). KOWALIK *et al*. (2007) proposed the reflections from the Maldive Islands and/or the Mascarene Ridge caused the second group of waves. As the dominant wave direction in the 2005 event was not directed towards the Maldives and Sri Lanka (Fig. 1), we could discount the islands of Sri Lanka and the Maldives as possible sources for wave reflection. Hence it was likely the Mascarene Ridge and Madagascar were the source of the reflections.

4.3. July 2006 Tsunami

Sri Lanka. The primary direction of the tsunami waves was southwards and away from Sri Lanka (Fig. 1); thus no evidence of the tsunami was detected in the Sri Lankan tide gauges.

Western Australia. The tide gauges along the WA coast, north of Geraldton, recorded the tsunami (Table 4), with the tsunami being most prominent at Dampier, which recorded a maximum wave height of 0.8 m (Fig. 10). The northern stations recorded higher water

Table 4

Characteristics of the 17 July 2006 tsunami as recorded by tide gauges

Station	Initial wave		Maximum wave	
	Arrival time/date (UTC)	Wave height	Elapsed time (number)	Wave height
Cape Lambert	12:30 17/07/06	0.09 m	40 m (3)	0.19 m
Dampier	12:30 17/07/06	0.27 m	40 m (3)	0.80 m
Carnarvon	12:40 17/07/06	0.19 m	35 m (3)	0.44 m
Geraldton	12:00 17/07/06	0.08 m	3 h 50 m (10)	0.36 m
Jurien Bay	12:10 17/07/06	0.12 m	10 m (3)	0.14 m
Fremantle	12:30 17/07/06	0.07 m	20 m (3)	0.09 m

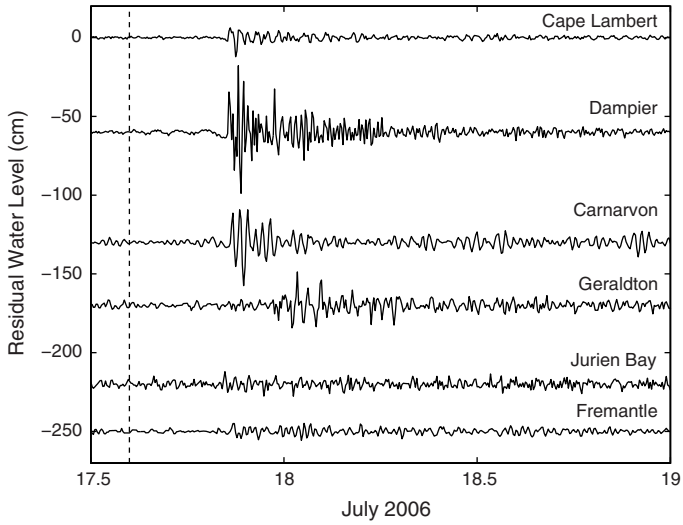

Figure 10
Time series of the residual water level records from Western Australia for 17–19 July, 2006. The dashed line shows the time of the earthquake. (Note: local time is +8 hrs UTC).

levels because the location of the earthquake epicentre was more eastward than it was during the 2004 and 2005 tsunamis. Thus the stations to the south of Geraldton were in the lee of the Cuvier Plateau (Fig. 2b). The existing shelf oscillations, unrelated to the tsunami, also obscured the tsunami signal at Jurien Bay, Fremantle, Bunbury, and Busselton (Figure 10—latter two stations are not shown).

The tsunami first arrived as a leading elevation wave at Geraldton, followed by Jurien Bay, Fremantle, Dampier, Cape Lambert, and Carnarvon. The maximum wave heights occurred within 10–40 minutes of the initial wave; the third wave was the highest at all stations except Geraldton. The absence of a second wave group was evident and could be

attributed to the propagation of the primary wave in a southerly direction (Fig. 1) away from regions which could result in wave reflection. At Geraldton, the maximum wave height was recorded $\sim$4 hours after the arrival of the initial wave. The delay in the arrival of the highest waves at Geraldton was also observed during the 2004 and 2005 events and appeared to be a phenomenon related to the local bathymetry: Geraldton has a complex offshore topography with a wide ($\sim$80 km) continental shelf and a string of offshore islands (the Houtman-Abrolhos Islands) located at the shelf break (Fig. 2b).

4.4. September 2007 Tsunami

Sri Lanka. Tide gauges at Trincomalee and Colombo (Fig. 2a) recorded the tsunami as a leading elevation wave with initial wave heights of 0.2 m and 0.3 m, respectively, and travel times to Trincomalee and Colombo of three hours and 48 minutes and four hours and two minutes, respectively (Fig. 11; Table 5). At Trincomalee, the second wave reached a maximum height of 0.6 m 52 minutes after the arrival of the first wave (Fig. 11). In contrast, at Colombo, the sixth wave (0.50 m), which arrived two hours and 38 minutes after the first wave, was the highest. This was in agreement with the 2004 and 2005 events and could be related to wave reflection from the Maldives Island chain. Trincomalee, along the east coast (Fig. 2a), was sheltered from the reflected wave and thus did not appear in the record.

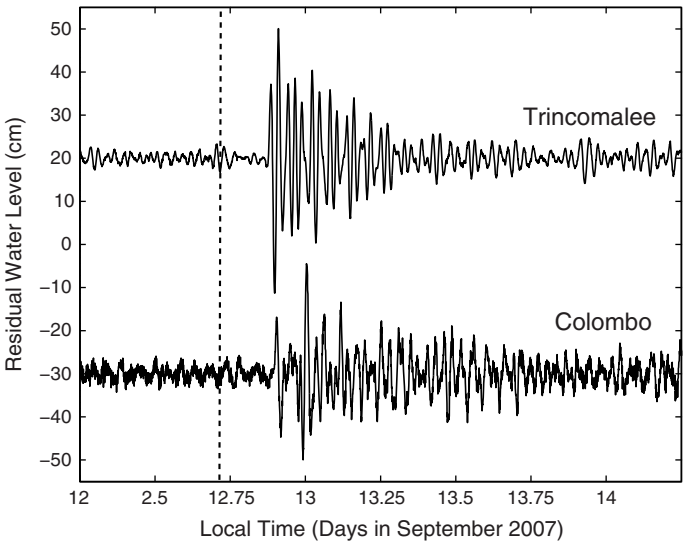

Figure 11
Time series of the residual water level records from Colombo and Trincomalee for 12–14 September, 2007. The dashed line shows the time of the earthquake. (Note: local time is +5.5 hrs UTC).

Table 5

Characteristics of the 12 September 2007 tsunami as recorded by tide gauges

Station	Initial wave		Maximum wave	
	Arrival time/date (UTC)	Wave height	Elapsed time (number)	Wave height
Colombo	15:12 12/09/07	0.3 m	2 h 38 m (6)	0.50 m
Trincomalee	14:58 12/09/07	0.2 m	52 m (2)	0.60 m
Onslow	15:55 12/09/07	0.15 m	5 h 15 m (7)	0.32 m
Carnarvon	16:25 12/09/07	0.09 m	6 h 25 m (11)	0.34 m
Geraldton	16:00 12/09/07	0.07 m	5 h 35 m (8)	0.64 m
Jurien Bay	15:35 12/09/07	0.13 m	1 h 20 m (2)	0.17 m
Fremantle*	-	-	-	-
Busselton	-	-	-	-

* Tsunami could not be identified because of background oscillations.

At both stations, there was no evidence of a tsunami generated by the second earthquake, which occurred $\sim$12 hours after the first earthquake (Table 1). If a tsunami occurred, its effects were small and could not be identified because of the oscillations set up by the first tsunami.

Western Australia. The tide gauges along the WA coast recorded the tsunami; however, at Fremantle (Fig. 12), the effect of the tsunami was obscured because of the passage of a storm system prior to the earthquake, which set up oscillations of the same order as that due to the tsunami. These oscillations were also present at Busselton, but the tsunami could be identified as higher oscillations, which occurred at a similar time to the tsunami's arrival at Jurien Bay. The tsunami arrival patterns along the west coast were similar to those of the 2004, 2005, and 2006 tsunamis: the leading elevation waves first arrived at Jurien Bay, followed by Geraldton, Onslow, and Carnarvon (Table 5). The maximum wave height was recorded at Geraldton (0.64 m), with the maximum wave heights at Onslow and Carnarvon being of similar magnitudes (0.32 m and 0.34 m, respectively) (Table 5). As per previous tsunamis, there was a time lag (5.5 hours) between the arrival of the initial wave and the recorded maximum wave height at Geraldton.

The residual time series, particularly for Onslow, Carnarvon, and Geraldton, indicated the occurrence of several wave groups. Here it should be noted that a second earthquake occurred at almost the same location ($\sim$250 km to the south; Table 1) $\sim$12 hours later. Through examining the time lags for the first tsunami and the arrival of the initial wave at the sea-level recording stations, the tsunami generated by the second earthquake could be identified (Fig. 12). The presence of secondary wave groups between the first and second tsunami could also be clearly identified in the residual times series (Fig. 12); however, the time lag between the arrival of the initial wave and the maximum wave in the wave group varied between five and six hours, which was much less than the $\sim$15 hours recorded during the 2004 and 2005 tsunamis. This indicated that local phenomena, rather

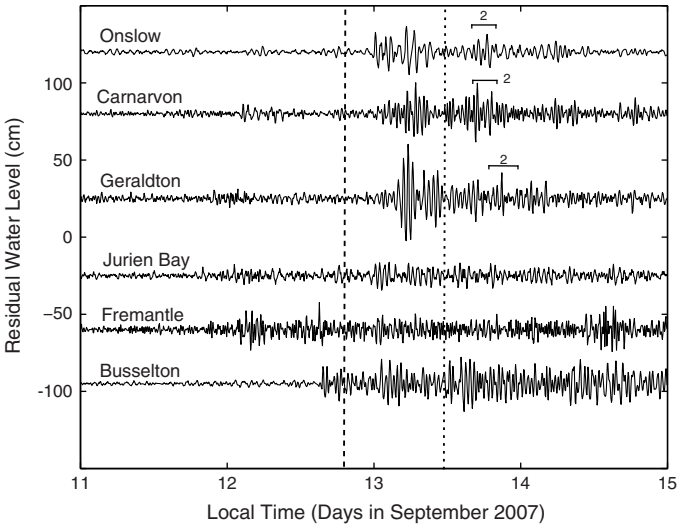

Figure 12
Time series of the residual water level records from Western Australia for 11–15 July, 2006. The dashed lines indicate the times of the earthquakes. The brackets and number 2 denote the tsunami due to the second earthquake. (Note: local time is +8 hrs UTC).

than wave reflection from distant sources, such as the Mascarene Ridge or Madagascar, caused these wave groups.

5. *Tsunami-induced Seiches*

A free oscillation in an enclosed or semi-enclosed body of water, similar to the oscillation of a pendulum where the oscillation continues after the initial force has stopped, is defined as a seiche (MILES, 1974). Several factors cause the initial displacement of water from a level surface, and the restoring force is gravity, which tends to maintain a level surface. Once formed, the oscillations are characteristic only of the system's geometry (length and depth) and may persist for many cycles before decaying under the influence of friction.

A common feature of the time series plots shown in Figures 3 to 12 is the presence of high frequency oscillations with periods ranging from minutes to hours, which persisted for several days after the tsunami. As a result of the tsunami impact, the energy contained in these periods increased by two to three orders of magnitude (RABINOVICH and THOMSON, 2007); this is illustrated in the spectra obtained from the Colombo and Geraldton tide gauge records (Fig. 13). These oscillations mainly consisted of two types: (1) Waves that comprise the tsunami. These waves are usually identified in tide gauge records during the first few hours of a tsunami. For the 2004 tsunami, these waves had energy in the periods

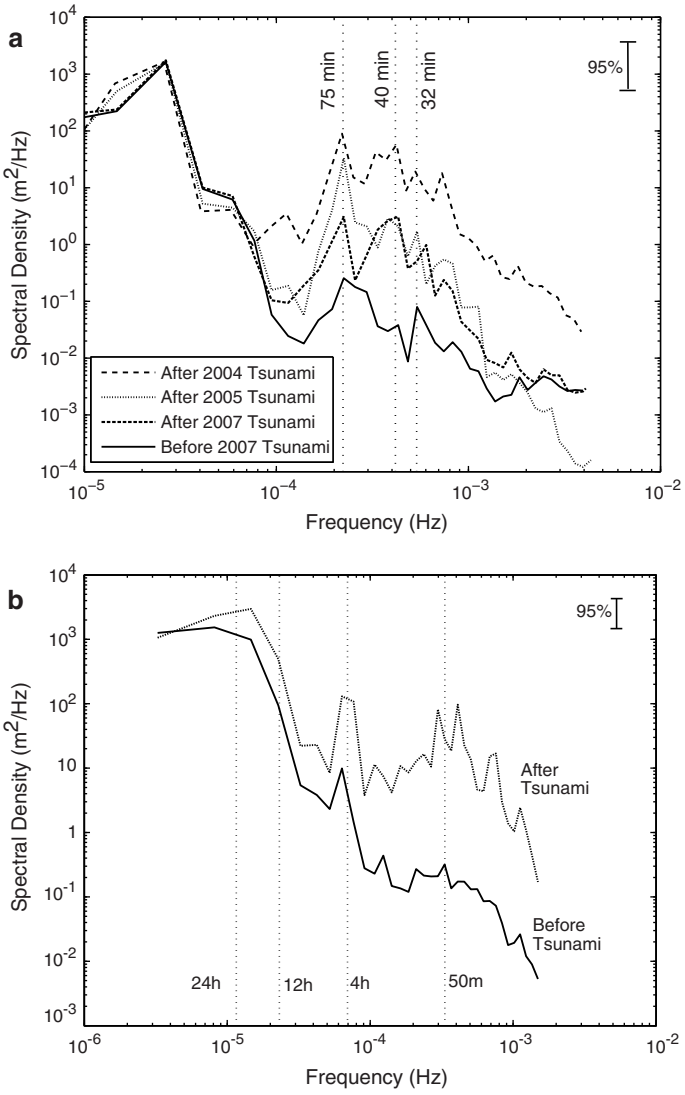

Figure 13
(a) Water level spectra from the Colombo tide record for the 2004, 2005 and 2007 tsunamis showing the spectral energy after the tsunami. Spectral energy before the 2007 tsunami is also shown. (b) Water level spectra from the Geraldton tide record for the December 2004 tsunami showing the spectral energy before and after the tsunami.

ranging from 20 to 85 minutes, with peak values ranging between 35 and 60 minutes (RABINOVICH and THOMSON, 2007). This was also reflected in the data recorded at Colombo and Geraldton (and other stations in Western Australia, not shown), where a significant increase in the spectral energy in this range of periods occurred subsequent to the tsunami (Fig. 13); (2) oscillations that are set up by the tsunami but whose periods are governed

by the local topography. These oscillations may continue for several days after the tsunami's impact, with energy in a particular period enhanced because of the tsunami. Examples of these oscillations were seen at Colombo, where the energy at the 75-minute period increased after the tsunami (for all tsunamis recorded in 2004, 2005 and 2007, Fig. 13a), and at Geraldton, where the oscillations at a period of four hours were enhanced (Fig. 13). We will now examine the features of these oscillations in more detail.

Several studies have been undertaken to examine water level oscillations with periods of O (hours) on the continental shelf. These studies showed atmospheric effects mainly generated these oscillations. CARTWRIGHT and YOUNG (1974) demonstrated that along the east Shetland coast (Scotland, UK), standing edge waves were generated through the passage of weather systems. HEATH (1982) indicated that along the east coast of New Zealand, atmospheric forcing, tsunamis, and edge waves along the continental shelf and slope caused sea-level oscillations with periods of two to three hours. Similarly, shelf oscillations off the Argentine coast (DRAGANI, 2007), Strait of Sicily (CANDELA *et al.*, 1999), and in the Balearic Islands (RABINOVICH and MONSERRAT, 1998) have been attributed to meteorological forcing.

In Colombo, after the first packet of waves from the December 2004 tsunami, enhanced high frequency oscillations superimposed on the tidal record were present for four to five days (Fig. 3). Spectral analysis of five days of data obtained before and immediately after each of the tsunamis in 2004, 2005 and 2007 indicated high frequency energy (e.g., at 75 minutes) was enhanced after the tsunami (Fig. 13a). Although the tide gauge was located in a harbour, the 75-minute oscillations were related to the study region's entire continental shelf, whose fundamental period is given by Merian's formula for an open system (PUGH, 1987):

$$T_n = \frac{1}{n}\frac{4L}{\sqrt{gh}},$$

where L is the width of the continental shelf; h is the mean water depth; g is acceleration due to gravity; and n is the mode number ($=1$ for the fundamental mode). The continental shelf adjacent to Colombo has a mean depth of 40 m and a width (to the 200-m contour where the shelf break occurs) of 22 km. Thus the tsunami enhanced the existing natural oscillation of the entire continental shelf. The time–frequency plot (Fig. 14) indicated higher frequency energy at the 75-minute band before the tsunami. During the tsunami, spectral energy increased across all frequencies, and subsequent to the tsunami, the energy at the higher frequencies decreased, nonetheless the energy at the 75-minute frequency band continued for almost 10 days (Fig. 14).

A similar pattern was found along the Western Australian coast (Fig. 2b). After the first packet of waves from the December 2004 tsunami, enhanced high frequency oscillations superimposed on the tidal record were present for four to five days (Fig. 5). At Geraldton, spectral analysis of five days of data obtained before and immediately after the tsunami showed the energy at the four-hour frequency band was enhanced after the

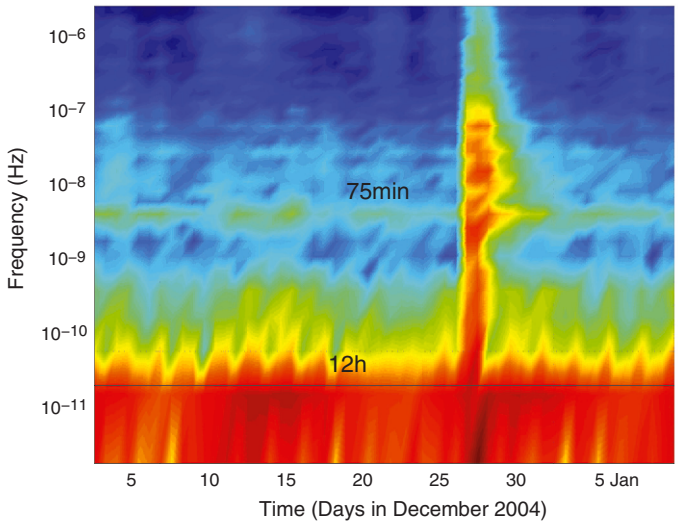

Figure 14
Time–frequency plot of the tidal record from Colombo for December 2004.

tsunami (Fig. 13b). The four-hour oscillations were related to the first mode of the study region's entire continental shelf. Here the continental shelf has a mean depth of 50 m and a width (to the 200-m contour) of 80 km; hence the tsunami enhanced the existing natural oscillation of the whole continental shelf.

The time–frequency plot (Fig. 15a) showed the presence of the enhanced energy at the four-hour band (before the tsunami) and the increased energy along all frequencies (during the tsunami). After the tsunami, the energy at the higher frequencies decreased, however the energy at the four-hour frequency band continued (Fig. 15a). Similarly, oscillations at 2.7 hours (Figs. 15c and 15d) were seen at Jurien Bay and Fremantle. A decrease in the shelf width caused these decreased period (cf. Geraldton), whereas further south at Busselton, the increase in shelf width increased the fundamental frequency to four hours (Fig. 15d).

The time–frequency plot also indicated events that caused higher energy levels across all the frequencies, similar to what was observed during the tsunami, although the maximum energy was lower than it was during the tsunami. In Western Australia, these events occurred on 5–6 December 2004, 9–10 January 2005, and 19–20 January 2005 (Fig. 15). These periods coincided with the passage of pressure systems, which enhanced the onshore (westerly) winds at the site. These results confirmed the findings of RABINOVICH and STEPHENSON (2004), who analysed sea-level records from the British Columbia coast and concluded that the oscillation periods identified from the sea-level records were related to the resonant properties of the local topography rather than the source characteristics and were the same as the background oscillations at each site.

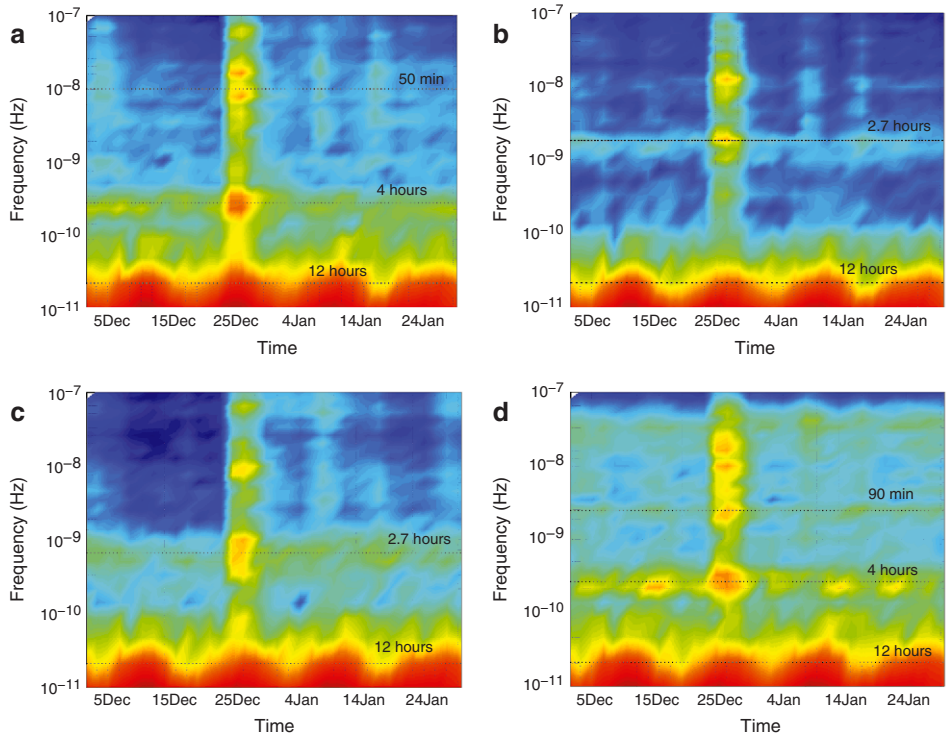

Figure 15
(a) Time–frequency plot of the tidal record from Geraldton for December 2004. (b) Time–frequency plot of the tidal record from Jurien Bay for December 2004. (c) Time–frequency plot of the tidal record from Fremantle for December 2004. (d) Time–frequency plot of the tidal record from Busselton for December 2004.

Thus the effect of the tsunami was to set up oscillations at the local resonance frequency. Because Sri Lanka and Western Australia have relatively straight coastlines, these oscillations were related to the fundamental period of the shelf oscillation. The actual nature of these oscillations in terms of standing or progressive edge waves trapped on the continental shelf (e.g., BRICKER *et al.*, 2007) was beyond the scope of this study.

6. *Conclusions*

Tide gauge data collected from Sri Lanka and Western Australia during five tsunamis—December 2004, March 2005, July 2006, and September 2007 (two tsunamis)—which occurred in the Indian Ocean, indicated that although the relative magnitudes of the tsunamis changed, the tsunami behaviour at each station was similar.

This was because the local and regional topography mainly controlled the tsunami characteristics at each station. Other major findings could be summarised as follows:

- At all stations in Sri Lanka and Western Australia, spectral energy corresponding to periods between 20 and 85 minutes increased during the tsunami.
- The sea-level data obtained from the west and south coasts of Sri Lanka (Colombo and Kirinda) indicated the importance of wave reflections from the Maldives Island chain, which produced the highest wave two to three hours after the first wave. In contrast, Trincomalee on the east coast did not show evidence of a reflected wave.
- Along the west coast of Australia, the highest waves occurred 15 hours after the arrival of the first wave. Here, based on travel times, we postulated that the waves were reflected from the Mascarene Ridge and/or the Island of Madagascar. Reflected waves were not present in the 2006 tsunami, in which the primary waves were propagated from topographic features.
- The effect of the tsunami was to set up oscillations at the local resonance frequency. Because Sri Lanka and Western Australia have relatively straight coastlines, these oscillations were related to the fundamental period of the shelf oscillation. For Colombo, this corresponded to the 75-minute period, whereas in Geraldton and Busselton (Australia), the four-hour period was most prominent; at Jurien Bay and Fremantle, the resonance period was 2.7 hours.

Acknowledgements

The authors would like to acknowledge Lanka Hydraulic Institute, Ltd. for the provision of offshore tidal data from Colombo, and Reena Lowry, Department for Planning and Infrastructure (WA), for providing the tidal data from Western Australia.

References

Bricker, J.D., Munger, S., Pequignet, C., Wells, J., Pawlak, G., and Cheung, K.F. (2007), *ADCP observations of edge waves off Oahu in the wake of the November 2006 Kuril Islands tsunami*, Geophys. Res. Lett. *34*, L23617, doi:10.1029/2007GL032015.

Candela, J., Mazzola, S., Sammari, C., Limeburner, R., Lozano, C.J., Patti, B., and Bonnano, A. (1999), *The "Mad Sea" phenomenon in the strait of Sicily*, J. Phys. Oceanogr. *29*, 2210–2231.

Cartwright, D.E., and Young, C.M. (1974), *Seiches and tidal ringing in the sea near Shetland*, Proc Roy. Soc. Lond. A. *338*, 111–128.

Choi, B.H., Pelinovsky, E., Kim, K.O., and Lee, J.S. (2003), *Simulation of the trans-oceanic tsunami propagation due to the 1883 Krakatau volcanic eruption*, Natural Hazards and Earth System Sciences *3*, 321–332.

Dominey-Howes, D. (2007), *Geological and historical records of tsunami in Australia*, Marine Geology *239*, 99–123.

DOMINEY-HOWES, D., CUMMINGS, P., and BURBIDGE, D. (2007), *Historic records of teletsunami in the Indian Ocean and insights from numerical modelling*, Natural Hazards *42*, 1–17.

DRAGANI, W.C. (2007), *Numerical experiments on the generation of long ocean waves in coastal waters of the Buenos Aires province, Argentina*, Continental Shelf Res. *27*, 699–712.

DRAGANI, W.C., D'ONOFRIO, E.E., GRISMEYERA, W., and FIOREA, M.E. (2006), *Tide gauge observations of the Indian ocean tsunami, December 26, 2004, in Buenos Aires coastal waters, Argentina.*, Continental Shelf Res. *26*, 1543–1550.

GREGSON, P.J., PAULL, E.P., and GAULL, B.A. (1979), *The effects in Western Australia of a major earthquake in Indonesia on 19 August 1977*, BMR J. Aust. Geology and Geophys. *4*, 135–140.

HEATH, R.A. (1982), *Generation of 2-3 hour oscillations on the east coast of New Zealand*, New Zealand J. Marine Freshwater Res. *16*, 111–117.

INOUE, S., WIJEYEWICKREMA, A.C., MATSUMOTO, H., MIURA, H., GUNARATNE, P.P., MADURAPPERUMA, M., and SEKIGUCHI, T. (2007), *Field survey of tsunami effects in Sri Lanka due to the Sumatra-Andaman earthquake of December 26, 2004*, Pure Appl. Geophys. *164*, 395–412.

KOWALIK, Z., KNIGHT, W., LOGAN, T., and WHITMORE, P. (2007), *The tsunami of 26 December, 2004: Numerical modeling and energy considerations*, Pure and Appl. Geophysics, *164*, 379–393.

LEGGET, S. (2006), *Modeling tsunami impacts on the Western Australian coast*. Unpubl Hon. Thesis, School of Environm. Sys. Engin. The University of Western Australia.

LITTLE, J.N., and SHURE, L. (1988), *Signal processing toolbox for use with MATLAB*, The Math Works Inc., 166 pp.

LIU, P., LYNETT, L.-F.P., FERNANDO, J., JAFFE, B.E., FRITZ, H., HIGMAN, B., MORTON, R., GOFF, J., and SYNOLAKIS, C. (2005), *Observations by the international tsunami team in Sri Lanka*, Science *308*, 1595.

MERRIFIELD, M.A., FIRING, Y.L., AARUP, T., AGRICOLE, W., BRUNDRIT, G., CHANG-SENG, D., FARRE, R., KILONSKY, B., KNIGHT, W., KONG, L., MAGORI, C., MANURUNG, P., MCCREERY, C., MITCHELL, W., PILLAY, S., SCHINDELE, F., SHILLINGTON, F., TESTUT, L., WIJERATNE, E.M.S., CALDWELL, P., JARDIN, J., NAKAHARA, S., PORTER, F.Y., and TURETSKY, N. (2005), *Tide gauge observations of the Indian Ocean tsunami, December 26, 2004*, Geophys. Res. Lett. *32*, doi: 10.1029/2005GL022610.

MILES, J. (1974), *Harbour seiching*, Ann. Rev. Fluid Mech., *6*, 17–33.

MURTY, T., and RAFIQ, M. (1991), *A tentative list of tsunamis in the marginal seas of the north Indian Ocean*, Natural Hazards *4*, 81–83

NAGARAJAN, B., SURESH, I., SUNDAR, D. SHARMA, R., LAL, A.K., NEETU, S., SHENOI, S.S.C., SHETYE, S.R., and SHANKAR, D. (2006), *The great tsunami of 26 December 2004: A description based on tide-gauge data from the Indian subcontinent and surrounding areas*, Earth Planets, Space *58*, 211–215.

ORTIZ, M., and BILHAM, R. (2003), *Source area and rupture parameters of the 31 December 1881 $M_w = 7.9$ Car Nicobar earthquake estimated from tsunamis recorded in the Bay of Bengal*. J Geophys. Res. *108*, doi:10.1029/2002JB001941.

PATTIARATCHI, C.B., and WOO, M. (2000), *Risk of tsunami impact at the Port of Dampier*, Centre for Water Research Report No. WP 1520 CP.

PUGH, D.T., *Tides, Surges and Mean Sea-level: A Handbook for Engineers and Scientists*, (Wiley, Chichester 1987), 472 pp.

RABINOVICH, A., and MONSERRAT, S. (1998), *Generation of meteorological tsunamis (large amplitude seiches) near the Balearic and Kuril Islands*, Natural Hazards *18*, 27–55.

RABINOVICH, A., and STEPHENSON, F.E. (2004), *Long wave measurements for the coast of British Columbia and improvements to the tsunami warning capability*, Natural Hazards *32*, 313–343.

RABINOVICH, A.B., and THOMSON, R.E. (2007), *The 26 December 2004 Sumatra Tsunami: Analysis of tide gauge data from the World Ocean. Part 1. Indian Ocean and South Africa*, Pure Appl. Geophys. *164*, 261–308.

RASTOGI, B.K., and JAISWAL, R.K. (2006), *A catalog of tsunamis in the Indian Ocean*, Science of Tsunami Hazards *25*, 128–143.

SYNOLAKIS C, IMAMURA F., TSUJI Y., MATSUTOMI H., TINTI S., COOK B., CHANDRA Y.P., and USMAN M. (1995). Damage, conditions of east Java tsunami of 1994 analyzed. EOS, Transactions American Geophysical Union, *76* (26), 257.

TITOV, V.V., RABINOVICH, A.B., MOFJELT, H., THOMSON, R.E., and GONZALES, F.I. (2005), *The global reach of the 26 December 2004 Sumatra tsunami*, Science *309*, 2045–2048.

WALTER, J. (ed.), *World Disasters Report 2005: Focus on Information in Disasters*, (Kumarian Press, Bloomfield, Connecticut 2005).

WOODWORTH, P.L., BLACKBURN, D.L., FODEN, P., HOLGATE, S., HORSBURGH, K., KNIGHT, P.L., SMITH, D.E., MACLEOD, E.A., and BRADSHAW, E. (2005), *Evidence for the Indonesian tsunami in British tidal records*, Weather *60*(9), 263–267.

(Received January 10, 2008, accepted June 18, 2008)
Published Online First: February 6, 2009

Pure appl. geophys. 166 (2009) 259–281
0033–4553/09/010259–23
DOI 10.1007/s00024-008-0431-8

Pure and Applied Geophysics

Reconstruction of Tsunami Inland Propagation on December 26, 2004 in Banda Aceh, Indonesia, through Field Investigations

Franck Lavigne,[1] Raphaël Paris,[2] Delphine Grancher,[1] Patrick Wassmer,[1] Daniel Brunstein,[1] Franck Vautier,[2] Frédéric Leone,[3] François Flohic,[4] Benjamin De Coster,[4] Taufik Gunawan,[5] Christopher Gomez,[1] Anggri Setiawan,[6] Rino Cahyadi,[6] and Fachrizal[5]

Abstract—This paper presents the results from an extensive field data collection effort following the December 26, 2004 earthquake and tsunami in Banda Aceh, Sumatra. The data were collected under the auspices of TSUNARISQUE, a joint French-Indonesian program dedicated to tsunami research and hazard mitigation, which has been active since before the 2004 event. In total, data from three months of field investigations are presented, which detail important aspects of the tsunami inundation dynamics in Banda Aceh. These include measurements of runup, tsunami wave heights, flow depths, flow directions, event chronology and building damage patterns. The result is a series of detailed inundation maps of the northern and western coasts of Sumatra including Banda Aceh and Lhok Nga.

Among the more important findings, we obtained consistent accounts that approximately ten separate waves affected the region after the earthquake; this indicates a high-frequency component of the tsunami wave energy in the extreme near-field. The largest tsunami wave heights were on the order of 35 m with a maximum runup height of 51 m. This value is the highest runup value measured in human history for a seismically generated tsunami. In addition, our field investigations show a significant discontinuity in the tsunami wave heights and flow depths along a line approximately 3 km inland, which the authors interpret to be the location of the collapse of the main tsunami bore caused by sudden energy dissipation. The propagating bore looked like a breaking wave from the landward side although it has distinct characteristics. Patterns of building damage are related to the location of the propagating bore with overall less damage to buildings beyond the line where the bore collapsed. This data set was built to be of use to the tsunami community for the purposes of calibrating and improving existing tsunami inundation models, especially in the analysis of extreme near-field events.

Key words: Tsunami, runup, tsunami bore, inundation, intensity scale, building damage.

[1] Laboratoire de Géographie Physique, UMR 8591 CNRS, 1 Place A. Briand, 92190 Meudon, France. E-mail: franck.lavigne@univ-paris1.fr

[2] Géolab UMR 6042 CNRS, Maison de la Recherche, 4 rue Ledru, 63057 Clermont-Ferrand, France.

[3] Department de Géographie, université Paul Valéry, Montpelliar, France.

[4] Planet Risk, 6 rue Marie-Thérèse, 91230 Montgeron, France.

[5] Badan Meteorologi dan Geofisika, Jl. Angkasa 1 No.2, Kemayoran, Jakarta Pusat, Indonesia.

[6] University Gadjah Mada (UGM), Jl Kaliurang, Yogyakarta, Indonesia.

1. Introduction

The 2004 Indian Ocean tsunami was triggered by a 9.15 magnitude earthquake (MELTZNER *et al.*, 2006; CHLIEH *et al.*, 2007) that occurred at 0:58:53 GMT, 7:58:53 LT (USGS) (t_{EQ}). The epicenter was located at 3.3 N, 95.8 E (Fig. 1) with a focal depth of approximately 30 km. The earthquake was responsible for a sudden fault slip estimated on average from 12–15 m (SYNOLAKIS *et al.*, 2005; LAY *et al.*, 2005) to 20 m (FU and SUN, 2006). The seismic moment estimate (Mo = 1.3 5 × 10^{30} dyne-cm), based on the

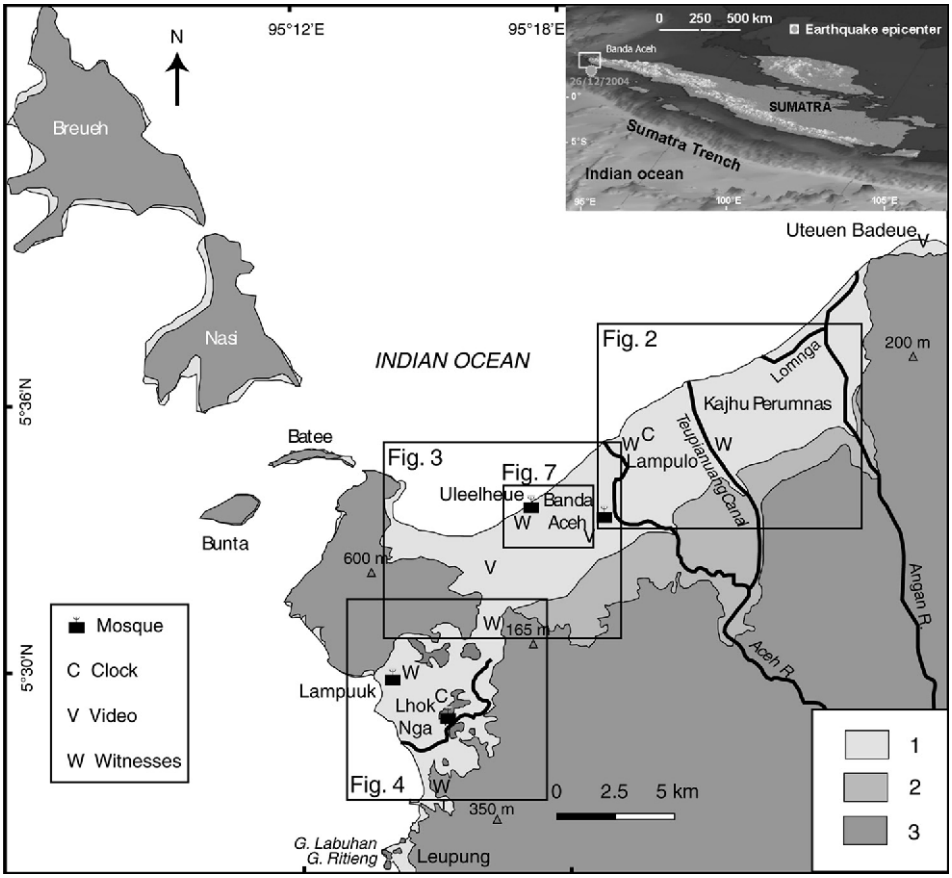

Figure 1

Locations of video recordings, recovered clocks, and reliable eyewitness observations. 1: Coastal plains flooded by the tsunami; 2: non-flooded coastal plains; 3: uplands. Insert 3D-map showing the Sumatra Island, the studied area, and the epicenter of the 26/12/2004 earthquake. The video taken at Uteuen Badeue, on the eastern edge of the Banda Aceh Bay, was recorded by the chief of the Fishery Regional Office from the top of a cliff. The movie that was shot near the Baiturrahman mosque in downtown Banda Aceh has been shown worldwide on TV. The one at Peukan Bada has been recorded during a wedding party. The last two movies were analyzed in detail in order to calculate the tsunami velocity (FRITZ *et al.*, 2006).

measurement of split modes of free oscillations of the Earth, is about three times larger than the $4\,5 \times 10^{29}$ dyne-cm measured from traditional long-period surface waves (STEIN and OKAL, 2005). In the model suggested by CHLIEH *et al*. (2007), the latitudinal distribution of released moment has three distinct peaks at about 4° N, 7° N, and 9° N, which compares well to the latitudinal variations seen in the seismic inversion and of the analysis of radiated T waves. The earthquake-induced damage to buildings was rather limited in Banda Aceh City. Along the coastline, the damage to structures was difficult to assess because the tsunami had totally destroyed the buildings.

Since the 1980s and the 1990s, the development of numerical modeling has increased the knowledge of offshore tsunami propagation (e.g., SYNOLAKIS, 1987; IMAMURA and SHUTO, 1990; CARRIER *et al*., 2003). Models currently in use include the French simulation code developed by the Commissariat à l'Energie Atomique (CEA) (HEINRICH *et al*., 1998; HÉBERT *et al*., 2001), the Method of Splitting Tsunami (MOST) model used by the Pacific Marine Environmental Laboratory of the National Oceanic and Atmospheric Administration (NOAA PMEL) (TITOV and SYNOLAKIS, 1998), the FUNWAVE model (developed by the Centre of Applied Coastal Research: KIRBY, 2003), and the code produced by workers from Japan called TUNAMI N2 (GOTO *et al*., 1997). Most of these models use linear or nonlinear shallow water assumptions, with or without dispersive effects, to study tsunamis generated by earthquakes and submarine landslides. Such models provide accurate simulations of far-field propagation of the tsunami waves. Some models like MOST have also been extensively validated against runup signatures, even for extreme events like the Okushiri tsunami (> 30 m runup). However, other models have not yet been used extensively in simulating near-field propagation and detailed inland wave behavior (e.g., transient bore propagation). This fact can be partially explained by a lack of a highly accurate DEM and source model, however mainly by a lack of accurate field data necessary to calibrate the models. Therefore, few inundation maps have been drawn following a major tsunami, and tsunami hazard mapping based on numerical modeling is still limited, except along the Japanese coast and the West coast of the USA (TITOV *et al*., 2004; WONG *et al*., 2005).

The December 26th, 2004 Indian Ocean earthquake and tsunami offers an opportunity to enhance our knowledge on tsunami processes and modeling, both near-shore and on land. Several research teams involved in the study of this unusual event thus far have focused their efforts on the tsunami origin — i.e. the earthquake mechanism — and/or trans-oceanic propagation (AMMON *et al*., 2005; GEIST *et al*., 2007; HÉBERT *et al*., 2007; ENGDAHL *et al*., 2007; VALLÉE, 2007). A few weeks after the disaster, other research groups conducted reconnaissance surveys along the Indonesian coasts in the framework of the International Tsunami Survey Teams (ITST) headed by BORRERO (2005a,b), BORRERO *et al*. (2006), YALCINER *et al*. (2005), and TSUJI *et al*. (2006). Such rapid field surveys were very useful in the aftermath of this exceptional tsunami that inundated hundreds of square kilometers of coasts and destroyed thousands of houses. For example, BORRERO (2005b) provided a table of overland flow depths and direction from throughout Banda Aceh, as well as a detailed map of the inundation extents and the first descriptions

of the wave crossing from Lhok Nga to the southwestern parts of Banda Aceh. Such data were enough to do preliminary modelling. However, additional data are needed to conduct in-depth analysis at a local scale.

An extensive database of tsunami propagation evidence has been collected for the Banda Aceh and Lhok Nga districts (Fig. 1). The data were collected under the auspices of TSUNARISQUE, a joint French-Indonesian program dedicated to tsunami research and hazard mitigation, which has been active since before the 2004 event. At the time of the Indian Ocean tsunami disaster, authors 1 and 2 accompanied the second ITST from 19 to 29 January 2005, and supplemented this preliminary survey by six subsequent trips conducted between August 2005 and August 2006. Finally, this program was completed after three months of field investigations, and with the help of more than 30 researchers, technicians, and students.

In this paper we synthesized the main data collected during these field trips in order to provide the most complete and accurate reconstruction of the dynamics of the tsunami inundation as possible. This analysis includes various aspects of the phenomenon, such as the time and space evolution of the different waves, tsunami height and runup variations, flow-depth distribution, as well as the contribution of backwash to coastal erosion. In addition, these parameters were discussed with several additional parameters, such as topography, location of tsunami bores, and building damages. Complementary analyses of the 2004 tsunami deposits and observations on the geomorphological effects of the tsunami were previously published (PARIS *et al*., 2007a, b). Beyond the direct contribution of this work to the understanding of the effects of giant tsunami waves on coastal areas, our database offers an opportunity to test, calibrate, and improve the existing numerical simulation codes, which are fundamental in assessing the hazards of future events. In this respect, a high-resolution DEM has been built from various datasets collected during the campaigns. The complete database, including this DEM, is available as open-source in a web page dedicated to the international community of tsunami modellers (www.tsunarisque.cnrs.fr).

2. Methods

The database contains 300 measurements of tsunami height, flow depth, runup, and inundation distance. For these measurements, a variety of standard tsunami field survey techniques were combined (e.g., TSUJI *et al*., 1995; OKAL *et al*., 2002), which has been previously published (LAVIGNE *et al*., 2006). Field data acquired using laser range finders (*LaserAce 300*) were calibrated from astronomical tide tables at Pulau Rusa and Uleelheue. The high density of field data allowed us to map the spatial distribution of tsunami height, flow depth, and runup, as well as the lines where the last transient tsunami bore collapsed several kilometers inland. At several sites, the highest marks on impacted trees or the upper limit of destruction traces on buildings decreased by several

meters in less than 100 m of distance, indicating a sudden energy loss attributed by the authors to collapse or "breaking" of a transient tsunami bore.

Flow directions for the tsunami waves, i.e., the angle with respect to the magnetic North, are evidenced by tilted trunks, pillars, and debris wrapped around trees. Two complementary methods were applied: (1) about 650 measures of flow orientation were collected using compass and GPS during two field surveys in January and August 2005; (2) About 400 additional data points (mostly coconut trunks in the rice fields) obtained through remote sensing and high-resolution air photograph as of June 2005 supplemented the database. For both methods, there is the potential for flow direction indicators to be biased due to the return flow. Therefore, landward flows and return flows were carefully distinguished in selecting only groups of parallel tilted trunks. This data set can be used to identify anomalous wave flow patterns such as interacting flows, and provide an additional means to evaluate the resolution of numerical simulations.

In order to complement these field data, interviews of eyewitnesses were conducted. Questionnaires were aimed at gaining a better understanding of the event's phenomenology. Information about the number of waves, the direction and timing of the flow, the location and shape of transient bores, and the sea retreat's distance was collected. However, forgetfulness, trauma, or influence of an official version of the event, may have influenced the testimonies given by local people, and the answers to our questionnaires were often approximate or even unreliable. For this reason, more reliable data to assess the arrival time of the tsunami waves were obtained through the analysis of three video recordings and the discovery of three broken clocks that stopped working when hit by a tsunami wave (see location in Fig. 1).

The patterns of building damage were investigated through the analysis of field survey, as well as aerial and satellite imagery. This technique compared existing buildings from before the tsunami to damage visible in post-event images. Over 6200 data points were collected and combined in a GIS framework using MapInfo® and Vertical Mapper® softwares, which allowed for a spatial representation of the building damage distribution. The damage level was classified based on structure vulnerability and level of damage (i.e., European Macro Seismic scale EMS98, Grunthal 1998, see Table 1).

3. Results

3.1. Earthquake Environmental Effects and Precursory Signs of Tsunami

In the Banda Aceh area, the great earthquake generated ground subsidence (MELTZNER *et al*., 2006), with amplitudes ranging from a few centimeters in Banda Aceh to about 2 meters along the west coast. Such large subsidence along the coast should have suggested to an aware observer the occurrence of a vertical displacement of the seafloor as a result of the earthquake, which was one natural warning signal of the incoming tsunami. In the

Table 1

Macro-tsunamic intensity scale based on buildings damages (from I to VI degrees). The term "Macro-tsunamic" is proposed by reference to the European Macro-Seismic intensity scale. This scale, developed by F. Leone, encompasses all building classes and damage levels

		Damage levels on buildings				
		D0 to D1	D1 to D2	D2 to D3	D4 to D5	D5 to D6
Buildings vulnerability classes	A	I	II	III	IV	V
	B	I	II	III	IV	VI
	C	II	III	IV	V	VI
	D	II	III	IV	V	VI
	E	II	IV	V	VI	VI

former swamp areas, transformed into shrimp basins or *tambak* along the north coast of Banda Aceh, liquefaction effects of clayed soils were observed. Eyewitnesses in Cotpaya or Miruk Taman (Fig. 2) described sulphurous, black water coming out of the ditches and sudden variations of well water levels, which were also mentioned by KITAGAWA *et al.* (2006). At Lampineung (Fig. 2), testimonies described malodorous black bubbles in water wells. Similar smells and colors were reported by fishermen roughly 1.5 km offshore. Along the karstic area of Lhok Nga, on the west coast, many wells were drained immediately following the earthquake.

Local people also reported hearing three detonations similar to bomb explosions that sounded between the main tectonic shock and the tsunami arrival. Similar noises were reported at the time of the 1933 Great Sanriku Earthquake in Japan (INOUYE, 1934) and of the 1977 Sumba earthquake and tsunami (KATO and TSUJI, 1995). These bangs are probably peculiar to earthquakes caused by the breaking of a sinking plate (KATO and TSUJI, 1995). However, SHUTO (1997) suggested that "thunder-like" sounds are generated and heard at distant places when tsunamis higher than 5 m hit coastal cliffs.

Another preliminary sign of the impending tsunami was a withdrawal of the ocean waters near the shore. The withdrawal related to the leading depression wave (SYNOLAKIS and TADEPALLI, 1996) was observed on the west coast about 10 minutes after the first shock of the earthquake. Testimonies reported similar observations at Meulaboh on the south coast (YALCINER *et al.*, 2005). The extent of the withdrawal exceeded 1 km off Banda Aceh and Lhok Nga, with the most reliable data being given by the Tuan Island, northwest off Uleelheue (Fig. 3). Located 1.2 km off the former coastline, the seawater surrounding this small island was drained during the leading depression wave related drawdown. The leading depression was estimated to 10 minutes. The corresponding lowering of the sea level has been estimated at 5 m $\pm$ 1 m by local fishermen. At Lampuuk (Fig. 4), the duration of the sea withdrawal lasted several minutes based on testimonies.

The last warning sign of the tsunami arrival was the massive migration of bird colonies flying landward from the open sea. Numerous eyewitnesses reported, after the disaster, to have heard bird calls which were interpreted by some villagers as a warning

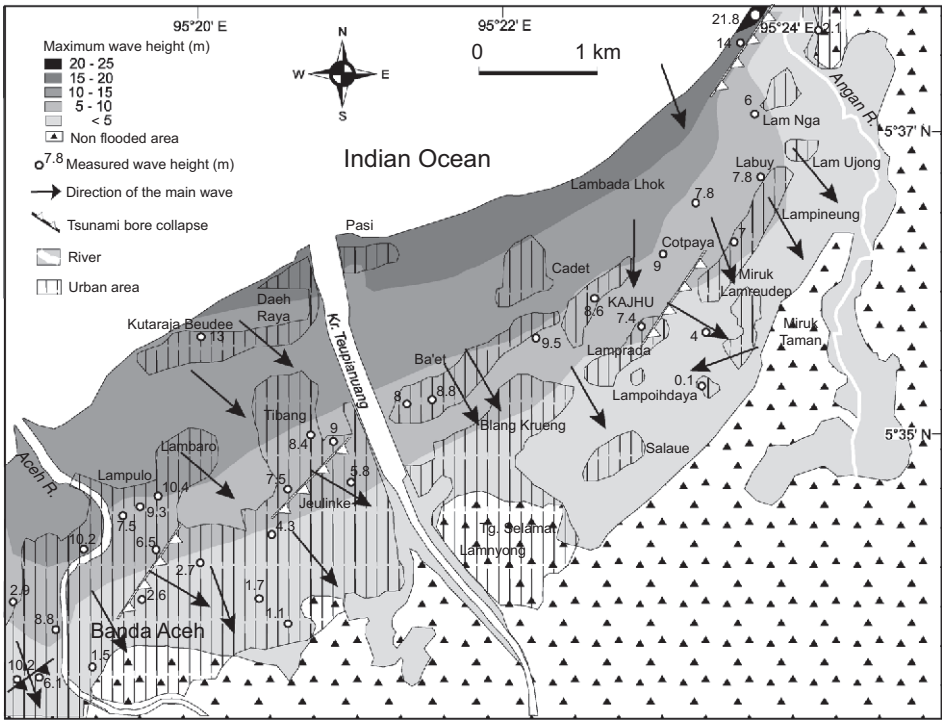

Figure 2
Tsunami propagation across the eastern part of the Banda Aceh plain.

for people threatened by the tsunami. This underlines the great efforts that still need to be focused on tsunami education and raising tsunami awareness.

3.2. Tsunami Waves and Velocities

Eyewitnesses reported between 10 and 12 waves along the coastlines all around the Banda Aceh area. The chief of the Fishery Regional Office at Uteuen Badeue (Fig. 1) recorded a dozen waves on videotape. Further west, eyewitnesses reported about ten waves from the bridge over the Teupianuang Canal, which was not inundated by the tsunami. Near downtown Banda Aceh, people who found shelter in the famous boat that overtopped a house at Lampulo also reported ten waves, like other eyewitnesses at Lampuuk and Labuhan (a military camp above the cement factory and the harbor: Fig. 4). However, several individual waves identified by the eyewitnesses may have resulted from the decomposition of single transient bores that have broken up into multiple waves.

Rather detailed descriptions were obtained for the first three waves. The leading wave moved rapidly landward as a turbulent flow with depths ranging from 0.5 to 2.5 m from

ground, depending on the local topography. The velocity of this flow was estimated to be approximately 8–10 $m.s^{-1}$, based on testimonies of some survivors at Lampuuk, who fled from this wave by motorcycle at a similar speed. The leading wave carried a large amount of debris. Several survivors reported that this wave was responsible for the destruction of most of the so-called *sederhana* and *semi-permanent* houses, as they are built using wood and bamboo. In spite of its limited depth and its solid waste, this flow moved as far as 2 km inland up to Ba'et village (Fig. 2), and as far as 3.5 km inland in downtown Banda Aceh. This first wave may have corresponded to the leading edge of the tsunami, i.e., the water that was being pushed by the second bore. Contrary to this leading wave, the second bore moved landward as a rapidly rising tide of dark color. Little is known about the following waves, which were lower than the subsequent waves, and thus came over areas already inundated and devastated. However, witnesses at Lampuuk, Uleelheue, Lamtengoh, northwest of Banda Aceh city, Figure 3, reported that the third wave was higher than the second one.

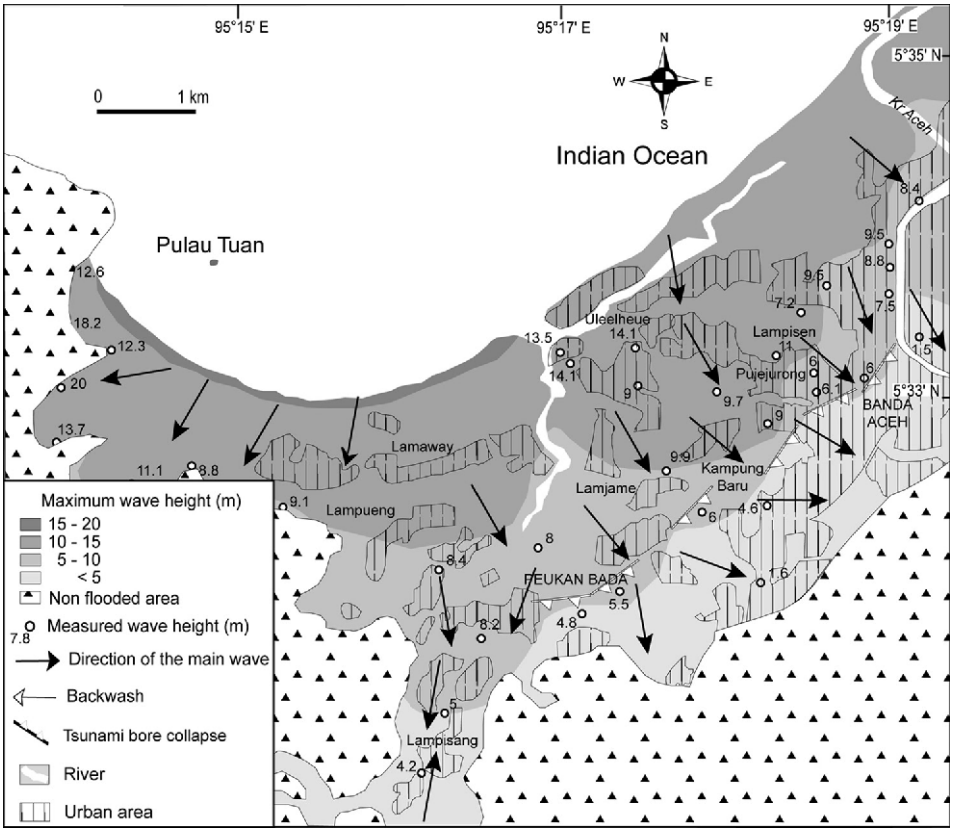

Figure 3
Tsunami propagation across the western part of the Banda Aceh plain.

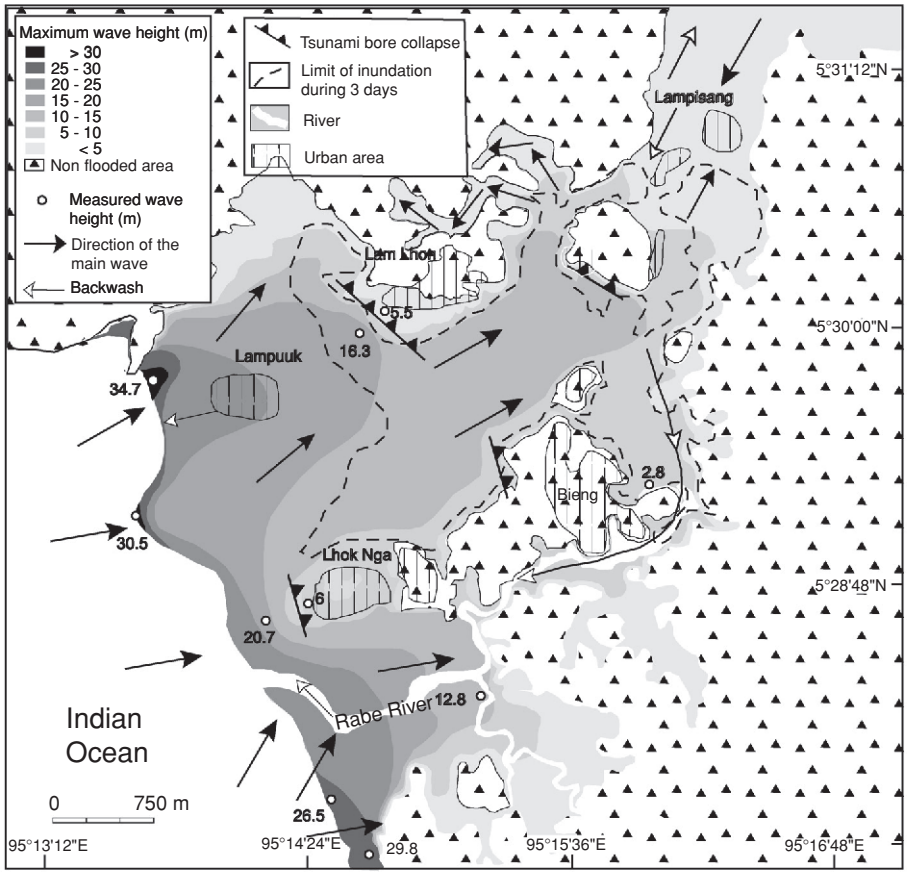

Figure 4
Tsunami propagation across the west coast (Lhok Nga subdistrict).

3.3. Tsunami Arrival Time

The tsunami arrival time is a fundamental parameter required to calibrate numerical models. However, accurate time data were difficult to obtain, due to contradictory testimonies and the scarcity of solid evidence that could be used to clarify the tsunami wave's chronology. Although also controversial, more accurate data based on stopped clocks and video sequences helped to estimate the tsunami velocity (Table 2).

On the west coast, the imam of Lhok Nga's main mosque heard people shouting "air laut naik" (the sea level raises) at 8:12 LT (t_{EQ} + 13 min), meaning that he heard the shouts when the sea started to return from its lowest receding level. The clock he found in his neighbor's house was broken by the leading wave at 8:20 LT (Fig. 5a) (t_{EQ} + 21 min). The second wave (the main one) occurred less than 5 minutes after the

Table 2

Characteristics of the tsunami waves on the 26 December 2004 in Banda Aceh District

		West coast		North coast			
		Lampuuk (mosque)	Lhok Nga (mosque)	Uleelheue (mosque)	Baiturrahman (mosque)	Lampulo (boat)	Teupianuang (bridge)
Coordinates (UTM)		747678 607764	748805 605982	753105 614607	756620 614340	757566 616755	760797 617865
Distance from coast (km)		0.7	1.3	0.1	2.5	1.5	2.2
Number of waves		~10	~10	> 3	2	~12	~10
Leading wave	Time	nd	8:20 LT (t_{EQ}+21 min)	nd	8:47 LT (t_{EQ}+48 min)	8:40 LT (t_{EQ}+41 min)	nd
	Direction (origin)	SW	SW	NW	NW	NW	NW
	Depth (m)	1.5	1	1.5	0.5	1	1
	Velocity ($m.s^{-1}$)	8-10	nd	very fast	1	nd	very fast
Second wave	Time	nd	8:25 LT (t_{EQ}+26 min)	nd	8:48 LT (t_{EQ}+49 min)	8:42/43 LT (t_{EQ}+43/44 min)	nd
	Direction	W	W	NW first, then NE & N	NW	NW first, then NE & N	NE first, then WNW & N
	Depth (m)	~20	8	~10	1.3	6	7 (Edge of the bridge)
	Velocity (m/s)	nd	nd	nd	4	nd	nd
Third wave	Time	nd	nd	nd		9:00 LT (t_{EQ}+61 min)	nd

LT: Local Time.
nd: no data.

Figure 5
Clocks stopped by the tsunami waves. A: Mr. Abu Abdul Rhaffar, Imam of Lhok Nga's main mosque, carrying a clock stopped by the first tsunami wave at 8:20 LT. B and C: Two clocks stopped by the second tsunami wave at Lampulo, 1.5 km from the open ocean. Located inside the same house near the boat, they stopped at 8:44 LT and 8:49 LT, respectively. (Photos: F. Lavigne).

first wave (t_{EQ} + 26 min) at Lampuuk and Lhok Nga, and no backwash was reported between these two waves at these locations. Although several testimonies reported the occurrence of a third wave higher than the second one, the exact chronology remains unclear.

At Lampulo, northeast of Banda Aceh (Fig. 1), a boat can still be found perched on the roof of a house 1.5 km from the ocean. The leading edge of the tsunami arrived along the north coast at approximately 8:40 LT. The second wave arrived 2 to 3 minutes after the leading wave (t_{EQ} + 42/43 min), and broke two clocks in a house (Fig. 5b). The first clock originally hung on a wall 2 m above the floor, stopped at 8:44 LT (t_{EQ} + 45 min), whereas the second one, hung at 3 m, stopped at 8:49 LT (t_{EQ} + 50 min). Considering a minimum flow velocity of 4 $m.s^{-1}$ calculated by Fritz *et al*. (2006) near the great mosque and at Peukan Bada, the front of the second wave reached the north coast less than 6 minutes before its arrival at the mosque (4 m/s × 1500 m), i.e. at t_{EQ} + 39 min or slightly less. The boat on the roof was carried by the third wave at about 9:00 LT (t_{EQ} + 61 min), i.e., about 10 minutes after the second wave. Eyewitnesses at Lampulo reported that the sea level withdrew by 1 m preceding the arrival of the third wave. This

small backwash between the second and the third wave was also observed in other locations, e.g., north of Cadet (Fig. 2).

At the Baiturrahman mosque in downtown Banda Aceh, the flow velocity of the leading wave did not exceed 1 $m.s^{-1}$ (Borrero, 2005b; Fritz *et al.*, 2006) due to the large amount of debris it was transporting. Based on a video frame analysis, the second tsunami wave arrived at the site only 40 seconds after its leading edge, with a flow velocity of 4 $m.s^{-1}$ (Fritz *et al.*, 2006). Assuming this velocity as constant from the shore to the mosque on a 2.5-km distance (whereas it was higher than this value), the second wave should have reached the city center in 10 minutes (4 $m.s^{-1} \times 2500$ m), i.e., at $t_{EQ} + 49$ min. This arrival time is twice the initial estimation of Borrero (2005b) who simply reported witness accounts during the immediate aftermath of the disaster. Such discrepancy underlines that the data obtained through broken clock and videos, although somewhat controversial, are still more reliable than information obtained by witnesses.

3.4. Flow Directions

Flow direction data obtained through eyewitness accounts and/or tilted trunks, pillars, and debris are of primary importance in reconstructing the wave's origin. Thus, a detailed analysis of the flow directions may help calibrate the numerical models.

The leading wave was almost perpendicular to the shore along the west coast, whereas it reached the northern shore from the northwest with an angle of 45° near the Aceh River mouth (Fig. 2) and Uleelheue (Fig. 3). The second wave reached Lhok Nga on the west coast from the southwest at an angle of about 45°. Therefore, its source may be attributed to the moment peak at about 4° N, rather than to the ones at 7° N and 9° N. This flow was moving as a single and massive tsunami front. On the northern coast, this front was divided into three segments of different directions, namely WNW, N and NE. On the eastern part of the Banda Aceh Bay, the northeast wavefront came first, whereas the northwest one came first at Uleelheue. These three segments of similar height (see below) probably resulted from the division of the second wave into separate waves after multiple refraction and diffraction effects near shore around the islands to the northwest of Banda Aceh (Fig. 1). In addition, some reflection effects may have enhanced the local effects of the tsunami, as also reported on Babi Island (Flores) in 1992 (Yeh *et al.*, 1994; Minoura *et al.*, 1997) and at Pangandaran (South Java) in July 2006 (Lavigne *et al.*, 2007). These waves collided with each other a few kilometers inland in several locations (e.g., at Jambutape, Lampulo, Lamprada, Lamjame: Fig. 2), as reported by testimonies or evidenced by trunks or pillars that were tilted in many different directions. The flow moving landward from Lhok Nga on the west coast interacted with the one moving from Uleelheue at Lampisang (Figs. 3 and 4). Such collision between waves may partly explain the differences in flow depth and orientations in neighboring areas.

3.5. Runup Heights

The apparent uniformity of the runup as indicated by the trim line (i.e., the upper limit of vegetation clearing by the tsunami on coastal hill slopes and cliffs) hundreds of kilometers along the west coast, typically 25 to 35 m, suggests that significant co-seismic submarine landslides were limited during the great Indian Ocean earthquake. Were this not the case, extreme runup values should have been locally identified (OKAL and SYNOLAKIS, 2003, 2004), as recently reported at Nusa Kambangan Island during the 17 July, 2006 tsunami that hit Java (FRITZ *et al*., 2007). A large mass failure capable of producing such a large wave has not been found yet for the 2004 tsunami event, even though marine surveys have taken place in search of such features along Sumatra's coast. Local geomorphological configurations of the coastline and/or the seafloor, however, were responsible for exceptional runup heights along the west coast of the Banda Aceh district. In Figure 6, the vegetation distribution along the cliff suggests that the runup heights varied from 27 m (left part of both pictures), which was the average tsunami height along the coast, to a maximum of 51 m (center of the picture). Even though this value is the highest recorded in human history for a non-landslide generated tsunami (cf. *NOAA National Geophysical Data Center*), this runup is roughly 10% of the 524 m runup marked by the trimline of the 1958 Lituya Bay landslide impact tsunami (MILLER 1960; FRITZ *et al*. 2001; FRITZ 2009, THIS ISSUE).

On the flat areas of the west coast, the tsunami height typically ranged from 25 to 35 m a.s.l., based on the height of the Filao trees near Lhok Nga's harbor. On the northeast coast, available data of tsunami heights are rather limited east of the Aceh

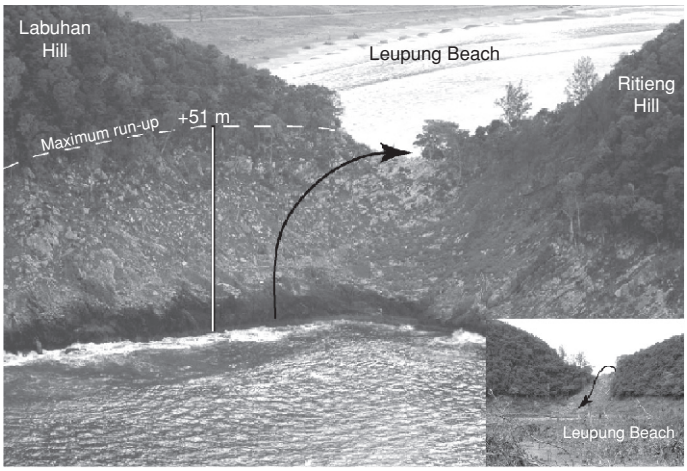

Figure 6
Runup height of 51 m a.s.l. measured on a cliff near Leupung, on the west coast (location in Fig. 1). The arrow displays the direction of the tsunami wave, which crossed the pass between Labuhan Hill and Ritieng Hill (Photos: F. Leone and F. Lavigne).

River, due to the lack of remaining trees and buildings. However, several reliable testimonies reported that the front of the second wave was as high as the coconut trees close to the shoreline, i.e., about 20 m a.s.l. On the eastern part of the bay, broken branches of Filao trees on sand dunes indicated runup values up to 22 m a.s.l. At Uleelheue, the maximum tsunami height did not exceed 13.5 m a.s.l. at the mosque.

3.6. Overland Tsunami Propagation

Landward motion of tsunamis is one of the lesser-known parameters for tsunami modeling. The rate that wave height and flow depth decrease with distance from the shoreline is poorly known, as are the factors that may explain the spatial variations of this rate. A recurrent question for the modellers is: Do the models require any additional basal friction to account for local topography, vegetation and buildings? Some results of our field investigations are presented below, which may help to answer this challenging question.

Before the collapse of the main tsunami bore two or three kilometers inland, the flow depth progressively decreased at a rate that ranged from 20 cm per 100 m to 60 cm per 100 m. At Lhok Nga on the west coast, this rate reached 50 cm per 100 m along the two first kilometers inland. Then was half this value across the 2-km long swamp further inland. On the coast north of Banda Aceh City, the flow depth decreased at various rates, i.e., 50 to 60 cm per 100 m on the eastern part of the bay (see Fig. 2), 25–30 cm per 100 m in the northeast suburbs of Banda Aceh City (e.g., at Lamparo or Jeulinke, Fig. 2), and 20 cm per 100 m on the northwest suburbs between Uleelheue and downtown Banda Aceh.

The above data may help define the role various factors play in controlling the rate at which flow depth decreases before the tsunami bore collapses.

The maximum rates were calculated at Lhok Nga and on the eastern part of the Banda Aceh Bay, where the maximum tsunami heights at the coastline were observed. Therefore the height of the main bore seems to play a key role in this rate, the higher the bore at the coastline, the higher the rate of decreasing flow depth. Indeed, the increase of flow depth due to a sudden increase of the nearshore slope (from 0.13% to 1.3% on the last 1.5 km) causes a drastic reduction of the tsunami velocity. This rapid dissipation of energy as the wave moves inland has also been inferred from the thickness, mean size, and sorting of the tsunami deposits in these areas (Paris *et al.*, 2007a; Jaffe *et al.*, 2006).

The local topography of the shore also played an important role in the landward reduction of flow depth. Indeed, huge sand dunes help to dissipate the wave's energy; at Lhok Nga and on the coast northeast of Banda Aceh, the dunes reaching elevations as high as 8 m a.s.l have been partly eroded by the tsunami. For an initial depth in excess of 20 m, the decreasing rate of the tsunami is about 50 cm per 100 m when the tsunami moves across a sand dune field. When the tsunami waves moved across swamps, shrimp basins or rice fields, the limited roughness of the ground explains lower decreasing rates, ranging around 20 cm per 100 m.

The role played by human settlements seems to be very limited before the collapse of the tsunami bore. Along the road between the Uleelheue mosque and downtown Banda Aceh, where the former traditional villages had previously been transformed into a residential area including concrete, two-story houses, the tsunami bore moved landward with a rather constant flow depth. The decreasing rate of flow depth was in the same order as the one calculated across non-built areas. Artificial dams and fringing reefs were also inefficient in locally reducing the tsunami velocity and depth (PARIS *et al*., 2007b).

3.7. Transient Tsunami Bores Formation and Collapse

For the first time since the major tsunamis crossed the Pacific in 1960 and 1964, the 26 December, 2004 event made it possible to accurately determine the location where the main tsunami bores collapsed due to the sudden energy dissipation of the second wave. Data based on field measurements (sudden decrease in flow depth) were always confirmed by relevant eyewitnesses, who used the Indonesian words "ombak pecah" (meaning "wave broke") to describe the collapse of the bores. Such data are of major importance when calibrating the numerical models that utilize this parameter. Thus far, the bore's collapse or "breaking" of tsunami waves has been analyzed mainly through physical modeling in artificial basins or through a mathematical approach (GRILLI *et al*., 1997). Our result will allow comparisons between these models and the 2004 field data.

Everywhere within the studied area, eyewitnesses described the shape of the propagating bore as similar to "standing cobra snake," meaning a high standing wave with vortex. Transient tsunami bores formed between 1.5 to 3 km inland (Figs. 3, 4, and 5). To the east of Banda Aceh Bay (Fig. 2), the bore related to the second wave collapsed in the rice fields south of the main road 1.7 km to 2 km from the coast line. In the northeast suburbs of Banda Aceh city, the propagating bore collapsed from 1.5 km, e.g., at Lamparo, to 3 km at Jeulinke, where the 7.5 m-high wave "broke" on the commercial buildings along the road. In the northwest suburbs of Banda Aceh City, the bore related to the second wave coming from Uleelheue collapsed near the Perusaahan Listrik Negara (PLN) boat, i.e., about 2.5 km inland from the open ocean. In this place, the flow depth suddenly diminished from 9–10 m to 1.5–2 m in a few hundred meters (Fig. 3).

The factors that contribute to the formation and disappearance of transient tsunami bores are difficult to assess. Some bores collapsed on contact with hill slopes. For example, Figure 5 shows a "breaking" line along the slope of a small hill covered with a coconut plantation, behind the golf course of Lhok Nga, located 1 km away from the shore. Due to the bore's collapse, the village was partially spared. Some survivors had taken refuge on the roofs of non-flooded houses. Another bore collapsed 2 km away from Lampuuk beach, at Lam Lhom village (Fig. 4). The flow depth suddenly decreased from about 16.5 m to 5.5 m over a distance of less than 100 m. Eyewitnesses described a "breaking wave" along a 5-m high palaeoshore covered by a coconut plantation that lies in front of the village. For the flat areas of the north coast, Figures 2 and 3 show that most

Figure 7 ▶

Investigation of tsunami-induced damage on building after the 26 December, 2004 tsunami. A. Studied area between Uleelheue and downtown Banda Aceh. B. Map of studied buildings. The selected area was divided in 25 ha squares. Within each square, the damaged building were precisely located using the freely available post-disaster high-resolution Quick Bird imagery (http://www.digitalglobe.com), and high resolution aerial photographs provided by Bakosurtanal (4970 units), from June 2005. C. Map of interpolated damage intensity for all building types (methodology and map conception: F. Leone).

of the bores collapsed where the flow depth ranges from five to ten meters. This may indicate a depth/velocity threshold for the destruction of the transient bores.

In addition with the local topographical settings, the collapse of the bores could have also been caused by the incoming flow interacting with the receding flow. However, the location of the interacting flows ("air beradu" in Indonesian language) reported by witnesses or enhanced through the flow direction map do not match with those of the bores' collapse. Furthermore, based on our field data, the density of human settlements did not play any role in the bore collapse process.

3.8. Flow Depth after Bores Collapses, Inundation Distance and Duration, and Backwash

Following the collapse of bores related to the second wave, the flow depth of the tsunami rapidly decreased. The runout flow spread over Banda Aceh City and its suburbs through foiled surges, sparing some districts and damaging others. The flow from Uleelheue encountered the one from Lampulo in the center of the city, where the flow depth did not exceed 2 m, based on the video recording analysis from FRITZ *et al*. (2006). The high density of buildings explains why the flow was reduced within the city. To the east of the Aceh River, the presence of old beach ridges (or palaeoshores) running parallel to the current shore drastically reduced both flow depth and velocity of the second wave. The propagation of the following waves was stopped by the backwash of the second wave. Therefore, the inundation line did not exceed 2 km inland (Fig. 2). As for the tsunami wave coming from the west coast, it continued moving inland as far as 6 km, at which point it met the wave coming from the north coast.

On the north coast, the flow started to recede towards the ocean at about noon. At Kajhu (Fig. 2), the backwash lasted several hours during the first night following the disaster. The sea withdrawal was not regular, but occurred by steps. The mud lines at different levels, usually three, in the houses are evidence of periods of stagnant water that lasted for hours. At Lampulo, the flow depth was still 1 m at 14:30 LT, two and a half hours after the peak flow of 9 m. Therefore, the average velocity of the drawdown was about 5.3 cm per minute during this time interval. Closer to the shore, the current generated by the backwash was reported to be very fast. However, several indications suggest a laminar receding flow rather than a series of concentrated flows parallel to each other, including the absence of new gullies or other erosional features created by the backwash (UMITSU *et al*., 2007), the lack of sedimentary features of backwash within the tsunami deposits, as well as several testimonies. Contrarily, at Lampuuk (west coast),

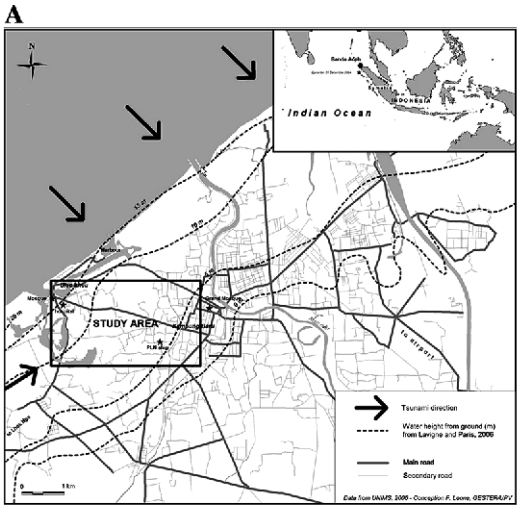
A
Indian Ocean
STUDY AREA
Tsunami direction
Water height from ground (m) from Lavigne and Paris, 2008
Main road
Secondary road
Data from DHAPS, 2005 - Conception F. Leone, GESTER/UPV

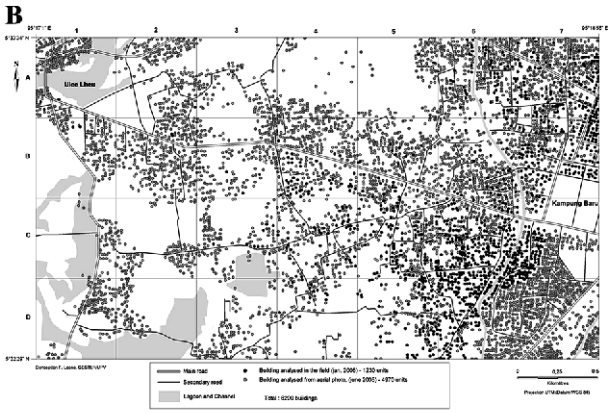
B
Lhoe Lhee
Kampung Baru
Main road
Secondary road
Lagoon and Channel
Building analysed in the field (jan. 2006) - 1230 units
Building analysed from aerial photo. (june 2005) - 4972 units
Total : 6200 buildings

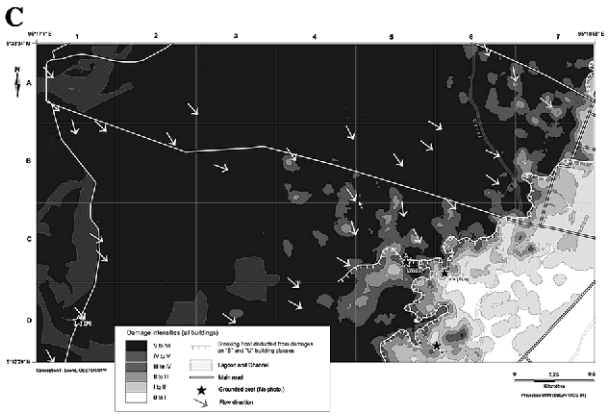
C
Damage intensities (all buildings)
Missing trees deducted from damages on "B" and "A" building classes
Lagoon and Channel
Main road
Grounded boat (file photo.)
Flow direction

the strong return current enlarged the river beds and created new gullies up to 20-m wide and 2-m deep (PARIS *et al.*, 2007b).

The inundation lasted for three days at several sites. On the north coast, the long inundation preceding the backwash was mainly due to coseismic subsidence, which reached 0.50 m at Lampulo. The destruction of the polders by the tsunami, e.g., west to Uleelheue, may have favored the inundation. On the west coast, the tsunami flooded an approximate area of 65 km^2 between Lampuuk and Lampisang (Fig. 4). The inundation lasted three days, due to the combination of two factors. Firstly, what had once been a mangrove forest had previously been transformed into rice fields. Thus, this area is lower than the sandy shore, even after most of the sand dunes at Lampuuk were eroded by the tsunami. Therefore, the return flow followed the Rabe River instead of reversing and returning along the runup course. Secondly, a natural dam formed by tons of trees and debris of all types interrupted the backwash. A breach through the dam allowed the drainage of the stagnant water only three days after the tsunami event (Fig. 4).

3.9. Tsunami Intensity Based on Building Destruction

The integration and interpolation of 6200 damaged buildings in a GIS enabled reconstitution of the damage gradient in the northwestern suburbs of Banda Aceh city (Table 1 and Fig. 7). Nearly all of the buildings suffered grade 5 damage (i.e., destruction/collapse) and only a few reinforced-concrete buildings (e.g., a big mosque, the hospital, and a school at Uleelheue) suffered very heavy structural damage (grade 4). No substantial to heavy damage (grade 3) has been observed. Artificial embankments collapsed, and big boulders from these embankments or from the near-shore sea floor were moved inland (e.g., 85 tons of coral boulders in Labuhan: PARIS *et al.*, 2007a). The tsunami also damaged port breakwaters, destroyed or washed away small vessels, and violently moved large vessels ashore. Figure 7c underlines a steep drop in the damage gradient around 2.7 km from the coast. Interestingly, four grounded boats are plotted exactly along the line of the bore's collapse, indicating a sudden drop in tsunami energy. This line was further refined using the Macro-tsunamic intensity scale (Table 1). The final shape of the line outlines digitations that can be associated with different wave heights or roughness variations of the topography. However, such lobes that are drawn on Figure 7 are difficult to interpret owing to the complex dynamics of the tsunami within the town.

4. Discussion and Conclusion

The 26 December, 2004 tsunami was an exceptional catastrophic event in the Banda Aceh area in every aspect.

The maximum tsunami height reached 35 m, i.e., approximately the height of a 10-story building, at the coastline of Lhok Nga, whereas historical records have rarely

exceeded 20 m. The maximum runup height reached 51 m on a high cliff at Labuhan. At least 3 factors may explain this record: (1) a "wave trap" morphology, i.e., a small bay oriented toward the wave train, (2) a 50° inclined cliff at the bay's upper two-thirds extent, and (3) a large continental shelf (25-km wide) with gentle slope gradient (0.13%).

The 26 December, 2004 tsunami caused the worst marine inundation ever reported in a large city located at more the 3 km from the shore. In almost every village, local eyewitnesses reported that the main tsunami waves were coming from two or three directions almost instantaneously. Trying to reconstruct the arrival time and flow direction of the main wave, which is supposed to have flattened most of the trees, was therefore quite challenging. Based on stopped clocks and video sequences, the front of the second wave reached the north coast about 40 minutes after the earthquake, i.e. twice the arrival time recorded on the west coast.

The tsunami's intensity in Indonesia ranked 6 (disastrous) on the Sieberg and Ambraseys' scale (AMBRASEYS, 1962), and XII (completely devastating) on the Papadopoulos and Imamura's scale (PAPADOPOULOS and IMAMURA, 2001). In both scales, it reached the highest intensity. Consequently, the tsunami is responsible for the deaths of more than 178,000 people in the Aceh province alone, including 90,000 in the city itself.

Many tsunami waves do not display any bore as they hit land, especially for slopes steeper than 12° (GRILLI *et al*., 1997). They simply surge, flooding low-lying areas. During the Indian Ocean tsunami event, tsunami bores were observed as far as 3 km inland. At such distance, it can be assumed that the waves were "breaking" for the second or third time. However, field data display everywhere a progressive decreasing of the flow depth at a rate that ranged from 20 cm per 100 m to 60 cm per 100 m until the bore collapsed. Such data seem to act contradictorily with an assumption of transient bores reforming and "breaking" again.

The tsunami bore propagation plays a key role in the destruction processes of the buildings. Before crashing down on itself, the bore washed away all types of buildings except the huge mosques (e.g., at Lampuuk). The houses were totally destroyed independently of the flow depth when this depth exceeded 10 m. After the bore collapsed, water penetrated inland taking the form of fast-moving floods that have considerably less destruction power. Indeed, "postbreaking" behaviors exhibit a rapid

Table 3

Tsunami Intensity Scale proposed by PAPADOPOULOS and IMAMURA (2001) versus revised scale proposed by F. Leone in this paper

Intensity from Leone et al.	H(m)	Intensity from Papadopoulos et al., 2001
I	< 1.5	I to V
II	2	VI
III	3	VII to X
IV	5	
V	8	
VI	> 11	XI to XII

(nondissipative) decay associated with a transfer of potential energy into kinetic energy. Wave velocity decreases in this zone of rapid decay, as previously demonstrated by GRILLI *et al*. (1997) through numerical modeling. Thus, the houses were damaged but not completely swept away after the bores' collapse. Our field observation on the aftermath of the July 2006 tsunami event in Java confirmed this affirmation. As the tsunami wave hit the Batukaras and the Permisan beaches of Java, the flow depth increased to over 10 meters (LAVIGNE *et al*., 2007). The houses close to the shore were completely destroyed, whereas houses were only slightly damaged beyond the line where the bore collapsed.

Our extensive field work made it possible to construct a tsunami damage intensity scale based upon quantitative data that includes all building classes and levels of damage. This scale is named here the "Macrotsunamic Intensity Scale" after the Macroseismic Intensity Scale of GRUNTHAL (1998). Our results should also enhance the Tsunami Intensity Scale proposed by PAPADOPOULOS and IMAMURA (2001; Table 3), which to date has not been calibrated for megatsunami events. In particular, the results of our comparison between damage gradients and flow depth suggest a need to revise the definition of the XI level of the PAPADOPOULOS and IMAMURA (2001) scale, which is the "devastating" level associated with a tsunami height of > 16 m. Indeed, this scale indicates a damage of grade 5 in many masonry buildings, grade 4 in a few reinforced-concrete buildings, and grade 3 for most of the other reinforced-concrete buildings. On the north coast of Banda Aceh City (wave height around 16 m), most all of the buildings suffered grade 5 damage and only a few reinforced-concrete buildings suffered grade 4 damage. No grade 3 damage has been observed. Actually, 10 m seems to be the depth of water where the correlation between water depth and damage levels breaks down.

The open-source database obtained in the frame of the TSUNARISQUE programme offers an opportunity for worldwide researchers to better calibrate numerical models. Data includes high-resolution DEM of near-shore and coastal areas at Banda Aceh and Lhok Nga, tsunami and runup heights, flow depth, flow directions measured in the field, chronology of the waves, location of the hydraulic jumps, damage maps using a new quantitative-based tsunami intensity scale, and additional studies on sediment deposits previously published (PARIS *et al*., 2006, 2007). Our field data will provide interesting challenges for mathematicians and earth scientists, including modeling of transient bore propagation and collapse, determining the friction and erosion processes of tsunami, modeling the turbulence, determining the effect of buildings and vegetation on the wave propagation, etc.

Acknowledgements

This paper is dedicated to the memory of our student and co-author Rino Cahyadi, who tragically died during a field trip in Thailand in 2007. The first measurements in January

2005 were achieved during the first ITST led by Prof. Tsuji. The following field surveys were carried out in the frame of the Tsunarisque Programme funded by the French Délégation Interministérielle pour l'Aide Post-Tsunami (DIPT), the French Embassy in Indonesia, and the French National Centre for Scientific Research (CNRS – ATIP Programme). The authors thank Waluyo, Syahnan, Laurent Mahieu and Nicolas Lespinasse, who contributed to field data acquisition, Marc Le Moullec and P.T. Enrique in Jakarta who provided high-resolution aerial photographs of the studied area. We also acknowledge the survivors of the disaster who have provided useful information about the event. We are also grateful to Chris Thissen for the correction of the English. J.-C. Borrero, K. Sieh, G. Greene, S. Bondevik, and an anonymous reviewer who provided thoughtful reviews of the early versions of the manuscript.

References

Ambraseys, N. N. (1962), *Data for the investigation of the seismic sea-waves in the Eastern Mediterranean*, Bull. Seismol. Soc. Am *52*, 895–913.

Ammon, C. J., Ji, C., Thio, H.-K., Robinsons, D., Ni, S., Hrorleifsdottir, V., Kanamori, H., Lay, T., Das, S., Helmberger, D., Ichinose, G., Polet, J., and Wald, D. (2005), *Rupture Process of the 2004 Sumatra-Andaman Earthquake*, Science *308*, 1133–1139.

Borrero, J.C. (2005a), *Field data and satellite imagery of the tsunami effects in Banda Aceh*, Science *308*, 1596.

Borrero, J.C. (2005b), *Field Survey of Northern Sumatra and Banda Aceh, Indonesia after the Tsunami and Earthquake of 26 December 2004*, Seismol. Res. Lett. *76*, 3, 312–320.

Borrero, J.C., Synolakis, C.E., and Fritz, H.M. (2006), *Field surveys of northern Sumatra after the tsunami and earthquake of 26 December 2004*, Earthq. Spectra *22*, S3, 93–104.

Carrier, G.F., Wu, T.T., and Yeh, H. (2003), *Tsunami runup and drawdown on a plane beach*, J. Fluid Mech. *475*, 79–99.

Chlieh, M., Avouac, J.-P., Hjorleifsdottir, V., Song, T.-R. A., Sieh, K., Sladen, A., Hébert, H. Prawirodirdjo, L., Bock, Y., and Galetzka, J. (2007), *Coseismic slip and afterslip of the great (Mw 9.15) Sumatra–Andaman Earthquake of 2004*, Bull. Seismol. Soc. Am *97*, 152–173.

Engdahl, E.R., Villaseñor, A., DeShon, H.R., and Thurber, C.H. (2007), *Teleseismic relocation and assessment of seismicity (1918–2005) in the region of the 2004 M_w 9.0 Sumatra–Andaman and 2005 Mw 8.6 Nias Island great earthquakes*, Bull. Seismol. Soc. Am. *97*, 1A, S43–S61.

Fritz, H., M., Kongko, W., Moore, A., McAdoo, B., Goff, J., Harbitz, C., Uslu, B., Kalligeris, N., Suteja, D., Kalsum, K., Titov, V., Gusman, A., Latief, H., Santoso, E., Sujoko, S., Djulkarnaen, D., Sunendar, H., and Synolakis, C. (2007), *Extreme runup from the 17 July 2006 Java tsunami*, Geophys. Res. Lett. *34*, L12602.

Fritz, H.M., Borrero, J.C., Synolakis, C.E., and Yoo, J. (2006), *2004 Indian Ocean tsunami flow velocity measurements from survivor videos*, Geophys. Res. Lett. *33*, L24605.

Fritz, H.M., Hager, W.H., and Minor, H.E. (2001), *Lituya Bay case: Rockslide impact and wave run-up*, Science of Tsunami Hazards *19*, 3–22.

Fritz, H.M., Mohammed Fi, and Yoo, Y. (2009), *Lituya Bay Landside Impact Generated Mega-Tsunami: 50th Anniversary*, Pure. Appl. Geophys. *166,* 1/2 (2009), this issue

Fu, G. and Sun, W. (2006), *Global co-seismic displacements caused by the 2004 Sumatra-Andaman earthquake (M_w 9.1)*, Earth Planets Space *58*, 149–152.

Geist, E.L., Titov, V.V., Arcas, D, Pollitz, F.F., and Bilek S. L. (2007), *Implications of the 26 December 2004 Sumatra–Andaman earthquake on tsunami forecast and assessment models for great subduction-zone earthquakes*, Bull. Seismol. Soc. Am. *97*, 1A, S249–S270.

Grilli, S.T., Svendsen, I.A., and Subramanya, R. (1997), *Breaking criterion and characteristics for solitary waves on slopes*, J. Waterway Port Coastal and Ocean Engineering *123*, 3, 102–112.

GOTO, C., OGAWA, Y., SHUTO, N., and IMAMURA, N., *Numerical method of tsunami simulation with the leap-frog scheme* (IUGG/IOC Time Project) (IOC Manual, UNESCO, New York 1997)

HÉBERT, H., HEINRICH, P, SCHINDELÉ, F., and PIATANESI, A. (2001), *Far-field simulation of tsunami propagation in the Pacific Ocean: Impact on the Marquesas Islands (French Polynesia)*, J. Geophys. Res. *106*, C5, 9161–9177.

HÉBERT. H., SLADEN A., and SCHINDELÉ, F. (2007), *Numerical Modeling of the Great 2004 Indian Ocean Tsunami: Focus on the Mascarene Islands*, Bull. Seismol. Soc. Am. *97*, 1A, S208–S222.

HEINRICH, P., SCHINDELÉ, F., GUIBOURG, S., and IHMLÉ, P.F. (1998), *Modeling of the February 1996 Peruvian tsunami*, Geophys. Res. Lett. *25*, 2687–2690.

IMAMURA, F., and SHUTO, N., *Tsunami propagation by use of numerical dispersion*. In *Proceedings, International Symposium Comp. Fluid Dynamics* (Nagoya, 1990) pp. 390–395.

INOUYE, W. (1934), *On sound phenomena of the Sanriku earthquake of March 3rd, 1933*, Bull. Earthq. Res. Instit. Extra *1*, 77–86 (in Japanese).

JAFFE, B.E., BORRERO, J.-C., PRASETYA, G.S., PETERS, R., MCADOO, B., GELFENBAUM, G., MORTON, R., RUGGIERO, P., HIGMAN, B., DENGLER, L., HIDAYAT, R., KINGSLEY, E., KONGKO W., LUKIJANTO, and MOORE A. (2006), *Northwest Sumatra and Offshore Islands field survey after the December 2004 Indian Ocean Tsunami*. Earthquake Spectra *22*, S3, S105-S135.

KATO, K. and TSUJI, Y. (1995), *Tsunami of the Sumba earthquake of August 19, 1977*, J. Natural Disaster Sci. *17*, 2, 87–100.

KIRBY, J.T. (2003), *Boussinesq models and applications to nearshore wave propagation, surf-zone processes and wave-induced currents*. In Lakhan V.C., ed., *Advances in Coastal Engineering*, (Elsevier, 2003) pp. 1–41.

KITAGAWA, M., KOIZUMI, Y., TAKAHASHI, M., MATSUMOTO, N., and SATO, T. (2006), *Changes in groundwater levels or pressures associated with the 2004 Earthquake off the west coast of northern Sumatra (M9.0)*, Earth Planets Space *58*, 173–179.

LAVIGNE, F., PARIS, R., WASSMER, P., GOMEZ, C., BRUNSTEIN, D., GRANCHER, D., VAUTIER, F., SARTOHADI, J., SETIAWAN, A., SYAHNAN, GUNAWAN, T., FACHRIZAL, WALUYO, B., MARDIATNO, D., WIDAGDO, A., CAHYADI, R., LESPINASSE, N., and MAHIEU, L. (2006), *Learning from a major disaster (Banda Aceh, December 26th, 2004): A methodology to calibrate simulation codes for tsunami inundation models*, Zeitschrift für Geomorphologie N.F., Suppl. *146*, 253–265.

LAVIGNE, F., GOMEZ, C., GIFFO, M., WASSMER, P., HOEBRECK, C., MARDIATNO, D., PRIOYONO, J., and PARIS, R. (2007), *Field observations of the 17th July 2006 Tsunami in Java*, Nat. Hazard and Earth Sci. Syst. *7*, 177–183.

LAY, T., KANAMORI, H., AMMON, C.J., NETTLES, M., WARD, S.N., ASTER, R.C., BECK, S.L., BILEK, S.L., BRUDZINSKI, M.R., BUTLER, R., DESHON, H.R., EKSTRÖM, G., SAKATE, K., and SIPKIN, S. (2005), *The great Sumatra-Andaman earthquake of 26 December 2004*, Science *308*, 1127–1133.

MELTZNER, A.J., SIEH, K., ABRAMS, M., AGNEW, D.-C., HUDNUT, K.-W., AVOUAC, J.-P., and NATAWIDJAJA, D. H. (2006), *Uplift and subsidence associated with the great Aceh-Andaman earthquake of 2004*, J. Geophys. Res. *111*, B02407, doi:10, 1029/2005JB003891.

MILLER, D.J. (1960), *Giant waves in Lituya Bay*, Alaska. U.S. Geological Survey Professional Paper 354C, 51–83.

MINOURA, K., IMAMURA, F., TAKAHASHI, T., and SHUTO, N. (1997), *Sequence of sedimentation processes caused by the 1992 Flores tsunami: Evidence from Babi Island*, Geology *25*, 6, 523–526.

OKAL, E.A., and SYNOLAKIS, C.E. (2003), *Theoretical comparison of tsunamis from dislocations and landslides*, Pure Appl. Geophys. *160*, 2177–2188.

OKAL, E.A., and SYNOLAKIS, C.E. (2004), *Source discriminants for near-field tsunamis*, Geophysical Journal International *158*, 899–912.

OKAL, E A., DENGLER, L., ARAYA, S., BORRERO, J.C., GOMER, B., KOSHIMURA, S., LAOS, G., OLCESE, D., ORTIZ, M., SWENSSON, M., TITOV, V.V., and VEGAS, F. (2002), *A field survey of the Camana, Peru tsunami of June 23, 2001*, Seismol. Res. Lett. *73*, 904–917.

PAPADOPOULOS, G.A. and IMAMURA, F., *A proposal for a new tsunami intensity scale*. In *Proc. Internat. Tsunami Conf.* 7–9 August 2001 (Seattle 2001) pp. 569 - 577.

PARIS, R., LAVIGNE, F., WASSMER, P., and SARTOHADI, J. (2007a), *Coastal sedimentation associated with the December 26, 2004 tsunami in Lhok Nga, West Banda Aceh (Sumatra, Indonesia)*, Marine Geology *238*, 93–106.

PARIS, R., WASSMER, P., SARTOHADI, J., LAVIGNE, F., BARTHOMEUF, B., DESGAGES, E., GRANCHER, D., BAUMER, P., VAUTIER, F., BRUNSTEIN, D., and GOMEZ, C. (2007b), *Tsunamis as geomorphic crisis: Lessons from the December 26, 2004 tsunami in Lhok Nga, West Banda Aceh (Sumatra, Indonesia)*, Geomorphology (in press).

SHUTO, N., *A natural warning of tsunami arrival*. In *Perspectives on Tsunami Hazard Reduction, Observation Theory and Planning, Advances in Natural and Technological Hazards Research* (ed. Hebenstreit G. T.) (Springer, 1997) pp. 157–173.

STEIN, S. and OKAL, E. (2005), *Speed and size of the Sumatra earthquake*, Nature *434*, 581–582.

SYNOLAKIS, C.E. (1987), *The runup of solitary waves*, J. Fluid Mech. *185*, 523–545.

SYNOLAKIS, C.E., OKAL, E.A., and BERNARD, E.N. (2005), *The Megatsunami of December 26 2004*, The Bridge *35*, 2, 26–35.

TADEPALLI, S. and SYNOLAKIS, C.E. (1996), *Model for the leading waves of tsunamis*, Phys. Rev. Lett. *77*, 2141–2145.

TITOV, V.V., and SYNOLAKIS, C.E. (1998), *Numerical modeling of tidal wave runup*, J. Waterways, Port, Coastal and Ocean Engin., ASCE *124*, 4, 157–171.

TITOV, V.V., ARCAS, D., KANOGLU, U., NEWMAN, J., and GONZALEZ, F.I. (2004), *Inundation modeling for probabilistic tsunami hazard assessment*, EOS Trans. AGU *85*, 47, Fall Meeting Suppl., Abstract OS23D–1340.

TSUJI, Y., IMAMURA, H., MATSUTOMI, H., SYNOLAKIS, C.E., NANANG, P.T., JUMADI, HARADA, S., HAN, S.S, ARAI, K., and COOK, B. (1995), Field survey of the east Java earthquake and tsunami of June 3, 1994, Pure Appl. Geophys. *144*, 3–4, 839–854.

TSUJI, Y., TANIOKA, Y., MATSUTOMI, H., NISHIMURA, Y., KAMATAKI, T., MURAKAMI, Y., SAKAKIYAMA, T., MOORE, A., GELFENBAUM, G., NUGROHO, S., WALUYO, B., SUKANTA, I., TRIYONO, R., and NAMEGAYA, Y. (2006), *Damage and height distribution of Sumatra earthquake-tsunami of December 26, 2004, in Banda Aceh City and its environs*, J. Disaster Res. *1*, 1, 103–115.

UMITSU, M., TANAVUD, C., and PATANAKANOG, T. (2007), *Effects of Landforms on Tsunami Flow in the Plains of Banda Aceh, Indonesia, and Nam Khem*, Thailand, Marine Geology (in press).

VALLÉE, M. (2007), *Rupture properties of the giant Sumatra earthquake imaged by empirical Green's function analysis*, Bull. Seismol. Soc. Am. *97*, S103–S114.

WONG, F.L., GEIST, E.L., and VENTURATO, A., J., *Probabilistic Tsunami Hazard Maps and GIS*. In Proc. 2005 ESRI Internat. User Conf., (San Diego California, July 2005), 11 pp.

YALCINER, A.C., PERINCEK, D., ERSOY, S., PRESATEYA, G.S., HIDAYAT, R., and MCADOO, B. (2005), *December 26, 2004 Indian Ocean Tsunami field survey (Jan. 21–31, 2005) at north of Sumatra Island*, http://yalciner.ce.metu.edu.tr/sumatra/survey/

YEH, H., LIU, P.L.F., BRIGGS, M., and SYNOLAKIS, C.E., (1994), *Tsunami catastrophe in Babi Island*, Nature, *372*, 6503–6508.

(Received January 20, 2001, accepted September 17, 2008)
Published Online First: February 13, 2009

Pure appl. geophys. 166 (2009) 283–300
0033–4553/09/010283–18
DOI 10.1007/s00024-008-0433-6

Pure and Applied Geophysics

The 1856 Tsunami of Djidjelli (Eastern Algeria): Seismotectonics, Modelling and Hazard Implications for the Algerian Coast

ABDELKARIM YELLES-CHAOUCHE,[1] JEAN ROGER,[2] JACQUES DÉVERCHÈRE,[3,4] RABAH BRACÈNE,[5] ANNE DOMZIG,[6] HELENE HÉBERT,[2] and ABDELAZIZ KHERROUBI[1]

Abstract—On August 21st and 22nd 1856, two strong earthquakes occurred off the seaport of Djidjelli, a small city of 1000 inhabitants, located 300 km east of Algiers (capital of Algeria). In relation to these two earthquakes, an important tsunami (at least one) affected the western Mediterranean region and the eastern Algerian coastline between Algiers and La Calle (Algero-Tunisian border). Based on historical information as well as on data recently collected during the Maradja 2 survey conducted in 2005 over the Algerian margin, we show that the tsunami could have been generated by the simultaneous rupture of a set of three *en echelon* faults evidenced off Djidjelli. From synthetic models, we point out that the area affected along the Algerian coast extended from Bejaia to Annaba. The maximum height of waves reached 1.5 m near the harbor of Djidjelli.

Key words: Djidjelli, Algeria, 1856 tsunami, Faults, Wave modelling, Runup.

1. Introduction

Although the Algerian margin demonstrated its ability to potentially generate hazardous tsunamis (e.g., YELLES *et al.*, 1991; SOLOVIEV *et al.*, 2000; LORITO *et al.*, 2008, and references therein) as for instance during the recent May 21, 2003 Boumerdes earthquake, little is known about the size and impact of past or future tsunami events on the western Mediterranean coasts and mainly on the Algerian coast. This could be attributed mostly to the lack of historical informations and the fact that tsunamigenic events are rare (YELLES-CHAOUCHE, 1991). Historically, although some reports mention a tsunami related to the destructive earthquake of Algiers in 1365 (IBN KHALDOUN, 1369) or to the moderate event of Gouraya of January 15, 1891 (SOLOVIEV *et al.*, 2000), the first

[1] CRAAG, Route de l'Observatoire, B.P.63, Algiers, Algeria. E-mail: a.yelles@craag.dz
[2] CEA-DASE, Bruyères-le-Châtel, 91297 Arpajon, France.
[3] Université Européenne de Bretagne, France.
[4] CNRS, UMR 6538, Domaines Océaniques, Institut Universitaire Européen de la Mer, Université de Brest, Place Copernic, 29280 Plouzané, France.
[5] Division Exploration, Sonatrach, Boumerdès, Algeria.
[6] Laboratoire de Planétologie et Géodynamique, UMR 6112, Université de Nantes, France. Now at Midland Valley Exploration, 144 West George Street, Glasgow G2 2HG.

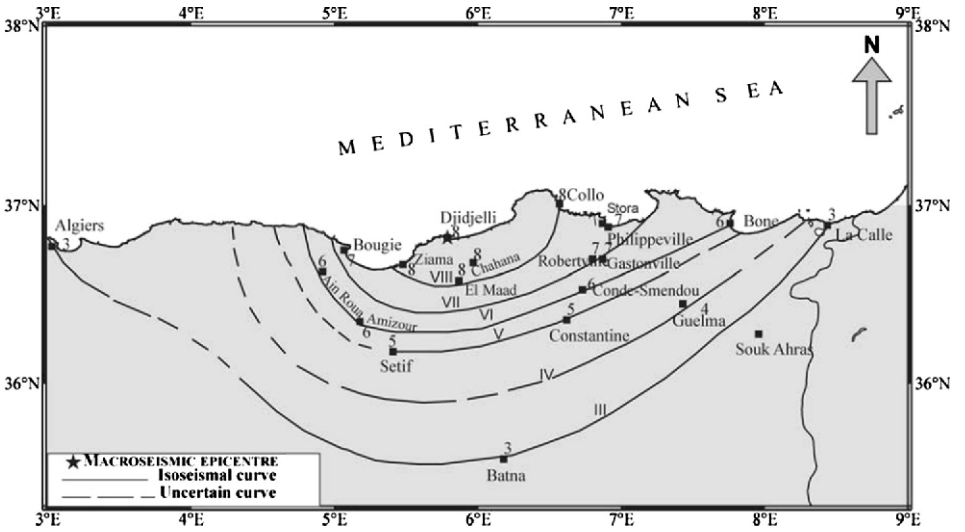

Figure 1
Isoseismal map of the Djidjelli earthquake of August 22, 1856 (I: VIII) after HARBI *et al.* (2003).

well documented event remains the Djidjelli tsunami associated with the seismic crisis of August 21–22, 1856 (ROTHÉ, 1950; AMBRASEYS, 1982; BENHALLOU, 1985; Fig. 1).

During the instrumental period, two tsunamigenic events are evidenced as they were the first recorded by geophysical instruments. The first one occurred after the destructive El Asnam event of October 10, 1980 (M_s: 7.3; OUYED *et al.*, 1981). Although located at a distance of about 60 km from the coast, the earthquake triggered a submarine landslide inducing a weak tsunami recorded by several tide gauge stations of southeastern Spain (SOLOVIEV *et al.*, 1992; PAPADOPOULOS and FOKAEFS, 2005). The second tsunami, the more recent one, is the tsunami of Boumerdes of May, 21, 2003. This event, one of the most important in the western Mediterranean region within the last century, was generated by an earthquake of magnitude M_w 6.8 that occurred on the offshore reverse fault of Zemmouri (YELLES *et al.*, 2003; ALASSET *et al.*, 2006). This thrust fault, with a length of about 50–55 km, is assumed to outcrop near the seafloor at about 10–15 km from the shoreline (DÉVERCHÈRE *et al.*, 2005). Effects of this tsunami were felt in the entire western Mediterranean region and especially along the Balearic coasts (ALASSET *et al.*, 2006). The Boumerdes tsunami demonstrated for the first time the high potential of the Algerian margin for tsunami generation.

If the Algerian tsunamis are mainly related to strong earthquakes that could happen along the coastal region, landslides along the margin could also be another potential source of tsunamigenic events as discussed by some authors for the Orleansville and the El Asnam earthquakes (AMBRASEYS, 1982; YELLES, 1991).

The recent swath bathymetry survey, Maradja 2 survey, conducted along the eastern Algerian margin in November 2005 allowed us to map the seafloor of the region between

Dellys and Annaba by using a high resolution swath bathymetric system (DOMZIG, 2006) (Fig. 2a). These new bathymetric data, together with seismic sections recently carried out in the area, offer the opportunity through seafloor mapping and densification of the seismic sources, to revisit and discuss on a new basis the origin of the important historical Djidjelli tsunami event. Using numerical modelling of the tsunami waves triggered by the earthquake only, the aim of this study is to estimate and to discuss the effects of the tsunami due to the source inferred, and to compare this modelling to the available historical observations along the Algerian coast, and more particularly in the Djidjelli harbor area.

2. The Djidjelli Earthquake of August 21 and 22, 1856

The tsunami occurred during the French occupation of Algeria. Based on several historical archives available (newspapers, reports, etc) the seismic crisis of Djidjelli was well described by authors like ROTHÉ (1950) and AMBRASEYS (1982) who reported many details on its effects on the Algerian and western Mediterranean coasts.

The Djidjelli sequence was marked by the occurrence of two main shocks, one on the night of August 21, and the second**,** more violent, on the night of August 22, 1856. The first shock, considered as a foreshock, happened at 21 h 45 mn (local time). It destroyed the old Genoese tower of the city and claimed the lives of a few people. Following the shock, ROTHÉ (1950) and AMBRASEYS (1982) indicated that the sea receded for some distance and suddenly flooded the low-lying parts of the coast. Damage was equally serious in the region between Djidjelli and Collo (Fig. 1). The earthquake was felt over a large area from Algiers in the West to La Calle in the East and from Batna in the South to Nice (France) to the North. At Mahon in Minorca (Balearic Islands), the shock was followed by a rapid flooding of the harbor. As a result of it, many boats broke their moorings (AMBRASEYS, 1982, SOLOVIEV, 2000).

The second shock occurred on August 22, at 11 h 40 min (local time). It was more violent than the first one and it is generally considered as the main shock. It destroyed what remained of local houses and killed few people, as the population was evacuated the day before. The shock triggered a sea wave of 2 to 3 meters high (observed at Djidjelli) that flooded the eastern Algerian coast several times. At Bougie (Bejaia) and Philippeville (Skikda), small towns located eighty kilometers west and east of Djidjelli, AMBRASEYS (1982) and SOLOVIEV (2000) reported that the sea rose from about 5 meters, flooding the shore five to six times. In Bone, the sea rose by about one meter, flooding the parade grounds in a succession of waves that continued for twelve hours. These authors also reported that the shock was felt at Cagliari (Island of Sardinia) and Caloforte (Island of S. Pietro) as well as at Mahon in Spain. There the shock was less intense than that of the previous day but it was stronger in Nice and in Genoa in Italy.

Considering all these pieces of information and on the basis of the isoseismal map (Fig. 1), the earthquake was located a few kilometers offshore of Djidjelli, with an

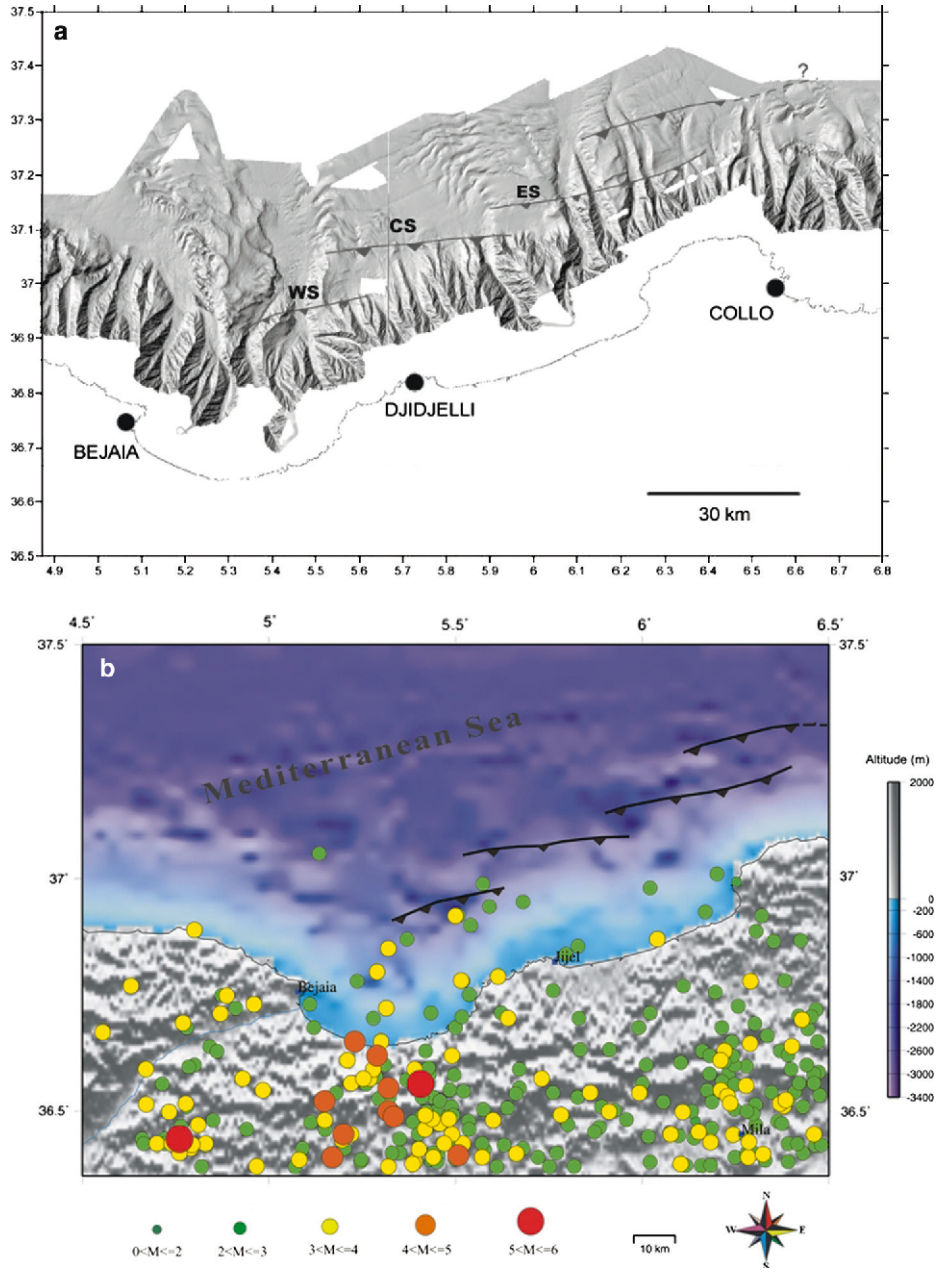

Figure 2

(a) Bathymetry offshore of Djidjelli with the four overlapping structures assumed active (Domzig, 2006). The three faults named WS (West Segment), CS (Central Segment), and ES (East Segment) are used in this study because they are thought to be at the origin of the 21 and 22 August, 1856 earthquakes and associated tsunamis (see text for details). (b) Recent seismic activity off Djidjelli (1980–2007 period, from CRAAG seismic catalogues).

estimated maximum intensity of VIII. PAPADOPOULOS and FOAKEFS (2005) estimate that the tsunami intensity of 21 August 1856 was equal to 3 on the 6-point tsunami intensity scale and 5 on the 12-point scale. This places this particular tsunami among the significant ones observed in the Mediterranean Sea in the last two centuries.

3. Physiography of the Margin off Djidjelli

Off the coast of Djidjelli, the bathymetric map has been obtained from the Maradja 2 survey data (Fig. 2a). This survey was conducted in November 2005 on the French R/V Suroit and aimed firstly at obtaining a precise bathymetric map of the structures between Dellys and Annaba (eastern Algeria). For this purpose, a Kongsberg EM300 Simrad multibeam echosounder (EM 1000 for the continental shelf) for bathymetry and reflectivity was used. Simrad EM300 is a 32-kHz multibeam system which allows for an overall swath coverage up to 5 times water depth, increasing with depth to a maximum width of 5000 m at 1000 m depth. The reached resolution was of 15 $\times$ 35 m at 1000 m depth with a vertical accuracy from 2 m (central beam) to 10 m (lateral beam).

The survey was limited to the continental slope and part of the deep basin (DOMZIG, 2006). Between Bejaia and Collo, the margin is marked by a narrow shelf and a steep slope in front of the massif of Lesser Kabylia. The continental shelf disappears totally near Collo. In the bay of Bejaia, the slope is outlined by two main canyons with a N-S direction (Fig. 2a). They correspond to the marine extension of the Soummam River (DOMZIG, 2006). Further east, between Djidjelli and Collo, the slope of the margin is incised by several canyons. Off Djidjelli, these canyons are short whereas off Collo they extend down to the abyssal plain. According to the bathymetric map (Fig. 2a), the deep basin depicts a series of elongated ridges that can be interpreted as sediment waves or contourites developing at the foot of the slope. However, several linear topographic anomalies that can hardly be due to sedimentary processes only are also observed at the foot of the slope and upslope. They present a general NE-SW to E-W strike as presented in Figure 2a.

4. Seismotectonics of the Djidjelli Margin

Northern Algeria lies along the Eurasian-African plate boundary. With an average rate of about 5 mm/yr in a N 60°W, the convergence between the two main plates is responsible for the seismic activity which affects Algeria. Seismicity on land is generated by active faults oriented mostly NE-SW, located along the Atlasic mountains and the Neogene basins. Strong earthquakes could occur in the northern region, as the last one of Boumerdes of May 21, 2003. For a long time, offshore seismicity remained poorly known due to the lack of investigations along the margin.

In the Djidjelli region, the seismic activity deduced from historical catalogs (MOKRANE *et al.*, 1994; BENOUAR, 1994) seems to be low with an activity mostly focused

along the southern suture between the internal and external domains. Nevertheless, since the recent installation of the Algerian Digital Seismic Network by the CRAAG (Centre de Recherche en Astronomie, Astrophysique et Géophysique), many seismic events were recorded recently along the coastline between Bejaia and Djidjelli. An updated seismic map of the region of Djidjelli (Fig. 2b) shows activity in proximity to the four scarp segments reported hereafter, which favors possible activity of these faults, and therefore, their ability to generate tsunamis.

From the analysis of the seismic lines carried out during the Maradja survey and of Sonatrach (Algerian Oil Company) commercial seismic lines (see location on Fig. 3a), cross sections along the margin in the region of Djidjelli were obtained. We observe that the central part of the margin is uplifted (Figs. 3b and c), whereas the lower slope is dominated by low-angle normal faults and slides rooted at the base of the Messinian salt layer (Fig. 3c). By correlating the bathymetry and the seismic lines, we find that uplifts are related to reverse faulting near the slope break or below the lower slope, although the geometry of thrusts is hardly visible (Figs. 3b and c). Thereafter, we could identify four *en echelon* segments, widely overlapping, which can be followed near the foot of the slope or in the lower slope (Fig. 2a). In front of Djidjelli, a first segment (named west segment) oriented NE-SW (N 75°E) has a surface extent of $\sim$25 km. This is a thrust fault related to an asymmetrical fold which produces the growth of a basin on its backlimb that is tilted towards the continent (Fig. 3b). The second one (named central segment) is observed north of the City of Djidjelli. This segment, about 30 km far from the coast is apparently slightly longer than the previous one ($\sim$35 km). This reverse fault striking N85°E is also related to another asymmetrical fold. Finally, two other scarps, with apparent lengths of $\sim$40–45 km and $\sim$30 km, are found northwest of Collo City. Among these two segments, the one located in the deep basin and striking N 80° is not clearly related to a deeper fault activity and could only result from salt tectonics; a process quite well identified in the eastern part of the studied area (Fig. 3c). We will therefore consider in the following only the segment located upslope and designate it east segment. Note that this segmentation pattern of the fault zone with similar lengths has also been observed during the May 21, 2003 Boumerdes earthquake rupture: Indeed, two main slip zones have been identified from a joint inversion of seismological waveforms and ground displacement observations (DELOUIS *et al.*, 2004) which are interpreted as being related to the two main cumulative scarps evidenced at the sea floor (DÉVERCHÈRE *et al.*, 2005).

Then, from bathymetric maps and seismic lines, the main characteristics of these three fault segments (length, width, depth) are determined (Table 1). It is worth to note that these parameters are only mean values deduced from the combination of observations made on bathymetry, seismic sections, and assumptions deduced from literature. Uncertainties remain, especially for strike and dip of faults that cannot be accurately determined from the available data set, since there is no means to directly describe the geometry of faults at depth and their spatial continuity.

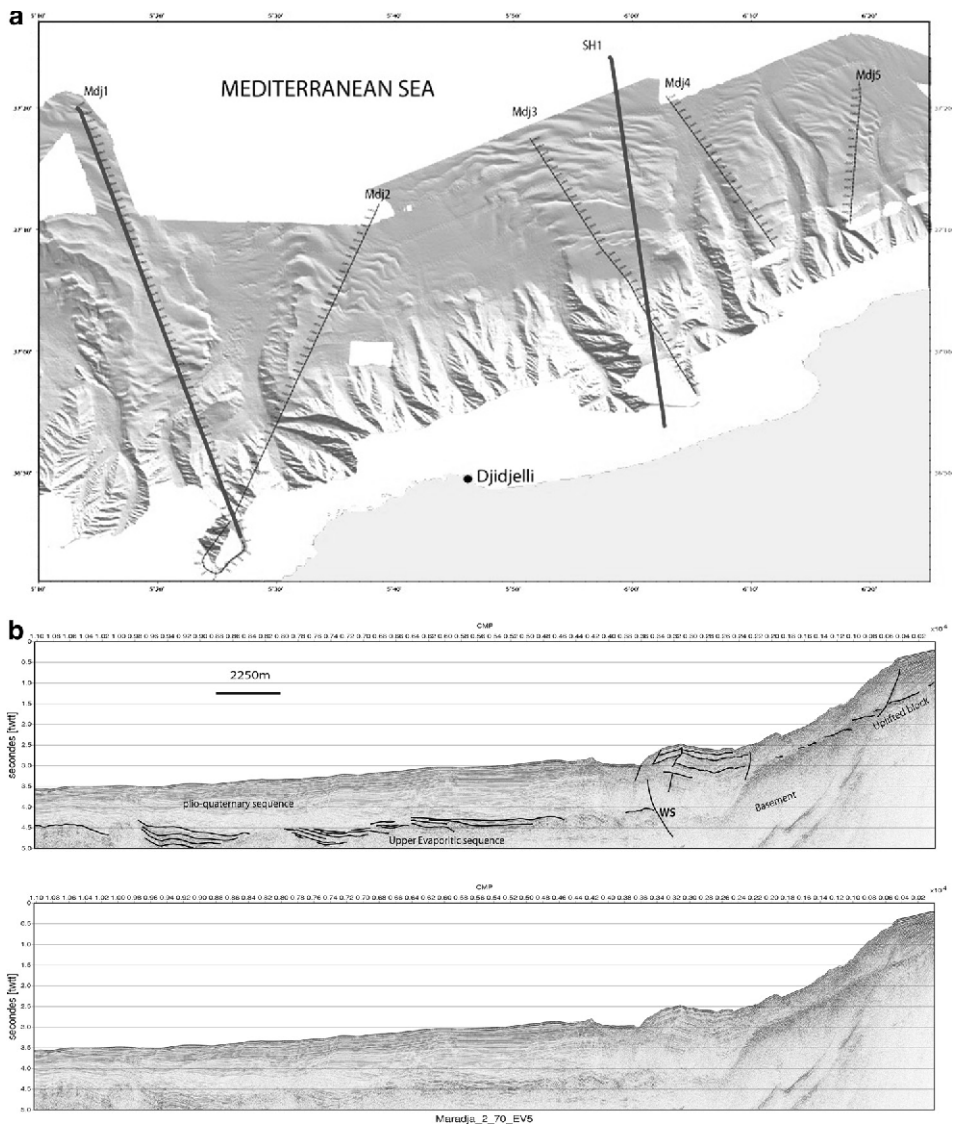

Figure 3

(a) Location map of the bathymetry with seismic lines shot during the Maradja 2 survey. Bold lines are the location of the seismic lines shown. One line from the industry (SH1) (dark line) is also plotted; (b): Seismic profile MDJ1 (in two-way travel time, TwT) across the West Segment WS (Fig. 2a) – Black line depicts the inferred position of WS according to the deposition pattern (growth strata) near the surface; (c): Processed commercial seismic section SH1 (480-channel, stacked and migrated) across the margin off Djidjelli and crosscutting the Eastern Segment ES (see location Fig. 2a). For (b) and (c) the upper one is the interpreted line, the lower one is the raw data.

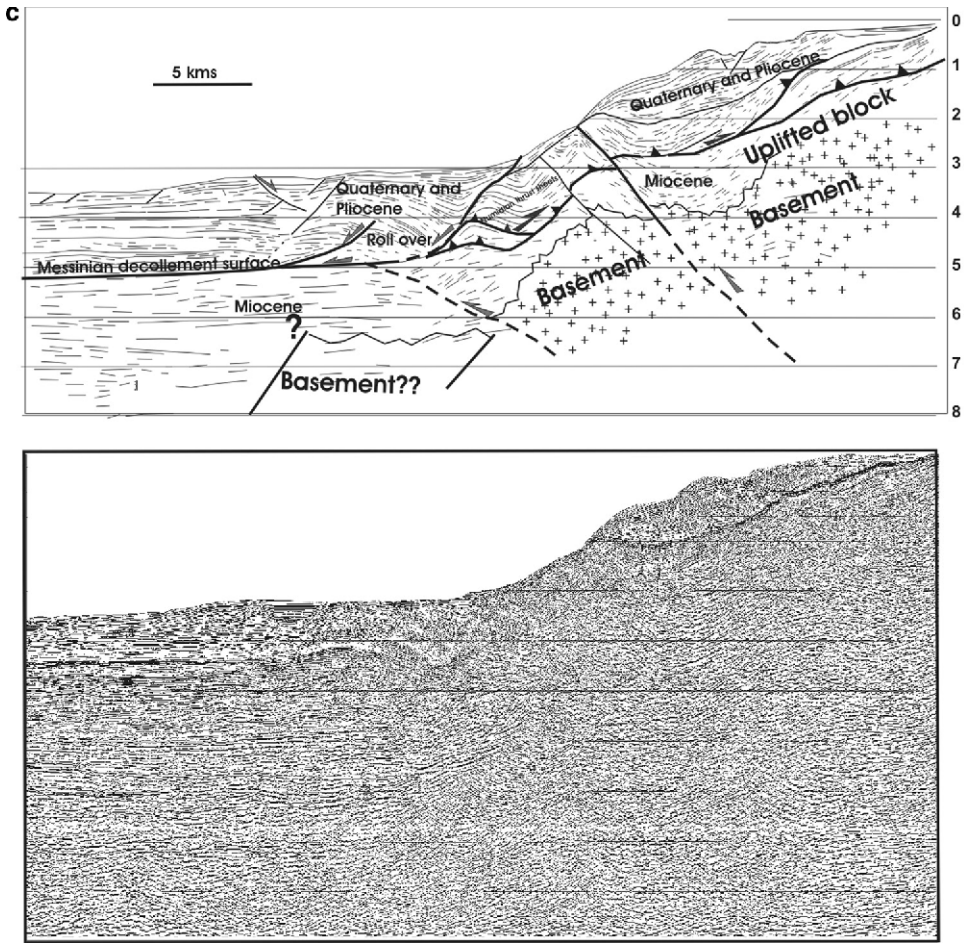

Figure 3
contd.

Table 1

	Longitude (°)	Latitude (°)	Center of fault plane deep (km)	Slip (m)	Strike (°)	Dip (°)	Rake (°)	Half length (m)	Width (m)	Shear modulus (Pa) = rigidity
West	5.4764	36.95	10	1.0	75	40	90	12500	20000	$4{,}5*10^{10}$
Center	5.736	37.0791	10	1.5	85	40	90	18500	20000	$4{,}5*10^{10}$
East	6.15	37.1784	10	1.5	75	40	90	22000	20000	$4{,}5*10^{10}$

Finally, we note that the overall length of the three segments considered here is about 100–105 km. According to WELLS and COPPERSMITH law (1994), this value is consistent with the approximate magnitude inferred for the 1856 earthquake sequence from the isoseismal map, i.e., $7^{1/2}$ (Fig. 1; HARBI *et al.*, 2003, and references therein). Therefore, considering their effects at the surface, their apparent connection to deformed areas at depth (see e.g., Figs. 3b and c) and the consistency of cumulative length with the magnitude hypothesized, we assume that these segments, which are distributed as *en échelon* faults, could be (for at least two of them) responsible for the Djidjelli events of August 1856 (YELLES *et al.*, 2007; ROGER and HÉBERT, 2008). Subsequently we propose to take into account these three western segments in order to model the tsunami of August 21–22, 1856, and we combine them in order to determine a range of possible triggering effects.

5. Modelling of the Tsunami

5.1. Method

For the generation of the tsunami wave, the coseismic deformation corresponds to an elastic dislocation model which involves the vertical deformation of the seafloor in the epicentral area as a function of the ground elastic parameters and the fault plane geometry (OKADA, 1985). The different parameters used are also related to each other by the seismic moment relation: $\mathbf{M_0 = \mu ULW}$ (AKI, 1966), where $\boldsymbol{\mu}$ is the rigidity constant, $\mathbf{U}$ the average slip in the fault, and $\mathbf{L}$ and $\mathbf{W}$ the length and width of the fault plane, respectively.

In order to model the propagation of the sea waves, we use the depth averaged, nonlinear hydrodynamical equations of continuity (1) and motion (2) conservation describing the conservation of mass and momentum:

$$\frac{\partial(\acute{\eta} \pm h)}{\partial t} + \nabla \cdot [v(\acute{\eta} + h)] = 0 \tag{1}$$

$$\frac{\partial v}{\partial t,} + (v \cdot \nabla)v = -g\nabla\acute{\eta} + \Sigma f \tag{2}$$

where $\mathbf{h}$ is the water depth, $\acute{\boldsymbol{\eta}}$ the water elevation above mean sea level, $\mathbf{v}$ the depth-averaged horizontal velocity vector, $\mathbf{g}$ the acceleration of gravity and $\mathbf{f}$ the bottom friction and Coriolis forces. Thus nonlinear terms are taken into account, and the resolution is carried out using a Crank Nicolson finite-difference method centered in time and using an upwind scheme in space.

Amplification of the sea waves from the seafloor are based on the use of the available bathymetric data. In this study we use the GEBCO world bathymetric dataset (BRITISH OCEANOGRAPHIC DATA CENTRE, 1997) mixed with the Maradja 2 data (200 m resolution)

along the eastern Algerian margin. Near the coast and due to the lack of swath bathymetry coverage of the continental shelf where the depth is less than 200 meters (a band of about 5 miles wide) digitized bathymetric maps from LECLAIRE (1972) were used.

On the other hand and in order to be complementary from other studies related to tsunamis in the western Mediterranean region (LORITO *et al.*, 2008; ROGER and HÉBERT, 2008), we choose to focus our study on the impact of the tsunami along the Algerian coastline and more specifically in Djidjelli. Figure 4 depicts the topography of the region of Djidjelli. The city is located along the coastline, at the foot of the Lesser Kabylian massif. This particular location could influence the runup on land, by stopping invasion of the water on the continent. One can also note that the present-day configuration of the lower part of the city with the old and new port of Djendjen (suburb of Djidjelli) is very different from the one of August 1856. Indeed, the harbor of the city, situated in the western part of the Djidjelli bay, depicts structures that directly develop over the seafloor

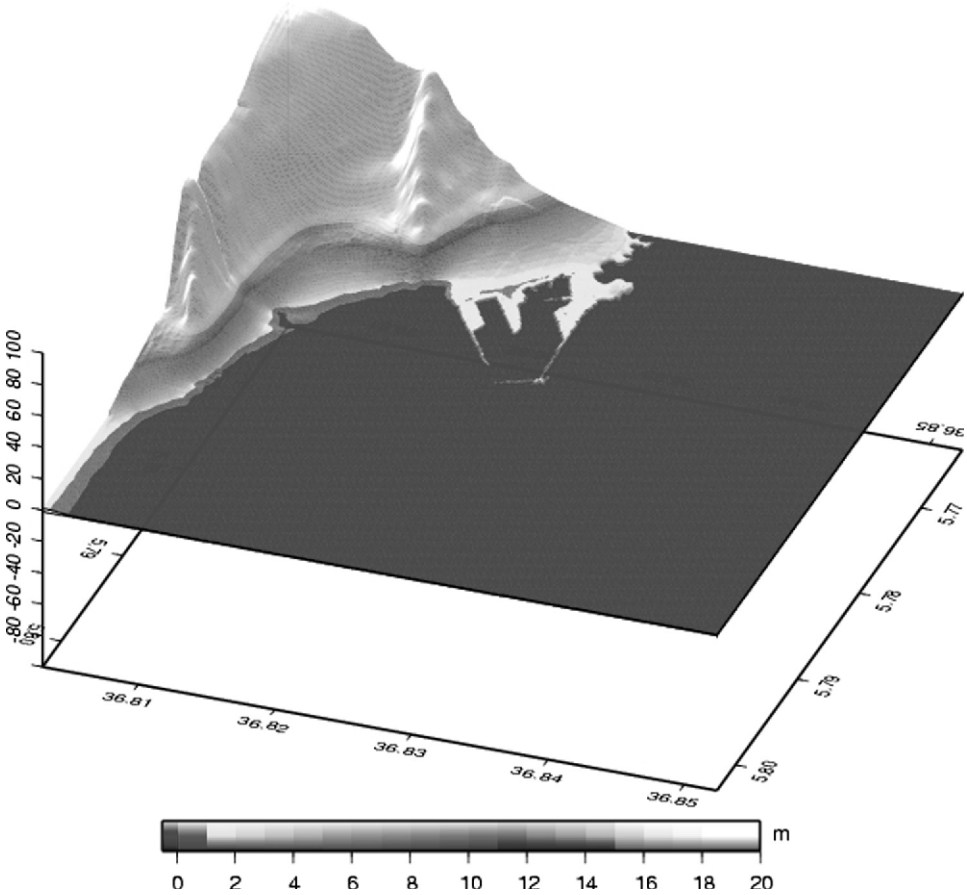

Figure 4
Topographic map on land in the region of Djidjelli.

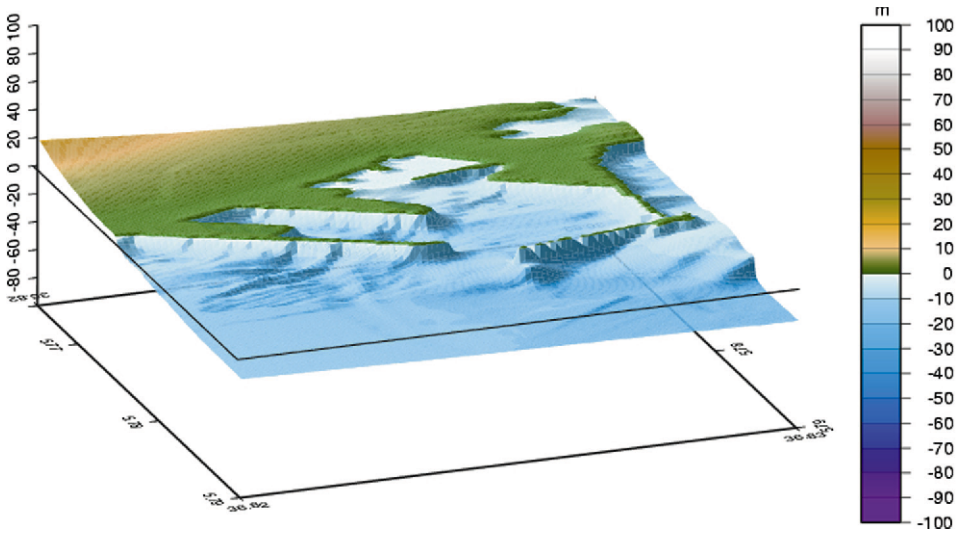

Figure 5
Submarine topography off the Djidjelli harbor.

(Fig. 5). Unfortunately, it was not possible to obtain topographic data of the new Djendjen harbor built in the 1990s. These structures could therefore play a role in the sea-wave propagation and amplification and seem to constitute a protection for the City of Djidjelli thanks to its long piers.

To set up our modelling, we created a set of three imbricated grids, the first one containing the sources with a resolution of 200 m; the second one being a zoom on the Djidjelli bay area with a resolution of 50 m; and the last one a zoom on the Djidjelli harbor with a resolution of 10 m (Figs. 4 and 5). Each grid has been built using krigging interpolation in order to unify the data coming from different origins. The last grid has been created from a combination of the previous cited data and from georeferencing and manual digitizing of a nautical bathymetric chart of the Djidjelli harbour with the same method as proposed by ROGER and HÉBERT (2008). Finally, the resolution of the bathymetric data increases from the abyssal region to the coast from a grid to another one, which is in direct relation with the slowdown of the waves and their amplification as they approach the coastline.

5.2. *Tested Seismic Sources*

In order to reproduce the tsunamis inferred by the two earthquakes, we tested several seismic sources in relation with the *en echelon* fault system evidenced by DOMZIG (2006) and further detailed in this study (Fig. 3). Different combinations of one fault, two or three faults (Fig. 6) were introduced in the model. As explained above, the fourth segment (the most eastern one) is apparently not related to an active fault and was not considered.

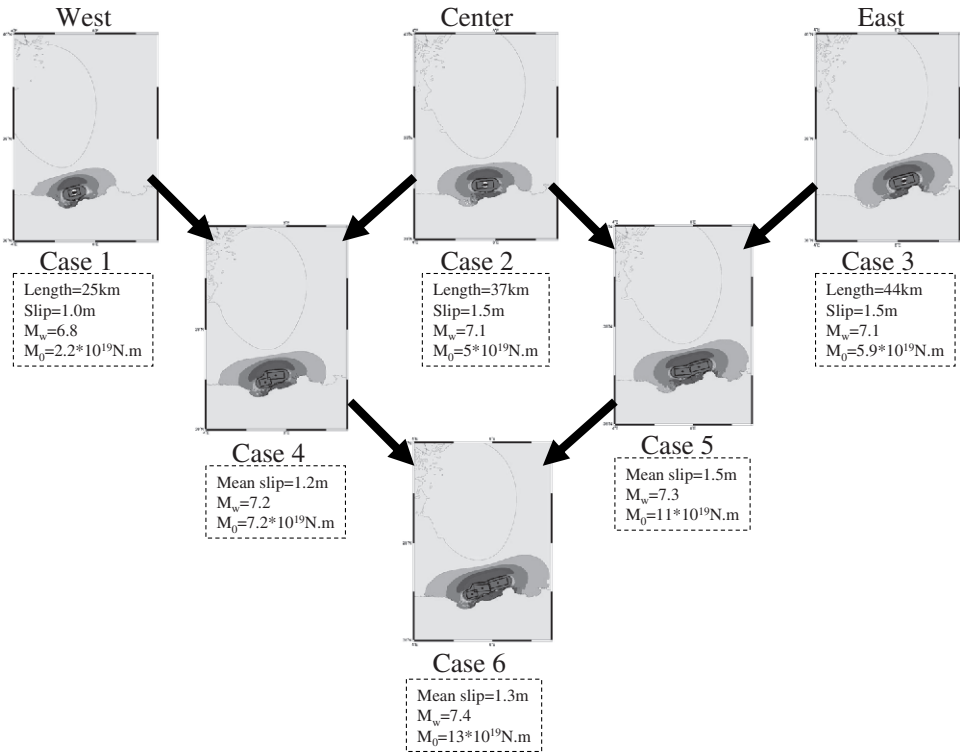

Figure 6
Initial deformation and location or assumed fault planes (black rectangle). Six models are proposed due to the complexity of the rupture and due to the presence of three active faults. The upper line is for each segment. The middle one corresponds to the combination of two segments. The lower model is the combination of the effects of the three segments.

Each hypothesis leads to a maximum earthquake magnitude (Fig. 6). In Table 1, we summarize the parameters chosen for the three main fault segments (West, Central and East) possibly involved in the rupture and the tsunami process. From the bathymetry and seismic lines, the strike, length, and width of the faults are estimated. The existence of some uncertainties discussed above on the different parameters (strike and length essentially) of these segments makes these tests only indicative. The main magnitude range expected is from 6.8 for the western segment to 7.4 for the combination of the three segments. This latter value is in agreement with the magnitude that can be assumed from the damage reported after the two earthquakes of 1856 (ROTHÉ, 1950; AMBRASEYS, 1982).

5.3. Maximum Amplitude of the Sea Waves for Historical Sites

Based on a selection of several sites on the Algerian coastline and the Balearic Islands, we plot on Figure 7 the maximum sea-wave amplitudes in several places affected

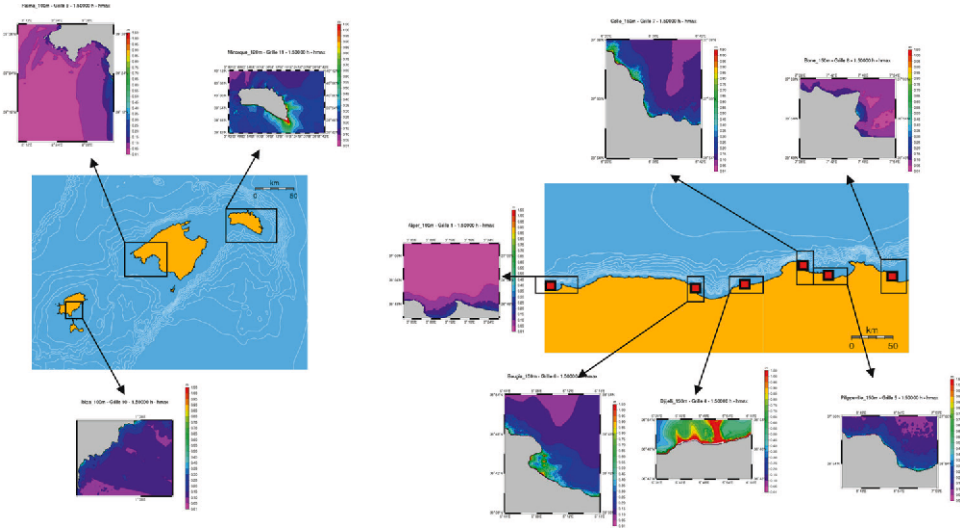

Figure 7
Maximum wave calculated amplitude for historical observations sites. This result is obtained from the combination of the three segments (case 6) and after a time propagation of 5400 s.

by the tsunami. We observe first, that in the Balearic Islands, some sites where the waves arrived an hour after the earthquake are more affected than others (ROGER and HÉBERT, 2008). The maximum is observed in the Minorca Island where the height reached 1.5 m at the southeastern point of the Island. This could be explained by the exposure of the sites to the sea wave propagation and also by the seafloor topography (HÉBERT *et al.*, 2007; ROGER and HÉBERT, 2007, 2008).

Secondly six sites were selected between Algiers in the west and Annaba in the east along the Algerian coastline. The maximum amplitude of the sea waves is measured near Djidjelli and Bejaia. Thus, in this region the maximum sea wave amplitude reaches respectively 1.5 m between 5° 42 E and 6° E. In Bejaia City the height does not exceed one meter. From Figure 7, one can see that on the Algerian coastline, the influence of the tsunami does not extend further than Algiers to the West and Annaba to the East. From our model, one can consider that the maximum energy of the tsunami dissipates more easily towards the North than laterally, indicating that the majority of exposed areas are located southward and northward of the seismic sources.

In order to measure the flooding of the lower part of the city of Djidjelli, a map of the zones invaded by the sea is proposed. Figure 8 shows a first attempt to quantify the maximum wave height and flooding limits in the Djidjelli coastline area. It is obtained by using the model of the three seismic sources with a maximum magnitude of $M_w = 7.4$. On this map we can see that the eastern part of the city is the most affected area, and that the runup may reach a height of 1.5 m. However, the use of our model does not allow us to reach runup values higher than two meters, whereas historical observations locally

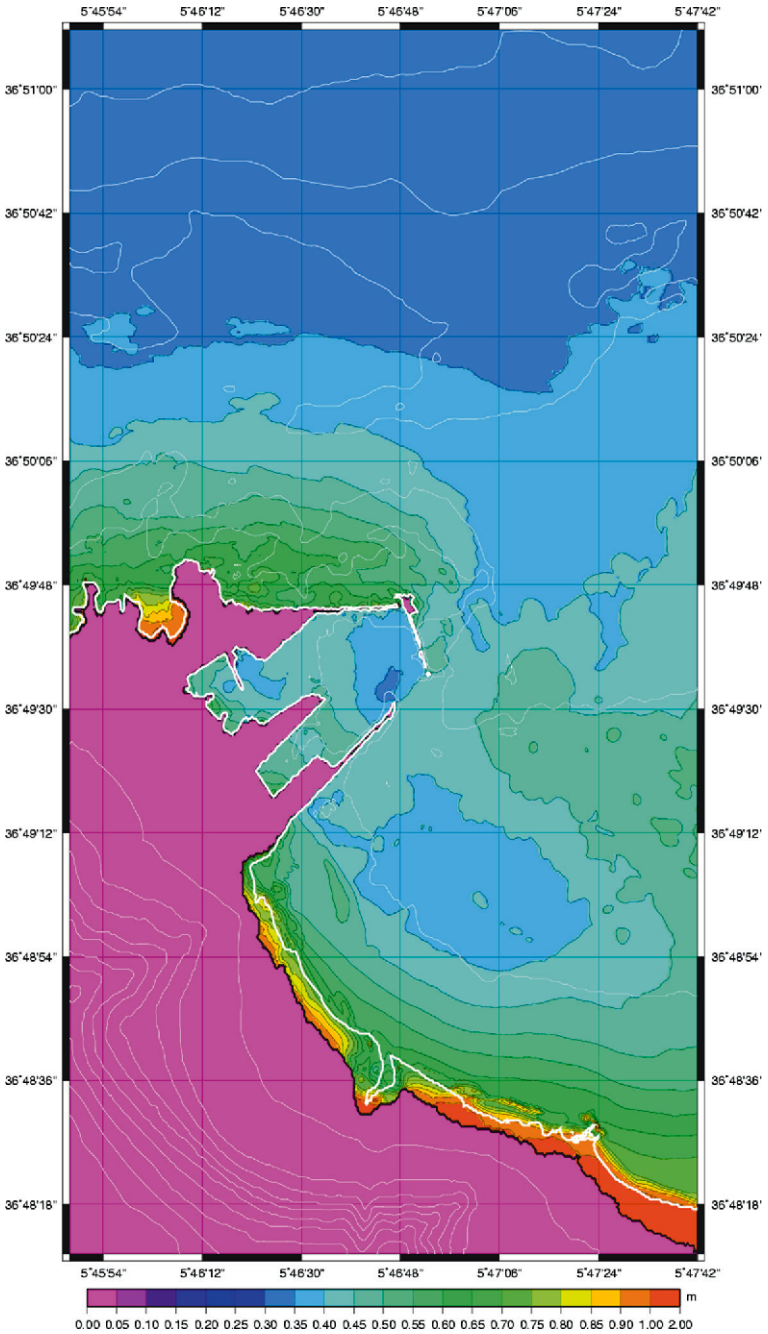

Figure 8

Maximum wave heights for a propagation of 30 minutes for the three segments source over bathy/topo grid (10 m each line). The blank line is the actual coastline of the city of Djidjelli. The dark line corresponds to the flooding limit area (runup).

provide values of more than 4 meters. This discrepancy could be attributed to the inaccuracy of the values reported by the observers at that time or to the poor bathymetric coverage near the shoreline, preventing us from predicting local wave amplifications. We also note that no flooding is evidenced in the western part of the city near the harbor, therefore the harbor with its present-day structure could play the role of a barrier to protect the old city.

6. Discussion and Concluding Remarks

The Djidjelli tsunami of August 1856 could be considered as one of the significant events in the Mediterranean region. Indeed, this is one of the well described tsunamigenic events which took place in the western Mediterranean region during the 19th century. Numerous observations on the impact of this event are available in literature, newspapers or reports. However, no attempt was made until now to explore the possible range of coastal impact of such an event, mainly because of the lack of knowledge related to the source of the event and regarding the bathymetry of the area. The Maradja 2 cruise conducted in 2005 is the first modern bathymetric survey carried out along the eastern margin and offers the opportunity to make a first approach of the implications of this active faulting occurring offshore. Based on the data collected during this survey and on a deep seismic section from the industry, the possible seismic sources of the Djidjelli tsunami (Algeria) of August 21 and 22 are hypothesized, and the possible triggered tsunami is presented. The *en echelon* pattern of the faults (3 segments) that have been identified for the first time near the foot of the margin expresses the deformation process of the margin as observed in other regions of the margin recently studied as Boumerdes or Annaba (Déverchère *et al.*, 2005; Domzig, 2006; Kherroubi *et al.*, in press). This set of faults with an NE-SW or E-W direction is in agreement with the deformation pattern on land (Meghraoui, 1988) which results from the slow convergence of the African and Eurasian plates with an estimate rate of about 0.5–0.7 cm/yr (De Mets, 1990). In accordance with literature, which mentioned two main shocks and many series of waves, we propose that the western fault segment (WS, Fig. 2) may have ruptured first, followed by the rupture of one or two other fault segments (CS and/or ES, Fig. 2) located further east. Despite the complexity of the rupture process, we propose that the use of the model with the involvement of the three segments is the more realistic scenario.

Based on the historical information on the area affected by the tsunami, our work proposes several sea-wave propagation scenarios, trying to reach the best fit to the historical observations. The tsunami affected mainly the eastern Algerian coast and the coast of the Balearic Islands. We would like to emphasize that, because of the proximity of the epicenter from the shoreline, all the tested sources gave the same effects in the harbor area. The discrepancy of sea-wave predictions with the historical observations could be explained by several factors, such the poor bathymetry coverage near the shore, which do not allow the creation of a very realistic bathymetric map for modelling.

Furthermore, we must mention the lack of precise temporal information on the arrival times of the tsunami on the Algerian and Balearic coasts. Indeed, the available archives do not report any approximate time delay between the earthquake and the sea-wave arrival on the coast. This could be related to the time occurrence of the first earthquake which struck in the evening and to the induced panic. Therefore, more temporal investigations of these data will be necessary to precisely determine the propagation of the tsunami.

In spite of our effort to build a realistic grid for the harbor with respect to the structures as piers, docks, etc. for the Algerian coast, the lack of very precise bathymetry as approaching the coast and especially in harbors prevents us from better knowing the role of the bathymetric structures, as submarine canyons for example, near the shore, on the wave amplification. Future bathymetric surveys on the Algerian continental shelf will allow to refine the runup model. Whatsoever, the occurrence of the Djidjelli tsunami indicates that waves of some meters could reach the different coastlines of the western Mediterranean region. LORITO *et al.* (2008) also demonstrate that the coastal area of Djidjelli could be affected by tsunamis triggered in the Sicily channel.

The tsunami hazard in Algeria became more obvious by the occurrence of the last Boumerdes tsunami of May 2003, also evidencing that the Algerian margin hosts several important active tsunamigenic faults that can cause damage on both parts of the western Mediterranean Sea. The acquisition of the recent data through the Maradja 1 and 2 surveys along the margin will allow us to re-assess the tsunamigenic hazard in Algeria, poorly constrained in the past owing to the lack of accurate and up-to-date surveys in this region.

Acknowledgments

We thank reviewers G.A. Papadopoulos and A.C. Yalciner for useful advice which enhanced clarification and improve the content and presentation of this paper. This work is a contribution to ANR (Agence Nationale de la Recherche) Projects ISIS and DANACOR (CATTELL: « Catastrophes telluriques et tsunamis » Programme, France). We have benefited from exchanges in the frame of the TASSILI CMEP (Comité Mixte d'Evaluation et de Prospective de la coopération scientifique franco-algérienne) Programme number 014MDU619.

REFERENCES

AKI, K. (1966), *Generation and propagation of G-waves from the Nigata earthquake of June 16, 1964, Part 2: Estimation of earthquake moment, released energy, and stress-strain drop from the G wave spectrum*, Bull. Earthquake Res. Inst. Tokyo, Univ. *44*, 73–88.

ALASSET, J.P., HÉBERT, H., MAOUCHE, S., CALBINI, V., and MEGHRAOUI, M. (2006), *The tsunami induced by the 2003 Zemmouri earthquake (M_w: 6.9, Algeria): Modelling and results,* Geophys, J. Int., doi:10.111/j.1365-246X.

AMBRASEYS, N.N. (1982), *The seismicity of North Africa: the earthquake of 1856 at Jijelli, Algeria*, Bollettino Di Geofisica a Teoritica ed Applicata, XXIV, *93*, 31–17.

BENHALLOU, H. (1985), *Les catastrophes sismiques de la région d'Echelif dans le contexte de la sismicité historique de l'Algèrie*. Thèse d'Etat. USTHB. Alger, 294 p.

BENOUAR, D. (1994), *The seismicity of Algeria and the Maghreb during the twentieth century*, Ph.D. dissertation, Imperial College London, U.K.

BRITISH OCEANOGRAPHIC DATA CENTRE (1997) *The Centenary Edition of the Gebco Digital Atlas,* Liverpool, U. K.

DELOUIS, B., VALLEE, M., MEGHRAOUI, M., CALAIS, E., MAOUCHE, S., LAMMALI, K., MAHSAS, A., BRIOLE, P., BENHAMOUDA, F. and YELLES, K. (2004), *Slip distribution of the 2003 Boumerdes Zemmouri earthquake Algeria from teleseismic, GPS and coastal uplift data*, Geophys. Res. Lett. *31*, L18607, doi 10 1029/2004 GL020687.

DE METS, C., GORDON, R., ARGUS, D.F., and STEIN, S.(1990), *Current plate motions*, Geophys. J. Int. *101*, 425–478.

DÉVERCHÈRE, J., YELLES, K., DOMZIG, A., MERCIER DE LÉPINAY, B., BOUILLIN, J.-P., GAULLIER, V., BRACÈNE, R., CALAIS, E., SAVOYE, B., KHERROUBI, A., LE ROY, P., PAUC, H., and DAN, G. (2005), *Active thrust faulting offshore Boumerdes, Algeria, and its relations to the 2003 M_w 6.9 earthquake*, Geophys. Res. Lett. *32*:L04311, doi:10.1029/2004GL021646.

DOMZIG, A. (2006), *Déformation active et récente et structuration tectono-sédimentaire de la marge sous marine algérienne*, Ph.D. Thesis, UBO-IUEM, Brest, France, 332 pp.

HARBI, A., BENOUAR, D., and BENHALLOU, H. (2003), *Re-appraisal of seismicity and seismotectonics in the north-eastern Algeria. Part I: Review of historical seismicity*, J. Seismol. *7*, 115–136.

HEBERT, H., ROGER, J., and SCHINDELE, F. (2007), *Advances in tsunami hazard assessment in the western Mediterranean sea,* Geophys. Res. Abstracts, *9*, 06341, EGU Vienna, 15–20 April 2007.

IBN KHALDOUN, A.Z.Y. (1369), *Kitab al-Ibar*, edited in 1959, Maison du Livre Libanais, Beyrut.

KHERROUBI, A., DEVERCHERE, J., YELLES, K., MERCIER LEPINAY, B., DOMZIG, A., CATTANEO, A., BRACENE, R., GAULLIER, V. and GRAINDORGE, D., *Recent and active deformation pattern off the easternmost Algerian margin: New evidence for tectonic reactivation*, Marine Geology, in press.

LECLAIRE, L. (1972), *La sédimentation holocène sur le versant méridional du bassin algéro-baléare (précontinent algérien)*, Mém. Mus. Nat. Hist. Nat. Paris, Nouv. Serv., C.24, 391 p.

LORITO, S., TIBERTI, M.M., BASILI, R., PIATANESI, A., and VALENSISE, G. (2008), *Earthquake-generated tsunamis in the Mediterranean Sea: Scenarios of potential threats to Southern Italy*, J. Geophys. Res., *113*, B01301, doi:10.1029/2007JB004943.

MEGHRAOUI, M. (1988), *Géologie des zones sismiques du nord de l'Algérie: Paléosismologie, Tectonique active et Synthèse Sismotectonique*, Thèse de Doctorat es Science, U. de Paris XI, France, 356 pp.

MOKRANE, A., AIT MESSAOUD, A., SEBAI, A., MENIA, N., AYADI, A., and BEZZEGHOUD, M. (1994), *Les seîsmes en Algérie de 1365 à 1992*, Publication CRAAG.

OUYED, M., MEGHRAOUI, M., CISTERNAS, A., DESCHAMPS, A., DOREL, J., FRECHET J., GAULON, R., HATZFELD, D., and PHILLIP, H. (1981), *Seismotectonics of the El Asnam earthquake*, Nature *292*, 26–31.

OKADA, E.A. (1985), *Surface deformation due to shear and tensile faults in a half-space*, Bull. Seismol. Soc. Am. *75*, 1135–1154.

PAPADOPOULOS, G.A. and FOKAEFS, A. (2005), *Strong tsunamis in the Mediterranean Sea: A re-evaluation,* ISET J. of Earthq. Technol. *42*, 159–170.

ROGER, J. and HEBERT, H. (2007), *Tsunami hazard in western Mediterranean: Preliminary study of scenarios for the Balearic*, EOS Trans. AGU, *88*(52), Fall Meet. Suppl., Abstract S53A–1009.

ROGER, J. and HEBERT, H. (2008), *The 1856 Djidjelli (Algeria) earthquake and tsunami: Source parameters and implications for tsunami hazard in the Balearic Islands*, Natural. Hazards Earth Syst. Sci., *8*, 721–731.

ROTHE, J.P. (1950), *Les seîsmes de Kerrata et la seîsmicité de l'Algérie*, Bull. Serv. Carte Geol. Algérie, Série *4*, 3.

SOLOVIEV, S.L., CAMPOS-ROMERO, M.L., and PLINK, N.L. (1992), *Orleansville tsunami of 1954 and El Asnam tsunami of 1980 in the Alboran Sea (Southwestern Mediterranean Sea)*, Izvestiya, Earth Phys. *28*(9), 739–760.

SOLOVIEV, S.L., SOLOVIEVA, O.N., GO, C.N., KIM, K.S., and SHCHETNIKOV, N.A., *Tsunamis in the Mediterranean Sea 2000 B.C.-2000 A.D: Advances in Natural and Technological Hazards Research* (Kluwer Publications 2007). Vol. 13, 237 pp.

WELLS, D.L. and COPPERSMITH, K.J. (1994), *New empirical relationships among magnitude, rupture length, rupture width, rupture area, and surface displacement,* Bull. the Seismol. Soci. Am. *84*(4), 974–1002.

YELLES-CHAOUCHE, A.K. (1991), *Coastal Algerian earthquakes. A potential risk of tsunamis in Western Mediterranean? Preliminary investigations*, Science Tsunami Hazards, *9*(1), 47–54.

YELLES-CHAOUCHE, A.K., DJELLIT, H., and HAMDACHE, M. (2003), *The Boumerdes Algiers (Algeria) earthquake of May, 21, 2003 (M_w: 6.8)*, CSEM Lett., *20*, 1–3.

YELLES-CHAOUCHE, A.K., DEVERCHERE, J., DOMZIG, A., MERCIER DE LEPINAY, B., BABONNEAU, N., HEBERT, H., ROGER, J., KHERROUBI, A., GRAINDORGE, D., BRACENE, R., CATTANEO, A., GAULLIER, V., SAVOYE, B., LEROY, P., and AIT OUALI, R. (2007), *The tsunami of Djidjelli (eastern Algeria) of August 21–22, 1856: The seismotectonic context and its modelling*, IUGG Meeting, Perugia, Italy, 2–13 July 2007.

(Received February 2, 2008, revised September 17, 2008)

Pure appl. geophys. 166 (2009) 301–324
0033–4553/09/010301–24
DOI 10.1007/s00024-008-0437-2

Pure and Applied Geophysics

Analysis of Observed and Predicted Tsunami Travel Times for the Pacific and Indian Oceans

PAUL WESSEL

Abstract—I have examined over 1500 historical tsunami travel-time records for 127 tsunamigenic earthquakes that occurred in the Pacific and Indian Oceans. After subjecting the observations to simple tests to rule out gross errors I compare the remaining reports to simple travel-time predictions using Huygens method and the long-wave approximation, thus simulating the calculations that typically take place in a tsunami warning situation. In general, I find a high correspondence between predicted and reported travel times however, significant departures exist. Some outliers imply significantly slower propagation speeds than predicted; many of these are clearly the consequences of observers not being able to detect the (possibly weak?) first arrivals. Other outliers imply excessively long predicted travel times. These outliers reflect peculiar geometric and bathymetric conditions that are poorly represented in global bathymetric grids, leading to longer propagation paths and consequently increased travel times. Analysis of Δt, the difference between observed and predicted travel time, yields a mean Δt of 19 minutes with a standard deviation of 131 minutes. Robust statistics, being less sensitive to outliers, yield a median Δt of just 18 seconds and a median absolute deviation of 33 minutes. Care is needed to process bathymetry to avoid excessive travel-time delays in shallow areas. I also show that a 2×2 arc minute grid yields better results that a 5×5 arc minute grid; the latter in general yielding slightly slower propagation predictions. The largest remaining source of error appears to be the inadequacy of the point-source approximation to the finite tsunami-generating area.

Key words: Tsunami travel-time prediction, statistics, bathymetry.

1. Introduction

Historically, the Pacific has experienced several basin-wide tsunamis following large tsunamigenic earthquakes from various areas of the subducting plate boundary (e.g., DUDLEY, 1998). Of particular importance is the April 1, 1946 Aleutian earthquake whose powerful tsunami led to widespread destruction and numerous deaths (e.g., SHEPARD *et al.*, 1950); it also gave birth to the early U.S. tsunami warning system. In contrast, tsunamigenic earthquakes in other oceans have been much less frequent and thus warning centers were generally lacking; the calamitous 2004 Sumatra tsunami has now ushered in a new era in tsunami detection and preparedness. Designed to monitor their regions for potentially destructive tsunamis, warning centers, such as the U.S. Pacific and Alaska

Department of Geology and Geophysics, School of Ocean and Earth Sciences and Technology, University of Hawaii at Manoa, 1680 East-West Rd. Honolulu, HI 96822, U.S.A. E-mail: pwessel@hawaii.edu

tsunami warning centers, must routinely evaluate predicted tsunami travel times from the epicenters of potentially tsunamigenic earthquakes. Typically, it is not known until tide gauge or tsunameter data become available whether or not a particular large earthquake has generated an ocean-wide tsunami. In the mean time, the authorities may calculate travel times to a large number of tide stations and warning points in the Pacific. These estimated times of arrival (ETA) are incorporated into various communications from the warning agencies to local, state, and international civil defense agencies so that first responders will have an accurate estimate of when the first wave is likely to arrive. Because the premium is on responding quickly in a possible emergency situation, many warning agencies employ a rapid first-arrival methodology where no dynamic calculation of the waves is performed; i.e., no prediction of wave amplitude is attempted. Such dynamic calculations require detailed knowledge of the source, are usually done after an event, and may require considerable computational power (e.g., KOWALIK *et al.*, 2005). Simple estimates can be obtained by using the long-wave approximation (e.g., MADER, 2004; MEI, 1989), i.e., it is assumed that the tsunami will propagate away from the epicenter at a velocity given by

$$v(\vec{x}) = \sqrt{g(\vec{x})z(\vec{x})}, \tag{1}$$

where g is the vertical gravitational attraction, z is the local water depth, and $\vec{x}$ is the position vector. The program TTT from Geoware (GEOWARE, 2007) calculates these velocities based on an input bathymetry grid and uses Huygens' constructions to propagate the wave front from the epicenter to all nodes on the grid.

There are several situations in which these predicted ETAs may not match observed arrival times of the tsunami waves, including but not limited to the following:

1. The bathymetry grid is not accurate.
2. The epicenter is not well located, or the origin time is uncertain.
3. The epicenter is on land and a pseudo-epicenter off the coast must be selected.
4. The point approximation to the epicenter inadequately represents the rupture zone.
5. Nonlinear propagation effects may be important in shallow water.
6. The observed travel times represent later arrivals.

It is therefore of interest to examine historical tsunamigenic events in the Pacific and Indian Oceans and compare observed travel times to predictions made with the methodology currently in place at many warning centers. Given such data one may derive statistical information about the accuracy of these rapidly calculated ETAs. In particular, I wish to examine the statistical properties of Δt, the discrepancy between observed and predicted travel times, and determine if there are significant systematic variations in Δt. For instance, given that earthquakes with epicenters on land can excite tsunamis, how does Δt vary with location of the pseudo-epicenter location chosen for such earthquakes? Finally, I will examine to what degree the various error sources listed above are

responsible for large Δt and what can be done to ensure the most accurate predictions in an emergency situation.

2. Methodology

I have examined the NGDC database of tsunamigenic earthquakes and associated observed first arrival tsunami travel times to numerous stations (NATIONAL GEOPHYSICAL DATA CENTER, 2007). From this database 127 tsunamigenic earthquakes were identified as having produced observable tsunamis with well-determined origin times and locations. In selecting this subset I examined definite tsunamis since 1800 with runup reports, an earthquake magnitude of 6 or above, and an epicenter in the Pacific or Indian Oceans (Fig. 1); the overwhelming majority of events are from the Pacific basin. Travel-time calculations relied on the global 2×2 arc minute bathymetry grid ETOPO2 (NATIONAL GEOPHYSICAL DATA CENTER, 2006) which itself derives most of its oceanic depths from the predicted/calibrated bathymetry based on satellite altimetry and shipboard bathymetry (SMITH and SANDWELL, 1994; 1997). To prevent excessive travel time overestimates in cases when the earthquake occurred beneath very shallow water (or for epicenters on land) I relocated the epicenter to the nearest node with a depth of

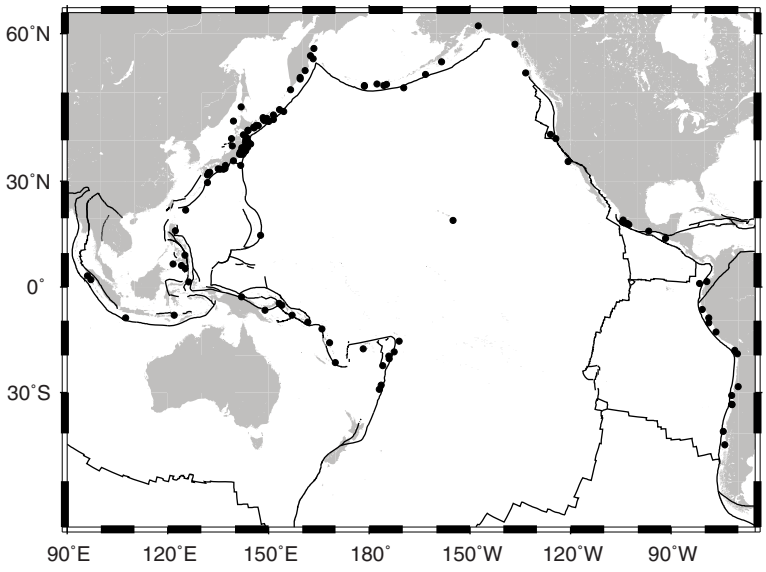

Figure 1
Location of 127 earthquakes identified as tsunamigenic events in the NOAA database. For each event I computed a global 2'×2' travel-time grid and sampled the travel times at all stations that reported an observed travel time, yielding over 1500 pairs of reported and predicted travel times.

at least 25 m. For consistency, and to examine far-field propagation of the most devastating tsunamis, global 2×2 arc minute travel-time grids were generated for each of the 127 events considered, even though only a few are known to have propagated beyond the Pacific (or Indian) basins. For warning center operations, typically only a regional (e.g., Pacific-wide or Indian-wide) calculation is required; at 2×2 arc minute resolution a Pacific-wide ETA grid is obtained within 1–2 minutes on a fast workstation; a slightly cruder 5×5 arc minute solution takes less than 10 seconds. Because most warning operations will automatically determine the epicenter and magnitude of an earthquake (or obtain this information from other agencies), the tsunami travel-time calculations may be launched automatically for earthquakes over a certain magnitude threshold and the resulting travel-time grid will be ready for analysis almost immediately. The output travel-time grids are compatible with the Generic Mapping Tools (e.g., WESSEL and SMITH, 1998), which were used extensively in this analysis, and are available upon request.

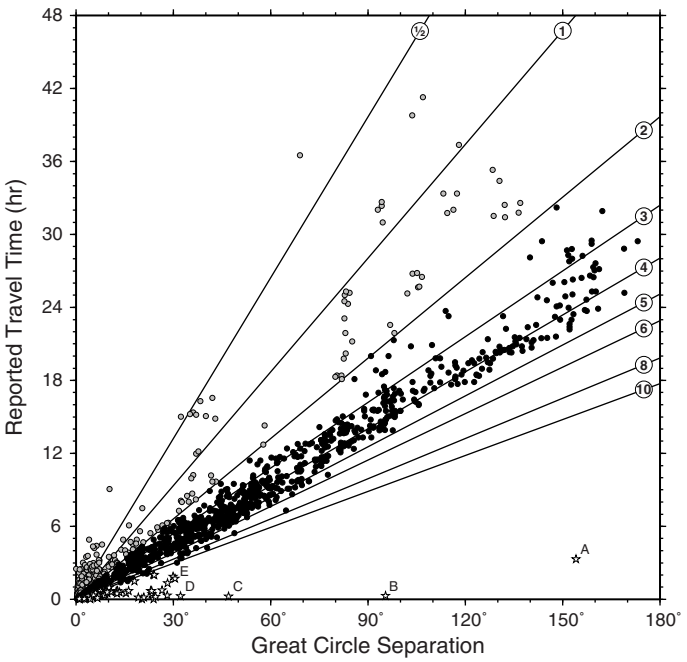

Figure 2

Reported travel times for the 127 earthquakes considered in the study, plotted versus the great circle distance between epicenter and recording station. Straight lines show travel times predicted by Eq. (1) for various average water depths (see labels, in km). Reported travel times above the 2 km-depth prediction (gray circles) are possibly late arrivals whereas times below the 11 km depth prediction may largely reflect erroneous tabulations (open stars), especially for the longer distances.

3. Analysis

3.1. Consistency of Reported Tsunami Travel Times

Prior to analyzing predictions I examined reported travel times versus the great circle separation between epicenter and reporting station; this distance represents the minimum path length traveled by any tsunami wave. Given Eq. (1) one can predict this relationship for a constant water depth. Figure 2 reveals several outliers that clearly indicate problems with the reported data. For instance, several reported travel times are much too short given the minimum distance the waves must have traveled. The outlier labeled "A" is the reported travel time from a 1922 earthquake in northern Chile to Aburatsubo, Japan. The distance is thus correct but one would expect a travel time closer to one day instead of the reported 198 minutes (3.3 hours). Perhaps the observed travel time originally was 19.8 hours (which is still too fast) but somehow ended up in the NOAA archive as 198 minutes. Outlier "B" from 2006 is more humorous, as the reasonable travel time from an Indonesian tsunami to Christmas Island (Indian Ocean) became associated with the other Christmas Island located in the Pacific, thus being archived with wrong metadata. Outlier C is simply a seiche registered in Freeport, Texas that was excited by the seismic tremors of the momentous 1964 Good Friday earthquake; thus, the travel time does not represent a typical tsunami phenomenon. Outlier D reflects another clerical error where the travel time from a 2006 earthquake in the Kuril Islands reportedly only took 16 minutes to reach the Shumagin Islands, Alaska over 3500 km to the west. Finally, outlier E is another Japanese recording (from Tsurushima) following a 1923 earthquake in Kamchatka. Again, I suspect the reported 10.2 minutes might originally have been 10.2 hours, and that many of the remaining outliers are likely to have similarly trivial explanations.

These data are further analyzed in Figure 3, which displays the equivalent average water depths, z_{ave}, required to reconcile reported travel times and their minimum distance of travel (via Eq. 1). All in all, 61 reports gave z_{ave} exceeding 11,022 m, which is the oceans' largest observed depth. These 61 are clearly all outliers and will be excluded from further consideration. Obviously, many others with slightly smaller z_{ave} are likely to be outliers as well but I have no clear cut-off criteria to apply and the distribution appears fairly continuous (see Fig. 3). Figure 2 also shows (as gray circles) reported travel times that appear too slow (equivalent average depth < 2 km). Certainly, for the more distant events these excessive travel times most likely reflect later arrivals, implying the first wave simply was too small to be noticed. Figure 3 suggests a possible hachured region where observations most likely come from later arrivals; again, no clear-cut criterion is available to separate these from first-wave arrivals and I will retain the remaining 1476 data pairs in the subsequent analysis.

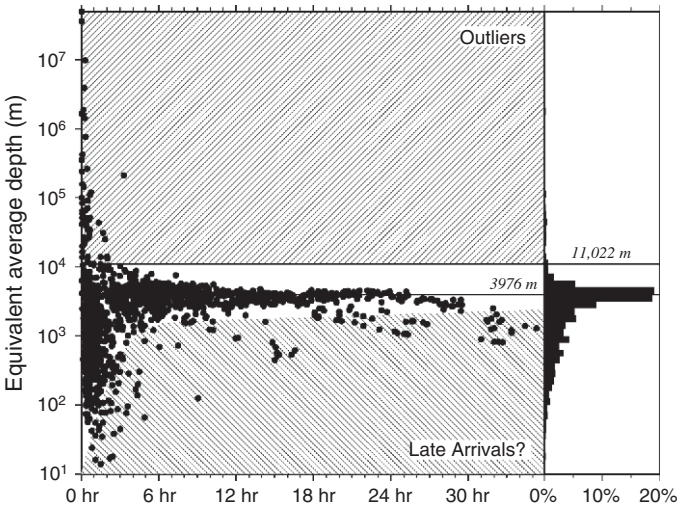

Figure 3

Equivalent average water depth (z_{ave}) versus reported travel times for data points in Figure 2. Most reported values are compatible with the Pacific mean ocean floor depth (3976 m). A total of 61 observations have a z_{ave} that exceeds the largest depth on Earth (11,022 m); these are considered clear outliers and are most likely clerical errors. Many values correspond to very shallow depths, probably reflecting overestimates of actual travel times (e.g., the detection of later rather than first arrivals). The lower hachured regions suggest an envelope for such later arrivals.

3.2. Simply Predicted Tsunami Travel Times

For each of the 127 events I calculated predicted travel-times on a global 2×2 minute grid, from which I made a detailed travel-time contour map, showing not only the (global) travel-time predictions but displaying the locations of stations from which reported travel times are available. These maps also include a simple graph of predicted versus observed travel time for these stations, and summarize the differences, Δt, between these pairs of values in standard box-and-whisker diagrams. In this paper I will only highlight some of these events individually; high-resolution PDF versions of all 127 event maps are available from the author's website (http://www.soest.hawaii.edu/pwessel/ttt). Figure 4 shows the results for the propagation of the tsunami wave front following the large 1960 Chile earthquake; here limited to the Pacific region only. The travel times are color-coded, with shading reflecting the shape of the underlying bathymetry. Over 100 tide stations, all in the Pacific, registered the arrival of this tsunami that took numerous lives, particularly in Hawaii and Japan, in addition to the local devastation in Chile (e.g., DUDLEY, 1998). None of the reported values have equivalent average depths exceeding 11,022 m. A direct comparison of observed and predicted travel times gives a correlation of 0.98, with a median Δt of only 14 minutes. However, note the several outlying points in the travel-time graph (Fig. 5). A closer inspection

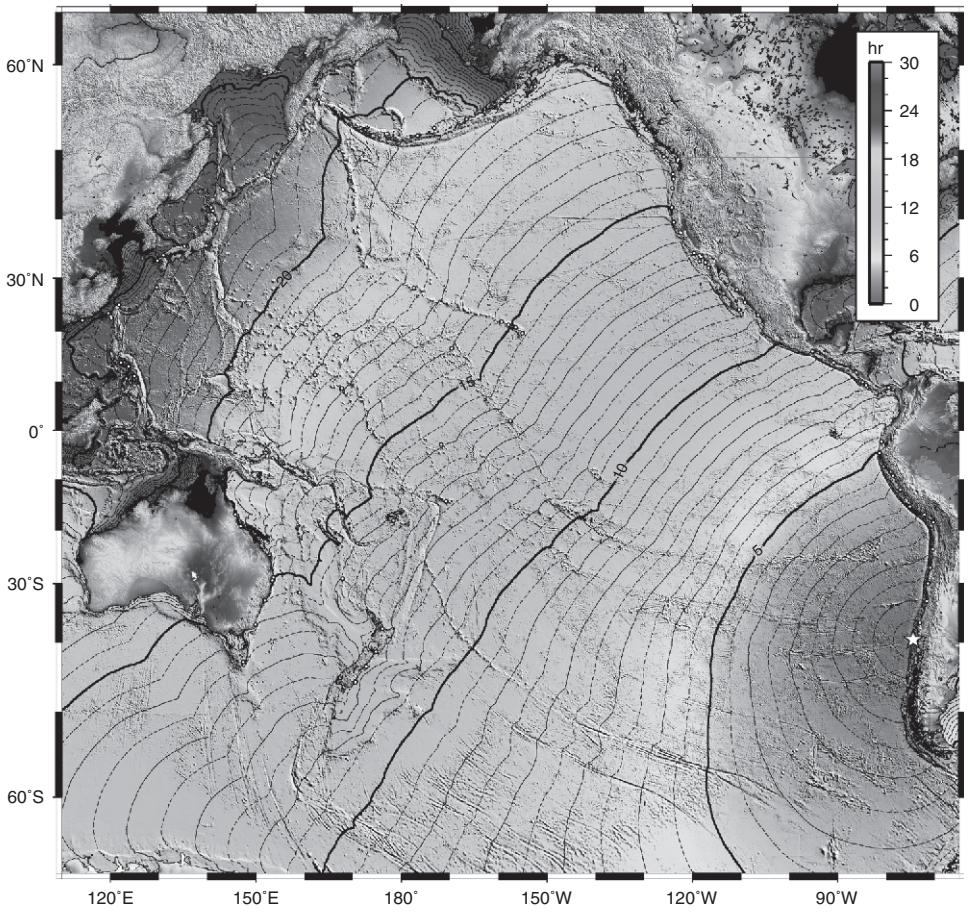

Figure 4
Predicted travel times for the Pacific-wide tsunami produced by the large 1960 Chile earthquake. Star indicates the point-source epicenter used for the calculation, with the 104 stations that reported travel times shown as white circles. Shading of travel times is provided by the bathymetry. Solid contours are hourly with 30-minute dashed contours in between.

shows that the single point for which the prediction exceeds the observed by several hours represents Punta Arenas in the far south of Chile. Given its sheltered position in the Strait of Magellan behind the Chilean Archipelago, the predicted travel time has been overestimated; it is likely that in this situation the simplicity of Eq. (1) poorly approximates the physics of wave propagation. Fortunately, the same island obstructions that lead to the excess in predicted travel time are also likely to attenuate truly dangerous waves before they arrive in Punta Arenas.

While the 1:1 correlation line is a remarkably good lower bound for all remaining observed travel times, there are several observations that are many hours slower than the

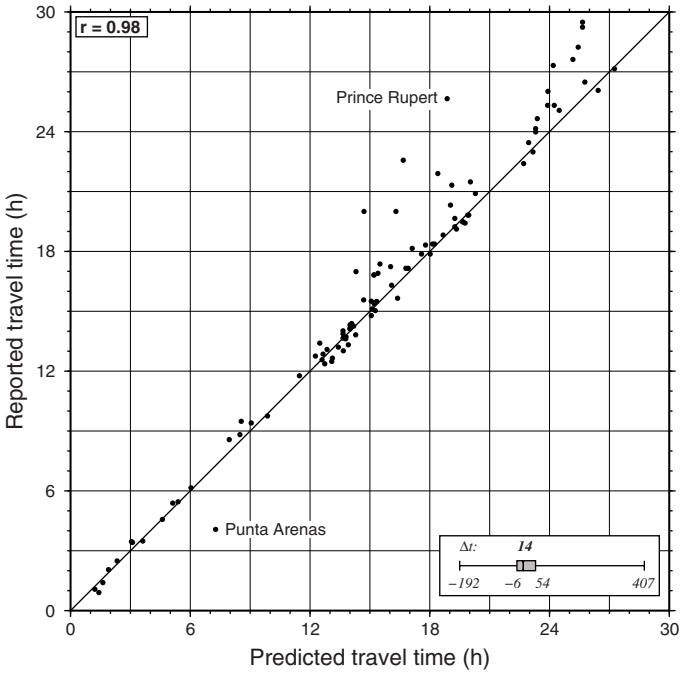

Figure 5
Reported versus predicted tsunami travel times for all 104 stations that observed the 1960 Chile tsunami. The 1:1 line represents perfect correlation. Large departures from this trend appear to be caused by excessive predicted travel times in shallow, narrow fiords (e.g., Punta Arenas, −3 hours) or a failure to detect the first arrivals (e.g., Prince Rupert, +6 hours). The box-and-whisker diagram summarizes the statistics of Δt; the differences between reported and predicted travel time (in minutes). The median Δt is +14 minutes.

corresponding predictions. Examining these points reveals that the slower observations for predictions in the 14–20 hour range are mostly associated with stations on the U.S. and Canadian west coast, many of which are sheltered in narrow inlets and sounds. Similarly, the slow arrivals after the first full day of propagation are mostly stations on the west-facing sides of Japan, Taiwan, and the Philippines. It would seem that these outliers represent later arrivals in locations where the first wave was not particularly energetic.

3.3. Statistical Analysis of Travel Times

Figure 6 shows all observed tsunami travel times plotted against the corresponding predicted travel times; the 61 points with excessive z_{ave} have been excluded. Again, if travel-time observations and predictions both faithfully reflected reality then all points should fall on a straight line with slope 1:1; clearly, this is not the case. However, as in the case of the 1960 event we do find a strong tendency for points to cluster around this

line, however there is significant scatter, some systematic offsets, and some large outliers. A peculiar feature of this plot is the appearance of a secondary trend that parallels the main 1:1 line but shifted by almost three hours of excess predicted travel time. During the analysis it became clear that the 1964 Prince Williams Sound, Alaska earthquake posed a particular problem when comparing predictions to observed travel times. Even a casual inspection of the travel-time correlation chart (white circles in Fig. 6) reveals that the predicted travel times are all close to three hours too long. This consistency for all observations points to a problem originating in the area near the epicenter. Early studies have demonstrated, by backward propagation of travel times, that the tsunami source area had to be located further out on the continental shelf, far from the epicenter (e.g., HATORI, 1981; PARARAS-CARAYANIS, 1967). Figure 7a presents a Mercator map of the Gulf of Alaska and indicates the reported location of the epicenter (star). As reported, the epicenter falls on land (e.g., SHERBURNE *et al.*, 1969) and therefore was relocated to the nearest ocean node of at least 25 m depth. The bathymetry in and near the area is

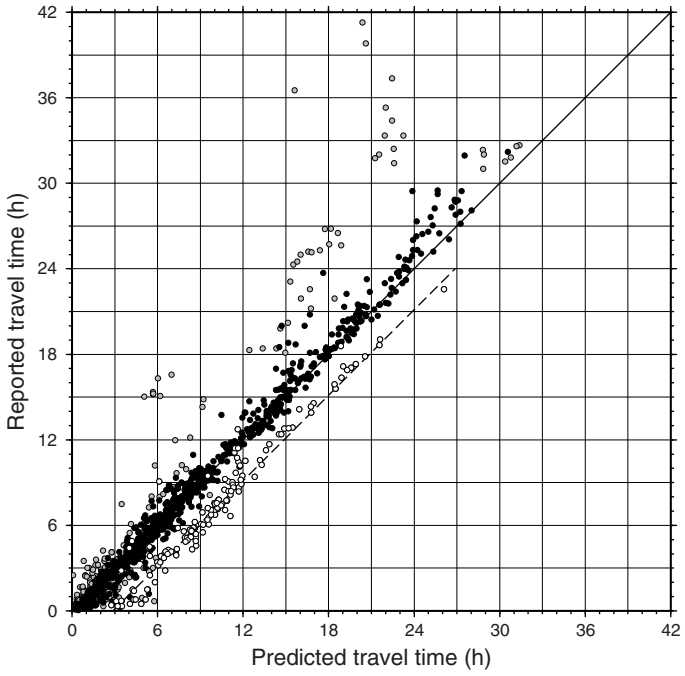

Figure 6
Correlation plot of all 1476 pairs of reported and predicted tsunami travel times. Color-coding as in Figure 2; outliers (stars) have been excluded. Other extreme outliers are noted, both above and below the trend line. The cluster of points (white) sub-parallel to the trend line ensues from reports of the great 1964 Prince Williams Sound earthquake in Alaska (see text).

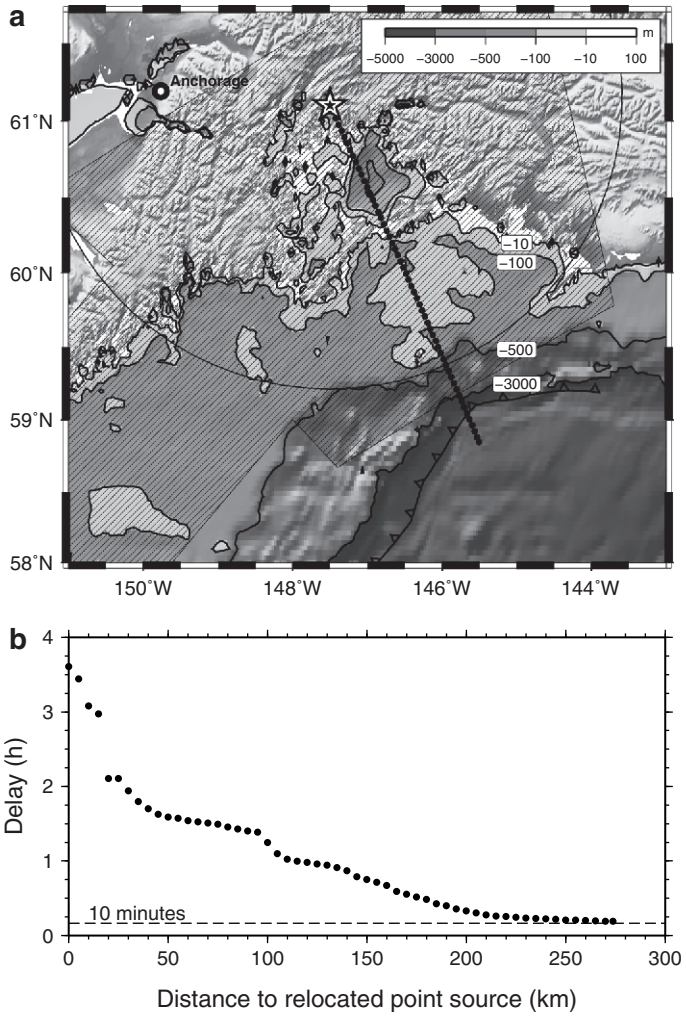

Figure 7

a) Coastlines and bathymetry near the site of the 1964 Alaska earthquake (star). Bathymetry shows extended shallow water depths on the continental margin. Hachured areas are uplifted blocks determined by joint geodetic and tsunami inversion by JOHNSON *et al.* (1996). Red dots indicate alternative point source locations for improved travel-time calculations, up to 275 km from the epicenter and toward the trench. **b**) Average delay (predicted minus reported tsunami travel time) obtained by using different point source locations. The major delays are caused by low propagation speed in shallow waters and the fact that the tsunami generation took place closer to the continental edge.

particularly shallow, which adds considerable propagation time to all stations. However, the main cause of the delays lies in the nature of the tsunami generation. Studies have shown that a large region of the continental shelf experienced significant crustal uplift in response to the earthquake (e.g., CHRISTENSEN and BECK, 1994; JOHNSON *et al.*, 1996; RUFF

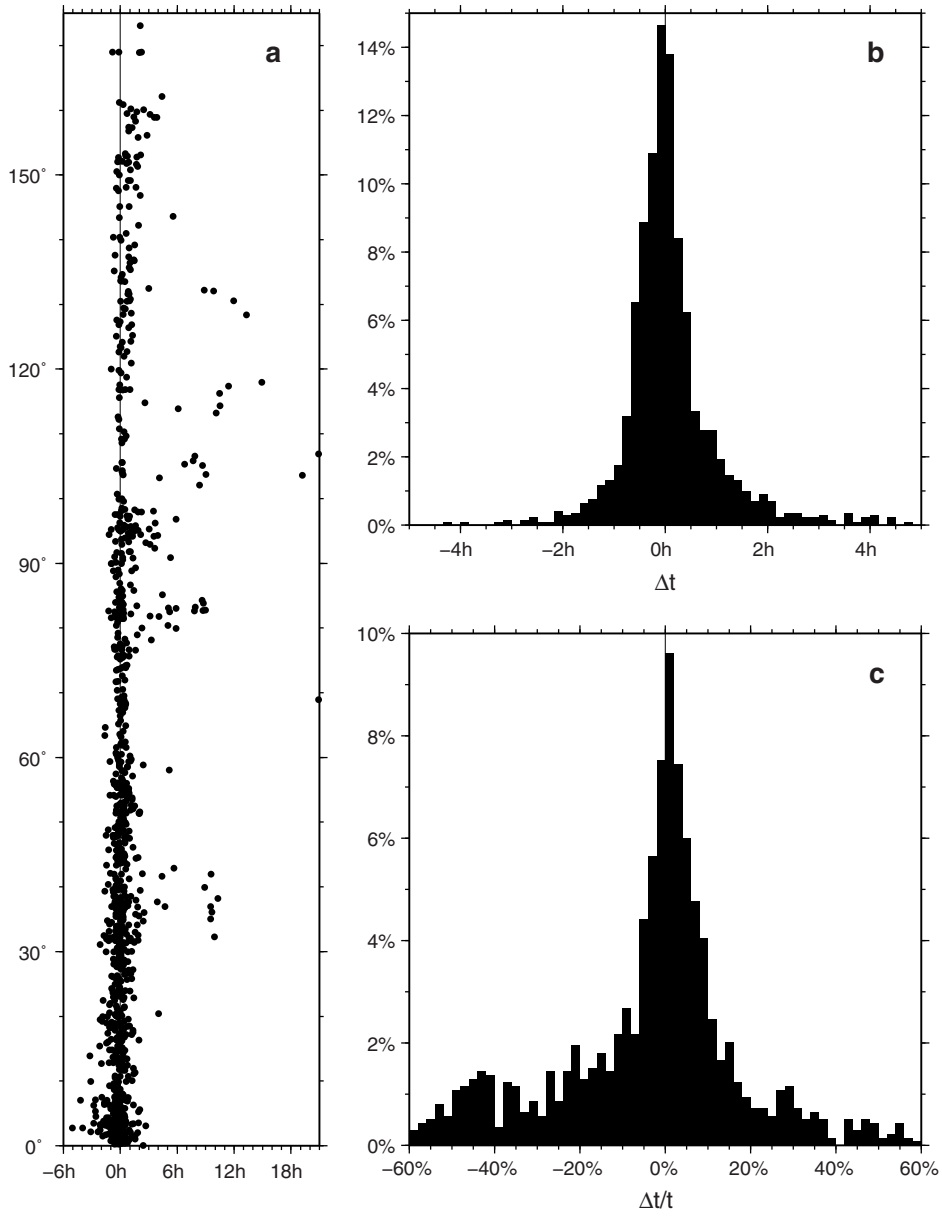

Figure 8

(a) Summary of Δt, the difference between reported and predicted tsunami travel times for all 1537 data pairs versus minimum travel distance (in degrees). (b) Histogram of Δt. The mean (median) value is 12 (−1.5) minutes with standard deviation (median absolute deviation) of 139 (35) minutes. Distribution has a longer tail to the right. (c) Same, but normalized by predicted travel time and reported in percent.

and KANAMORI, 1983), and it is this wide uplift of the water on the continental shelf that initiated the tsunami. In other words, a point source approximation turns out to be particularly poor for this event; however, this realization is in general not achieved until some time after the event.

To test this explanation I relocated the point source to increasingly more distant locations along a great circle from the epicenter to the nearest point on the trench

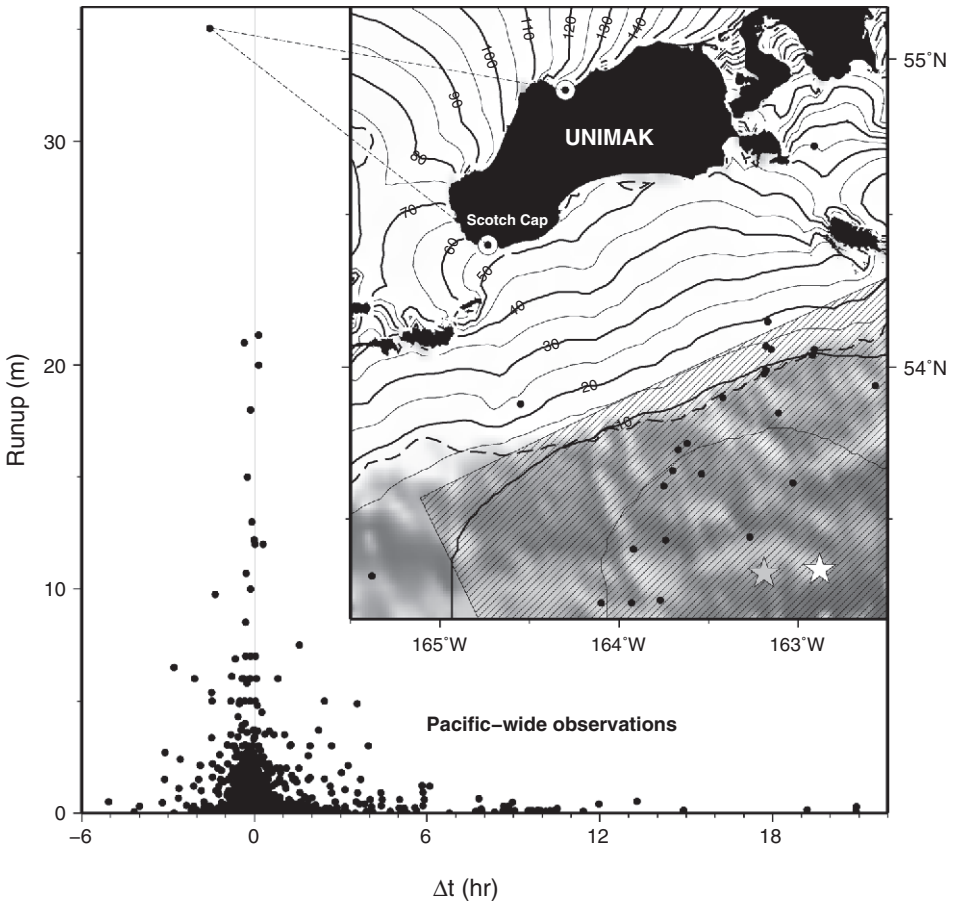

Figure 9

Distribution of tsunami runups (m) versus Δt. The larger runups have small Δt, suggesting larger Δt values may involve later arrivals. Note the large runup for the 1946 tsunami and its substantial travel-time prediction delay of $\sim$1.5 hrs. Inset: Travel-time contours (in minutes) from epicenter (star) of 1946 Aleutian tsunami on shaded bathymetry. Gray star is epicenter reported in NOAA runup catalog. White star, solid circles, and hachured region are relocated epicenter, aftershocks, and best estimate of minimum rupture area, respectively (LOPEZ and OKAL, 2006). Dashed contour is 200-m isobath. The marked delay Δt for the largest runup reflects incorrect coordinates used for Scotch Cap (see text).

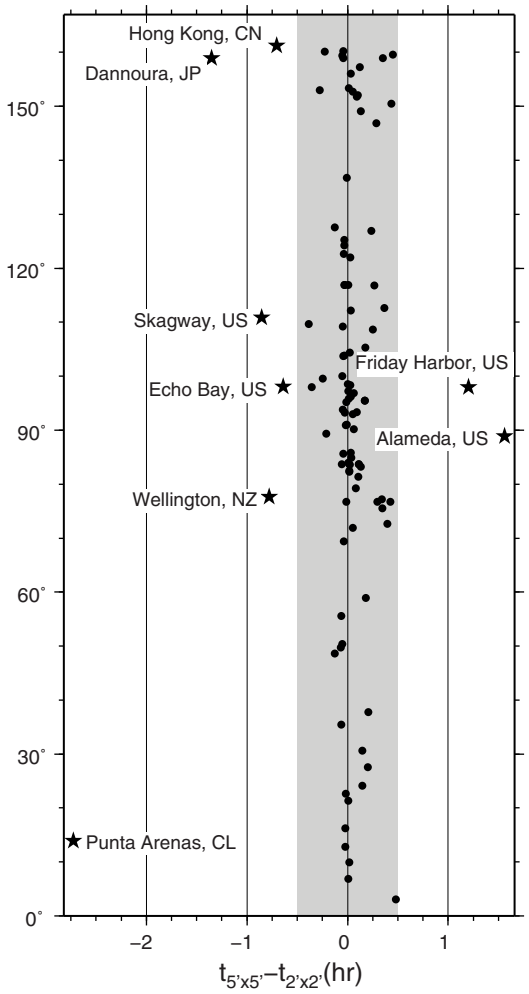

Figure 10
Sensitivity of predicted travel time due to bathymetry grid resolution. Differences in travel times (solid dots) calculated from 5×5 and 2×2 arc minute grids are shown at all stations reporting arrivals for the 1960 Chile event. I thoroughly investigated the causes of the largest discrepancies (named stations; solid stars) which all were related to geometry changes for shallow water pathways near the station (see text).

(Fig. 7a). I then ran the travel-time calculations on the 2×2 arc minute grid for the different point sources. The various travel-time delays were found by computing the mean Δt for each solution. Figure 7b shows the prediction delays versus the distance between reported epicenter and point source used. The delay is gradually reduced with distance and appears to approach asymptotically a ∼10-minute level (for distances > 250 km). This distance corresponds to the outer boundary of the uplifted

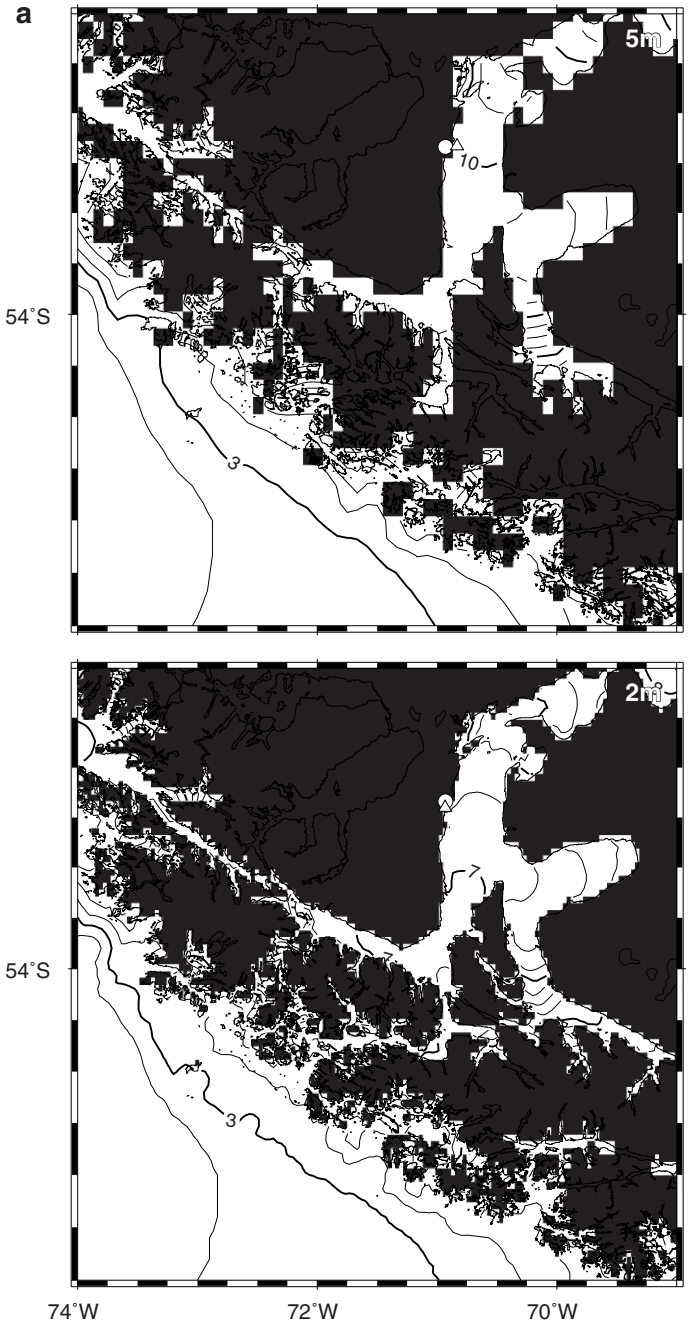
a
5m
10
3
2m
7
3
54˚S
54˚S
74˚W
72˚W
70˚W

◀ Figure 11
Comparison of bathymetry grid and predicted travel times for the 2×2 min (lower) and 5×5 min (upper) grids for the 1960 Chile event. Open circle is reported station location whereas open triangle is nearest node located in the water. (a) Punta Arenas, Chile, is located in the Strait of Magellan sheltered by the Chilean Archipelago. The different bathymetry resolutions result in different pathways and a shallower average depth. (b) Alameda, California, US in the San Francisco Bay. In the courser 5-min-grid the bay entrance is closed off, forcing the station to be relocated all the way to the Pacific coast and shortening the predicted time. (c) Dannoura, Japan is similar to Alameda, as the relocated station falls on the Japan Sea coast instead of in the Seto Inland Sea to the east of the artificial barrier blocking the Kanmon Strait.

blocks (hachured areas in Fig. 7a) determined from a joint inversion of geodetic data and tsunami waveforms (JOHNSON *et al.*, 1996). The remaining $\sim$10 minute delay most likely reflects the non-point-source nature of the disturbance as well as other causes such as inaccurate bathymetry at reporting stations and inability to identify the arrival of the first wave.

Figure 8 presents a summary and histograms of Δt implied by the data in Figure 6 and augmented by the data for the 1964 tsunami after correcting for the inferred 2.92-hour bias. Figure 8a shows how Δt varies with epicenter-station separation. We clearly see late arrivals (positive Δt) increase for tsunami waves that traveled long distances, while prediction errors ($\Delta t < 0$) are most prevalent for stations not too distant from the tsunami nucleation area. Two different forms of analysis were pursued: (1) Figure 8b gives the standard histogram of the Δt distribution in terms of departures from the predicted value; (2) Figure 8c shows the same departure as a percentage relative to the predicted travel time. This approach was undertaken to show how the misfit varied with travel time. We note that the former quantity appears more normally distributed than the latter, nonetheless both have long tails, suggesting nonparametric statistics should be used to characterize the distributions. Whereas the mean and standard deviation of Δt are 19 and 131 minutes, respectively, the median and the median absolute deviation (MAD) are only -0.3 and 33 minutes, respectively. Clearly, the presence of late arrivals skews the mean away from the expected zero, which is well represented by the median. The percentages also are vulnerable to large scatter due to the normalization by small travel times; I find a median percentage of -0.2 and a MAD of 15%. These robust values represent typical uncertainties and exclude the few extreme cases.

3.4. Runup and Predicted Travel Times

One of many concerns for agencies responsible for issuing warnings is the possibility of overestimating travel times to some stations, such as would have been the case if the 1964 Alaska tsunami travel-time predictions were to be taken at face value. In comparing reported runups to both predicted and reported travel times I note: (1) The largest runups are associated with stations very close to the epicenter. For people in proximal regions of large earthquakes the best defense is to leave the coastal region and seek safety inland while there is still time. (2) Runups at stations with poor correlation between reported

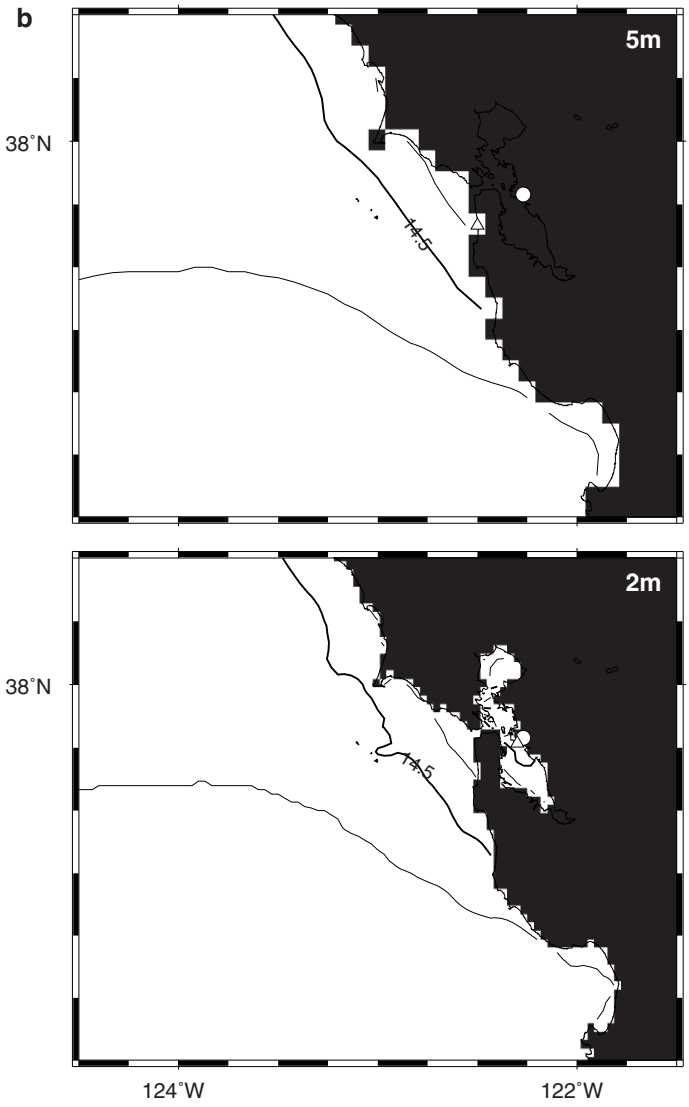

Figure 11
Contd.

and predicted travel times are insignificant. This is highlighted in Figure 9, which displays runups for all 1476 records; it is clear that, in general, the largest values have very small Δt. However, we note that the largest runup (> 35 m) has a disturbingly large prediction delay of 1.6 hours (as do some other runups in the 5–10 m range). This particular observation comes from Scotch Cap on Unimak Island, Alaska following the April 1, 1946 tsunami that originated on the slope to the south of Unimak Island. This

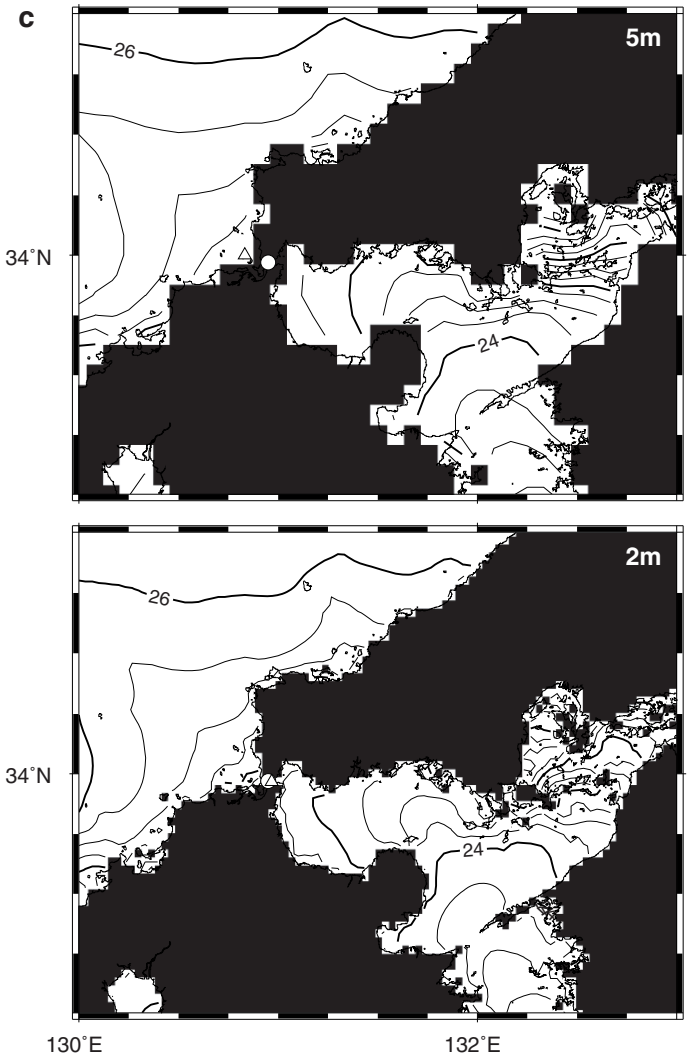

Figure 11
Contd.

tsunami is unusual in that it is generally assigned a relatively small magnitude (e.g., PACHECO and SYKES, 1992), yet its tsunami magnitude is 9.3 (ABE, 1979) and it produced very large runups focused in a narrow beam normal to the strike of the trench (FRYER *et al.*, 2004). A recent revision to the Scotch Cap runup even raises the value to 42 m (OKAL *et al.*, 2003), and a reanalysis of long-period seismographs suggests the magnitude was probably closer to 8.5 (LOPEZ and OKAL, 2006). Several studies have determined

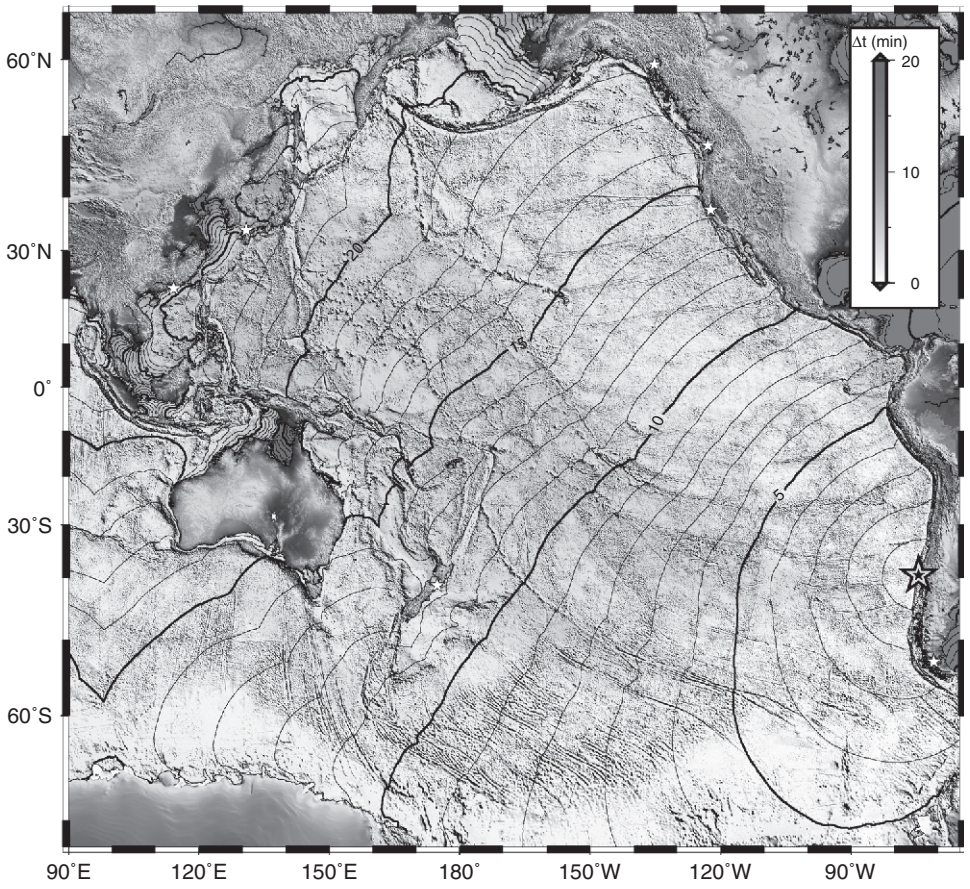

Figure 12

Color-coded differences between travel-time predictions for 2×2 and 5×5 arc minute bathymetry, with superimposed hourly travel-time- contours. Yellow star is epicenter location. The largest differences occur in shallow coastal areas such as between Australia/Papua New Guinea and the Yellow Sea between China and Korea. For > 97% of the Pacific nodes the difference in predicted travel time is less than 5 minutes. White stars denote locations of 8 outliers in Figure 10.

approximate fault plane solutions from the distribution of aftershocks (e.g., JOHNSON and SATAKE, 1997; LOPEZ and OKAL, 2006); hence the point source epicenter solution employed herein to obtain travel times may likely be inadequate in this case as well. However, from the map inset we can determine the main cause of the large Δt: While the NOAA runup data base correctly reports the Scotch Cap observed travel time (48 minutes) and runup, it incorrectly lists as location the coordinates of a point on the north side of Unimak Island, near Cape Mordvinof. Using the Scotch Cap coordinates yields a revised predicted travel time of 53 minutes and an improved Δt of only 5 minutes.

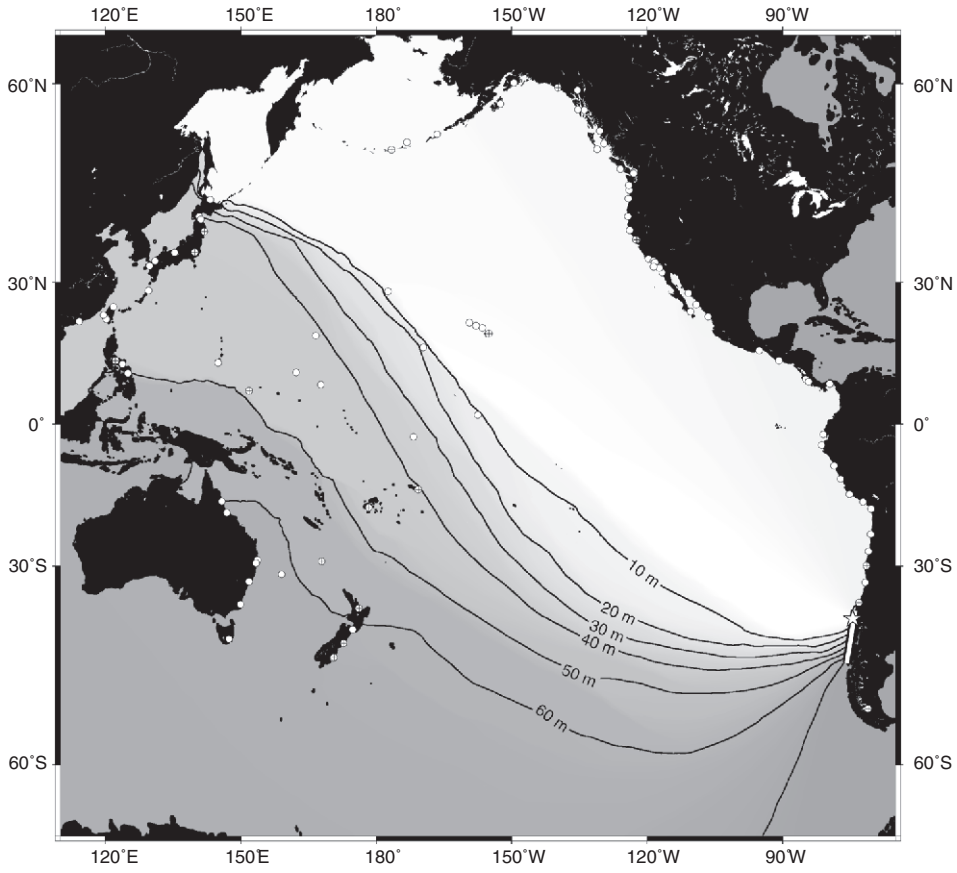

Figure 13
Differences in travel-time predictions for the 1960 Chile tsunami using a close approximation to the actual rupture area (white rectangle) versus the point-source epicenter solution (star). Contours (in minutes) project the effect being limited to the southern and western Pacific (shaded areas). Circles represent recording stations; crossed circles have predicted travel times that are slower than observed by 10 minutes or more.

3.5. Effect of Using Coarser Bathymetry Grids

Regardless of the method used to calculate travel times, any uncertainties in water depth will translate into uncertainties in the predictions. Equation (1) suggests uncertainties in depth are more critical for areas of shallow water where an underestimated depth can give rise to significant travel-time delays. One source of depth uncertainty comes from the preparation of gridded bathymetry. Given the 104 stations that reported observed travel times for the 1960 Chile tsunami, I repeated the travel-time calculation using a coarser, 5×5 arc minute global grid derived by filtering ETOPO2 with a 17-km median filter to avoid aliasing and to reduce the influence of

narrow, shallow features in the derived grid. I then computed the difference in predicted travel-time to the 104 stations and plotted these differences versus the corresponding epicenter-to-station great circle distances (Fig. 10). While the differences have $\sim$ zero mean we find a handful of significant outliers as well as a general variability with standard deviation of $\sim$5 minutes. To determine the source of the larger outliers (stars) I thoroughly investigated each of the bathymetry grids near the eight named stations; here I discuss three representative examples that highlight the typical causes of such discrepancies. The remaining examples have similar albeit less severe characteristics.

Figure 11a shows travel-time grids for the 5×5 minute (upper) and 2×2 minute (lower) bathymetry grids. Black indicates nodes on land. The circle indicates the location of Punta Arenas in southern Chile where the two travel-time grids differ by almost 2 hours. Examination of the nodes quickly reveals differences between the two grid resolutions. While the finer 2×2 minute grid is able to preserve some of the narrow waterways between the numerous islands in the Chilean Archipelago and the Strait of Magellan, the 5×5 minute grid has closed off many of these pathways, resulting in two significantly different paths from epicenter to station. In this extreme case the 5×5 minute grid prediction would be almost 10 hours. Neither solutions come particularly close to the reported travel time of $\sim$4 hours (7.3 vs. 10 hours).

Figure 11b shows the opposite situation occurring at the Alameda tide station inside San Francisco Bay, USA. Here, the narrow inlet (spanned by the Golden Gate Bridge) could not be represented in the coarser grid, resulting in the entire bay being land-locked. In such cases, the travel-time grid must be sampled at the ocean node nearest the tide station (triangle), which in this case is relocated to the Pacific coast. In comparison, the finer grid allows for propagation into the shallow bay, thus resulting in almost one hour longer travel time and a much better fit to the observed travel time.

Finally, Figure 11c displays the travel-time grids near the Japanese station Dannoura (circle). Again, the coarser grid is unable to represent the narrow Kanmon Strait connecting the Japan Sea to the Seto Inland Sea, and when the nearest node in the ocean is selected it falls on the western rather than eastern side of the artificial barrier. Hence, as the waves must propagate around Kyushu to reach the station, we find a delay of almost 2 hours relative to the 2×2-minute grid prediction. Interestingly, the reported travel time to Dannoura is 29.5 hours, which is about 4 hours longer than the 2×2-minute prediction. Based on Figure 2 it would appear that the reported arrival time corresponds to a later arrival; the bathymetry near the station is not as complicated as in the case of Punta Arenas, and hence the 4-hour difference is unlikely to reflect a prediction error.

By resampling the 5×5 minute travel time prediction grid onto a 2-minute grid we may compute the predicted differences for the entire Pacific (Fig. 12). It is noteworthy that the two grids differ by less than 5 minutes at $\sim$97% of the grid nodes. The only significant deviations visible at this scale are differences in the 20–60 minute range for shallow areas between Australia and Papua New Guinea and in the Yellow Sea. The extreme cases in Figure 10 (white stars in Fig. 12) are not typical nodes in this regard, yet

many tide stations are obviously located in shallow water near land and hence are affected locally by the grid resolution effect. We can also see a subtle delay effect due to the denser seamount populations in the Western Pacific. While the 5×5 minute predictions in general are slightly slower than the 2×2 minute predictions, a few areas show the opposite effect (e.g., off Alaska), again reflecting the difference in pathways when narrow waterways are not adequately represented in one of the grids.

4. Discussion

This investigation has found several characteristics of observed and predicted travel times and their statistical distribution and depth-dependency that may be of interest to both warning centers and tsunami researchers. However, given the simple approach used to predict travel times, the observations made in this study are more germane to the near-real-time response to a tsunami in progress when quick and accurate estimates of travel times are required. It is reassuring that the simple predictions based on Eq. (1) and the standard 2×2 minute bathymetric grid are quite consistent with reported travel times for the 127 tsunamis studied here (e.g., Fig. 6). However, there are clear departures from the expected 1:1 correlation and these have been examined in some detail. I have demonstrated that predictions in some cases have considerable delays and determined three main causes for these delays: (1) The inability of the epicenter point source to adequately represent the actual water impact that generated the tsunami, (2) occasional large changes in propagation geometry due to the finite spatial resolution of the global grids, and (3) uncertainties in depth for shallow water regions. Given Eq. (1), all significant bathymetric bias will occur in shallow waters. For any event, these areas are most likely to include the immediate regions surrounding both epicenter and observation points (or warning points). Warning agencies and tsunami researchers should therefore strive to acquire the best available local bathymetric data in all regions that fall in this category.

To exemplify the bias that may result from using a point source (i.e., the epicenter) for tsunami travel-time evaluation I contrast the predictions from the 1960 Chile tsunami using two different sources: (1) The reference calculation uses the reported epicenter (Fig. 4) which is what warning centers must use in a real-time warning situation, and (2) the rupture zone identified by PLAFKER and SAVAGE (1970). The latter source region extends over 1000 km southward from the epicenter and hence prediction of travel times south of the epicenter can be expected to differ. Figure 13 shows the difference in predicted travel time (in minutes) between the point- and line-source calculations. As anticipated the largest discrepancies are found to the south of a line from the epicenter to Japan, i.e., the shaded region. In particular, at stations in New Zealand and Australia the difference in predicted travel time is almost 1 hour. Stations that reported an observed travel time shorter than the reference prediction are shown with a crossed circle; the majority of such stations fall in the affected region. Of course, slow propagation in

shallow waters near some stations and failure to detect first arrivals may have obscured the predicted trend to some extent.

In a warning situation the emphasis lies on preparing as accurate estimated times of arrival as possible. It is therefore of great concern that certain combinations of epicenter locations and station placements, when used with Eq. (1) and standard global bathymetric grids, yield travel times that are unacceptably delayed. Should such delayed predictions be presented as accurate they may cause considerable damage directly (by giving wrong information) and indirectly (by reducing the confidence the community has in warning centers). However, large tsunamigenic earthquakes do not occur daily, hence there is ample time between events to lay the groundwork required to avoid such overestimates. Given the rapidity with which travel-time estimates can be obtained, warning centers may explore the effects that epicenter and station location and bathymetry grid quality have on the predicted values. For instance, the finite number of tide stations and warning points could be explored in detail (such as was done in Fig. 11) to determine if the coordinates of the station should be adjusted to avoid particularly shallow areas and if important, but narrow water ways are well represented in the grid. Special processing of the bathymetry may be required to reduce delays and optimize travel-time predictions. Similarly, precalculations of tsunamis from anywhere along the ring of fire could be examined and used to identify regions where point source solutions may be particularly susceptible to error (such as along wide continental margins, e.g., Fig. 7). Since such numerical experiments are not subject to the time-constraints of an emergency response, higher resolution grids (requiring longer calculation times) may be employed in order to map the sensitivity of the predictions to the grid spacing used during emergency operations. Finally, assessment of travel times from model-based forecast systems may be used to address the uncertainties of point-source based solutions (e.g., GREENSLADE and TITOV, 2008). The goal of such efforts would be to enable warning centers to calculate and report reasonable error bounds on any estimated time of arrival released to the public.

5. *Conclusions*

1. Simple long-wave predictions of tsunami travel times calculated from a global grid of bathymetry yields approximate results that correlate highly with ~ 1500 reported travel times from 127 separate events.
2. Large outliers exist on both sides of the expected trend. Observation times that greatly exceed the simple predictions are most likely later arrivals. In cases when predictions greatly exceed observation times we find that either the reports had clerical errors or there were peculiar circumstances with respect to the geometry of the pathways and their depths near a particular station. Because most stations are located next to land, these conditions do occur in enough places to warrant concern.

3. The largest significant causes of uncertainty for predicted travel-times are the inadequate approximation of the tsunami source by the epicenter point source and the poor characterization of shallow bathymetry near stations and some epicenters. Depending on circumstances, the travel-time delays from these errors sources can be significant (i.e., hours).
4. Numerical simulations of hypothetical tsunamis from any point along subduction zones can be performed and used to delineate areas from which the simple travel-time solutions may be inadequate. Likewise, the examination of the variability of travel times near all stations of points of interest can be used to map which regions need special consideration in a warning situation and to guide special processing of bathymetry to ensure the proper representation of key waterways near stations.

Acknowledgments

Diana Greenslade, Gerard Fryer, editor Kenji Satake and an anonymous reviewer made numerous suggestions that lead to improvements in the text. This is SOEST contribution no. 7606.

References

Abe, K. (1979), *Size of great earthquakes of 1837–1974 inferred from tsunami data*, J. Geophys. Res. *84*, 1561–1568.

Christensen, D. H. and Beck, S. L. (1994), *The rupture process and tectonic implications of the great 1964 Prince William Sound earthquake*, Pure Appl. Geophys. *142*, 29–53.

Dudley, W., T*sunami*!, 2nd ed., 380 pp. (Univ. Hawaii Press, Honolulu, 1998).

Fryer, G. J. *et al*. (2004), *Source of the great tsunami of 1 April 1946: A landslide in the upper Aleutian forearc*, Marine Geology *203*(3–4), 201–218.

Geoware (2007), *TTT - A tsunami travel-time calculator*, http://www.geoware-online.com

Greenslade, D. J. M. and Titov, V. V. (2008), *A comparison study of two numerical tsunami forecasting systems*, Pure Appl. Geophys. *165*, 1991–2001.

Hatori, T. (1981) *Tsunami magnitude and source area of the Aleutian-Alaska tsunamis*, Bull. Earthquake. Res. Inst., Univ. Tokyo *56*, 97–110.

Johnson, J.M. *et al*. (1996) *The 1964 Prince William Sound earthquake: Joint inversion of tsunami and geodetic data*, J. Geophys. Res. *101*(B1):523–532.

Johnson, J. M. and Satake, K. (1997), *Estimation of seismic moment and slip distribution of the April 1, 1946, Aleutian tsunami earthquake*, J. Geophys. Res. *102*(B6), 11, 765–711,774.

Kowalik, Z. *et al*. (2005), *Numerical modeling of the global tsunami: Indonesian tsunami of 26 December 2004*, Science of Tsunami Hazards *23*(1), 40–56.

Lopez, A. M. and Okal, E. A. (2006), *A seismological reassessment of the source of the 1946 Aleutian 'tsunami' earthquake*, Geophys. J. Internat. *165*(3), 835–849.

Mader, C.L. (2004), *Numerical Modeling of Water Waves*, 2nd ed., 274 pp. CRC Press, Baton Rouge.

Mei, C. C. (1989), *The Applied Dynamics of Ocean Surface Waves*. (World Scientific, Singapore).

National Geophysical Data Center (2006), *2-minute gridded global relief data (ETOPO2v2)*, U.S. Department of Commerce, National Oceanic and Atmospheric Administration.

National Geophysical Data Center (2007) *NOAA/WDC historical tsunami database at NGDC*, edited, http://www.ngdc.noaa.gov/seg/hazard/tsu_db.shtml.

Okal, E. A. *et al*. (2003), *Near-field survey of the 1946 Aleutian tsunami on Unimak and Sanak Islands*, Bull. Seismol. Soc. Am. *93*(3), 1226–1234.

Pacheco, J. F. and Sykes, L. R. (1992), *Seismic moment catalog of large, shallow earthquakes, 1900–1989*, Bull. Seismol. Soc. Am. *82*, 1306–1349.

Pararas-Carayanis, G. (1967), *A study of the source mechanism of the Alaska earthquake and tsunami of March 27, 1964, I. Water waves*, Pac. Sci. *21*, 301–310.

Plafker, G. and Savage, J. C. (1970), *Mechanism of the Chilean Earthquake of May 21 and 22, 1960*, Geol. Soc. Am. Bull. *81*, 1001–1030.

Ruff, L. and Kanamori, H. (1983), *The rupture process and asperity distribution of three great earthquakes from long-period diffracted P-waves*, Phys. the Earth and Planet. Inter. *31*, 202–230.

Shepard, F. P. *et al*. (1950), *The tsunami of April 1, 946*, Bull. Scripps Inst. Oceanogr. Univ. Calif. *5*, 391–528.

Sherburne, R. W. *et al*. *The hypocenter, origin time, and magnitude of the Prince William Sound earthquake of March 28, 1964*. In *The Prince William Sound, Alaska Earthquake of 1964 and Aftershocks* (ed. L. E. Leipold), pp. 49–69 (US Dep. of Comm., Environ. Sci. Serv. Admin., Washington, D.C. 1969).

Smith, W. H. F. and Sandwell, D. T. (1994), *Bathymetric prediction from dense satellite altimetry and sparse shipboard bathymetry*, J. Geophys. Res. *99*(B11), 21,803–821,824.

Smith, W. H. F. and Sandwell, D. T. (1997), *Global seafloor topography from satellite altimetry and ship depth soundings*, Science *277*(5334), 1956–1962.

Wessel, P. and Smith, W. H. F. (1998), *New, improved version of Generic Mapping Tools released*, EOS Trans., AGU, *79* (47), 579.

(Received January 27, 2008, accepted May 10, 2008)
Published Online First: February 6, 2009